



THESIS / THÈSE

DOCTOR OF SCIENCES

Fundamental study of the adhesion phenomena in polymer-metal hybrid materials obtained by laser welding

Hirchenhahn, Pierre

Award date:
2021

Awarding institution:
University of Namur

[Link to publication](#)

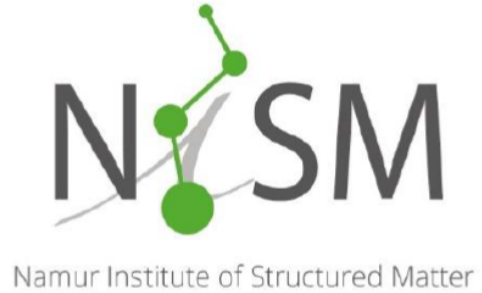
General rights

Copyright and moral rights for the publications made accessible in the public portal are retained by the authors and/or other copyright owners and it is a condition of accessing publications that users recognise and abide by the legal requirements associated with these rights.

- Users may download and print one copy of any publication from the public portal for the purpose of private study or research.
- You may not further distribute the material or use it for any profit-making activity or commercial gain
- You may freely distribute the URL identifying the publication in the public portal ?

Take down policy

If you believe that this document breaches copyright please contact us providing details, and we will remove access to the work immediately and investigate your claim.



FACULTÉ DES SCIENCES
Département de physique
Laboratoire Interdisciplinaire de Spectroscopies Électronique

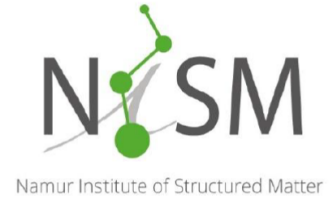
Fundamental study of the adhesion phenomena in polymer-metal hybrid materials obtained by laser welding

Janvier 2021

Dissertation en vue de l'obtention du grade de Docteur en Sciences présentée par
Pierre HIRCHENHAHN

Membres du jury:

- Prof. Robert SPORKEN (Université de Namur, président du jury)
- Prof. Peter PLAPPER (Université du Luxembourg)
- Prof. Herman TERRYN (Vrije Universiteit Brussel)
- Prof. Didier LEONARD (Université de Lyon - CNRS)
- Dr. Céline NOËL (IMEC)
- Prof. Laurent HOUSSIAU (Université de Namur, promoteur)

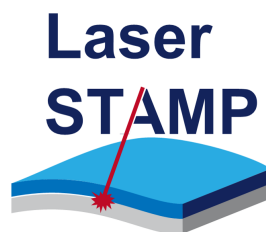


FACULTÉ DES SCIENCES
Département de physique
Laboratoire Interdisciplinaire de Spectroscopies Électroniques

Fundamental study of the adhesion phenomena in polymer-metal hybrid materials obtained by laser welding

Janvier 2021

Dissertation en vue de l'obtention du grade de Docteur en Sciences présentée par
Pierre HIRCHENHAHN



Membres du jury:

- Prof. Robert SPORKEN (Université de Namur, président du jury)
- Prof. Peter PLAPPER (Université du Luxembourg)
- Prof. Herman TERRYN (Vrije Universiteit Brussel)
- Prof. Didier LEONARD (Université de Lyon - CNRS)
- Dr. Céline NOËL (IMEC)
- Prof. Laurent HOUSSIAU (Université de Namur, promoteur)

«Le progrès est une idée saugrenue.»

René Magritte

Contents

Foreword	ix
1 Introduction	1
2 Assemblies	5
2.1 Mechanical fastening methods	5
2.2 Adhesive methods	5
2.3 Welding or fusion bonding methods	6
2.3.1 Spin-welding or rotary friction welding	7
2.3.2 Vibration welding	7
2.3.3 Ultrasonic welding	8
2.3.4 Friction stir welding	8
2.3.5 Induction welding	9
2.3.6 Microwave welding	9
2.3.7 Dielectric or radio frequency welding	10
2.3.8 Resistive implant or resistance welding	10
2.3.9 Hot tool welding	11
2.3.10 Hot gas welding	11
2.3.11 Extrusion welding	12
2.3.12 Infrared welding	12
2.4 State of the art in laser welding	12
2.4.1 Bibliometry	12
2.4.2 General principle and applications	13
2.4.3 Advantages and drawbacks	13
2.4.4 Advancement in laser welded polymer-metal assemblies	16
3 Adhesion theory	19
3.1 Introduction	19
3.2 Mechanical interlocking	19
3.2.1 General description	19
3.2.2 State of the art	21
3.3 Bonding	22
3.3.1 Different bonding type	23
3.3.2 Chemical bonding in adhesion: state of the art	26
3.4 Diffusion	29
3.4.1 General description	29
3.4.2 State of the art	31
3.5 Electrostatic interaction	32
3.5.1 General description	32

3.5.2	State of the art	34
3.6	About failure modes	34
4	Materials and Methods	37
4.1	Strategy	37
4.1.1	Pre-welding surface modification	37
4.1.2	Chemical bonding	37
4.1.3	Strategy of interpretation of the data collected in XPS and ToF-SIMS	40
4.1.4	Diffusion	40
4.2	Materials	41
4.2.1	Metals	41
4.2.2	Organic materials	42
4.3	Sample preparation	43
4.3.1	Laser ablation (done at the University of Luxembourg)	43
4.3.2	Mirror polishing	43
4.3.3	Spin-coating	44
4.3.4	Dip-coating	44
4.3.5	Laser welding (done at the University of Luxembourg)	44
4.3.6	Accessing the interface	44
4.4	Sample analysis	45
4.4.1	Roughness (done at LIST)	45
4.4.2	Profilometry - Spin-coating thickness (done at LIST)	45
4.4.3	Scanning electron microscopy – SEM (done at LIST)	45
4.4.4	Joint area assessment (done at the University of Luxembourg)	45
4.4.5	Laser flash analysis – LFA (done at the University of Luxembourg)	46
4.4.6	Shear load tests (done at the University of Luxembourg)	47
4.4.7	X-ray Photoelectron Spectroscopy - XPS	47
4.4.8	Time of Flight Secondary Ion Mass Spectrometry - ToF-SIMS	52
4.4.9	Principal Component Analysis - PCA	55
5	Surface pretreatments	59
5.1	Laser ablation on aluminum	59
5.1.1	Sum up of the results from the article “Influence of aluminum laser ablation on interfacial thermal transfer and joint quality of laser welded aluminum-polyamide assemblies” published in <i>Coatings</i> in 2019	59
5.1.2	XPS results on the laser ablated aluminum	62
5.1.3	Conclusions on the laser ablated aluminum	67
5.2	Laser ablation on titanium	68
5.2.1	Sum up of the article “Influence of titanium alloy (Ti64) laser ablation on joint quality and interfacial thermal transfer between laser welded titanium – polyamide joints” still in preparation for publication	68
5.2.2	XPS results on the laser ablated titanium	70
5.2.3	Conclusions on the titanium laser ablation	75
5.3	Conclusions	76
6	Aluminum-polyamide bonding?	77
6.1	Welded samples	77
6.1.1	Adhering polymer on the aluminum surface in the weld	78
6.1.2	Identification of the bond’s nature	82
6.1.3	Discussion about PCA	86

6.1.4	Conclusions on the welded samples	91
6.2	Ablated welded samples	93
6.2.1	XPS results	93
6.2.2	ToF-SIMS results	95
6.2.3	Conclusions on the ablated welded samples	99
6.3	Spin-coated samples	99
6.3.1	Polyamide adsorption/adhering on the aluminum surface	99
6.3.2	Chemical reactivity	101
6.3.3	Discussion about PCA	106
6.3.4	Conclusions on the spin-coated samples	112
6.4	Model samples	112
6.4.1	Deposition of the molecule on the aluminum surface	112
6.4.2	Chemical reactivity	114
6.4.3	Discussion about PCA	118
6.4.4	Conclusions on the model samples	122
6.5	Conclusions	123
7	Titanium-polyamide bonding?	127
7.1	Welded samples	127
7.1.1	Traces of polyamide-6.6 in the adhesive failure mode zone in the weld	128
7.1.2	Nature of the chemical bond	131
7.1.3	Discussion about PCA	138
7.1.4	Conclusions on the welded samples	139
7.2	Spin-coated samples	143
7.2.1	XPS results	143
7.2.2	Principal component analysis on the ToF-SIMS data	144
7.2.3	Conclusions on the spin-coated samples	157
7.3	Model samples	159
7.3.1	Deposition of the molecule	160
7.3.2	Chemical reactivity	163
7.3.3	Discussion about PCA	169
7.3.4	Conclusions on the model samples	171
7.4	Conclusions	171
8	Diffusion	175
8.1	Results and discussion	175
8.2	Conclusion	178
9	Conclusions	181
	Appendix to surface pretreatments	185
	Appendix to aluminum and polyamide bonding?	203
	Appendix to titanium and polyamide bonding?	225
	Appendix to diffusion	235
	Bibliography	237

Foreword

The whole thesis is written in English, but I took the liberty to change language for the acknowledgements. As a French living in another French speaking country, it is just but normal to write this part in his mother language, French and even a part in Alsatian dialect. It is also more natural, as this part is generally the most read by the family and friends, that not necessarily do understand English. With that written, I will now switch to French.

Faire une thèse est une aventure tant scientifique qu'humaine. Les remerciements sont la seule partie d'un manuscrit de thèse où cette composante humaine peut s'exprimer librement. De ce fait, et aussi parce que la majorité des personnes à lire cette partie ne sont pas anglophones, notamment les membres de la famille, j'ai fait le choix de la rédiger en français, et aussi une partie en alsacien.

Je commence par remercier les membres du jury, qui se sont pris le temps pour lire et évaluer ce travail, afin d'y apporter des améliorations par leurs remarques constructives et les discussions de fond sur différents aspects de ce travail.

Je vais continuer en adressant des remerciements au promoteur de cette thèse, le professeur Laurent Houssiau. Au début cela me paraissait un peu exotique de parler de « promoteur » plutôt que de « directeur de thèse », mais les années passant je trouve que ce terme est sans doute plus approprié. En France, souvent un directeur de thèse « dirige » le travail de thèse du doctorant, avec tout ce que ça implique d'autorité et de frustration créée chez le doctorant. J'ai été un peu décontenancé en comprenant que je vivais l'exact opposé. En effet, dès le départ j'ai joui d'une grande liberté dans mon travail avec de temps en temps une indication toujours formulée avec la plus grande diplomatie. Cela ne convient pas à tout le monde une telle liberté, mais personnellement elle m'a permis de mieux m'approprier le sujet de thèse et sans doute de creuser plus loin. Cette liberté était accompagnée d'une bonne dose d'humour (plus ou moins fin en fonction du jour de la semaine). En définitive, je sors de ma thèse en ayant appris énormément tant scientifiquement qu'humainement, et cela n'aurait pas été possible sans ton aide précieuse. En fait, plutôt que promoteur je pense qu'on devrait dire « sensei ». D'une part à cause de ton intérêt pour la culture nippone. D'autre part, parce que tu nous fais apprendre des choses en nous faisant observer et écouter, c'est comme ça que certains instruments de musique traditionnels sont enseignés où les premières années de pratique, l'enseignant ne dit rien, mais demande à son élève d'observer et d'écouter pour ensuite essayer de refaire par lui-même.

Un travail de recherche, et en particulier celui-ci qui s'est fait dans le cadre d'un projet européen, ne peut pas se faire sans collaboration. Ainsi je souhaite remercier chaleureusement Julien Bardon et Adham Al Sayyad pour l'entraide et le soutien mutuel, notamment dans la réalisation pratique des expériences, pour arriver au bout de ce travail. Je souhaiterais joindre aux remerciements le prof. Peter Plapper de l'Université du Luxembourg et Alain Biernaux d'Optec pour les échanges, les questions et remarques qui ont permis d'approfondir ces recherches. Cela m'a aussi permis d'améliorer mes compétences en communication, que ce soit pour la langue (tout se faisant en anglais), mais surtout pour présenter des résultats de physico-chimie à des personnes plus spécialisées en ingénierie.

De même, mon travail n'aurait pu bien se dérouler sans une bonne entente avec les collègues du LISE. Je voudrais remercier Céline et Alexandre pour m'avoir beaucoup aidé pour les mesures en ToF-SIMS, pour mieux comprendre la technique, qui au début de ma thèse était complètement nouvelle pour moi. Pour l'XPS, je souhaiterais de nouveau remercier Alexandre, mais surtout Pierre, pour la patience et l'humour dont il fait preuve suite à un petit incident sur le K-alpha. Je voudrais aussi remercier Mathieu, avec qui j'ai pu avoir des discussions intéressantes sur l'XPS, sur le Japon, et bien d'autres sujets. Enfin, je ne peux pas ne pas remercier le pilier du LISE, celui qui fait tout le charme et le caractère de l'équipe, j'ai nommé Fred, LE technicien du LISE. En effet, on ne saurait vivre au LISE pendant 4 ans, sans « subir » le potentiel de médisance, l'humour parfois très pointu ou bien les petites farces, mais ce ne serait pas lui faire justice, si on ne parlait pas de sa disponibilité et de son engagement pour le laboratoire. Je voudrais aussi le remercier pour la patience et l'écoute dont il a fait preuve pour me soutenir dans certaines périodes plus difficile à vivre, mais qui sont inhérentes à une vie de thésard.

Il n'y a pas eu que les relations avec l'équipe du LISE, mais aussi avec les autres membres du département de physique. La proximité géographique entre les différentes équipes permet beaucoup d'échanges sur le plan scientifique, mais pas que. Que ce soit en ce croisant dans le couloir ou en partageant un moment à la salle de pause (repas ou pause café). C'est ce qui fait la richesse du quotidien. Certains en plus d'être des collègues sont devenus de vrais amis. Je pense notamment à Pauline, Sylvain, Julie, les deux Nicolas (Roy et Reckinger), Bruno, Mathilde, Sébastien, Xavier, Céline (Molinaro), Lorena, . . . Amis avec lesquels on a partagé repas, pause café (parfois exagérément longue), glace, bière et j'en passe, mais qui ont rendu la recherche scientifique beaucoup plus agréable et qui m'ont un peu manqué ces derniers mois crise sanitaire oblige.

Il n'y a pas eu que les amis et les relations avec les collègues et amis du département de physique, mais aussi en-dehors du département. On peut citer les rencontres faites lors du certificat U2ES, qui a occupé un certains nombres de soirée et de samedis matins pour arriver à la fin et finalement le valider. Mais sans ce certificat, qui outre nous apprendre un nombre certain de choses sur nos compétences transversales, nous a permis de rencontrer des gens d'autres départements. Je n'en citerais que quelques-uns, mais ce n'est pas par volonté d'oublier les autres. Je pense notamment à Joanna et à Delphine de la faculté de médecine, avec qui on a partagé quelques bons moments de partage, autant de rire que de discussions scientifiques ou artistiques. La dernière que je voudrais citer c'est Sophie, du département de biologie. Je ne compte plus les soirées, les petites bières, même des voyages, que nous avons partagé avec d'autres (Géraldine, Salomé, Damien, . . .) et puis c'est grâce à Sophie que je pouvais aller partager une bière le vendredi soir après le travail, à la fameuse « beer hour » de l'URBC. Je voudrais aussi la remercier pour l'idée de faire du coworking durant le confinement, dès que les règles sanitaires l'ont permis, pour se motiver mutuellement, et se donner du courage dans la rédaction.

Durant ma thèse je n'ai pas fait que des rencontres au sein de l'Université, mais aussi en-dehors. Je vais commencer par mentionner les personnes que j'ai eu la chance de rencontrer durant mes aventures musicales accompagné de mon violoncelle. D'abord, je voudrais remercier Matthieu Widart, mon professeur de violoncelle, tant pour son humour et sa pédagogie que pour sa patience. Plus qu'un professeur, j'ai rencontré un ami avec qui partager une passion pour le violoncelle. Il me faut aussi remercier son comparse au piano, Etienne Rappe, qui en plus de m'accompagner de temps en temps au piano, m'a convaincu (à grand renfort de bière) de rejoindre l'Orchestre Terra Nova. Pour me « convaincre » il n'a pas été seul, mais accompagné de Laurence, Sarah, Isabelle, et Quentin. Avec du recul, je ne regrette absolument pas d'avoir rejoint cette aventure, dans ces différents projets, avec ces rires, ces moments de grande concentration, mais tout ça pour la musique. Parmi ces projets de l'orchestre, un en particulier a retenu

grandement mon attention. A l'aide de Matthieu et d'Etienne, nous avons préparé et monté tout un concerto, celui en mi mineur pour violoncelle d'Edward Elgar. Quasiment trois ans de travail pour arriver à finalement le jouer accompagné par un orchestre. J'ai déjà eu la chance de remercier tous les acteurs de ce projet (un peu fou) par ailleurs, Matthieu et Etienne, le président de l'Orchestre, tous les musiciens et toutes les personnes qui aide à la réalisation et au succès de ces concerts, mais je souhaiterais le refaire ici, parce que en temps qu'amateur (et surtout en étant amateur) il n'est pas courant de pouvoir jouer un concerto en entier accompagné par un pianiste, mais d'autant moins avec un orchestre.

Après la musique, la danse. C'est durant les cours de Lindy Hop que j'ai fait la rencontre de ce qui allait devenir une sacré clique : Laura, Zaïna, Florence, Fiona, Kathi, Andrea, François, Guillaume, Fabrice, et tous les autres. Je voudrais les remercier pour tous ces moments de partage, de danse, d'amusement, de rire. Une bande de joyeux lurons toujours prêt pour s'amuser et faire les quatre cent coups. J'en profite aussi pour remercier nos joyeux professeurs, Elise et Didier, mais aussi Briec et Ayumi. Ils nous ont et nous transmettent non seulement une danse mais de la joie de vivre, et le fait de savoir qu'il y avait cours de Lindy Hop le jeudi soir, m'a toujours redonner le sourire et du courage pour avancer dans le travail de thèse qui n'est pas simple au quotidien. Le Lindy Hop ça a aussi été l'occasion de faire des voyages pour des stages de quelques heures, d'un week-end ou plus long. Que ce soit les petits « workshop » en Belgique, les Crazy Swing Camp, ou bien cette semaine de folie à Herräng en Suède, ça a toujours été un plaisir de rencontrer des gens qui partage à la fois cette joie de vivre et la passion de la danse, et ce toujours dans le respect et la bienveillance.

Pour finir ce chapitre, je souhaiterais adresser des remerciements à ma famille, et pour ce faire je vais me permettre de changer de langue encore une fois, et passer en Alsacien. C'est un peu ma « seconde langue maternelle » ; langue que j'utilise principalement, et depuis mon installation en Belgique quasiment exclusivement, dans le cercle familial. Je pourrais tout à fait les rédiger en Français, mais ce serait se priver de la richesse linguistique et sonore de ce dialecte, qui pourrait disparaître dans les prochaines décennies. Je me rappelle de ce qu'un jour mon professeur de littérature allemande du lycée nous avait proposé. Une langue ou un dialecte n'est qu'un vecteur pour transmettre une idée, mais d'une langue à l'autre, les mêmes mots pour exprimer la même idée, ne peuvent jamais la transmettre totalement de manière identique. En conséquence de quoi, maîtriser le plus de langue possible et en préserver le maximum est un des meilleurs moyens de garantir la richesse et le foisonnement d'idée. Ce n'est donc pas par régionalisme égocentrique que je fais ce choix, mais bien parce que je pense que la langue choisie a une importance dans le message transmis et pour soutenir la diversité –la richesse– linguistique.

All de Johre lang, han ihr mi unterstétzt, obwohl es net unbedingt einfach isch gseh. Von Strossburi bis jetzt i Namur, sen ihr immer fer mi do gseh, defer wod ich eich Merci sawe. Alles han ihr worschlich net mitbekome, von was ich shaff, oder wie d'Forschung funktionert, awer ihr sen immer do gewann un am mich ofgemontert dass ich wiedersch komm un des bis ans And. Ich hab auch a Danke fer d'Mamie un de Babeba wie nimm do sen, ver des alles zu san un mitzuerlawe un wie worschlich auch eins met uns gedronke hatte.

Chapter 1

Introduction

Combining dissimilar materials to create hybrid assemblies is often achieved to gain new properties, but it still remains a challenge nowadays. The idea of combining two or more materials presenting different properties to get new and improved materials is not new. Indeed, the first men already did it by fixing a stone spear head, later on in metal, on a wooden spear hand [1]. This combination allowed to ally the resistance of the stone or the metal, and the lightness and pliancy of the wood. Hybrid materials have evolved a lot since then, and are not focused on hunting materials, but rather on applications to address environmental, energetic or even biomedical questions. Hence, the development of such materials is of strategic importance for automobile, aerospace and biomedical industries.

Addressing different needs lead strangely to the same solution. Indeed, for the automotive and aerospace industries saving energy and consuming less fossil fuels is of the utmost importance. Therefore, the structures must be lighter. Traditionally the car structures were made out of steel, but to lighten up the structures nowadays, more and more parts are made of aluminum and polymers, explaining the need for hybrid polymer-metal structures. For the biomedical industry, the development of new generation implants increases the need for biocompatible hybrid structures also composed of polymer-metal assemblies, the metal being generally titanium. Polymer-metal assemblies present many advantages, such as the strength and the resistance of the metal and the lightness of the polymer. The polymer can also serve as an anticorrosion layer [2]. The work is done in the frame of the project Laser-STAMP (detailed below). In this frame an industrial advisory board (IAB) was assembled in order to advise on the materials, which would best fit for their industrial needs. From the IAB two metals were chosen: aluminum and titanium. They also advised on specific alloys: aluminum EN-AW1050A and Ti-6Al-4V. For the polymer, two choices came out: polyamide-6.6 (or Nylon66 ®) and polyetheretherketone (PEEK).

There is a wide variety of applications for hybrid assemblies, but assembling them is still an issue nowadays. Indeed, hybrid assemblies join dissimilar materials, which by essence will be difficult to assemble. Three different methods to assemble materials exist: mechanical fastening, adhesive bonding and welding. Mechanical fastening does not allow to reduce the weight as much as desired, while creating mechanical stresses on the assemblies and lowering the corrosion resistance. Adhesives are generally toxic, which is detrimental for the biocompatibility. In this case, welding appears as the best solution. Amongst the high variety of welding techniques that exist, laser welding is attracting more and more attention. It consists in heating the interface by means of a laser, which will melt the polymer. Hence the polymer and the metal will come into a more intimate contact, which will cause the seeked adhesion phenomenon between both materials. Laser welding presents many advantages, such as being a fast process, allowing a wide geometry freedom, and so on. The main drawback is its price for implementation in a production

line. Many improvements have been achieved in the last years in laser welding technologies [3–5]. Maybe the most important improvement is the impact of surface pretreatment on the mechanical resistance of the assemblies [6]. Nonetheless, at the moment, the root causes of this adhesion phenomenon are still unknown.

To put it clearly, there is an industrial interest in the development of laser welding technologies and at the same time a lack of fundamental knowledge of these technologies. Both ideas are the ground stone of the European project Laser-STAMP, which stands for “Laser and Surface Treatment Assisted Metal Polymer assembly”. This project is funded within the framework of the M-Era.Net program. It gathers three research institutions and a company. One of the research institutions is the University of Luxembourg, which has the know-how of laser welding. The second research institution is the LIST (Luxembourg Institute of Science and Technology) in charge of the surface treatments and some surface characterization. The last research institution is the University of Namur in charge of some of the surface characterization and the interface characterization. The Belgian company Optec is in charge of the development and the selling of a laser welding machine. It is in this frame that the work presented here is set and was carried out. The objectives of the Laser-STAMP project are to develop a laser welding station, as well as to get a deeper insight into the adhesion phenomenon and understanding the impact of surface pretreatment on the laser welded assemblies. In order to achieve these goals, the work is separated in seven work packages. The first one is the coordination of the whole project lead by the University of Luxembourg. The second consists in the definition of the industrial and research requirements lead by OPTEC. The third work package concerns the application of the selected surface treatment and the surface characterization lead by the LIST. The fourth one investigates the process parameters for the laser joining of the samples. The fifth work package concentrates on the interfacial analysis, more specifically the physicochemical bonding but also the mechanical testing of the joined partners, lead by the University of Namur. The sixth one is centered on the development of a demonstrative welding station, and the translation of the know how from laboratory scale to industrial application, lead by OPTEC. The seventh and last work package is the dissemination of the knowledge acquired in various forms, such as scientific articles, conferences, or fairs, lead by the University of Namur. Within this large project, the specific objectives of present PhD thesis focuses on the two latter goals: helping in understanding the surface pretreatment impact on the mechanical resistance and more importantly to broaden the knowledge on the adhesion phenomenon in the assemblies.

At first glance, the word “adhesion” does not seem peculiarly difficult to define, yet it is not trivial to describe. The Oxford dictionary [7] defines it as “the action or process of adhering to a surface or object”. A more scientific definition was proposed by Bischof et al. [8] in 1989: “adhesion describes the state of a boundary layer the two condensed phase have by being in contact. This state is characterized by the atomic or molecular interactions that are source of cohesion between both phases.”¹ In a more practical sense, four effects characterize the adhesion phenomenon, giving birth to the adhesion theory [9] mechanical interlocking [10], chemical and physical bonding [11], diffusion [12] and electrostatic attraction [13]. Studying all four effects represents a tremendous amount of work, that’s why this work will be restricted to physicochemical bonding, even if an exploratory work on diffusion was attempted. The mechanical interlocking has already been thoroughly studied in many different systems and does not require much more fundamental work [14]. The electrostatic effect is considered as a secondary effect, in terms of adhesion energy [9]. Nevertheless, it is maybe the hardest effect to study, because for

¹Originally in German in the article. Here is the original version: “Adhäsion bezeichnet den Zustand einer Grenzschicht, die zwischen zwei kondensierten Phasen entsteht. Dieser Zustand ist gekennzeichnet durch den von atomaren bzw. molekularen Wechselwirkungskräften in der Grenzschicht hervorgerufenen mechanischen Zusammenhalt der beteiligten Phasen.”

the moment measuring the electrical state of an insulating material is experimentally extremely difficult. In our case, the polymer chosen is an insulator. Different surface pretreatments are possible, but only two of them attracted specifically our attention: anodization [15] and laser ablation [16, 17].

To summarize, three different materials were chosen, giving two different materials combinations: aluminum/polyamide-6.6 and titanium/polyamide-6.6. Both material combinations will be submitted to laser welding, which will allow to investigate the physico-chemical bonding at the interface. The metals will be subjected to surface pretreatments and their surface chemistry will be assessed, which will allow to deepen the knowledge on the impact of these surface pretreatments on the mechanical resistance of the assemblies.

All the different questions will be addressed in seven chapters. Chapter 2 is focusing on the assembling methods. All the methods will be presented shortly and list their advantages and drawbacks, and at the end a review on laser welding is done. Chapter 3 is introducing the adhesion theory and detail all the four adhesion effects as well as a review on these effects and their characterization. Chapter 4 is summing up all the materials and methods used in the four following result chapters. Chapter 5 is centered on surface pretreatments, laser ablation, on both aluminum and titanium. Chapter 6 is gathering the results on chemical bonding for all the samples studied for the aluminum/polyamide-6.6 assembly. Chapter 7 is collecting the results on chemical bonding for all the samples studied for the titanium/polyamide-6.6 assembly. Chapter 8 is piling up the exploratory work on diffusion on the aluminum/polyamide-6.6 assemblies.

Chapter 2

Assemblies

There are many ways to assemble materials, depending on the materials joined, the usage of the assembly, economical factors, and so on. This high diversity can be classified into three categories: mechanical fastening methods, adhesive methods, and welding methods.

2.1 Mechanical fastening methods

Maybe the oldest way of assembling materials together, as it was already used by the first men to assemble their tools [1]. It is a way of fixing several materials together by mechanically blocking them together. Most known industrial applications are riveting, screwing, clinching, nailing, inserts, boss caps, press-on fasteners, and panel fasteners [18,19]. The idea of mechanical fastening can be extended to other technologies, as for example: sewing, stapling, knotting, . . . It can also lead to more complex structures for instance in carpentry where it is possible to assemble pieces by mechanical fastening without any nail or screw [20,21].

In general mechanical fastening present many advantages [18] as: ability of disassembling making the assemblies easily reparable, easy technology making it cost efficient, little surface preparation before assembling needed, possibility to join dissimilar materials, well-known prediction models and ease of joint inspection making it the easiest way to follow aging and wearing of the assemblies.

There are also some disadvantages [18]: increased weight due to fixation parts, loosening of fasteners due to stress relaxation, moisture and creep, low wear resistance because of high resistance stresses, increased residual stresses due to different thermal expansion coefficient in case of dissimilar material assemblies, and high number of processing steps to produce the assemblies.

2.2 Adhesive methods

At this day the oldest known use of adhesive bonding was dated from 200,000 years ago in Italy [22]. At the time the adhesives used originated from green plants and in this case from birch-bark-tar ¹ and was used on hunting material to increase its mechanical resistance. Nowadays adhesives can still be of natural origin, but it is more common that they are obtained by chemical synthesis. The applications of adhesives are extremely diverse, from pasting two papers together to automotive applications, for post-its, or biomedical needs.

The principle advantages of adhesives are [9, 18, 19, 23]: bonding of dissimilar materials, low stress concentration, improvement of fatigue resistance, sealing, weight reduction, good surface

¹In french : goudron d'écorce de bouleau. In german : Birkenrindenteer.

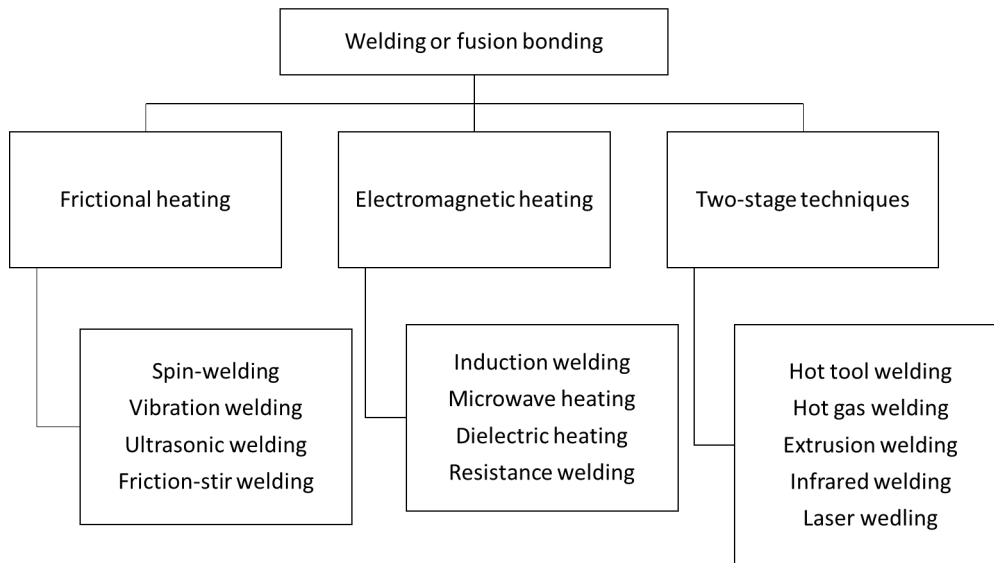


Figure 2.1: Classification of the different welding methods by heating source.

finishing, assembly of thin or flexible substrates, no holes required, and a good repair method.

The drawbacks of adhesives are [9, 18, 19, 23]: difficulty of disassembling making any reparation difficult, good surface preparation is required, engineering design confidence is lower compared to mechanical fasteners, resistant only to shear load, difficulty to predict bond failure, temperature sensitivity, high buying and disposal costs, assembly rate limitations, special handling because of toxic solvent and chemicals, adhesive may suffer thermal and environmental degradation.

2.3 Welding or fusion bonding methods

Dating the apparition of welding technologies is very difficult, but it must coincide with the apparition of metallurgy during the Bronze age from 3,300 BC to 1,000 BC. The principle is to heat the interface in order to melt the materials together, and by cooling they will stick together. There are a lot of different welding techniques. Therefore, Ageorges et al. [24] proposed a classification of the different welding techniques depending on the heating source as presented in Figure 2.1. The classification was modified, because Ageorges et al. [24] added as welding technologies a category they named “bulk heating”, which comprised: co-consolidation, hot-weld adhesive and dual resin bonding. The principle of the three techniques is to add an interstitial material, that will generate the bonding (like an adhesive), but that needs an external activation, heating or light for instance. The choice we made is to consider them as adhesive methods. The hereafter presented techniques is not an exhaustive list of all existing welding techniques, but aims at presenting the most used techniques for polymer-metal assemblies. Since the work is centered on laser welding, it will not be presented in this part, but presented in section 2.4 with much more details.

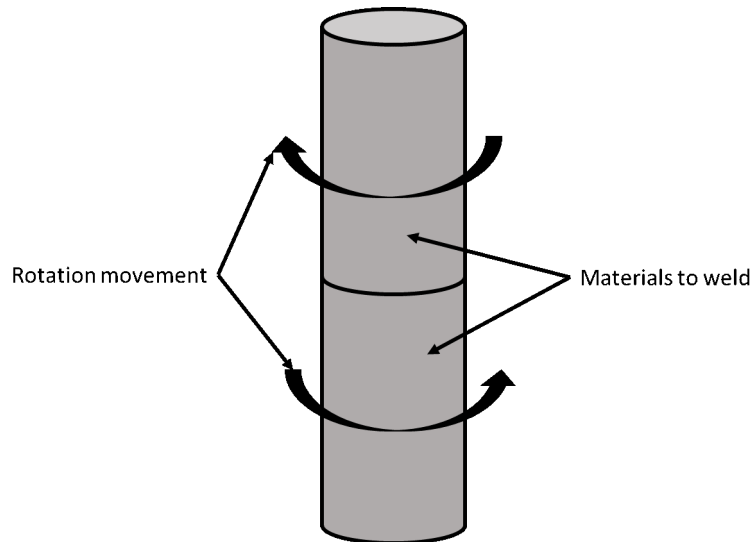


Figure 2.2: Scheme of spin-welding.

2.3.1 Spin-welding or rotary friction welding

The principle of this welding technique is very simple: the two pieces are put together and rotated in order to have heat generated by friction [25], as shown in Figure 2.2. The pieces must have symmetric contact surfaces. The process allows to rotate only one part or to rotate both parts. The quality of the weld is mostly influenced by the rotation speed, the friction pressure, the time and the burn-off or axial displacement of the moving joining partner². It is generally used for PVC-pipes and fittings, polypropylene ball floats for WC-cisterns, transmission shafts, aerosol bottles or car intake manifolds [25, 26].

The advantages presented by this technique are [18, 27] the ease of assembly, no additional filler material needed, the sealing is hermetic, a high energy efficiency, large parts can be welded, the equipment is cheap, and there is a low level of emission.

The disadvantages of the this welding technique are [18, 27]: the limitation to circular geometries and low level of geometric tolerance, and the limited production rate.

2.3.2 Vibration welding

Like in spin welding, the heat is generated by frictions between the two materials, but instead of having a rotational movement, the movements here can be linear, orbital or bidirectional [19, 28–31] as depicted in Figure 2.3. This technique is used in automotive, aeronautical and white goods industries. In automobile it is applied for car bumpers, air intake manifolds, or dashboards.

The advantages are [18]: a high controllability, a high process flexibility, a high production rate, welding large parts possibility, a certain design freedom, the possibility to perform internal joints with hermetic seals and entrapment of parts, the ease of assembly, the low level surface preparation needed, and no filler materials are required.

The disadvantages are [18]: only flat surface shapes can be welded, the vibration can cause damage to the welded pieces, a limited availability of joint geometries, expensive machinery and the process is noisy due to the vibration (90-95 dB).

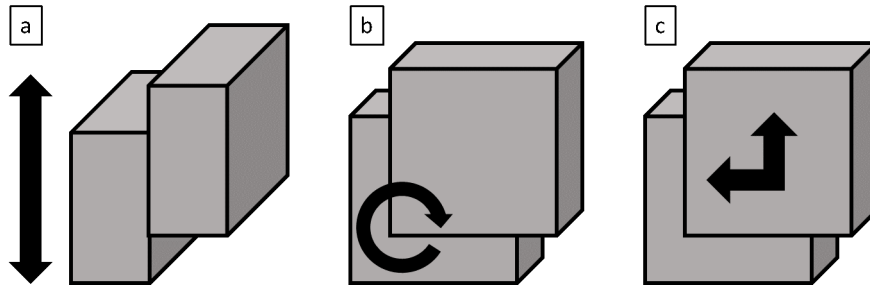


Figure 2.3: Scheme of the different configurations of vibration welding (a) linear configuration, (b) orbital configuration and (c) bidirectional configuration.

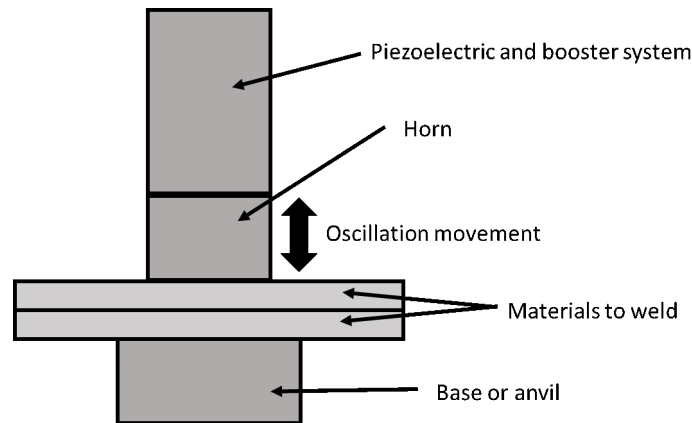


Figure 2.4: Scheme of ultrasonic welding.

2.3.3 Ultrasonic welding

In ultrasonic welding the heat is also produced by frictions, which are caused by applying ultrasonic waves on the materials to weld [32, 33] (see Figure 2.4). The important parameter to perform ultrasonic welding is the base material stiffness. In general, the higher the stiffness, the better the weldability. It is mostly used in white goods, medical industries, and in automotive industry.

The advantages are [18, 27]: high production rates, energy efficiency, design freedom, embedding of extra pieces, ease of assembly, and no filler materials required.

The drawbacks are [18, 27]: sample size limitations, usually only for compatible materials, noisy process, and expensive equipment.

2.3.4 Friction stir welding

Friction stir welding also creates heat through friction, but here the friction is coming from a welding head equipped with a pin that will rotate at high speed to melt the materials and weld them (see Figure 2.5 and/or <https://www.youtube.com/watch?v=y7rCTdxvGlg> consulted 04/01/21). This technique is generally used to weld metals together but development were made to use it also with plastics [34–39]. The applications are mainly in naval, railway, aircraft and automotive industry.

The advantages of this technique are [40]: no prior surface preparation needed, easily automated, low distortion and residual stresses, generally good weld appearance, and low environmental impact.

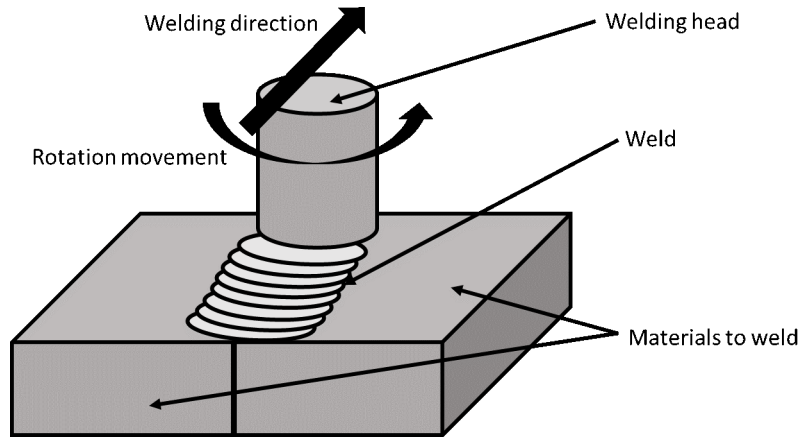


Figure 2.5: Scheme of friction stir welding.

The following disadvantages are [40]: a low design flexibility, the presence of an exit hole at the end of welding, relatively slow process.

2.3.5 Induction welding

The principle of induction welding is simply to induce heat at the interface by applying an alternative electromagnetic field (see Figure 2.6). The heat is produced by energy dissipation due to Joule effect and the magnetic hysteresis can be described by the following equation [41]:

$$Q = I^2 R t \quad (2.1)$$

where Q is the heating, I the induced electric current, R the ohmic resistance and t the time.

The technique is naturally used on conductive materials, metals or polymers, but can also be applied on insulating materials. To this purpose a conductive insert (a metal or carbon strip) will be placed at the interface of the materials [26,41–44]. Induction welding is used for sealing of plastic-coated metal foil tops, or for automotive parts, and domestic white goods. In the automotive industry, it is generally used for glass-fiber reinforced polypropylene seatbacks in estate car.

This method presents many advantages [18,19]: welding of large parts, the possibility to weld any kind of materials with a precisely controlled heating, generally high mechanical resistance, high production rates, the seals are hermetic, and the entrapment of parts.

The disadvantages are [18,19]: depending on the welded parts an insert is required, which can corrode and decrease the joint strength, the insert may also increase the stress concentration, the assembly operations are complicated, and the machinery is expensive.

2.3.6 Microwave welding

The principle is the same as the common microwave oven. Microwaves will heat up the materials and create the weld. The technique is used to weld plastics in general, but most of them are transparent to microwaves, so a metal part is inserted to heat up the materials to weld. Even if the technique is quite old (developed in the 1990's), to the best of our knowledge, the applications of this technique are quite rare in industry, and the use stays in the research area [45].

The advantages are [18,46]: high design freedom with three-dimensional weld or internal joints and low energy consumption, possibility to repair.

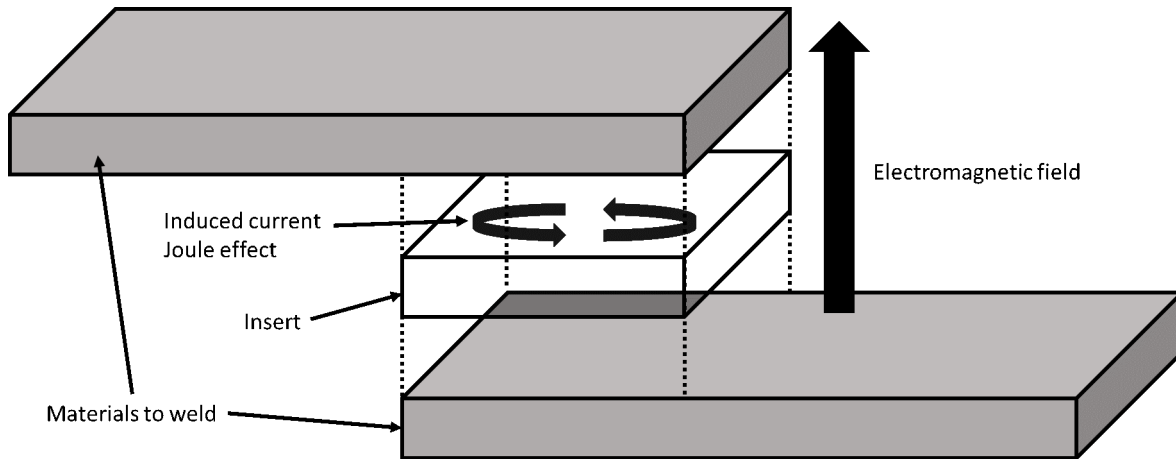


Figure 2.6: Scheme of induction welding.

The drawbacks are [18, 46, 47]: use of insert for most materials, inhomogeneous heating because of the microwaves.

2.3.7 Dielectric or radio frequency welding

This technique is a variation of the induction welding specific to weld polar thermoplastics. The heating is originating from the dielectric hysteresis losses of the polar materials. The polar polymers will see their dipole reoriented in a high frequency alternating electric field, which will cause the materials to heat. As the temperature is high enough to melt the faying materials they will be welded. Applications comprises medical blood and fluid bags, ring binders and stationary wallets² [18, 27, 48]. More generally it can be used for thin film or sheet applications.

The advantages are [18, 27, 48]: high production rate, short welding times, the joint interfaces are not exposed to ambient atmosphere so less oxidation degradation.

The disadvantages are [18, 27, 48]: the materials must be polar and have a low conductivity, thick materials cannot be welded, and in certain cases an insert is needed.

2.3.8 Resistive implant or resistance welding

The idea here is to insert a metallic wire in which current will be applied. The heating will be generated by Joule effect (see Figure 2.7). After welding the metallic wire stays entrapped [18, 24, 47]. It is mostly used to assemble plastic materials. It finds applications in automotive industry [24] for car bumpers and panels, as well as in aircraft industry [47], or for joints in plastic pipes [49, 50], containers and medical devices [51].

The advantages are [18, 27]: easy workability, reduced risk of air contamination of the molten phase, high joint design flexibility, cheap equipment (compared to other techniques), possibility to disassemble the parts by reheating the insert, adapted to large part, and theoretically all thermoplastics can be welded by resistive heating.

The disadvantages are [18, 27]: the mandatory use of an insert, long welding times, limited recycling of the welded component due to the insert, to perform the welding high operating skills are required, and it is inadequate for line production due to high welding times.

²In French: porte-document en plastique, portefeuilles. In German : plastik Dokumentenhalter, Brieftasche.

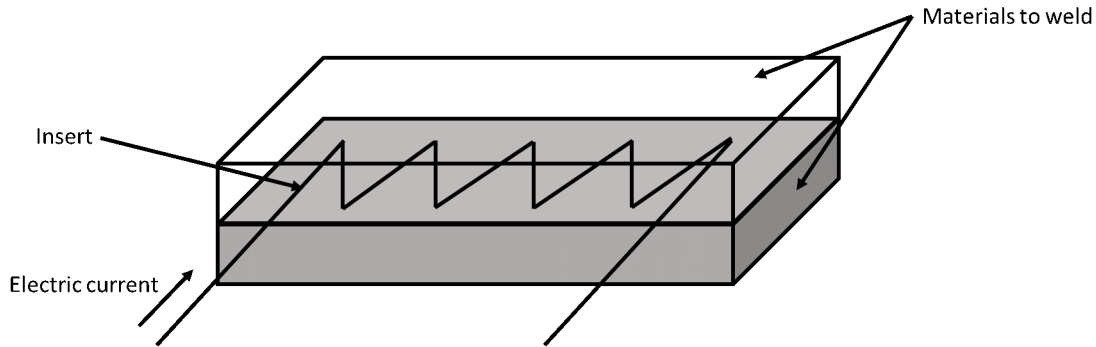


Figure 2.7: Scheme of resistance welding.

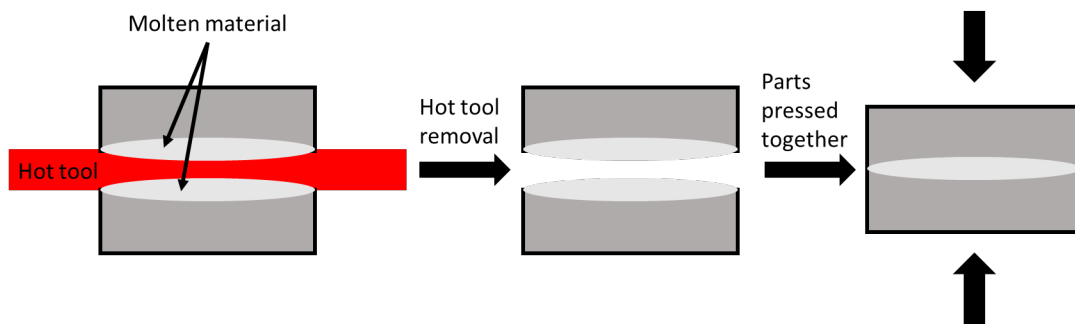


Figure 2.8: Scheme of hot tool welding.

2.3.9 Hot tool welding

The principle, depicted in Figure 2.8, is very simple. First the parts to weld are pressed on a hot tool, the materials will melt. At this point they will be removed from the hot tool and then pressed together and let to cool down to consolidate the joint. It is mostly used automotive, construction and pipeline industries for pieces like hydraulic reservoirs, fitting/filter pipes or battery cases. It can also be used for cooking, to make chocolate sculptures or assembling chocolate eggs for instance.

The advantages are [18, 19]: no filler materials required, ease of assembly, embedding of parts possible, large choice of weldable materials, shape freedom, hermetic seals possible, low emission levels, high productivity and welding of large parts possible.

The drawbacks are [18, 19]: high energy consumption, slow start until the hot tool is effectively hot, residual stress existence, need to clean the hot tool regularly to remove accumulated material on the hot tool's surface.

2.3.10 Hot gas welding

The principle is very simple. The parts to join are put together, a hot gas is blown on the joint and a filler materials is introduced to weld the parts [52]. The process might be difficult, because of the necessity to control the purity of the gas, because contaminants might oxidize the joined parts and decrease the resistance of the weld. This technique is generally used to weld plastic parts together and applied in the automotive industry for car bumpers or for chemical storage tanks.

The advantages are [18, 52]: cheap welding equipment, high shape freedom for the joined parts, possible portable equipment, great range of materials can be welded, low operating skill

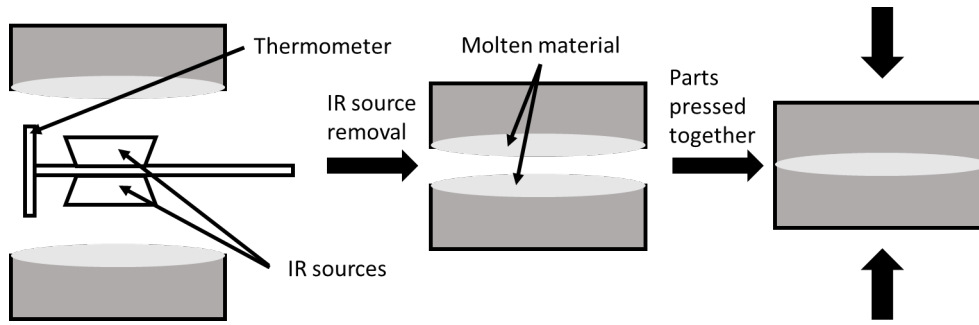


Figure 2.9: Scheme of infrared welding.

level required.

The disadvantages are [18, 52]: slow welding process, use of filler materials and manual operation and need to control the gas purity.

2.3.11 Extrusion welding

The principle here is very similar to hot gas welding and is actually a development of it made in the 1960s. The welding head is composed of a hot air nozzle and a filler extruder. The joining parts are put together, the hot air nozzle will heat them and then the extruder will introduce filler material to complete the welding. It can be automated or performed manually. The process is used to weld polymers for various applications as: storage tanks, containers, and pipelines [53, 54].

The advantages are : fast welding process, possibility to get very good quality joints, cheap equipment, and portable equipment if done manually.

The drawbacks are: use of filler material, and if performed manually the user must be skilled and well trained to perform a good weld.

2.3.12 Infrared welding

The principle of infrared weld looks like hot tool welding, but replacing the hot tool by an infrared source, as shown in Figure 2.9. Even if the technique exist since the 1960's, its development and usage began only in the 2000's [55, 56]. The technique is applied to weld pipes, window frames, biomedical products and fabrication laminates.

The advantages are [18, 27, 57]: higher welding speed and less contaminations than hot tool welding, joining of low modulus materials, and good joint quality.

The drawbacks are [18, 27, 57]: detrimental effect on the joint quality of colorants and pigments due to lower thermal transmission rate causing overheating leading to polymer degradation, and possibility of fumes generation which can be hazardous.

2.4 State of the art in laser welding

2.4.1 Bibliometry

In the 1950's the first masers-lasers were built, but a real laser or "light amplification by stimulated emission of radiation" was only built for the first time in 1960 by Theodore Maiman. Very quickly ideas for the usage of lasers were proposed, and of course laser welding in 1963 [58]. Since then laser welding has grown to a subject of interest, with more and more publications on the subject as shown in Figure 2.10a. More than 75 % of the publications are related to

engineering, materials science, and physics (see Figure 2.10b), but laser welding is also a subject of interest for other domains such as medical science, economics or even arts. The few economics article about laser welding are centered on the productivity and income gains the application of laser welding would have if used in the automobile industry [59, 60]. The arts articles found describe the possible use of laser welding for restoration purposes [61, 62]. The topic “laser welding” is attracting more and more attention, not only in the engineering domain, but also in the “welding field” in general. Indeed in 2019, Scopus gives a number of publication of 8 439 for the key word “welding”, and for “laser welding” there were 1 421 publications, which makes roughly 1/6th of the overall publications linked to “welding”.

2.4.2 General principle and applications

The principle is to heat the interface to create a weld by shining a laser beam on the materials. The laser might heat up the materials by being directly shining on the interface or indirectly, and in this case the heat is just conducted through one material to the interface. This will depend on the materials welded. Indeed, different material combinations can be assembled: metal-metal [63–65], metal-ceramic [63–65], ceramic-ceramic [63–65], ceramic-polymer [66], polymer-polymer [67–69], and metal-polymer [2, 4, 5, 70]. The weld configuration can be very diverse, depending on the use after welding; they are represented in Figure 2.11.

Even if there are several configuration possibilities, bringing the laser beam energy to the interface to weld polymers remains a challenge. Therefore several options exist, as depicted in Figure 2.12. To weld polymers to metals or ceramics, two options are possible: welding directly [5] (case (a)) or indirectly [70] (case (b)). In case (a) the laser beam is shone through the polymer to the interface and the metal (or ceramic) will absorb the heat, bringing the polymer to melt and so creating the weld. To achieve case (a), the polymer must be wisely chosen to be sufficiently transparent to the used laser beam. Therefore, the number of polymers that can be welded are limited. On the opposite, in case (b), the laser beam is shone on the metal (or ceramic) side without reaching the interface, the heat will diffuse by conduction to the interface, the polymer melts and the weld is created. So in this case, there is theoretically no limitation in materials that can be welded. The parameters of the laser (generally the beam power) can easily be adapted to the thickness of the metal, the heat can also be adjusted to the polymer’s fusion temperature. To weld two polymers, there are also two possibilities. In case (c), the two polymers are transparent to the laser used, so to absorb the energy of the laser beam, a metallic insert is put at the interface. Case (d), one of the polymers absorbs the laser beam, and the weld is performed like in case (a). The absorption of the polymer can be increased by adding pigments for instance, but case (d) is in general challenging to perform, because the polymers tend to degrade during the welding process.

Applications are very diverse and can be found in transport industry, especially in automobile industry, where it tends to replace screws and bolts, to make lighter structures. It is also used for biomedical applications, especially in dentistry, where it replaces adhesives, to make the implants more easily biocompatible.

2.4.3 Advantages and drawbacks

Laser welding offers a large design freedom. The design freedom can be expressed in the materials chosen as described above, in the form of the pieces to be welded, and the form of the joint. Indeed, laser welding has the ability to assemble pieces that are very small or very big, but also flat or round parts and so on. The configuration of the joint can have some freedom as depicted in Figure 2.12, but it will depend on the materials joined. The joint can be performed in straight lines or in more fancy ways. Basically the limitation here will be the capacity to

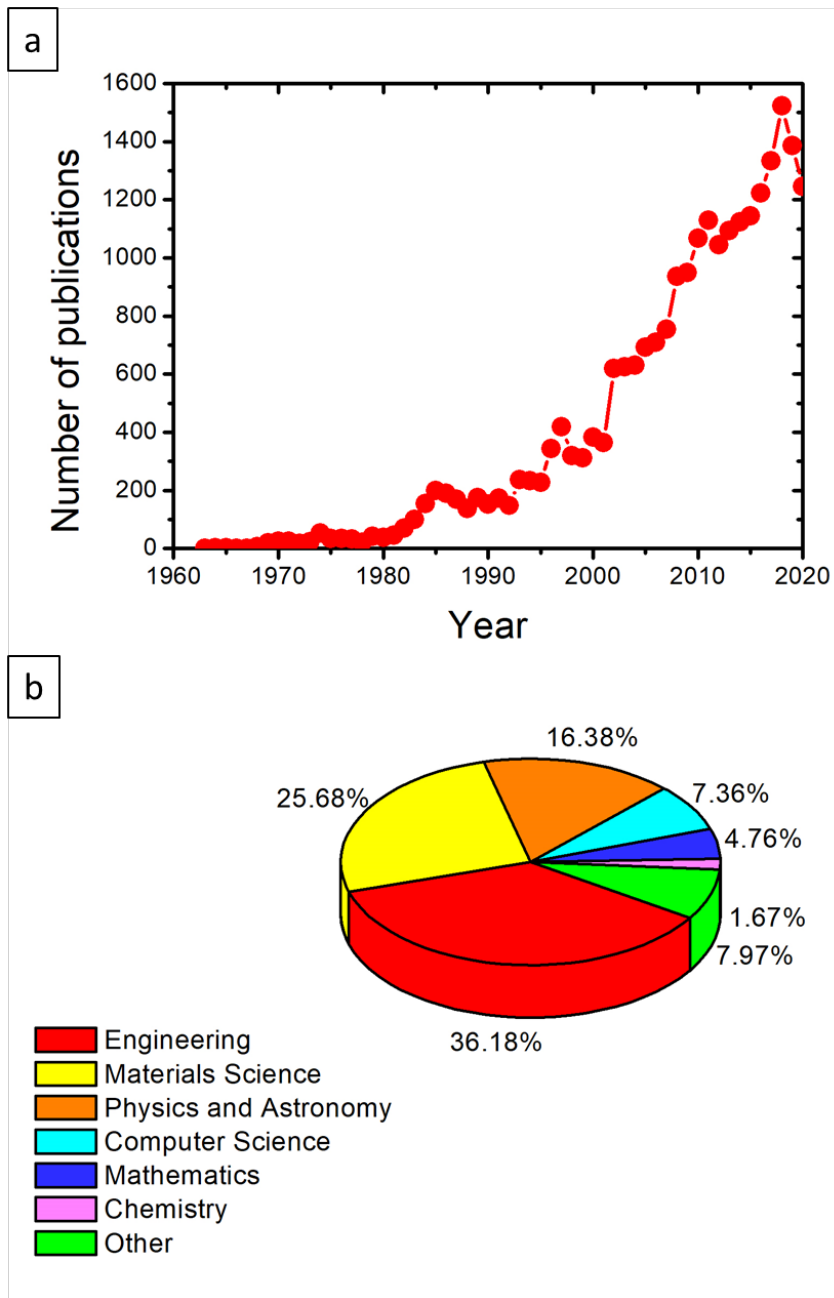


Figure 2.10: (a) Number of publications on laser welding per year and (b) pie chart of the publications per area. The data has been extracted from Scopus with the key words “laser welding”(consulted 19/11/2020).

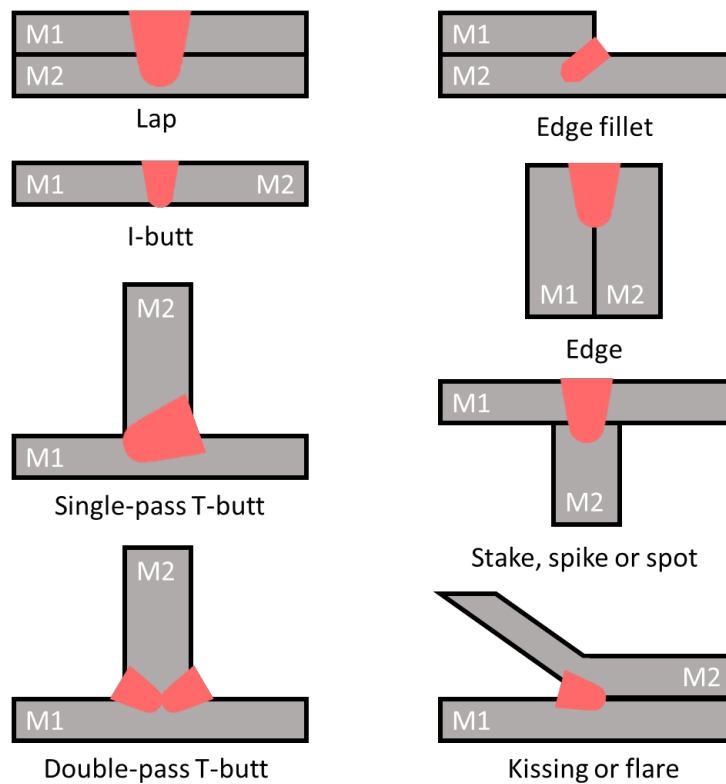


Figure 2.11: Scheme of the different possibilities of joint configuration in laser welding [71].

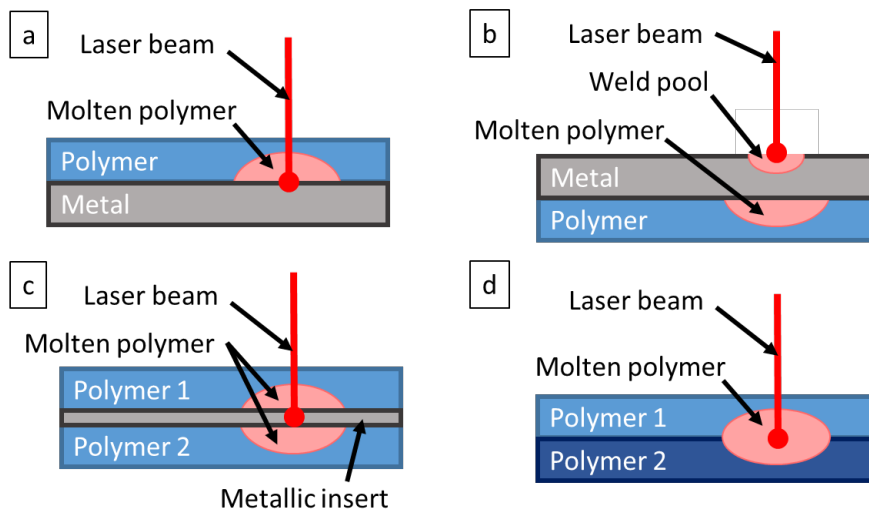


Figure 2.12: Scheme of the ways to weld polymers: (a) dissimilar direct weld [5], (b) dissimilar indirect weld [70], (c) polymer-polymer weld with insert [67,68], and (d) polymer-polymer weld without insert [67,68].

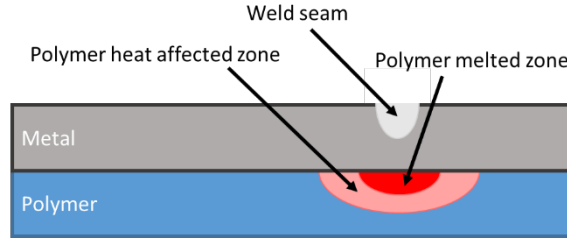


Figure 2.13: Scheme of the polymer melted and heat affected zone after laser welding.

move the pieces or the laser in order to achieve the wanted weld. Another great advantage is the rapidity of the process. The binding process in itself is quick, but the overall process is also fast because it can be performed without further pretreatment. Generally, no insert or interstitial material is needed, unless two polymers are to be welded. Furthermore laser welding can easily be automated.

The main disadvantage of the technique is that it is expensive to implement the process in a production line. To weld polymers, one must ensure that the polymer –or at least one of them in case of polymer-polymer assembly– must melt without degradation. Another disadvantage may appear in welding polymers with polymers or metals if the configuration chosen is to weld through the polymer (see Figure 2.12), is that the polymer must necessarily be transparent to the chosen laser wavelength.

2.4.4 Advancement in laser welded polymer-metal assemblies

Over the years, several hybrid polymer-metal combinations have been successfully tested, a non-exhaustive list has been summarized in Table 2.1. Most of the work done in polymer-laser welding are still concentrated on showing the possibility to weld specific materials combination and show possibilities to optimize the mechanical resistance, generally measured with shear load tests. Some authors also try to modify the surface prior to welding by different techniques, in order to increase the resistance. The surface modifications techniques used are laser ablation, anodization and surface cleaning. To the best of our knowledge, the only article presenting a study presenting a possible chemical bond between a polymer and a metal was done by Katayama et al. [5] in 2008. They welded chromium to PET (polyethylene terephthalate). In order to access the interface they dissolved the polymer, which permitted them to conduct XPS (X-ray photoelectron spectroscopy) and ToF-SIMS (time of flight secondary ion mass spectroscopy) measurement. In conclusion of their work they propose the possibility of a Cr-O-C bond between the polymer and the metal. Sadly, the article is too short to have more details about this work. Nevertheless, still to the best of our knowledge, no one ever tried to characterize the possibility of diffusion and electrostatic effect on laser welded materials (see Chapter 3). It is noticeable that there are few works about the polymer modifications after laser welding, which will be detailed hereafter.

Schricker et al. [85] analyzed the microstructure and measured the hardness of the polymer layer in the weld. The results show the existence of a heat affected zone around the melting zone. Indeed, between the bulk polymer and the melted zone, there is a transition zone, where the polymer has a different microstructure and is harder.

Katayama et al. [5] and Schricker et al. [86] studied the formation of bubbles in the melted zone during the welding process. These bubbles appear as detrimental to the shear load resistance. Both studies conclude, that the bubbles are composed of water and products resulting from pyrolysis –degradation– of the polymer. The water is coming from the natural moisture

Table 2.1: List of some the materials combination tested by laser welding and the type of welding used. (PA = polyamide, GF = glass fiber, CF = carbon fiber, PET = polyethylene terephthalate, PC = polycarbonate, PP = polypropylene, PTFE = polytetrafluoroethylene or Teflon®, PI = polyimide)

Metal	Polymer	Authors	Direct welding	Indirect welding
Steel	PA-6.6	Bergmann and Stambke [2]	X	X
	PA-6.6 GF			
Stainless Steel	PA-6	Cenigaonaindia et al. [72]	X	
	PA-6 GF laminate	Engelmann et al. [73]		X
	PA-6.6, PA-6.6 GF, PA-6.6 CF	Fortunato et al. [74]	X	
		Roesner et al. [4]		X
	PET	Kawahito et al. [75]	X	
		Niwa et al. [76]	X	
		Katayma and Kawahito [5]	X	
		Hao et al. [77]	X	
PC	Kawahito et al. [75]	X		
PP				
Magnesium	PET	Wahba et al. [6]		X
Aluminum	PC	Amend et al. [3]	X	X
	PA-6, PA-6 GF			
	PA-6.6	Lamberti et al. [70]		X
	PP	Gower et al. [78]		X
	PET	Yusof et al. [79]	X	
Titanium	PET	Wang et al. [80]	X	
		Wang et al. [81]	X	
		Chan et al. [82]	X	
	PTFE	Georgiev et al. [83]	X	
	PI	Mian et al. [84]	X	

of the polymer [87]. It can also be noticed that some work has been done on the effect of polymer moisture [88–90] on the shear load resistance after welding. From those works, it can be concluded that in general moisture in the polymer is detrimental to the mechanical resistance of the weld, but that it should be tested for each specific material combinations.

Chapter 3

Adhesion theory

3.1 Introduction

The phenomenon of adhesion has led to various applications for ages and can be traced down to prehistoric times. Nonetheless, the first fundamental studies on adhesion began in the 1920s. Baldan estimates that the field of adhesion really developed and became interesting only about 70 years ago [9]. Scientists of various backgrounds have worked to explain this phenomenon, and because of their different backgrounds have gone different paths to propose an explanation for it. Some people even speak of ‘adhesion theories’ in the plural, because all the explanations proposed are of very different nature. The first proposed explanation was mechanical interlocking in 1925 by Mc Bain and Hopkins [10]. Adsorption, composed of chemical and physical bonding, was the second explanation proposed and is attributed to Sharpe and Schonhorn [11]. The third proposition, diffusion, was done in the 1960s by Voyutski [91]. And finally the fourth explanation, electrostatic attraction, was done in 1967 by Derjaguin [13]. So to explain adhesion there are four effects: mechanical interlocking, chemical and physical bonding, diffusion and electrostatic attraction. The four phenomena explaining adhesion are complementary and sometimes even entangled, yet described separately. They have not been unified in one common description for the moment. The energy of adhesion, E_a , corresponds to the energy needed to separate to adhering materials at their interface and can be written as:

$$E_a = E_m + E_b + E_d + E_e \quad (3.1)$$

where E_m is the energy coming from the mechanical interlocking, E_b the bonding energy due to chemical and physical bonds, E_d the energy originating from the diffusion, and E_e the electrostatic attraction energy.

In this chapter, we will only describe all the four effects of adhesion: mechanical interlocking, adsorption, diffusion and electrostatic effect. Some authors [9,92] also include thermodynamics and wetting, but these phenomena do not explain adhesion by their nature. The last part will focus on how adhering materials can separate: failure modes.

3.2 Mechanical interlocking

3.2.1 General description

In 1925, Mc Bain and Hopkins [10] introduced the idea of mechanical interlocking as the first explanation for adhesion. It is also sometimes called “roughness effect”. They studied the interaction of adhesives and metal surfaces. The idea is that the adhesive when deposited will fill the groves of the metal’s roughness. This will lead to two effects. The first is a mechanical

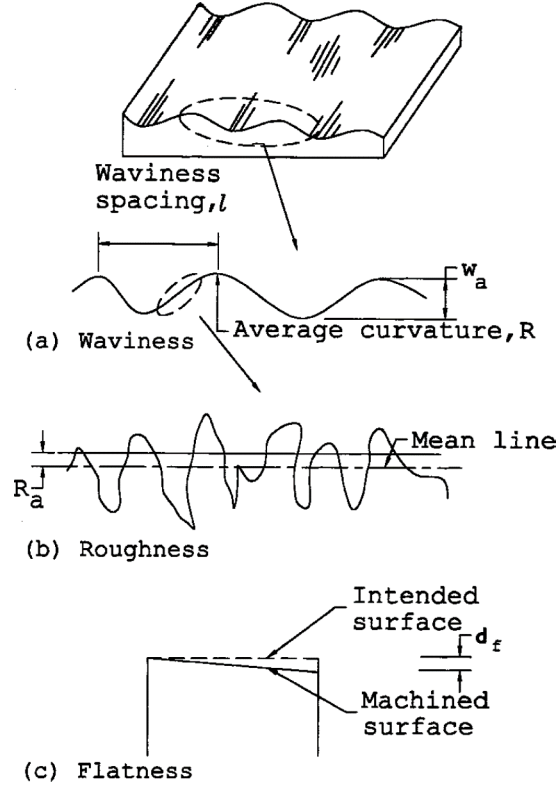


Figure 3.1: Illustration of the different surface characteristics [94].

anchoring on the metal because of the roughness, comparable to the Velcro fixation. The second is that the total surface of interaction available is higher than with a perfectly flat surface, allowing for more bonding to happen. So the main parameter for mechanical interlocking is the roughness. Roughness is easy to understand, but not to describe. When characterizing a surface, out of the roughness, there are two more parameters to take into account: the waviness and the flatness (see Figure 3.1). A series of parameter are used to describe completely the roughness of a surface and have been defined in an ISO norm [93]. These parameters are sorted in six categories: amplitude parameters (peak and valleys), amplitude average parameters, spacing parameters, hybrid parameters, height characteristic average parameters, and parameter from bearing ratio curve and profile height amplitude curve.

In this high variety of parameters, two are generally used alone to describe the roughness: the arithmetical mean deviation R_a , and the root mean square deviation R_q . The arithmetical deviation is calculated as follow:

$$R_a = \frac{1}{L} \int_0^L |Z(x)| dx \quad (3.2)$$

where L is the sampling length, and $Z(x)$ are the ordinate values. While R_q is defined, with the measurement parameters as:

$$R_q = \sqrt{\frac{1}{L} \int_0^L Z^2(x) dx} \quad (3.3)$$

Instinctively one could think that the rougher the surface, the stronger the assembly is. It is true until an optimum is reached (phase I in Figure 3.2). After that the assembly strength decreases, because the adhesive does not fill the valleys completely, so that in fact the contact surface between both materials is decreasing (phase II in Figure 3.2). It decreases till the valleys

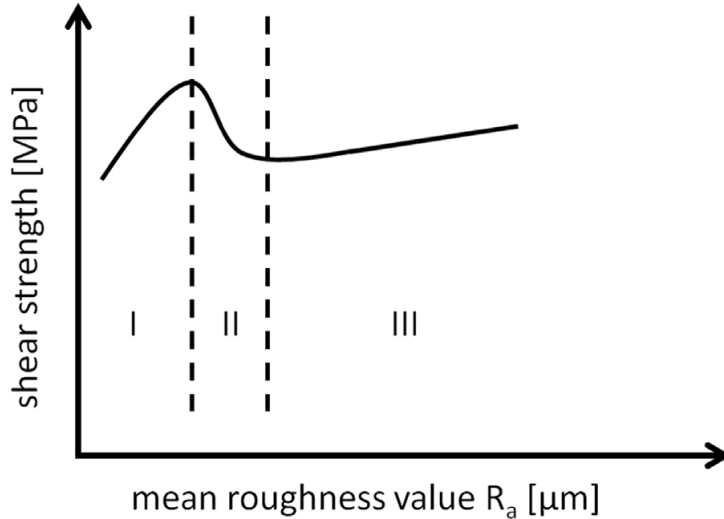


Figure 3.2: Schematic graph of the evolution of the shear strength towards the mean roughness value R_a [14].

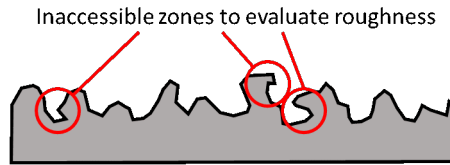


Figure 3.3: Scheme of the inaccessible zones in roughness measurement.

become so large that the material can flow in them very easily, and there the shear strength increases again, but never reaches the level of the optimum (phase III in Figure 3.2).

Roughness can be tricky to measure, as in some cases there are inaccessible zones on the surface (see Figure 3.3). This is even more true if the surface is porous. Porosity can be a way to maximize the mechanical interlocking, but the porosity must be large enough to allow the adherent to flow and fill the whole.

3.2.2 State of the art

It appears that there are two general trends when it comes to modify the surface roughness in order to tune the adhesion to the optimum point for the application. The first trend consist in imprinting a repetitive pattern that is very symmetrical, like grooves or nano-blocks. The second trend is to have less organized surfaces, but with precise roughness parameters, for instance by sandblasting them.

The idea of patterning surface to enhance adhesion was developed by mimicking nature. The most famous example for that, are the studies done on geckos' ability to adhere to surfaces defying gravity [95,96]. Indeed the geckos legs are covered with nanostructures allowing them to adhere on surfaces, and by retracting those structures, reverse the adhesion. Hensel et al. [97] did a great review on the applications for dry adhesive inspired by examples in nature. In the nano-range patterning, improvement in lithography technologies allowed to develop "mushroom-like" patterning, as Seong et al. did in 2019 [98]. Even if the improvements in photolithography allow now to obtain nano-structures, micro-structures are still developed with it [99]. Hopmann et al. [100] in 2016 tested different types of microstructurations by using various techniques, such

Table 3.1: Energy scale of the different type of bonding

Bonding type	Energy scale (in kJ.mol ⁻¹)
Van der Waals	≈ 2-40
Hydrogen bond	< 20-25
Metallic bond	110-350
Ionic bond	335-1050
Covalent bond	63-920

as selective laser melting (SLM) or by welding a metallic tissue on the metallic surface. Those structures were applied to weld metals to polymers, the polymer by melting filling the gaps of the structures. Another way to get well structured surfaces, is to use laser ablation. It is an interesting process as it allows to obtain very diverse structures, as well as it is fast and easily automated [17, 101, 102].

Patterning very strictly is generally expensive and time consuming, so generally for industrial applications, the surface roughness is tuned with less control on the structure, but not less control on the surface roughness parameters. Various techniques exist depending on the application aimed: mechanical abrasion, sandblasting, chemical and electrochemical. This year, Van Dam et al. [103] did a remarkable work on steel-epoxy adhesion, by varying the steel alloys and the surface treatments, which enabled them to conclude that mechanical interlocking is the first important parameter for a good adhesion, but combined to fine tuned surface chemistry adhesion can be enhanced even more. Abrasion might be the most used technique in industry to enhance mechanical interlocking for better adhesion [104]. Sandblasting is quite popular to change surface morphology, as did Zou et al. [105] in 2011 and Li et al. [106] in 2018. As for the chemical and electrochemical ways, they consist mostly in dipping the surface that has to be treated in an aggressive bath of a solvent that will attack the surface and so change its roughness. The solvent used might be acidic, basic, or zirconium solutions. In the case of electrochemical treatment, the attack is activated and accelerated by applying a current [107–109]. The last methodology found is plasma treatment, even if the changes are mainly on the chemical level, the roughness can also be modified and so enhance the adhesion properties [110–112].

Work on mechanical interlocking is mostly experimental, because of the large variety of techniques allowing to tune the roughness. Nonetheless there is also development of simulations and theoretical work on the matter, even if there is a high complexity in modelling surface roughness, especially for more random surfaces [14, 113–115].

3.3 Bonding

Leucippus and his pupil Democritus in the 5th century BC proposed the idea of atom, in ancient Greek “atomos” which means uncuttable. This is a well-known fact, what is less known is that at the same time they proposed an interaction, that allows these atoms to stick together to form bigger materials. The idea of chemical bonding was born. This idea was refined in the following centuries by other philosophers and alchemists, allowing Isaac Newton to write in the “Question 31” of his treaty “Opticks” [117]: “particles attract one another by some force, which in immediate contact is exceedingly strong, at small distances performs the chemical operations, and reaches not far from the particles with any sensible effect”. The real development of bonding, by separating different kind of bonding and proposing models to describe them appear during the 19th century and beginning the 20th century. This is possible because the atoms are better understood and described (Bohr’s model), and the development of quantum physics.

There are several types of bonds, generally separated in two categories: physical and chemical

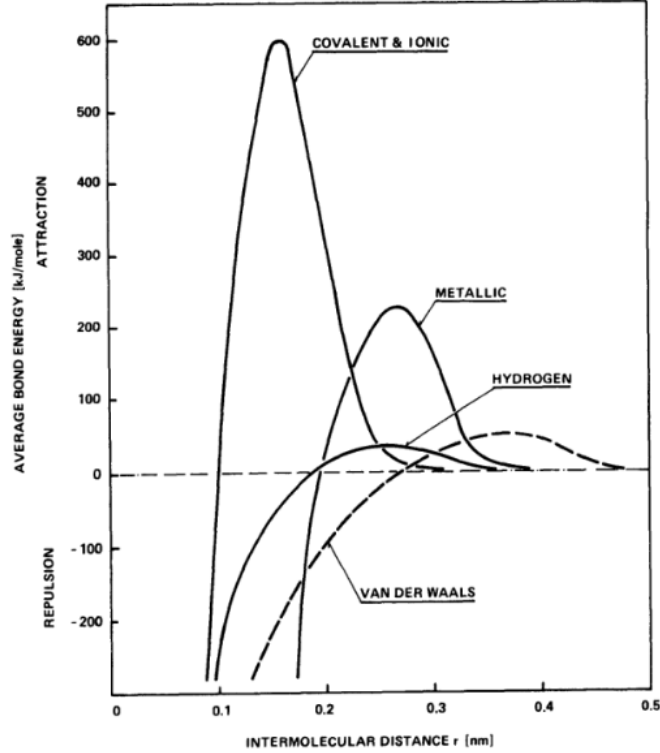


Figure 3.4: Average bond energy in function of the intermolecular distance for the different type of bonding [116].

bonds. These categories are also named: weak and strong bonds. The weak bonds include the Van der Waals and hydrogen bonds. While the strong bonds include ionic, metallic and covalent bonds. As they have different ways of acting, they also intervene at different energy scales and distances, which are presented in Table 3.1 and Figure 3.4. There are less known type of weak bonds: halogen bonds and chalcogen bonds. They will be described briefly in order to be complete. Unfortunately, they are not much studied, and their occurrence at interfaces is very rare.

3.3.1 Different bonding type

3.3.1.1 Van der Waals interactions

Van der Waals interactions are interactions between molecular dipoles. This makes Van der Waals interaction an electrostatic interactions at molecular range (3-5 Å). The dipoles can be of two nature: permanent dipoles or induced dipoles. This leads to three different interactions: permanent – permanent dipole, permanent – induced dipole, and induced – induced dipole. These three different interactions can be described respectively by three different forces: the Keesom force, the Debye force, and the London dispersion force.

The potential energy of the Keesom force can be written as:

$$\langle V \rangle = -\frac{2\mu_1^2\mu_2^2}{3(4\pi\epsilon_0)^2kT} \frac{1}{r^6} = -\frac{C_k}{r^6} \quad (3.4)$$

where μ_1 and μ_2 are the dipolar moment of the two molecules interacting, ϵ_0 the vacuum permittivity, k the Boltzmann constant, T the temperature and r the distance between the two molecules.

While the potential energy of the Debye force is given by the following expression:

$$\langle V \rangle = -\frac{\mu_1^2 \alpha'_2}{4\pi\epsilon_0} \frac{1}{r^6} = -\frac{C_D}{r^6} \quad (3.5)$$

where μ_1 is the dipolar moment of the dipole, α'_2 is the polarizability volume of the second molecule (the induced dipole).

Finally the potential energy of the London dispersion force is written as:

$$\langle V \rangle = -\frac{3}{2} \alpha'_1 \alpha'_2 \frac{I_1 I_2}{I_1 + I_2} \frac{1}{r^6} = -\frac{C_L}{r^6} \quad (3.6)$$

where α'_2 and α'_2 are the polarizability volume of the two molecules, I_1 and I_2 are the ionization energies of the two molecules.

It is noticeable that these three potentials are inversely proportional to the distance to the power six.

3.3.1.2 Hydrogen bonding

The definition of the hydrogen bond as given by the IUPAC [118] is: “A form of association between an electronegative atom and a hydrogen atom attached to a second, relatively electronegative atom. It is best considered as an electrostatic interaction, heightened by the small size of hydrogen, which permits proximity of the interacting dipoles or charges. Both electronegative atoms are usually (but not necessarily) from the first row of the Periodic Table, i.e. N, O or F. Hydrogen bonds may be inter-molecular or intramolecular. With a few exceptions, usually involving fluorine, the associated energies are less than 20-25 kJ.mol⁻¹ (5-6 kcal.mol⁻¹).” This definition can be completed by that given by Steiner [119] in 2002 in his review on hydrogen bond: “An $X - H \cdots A$ interaction is called a hydrogen bond, if (1) it constitutes a local bond, and (2) $X - H$ acts as proton donor to A.” A “local bond” is described by Steiner in his review, as a near interaction (about 2-4 Å), which is lower than Van der Waals interactions radii (about 3-5 Å), as shown in Figure 3.4. He also mentions the fact that generally Hydrogen bonds are spatially oriented in a linear configuration.

Hydrogen bonds are present quasi everywhere. The best example of presence of hydrogen bond is of course water (see Figure 3.5) [120, 121]. They revealed themselves as extremely important for biological systems; one example is its role played in protein conformation [122] (see Figure 3.5). In materials science hydrogen bond can also play an important role, and is typically responsible for the creation of gels [123, 124]. Hydrogen bonds may seem weak, and indeed it is when taken separately, but in sufficient amount, it can create extremely strong materials, as Poly-paraphenyleneterephthalamide better known as Kevlar [125]. The polymer chains have a linear organization, which allows hydrogen bond (or bridges) between the chains (see Figure 3.5), explaining the robustness of the material, allowing it to be used for bulletproof vest.

3.3.1.3 Halogen and chalcogen bonding

Halogen [127, 128] and chalcogen [129] bonds are very similar to hydrogen bonds and the hydrogen is replaced by a halogen or chalcogen atom (see Figure 3.6). They share the same nature: electrostatic interaction, the same distance range: 2-4 Å, and the same spatial orientation: generally linear. For the energy scale no information could be found, but assumption can be made that they have similar energies. Because of all these similarities, these three bonds are of the same nature and one day will be unified under one denomination [130].

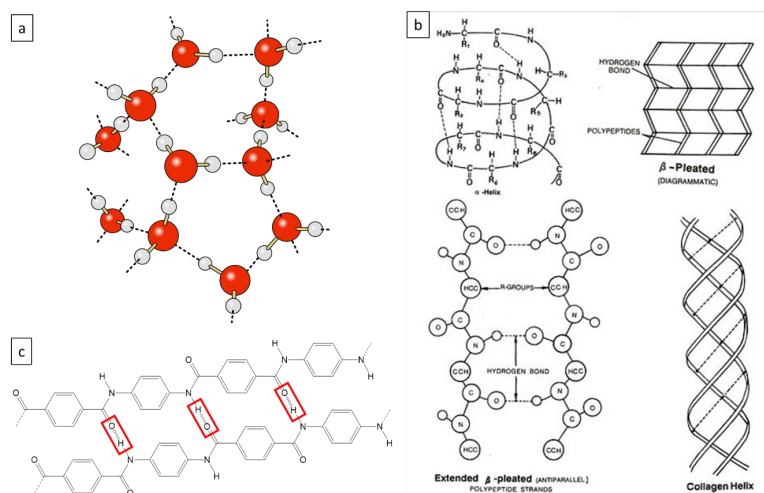


Figure 3.5: (a) hydrogen bonds structuring water, (b) hydrogen bonds responsible for the protein conformation [126] , and (c) hydrogen bonds between Kevlar chains.

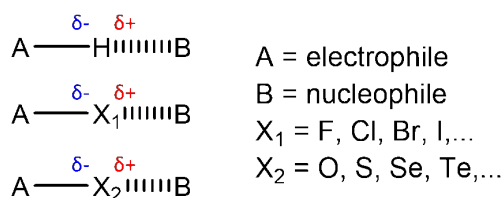


Figure 3.6: Parallel between hydrogen, halogen and chalcogen bond.

3.3.1.4 Covalent bonding

In 1916 Lewis [131] described the covalent bond as a sharing of valence electrons between two atoms. Heitler and London [132] in 1927 completely described a covalent bond between two atoms of hydrogen using quantum physics, and so gave birth to quantum chemistry. These work allow now to describe a covalent bond as the sharing of two valence electrons between two atoms. To share the electrons the atomic valence orbitals of the combining atoms must be able to recover, creating molecular orbitals centered on the two atoms, so that the electrons are “shared” between the two atoms (see Figure 3.7(a)). Depending on the configuration of the recovery and the involved atomic orbitals, they will be named σ -bonds, π -bonds or even δ -bonds.

3.3.1.5 Ionic bonding

From a quantum chemical point of view, the ionic bond can be described in the same manner as a covalent bond, the difference resides in the main localization of the bonding electrons, subsequently a main difference in the localization of the molecular orbitals. The atoms have different electronegativities –capacity to attract electrons– so that when a strongly electronegative atom bonds to a weakly electronegative atom, the electrons are not “shared” anymore and localized on the two atoms, but strictly localized on the strongly electronegative atom. Formally this creates charges on the two atoms, respectively negative for the electronegative atom and positive for the electropositive atom, leading to the formation of ions, explaining the name of the bond. Ionic bonds are generally stronger than covalent bond, because of the charges created by the bond, leading to the appearance of electrostatic forces (Coulomb’s law) between the two atoms. Practically, to differentiate an ionic bond from an covalent bond, the atoms must have a

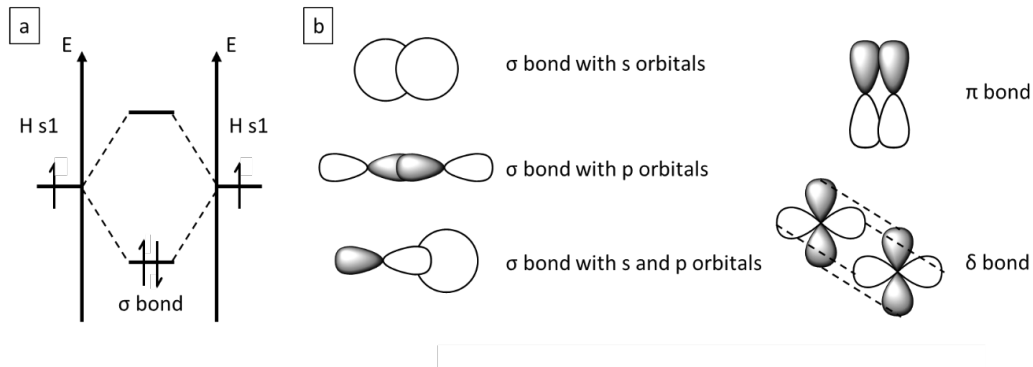


Figure 3.7: (a) energy diagram for the formation of H₂, (b) the different type of covalent bond.

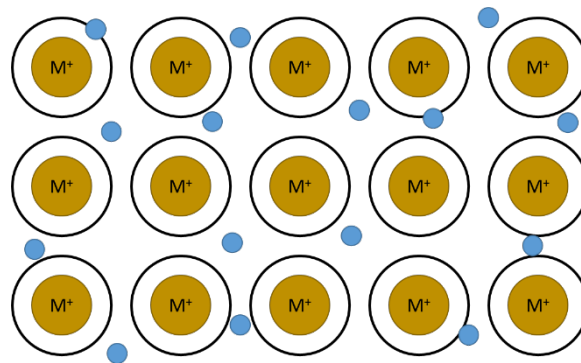


Figure 3.8: Illustration of metallic bonding, where the electrons (blue circles) move freely in the positive metallic matrix.

difference of electronegativity value higher than 1.7. Naturally, the transition is not steep, but rather continuous, giving birth to ionic-covalent bonds. In these cases, the electrons (and the molecular orbitals), are more centered on the more electronegative atom from the bond, but are not exclusively centered on him. There are many examples of ionic bond, but maybe the most famous is NaCl compound.

3.3.1.6 Metallic bonding

Metallic bonds occur in metals. Metal atoms share their valence electrons in common, so that in the end, the atoms are formally positively charged and are “floating” in a “sea” of electrons (see Figure 3.8). This is possible because the valence atomic orbitals of the metal, by mixing together at large scales (actually the size of the crystallites, what could be considered in a sense as a big molecule) create energy bands, instead localized energy levels, allowing the electrons to move freely around in the metal. This explains also the conductive nature of metals.

3.3.2 Chemical bonding in adhesion: state of the art

From all the bonding possibilities, covalent bonding is the most studied at interfaces in adhesion science. Van der Waals interactions and hydrogen bonding are studied as well. For ionic and metallic bonds nothing relevant to adhesion could be found.

3.3.2.1 Van der Waals interactions

When Van der Waals interactions at interfaces are studied, they are generally combined with characterization of the electrostatic effect (detailed in part 3.5). It is understandable because of the electrostatic nature of the Van der Waals interactions. Nonetheless, Van der Waals interactions describe the interactions between dipoles, while the electrostatic effect describes the creation of a dipole at the interface. The difference is small, and is quite impossible to distinguish in experiments.

To characterize Van der Waals interactions experimentally, mechanical measurement are generally performed. Howe et al. [133] used “pendulum-type apparatuses” to measure the adhesion force between pyrex glass surfaces. To study graphene adhesion on silicon oxide wafer Koenig et al [134] did a pressurized blister test. Lu and Dunn [135] did simulation studies to model pressurized blister tests for graphene adhering to silicon oxide with quasi only Van der Waals interactions and obtained satisfactory results, compared to experimental works. Theoretical and simulation work seems to be the most commonly used tool to assess Van der Waals interactions coupled to mechanic measurements [136–139]. Some works were also centered on bioadhesion, and more specifically on the capacity of Geckos to have reversible adhesion on their paws, allowing them to climb to walls and roofs [95].

3.3.2.2 Hydrogen bonding

Hydrogen bonds are not easy to observe and characterize experimentally. Inside materials, such as water, they are mostly highlighted by the use of spectroscopies, and by the use of X-ray diffraction completed with simulations for crystals [119].

In adhesion works, hydrogen bonds are commonly studied for polymer and organic materials. Thomas et al. [140] did use interfacial force microscopy to characterize them. While Frihart [141], Kajtna et al. [142] and Park et al. [143] did rheological measurement to characterize them. Owens [144] tested the autohesion of poly(ethylene terephthalate) (PET) plates after ultraviolet and corona treatment and evaluated the adhesion force by mechanical pulling tests. Faghihnejad et al. [145] also used mechanical testing with a surface forces apparatus to test hydrogen bonds in self-healing polymers. There were also works centered on chemical interactions in general using XPS, for polymer/metal assemblies, by depositing ultra-thin films of different acrylic polymers on different metal oxides, which allowed to characterize covalent as well as hydrogen bonds at the interface [146–150]. The last technique found to characterize directly hydrogen bonding at interfaces was sum frequency generation (SFG) vibrational spectroscopy, as used by Loch et al. [151] to analyze the interface of PET and silane coupling agents.

3.3.2.3 Covalent bonding

The major trouble to characterize chemical bonds at interfaces is to access deeply buried information. Therefore, Pletincx et al. [152] proposed four main ways to characterize chemical bonding at interfaces: doing cross-sections, etching and sputtering, thin film depositions, and the deposition of model molecules. These major strategies can be completed with: dissolving one of the two materials and direct analysis in case of adhesive failure of the assembly (see part 3.6).

Cross-sectioning is quite common to analyze interfaces, but represent a challenge to perform [153, 154]. Generally the samples are cut mechanically, which might mix the materials at the interface and so completely alter it. The samples might also break during the process. Alternate solutions exist, like cross section polishing (CSP) or focused ion beam (FIB) [155–158]. Both techniques limit the damages at the interface, but direct environmental effects are impossible to

study. For CSP the interface is exposed to the surroundings, which will alter the interface before its analysis. Another way to do cross sections is to use ultra low angle microtomy [159–161]. It is performed using a microtome combined with ultralow angle sectioning blocks. This allows to expose the interface and enables direct analysis, generally XPS with a small spot-size and ToF-SIMS. The technique is limited to rather thin and soft assemblies, so that the microtome can cut through.

Depth profiling is commonly used, and also represent a challenge to perform [153,154]. The principle is to sputter through one of the materials to get to the interface. The sputtering is done by an ionic source. Depending on the materials different sputtering sources can be used with adapted energetic parameters [162,163]. With the development of new cluster sources, C_{60}^+ and Ar_n^+ , depth profiling organic materials is possible, even if Cs^+ source is still performing when analyzing hybrid assemblies [164–167]. Characterization is mostly done by XPS and ToF-SIMS in case of depth profiling.

Studying chemical interfacial state using thin films is also commonly used. In this case vibrational spectroscopies can be easily applied, especially for polymer metal assemblies. Infrared reflectance absorbance spectroscopy (IRRAS) is one of the possibilities, as displayed by the work of Konstadinidis et al. [168], Tannenbaum et al. [169] or for the study of self-assembled monolayers (SAM) [170,171]. In the infrared techniques family, the use of attenuated total reflectance Fourier transform infrared spectroscopy (ATR-FTIR) is also a good option, especially when used in the Kretschmann configuration [172–175]. Simple Raman spectroscopy is also a good solution in the case of thin film [176]. It can also be upgraded to surface enhanced Raman spectroscopy (SERS). Even if SERS is a powerful tool, it is complicated to use, since the signal needs to be enhanced by depositing gold or silver nanoparticles at the interface, thus damaging the interface [177,178]. XPS is quite an easy tool to use to characterize the chemical state, allowing to characterize covalent bonds [146–150]. It is also quantitative. Unfortunately, XPS has to be performed under ultra-high vacuum, which is detrimental for some samples or more simply to study the environmental effects in situ, like humidity for example. Yet the development of near-atmosphere pressure XPS (NAPXPS) proves to be a good solution to tackle these issues [179,180]. González-Orive et al. [181] did an excellent review on studying the chemistry with techniques under ambient conditions.

The principle of using model molecules is to deposit only the (or one of the) reactive part of the molecule. The molecule deposited is thus smaller, but mimics the bigger molecule studied (generally a polymer). This simplifies the interface access. Since the deposit is ultra-thin it is easy to perform classic surface analysis. To study chemical interactions, vibrational spectroscopies are well suited [182]. Infrared reflectance absorbance spectroscopy (IRRAS) has shown the possibility to study molecular adsorption and desorption [183–185]. This technique requires a highly reflective substrate on which only ultra-thin film can be deposited. Polarizing the infrared beam allows to determine the orientation of the deposited molecules [186]. XPS and ToF-SIMS are classical tools for chemical surface evaluation and are widely applied in such cases [187–191].

Dissolution of one of the materials to access the interface is seldom used. Two examples could be found. Watts et al. [192,193] studied by XPS metals coated with epoxy layers, approaching the interface by the metal side. Thus, the metal layer was dissolved without destroying the metal oxide layer. Pletincx et al. [180] deposited PMMA on aluminum surfaces. The PMMA layer was dissolved to study the chemical state at the interface. From the two examples cited here, one can conclude that it is an interesting strategy to study interfacial chemical states, but the solvent has to be chosen wisely. Indeed an unwisely chosen solvent could alter the interface dramatically, making it impossible to study the chemical state.

Breaking the assemblies to reach the interface is the last strategy possible. This technique should be used in case of adhesive failure, or in case of mixed failure mode, in the adhesive mode

zone. In cohesive failure mode zones, generally the thickness to the interface is not controlled and rather rough, which makes depth profiling quite dubious. To analyze the interface, XPS is the most commonly used technique, always combined to another technique, such as SEM [194], or ToF-SIMS [195] or impedance measurements [196].

3.3.2.4 Ionic bonding

In 2000 Yoshida et al. [197] studied the chemical interactions of polyalkenoic acids with synthetic enamel and synthetic hydroxyapatite, using only XPS, and showed the formation of ionic bonds. More recently, Pletincx et al. [179] showed the ionic nature of the bonds formed between PMMA and aluminum oxide, by combining the results of AP-XPS, ToF-SIMS and FTIR in the Kretschmann configuration. Pletincx et al. [198] extended their work, by studying and comparing PMMA and polyacrylic acid (PAA) on aluminum oxide this time using random phase multisine electrochemical impedance spectroscopy (ORP EIS) and FTIR in the Kretschmann configuration. Many works combine experimental measurement and simulation or theoretical calculations to characterize an ionic bond. Kiguchi et al. [199] studied alkali heterostructures interfaces. They observed positive and negative misfits in reflection high energy electron diffraction (RHEED), in electron energy loss spectroscopy (EELS) and Auger electron spectroscopy. They could explain these misfits because of ionic bonds formed at the interface using Monte Carlo simulations. Bowers et al. [200] in 2014, showed that the formation of ionic bonds does not affect the electrical properties at the interface in $S(\text{CH}_2)_n\text{T}/\text{Ga}_2\text{O}_3$, with T being different Lewis acids. In 2019 Wróbel et al. [201] combined static SIMS and DFT calculations to study the ionic bond formation in $\text{BP}_n\text{COO}/\text{Ag}$ systems (BP = biphenyl). There are also works dealing solely with theoretical calculations and simulations. In 2002, Siegel et al. [202] made theoretical calculations on aluminum oxide and pure aluminum interfaces and showed the ionic character of the bond. In 2004, Peacock et al. [203] simulated the evolution of the band gap of Si/ZrO_2 and Si/HfO_2 systems. They showed that the ionic bonding does not affect the electrical state if it is an oxygen layer that is in contact with the Si substrate. Hu et al. [204] in 2019 showed the possibility to activate the dissociation of ionic bonds on ferroelectric systems by simply applying a magnetic field.

3.4 Diffusion

3.4.1 General description

The idea of diffusion is quite old, as the first model was described by Adolf Fick in 1855 [205]. Nonetheless, the idea that diffusion could play a role in adhesion was proposed only a century later, by Voyutskii in 1949 [206]. This article was originally published in Russian, but got finally published in English in 1957 [12]. Nonetheless, the recognition of the diffusion as a phenomenon responsible for adhesion, occurs only in the 1960's [91, 207]. A bit later, in the 1970's, this work was completed by De Gennes [208], adding the idea of polymer reptation to explain their movement, and so their diffusion.

Voyutskii and later De Gennes, described the diffusion or interdiffusion only in polymers. The idea is that if the two materials joined together are miscible, an interphase will appear where the two materials are mixed following a gradient of concentration (see Figure 3.9). Fourche [209] mention two main criteria to obtain adhesion by diffusion: as already mentioned the miscibility of the two materials, but also the high mobility of the polymer chains. The mobility of the molecules increases with the temperature (as long as the molecules are not decomposed). Therefore, the cases studied in interdiffusion, are frequently cases of autohesion (joining of the same materials),

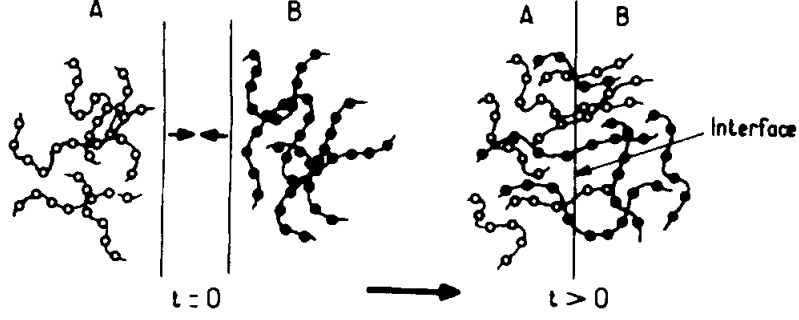


Figure 3.9: Scheme of the phenomenon of diffusion at an interface [209].

and cases where two polymer materials are welded, because heat is needed for the molecules to diffuse and to create the interphase.

In the case of autohesion, under constant assembly pressure, the diffusion follows Fick's law, and will depend on the temperature and the time of contact. Thus, the average interpenetration depth, x , can be written as:

$$x \propto \exp\left(-\frac{E_a}{2RT}\right) t^{\frac{1}{2}} \quad (3.7)$$

where E_a is the diffusion activation energy, R is the molar gas constant, T is the temperature and t the contact time [9, 209]. Since the diffusion follows Fick's law, if the concentration is constant during the time, which is the steady state of diffusion or the first Fick law, the flux F_x in the x direction, can be written as:

$$F_x = -D \left(\frac{\partial C}{\partial x} \right) \quad (3.8)$$

where D is the diffusion constant. If the concentration varies with time, the second Fick law is used:

$$\left(\frac{\partial C}{\partial t} \right) = D \left(\frac{\partial^2 C}{\partial x^2} + \frac{\partial^2 C}{\partial y^2} + \frac{\partial^2 C}{\partial z^2} \right) \quad (3.9)$$

The diffusion coefficient is defined as follow:

$$D_\eta = \left(\frac{A\rho kT}{36} \right) \left(\frac{R^2}{M} \right) \quad (3.10)$$

where η is the bulk viscosity, A the Avogadro number, ρ the density, k the Boltzmann constant, T the absolute temperature, R the molar gas constant, and M the molar mass distribution [210].

It is possible to evaluate the depth of interpenetration x , and the number of macromolecular chains crossing the interface L_0 , from the contact time t and the number of monomer N with these both equations [9]:

$$x(x) \approx t^{\frac{1}{4}} N^{-\frac{1}{4}} \quad (3.11)$$

$$L_0(t) \approx t^{\frac{3}{4}} N^{-\frac{7}{4}} \quad (3.12)$$

A similar model of diffusion for metals, or polymer-metal interfaces has not been developed yet. Even if diffusion is observed at such interfaces, the role of diffusion on adhesion properties is not clearly understood at the moment.

3.4.2 State of the art

As mentioned previously, most of the work on diffusion in adhesion has been done on polymer assemblies, generally self-adhesion or autohesion cases. For example Roland and Bohm [211] in 1985 studied the autohesion of polybutadiene using small angle neutron scattering. They concluded that diffusion is the main cause of the adhesion. The same conclusion was obtained by Brown et al. [212] in 1988 on polyimides PMDA-ODA assemblies. Mikos and Peppas [213] in 1989 compared their experimental results obtained in rheology with their simulations, which are in good agreement with one another, and also showed the importance of diffusion in the adhesion process for poly(methyl methacrylate) assemblies. In 1997, Sahlin and Peppas [214] tried successfully to increase the adhesion of hydrogel blocs by adding poly(ethylene glycol), PEG, which diffused at the interface of the hydrogels. Ghanem and Lang [215] in their book about polymer adhesion shows some examples where the surface pretreatments helped the adhesion by favoring the interactions between both polymers and so the interdiffusion. Zhang et al. [216] improved the adhesion of two polypropylene sheets by intercalating a blend of polypropylene/acrylate copolymer at the interface, which allowed higher diffusion and hence better adhesion. In 2019, Mocellin et al. [217] studied the adhesion of two PTFE sheets by rheology measurements, and concluded that the diffusion is indeed present but is not the main factor for adhesion because the time of contact is too short.

It is also interesting to mention that diffusion was also studied on polymer metal assemblies, and especially in the case of polymer metallization. Nonetheless, the effect of the diffusion on the adhesion was not reported, and generally the diffusion is avoided in the application such systems are used for [218–221].

Some recent experimental examples were also found on diffusion in metal assemblies impacting the adhesion. Campos-Silva et al. [222] studied borided steel and its adhesion on steel. They obtained the borided steel by diffusing boron on the steel surface. After the diffusion they tested annealing and demonstrated that the annealing treatment allowed to change the failure mode from adhesive at the interface (borided steel – steel) to a cohesive mode in the steel. Vieira et al. [223] studied Si/Si₃N₄/TiO_x/Pt/LiCoO₂ systems for microbattery applications. The problem was that the titanium was diffusing in the platinum layer which led to oxidation of the system and adhesion failure. Therefore they replaced the original pure titanium layer directly by an oxidized titanium layer, which demonstrated no diffusion and better adhesion properties. Ma et al. [224] functionalized WC-Co substrate by diffusing tantalum in it, in order to successfully increase the adhesion with an afterward deposited diamond layer. With these few examples, diffusion as an adhesion effect in metal assemblies is more difficult to apprehend, and this might explain the absence of model for it.

Theoretical and simulation work were also performed. Of course the work of Voyutskii [12, 206, 207, 225] must be mentioned, as well as the work of De Gennes [208] and the work of Campion [226] in 1975 on polymer autohesion. Still for polymer and organic compounds He et al. [227] recently presented a model for viscoelastic solids, where the adhesion is explained by diffusion, chemical interactions, but also deformation creep of the solid. Du and Zhu [228] in 2019 used molecular dynamics to simulate and try to explain the effect of diffusion of asphalt binders in mineral aggregates, which is of high interest to increase the roads lifetime. In 2017 Martinez et al. [229] used density functional theory (DFT) to study the adhesion of TiO₂/TiN assemblies and the diffusion of oxygen atoms at the interface by varying the surface crystalline structures of both materials, as well as the available sites. Finally in 2020, Han et al. [230] also used DFT to study diffusion and adhesion energy on Cu/2H-MoS₂ assemblies. Their conclusion seems that the diffusion did not strongly affect the adhesion, but changed the magnetic properties of the material.

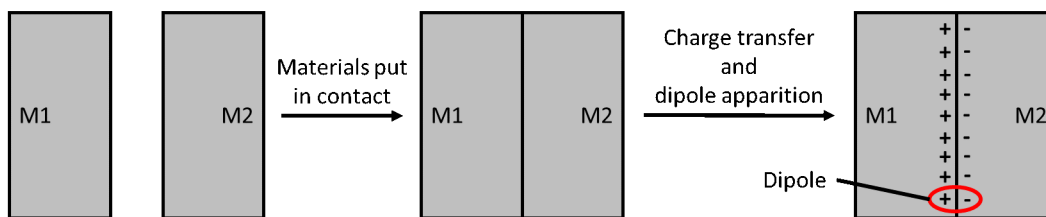


Figure 3.10: Schematic view of the apparition of the electrostatic effect when two materials are put in contact.

3.5 Electrostatic interaction

3.5.1 General description

The electrostatic effect is introduced in 1967 by Derjaguin and his coworkers [13] as a possible phenomenon to explain adhesion. The principle is that when two different materials are put in intimate contact, there is a possible charge transfer, creating a dipole at the interface, as depicted in Figure 3.10. It is often compared to what happens at the surface of a capacitor. But to illustrate the electrostatic effect in adhesion, the image of hair sticking on a plastic balloon after being scrubbed on it, seems way more didactic. This is the general (not to say simple) idea, but this does not explain the physical reason of such phenomena.

The concept of molecular orbitals was briefly introduced when describing covalent bonds in section 3.3.1.4. These molecular orbitals result from a mixing of the atomic orbitals involved in the bonding. In larger materials, e.g. metals, the number of atomic orbitals mixed is very high, making the molecular orbitals number very high, with quite close energies, and when the number is sufficient, instead of having discrete molecular orbitals, a band structure is obtained. This idea illustrated in Figure 3.11 (a) is called the band structure theory. Depending of the nature of the material, the bands will be filled by the electrons very differently. The electrons will fill the bands following a Fermi-Dirac distribution and at 0 K the highest energy level occupied is defined as the Fermi level. In metals the valence band, the highest band filled with electrons (comparable to a HOMO in molecules), is not completely filled. The energy needed to make an electron move around freely in the metal is extremely low, explaining why metals are conductors and also the basic description of metallic bonds where “the atoms are in a sea of electrons” (see section 3.3.1.6). In semi-conductors the valence band is completely filled, but the gap between the valence band and the conduction band (the lowest empty band, equivalent to the LUMO) is low in energy. By definition the band gap must be lower than 2 eV. The energy difference is sufficiently low to promote electrons into the conduction band, which is the principle used for photovoltaic cells. Above 2 eV energy gap, the material is considered as an insulator (see Figure 3.11 (b)). In semi-conductor and in insulator, the Fermi level is in the gap. This does not mean that electrons are in forbidden states, but that statistically there are electrons present in the conduction band. The Fermi level is defined and different for each material as the HOMO and the LUMO are different for every atom.

Two different materials have different Fermi levels as stated above. So when the materials are contacting each other, electrons will cross the interface in order to equalize the Fermi levels. The direct consequence is that charges are created at the interface (see Figure 3.10 and Figure 3.12), leading to the apparition of a dipole, so the apparition of electrostatic forces, explaining a part of the adhesion phenomena. The equalization of the Fermi levels is also called "band curvature". The example shown in Figure 3.12 is between two metals, but this also works for semi-conductors and normally also for insulators.

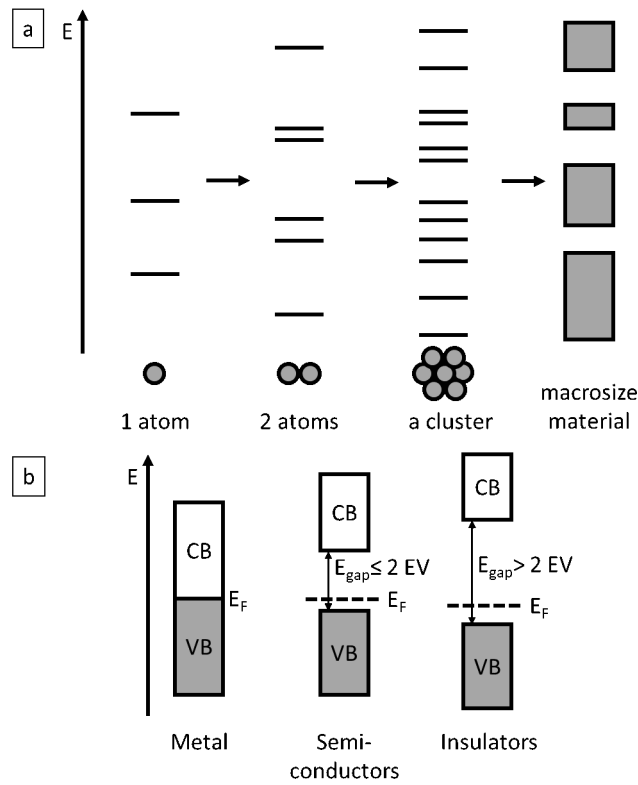


Figure 3.11: (a) scheme depicting the formation of energy band structure, and (b) scheme illustrating the energetic nature of metals, semi-conductors and insulators where VB stands for valence band, CB for conduction band, E_F for the Fermi level and E_{gap} for the gap energy.

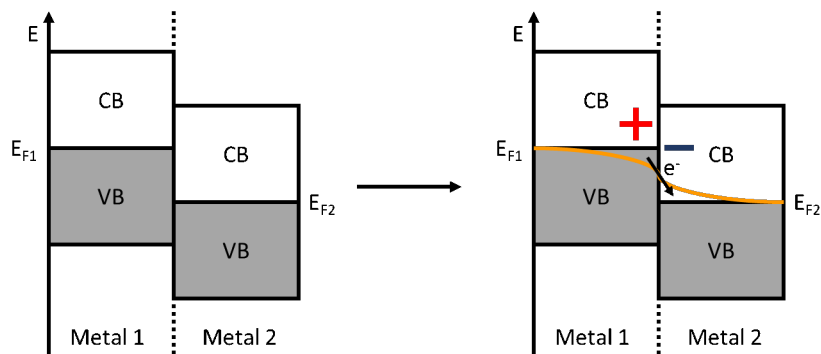


Figure 3.12: Example of band curvature phenomena and apparition of a dipole at the interface of two metals.

3.5.2 State of the art

The easiest materials on which an electrostatic effect could be observed are metals and semiconductors. As they conduct electricity, electrical conduction measurement can be made and hence demonstrate charge transfers at the interface. Though such characterization are common, for metals and semiconductors, the main focus of such work is rarely the adhesion, but rather the conductivity of electrons and holes. As metals and semiconductors are generally inorganic, it is no wonder that inorganics are more studied regarding this matter [231–233].

Nonetheless, with the rash development of organic conducting materials – organic electronics – for instance for light emitting devices (OLEDs), photovoltaics, or transistors and so on, studies on conducting organics are performed. As for inorganics, the greatest concern here is not the adhesion and the existence of an electrostatic effect, but also the conductivity at the interface. Different characterization methodologies exist, Zhang et al. [234] listed the main techniques: surface voltage measurement, photoluminescence spectroscopy (SPL), scanning probe microscopy (SPM), O₂ photostimulated desorption (PSD) and electron stimulated desorption (ESD), X-ray photoelectron spectroscopy (XPS) and ultra-violet photoelectron spectroscopy (UPS). The UPS principle is similar to XPS, but instead of shining an X-ray beam onto the surface of interest, an ultra-violet beam is used. Since the photoemission cross-section and the energy of the UV beam is lower, the photoelectrons originate from the upper shells of the atoms, allowing to characterize the Fermi level, and the conduction band. In the case of organic materials, the HOMO and the LUMO levels [235,236]. With this technology, Ishii and Seki [237] in 1997 demonstrated charge transfer and dipole formation at organic/metal interfaces. Two years later, in 1999, Ishii et al. [238] were able to study the same phenomena between two fully organic materials. At the same time Kugler et al. [239] studied this effect between a polymer and a ZnO substrate for LED applications. Hayashi et al. [240] studied the interface between fullerenes and metals and also observed charge transfer and band bending. Finally in 2004, Ishii et al. [241] demonstrated that the model applied for interfaces between metals and inorganic semiconductors, can be applied as well for metals and organic semi-conductors. Timpel et al. [242] combined UPS, XPS and simulation to characterize a charge transfer between indium tin oxide (ITO) and phosphonic acids. In 2018, Li and Lu [106] showed the importance of characterizing the interface dipole in order to get a better understanding of the charge transfer – the conduction – at interfaces.

The characterization of dipole apparition at the interface between conductive materials (metals and semiconductors) has been extensively studied, but the difficulty resides in doing the same characterization work for insulating materials. All the measurement involving current measurement are impossible to perform. In UPS insulator characterization is difficult, since no charge compensation system can be applied. Salaneck [235] did measurement on ultra-thin films of polymers deposited on metals, but it was rather unsatisfactory, because the electrostatic effect takes place, and the HOMO and LUMO levels measured are different from the bulk levels. The works of Possart [243], Brazovskii and Kirova [244], and Ettedgui et al. [245] are also worth mentioning. To the best of our knowledge since then, there has been little to no work done on this question in theory and simulation.

3.6 About failure modes

Two adhering materials can eventually experience failure, because of stress and fatigue, or for testing. In 1921, Griffith [246] studied the failure modes and has given the basis for the theory of fracture. The root cause of failure comes from defects in the materials and the failure propagates from these defects. These defects can be located at different places in an assembly and lead to different failure modes: adhesive, cohesive and mixed [247]. Schemes of the different

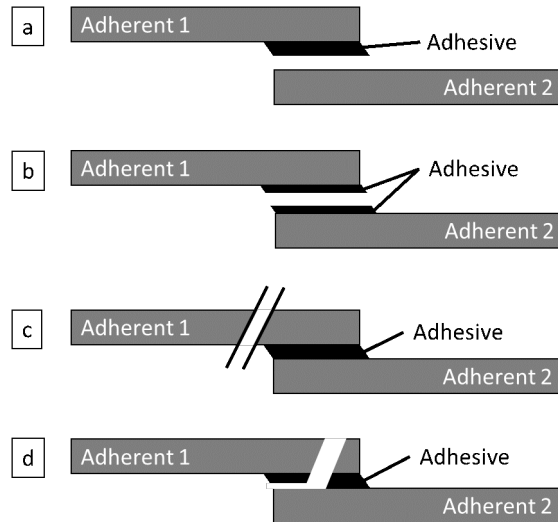


Figure 3.13: Schemes of the different failure modes, (a) adhesive failure mode, (b) cohesive failure of the adhesive, (c) cohesive failure of one the adherent, and (d) mixed failure mode.

failure modes can be seen in Figure 3.13. The examples shown depict the cases for adhesive assemblies, because they have the most possibilities in failure mode, but the described cases can easily be transferred to mechanical or welded assemblies.

When the assembly fails at the interface between the adhesive and one of the adherent, without leaving any traces on the separated materials, the failure is called adhesive. Nowadays it is seen that it is extremely rare to have such failure, since with powerful surface analysis tools, traces of the adhesive are generally found on the adherent. This is why some people introduced the idea of “apparent adhesive failure” [247]. When the assembly breaks in one of the assembled base materials, the failure is called cohesive. Cohesive failure can happen in one of the adherent, or in the adhesive layer if there is any.

The last failure mode is a mixed failure, where at some places the failure is adhesive and at others the failure is cohesive.

Generally a “good” failure is considered as cohesive, especially for adhesive assemblies. It is considered a good adhesion because it is supposed to mean that the adhesion between the adhesive and the adherent is stronger than the base material, so that failure happens in the adhesive base material. But physically it just signifies that the weak point is not at the interface, but does not necessarily mean that the adhesion is stronger than the base material. Indeed the process of assembling might create weak points in the base materials, like cracks or voids, which will result in a cohesive failure without improving the mechanical resistance. Examples show that in an assembly that has apparently an adhesive failure mode, the failure can be displaced to be completely cohesive in the adhesive layer, by adding some mineral charges in the adhesive, but the overall load resistance was not improved at all. So the conclusion is that the place of the failure is not necessarily a sign of strength of the bonding between the two materials, but only shows where the weak points of the assembly are.

Chapter 4

Materials and Methods

As a general comment for this chapter, some sample preparations and analysis have not been carried out at the University of Namur, but by other members of the Laser-STAMP project. In this case, it will be specified. If there is no specification, it has been carried out at the University of Namur.

4.1 Strategy

4.1.1 Pre-welding surface modification

The surface parameters, like chemistry, roughness, . . . are very important factors for welding, that's why great attention was paid to the surface preparation to get the highest mechanical resistance. Therefore in the Laser-STAMP project several pretreatments (laser ablation, anodization, and silanization) were tested to increase the shear load. In the frame of the thesis only the laser ablation was investigated by XPS properly enough to be presented. The laser ablation was studied on the aluminum and the titanium.

4.1.2 Chemical bonding

To highlight the existence, the nature and also the reaction mechanism for a chemical bonding between the metal (aluminum or titanium) and the polymer (polyamide-6.6), three types of samples were prepared: welded, spin-coated and model samples.

4.1.2.1 Welded samples

These samples were initially prepared to perform shear load strength tests, but the idea to analyze their interface chemistry came to test the possibility to characterize a chemical bonding in "industrial-like" samples.

First the materials –metals and polymer- were ethanol cleaned. After that they were clamped and laser welded. The interface is deeply buried and hardly accessible with XPS and ToF-SIMS even by depth profiling. It was therefore necessary to break the samples to reach the interface. On the titanium samples the failure is mixed (adhesive and cohesive), so part of the interface is directly accessible. On the aluminum samples the failure is only cohesive in the polymer close to the interface. A large residue (up to several micrometers) of polymer remains on the Al sheet. To access the interface, the polyamide-6.6 residue was dissolved. The idea of dissolving was already used previously by Katayama et al. [5] in 2008 for laser welded PET and chromium and Pletincx et al. [180] in 2017 for PMMA and aluminum oxide assemblies. The novelty resides in combining breaking of the samples with the dissolution of one of the joining partners. Nonetheless, finding

a solvent for polyamide-6.6 is quite difficult, because the only choices found in the literature were acetic and formic acid, hot phenols and 2,2,2-trifluoroethanol [248]. The 2,2,2-trifluoroethanol was preferred. To get a good overview on the action of the welding process, the welded zone was compared with the non-welded zone, which will be called “the out of weld” (see Figure 4.1).

As the laser ablation revealed itself as an easy way to enhance the mechanical resistance, the idea came to test such samples. The methodology was the same as for the simple welded samples, but here the surface were ablated prior to welding. The time allowed to analyze only the aluminum ablated samples and not the titanium. For the aluminum the failure was also cohesive, so a dissolution step was needed and performed following the same procedure as for the simple welded samples.

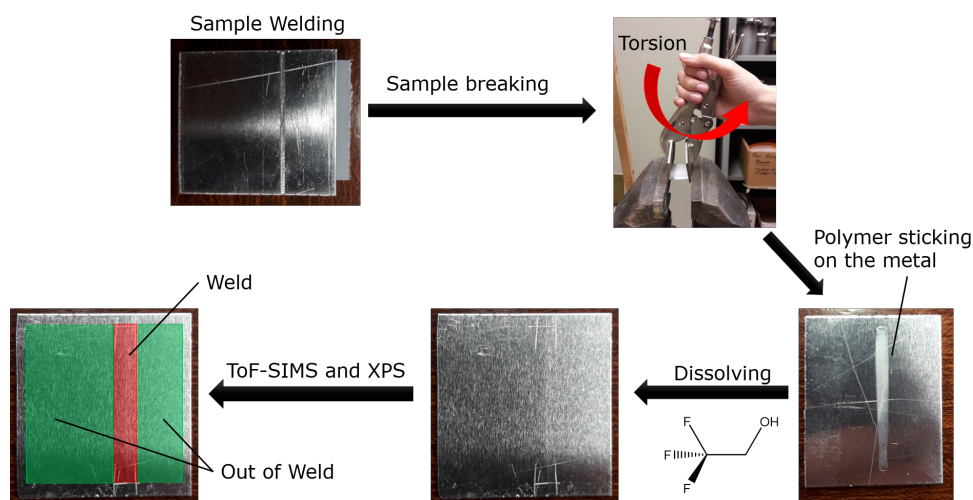


Figure 4.1: Strategy of preparation of the welded samples.

4.1.2.2 Spin-coated samples

These samples were prepared in order to really evaluate the influence of the welding at the interface. If possible also get insights on the reaction mechanism, and to study the diffusion phenomena. To prepare the spin-coated samples (see Figure 4.2) metal surfaces were first mirror polished, then ethanol cleaned, allowing the deposition of a polyamide-6.6 layer by spin-coating. The mirror polishing was done to study the diffusion and to limit the roughness impact on the experiments. Some of these samples were then treated by laser welding. The welded and not welded samples were then immersed in a 2,2,2-trifluoroethanol bath, to remove the residual polymer layer and so reach the interface. Three different zones were analyzed: reference, the out of weld and the weld. The reference was obtained with the non-welded samples. The out of weld and the weld were taken on the same samples and follow the same distinction as on the previous welded samples (see above).

4.1.2.3 Model samples

The model samples were designed for two reasons: checking in a third manner the nature of the chemical bond, and explaining the bond formation mechanism. Therefore, a molecule composed only of the chemically reactive part of the polymer (the amide function part) and easily processable for dip-coating was chosen: N-methylformamide. It was preferred to N-methylethanamide because it is liquid at room temperature. Indeed the melting point of N-methylethanamide is 28 °C. The metal surfaces were simply ethanol cleaned and then underwent

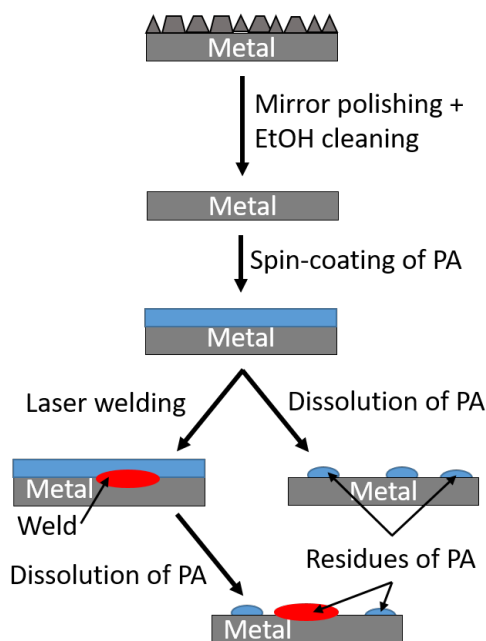


Figure 4.2: Strategy of preparation of the spin-coated samples.

a UV/O₃ cleaning. They were then dipped in pure liquid N-methylformamide (used as received). After the dipping, some were let to air dry and some were heated on a hot plate at 150 °C to simulate the effect of the welding. This temperature was chosen below the boiling point temperature of the molecule [249] which is around 186 °C (see Figure 4.3). The heating simulates the welding, even if it is half the welding temperature. As the reaction already occurs at room temperature as seen on the spin-coated samples (see chapter 6 part 6.3), heating at only 150 °C is sufficient to activate the reaction without desorbing or degrading the molecule too much.

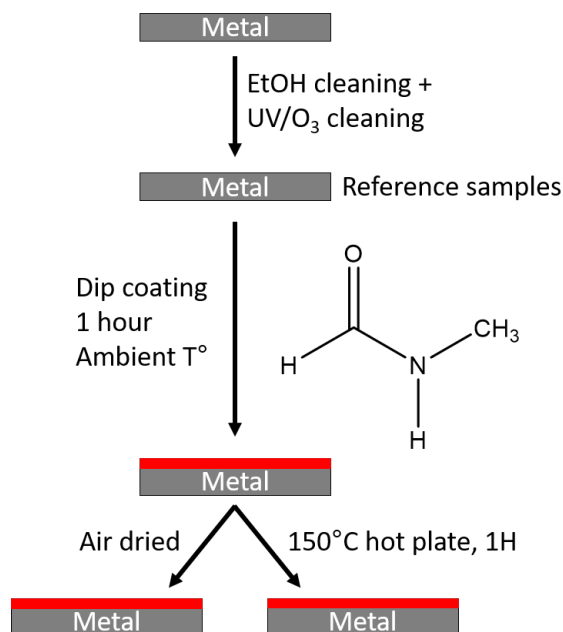


Figure 4.3: Process of preparation of the model samples.

4.1.3 Strategy of interpretation of the data collected in XPS and ToF-SIMS

For all samples, the XPS data was collected and analyzed first. This allowed to have a first insight, to verify the presence or absence of polyamide-6.6 or N-methylformamide. In XPS first the data was checked to see if there was any charging effect or any problems of that sort. Then, the survey spectra were interpreted using the combination of the automatic peak selection tool and the hand peak selection tool if needed (particularly the case for the titanium samples to find the vanadium peak). After that the high resolution spectra were calibrated using the C1s region by imposing the C-C/C-H bond at 284.8 eV. From the survey spectra, the presence of polymer is directly suspected or not, by looking at the nitrogen percentage. Knowing the composition, and based on the samples preparation (polymer, N-methylformamide, aluminum or titanium), the respective peak adapted to the bonding states for the different atoms were applied. For instance, in the N 1s region, as there are amide functions in the organic matter deposited on the surfaces, a peak around 399.8 eV should be present at least in the weld or heated samples. The same idea was followed for the other studied region. The peaks width was set to be equivalent for all peaks of the sample, with a slight difference tolerance of 0.2 eV. If the fit, using the peaks as described above, could not be made sufficiently satisfying (flatten sufficiently the residuals, i.e. the difference between the measured data and the fit), adding more peaks was considered. This addition was made in order to fit the data, then only the possible interpretation was considered using again the XPS database. If a possible interpretation was found, the peak was kept, if not it was moved in the binding energy in order to still fit the data but also fit a possible interpretation.

The ToF-SIMS measurement were performed after the XPS measurement and analysis as said above. With the knowledge gained during the XPS analysis, the interpretation of the mass spectrometry data is way easier. But prior to any analysis, the data needed a calibration. The spectra were calibrated using the same calibration peak list. This peak list was adapted to each type of sample. The peaks were chosen by looking at their ppm shift in order that this shift stays the lowest as possible. As the samples contained polymer and metal, peaks related to both materials were chosen to establish the calibration peak lists. After that the real work of data analysis was done. As the XPS demonstrated the presence of both metal and polymer (or N-methylformamide), peaks associated to both were selected for the peak list based on the data present in the library of the software. Since the goal was to analyze the interfacial chemistry, hybrid ions were carefully identified. For each family of hybrid ion, the selection was made as systematical as possible, by changing the chemical formula one element after another. For instance for the family $C_xH_yAl_z^-$, first the ion CAI^- , then $CHAI^-$, CH_2Al^- , ... then C_2Al^- , C_2HAl^- , and so on. If in the right region there was a peak, it was investigated to see if there could be an interference with another mass of an ion that would more surely occur or not. If there was no peak, the next ion was looked for. With these peak lists, the data could generally be understood and explained without the use of PCA. There was one type of sample, the titanium spin-coated samples, where this procedure could not allow to understand the data, so that a PCA was necessary on the selected peak list. Nonetheless, PCA was performed for all the samples in order to confirm the observation made and to acquire the skills to understand PCA. It is only at the end that automatically generated peak lists were used for PCA analysis. Even if they were not needed to get more knowledge and better understand the data, they allowed to show the strength of the hand made peak lists, as the results are sensibly similar in each case.

4.1.4 Diffusion

In order to highlight a possible diffusion phenomenon due to laser welding, specific samples have been prepared and analyzed. Time was lacking to perform a comprehensive diffusion analysis and only diffusion analysis was attempted on aluminum samples. The aluminum surfaces

were mirror polished. The polishing is necessary to reduce the roughness which would reduce the ability to characterize properly a diffusion effect. The next step is to spin-coat the samples with a layer of polyamide-6.6, like on the spin-coated samples. The samples were then welded. Then the samples were introduced in the ToF-SIMS instrument for depth profiling. Two depth profiles are obtained: one in the welded area, and one outside of the weld (see Figure 4.4).

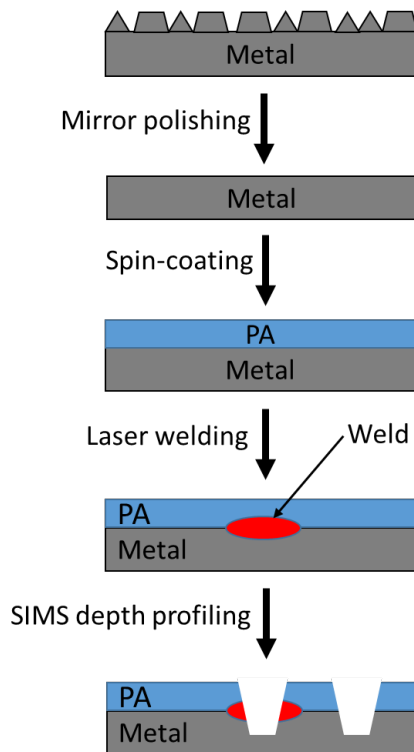


Figure 4.4: Scheme of the strategy to study the diffusion in laser welded metal/polymer systems.

4.2 Materials

4.2.1 Metals

4.2.1.1 Aluminum

Two different aluminum alloys were used: EN-AW1050A aluminum and 99.999% pure aluminum.

The first alloy, used for the pretreatment work, the welded and ablated welded samples, in 0.5 mm sheets was cut to $30 \times 70 \text{ mm}^2$. The alloy is composed of min. 99.5% of Aluminum, max. 0.05% of copper, max. 0.4% of iron, max. 0.05% of magnesium, max. 0.05% of manganese, max. 0.25% of silicon, max. 0.03% of titanium, max. 0.05% of vanadium and max. 0.05% of zinc.

The ultra-pure aluminum alloy was purchased from Goodfellow in plates of 1 mm thickness. They were processed into pieces of $20 \times 20 \text{ mm}^2$. The impurities present are: less than 0.2 ppm of copper, 0.577 ppm of iron, 0.439 ppm of magnesium and 0.847 ppm of silicon.

Table 4.1: Elemental composition of the two alloy used.

Alloy	%Al	%Cu	%Fe	%Mg	%Mn	%Si	%Ti	%V	%Zn
EN-AW1050A	99.5 %	max. 0.05 %	max. 0.4 %	max. 0.05 %	max. 0.05 %	max. 0.25 %	max. 0.03 %	max. 0.05 %	max. 0.05 %
Ti-6-4	6 %	/	/	/	/	/	90 %	4 %	/

4.2.1.2 Titanium

For the work on titanium, the only alloy studied was titanium-Al6-V4. This means that the alloy is composed by 90% of titanium, 6% of aluminum and 4% of vanadium. For the welded samples, the alloy purchased from Dutec, had a geometry of $0.5 \times 25 \times 75 \text{ mm}^3$. As for the spin-coated and the model samples, the same alloy was purchased from Goodfellow and cut down to $1 \times 20 \times 20 \text{ mm}^3$.

4.2.2 Organic materials

4.2.2.1 Polyamide-6.6 - Nylon66

Polyamide-6.6 or Nylon66, depicted in Figure 4.5, was used in two forms. The first one for the welded and ablated welded samples were plates cut to $25 \times 75 \times 4 \text{ mm}^3$ and obtained from Dutec (Germany). The second form used for the spin-coated samples and the diffusion was in pellets purchased at Sigma-Aldrich and used as received. Polyamide-6.6 has a glass transition temperature of around 70°C , a melting point at 264°C and a decomposition temperature of 466°C .

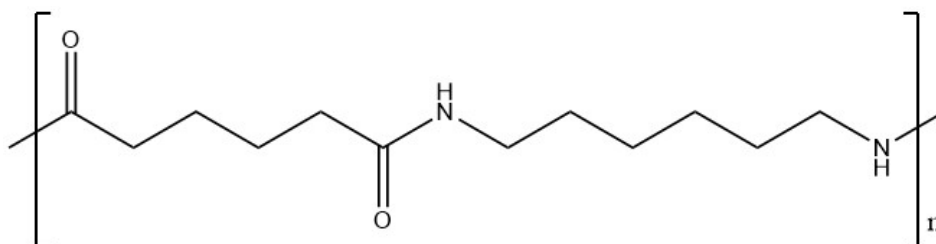


Figure 4.5: Chemical formula of polyamide-6.6.

4.2.2.2 N-methylformamide

N-methylformamide was purchased by Sigma-Aldrich and used as received. The chemical formula is represented in Figure 4.6. The melting point is at -4°C , the flash point is 111°C and the boiling point 186°C .

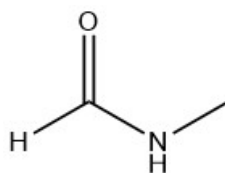


Figure 4.6: Chemical formula of N-methylformamide.

4.2.2.3 2,2,2-trifluoroethanol

2,2,2-trifluoroethanol was purchased by Alfa Aesar and used without further purification. The chemical formula is represented in Figure 4.7. The melting point is -44°C , the flash point 29°C and the boiling point 74°C .

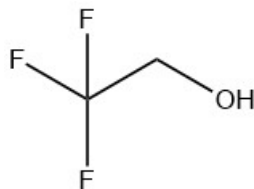


Figure 4.7: Chemical formula of 2,2,2-trifluoroethanol.

4.3 Sample preparation

4.3.1 Laser ablation (done at the University of Luxembourg)

Metallic surfaces were ablated by means of short pulsed (ns) Nd:YVO₄ laser, a TruMark 6130 from TRUMPF. The wavelength was 1064 nm and the spot size 45 μm . The parameters for all samples (aluminum and titanium) are presented in Table 4.2.

Table 4.2: Laser ablation parameters for the aluminum and titanium samples.

Samples	Pulse frequency (kHz)	Speed (mm.s ⁻¹)	Peak pulse power (kW)	% power
Al_1	85	250	11.00	100
Al_2	40	1000	35.00	100
Al_3	70	1000	15.00	100
Al_4	85	1750	11.00	100
Al_5	120	1750	5.00	100
Al_6	120	1750	4.75	95
Ti_1	43.89	160	32.00	100
Ti_2	40	160	37.37	100
Ti_3	23.89	193.5	65.00	100
Ti_4	34.17	3772.8	41.70	100
Ti_5	120	2500	5.00	10

4.3.2 Mirror polishing

The metal plates (aluminum and titanium) were mirror polished using an EcoMet 250 pro from Buehler. The first step was to polish the plates with a SiC foil of 1200 grit from Struers. Then diamond paste DiaDuo-2 from Struers of successively 9 μm , 3 μm and 1 μm were used to polish. The rotation was set at 120 rpm for the sample holder and 40 rpm in counterclockwise rotation for the grit plate with 22 N pressure during 5 min. The final polishing step was made using a 40 nm colloidal silicon OP-S from Streuers with 22 N pressure, 180 rpm sample holder speed and 40 rpm grit speed counterclockwise during 3 min.

4.3.3 Spin-coating

A 1% w/w PA-6.6 solution in 2,2,2-trifluoroethanol was spin-coated on the previously polished metal plates, using a Laurell WS-650-23B spincoater. The speed rotation was 1000 rpm for 1 min. After the samples were left to dry for one hour on a hot plate at 37 °C. The same conditions were used for the aluminum and the titanium samples.

4.3.4 Dip-coating

The aluminum surfaces were cleaned using a UVO cleaner model N° 42-220 from Jelight Inc. for 5 minutes. The samples used as reference were directly put into the XPS and ToF-SIMS machine for analysis. After the cleaning, the samples were immediately dipped in pure N-methylformamide for an hour at ambient temperature and pressure. For drying, the samples were then separated into two series. The first one was left to dry in ambient conditions overnight, and the second was put on a hot plate at 150 °C for an hour.

4.3.5 Laser welding (done at the University of Luxembourg)

The laser welding methodology we used has already been described by Lamberti [250] in 2014. The process is presented in Figure 4.8. The laser beam was obtained using fiber laser (TruFiber 400) from TRUMPF. The laser has a wavelength of 1070 nm with a spot size of 31 μm . The focus of the laser was set to the metal surface. The beam followed a wobbling trajectory in order to diminish the energy flux deposited at the surface. The beam was pulsed at the same time to avoid material deterioration (especially the polymer). The parameters are detailed in Table 4.3.

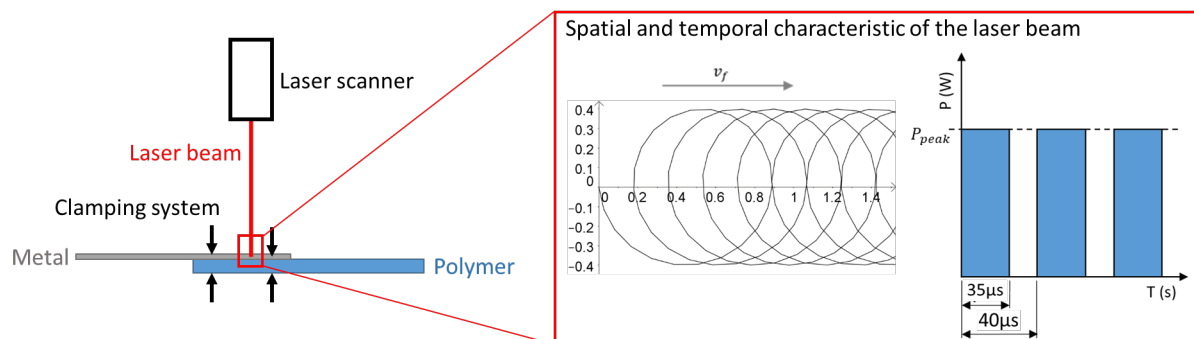


Figure 4.8: Scheme of the laser welding process.

4.3.6 Accessing the interface

4.3.6.1 Assembly breaking

The welded samples were clamped in a bench vice by the metal part. Using clamps a torsional load was applied to the polymer so that it breaks near the interface. On the aluminum samples the failure mode is cohesive in the polymer, leaving a thick polymer residue on the aluminum surface. So, no direct analysis of the interface can be performed. On the titanium samples, the failure mode is mixed, adhesive and cohesive in the polymer. The XPS and ToF-SIMS measurements were done on the adhesive failure mode parts.

Table 4.3: Welding parameters.

Samples	Al-PA welded	Al-PA spin-coated	Ti-PA welded	Ti-PA spin-coated
Peak pulse power (in W)	400	400	60	60
Speed (mm.s ⁻¹)	88.8	40	900	900
Temporal frequency (in Hz)	25000	25000	25000	25000
Pulse duration (in μ s)	35	35	35	35
Wobble amplitude (in mm)	0.4	0.4	0.4	0.4
Circular oscillation frequency (in Hz)	500	500	500	500

4.3.6.2 Dissolving

The residual polymer sticking on the samples' metallic side was dissolved by dipping the samples in 100 mL 2,2,2-trifluoroethanol at room temperature under mechanical agitation at 150 rpm overnight.

4.4 Sample analysis

4.4.1 Roughness (done at LIST)

3D profilometry measurement was performed on the polished metal plates on a KLA Tencor P17 according to ISO 4287. Areas of $0.1 \times 0.1 \text{ mm}^2$ were analyzed with a resolution of $1 \times 1 \mu\text{m}$ in order to calculate the mean arithmetical height value R_a , the average quadratic height R_q and the average quadratic slope R_{dq} .

4.4.2 Profilometry - Spin-coating thickness (done at LIST)

The polyamide-6.6 coatings were peeled-off locally by means of a rigid polymer tip. Step height measurements, 3 experiments per sample, were performed by a Asylum MFP3D Infinity atomic force microscope (AFM) purchased from Oxford instruments. Measurements were performed in AC air topography (intermittent contact) mode with a AC160 tip from Asylum Research, whose resonance frequency and stiffness are approximately 300 kHz and 26 N/m, respectively.

4.4.3 Scanning electron microscopy – SEM (done at LIST)

A pressure-controlled FEI Quanta FEG 200 scanning electron microscope from FEI Company is used in secondary electron mode to get information about the samples morphology. The acceleration voltage is generated at 10 kV.

4.4.4 Joint area assessment (done at the University of Luxembourg)

In order to quantify the joint area, a dedicated experimental approach was developed. First, macroscopic images of the joint interface after failure were obtained using a digital FUJIFILM

X-Pro2 camera. Next, the dimensions of a single pixel was measured using GIMP software by correlating to a predefined scale positioned on the sample close to the weld zone. Then, the coordinates outlining the joint area were allocated and the joint area was measured by counting the number of pixels and correlating them to the measured pixel dimension. Stitched and polarized microscopic images of the joint area were used to confirm the measurements.

4.4.5 Laser flash analysis – LFA (done at the University of Luxembourg)

In order to prepare ablated samples for LFA, they were cut to 1cm² squared geometry using an Accutom 50 dicing tool from Struers. Then, ablated samples were arranged in layered configuration together with 1 mm thick polished aluminum sample having the same dimensions as the ablated ones as shown in Figure 4.9. Samples were coated on both external faces using Graphit 33 spray from Kontakt Chemie containing 1-5 w/w % of graphite powder in order to have a consistent absorbance to the laser beam, and consistent emissivity to the IR detector.

Laser Flash Analysis (LFA) test was performed by a Netzsch LFA 457 Microflash machine at room temperature. A single flash (0.5ms) from Nd-Yag laser was irradiated on the untreated surface of the ablated aluminum sample as illustrated in Figure 4.9. The LFA chamber was filled with a dry argon gas during the experimentation in order to reduce the influence of moisture on the measurement of the thermal properties. An infrared detector (InSb photodiode) was used to monitor the temperature transient at the back face. The output voltage of the laser was fixed at 1922 V for all experiments. A duration of 60 ms was used for the acquisition time of the IR detector.

Layered configuration (Figure 4.9) was used in order to calculate TCR generated by the particular geometry of the rough ablated surface in contact with a flat surface [251]. It is difficult to calculate the exact TCR between PA and Al using LFA with such layered configuration due to experimental challenges resulting from the low thermal conductance of PA. Therefore, the rough ablated aluminum is brought into contact with another flat aluminum sample. Thermal diffusivity of the layered system is evaluated from the measurement of temperature increase as a function of time at the back face of the polished aluminum, i.e the side facing the IR sensor. Then the density, thickness, thermal diffusivity, and specific heat of both materials were predefined to that of pure aluminum, kept constant for all tested samples, and used to calculate TCR based on the algorithm developed by Hartmann et al. [252].

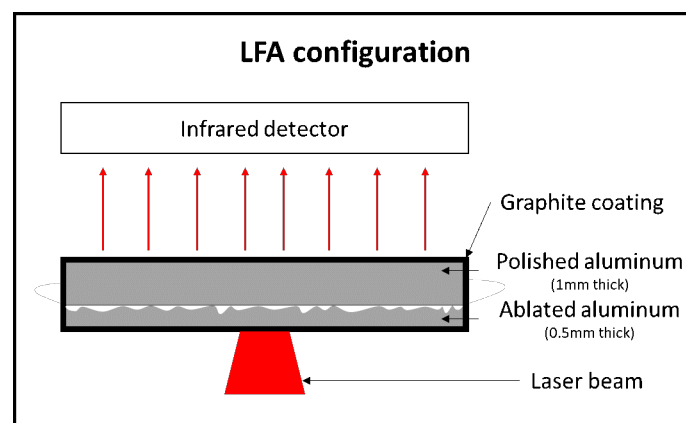


Figure 4.9: laser flash analysis layered configuration.

4.4.6 Shear load tests (done at the University of Luxembourg)

The joints' resistance to failure was quantified by performing single lap shear tests using a Z010 tensile testing machine from Zwick/Roell. During those tests, samples were clamped in vertical alignment having a jaw-to-jaw distance of 75 mm, and a crosshead speed of 2.21 mm/min.

4.4.7 X-ray Photoelectron Spectroscopy - XPS

4.4.7.1 General principle

XPS measurements are based on the photoelectric effect, which was historically first observed by Antoine Becquerel and his son Alexandre Edmond Becquerel in 1839. They could not explain it and did not perform further experiment on it. Nearly fifty years later, in 1887, Heinrich Rudolph Hertz performed more detailed experiments on this phenomenon, but neither could give a satisfactory explanation for it. Finally Albert Einstein proposed a complete explanation in 1905, for which he received the Nobel Prize in Physics in 1921. Nevertheless, it is only in the 1960s that Kai Siegbahn developed the ESCA (electron spectroscopy for chemical analysis) later known as XPS, for which he got the Nobel Prize in Physics in 1981.

The photoelectric effect is the capacity of materials to emit electrons by absorbing a photon (see Figure 4.10). The electrons are then called photoelectrons. The higher the energy of the photons the deeper in energy the emitted photoelectrons will be. For instance, if UV light (3.2-124 eV) is shone on a metallic surface only the electrons from the valence level can be detected, but if X-rays (0.124-124 keV) are shone then core electrons can be detected.

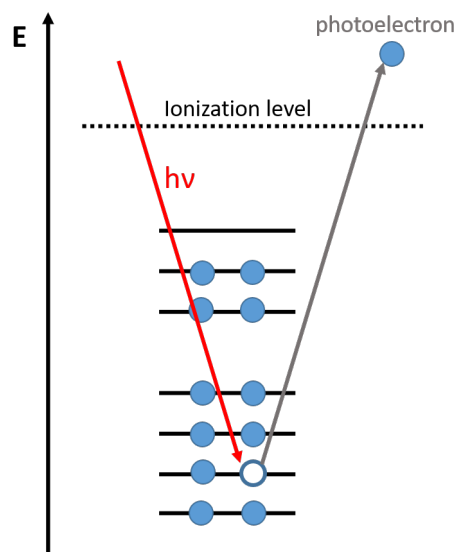


Figure 4.10: scheme of the photoelectric effect.

Figure 4.11 depicts the measurement process of an XPS spectrum. The sample, placed in ultra high vacuum, is illuminated with a monochromated X-ray gun generating photoelectrons from the studied material. The created charges at the surface of insulators are compensated with the help of an electron flood gun. The emitted photoelectrons are guided to the energy analyzer through a lens system. The photoelectrons arriving in the energy analyzer do have different kinetic energies depending on the nature of the atoms, the electronic level and the chemical environment they originate from. The energy analyzer deflects the photoelectrons in order to measure their kinetic energy. Since the X-ray beam is monochromated, the binding

energy (BE) can be calculated by subtracting the kinetic energy (E_c) and the work function (ϕ) to the X-ray beam energy ($h\nu$):

$$BE = h\nu - (E_c + \phi) \quad (4.1)$$

As written above the kinetic energy of the photoelectrons differs depending on the nature of the atom, the electronic level and the chemical environment. The first separation is done by the nature of the atom and the electronic level studied, for example C 1s appears around a binding energy of 285 eV, while Al 2p appears around 73 eV, but Al 2s will be measured around 118 eV. Since the different atoms are well defined in energy in an XPS spectrum, and since the number of photoelectrons, or their measured intensity, is directly related to the number of atoms present in the measured volume, the amount of each element can be calculated. The second separation is due to the chemical environment, which is called chemical shift. The chemical environment will slightly perturb the energy level, which is measurable in XPS, and allows to make chemical characterization. As a general rule, the higher the oxidation state of an atom, the higher the binding energy and vice versa. For instance, looking at the C 1s region an aliphatic carbon will be characterized by a peak at 284.8 eV and if there is an alcohol function in the chain a peak around 286 eV will be visible. The last term of the equation (ϕ) is the work function term, and characterizes the energy needed to extract the photoelectrons from the materials.

The energy analyzer is composed of two hemispherical electrodes, with different radii R_1 and R_2 . Different potentials can be applied to the hemispheres V_1 and V_2 respectively. The photoelectrons arrive with an energy E in the electric field created by the hemispheres, where the electric force will deflect them:

$$F_e = -e|E(r)| \quad (4.2)$$

where F_e is the electric force, e the charge of an electron and $E(r)$ the electric field, which can be written as:

$$|E(r)| = \left(\frac{V_2 - V_1}{R_2 - R_1} \right) \frac{R_1 R_2}{r^2} \quad (4.3)$$

or:

$$V(r) = \left(\frac{V_2 - V_1}{R_2 - R_1} \right) \frac{R_1 R_2}{r} + const. \quad (4.4)$$

In order that the photoelectrons with an energy E_0 follow a circular trajectory, the electrical force must act as a centripetal force. The circular trajectory has a radius of R_0 that is the middle of the distance between the two hemispherical electrodes. These electrons are subjected to an electric potential V_0 that can be expressed in eV:

$$V_0 = \frac{E_0}{e} \quad (4.5)$$

This equation can be applied to define the pass energy, which allows to select the energy:

$$E_0 = |e|V_0 \quad (4.6)$$

Using those equations, one can calculate the potential difference between the two hemispheres that needs to be applied:

$$V_2 - V_1 = V_0 \left(\frac{R_2}{R_1} - \frac{R_1}{R_2} \right) \quad (4.7)$$

During the measurement the potential difference will remain the same for each pass energy. In order to be able to measure different zone in the spectra, the electrons first go through an electro-optical system, that collects and decelerates the electrons to the kinetic energy E_0 . The electron detector consists simply in several channeltrons assembled together. The principle of a channeltron uses secondary generated electrons to increase the number of electrons, which can be detected at the end. So when the photoelectrons enter the channeltron, they will necessarily hit the walls of the channeltron and generate more electrons, which will also hit the walls and generate even more electrons and so on till the end of the channeltron where a current can be measured. The energy resolution depends on the geometrical properties of the analyzer and the angular divergence of the incoming electrons:

$$\Delta E = E_0 \left(\frac{\omega}{2R_0} + \frac{\alpha^2}{4} \right) \quad (4.8)$$

where ω is the average width of the two slits (aperture of the analyzer at the entrance and at the detector) and α the incident angle of the photoelectrons. From this equation, it can be seen that the higher the pass energy (E_0), the higher the ΔE , so the lower the resolution. The survey spectra are taken with a high pass energy (200 eV), meaning that the spectra have a low resolution. They can only be used to determine the elemental composition, since the resolution does not permit to characterize precisely the chemical shift. Therefore high resolution spectra of the studied element are acquired, by using a low pass energy (20 eV), which diminishes the ΔE , and increases the resolution up to 0.1 eV in our case.

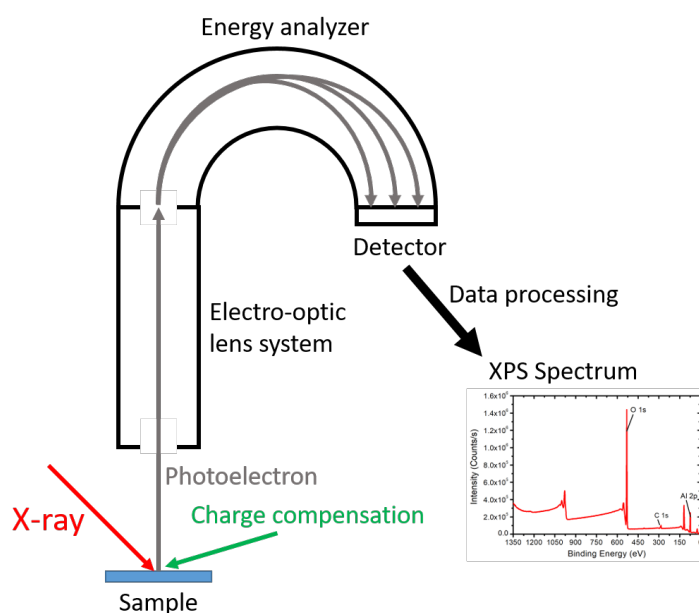


Figure 4.11: scheme of the principle of XPS measurement.

The measurement has a limited probing depth, which depends on the mean free path of the photoelectron. The photoelectron mean free path depends directly on the photoelectron energy, therefore on the wavelength of the incident beam. Generally the probing is then estimated to be between 10-15 nm, which explains why XPS is referred to as a surface sensitive technique [253–255]. Though XPS is considered as non-destructive, this should be nuanced, since there are several studies showing damaging of the surfaces due to XPS measurements [255–257]. In order to analyze materials in the bulk or for multilayered materials, the possibility exists to do

depth profiling. The measurement is then alternated with an etching step performed by an ion beam.

4.4.7.2 Measurement parameters

All the measurement were performed on a Thermo Fisher Scientific K-alpha spectrometer equipped with a monochromated Al $K\alpha$ X-ray source at 1486 eV. The same measurement parameters were used for all samples and have been summarized in Table 4.4. Depending on the samples the high resolution spectra were taken for different elements (see Table 4.5). The number of measurement points was adapted to check reproducibility enabling statistically meaningful results. If possible three samples of teh same types were prepared on which three measurement point were taken, leading to nine points for each samples. For instance, on the spin-coated samples, the measurement on the reference samples, leaded to nine points.

Table 4.4: XPS measurement parameters.

Spectra type	Number of scans	Pass energy (in eV)
Survey	3	200
High resolution (C 1s, Al 2p, O 1s,...)	20	20

Table 4.5: High resolution spectra measured per type of sample.

Sample type	Region measured
Aluminum surfaces	Al 2p, C 1s, O 1s, N 1s
Titanium surfaces	Ti 2p, C1s, O 1s, N1s, Al 2p, V 2p
Polyamide-6.6 surfaces	C 1s, O 1s, N 1s

4.4.7.3 Some comments on the spectra analysis

The strategy of data analysis used for all the samples is detailed in part 4.1.2.4. As a reminder, first the survey spectra were analyzed to get the surface elemental composition. This allowed to test the hypothesis of the residual polymer or molecule, as their presence is characterized by a higher nitrogen percentage. If it was confirmed, the high resolution spectra were calibrated using the C 1s region, by imposing the C-C/C-H bond at 284.8 eV. The peaks were then added to fit the spectra at best regarding the existing XPS database (www.xpsfitting.com for instance) and the literature. The width of the peak measured by the FWMH was systematically set to be equivalent with a tolerance of 0.2 eV.

4.4.7.3.1 Estimation of the aluminum oxide thickness

In 1990, Strohmeier [258] proposed a way of calculating the oxide thickness on a metal. The study is centered on the aluminum oxide thickness, but the author claims that it could be used for any metal, by adapting the parameters in the calculus. To the best of our knowledge no one uses this on any other metal than aluminum. The model makes some assumptions. The first one is to consider a “uniform overlayer model”, that is to say that the top surface of the oxide and the interface metal/oxide are considered as atomically flat. The second assumption is to consider the chemical composition of the oxidized layer similar to that of γ -Al₂O₃, even if the oxidized layer is a mixture of hydroxide and oxide [259]. This assumption allows then to consider the molecular volume of the oxidized layer as constant and nearly 1.5 times larger than

that of pure metal. Based on those assumptions and the work of Carlson [260] who proposed in 1982 the following equation:

$$\frac{I_m}{I_o} = \frac{N_m \lambda_m}{N_o \lambda_o} \frac{\exp\left(-\frac{d}{\lambda_o \sin \theta}\right)}{1 - \exp\left(-\frac{d}{\lambda_o \sin \theta}\right)} \quad (4.9)$$

where I_m and I_o are respectively the intensity of the metal and the oxide peak in the Al 2p high resolution spectrum; N_m , N_o are the volume densities of metal atoms in the metal and the oxide respectively; λ_m and λ_o are the inelastic mean free paths of the photoelectron for the metal and the oxide respectively; d the oxide thickness (in Å) and θ the electron take-off angle. This equation can easily be transformed to calculate the oxide thickness:

$$d = \lambda_o \sin \theta \ln \left(\frac{N_m \lambda_m}{N_o \lambda_o} \frac{I_o}{I_m} + 1 \right) \quad (4.10)$$

Since the XPS machine used has an Al K α X-ray radiation (1486.6 eV), the parameters are set at $\lambda_m = 26$ Å, $\lambda_o = 28$ Å and $N_m/N_o = 1.5$, the equation can be transformed into:

$$d(\text{Å}) := 28 \ln \left(1.4 \frac{I_o}{I_m} + 1 \right) \quad (4.11)$$

This calculation gives a good estimate of the oxidized layer thickness, but should be used with caution, because the model does completely neglect the roughness and the real chemical composition of the oxidized layer.

4.4.7.3.2 Estimation of the aluminum hydroxide/oxide ratio

In order to calculate the ratio of aluminum hydroxide/oxide, two information are needed: the percentages of oxygen and aluminum involved in the oxidized layer. For example, if on the survey spectrum there is 20 % of oxygen and by analyzing the high resolution spectra 50 % of the oxygen is involved in the aluminum oxide, the oxidized oxygen percentage is then 10 %. The same goes for aluminum.

To get the oxidized aluminum percentage $X_{Al,ox}$, the high resolution Al 2p spectrum is analyzed. Generally there are two main contributions, one metallic and one from oxidized aluminum. Since the two contributions are clearly defined, one can calculate the percentage of aluminum that is oxidized $x_{Al,ox}$. With this value, and the percentage of aluminum from the survey spectrum X_{Al} it is very easy to calculate $X_{Al,ox}$, using this formula:

$$X_{Al,ox} = \frac{X_{Al} \times x_{Al,ox}}{100} \quad (4.12)$$

For the oxide oxygen percentage $X_{O,ox}$, it is more complicated since the high resolution O 1s spectrum is quite difficult to analyze surely, because the chemical shifts are very low for oxygen, so all oxygen contribution have pretty similar energies. On the aluminum surfaces, there are two oxygen contribution: from the aluminum oxide and from the adventitious oxygen. The contribution of the “adventitious oxygen” can be calculated from the carbon spectrum. The methodology was proposed in 2011 by Payne et al. [261]. The calculation they proposed is to take the percentage of each type of contribution: C-OH, C-O-C, C=O, O-C=O, and CO₃⁻ from the C 1s spectrum, and the total percentage of carbon and oxygen to calculate the oxidized oxygen percentage, following the equation:

$$X_{O,ox} = X_O - \frac{X_C}{100} \left[3x_{CO_3} + \frac{3}{2}x_{O-C=O} + x_{C=O} + \frac{2}{3} \left(x_{C-OH,C-O-C} - \frac{1}{2}x_{O-C=O} \right) \right] \quad (4.13)$$

As written above the oxidized aluminum layer is composed of a mixture of oxide (Al_2O_3) and hydroxide ($\text{Al}(\text{OH})_3$), which can be summarized in the following chemical formula: $\text{AlO}_x(\text{OH})_y$. In order to calculate x and y , the first step is to define the ratio R of the corrected percentages of oxygen and aluminum:

$$R = \frac{X_{O,ox.}}{X_{Al,ox.}} \quad (4.14)$$

because of the chemical formula defined above, the ratio R can also be written like:

$$R = x + y \quad (4.15)$$

the assumption is made that the oxidized layer has a neutral charge, so that the atomic valences of the atoms gives this equation:

$$3 = 2x + y \quad (4.16)$$

by solving the two last equations, x and y can be written as:

$$\begin{cases} x = 3 - R \\ y = 2R - 3 \end{cases} \quad (4.17)$$

which in the end allows to calculate the ratio of hydroxide and oxide like that:

$$R_{Hydr./Ox.} = \frac{y}{x} = \frac{2R - 3}{3 - R} \quad (4.18)$$

The calculation is limited by the fact that R , by definition, has to be comprised between 1.5 and 3. These are the extreme values to get respectively a pure oxide or a pure hydroxide. The final ratio $R_{Hydr./Ox.}$ should be considered as an estimate, because the calculated percentages $X_{Al,ox}$ and $X_{O,ox}$ depend directly from the user's fitting of the different spectra. Indeed each user might analyze the spectra slightly differently which as consequence will give different peak area for the different contributions, leading to differences in the calculations. Nonetheless, it seems an interesting way of estimating if the surface chemical composition.

4.4.8 Time of Flight Secondary Ion Mass Spectrometry - ToF-SIMS

4.4.8.1 General principle

Thomson made the first observations of ion sputtering in 1910. The basic work to develop the first SIMS technology was only done around 1949 by Herzog and Viehboek at the University of Vienna. In the late 1950's two independent projects of SIMS machine were developed, the first one in the United States of America and the second one in France. This led to the commercialization of two machines by GCA Corp. and CAMECA. At the time the mass analyzer was a magnetic analyzer. In the 1970's prof. Alfred Benninghoven and Klaus Wittmack developed the use of quadrupole analyzer, and finally in the early 1980's time-of-flight analyzer were integrated on SIMS machines. Since then several developments were made, by adding different ion gun sources (Ga, Bi_n, Ar_n, O₂, Xe, Cs, Cn), broadening the possibility to do profiling with different etching sources and analyze different materials, and so on. For more details on the history the reader is advised to read "*ToF-SIMS: Materials Analysis by Mass Spectrometry*" [163].

Figure 4.12 depicts the working principle of a ToF-SIMS measurement. First the sample is bombarded by a primary ion beam, which will sputter fragments away from the surface. These fragments can be of different nature: neutral molecular fragments and ionic molecular fragments. The ionic molecular fragments are called secondary ions and can be positive or negative ions.

They are then extracted to the time of flight analyzer with the help of a high electric field. The voltage is positive to extract negative ions and negative for positive ions.

The analyzer used is a time-of-flight analyzer. The principle of this analyzer is to measure the time a particle takes to go from the extractor to the detector, the so-called time-of-flight. The particles are extracted using the same voltage U , meaning that the potential energy E_p of the particles is equal to:

$$E_p = qU \quad (4.19)$$

where q is the charge of the particles. In the time-of-flight analyzer the potential energy is completely converted into kinetic energy E_c :

$$E_c = E_p \quad (4.20)$$

since all the particles receive the same potential energy, and so the same kinetic energy, their velocity depends directly of their masses:

$$v = \sqrt{\frac{2qU}{m}} \quad (4.21)$$

with v the velocity of the particles and m their mass. Since the time-of-flight analyzer is free of any field, the velocity remains constant and can also be written as dependent from the distance d (the distance of the trajectory in the analyzer which is known) and the time t :

$$v = \frac{d}{t} \quad (4.22)$$

therefore the time can be expressed as:

$$t = \frac{d}{\sqrt{2U}} \sqrt{\frac{m}{q}} \quad (4.23)$$

As shown in Figure 4.12, the analyzer used is indeed an ion mirror –also called a reflectron– which does not significantly change the equation presented above, and presents two advantages. The first and simple one, is that for the same distance, the tool takes less place; it is more compact. The second advantage and the most important, is that it improves the mass resolution, by compensating the slight kinetic energy differences between fragments of the same mass. Another great advantage of the time-of-flight analyzer is the capacity to measure all the sputtered ions at the same time (parallel acquisition). In conclusion the ToF analyzer is a good compromise between the mass resolution and the mass range. The analysis beam is pulsed for synchronization purposes, but the shorter the pulse is, the better the mass resolution is.

There are three different analysis modes: static mode, imaging mode, and profiling mode. The static mode consists in acquiring a mass spectra on surfaces to characterize materials. The imaging mode allows to make a chemical image showing where specific ions are originating from on the analyzed surface. Large chemical images may be obtained by using the stitching mode, which is simply the assembly of several smaller pictures, taken in siding zones, to obtain a greater picture. The profiling mode is simply the analysis in depth of materials. This is done by interlacing the analysis –primary ion beam, extraction and detection– and an etching beam. Since there are two different beams (analysis and etching), it is called dual beam analysis. In some cases, the two beams are the same. The data obtained is three dimensional with a high depth resolution.

When the primary ion beam reaches the surface a collision cascade takes place, leading to the ejection of some fragments. The number of ejected ionized species (called the intensity) depends

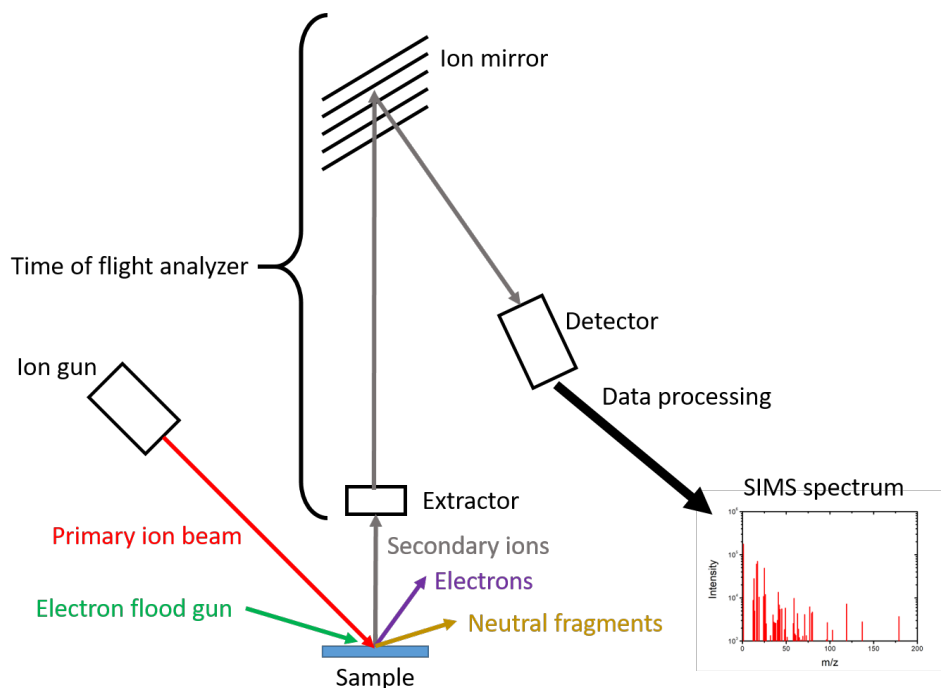


Figure 4.12: Scheme of SIMS measurement.

on the primary ion beam (chemical nature and energy), but also on the nature (chemistry and structure) of the studied materials which is called the matrix effect. The intensity of the measured species depends on the sputter yield of the ejected fragments and more importantly on the probability of ionization of the ejected species. This is well described by the “basic SIMS equation”:

$$I_m = I_p y_m \alpha^\pm \theta_m \eta \quad (4.24)$$

where I_m is the secondary ion current of species m , I_p the primary particle flux, y_m is the sputter yield, α^\pm the ionization probability to positive or negative species respectively, θ_m is the fractional concentration of the molecular or elemental species, m in the surface layer and η the transmission of the analysis system. These parameters make SIMS a very sensitive, semi-quantitative as well as a destructive analysis technique.

After the sputtering due to the primary ion beam bombardment, there is an ionic gas very near the surface called the selvedge [262–264]. Secondary ions expelled from this selvedge have three different origins: direct emission, rearrangement, and recombination (see Figure 4.13). Direct emission consists simply in secondary ions directly expelled from the surface, that undergo no changes until they reach the detector. Rearrangement occurs when the expelled secondary ions, reorganize themselves to be more stable. The last phenomenon is recombination, when the expelled secondary ions react with each other, because of chemical affinity (generally due to the charges of the ions). To the best of our knowledge, studies dealing with recombination are rare and generally old before the 2000’s [265–273].

4.4.8.2 Measurement parameters

Mass spectra were measured using an ION TOF IV. All the spectra of the same type of samples were calibrated using the same peaks and the peak list was the same. The strategy of the data analysis used is detailed completely in part 4.1.2.4. To sum up, the XPS data was

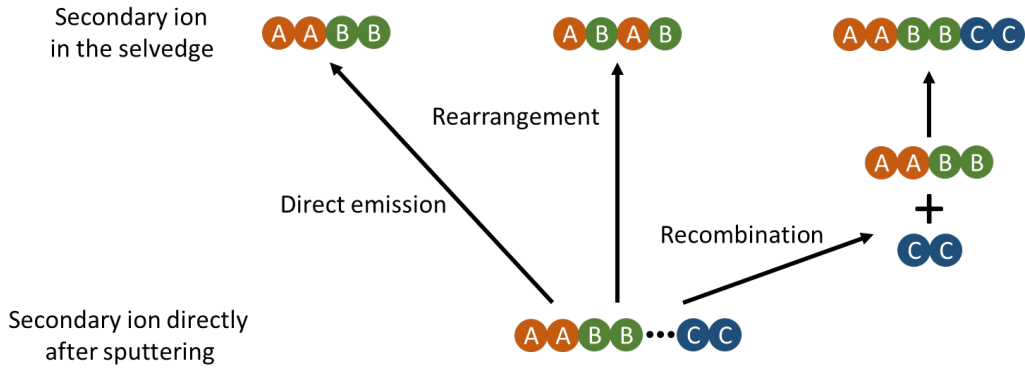


Figure 4.13: Scheme of the possible reactions for secondary ions in the selvedge.

analyzed before analyzing the samples in SIMS. From the XPS data, the presence of polymer or N-methylformamide and the metal was already confirmed, so looking for their respective characteristic peaks was natural. The selection of the hybrid peaks was made systematically by looking at each possibility. With the peak lists obtained, the data could be interpreted correctly and PCA analyses were generally not required, out of the titanium spin-coated samples, where it helped to analyze the data.

4.4.8.2.1 Static spectra

Static spectra were acquired using a 25 keV Bi_3^+ analysis beam with a pulsed current in both positive and negative mode during 60 s at 45° from normal. The raster size, so the size of the analyzed area, was of $200 \times 200 \mu\text{m}^2$. In Table 4.6, the measurement currents and the calibration peak list for each type of sample in positive and negative mode are presented. For each sample type and mode, the same calibration peak list was used, as well as the same peak list was applied. The spectra were normalized on their respective total intensity for comparison purposes.

4.4.8.2.2 Large area images

Large area images in stitching mode (combination of several small images to make a larger image) at the border between the weld and the out of weld were obtained in both positive and negative mode. A 25 keV Bi_3^+ ion beam has been used. The size of the images was set to $1500 \times 1500 \mu\text{m}^2$ with the stitching of 3×3 images of $500 \times 500 \mu\text{m}^2$. Images were taken only on the welded and ablated welded for both aluminum and titanium, and the same calibration and peak list were used as for the static spectra of the same sample type (see Table 4.6).

4.4.8.2.3 Depth profiling

The depth profiles were performed using a 500 eV Cs^+ beam with a current of 31.4 nA combined with a 25 keV Bi_3^+ analysis beam during 20 min. The current and the calibration peak list can be found in Table 4.7. The raster sizes of the profiling beam was of $400 \times 400 \mu\text{m}^2$ and $200 \times 200 \mu\text{m}^2$ for the analysis beam.

4.4.9 Principal Component Analysis - PCA

Principal component analysis (PCA) was introduced first in 1901 by Karl Pearson [274]. The methodology was further developed in the 1930's by Harold Hotelling [275]. PCA is one of many multivariate analysis techniques, but the most commonly used in the SIMS community. Two

Table 4.6: Measurement current, and calibration peak list in the positive and negative mode for each sample type.

Samples	Measurement current	Mass resolution in positive/negative	Calibration peak list in positive mode	Calibration peak list in negative mode
Aluminum welded	0.42 pA	6400 (CH ₄ N ⁺) / 5500 (Al ⁻)	CH ₃ ⁺ , Mg ⁺ , AlH ⁺ , Ca ⁺ , C ₂ H ₃ O ⁺ , CH ₂ NO ⁺ , CH ₄ OAl ⁺ , C ₅ H ₁₂ N ₃ ⁺	C ⁻ , CH ⁻ , Al ⁻ , C ₂ HO ⁻ , C ₂ H ₃ O ₂ ⁻ , C ₅ ⁻ , C ₆ ⁻ , Al ₃ O ₄ ⁻
Aluminum ablated welded	0.28 pA	3700 (CH ₄ N ⁺) / 3400 (Al ⁻)	CH ₃ ⁺ , Mg ⁺ , AlH ⁺ , Ca ⁺ , C ₂ H ₃ O ⁺ , AlOH ⁺ , C ₃ H ₉ NO ₂ ⁺	CH ⁻ , NH ⁻ , C ₂ H ⁻ , Cl ⁻ , C ₃ ⁻ , AlO ⁻ , C ₅ H ⁻ , Al ₃ O ₄ ⁻
Aluminum spin-coated	0.43 pA	5500 (CH ₄ N ⁺) / 4400 (Al ⁻)	CH ₃ ⁺ , Mg ⁺ , AlH ⁺ , Ca ⁺ , C ₂ H ₃ O ⁺ , CH ₂ NO ⁺ , CH ₄ OAl ⁺ , C ₅ H ₁₂ N ₃ ⁺	C ⁻ , CH ⁻ , C ₂ ⁻ , C ₂ HO ⁻ , AlO ⁻ , AlO ₂ ⁻ , C ₂ H ₃ O ₂ ⁻ , C ₅ ⁻ , C ₆ ⁻
Aluminum model	0.31 pA	6500 (CH ₄ N ⁺) / 5800 (Al ⁻)	CH ₃ ⁺ , CH ₂ N ⁺ , C ₃ H ₃ ⁺ , AlOH ⁺ , C ₄ H ₇ ⁺ , AlO ₂ H ⁺ , AlO ₂ H ₂ ⁺	C ⁻ , CH ⁻ , C ₂ ⁻ , Al ⁻ , Cl ⁻ , AlO ⁻ , C ₂ H ₃ O ⁻ , C ₂ H ₂ O ₂ ⁻ , AlO ₂ ⁻
Titanium welded	0.23 pA	5300 (CH ₄ N ⁺) / 3900 (CN ⁻)	C ⁺ , CH ⁺ , CH ₂ ⁺ , CH ₃ ⁺ , C ₂ H ₃ ⁺ , C ₂ H ₅ ⁺ , Ti ⁺ , TiO ⁺ , C ₅ H ₁₂ N ⁺	C ⁻ , NH ⁻ , F ⁻ , C ₂ ⁻ , C ₃ ⁻ , C ₄ ⁻ , C ₃ H ₂ N ⁻ , C ₅ ⁻ , TiO ⁻ , C ₆ ⁻
Titanium spin-coated	0.20 pA	4700 (CH ₄ N ⁺) / 4700 (CN ⁻)	CH ₃ ⁺ , CH ₂ N ⁺ , C ₂ H ₅ ⁺ , CH ₄ N ⁺ , C ₃ H ₅ ⁺ , C ₄ H ₅ ⁺ , C ₅ H ₅ ⁺ , TiO ₂ H ⁺ , C ₇ H ₇ ⁺ , Ti ₂ O ₄ H ₂ ⁺	CH ⁻ , NH ⁻ , Cl ⁻ , C ₃ ⁻ , C ₄ ⁻ , C ₅ ⁻ , TiO ⁻ , C ₆ ⁻ , TiO ₂ ⁻ , CHNOTi ⁻
Titanium model	0.34 pA	5400 (CH ₄ N ⁺) / 4400 (CN ⁻)	CH ₃ ⁺ , CH ₂ N ⁺ , CH ₃ O ⁺ , Ca ⁺ , C ₂ H ₃ O ⁺ , C ₄ H ₅ ⁺ , C ₅ H ₅ ⁺ , TiO ₂ H ⁺ , C ₇ H ₇ ⁺ , Ti ₂ O ₄ H ₂ ⁺	CH ⁻ , NH ⁻ , F ⁻ , C ₂ ⁻ , Cl ⁻ , C ₃ ⁻ , C ₄ ⁻ , C ₅ ⁻ , TiO ⁻ , TiO ₂ ⁻ , CHNOTi ⁻

Table 4.7: Measurement current, and calibration peak list.

Sample	Measurement current	Mass resolution	Caibration peak list
Aluminum coated	0.45 pA	3600 (Al ⁻)	CH ⁻ , CH ₂ ⁻ , Cl ⁻ , C ₃ ⁻ , C ₅ H ⁻ , C ₆ ⁻ , Al ₂ O ₂ ⁻ , Al ₃ O ₄ ⁻

books serve as reference for introduction to PCA in the SIMS community: “Surface Analysis: The Principal Techniques” written by John C. Vickerman and Ian S. Gilmore [162], and “ToF-SIMS: Materials Analysis by Mass Spectrometry” written by John C. Vickerman and David

Briggs [163]. To use PCA for SIMS data analysis, Daniel Graham gathered on a website: www.nb.uw.edu/mvsa/multivariate-surface-analysis-homepage (last checked 06/10/2020) courses on multivariate analysis, but also a link to download a free software “spectragui”, that easily allows to perform PCA on SIMS data. All PCA presented in this thesis were performed with this software.

PCA is generally used, when one is confronted to a complicated set of data to analyze. Indeed there can be correlations or redundancies for instance, making the samples undistinguishable from one another with direct analysis. A random example is shown in Figure 4.14. The left graph presents the measured data in the ‘ xy ’ space, but to draw any analysis is difficult, because the variations visible depends on the ‘ x ’ and the ‘ y ’ axis at the same time, they are correlated. The intuitive representation of PCA is an axis rotation, which is done in the two next pictures. In practice the data is introduced in a matrix where the columns correspond to one mass spectrum and the lines to a specific mass:

$$M = \begin{bmatrix} X_{1,1} & \cdots & X_{1,m} \\ \vdots & \ddots & \vdots \\ X_{n,1} & \cdots & X_{n,m} \end{bmatrix} \quad (4.25)$$

so for instance $X_{35,2}$ corresponds to the intensity of the 35th mass peak in the list from the 2nd spectra.

The principal component analysis will decompose the matrix M by calculating the covariance matrix as follow:

$$M = t_1 p_1^{t_1} + t_2 p_2^{t_2} + \dots + t_m p_m^{t_m} + E \quad (4.26)$$

where t_x represents the scores matrix of the principal component x , p_x the loadings matrix of the principal component x and E the residuals. The scores show the similarity between the spectra, i.e. the samples, and also give an idea of their reproducibility. The loadings show which variables –which mass peak– are responsible for the spectra differences or more globally the samples differences.

Data must be correctly collected before feeding data to PCA. The first point is to acquire sufficient spectra of each samples to check reproducibility and give more robustness to the outcoming model and interpretation. The acquired spectra must have the same calibration and the same peak list (interesting ions) must be used. This is the first step to make the data comparable. After that the data is normalized in intensity. Normalization is an important step to remove the differences due to topography, sample charging or instrumental conditions. There are several possibilities: normalization over total intensity, normalization over sum of selected peaks, normalization over highest peak in spectrum and normalization over user selected peak. All normalization are good, but generally total intensity normalization is preferred. The last preparation step would be the centering. The idea is to center the data around the mean value of each sample to make the data vary around the same zero value. It removes a common offset from the data and removes the differences in the means between values. There are two possibilities: a simple mean centering, or a square root mean centering. The first one just subtracts the mean of each variable from each measurement from that variable. The second method does the same, and applies a square root to the whole. A square root mean centering was preferred in this work, because it equilibrates the role of low and high masses in the end result, which is not the case in the simple mean centering.

To sum up, to perform PCA in this work, the different data sets, after being calibrated and having the same peak list, were normalized using a total intensity normalization and centered using a square root mean centering.

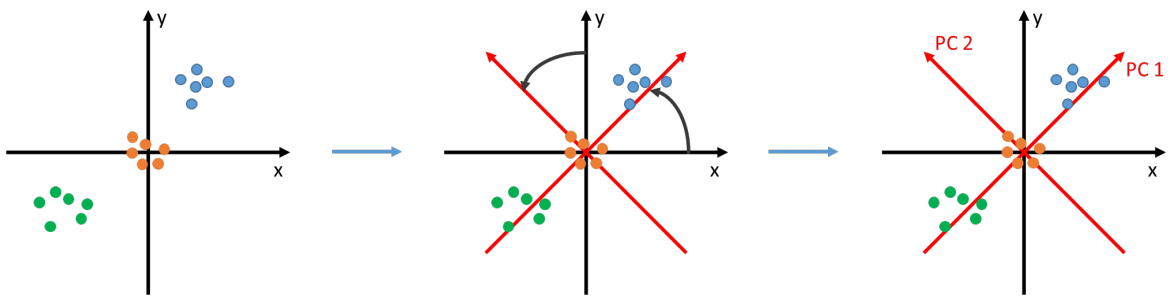


Figure 4.14: Schematic representation of the working of a principal component analysis [276].

Chapter 5

Surface pretreatments

The Laser-STAMP project, as described in the introduction, contains a work package on surface pretreatment. The experiments planned in this work package were mainly carried out by the partners at the University of Luxembourg and the LIST. Our participation is restricted to surface characterization using XPS. Several surface pretreatment were tested: laser ablation, anodization and silanization. As the analysis performed with XPS for anodization and silanization is not deep and thorough enough, they will not be presented here. However, the results on anodization were presented at the conference Adhesion'19 in Bristol in 2019 and are accessible through the conference proceedings [15].

Laser ablation treatments were performed on aluminum and titanium surfaces. The results on aluminum presented here, are extracted from one article published in *Coatings* in 2019 [277]. Concerning the titanium, the data presented are part of an article currently in preparation. Both parts will be organized in the same way. First a detailed sum up of the results of the articles illustrating their main conclusions, in order to better understand the context of these studies. Secondly a focus on the XPS data obtained. For the aluminum ablation part, the article from which the data are extracted can be found in annex

5.1 Laser ablation on aluminum

5.1.1 Sum up of the results from the article “Influence of aluminum laser ablation on interfacial thermal transfer and joint quality of laser welded aluminum-polyamide assemblies” published in *Coatings* in 2019

Six different laser ablation conditions were chosen and are based on the results obtained in a previous article [278] on the optimization of the ablation conditions. These different ablation conditions underwent several analysis. The joint area was assessed using optical images. The roughness was evaluated using scanning electron microscope (SEM) and a mechanical profilometer equipment. The surface chemistry was investigated both with XPS and with energy-dispersive X-ray spectroscopy (EDX). At last the laser flash analysis allowed to assess the thermal conductivity resistance. All the results will not be fully detailed here, but the whole article is available in annex. In order to fully understand the following part on XPS, only the joint assessment, the EDX measurement and the thermal conductivity will be detailed here.

The joint area was assessed for all samples, it was noticed that for the reference the joint area measured on the metal was 58% of that measured on the corresponding polyamide surface. This is a demonstration of a mixed failure mode between adhesive and cohesive failure mode. For the ablated samples the joint area measured on the metal matches that of the polymer indicating a cohesive failure mode in the polymer. The shear load was plotted as a function of the joint area

Table 5.1: Shear load of the different aluminum laser ablated samples.

Samples	Ref	Al_1	Al_2	Al_3	Al_4	Al_5	Al_6
Shear Load (in N)	718 (±92)	580 (±41)	800 (±65)	1222 (±143)	1341 (±172)	1415 (±113)	1465 (±65)

measured on both the metal and the polymer in Figure 5.1. A linear model was set to describe the evolution. The coefficient of determination (R^2) is extremely high at 98%. This indicates a low variability of the slope of the linear fit, which corresponds to the strength and is equal to 34.69 MPa for the ablated samples. This shows that the ablation parameters only affect the joint area, maybe because of a better thermal contact. So the ablation parameters are impacting directly the joint area, but are unlikely to affect the interfacial chemical bonding mechanisms, as the joint strength per unit area is kept constant. This is in favor for a constant interfacial “bond density”. Nonetheless, the weak point of the assembly is the polymer base material, so increasing the number of bonds at the interface might not be the best solution to increase the shear load.

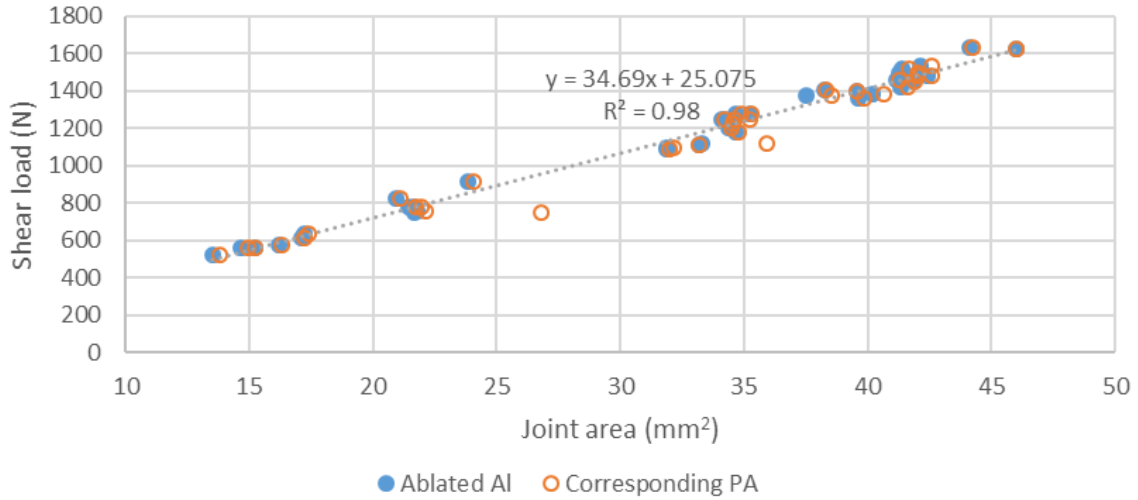


Figure 5.1: evolution of the shear load along the joint area for the ablated samples.

The atomic percentages calculated from the EDX measurements are presented in Figure 5.2. The depth of analysis yielded by the measurement parameters and the materials studied is close to 2 μm . Comparing the oxygen percentages the ablated samples can be separated into two groups. The first group, containing Al_1 to Al_4, presents higher oxygen percentages than the reference. While the second group, composed of Al_5 and Al_6, presents oxygen percentages comparable to the reference. A higher oxygen percentage indicates a thicker oxidized aluminum layer. This is consistent with the ablation conditions, which are softer going from Al_1 to Al_6. Comparing these results with the shear loads shown in Table 5.1, it appears clearly that softer ablation conditions leading to a lower oxidized aluminum thickness allow to get a higher shear load. As seen before, the strength is constant, the variable affected is the joint area. A thinner oxidized layer leads to a larger joint area. It can be explained by a better heat conduction in pure aluminum (94 mm^2/s at 300K) than in aluminum oxide (12 mm^2/s at 300K) [279, 280].

The thermal contact resistance (TCR) measurement obtained using laser flash analysis, presented in Figure 5.3, shows a clear correlation between the TCR and the shear load. The Pearson correlation coefficient is equal to -0.94. This shows that the lower the TCR, the better the shear

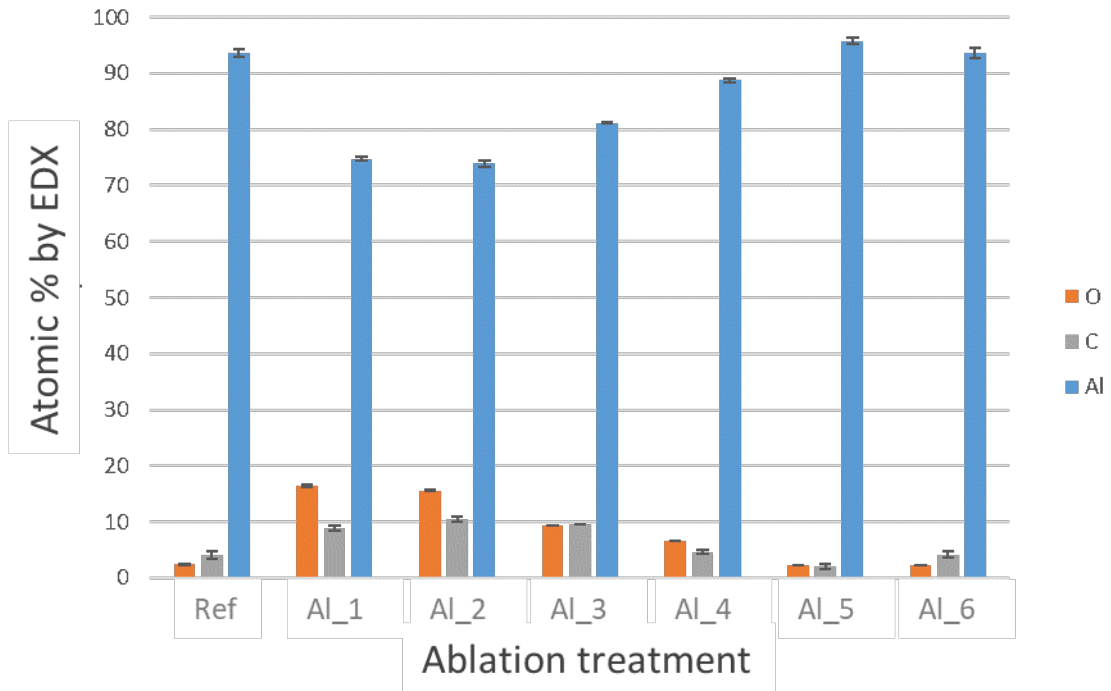


Figure 5.2: Elemental composition observed in EDX.

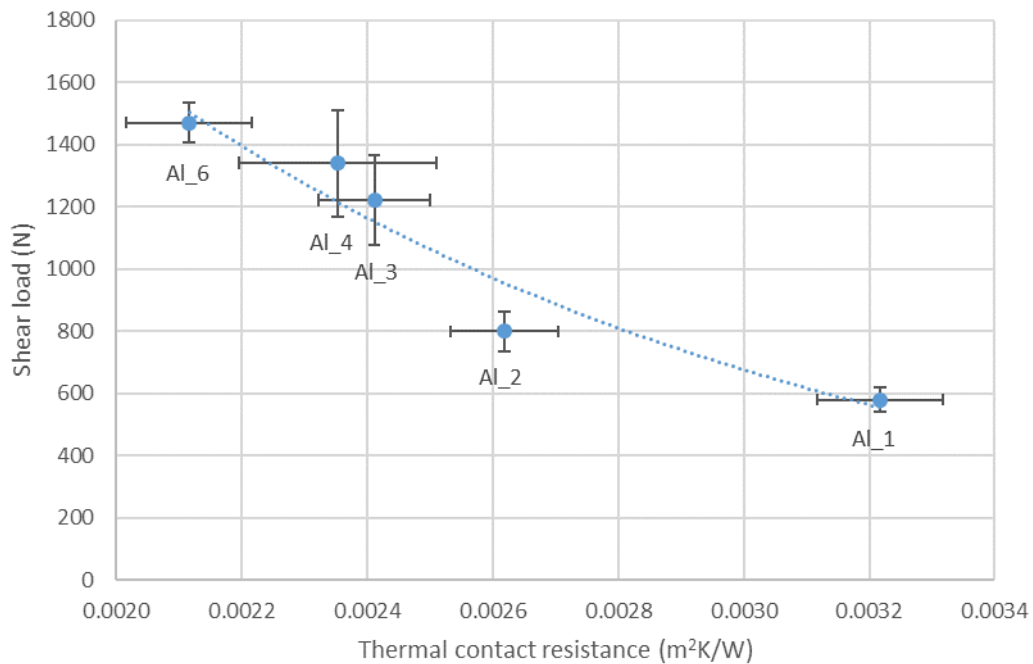


Figure 5.3: Relation between thermal contact resistance and joint's resistance to failure.

load. Multiple factors can explain this behavior. As mentioned above the fact that the oxidized layer is thinner for softer ablation conditions is one of the explanations possible. The roughness also plays an important role, leading to more or less contacts between the two materials. Sum-

Table 5.2: XPS average elemental composition for aluminum laser ablation.

Samples	% Al	% O	% C	% N	% Mg	% S	% Na
Ref	27.5 (± 2.6)	41.1 (± 3.1)	29.5 (± 5.7)	0.0 (± 0.0)	0.3 (± 0.0)	1.0 (± 0.1)	0.5 (± 0.1)
Al_1	32.4 (± 0.7)	61.0 (± 1.3)	6.0 (± 1.3)	0.7 (± 0.1)	0.0 (± 0.0)	0.0 (± 0.0)	0.0 (± 0.0)
Al_2	32.9 (± 0.7)	60.7 (± 0.5)	5.7 (± 1.1)	0.7 (± 0.1)	0.0 (± 0.0)	0.0 (± 0.0)	0.0 (± 0.0)
Al_3	32.0 (± 0.6)	59.7 (± 0.4)	8.0 (± 1.0)	0.5 (± 0.1)	0.0 (± 0.0)	0.0 (± 0.0)	0.0 (± 0.0)
Al_4	32.3 (± 0.7)	59.9 (± 0.5)	7.8 (± 1.1)	0.0 (± 0.0)	0.0 (± 0.0)	0.0 (± 0.0)	0.0 (± 0.0)
Al_5	32.8 (± 0.4)	58.7 (± 0.3)	8.5 (± 0.7)	0.0 (± 0.0)	0.0 (± 0.0)	0.0 (± 0.0)	0.0 (± 0.0)
Al_6	32.4 (± 0.4)	57.4 (± 0.1)	10.2 (± 0.5)	0.0 (± 0.0)	0.0 (± 0.0)	0.0 (± 0.0)	0.0 (± 0.0)

marizing the results of the roughness, it is to be noticed that the smoother the surface, the more intimate the contact is between the materials, the lower the TCR, leading to a larger joint area.

To sum up, in order to increase the shear load, the best way is to increase the joint area, as the strength is constant. This can be achieved by two factors, lowering the surface roughness and decreasing the oxidized layer thickness.

5.1.2 XPS results on the laser ablated aluminum

In Table 5.2, the chemical compositions of the different ablated surfaces are presented. It is noticeable that the aluminum percentage does increase after laser ablation, but that all the treatments present similar percentages around 32.4%. At the same time, the carbon percentage diminishes clearly as soon as there is some ablation treatment. The pretreatment has a cleaning effect, and the carbon percentage follows roughly the peak pulse power. The higher the peak pulse power, the less adventitious carbon there is. Compared to the reference, the oxygen percentage is much higher on the ablated samples, even if it decreases from nearly 61% to 57.4% from sample Al_1 to sample Al_6. Some nitrogen is detected on the Al_1, Al_2 and Al_3 samples. Nitrogen contaminations were already observed on samples from the same batch of metal [278,281], but not detected every time without any explanation. While on the reference low amounts of magnesium, sulfur and sodium are detected, they are completely absent on the ablated samples, even if they are naturally present in this aluminum alloy.

Figure 5.4 presents the high resolution spectra of the C 1s region for all the samples. The chemical nature of the carbon between the reference and the ablated samples can be directly observed. Indeed to interpret the spectra in the reference, three contributions were used: a C-C/C-H one set at 284.8 eV (serving as calibration peak), a C-O/C-N peak at 285.7 eV and a O-C=O contribution at 288.6 eV [282]. This interpretation is coherent with the literature on adventitious carbon [283–285]. While for the ablated samples only two peaks were used to fit the spectra: a C-C/C-H contribution at 284.8 eV and O-C=O contribution around 288.9 eV [282]. The nature of the peaks used for the interpretation indicates a recontamination of the surfaces after the laser ablation, but in lower amounts than before. Because of the ablation, the oxide layer has a composition nearer to pure aluminum oxide, which might present less reactive sites explaining the lower recontamination of the ablated surfaces.

Table 5.3: XPS binding energies in eV of the peaks in the O 1s region for each sample.

	Ref	Al 1	Al 2	Al 3	Al 4	Al 5	Al 6
Oxide peak	531.5	530.5	531.1	531.1	530.9	530.6	530.9
Hydroxide peak	532.3	531.9	533.0	533.2	532.9	532.5	532.6

The high resolution spectra of the Al 2p region, presented in Figure 5.5, mark a clear difference between the reference and the ablated samples. Indeed on the reference, the presence of two peaks associated to Al 2p_{3/2} and Al 2p_{1/2} respectively at 72.9 eV and 73.3 eV, are due to metallic aluminum [286], while none is visible on the ablated samples. A third contribution related to oxidized aluminum at 75.0 eV was added to fit the reference spectra [286]. On the ablated samples a single contribution, associated to oxidized aluminum, was used to fit the spectra around 74.2 eV [286]. The binding energy is very different than for the reference, but the oxidized form presents a huge standard deviation of 1.0 eV [286]. Statistics on the binding energy of this peak for all the samples showed no difference. Since there is no metallic contribution, the first 10 nm of the metal surface are oxidized, so that Strohmeier’s formula [258] of oxide thickness calculation cannot be used on these samples.

For the fitting of the O 1s regions of all the samples, only two contributions were used: one associated to aluminum oxide and one linked to hydroxide [282, 284, 285]. The binding energies variate a lot from one sample to another; the values are presented in Table 5.3. These variations might be induced by the calibration. As mentioned above the use of the C-C/C-H peak to calibrate the XPS spectra is criticized and it was shown that it might not always be the best solution to adequately calibrate the spectra [253, 255]. A contribution from organic compounds should be expected around 533.0 eV, but none was necessary to fit reasonably the O 1s regions. On the ablated samples, this can be explained by the very low percentage of carbon, which makes this contribution very low in intensity. This contribution might also simply be mixed with the hydroxide one, explaining why no organic contribution was needed on the reference. The hydroxide/oxide peak intensity ratio show some differences between the samples when just looking at the graphs, but by calculating this ratio on all the samples, only one trend can be taken out. The ratio between the hydroxide and oxide peaks is higher on the reference (0.7 ± 0.5) than the ablated samples. They all present a similar ratio of about 0.3 ± 0.1 . An estimate of the hydroxide/oxide ratio was obtained using the formula described in Chapter 4: Materials and method, part 4.4.7 (see Table 4). Looking at the obtained values, they are quite low, showing that the surfaces are in majority in the aluminum oxide state and not in the hydroxide form, within the sampling depth of XPS. At least this information is in good agreement with the O 1s fittings. The calculated ratio, show an inversed evolution with the shear load (see Figure 5.7). The lower the hydroxide/oxide ratio is, the higher the shear load is. If a linear correlation is tested, the model fits with a R²-value of 92% (see Figure 5.7). This appears as counterintuitive, as the hydroxide groups are supposedly needed at the interface to create more bonds (see Chapter 6), but the failure is systematically cohesive. However, XPS is not very sensitive to hydroxyl groups located at the extreme surface, as it has a sampling depth of ca. 10 nm. That’s why absolute adhesive strength is unknown, so that no conclusion can be made on the interfacial chemistry. Nonetheless, the chemical composition of the oxidized layer evolves towards a purer oxide. This can play a role in the thermal conductivity. It seems that an oxide layer, which is purer might have a better thermal conductivity, so a lower TCR. To the best of our knowledge, the thermal conductivity of pure aluminum hydroxide is not described in literature, which could give a clue in this matter. In addition, even if the chemical composition indicates a purer oxide, there is no indication on the crystalline structure and the crystallite size, which will have a determinant impact on the heat conduction.

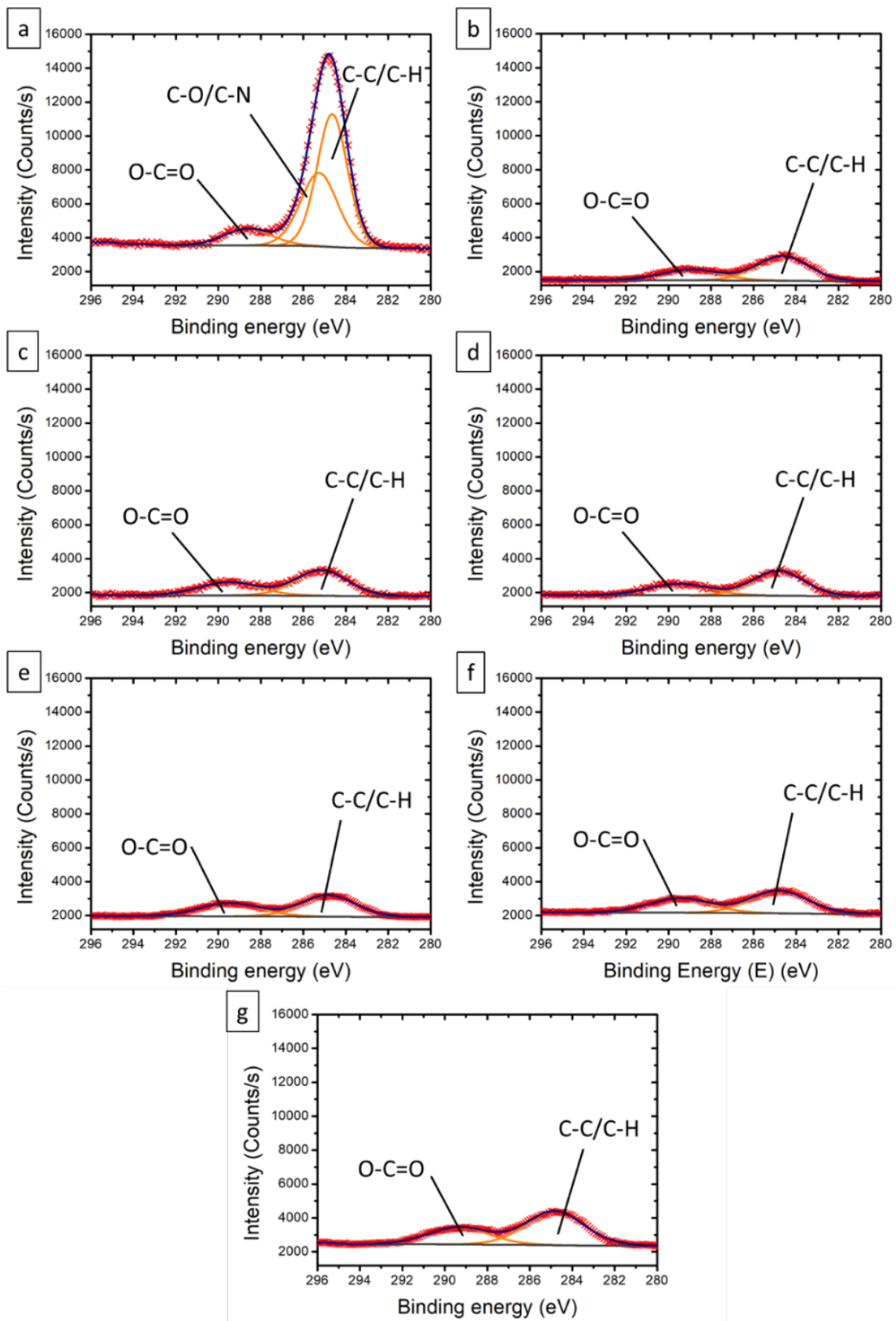


Figure 5.4: XPS high resolution spectra of the C 1s region (a) on the reference, (b) on Al_1, (c) on Al_2, (d) on Al_3, (e) on Al_4, (f) on Al_5, (g) on Al_6.

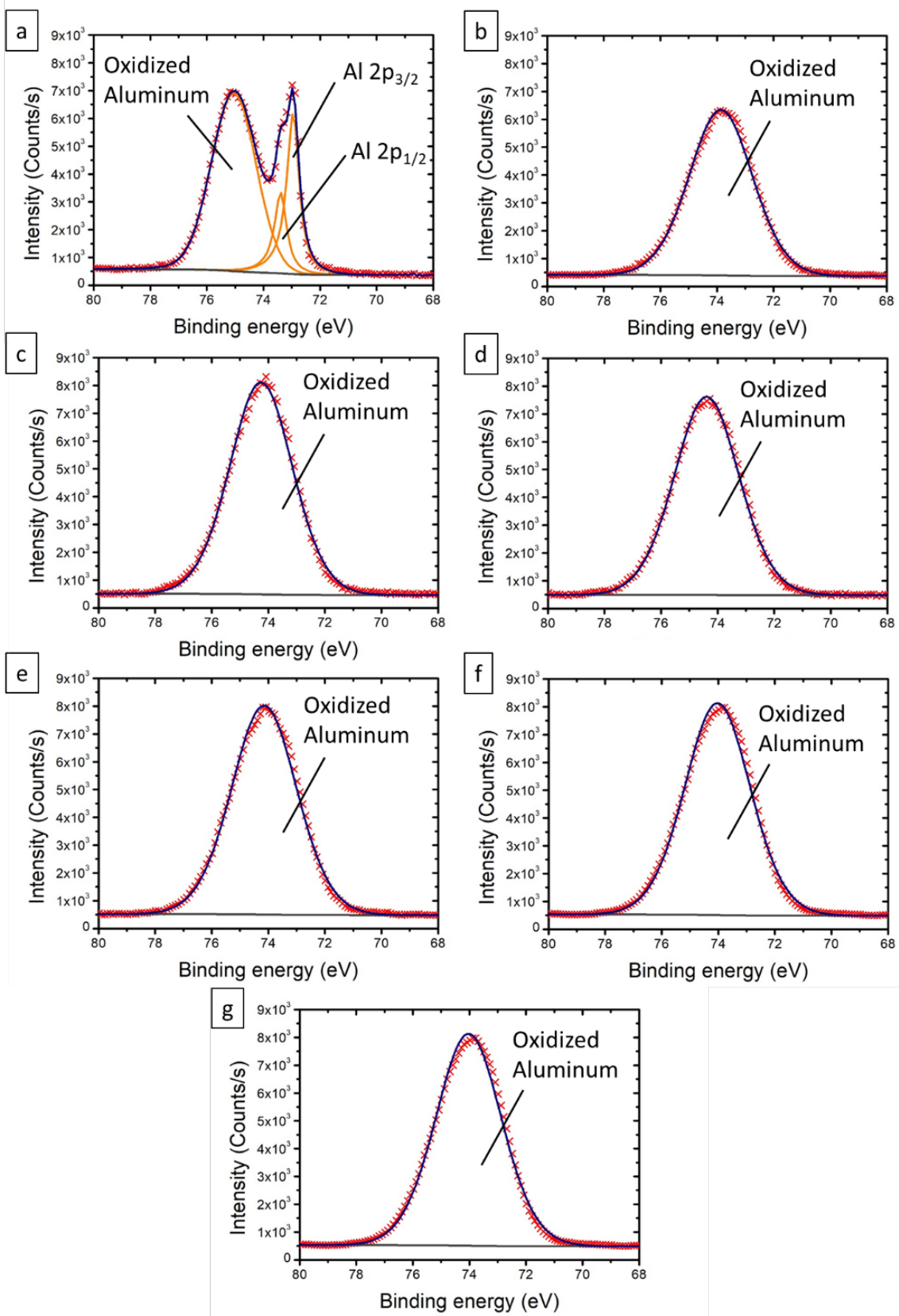


Figure 5.5: XPS high resolution spectra of the Al 2p region (a) on the reference, (b) on Al₁, (c) on Al₂, (d) on Al₃, (e) on Al₄, (f) on Al₅, (g) on Al₆.

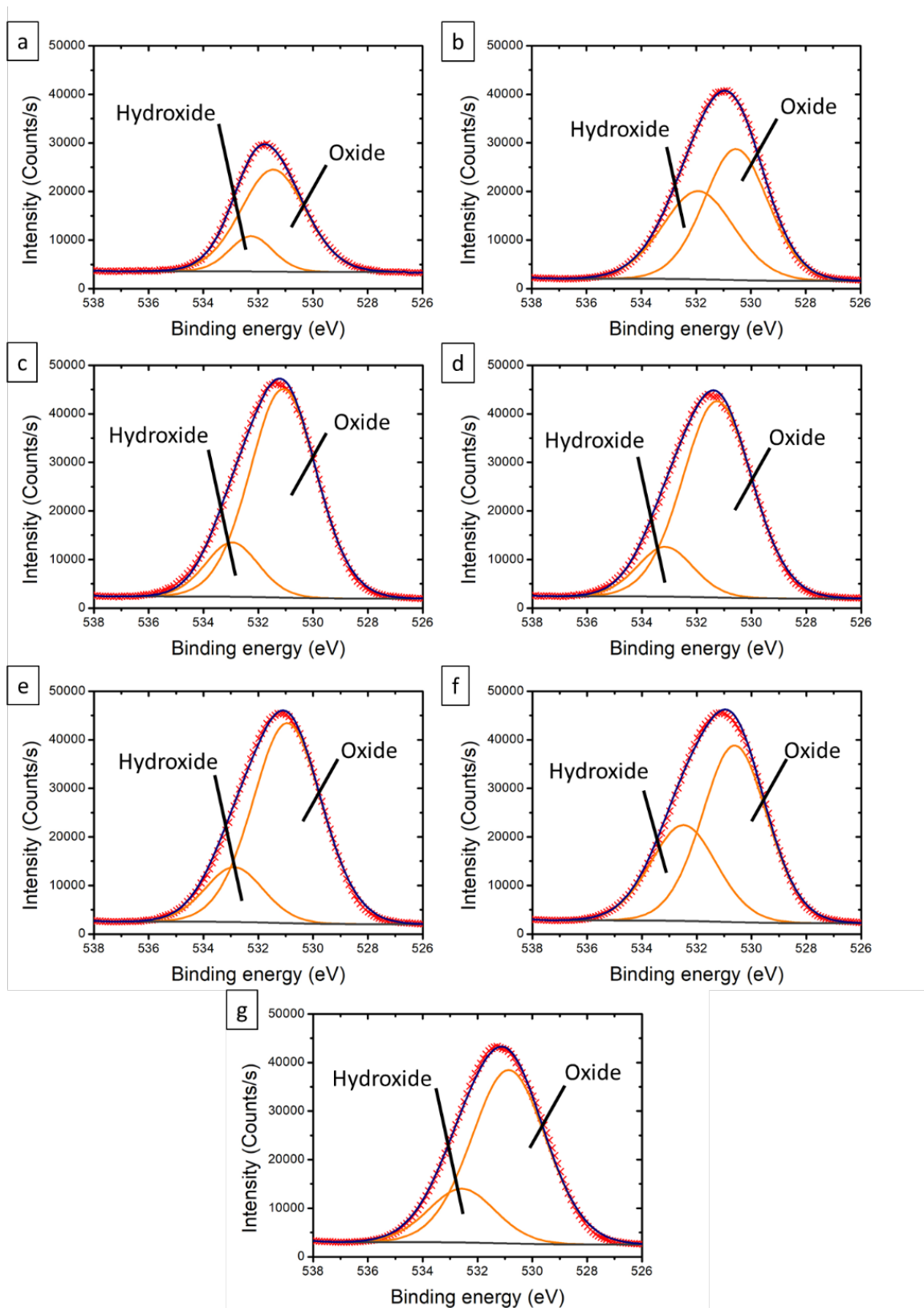


Figure 5.6: XPS high resolution spectra of the O 1s region (a) on the reference, (b) on Al_1, (c) on Al_2, (d) on Al_3, (e) on Al_4, (f) on Al_5, (g) on Al_6.

Table 5.4: XPS calculated data: oxide thickness, oxidized percentages of aluminum and oxygen and the hydroxide to oxide ratio.

Samples	Shear load (in N)	Oxide thickness (in nm)	X _{O, ox.}	X _{Al, ox.}	R	R _{hydr./ox.}
Ref	718 (± 92)	5.5 (± 0.0)	22.4 (± 2.0)	35.2 (± 3.6)	1.57 (± 0.03)	0.10 (± 0.04)
Al_1	580 (± 41)	<20 nm	32.4 (± 0.7)	54.2 (± 1.5)	1.67 (± 0.02)	0.26 (± 0.03)
Al_2	800 (± 65)	<20 nm	32.9 (± 0.7)	53.9 (± 1.5)	1.63 (± 0.02)	0.20 (± 0.03)
Al_3	1222 (± 143)	<20 nm	32.0 (± 0.6)	51.1 (± 1.4)	1.60 (± 0.01)	0.14 (± 0.03)
Al_4	1341 (± 172)	<20 nm	32.3 (± 0.7)	50.7 (± 1.7)	1.57 (± 0.03)	0.10 (± 0.04)
Al_5	1415 (± 113)	<20 nm	32.8 (± 0.4)	49.8 (± 0.7)	1.52 (± 0.01)	0.02 (± 0.01)
Al_6	1465 (± 65)	<20 nm	32.4 (± 0.4)	48.9 (± 0.5)	1.51 (± 0.00)	0.01 (± 0.00)

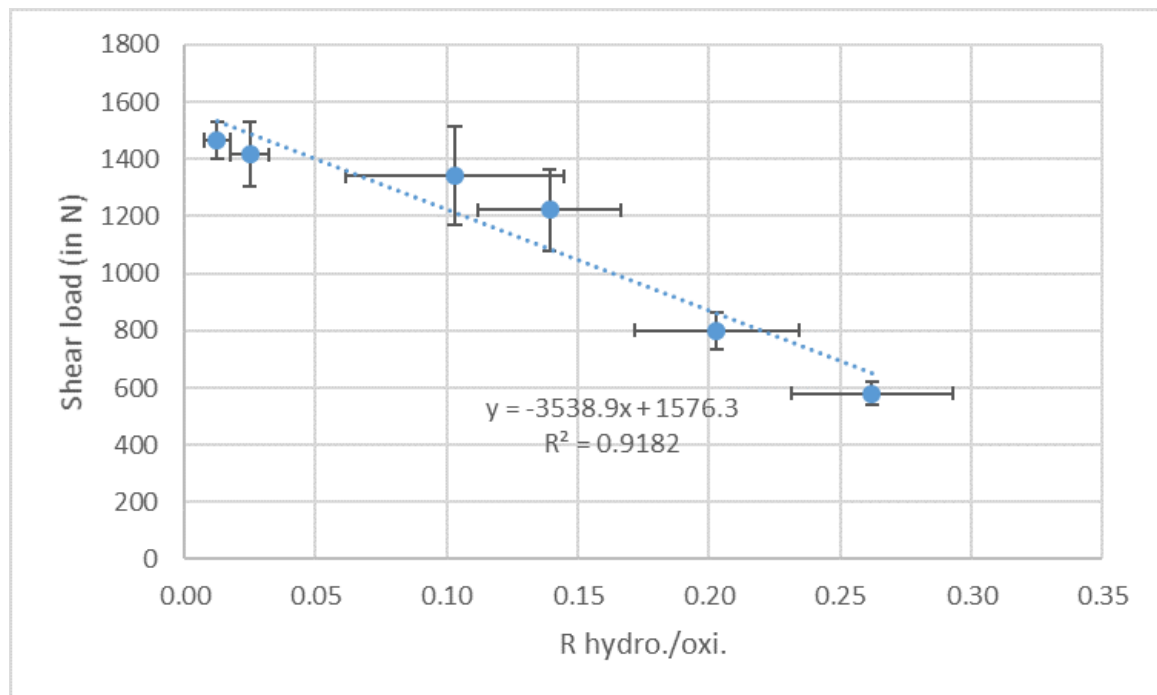


Figure 5.7: graph showing the correlation between the R_{hydro./oxi.} and the shear load.

5.1.3 Conclusions on the laser ablated aluminum

As a conclusion to heighten the shear load, the best way is to enlarge the joint area. In order to achieve that, one has to lower the thermal contact resistance. From this study two ways can be used and a third needs more investigation: (1) narrow the oxidized layer thickness, (2) minimize the roughness and (3) apparently having a purer oxide allows to increase the shear load, but

Table 5.5: Shear load of the different titanium ablated surfaces.

Samples	Ref	Ti_1	Ti_2	Ti_3	Ti_4	Ti_5
Shear Load (in N)	772 (± 70)	387 (± 117)	690 (± 57)	1064 (± 28)	1186 (± 11)	764 (± 5)

this needs more investigation. However the crystalline structure as well as the crystallite size also have an impact on the TCR and should be investigated.

5.2 Laser ablation on titanium

5.2.1 Sum up of the article “Influence of titanium alloy (Ti64) laser ablation on joint quality and interfacial thermal transfer between laser welded titanium – polyamide joints” still in preparation for publication

Four different ablation conditions were investigated following the same methodology as for the aluminum. The ablation conditions were chosen based on a published article on the optimization of the laser ablation process using a design of experiment approach [287]. Four surface characteristics were analyzed: (1) the joint area, (2) the surface chemistry by EDX and XPS, (3) the surface roughness by SEM, profilometry and sessile drop test, and (4) thermal contact resistance by laser flash analysis. As the article is still in preparation the sum up will rapidly introduce all the aspects.

The measured joint area on the polymer and the metal are plotted along the shear load in Figure 5.8. As for the aluminum samples, the shear load is linearly correlated to the joint area with a R^2 -value of 91%. The slope corresponding to the strength per unit area is of 36.5 MPa. Again the ablation is directly impacting the joint area, by tuning the thermal conductivity of the metal. Indeed, as the failure mode is cohesive, the impact on the interfacial interactions between both materials are not directly evaluated here also.

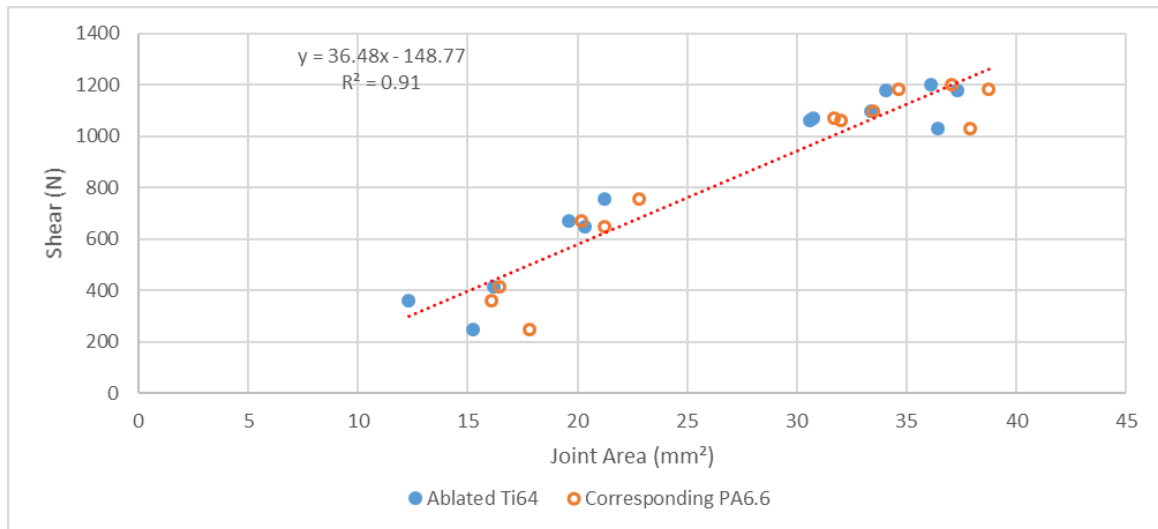


Figure 5.8: evolution of the shear load along the joint area for the ablated samples.

The EDX results are presented in Figure 8. The depth of analysis is estimated at maximum 1-2 μm . It is noticeable that the oxygen percentage is much higher on the ablated samples, than on the reference. This illustrates the oxide growth happening during the ablation process. For

the samples Ti_1, Ti_2 and Ti_3 the percentage of oxygen is similar, which implies a similar oxide thickness. Yet the shear load (see Table 5.5) is increasing a lot between the three samples. However, Ti_4 presents a lower percentage of oxygen, meaning a thinner oxide layer. The shear load is the highest for this sample. This illustrates well the fact that the heat transfer is governed by multiple factors. The evolution of the carbon percentage must be taken with great care, as in EDX it is difficult to quantify correctly the carbon percentage. It seems that the higher the carbon percentage, the higher the shear load, but this must be confirmed by XPS. The evolution of the aluminum and vanadium percentages are not significant and do not correlate with the shear load.

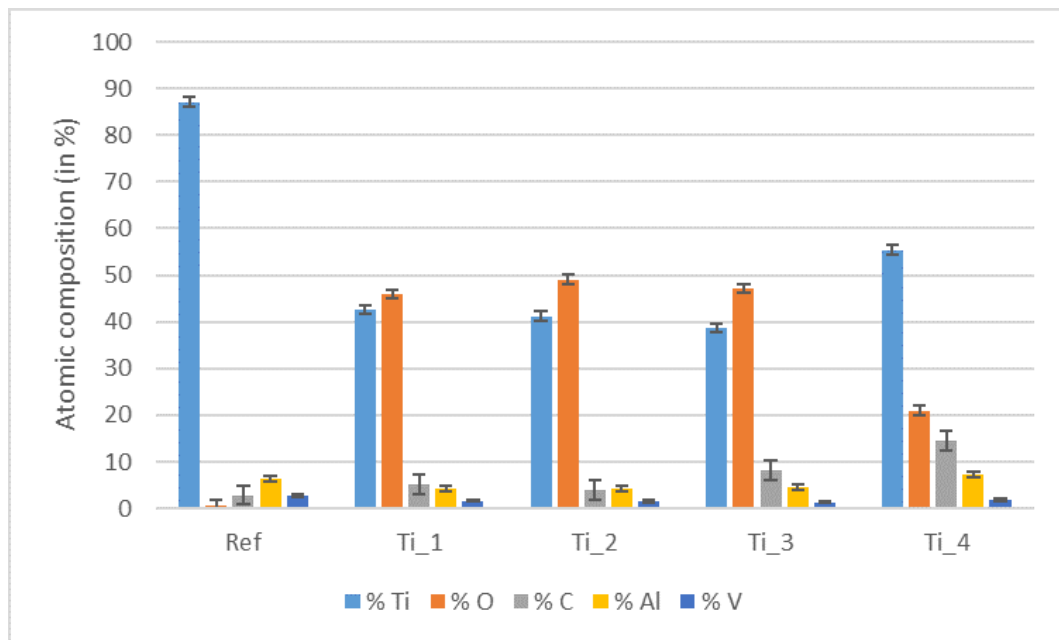


Figure 5.9: EDX atomic composition measured for each sample.

Looking at the SEM images in Figure 5.10, the high roughness differences are directly visible. Comparing Ti_1, Ti_2, Ti_3 and Ti_4, it appears clearly, that the smoother the surface, the higher the shear load. This is even more visible in Figure 5.11, showing the TCR coefficient versus the shear load. The TCR coefficient was obtained using the R_q and R_{dq} values (a complete description of the model can be found in annex in the article). The TCR coefficient is strongly related to the roughness, the higher this coefficient is, the rougher the surface. As the shear load decreases with a higher TCR coefficient, the conclusion is again, the smoother the surface, the more intimate is the contact between the two materials, allowing for more heat transfer, which will enlarge the joint area and so the shear load.

The shear load also displays a strong correlation towards the thermal contact resistance TCR, measured using laser flash analysis, as presented in Figure 5.12. The conclusion is the lower the thermal contact resistance the higher the shear load. The samples displaying the lowest shear load are Ti_1 and Ti_2, they also present the highest roughness, as well as the highest TCR. The SEM images (see Figure 5.10) clearly show that on these samples the roughness is characterized by high peaks and deep valleys. This diminishes the possible contact points between the metal and the polymer, explaining why the thermal contact resistance is higher on these samples than on the smoother ones. A second argument using the roughness, is that when the polymer melts, it does not have the time or the possibility to flow into the deep valleys, lowering the intimate contact area. This possibility was not thoroughly investigated, as the

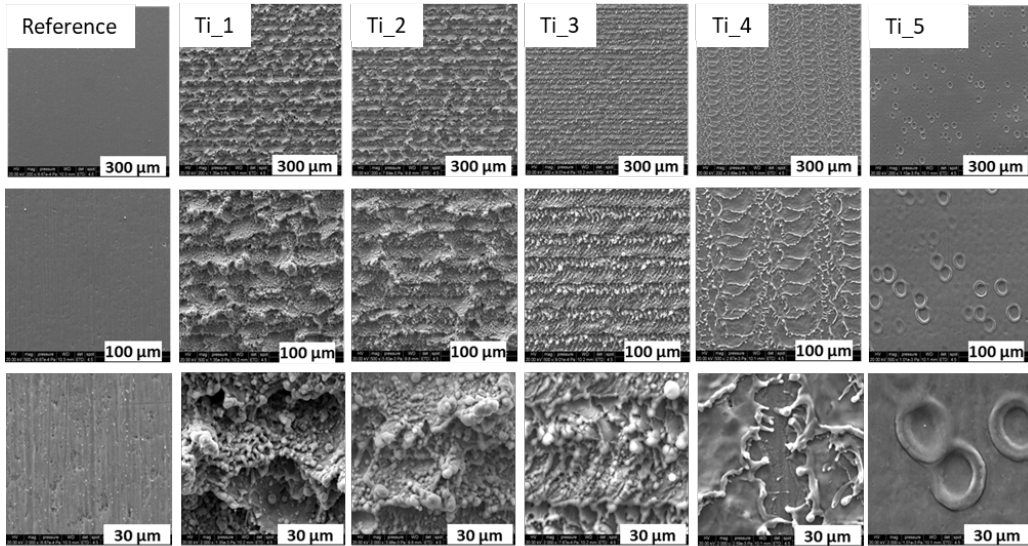


Figure 5.10: SEM images of ablated surfaces.

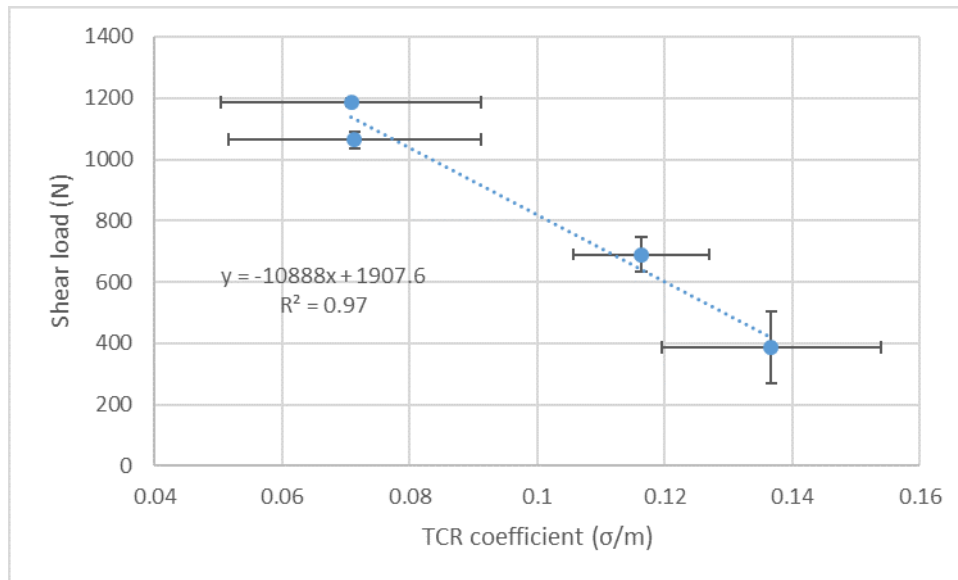


Figure 5.11: Relation between surface topography and joint's resistance to failure.

samples present a cohesive failure mode in the polymer, meaning that the weak point of the assemblies are not at the interface, but in the polymer itself.

5.2.2 XPS results on the laser ablated titanium

The average elemental composition of the different titanium ablated samples is presented in Table 5.6. The ablation treatments systematically increase the percentage of titanium. Ti_4 has a lower percentage than the other ablation conditions but still higher than the reference. This might be due to the high speed of the laser, which makes this treatment extremely fast, diminishing its impact. The oxygen percentage also increases for the ablated samples. The carbon percentage is lower on the three first ablation treatment, but not for Ti_4. For Ti_4, the explanation is also that the speed of the laser is extremely high, making the ablation fast,

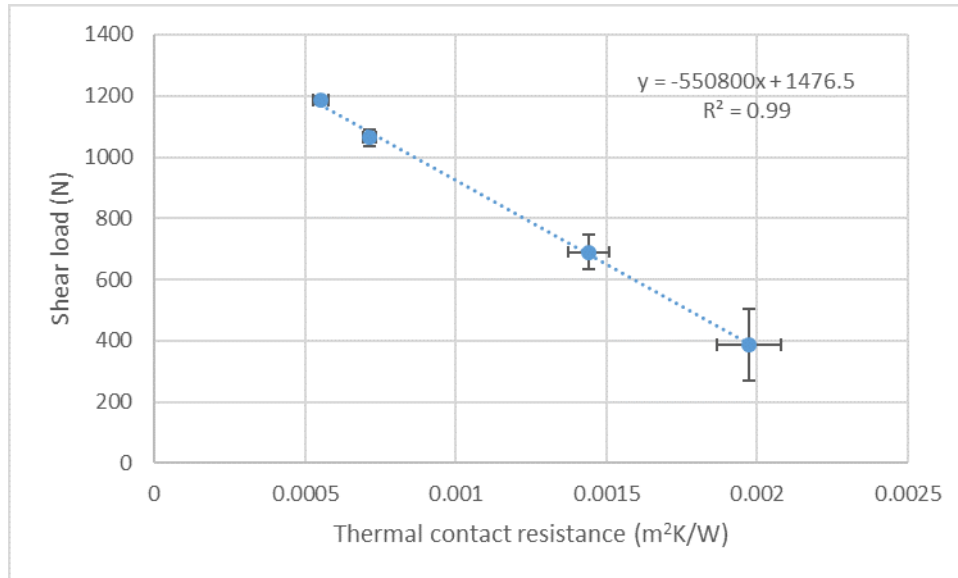


Figure 5.12: Relation between thermal contact resistance and joint's resistance to failure.

diminishing its impact. The aluminum percentage is increased with the laser ablation treatments. The vanadium percentage is higher due to the ablations. The nitrogen percentage is similar for the reference and the four ablation treatment. The reference, even if cleaned by ethanol wiping, presents surface contaminations, such as silicon, sulfur, calcium, zinc, and iron. The ablation removes these contaminants.

The high resolution spectra of the C 1s region, displayed in Figure 5.13, show a high disparity of chemical environment depending on the laser ablation treatment. To fit the reference, five peaks were used: one C-C/C-H peak set at 284.8 eV, one C-O/C-N peak at 286.5 eV, one CO₃ peak at 288.7 eV, one C-F peak at 292.9 eV, and a C-Ti peak at 291.9 eV [282, 286]. The presence of the C-F peak is consistent with the small amount of fluorine present on the reference samples. A titanium carbide peak (C-Ti) is observed at a normal energy for a metal carbide, but such peaks on adventitious carbon have not been described in literature to the best of our knowledge. For Ti_1, Ti_2, Ti_3 and Ti_4, the same contributions were used to fit the C 1s regions: one C-C/C-H contributions at 284.8 eV, one C-O/C-N contribution at 286.2 eV and a CO₃ contribution at 288.9 eV. This is typical for adventitious carbon [283, 284]. Even if the ablation has a cleaning effect, adventitious carbon is measured because of the recontamination due to the time to bring the samples to the XPS machine.

The high resolution spectra obtained in the O 1s region, presented in Figure 5.14, demonstrate two groups of samples: the reference on one side, and on the other side Ti_1, Ti_2, Ti_3 and Ti_4. The reference was interpreted using three peaks: one around 530.1 eV related to titanium oxide, and the two others around 531.4 eV and 532.5 eV respectively associated to organic compounds (adventitious carbon), and oxidized aluminum and vanadium [288–290]. On Ti_1, Ti_2, Ti_3 and Ti_4, only two peaks were used to fit this region: one around 530.2 eV associated to titanium oxide, and one associated to organic compounds as well as to oxidized aluminum and vanadium around 532.1 eV [288–290]. Maybe in the contribution at higher binding energy, titanium hydroxide can also be a possible interpretation, but to the best of our knowledge, no one detailed such observation, nor in the Ti 2p, nor in the O 1s high resolution spectra.

The interpretation of the high resolution Ti 2p region is presented in Figure 5.15. The reference samples were interpreted using nine peaks related to five contributions because of the

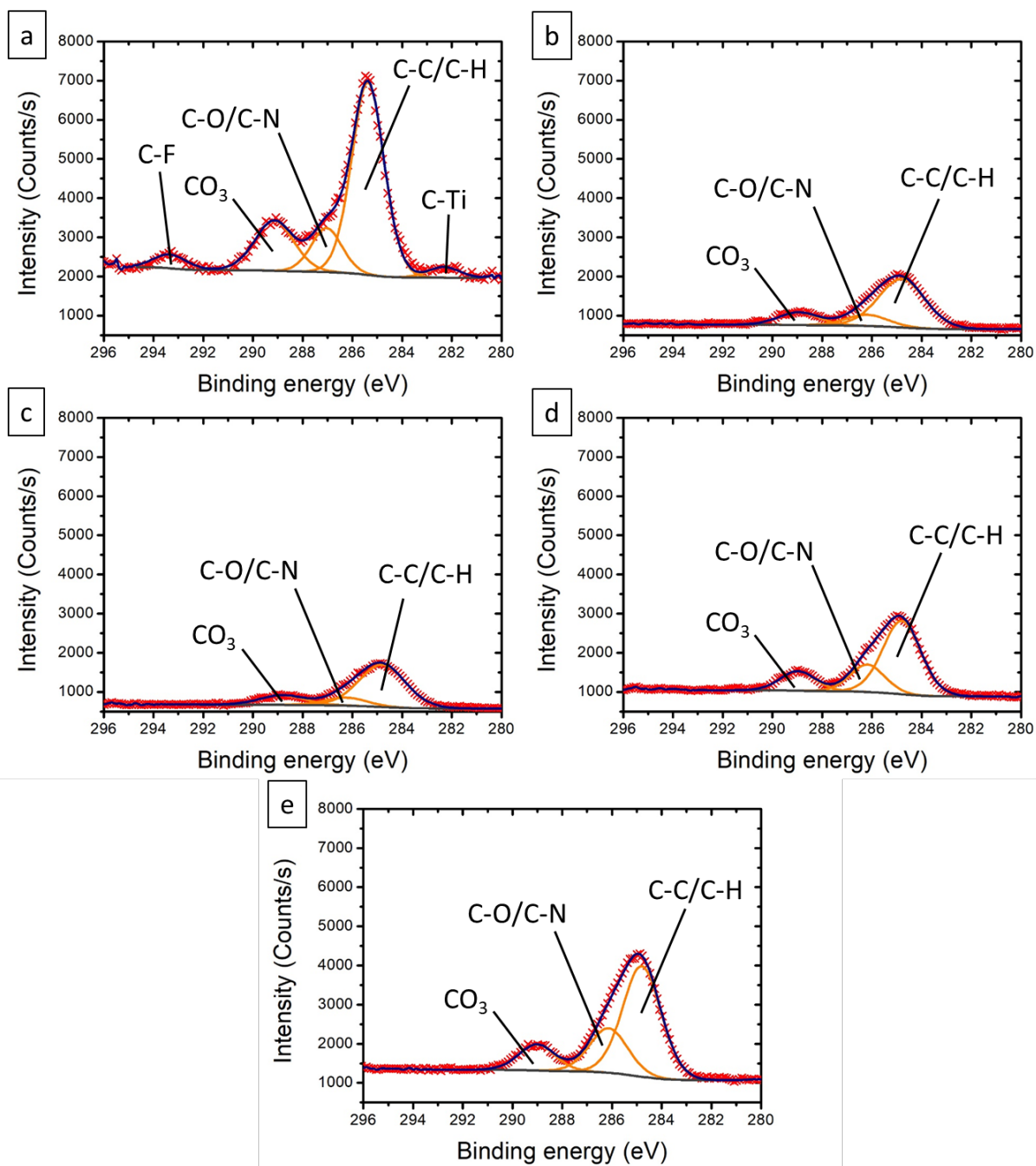


Figure 5.13: XPS high resolution spectra of the C 1s region (a) on the reference, (b) on Ti_1, (c) on Ti_2, (d) on Ti_3, and (e) on Ti_4.

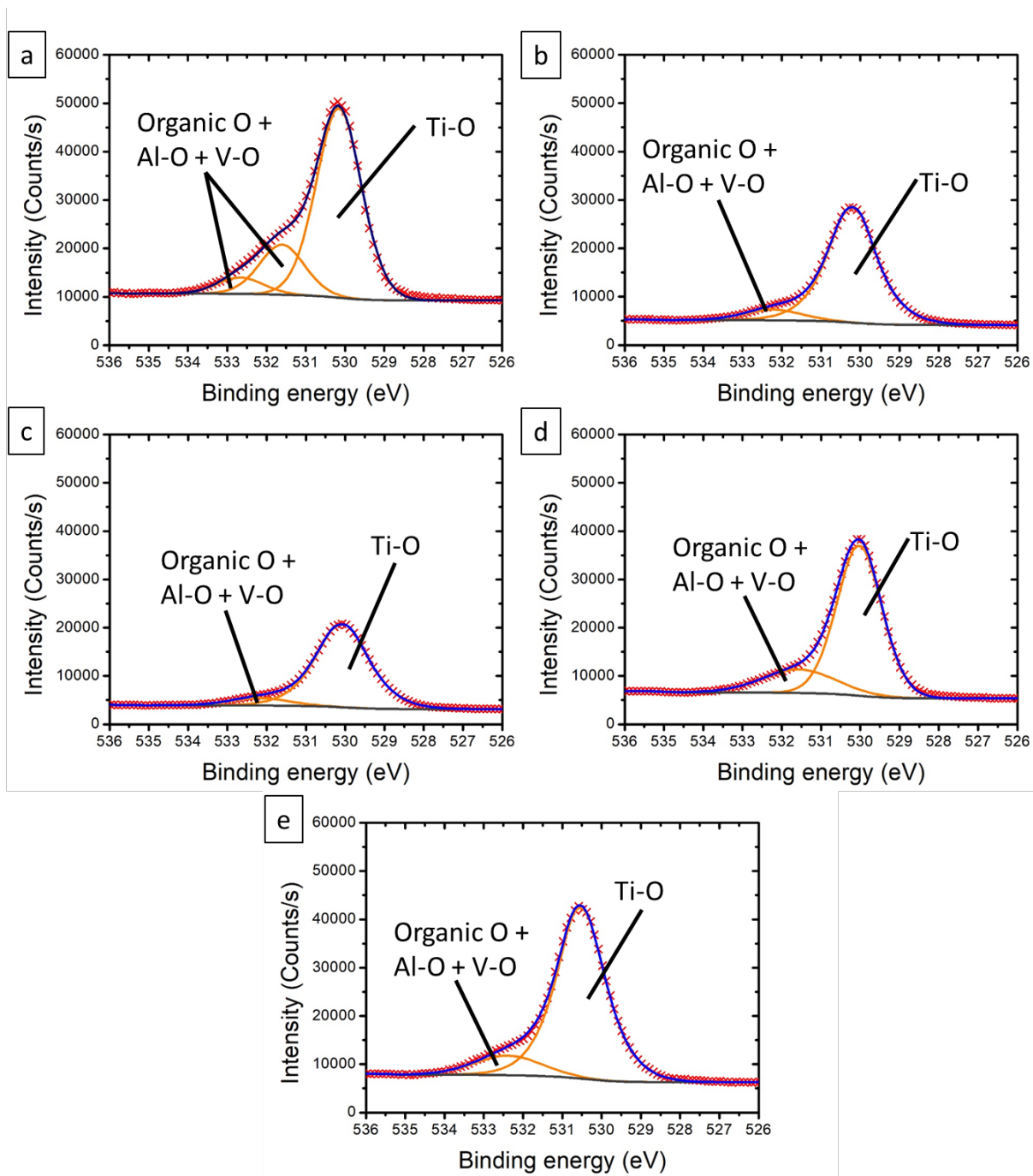


Figure 5.14: XPS high resolution spectra of the O 1s region (a) on the reference, (b) on Ti_1, (c) on Ti_2, (d) on Ti_3, and (e) on Ti_4.

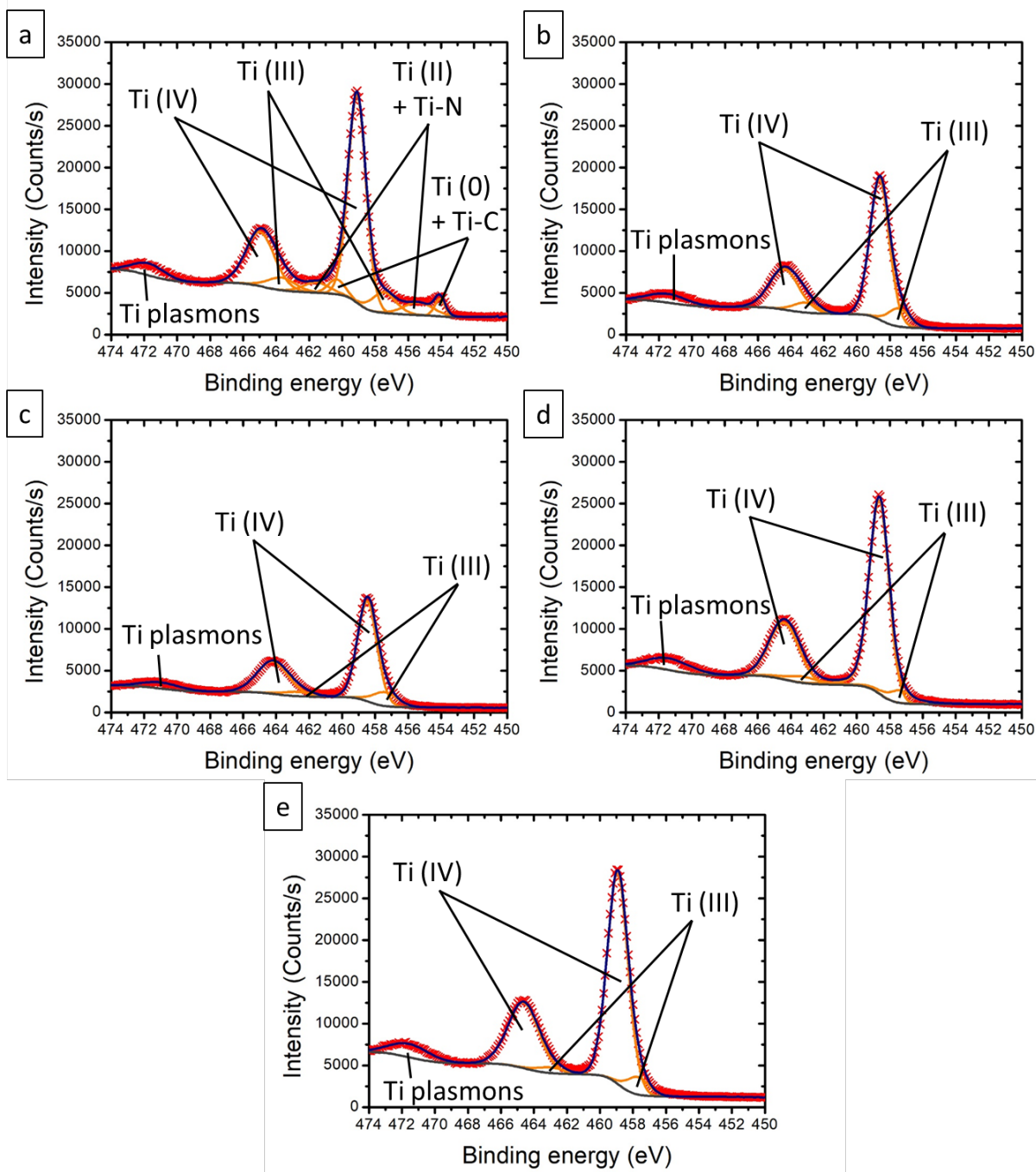


Figure 5.15: XPS high resolution spectra of the Ti 2p region (a) on the reference, (b) on Ti₁, (c) on Ti₂, (d) on Ti₃, and (e) on Ti₄.

Table 5.6: XPS elemental average composition for titanium laser ablation treatment.

	%Ti	%O	%C	%Al	%V	%N	%Si	%S	%Ca	%Zn	%Fe	%F
Ref	17.0 (± 0.9)	50.3 (± 1.3)	22.2 (± 2.2)	2.7 (± 0.3)	0.5 (± 0.0)	1.3 (± 0.5)	1.4 (± 0.2)	1.0 (± 0.2)	2.1 (± 0.2)	0.5 (± 0.1)	0.6 (± 0.1)	0.5 (± 0.1)
Ti_1	21.5 (± 0.3)	54.9 (± 0.1)	17.4 (± 0.4)	4.3 (± 0.4)	1.0 (± 0.1)	1.0 (± 0.1)	0.0 (± 0.0)	0.0 (± 0.0)	0.0 (± 0.0)	0.0 (± 0.0)	0.0 (± 0.0)	0.0 (± 0.0)
Ti_2	21.4 (± 0.3)	55.6 (± 0.3)	15.9 (± 0.6)	4.9 (± 0.4)	1.0 (± 0.0)	1.1 (± 0.1)	0.0 (± 0.0)	0.0 (± 0.0)	0.0 (± 0.0)	0.0 (± 0.0)	0.0 (± 0.0)	0.0 (± 0.0)
Ti_3	21.9 (± 0.4)	55.4 (± 0.2)	17.0 (± 0.2)	3.6 (± 0.4)	0.8 (± 0.0)	1.3 (± 0.1)	0.0 (± 0.0)	0.0 (± 0.0)	0.0 (± 0.0)	0.0 (± 0.0)	0.0 (± 0.0)	0.0 (± 0.0)
Ti_4	20.4 (± 0.1)	53.0 (± 0.2)	20.7 (± 0.5)	3.6 (± 0.1)	0.7 (± 0.0)	1.6 (± 0.1)	0.0 (± 0.0)	0.0 (± 0.0)	0.0 (± 0.0)	0.0 (± 0.0)	0.0 (± 0.0)	0.0 (± 0.0)
Ti_5	22.0 (± 1.3)	46.6 (± 2.3)	21.9 (± 4.2)	4.1 (± 0.3)	0.2 (± 0.0)	2.5 (± 0.1)	0.0 (± 0.0)	0.0 (± 0.0)	0.0 (± 0.0)	0.0 (± 0.0)	0.0 (± 0.0)	0.0 (± 0.0)

spin-orbit splitting. The first contribution is related to Ti (0) and Ti-C at 454.1 eV (Ti 2p_{3/2}) and 460.3 eV (Ti 2p_{1/2}). The second contribution is related to Ti (II) and Ti-N at 455.4 eV (Ti 2p_{3/2}) and 461.6 eV (Ti 2p_{1/2}). The third contribution is related to Ti (III) at 457.5 eV (Ti 2p_{3/2}) and 463.7 eV (Ti 2p_{1/2}). The fourth contribution is related to Ti (IV) and is found at 459.1 eV (Ti 2p_{3/2}) and 465.0 eV (Ti 2p_{1/2}). The fifth contribution is related to titanium surface plasmons and is found at 471.7 eV. These interpretations are in good agreement with the literature [288–290]. For the Ti_1, Ti_2, Ti_3 and Ti_4 samples, the same contributions were used, giving five peaks displaying similar binding energies for all these samples. The first contribution is associated to Ti (III) around 457.5 eV (Ti 2p_{3/2}) and around 463.0 eV (Ti 2p_{1/2}). The second contribution is associated to Ti (IV) around 458.6 eV (Ti 2p_{3/2}) and around 464.4 eV (Ti 2p_{1/2}) [288–290]. The third and last contribution is associated to titanium surface plasmons around 471.4 eV. The laser ablation parameters modifies both the oxide thickness and chemistry. Since no metallic titanium is detected on Ti_1, Ti_2, Ti_3 and Ti_4 samples, the oxide layer is much thicker than on the reference, which is also confirmed by the EDX measurement above. At the same time, the chemical nature of the oxide has changed, since there is no Ti (II) detected, but mostly Ti (IV) and a bit of Ti (III). The ratio between Ti (III) and Ti (IV) did not show significant changes between the different samples (systematically about 0.13). The metal oxide layer is chemically more homogeneous than on the reference and tends to the composition of pure TiO₂. Even if the data demonstrates an evolution towards a more chemically homogeneous oxide layer, no data has been collected on the crystallinity of this oxide. As for the aluminum it plays a role in the thermal conductivity and should be investigated in order to draw conclusions on the question of the thermal conduction.

5.2.3 Conclusions on the titanium laser ablation

To put it in a nutshell, the shear load is linearly correlated to the joint area. The determining parameter that increases the mechanical resistance is the thermal contact resistance. Indeed, the

samples presenting the highest shear load have the lowest TCR. It is influenced by the thickness of the oxidized layer, its chemical nature and its surface roughness. The thickness is similar for the samples Ti_1, Ti_2 and Ti_3, while thinner for the Ti_4 samples from the EDX results. Regarding the chemical nature, from the XPS results, observation was made that the ablated surfaces are strongly oxidized and that the chemical nature tend towards stoichiometric TiO₂. However, as the crystallinity was not evaluated no clear statement can be made on the effect on the thermal conductivity. The last parameter, the roughness, shows an inversely proportional behavior: the smoother the surface the higher the shear load. This can be explained by a more intimate contact between the materials leading to a better heat transmission.

5.3 Conclusions

Different surface treatment were tested during the Laser-STAMP project, but only the experiments on the ablation are presented, as they are the only ones relevant for this thesis. The ablation was tested on both aluminum/polyamide-6.6 and titanium/polyamide-6.6 assemblies.

On the two assemblies similar observations were made. The shear load is each time linearly correlated to the joint area. The larger the joint area, the higher the shear load. The strength (shear load per unit area) for both samples is constant. More importantly, the failure is cohesive, which means that the interactions at the interface are stronger than the base material. From this, the goal is to increase the joint area. Therefore, looking at the TCR for both combinations, it appears that the lower the TCR, the higher the shear load. Larger joint area are observed on the samples presenting the lowest TCR. So to increase the joint area, the best way appears to be the decrease of the TCR. Looking at the EDX results, it appears that a thinner oxidized layer is better. Indeed, as the oxide presents a lower heat conductivity than the pure metal, diminishing this layer is of great interest to increase the heat conduction and so the joint area. The roughness of the surfaces is also playing an important role in the heat conduction at the interface. Here also for both assemblies, the smoother the surface the higher the shear load. A lower roughness allows for more intimate contact between the joining partners, which allows the heat to be transferred more easily. The last point is the chemical nature of the oxidized layer. On aluminum, the ablation allowed to tune the chemical formula of the oxide towards a stoichiometric aluminum oxide Al₂O₃. This means a lower presence of hydroxide and is correlated to a higher shear load. However, the chemical composition alone does not explain such behavior, and the crystallinity should be investigated in order to draw solid conclusions on the matter. The data on the titanium tends to show the same behavior, a purer oxide leads to a stronger assembly, but here also the crystallinity should be investigated.

Chapter 6

Aluminum-polyamide bonding?

In this chapter, all the results from all the experiences done, in order to show the existence and the nature of a chemical bond between aluminum sheets and polyamide-6.6, are presented. The results are presented in a “top-down” approach. First the more industrial-like samples are presented: the welded and the ablated welded. The welded samples consist in ethanol wiped aluminum sheets welded to polyamide plates. The ablated welded samples are similar to the welded samples, only the aluminum sheets are laser ablated prior to welding. To access the interface on those samples, they were broken, and the remaining polyamide residue was then dissolved using 2,2,2-trifluoroethanol. Then the spin-coated samples will be discussed and finally the model samples, which will allow to draw the conclusions of this chapter. The spin-coated samples are mirror polished aluminum plates spin-coated with polyamide, some of them were welded, some not, which are used as reference samples. The deposited polyamide layer was then removed also using 2,2,2-trifluoroethanol as solvent. The model samples were prepared using a molecule, N-methylformamide, presenting only the reactive part of the polymer. This molecule was dip-coated on UV-cleaned aluminum plates. UV-cleaned surfaces were used as reference, while the dip-coated samples were separated into two groups, some were just air dried, and the others were heated to mimick the welding procedure. All those different samples were analyzed using XPS and ToF-SIMS. The welded samples were prepared in order to have samples near to industrial preparation conditions. The ablated welded were prepared in order to see if there are noticeable changes at the interface due to the ablation pretreatment. The spin-coated samples were prepared in order to better understand the impact of the welding at the interface of a polymer already in intimate contact with the metal. The model samples were prepared at the same time as the spin-coated samples also in order to confirm the observations and help in determining the reaction mechanism. The complete description of the strategy and the preparation of the samples can be found in Chapter 4 Materials and Method.

6.1 Welded samples

The data presented in this section have been published in the article “Highlighting Chemical Bonding between Nylon-6.6 and the Native Oxide from an Aluminum Sheet” published in June 2020 in *ACS Applied Polymer Materials* [281], but some changes were done, in order to fit in the text, and some data was added. At the end of this part the interest and limitations of PCA will be discussed.

Table 6.1: Average XPS elemental composition of bulk polyamide-6.6 (PA-6.6 ref.), aluminum surface prior welding (Al ref.) out of the weld and in the weld.

Samples	%O	%Al	%C	%N	%F	%Mg	%Ca	%Zn
PA-6.6 ref.	12.3 (± 0.3)	0.0	75.9 (± 0.1)	11.8 (± 0.2)	0.0	0.0	0.0	0.0
Al ref.	41.1 (± 3.1)	27.5 (± 2.6)	29.5 (± 5.7)	0.8 (± 0.3)	0.0	0.3 (± 0.0)	0.5 (± 0.1)	0.2 (± 0.2)
Out of weld	43.8 (± 2.0)	28.6 (± 0.7)	24.6 (± 2.5)	0.7 (± 0.3)	1.4 (± 0.2)	0.3 (± 0.1)	0.5 (± 0.1)	0.1 (± 0.1)
Weld	36.6 (± 1.7)	23.9 (± 2.3)	32.8 (± 3.2)	4.4 (± 0.7)	1.7 (± 0.2)	0.1 (± 0.2)	0.5 (± 0.1)	0.0

6.1.1 Adhering polymer on the aluminum surface in the weld

By comparing the values of the elemental composition per zone (out of the weld and in the weld) measured with XPS, given in Table 6.1, significant differences in the elemental composition are measured between the two zones. Aluminum concentration is significantly lower in the weld, while carbon concentration is significantly higher. This can be explained by the presence of a thin polymer layer (nanoscale) bound to the surface and covering the aluminum. This is validated by the significant increase of the nitrogen percentage which is multiplied by more than six. It is also confirmed by the strong decrease of the oxygen percentage, since the concentration of oxygen in polyamide is much lower than in aluminum oxide, their respective chemical formula, Al_2O_3 and $(\text{C}_{12}\text{H}_{22}\text{N}_2\text{O}_2)_n$, giving respectively a ratio of 3/5 and 1/8. For comparison purposes the elemental composition of bulk polyamide-6.6 is also presented in the table as “PA-6.6 ref.” and the detailed spectra are displayed in the annex. Some calcium was identified which is a contamination from an unknown source. As for magnesium and zinc, they are present in the aluminum alloy and their percentage is very small. As for the fluorine, it is observed in relatively low levels (1-2 %) both in and out of the weld. It originates from the dissolution step, since 2,2,2-trifluoroethanol containing fluorine was used. J. Vaynberg and L.M. Ng [291] in 2005 demonstrated that this molecule adsorbs onto aluminum oxide surfaces at 300 K, without reaction or decomposition on the surface, therefore not chemically altering the surface. This is supported by the XPS high resolution spectra of the Al 2p region out and in the weld presented in Figure 6.1 (a) and (b), because no Al-F contribution can be seen around 76-77 eV [292–294]. In these spectra, two contributions attributed to metallic aluminum are observed at 72.7 eV and 73.2 eV for Al 2p_{3/2} and Al 2p_{1/2} respectively, the last contribution at 74.7 eV is attributed to oxidized aluminum [282]. In ToF-SIMS data, no ions related to fluorine incorporated to the aluminum surface could be identified (ions containing aluminum and fluorine atoms). Nonetheless ions corresponding to the solvent could be identified and prove that residual solvent molecules remain adsorbed onto the surface (see annex). Their intensities out and in the weld are equivalent, implying that the perturbation induced by the solvent in this analysis is of the same amplitude out and in the weld, so that in the end it can be neglected.

Figure 6.1 (c) and (d) show two examples of representative carbon high-resolution spectra from out of the weld and in the weld. The “out of the weld” spectrum is a typical adventitious carbon spectrum with a C-C/C-H contribution at 284.8 eV (reference), a C-O/C-N at 286.1 eV and a O-C=O contribution at 288.8 eV [283, 284, 295, 296]. The weld spectrum is very close to the one of polyamide with the C-C/C-H bond at 284.8 eV, C=O contribution at 288.1 eV and finally the C-N/C-O contribution at 286.0 eV [282]. The measured ratio between the peak C-N/C-O contribution and the C=O one (1.1 in average) is close the theoretical ratio expected

for PA (1.0). The spectra in the weld are very similar to those of bulk polyamide-6.6 (presented in the annex), confirming that polyamide-6.6 is still adhering on the surface in the weld after dissolution. Ethanol wiping removes some surface contamination from the aluminum but does not provide a perfectly clean surface before welding. In order to get a perfectly clean surface, the work should have been realized in a glove box in inert atmosphere, which is far beyond the aims of this study. Indeed, the current investigations aim at studying materials prepared and joined in conditions close to the industrial ones.

Figure 6.1 (e) and (f) present the O1s high resolution spectra. Out of the weld, the spectral decomposition is typical for aluminum oxidized surfaces with a contribution at 531.5 eV attributed to aluminum oxide, one contribution at 532.5 eV due to hydroxide and the third one at 533.4 eV attributed to both water and organic compounds from adventitious carbon [150, 282, 297]. The same fitting approach was used for the spectra in the weld resulting in an oxide peak at 531.3 eV, a hydroxide peak at 532 eV and a peak at 532.9 eV. This last peak is a mix of water in the aluminum oxidized layer, the polymer layer and adventitious carbon. This contribution is much higher than out of the weld, also supporting the fact that a thin layer of residual polymer binds to the surface.

The N1s high resolution spectra out and in the weld are also shown in Figure 6.1 (g) and (h). In both spectra there was only one contribution at 400 eV and 399.7 eV out and in the weld respectively. In the weld the peak can without any doubt be attributed to the presence of polyamide-6.6 on the aluminum surface [282]. This is also confirmed by comparing the spectra to those of bulk polyamide-6.6. Out of the weld the chemical binding state is less clear: it is an organic compound, possibly an amine [282, 286, 298]. The important fact is that the nitrogen out of the weld is not related to polyamide-6.6, which during the dissolution process would have reabsorbed onto the surface. Indeed the same type of nitrogen (similar N 1s spectra) is found on simply ethanol wiped aluminum (see annex).

The XPS data obtained on the aluminum surface seem to be in good agreement with previous characterization [191, 195, 198, 299–305], though the observation of nitrogen on simply ethanol wiped aluminum surfaces is rather uncommon, it has already been observed elsewhere [148, 306].

The presence of polymer in the weld is confirmed by ToF-SIMS measurements by looking at some specific ions of the polyamide-6.6, presented in Figure 6.2. For comparison purposes, the intensity of the different ions were normalized on the total intensity of the spectrum. Their relative intensity is increasing up to 6 times, and ions having a chemical formula near the one of the monomer can be identified (see in particular Figure 6.2 (d)).

Some specific ions relative intensity in both positive and negative ion mode of the aluminum surface are presented in Figure 6.3. The ions are still present in the weld, even though their intensity has been nearly divided by two. In addition, when the samples are taken out from the solvent after dissolution, there is no trace of polymer visible by eye in the welded area. Therefore the residual polymer layer bound to the aluminum surface is a very thin film, with a thickness in the order of the ToF-SIMS sampling depth (~ 1 nm). This film can present holes, but these would be of sub-micron size, as the images in Figure 6.4 (a), (c) and (e) do not show any hole of micrometric size and the lateral resolution is of micrometer scale.

Images were also acquired in the border region between the weld and outside of it. The images and their area integration along the x axis of some specific polymer ions are presented in Figure 6.4 (a) to (f). Going from left to right, in all images there is a high intensity zone and then a low intensity zone. The high intensity zone corresponds to the weld, as indicated on the images, and the low intensity zone to the out of weld. The separation between both zones is rather steep. The dashed line in the area integrations represents the separation between the weld and outside the weld. One will also observe that the separation is not at the same place on the x axis between the negative ions ($x = 0.7$ mm) and the positive ions ($x = 1.0$ mm), this is

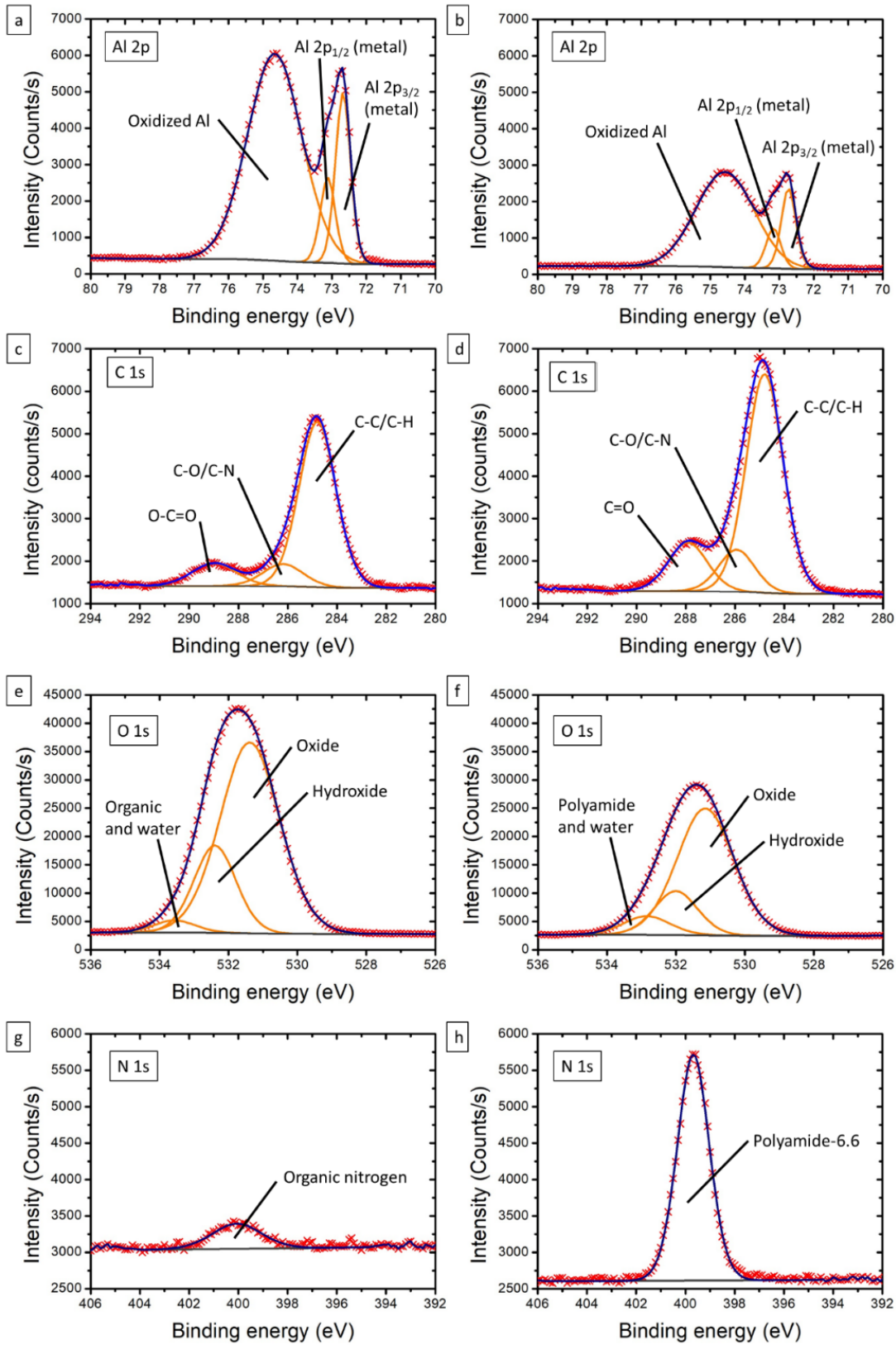


Figure 6.1: High resolution spectra of the Al 2p region (a) out and (b) in the weld, of the C 1s region (c) out and (d) in the weld, of the O 1s region (e) out and (f) in the weld, and of the N 1s region (g) out and (h) in the weld.

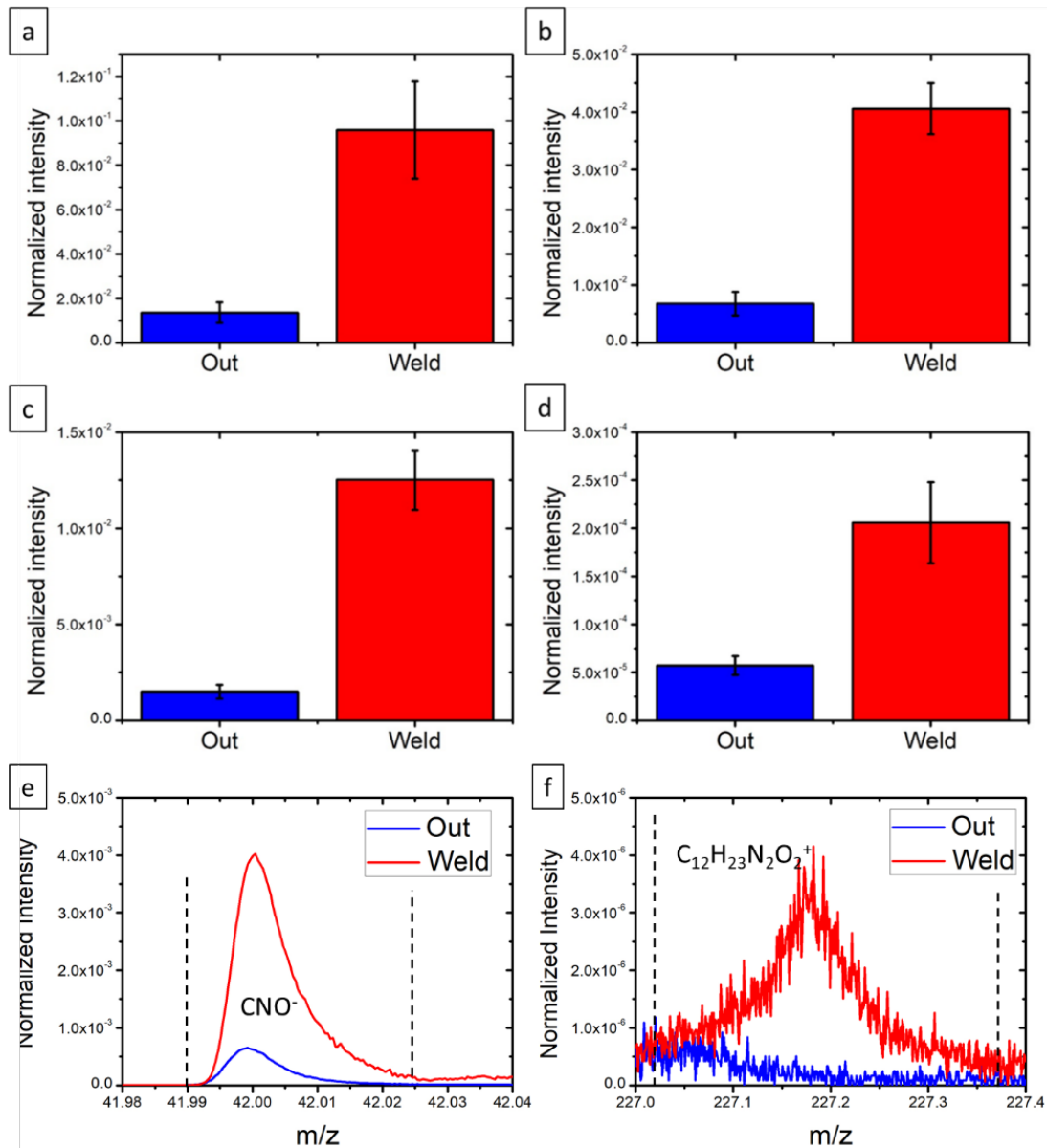


Figure 6.2: ToF-SIMS characteristic polyamide-6.6 ions in the negative and positive mode, presented in intensity normalized to total counts per zone, in blue the out of weld and in red the weld. (a) CNO^- , (b) CH_4N^+ , (c) CH_2NO^+ and (d) $\text{C}_{12}\text{H}_{23}\text{N}_2\text{O}_2^+$. Mass spectra zone with the range of interest marked by dashed lines of (e) CNO^- , and (f) $\text{C}_{12}\text{H}_{23}\text{N}_2\text{O}_2^+$.

simply due to the fact that both images were not acquired at the same place, which is common when switching from one polarity to another.

Looking at Figure 6.4 (g) and (h), presenting the image and its area integration along the x axis of the intensity of Al^+ , the separation between both zones is clear but not as sharp as for the polyamide ions. The high intensity zone now corresponds to the uncovered Al surface out of the weld, whereas the low intensity zone corresponds to the Al material covered with an ultrathin film of residual polyamide, in the weld zone. By comparing PA and Al images one can identify a complementary pattern, so that the separation between the out and in the weld can be located at the very same place.

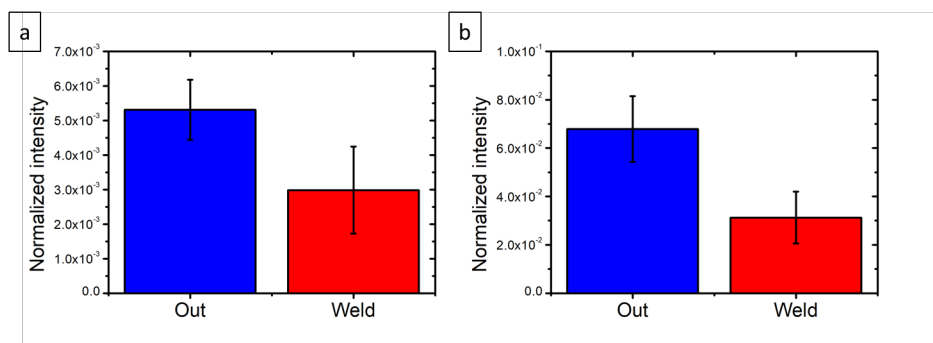


Figure 6.3: ToF-SIMS characteristic aluminum ions in the negative and positive mode, presented in intensity normalized to total counts per zone, in blue the out of weld, and the weld in red. (a) AlO^- , (b) Al^+ .

6.1.2 Identification of the bond's nature

As an ultrathin polymer layer still binds to the surface after dipping it overnight in the solvent, it implies that the interactions between the Al native oxide and PA are stronger than the interactions with the solvent leading to dissolution. As written above, the adhesion theory proposes four effects: mechanical interlocking, diffusion, chemical-physical bonding, and electrostatic interactions. Diffusion to the best of our knowledge cannot explain why polymer sticks to the surface even after the dissolution step. This step consists in dipping the samples overnight in 2,2,2-trifluoroethanol under mechanical agitation in a volume more than able to dissolve the polymer residue. A diffusion effect exists (see Chapter 8), but its effect on the interfacial interactions has yet to be investigated. Electrostatic interactions at interfaces between polymers, especially insulating ones, and metals are not well understood yet and are qualified as secondary effects for adhesion [9, 243], so insufficient to explain the adhering polymer. The last explanation is chemical bonding (see chapter 3 part 3.3). During the welding process the temperature increases up to nearly 300°C [250] and the polymer melts briefly. The liquid polymer can then wet the native aluminum oxide and react with it. The reaction rate may be enhanced by the temperature, but temperatures way above the melting point degrade the polymer and are not desirable [250]. Looking at the polymer chain presented in Figure 6.5, several reactive sites can be identified, marked by red dots. We distinguish three different types of reactive sites: the first one is the oxygen atom of the amide function, the second one is the nitrogen atom of the amide, and the third are the carbon atoms near the amide functions which are more reactive than the other carbon atoms. One is connected to the oxygen and the nitrogen, the second one in alpha of the carboxyl and the third one connected to the nitrogen. This gives three bonding possibilities between the polymer and the metal: one involving only carbon atoms, one involving only a nitrogen atom and one involving only an oxygen atom. Now looking at the reactive sites of the aluminum surface, two different types of sites exist: oxide and hydroxide sites. Generally the reaction occurs with the hydroxyl free groups present at the surface [152, 198, 307].

6.1.2.1 Reaction with the carbon sites

The high resolution spectrum of the carbon C 1s region in the weld, which is presented in Figure 6.1 (d), does not show any peak around 283 eV, which would be the signature of metal-carbon (carbide) bonds. This absence means that there are no such bonds between the polymer and the metal, or too few to be detected with XPS. Figure 6.6 presents the relative intensity of ions from the $\text{C}_x\text{H}_y\text{Al}_z^{-/+}$ family obtained in ToF-SIMS. Most of them have decreasing or

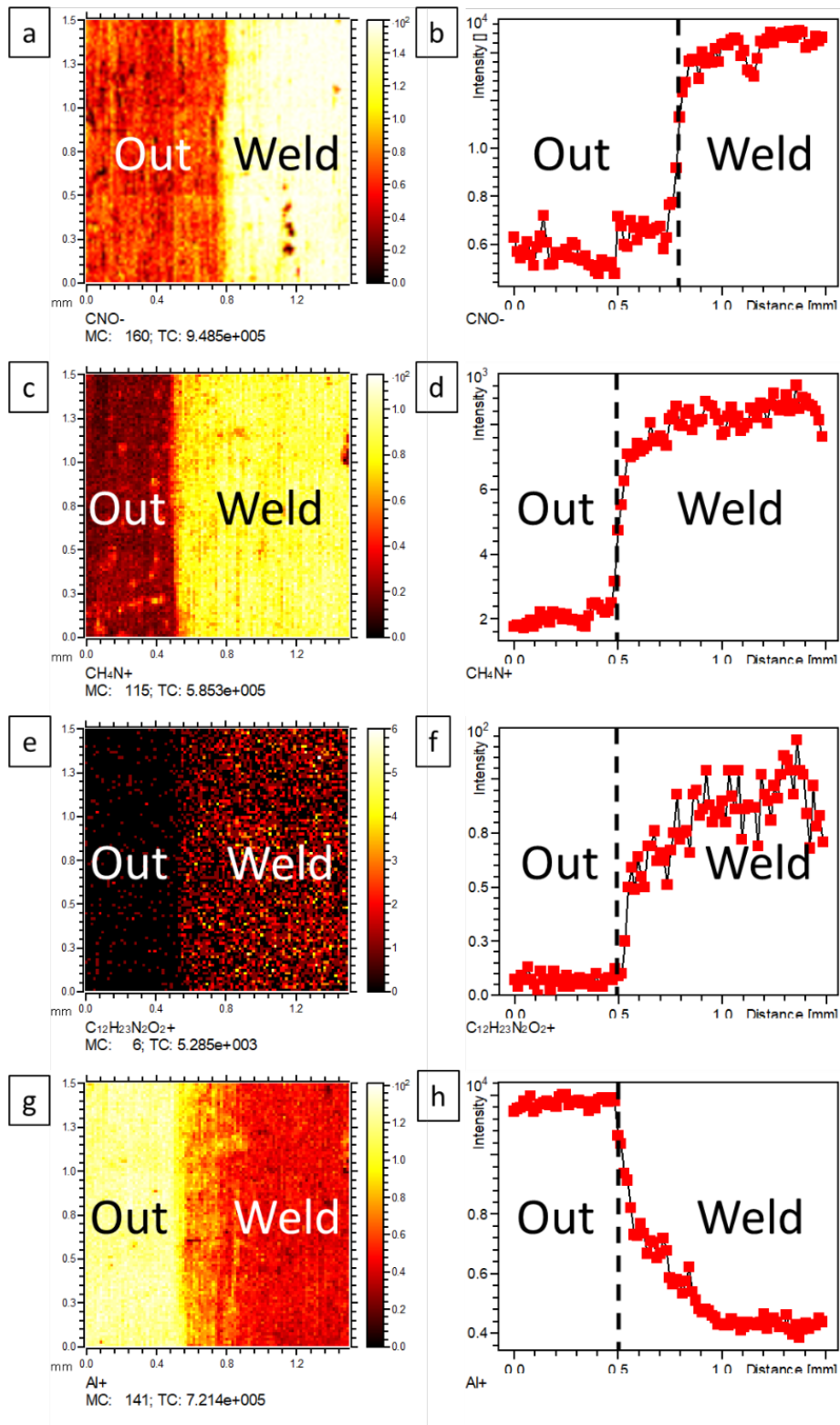


Figure 6.4: ToF-SIMS large area images and their area integration along the x axis (a) and (b) CNO⁻, (c) and (d) CH₄N⁺, (e) and (f) C₁₂H₂₃N₂O₂⁺, and (g) and (h) Al⁺.

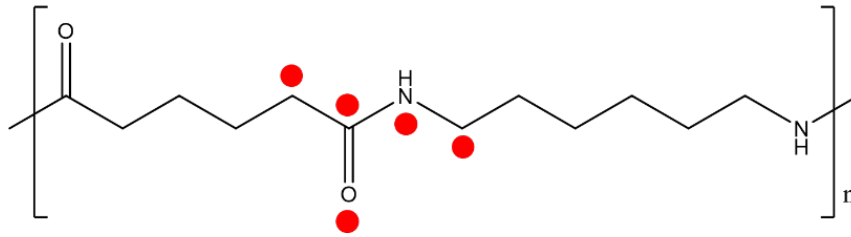


Figure 6.5: Chemical formula of nylon-6.6 showing the reactive sites by red dots of the chain.

constant intensities. Since in general, the relative intensity is decreasing or constant while the carbon concentration increases in the weld compared to the out of weld (see Table 6.1), the conclusion is that no carbon bond occurs between the metal and the polymer.

Some other studies suggest the existence of a carbon bond [308, 309]. Bou et al. [308] are interpreting the C 1s region by adding a C-Al peak around 282-283 eV, which is in good agreement with XPS database [286], but at the same time in the Al 2p region no C-Al peak is visible. Liu et al. [309] based their work on that of Bou et al., but they interpreted the Al 2p region with an Al-C peak at 73.0 eV, which is not impossible, but should rather be interpreted as a peak of metallic aluminum. Furthermore, synthesizing pure aluminum carbide is difficult [310–316], because of its instability towards moisture and in general towards the presence of oxygen atoms. It is rather unlikely that an Al-C bond forms that would explain the adhesion between welded polyamide and aluminum. As a matter of fact, polyamide contains oxygen in its structure and also contains moisture [87].

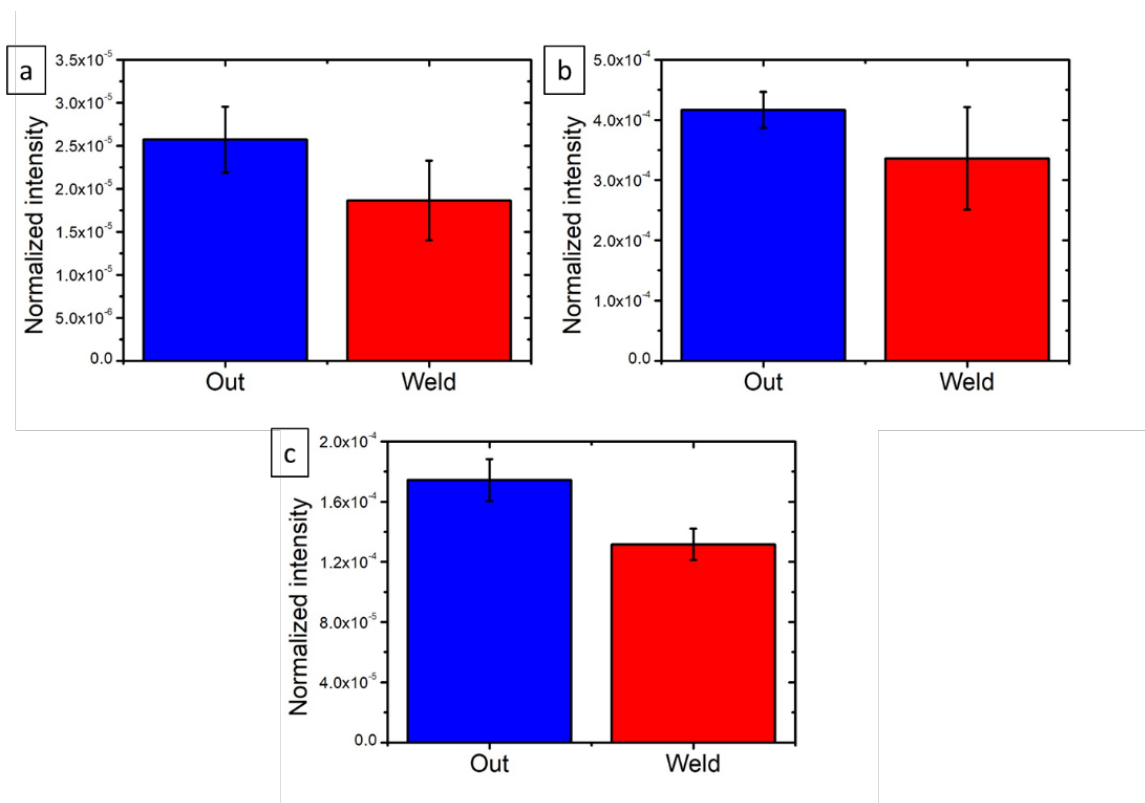


Figure 6.6: ToF-SIMS intensity normalized to total counts per zone, in blue the out of weld and in green the weld, of (a) CAI^- , (b) C_2Al^- , (c) C_2Al^+ .

6.1.2.2 Reaction with the nitrogen sites

Figure 6.1 (h) presents a typical N1s high resolution spectrum in the weld zone. As written above, a single peak at 399.7 eV is an evidence of the presence of polyamide-6.6. Since there is no peak around 396 eV, which is the expected binding energy of the Al-N bond [317–319], one can conclude that there is no Al-N bond. However, looking in detail at the ToF-SIMS data shown in Figure 6.7, two specific ions are shown: CHNAI^- and CHNAI^+ . These ions could originate from nitrogen bonding with aluminum, but also from recombination of sputtered ions or atoms such as CN^- , Al or H during the measurement. The first argument to assume a recombination is the low intensity of these ions, maximum $\sim 1.10^{-4}$ relative intensity, compared to other ions such as $\text{CHNOAl}^{+/+}$ (see section 6.3.2.3). The second argument is that the $\text{C}_x\text{H}_y\text{N}_z\text{Al}_w^{-/++}$ ions are rare in the spectra, only $\text{CHNAI}^{+/+}$ and CH_2NAI^- are observed, with a low intensity. Looking at the border region images in Figure 6.7 (c) to (f), the intensities of the ions are very low. On the images of the intensity of CHNAI^- , one can distinguish two plateaus of intensity corresponding to the weld and the out of weld. This separation is barely noticeable for the intensity of CHNAI^+ , even by binning the pixels.

As far as the authors know, pure nitrides are difficult to synthesize: several steps are needed in chemically hard conditions; and these compounds are rather unstable in the presence of moisture [320–323]. This makes the occurrence of a pure nitrogen bond between both materials rather unlikely, but local specific conditions cannot be excluded. Therefore, further investigations are necessary to shed light on this matter.

6.1.2.3 Reaction with the oxygen sites

Figure 6.1 (f) presents an example of XPS high resolution spectrum of the O 1s region in the weld. As written above three peaks have been considered to interpret these spectra. The first one at 531.3 eV is related to the oxidized aluminum in the Al_2O_3 form [258,324]. The second one at 532 eV is related to aluminum hydroxide. The third one at 532.9 eV can be associated to two contributions, carboxyl group of the amide function of the polymer and possibly a C-O-Al bond. To the best of our knowledge, no author describes C-O-Al bonds in the O 1s spectra. Despite the lack of data, it seems reasonable to think that the contribution of a C-O-Al bond is around 532.9 eV, since the contribution of C-O-C is found in the same region, ranging from 532.5 eV to 532.8 eV [282]. Some authors [308,309] previously reported such a bond in their C1s spectra. They both report a C-O-Al peak around 283.3 eV. This seems to be a fairly low binding energy, since in XPS the chemical shifts (and so the binding energy) depends on the electronegativity of the neighboring atoms. The more electronegative the neighbor the higher the binding energy will be and vice versa, so C-O-Al bonds should give rise to C1s binding energies higher than 285 eV. Unfortunately, the authors of both papers do not justify their assumption any further.

The SIMS data analysis allowed to identify two families of ions related to a C-O-Al bond: the $\text{C}_x\text{H}_y\text{O}_z\text{Al}_w^{-/++}$ and the $\text{C}_x\text{H}_y\text{N}_z\text{O}_w\text{Al}_n^{-/++}$.

The ions from the $\text{C}_x\text{H}_y\text{O}_z\text{Al}_w^{-/++}$ family have an erratic behavior (see Figure 6.8), indeed some of them have equivalent or lower intensities in the weld than outside (COAl^- , CH_2OAl^- , C_2OAl^- , C_2HOAl^- , $\text{C}_2\text{H}_5\text{OAl}^-$, CO_2Al^- and CH_3OAl^+ , CH_4OAl^+ , CH_5OAl^+ , $\text{C}_2\text{H}_2\text{OAl}^+$, CHO_2Al^+) whereas others have higher intensities in the weld ($\text{C}_2\text{H}_2\text{OAl}^-$, $\text{C}_2\text{H}_3\text{OAl}^-$, and CHOAl^+ , $\text{CH}_2\text{OAl}_2^+$, $\text{C}_2\text{H}_4\text{OAl}^+$, $\text{C}_3\text{H}_4\text{OAl}^+$). The first ions, lower in intensity, can be explained by adventitious carbon and CO_2 adsorption on the aluminum surface [283, 296, 325]; while the second ions, higher in intensity, can be interpreted as originating from a C-O-Al bond.

Ions from the family $\text{C}_x\text{H}_y\text{N}_z\text{O}_w\text{Al}_n^{-/++}$ were confidently identified, as CHNOAl^- , CH_2NOAl^- , CHNO_2Al^- , $\text{CH}_2\text{NO}_2\text{Al}^-$, $\text{CH}_3\text{NO}_2\text{Al}^-$, and CHNOAl^+ , CHNO_2Al^+ and $\text{CH}_3\text{NO}_2\text{Al}^+$. Some of these ions' relative intensity are depicted in Figure 6.9. The intensity of all ions of this family

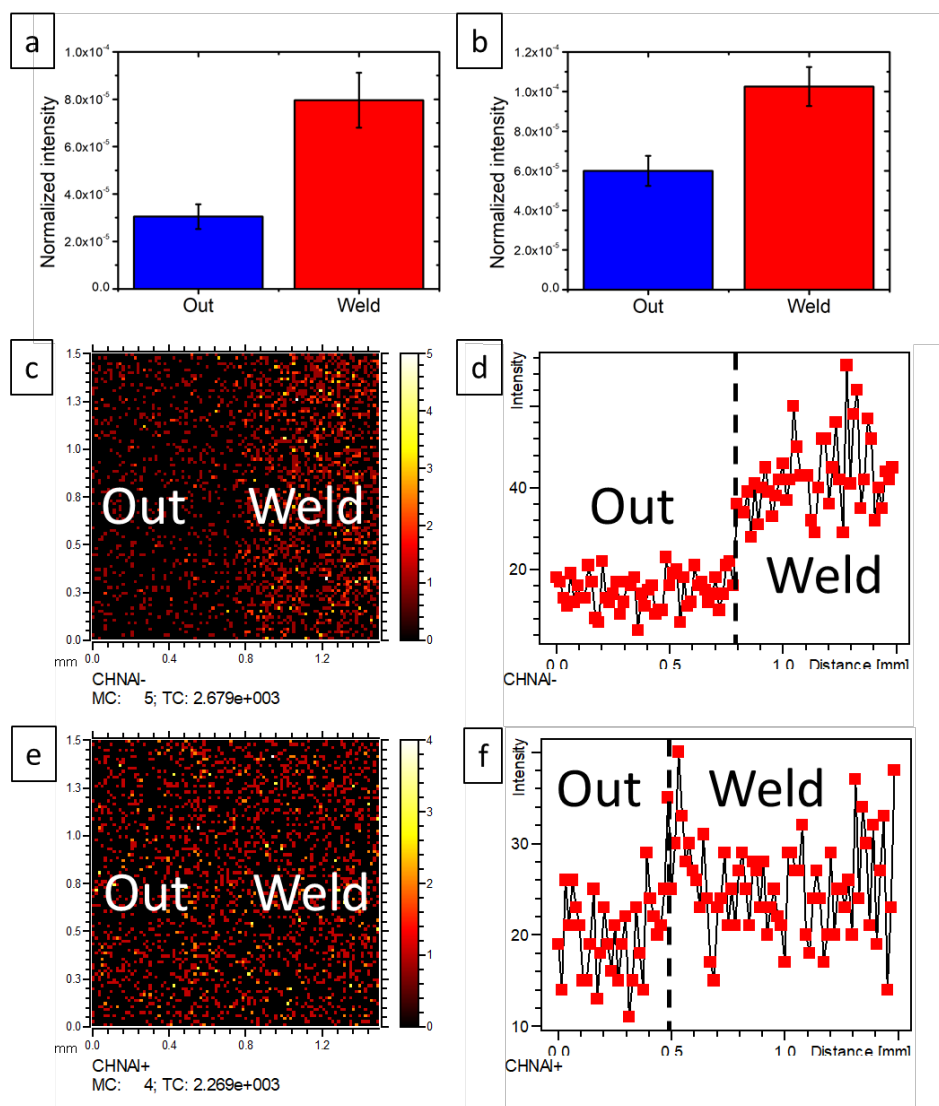


Figure 6.7: ToF-SIMS intensity normalized to total counts of (a) CHNAI⁻, (b) CHNAI⁺. Large area images obtained in ToF-SIMS at the border region for (c) CHNAI⁻ and (d) its area integration along the x axis, and (e) CHNAI⁺ and (f) its area integration along the x axis.

increases in the weld zone compared to outside of the weld. The comparison of the mass spectra in the regions of CHNOAI^{-/+} show that the intensity outside the weld is due to background in the spectra, as no peak can be assigned in these regions, whereas in the weld clear peaks can be identified (see Figure 6.9 (b) and (e)). The images in Figure 6.10, presenting the large area images of the border region and their area integration along the x axis, show that these ions are also more present in the weld than outside. Here also the separation between the weld and outside is at the very same place than for the polymer ions (Figure 6.4).

6.1.3 Discussion about PCA

The PCA analyses presented below were done after the direct analysis above. Two sets of peak list will be analyzed: the hand-selected peak lists and the automatic generated peak lists. The automatic generated peak list was obtained by using the automatic peak selection tool in the SurfaceLab 7.0 software. The parameters chosen were 100 counts as minimum intensity on

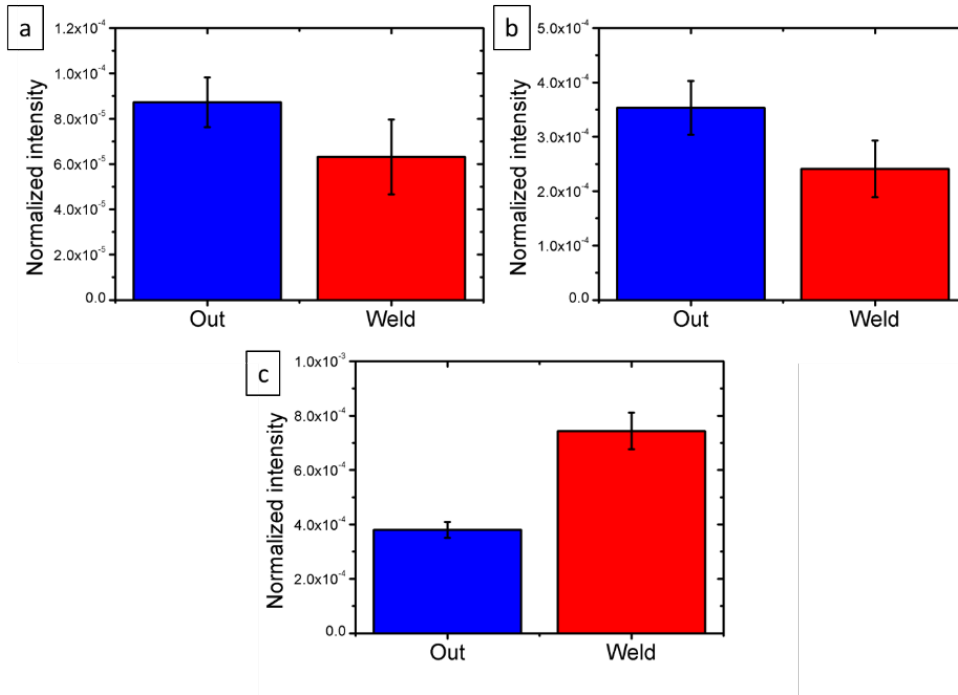


Figure 6.8: ToF-SIMS intensity normalized to total counts of (a) COAl^- , (b) CH_3OAl^+ , and (c) $\text{C}_3\text{H}_4\text{OAl}^+$.

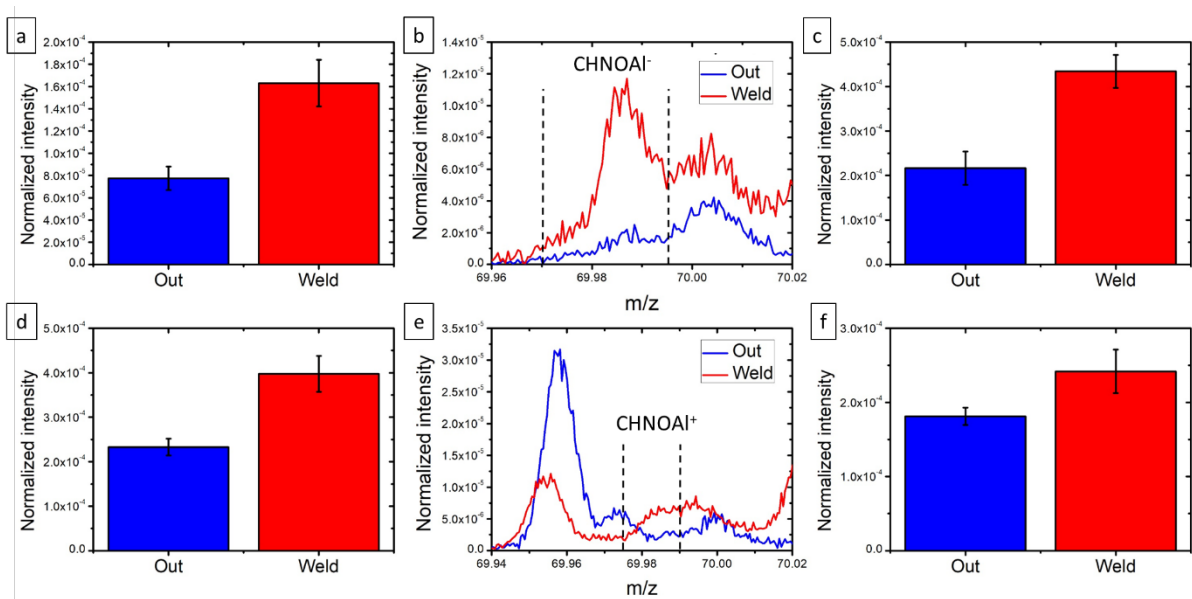


Figure 6.9: ToF-SIMS intensity normalized to total counts of (a) CHNOAl^- , (c) CHNO_2Al^- , (d) CHNOAl^+ and (f) CHNO_2Al^+ . Mass spectra comparison between the weld (in red) and out of the weld (in blue) in the region of (b) CHNOAl^- and (e) CHNOAl^+ for both with the range of interest marked with dashed lines.

a range from 0 to 300 m/z . This is done in both the negative and the positive mode.

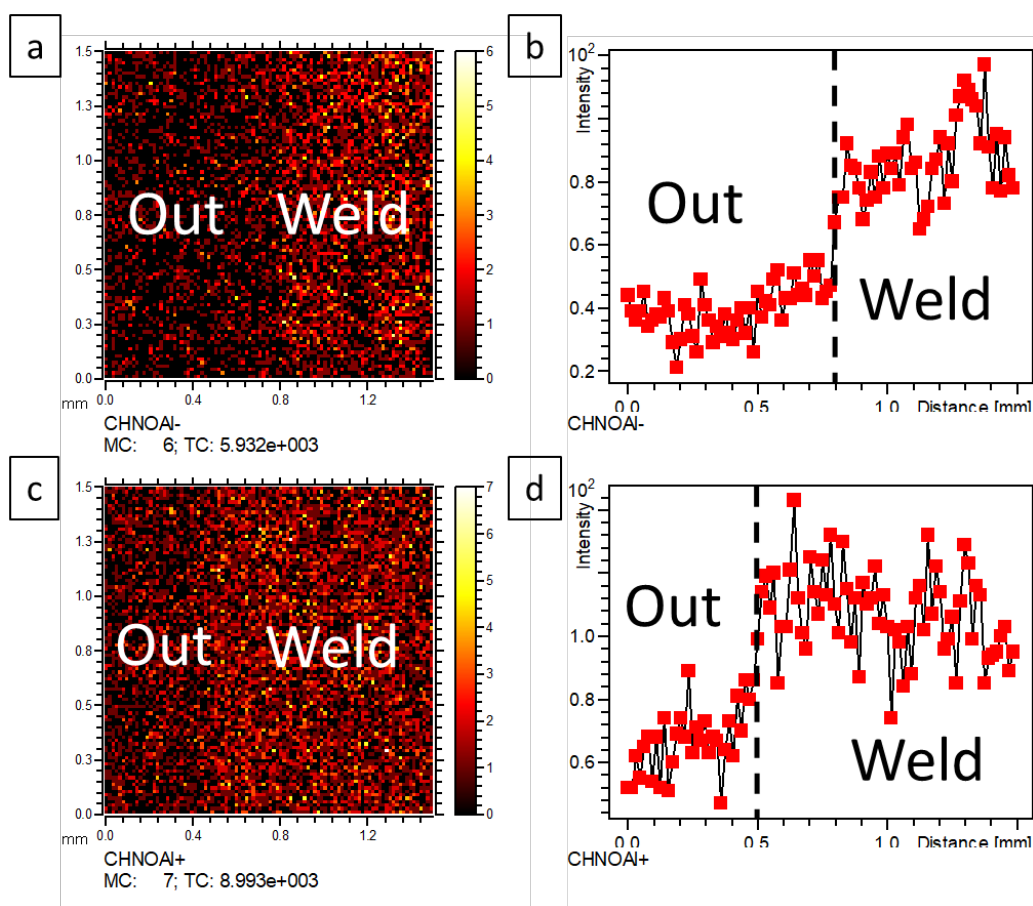


Figure 6.10: ToF-SIMS large area images and their area integration along the x axis (a) and (b) for CHNOAl⁻, and (c) and (d) CHNOAl⁺.

6.1.3.1 PCA on the hand-selected peak lists

The hand-selected peak lists are the ones used for the direct analysis. The scores of the PCA on the hand-selected peak lists in both polarities are depicted in Figure 6.13. The samples are separated directly with PC1 and PC2 does not discriminate the samples. This is even more visible on the plots of PC1 versus PC2. All the information for the sample separation are present in PC1 for both polarities. So only the loadings of PC1 are needed to analyze the differences between the samples. They are represented in Figure 6.14. In both polarities the loadings display the same behavior. Positive loadings are associated to ions having higher intensities in the weld than out of it, while the negative loadings are related to ions presenting lower intensities in the weld than out of it. The ions presenting high positive loadings for both polarities are associated to ions originating from the polymer. For instance in the negative mode, mass 26 is CN⁻, mass 40 is C₂H₂N⁻, mass 42 is CNO⁻, or mass 83 is C₅H₉N⁻. In the positive mode mass 30 is CH₄N⁺, mass 44 is CH₂NO⁺, mass 55 is C₃H₃O⁺, mass 100 is C₅H₁₀NO⁺, or mass 111 is C₆H₇O₂⁺. The negative loadings are related to the aluminum and contaminations. For instance in the negative mode, mass 17 is OH⁻, mass 59 is AlO₂⁻, and mass 77 is AlH₂O₃⁻. In the positive mode, mass 23 is Na⁺, mass 27 is Al⁺, mass 39 is K⁺, and mass 43 is C₃H₇⁺. This shows that polymer is detected in the weld, which is coherent with the XPS data. Out of the weld the metal surface is not covered by polymer, so more metal and some contaminations are observed, which is also in good agreement with the XPS data. The hybrid ions are not visible in the high loadings, because

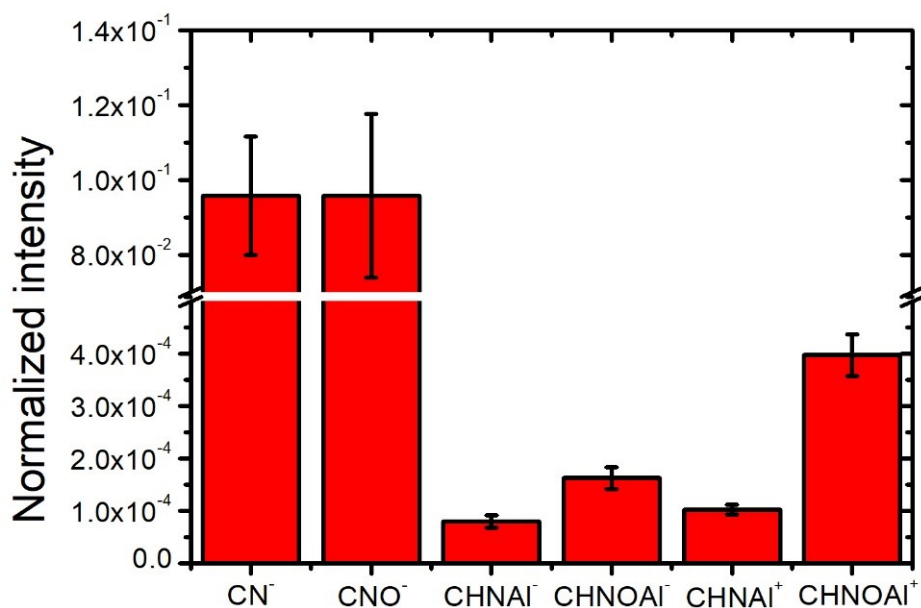


Figure 6.11: Comparison of the normalized intensity of CN⁻, CNO⁻, CHNOAl⁻, CHNOAl⁺, CHNAI⁻ and CHNOAl⁺ in the weld.

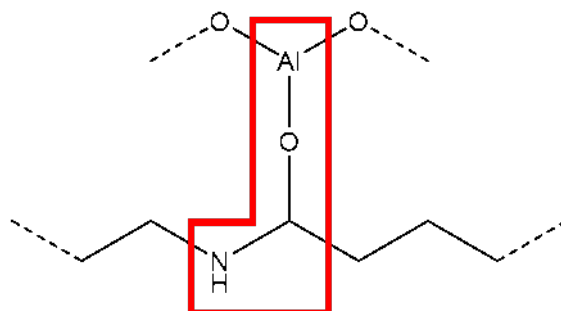


Figure 6.12: Scheme of the chemical bond between the aluminum surface and the polyamide-6.6. The fragment CHNOAl^{-/+} is shown with a red frame.

they present low intensities compared to the other ions selected. Here the PCA strengthen the observation made above, that polymer is detected in the weld and not out of it, but does not help directly to understand the nature of the bonding.

6.1.3.2 PCA on the automatic generated peak lists

Two peak lists were obtained by using the automatic peak selection of the SurfaceLab software, one for each polarity. All the peaks within the 0-300 m/z range with an intensity higher than 100 counts were selected. The number of peaks obtained were 366 and 372 for the negative and the positive mode respectively. In Figure 6.15, the scores of the two first principal components are depicted for the negative and positive mode. It is directly observable that for both modes, the samples are directly separated by the first principal component, while the second one does not differentiate them. This is emphasized in the graph plotting the scores of the two

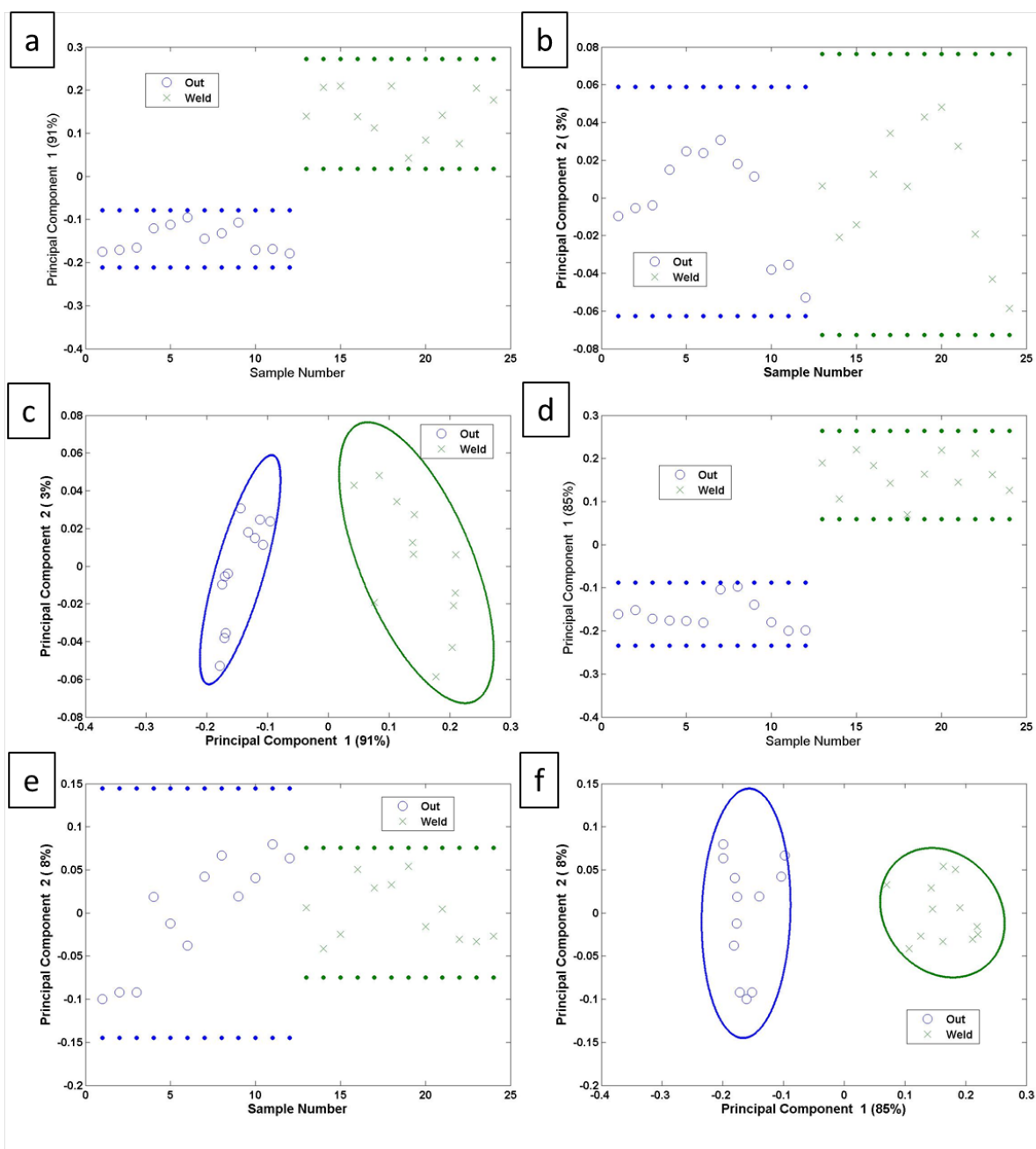


Figure 6.13: Scores of the hand-selected peak list. In the negative mode (a) PC1, (b) PC2, and (c) PC1 versus PC2. In the positive mode (d) PC1, (e) PC2, and (f) PC1 versus PC2.

principal components. Only one PC is needed to separate the samples, so that the difference between both samples in both modes can be seen and analyzed with bare eyes. This explains the choice of not using a PCA at the first place.

Since the separation of the sample is done by PC1 alone, only the loadings of PC1 were investigated. They are displayed in Figure 6.16. The pattern is the same for both polarities. The positive loadings indicate a higher intensity in the weld than out of it, and negative loadings the opposite. The ions presenting positive loadings in both the negative and the positive mode are related to the polymer. For instance, in the negative mode mass 26 is CN^- , mass 40 is $\text{C}_2\text{H}_2\text{N}^-$, mass 42 is CNO^- , or mass 83 is $\text{C}_5\text{H}_9\text{N}^-$. In the positive mode mass 30 is CH_4N^+ , mass

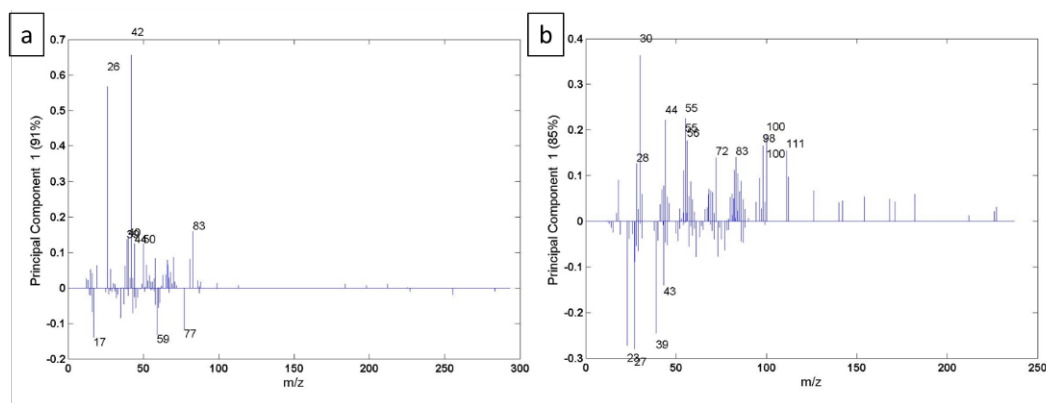


Figure 6.14: Loadings of PC1 (a) in the negative mode and (b) in the positive mode.

44 is CH_2NO^+ , mass 55 is $\text{C}_3\text{H}_3\text{O}^+$, mass 100 is $\text{C}_5\text{H}_{10}\text{NO}^+$, or mass 114 is $\text{C}_7\text{H}_{14}\text{O}^+$. The ions presenting negative loadings are related to the aluminum and contaminations. For example, in the negative mode, mass 59 is AlO_2^- , mass 119 is $\text{Al}_2\text{O}_4\text{H}^-$, mass 239 is $\text{Al}_4\text{O}_8\text{H}_3^-$, or mass 281 is $\text{Al}_5\text{O}_9\text{H}_2^-$. In the positive mode, mass 23 is Na^+ , mass 27 is Al^+ , mass 39 is K^+ , mass 43 is C_3H_7^+ , and mass 91 is C_7H_7^+ . More metal is visible out of the weld while in the weld polymer is detected. This is in good agreement with the XPS data and the direct analysis made above. Nonetheless, the hybrid ions do not present high loadings, which is coherent with the fact that they present low intensities.

6.1.4 Conclusions on the welded samples

This part investigates the nature of the interface in a joint formed by laser welding between an aluminum sheet and a polyamide plate. This part defines a new methodology to access the aluminum-polyamide interface, by breaking the joint and dissolving the residual polymer, allowing characterization with XPS and ToF-SIMS. The fracture leaves a polymer residue which was dissolved subsequently by 2,2,2-trifluoroethanol. The effect the solvent had on the interface proved to be negligible, because it adsorbs on the surface out and in the weld in the same manner, inducing the same perturbation in both compared zones.

It was shown that an extremely thin polymer film was still detected in the welded zone, whereas no residual polymer layer could be identified outside the weld region. Large area images were obtained to observe the border region between the weld and outside of the weld. The transition between the two regions occurs on a rather thin line (some tenth of microns), in particular when ions coming from the polymer are considered. The presence of such a residue can only be explained by strong chemical bonding between the polymer and the metal native oxide, as it is not displaced by the solvent. The welding process actually melts the polymer at the interface, allowing it to wet and react with the native aluminum oxide and hydroxide.

Different reactive sites able to react with the aluminum surface were identified in the polyamide molecule: carbon, nitrogen and oxygen sites, leading to three different bonding configurations. The carbon reactive sites, giving a C-Al bond, proved not to be the source of a chemical bonding with the aluminum. The nitrogen sites, were more difficult to analyze. The assertion can be made that an Al-N-C bond is not responsible for the polymer adhesion on the surface on a large scale. Nonetheless, such a bond formed in very specific and local conditions during the welding cannot be excluded and should be investigated more in details. At last the oxygen sites were studied and the combined results from XPS and ToF-SIMS proved that a C-O-Al bond is formed during the welding (as shown in Figure 6.12) and explains the adhesion

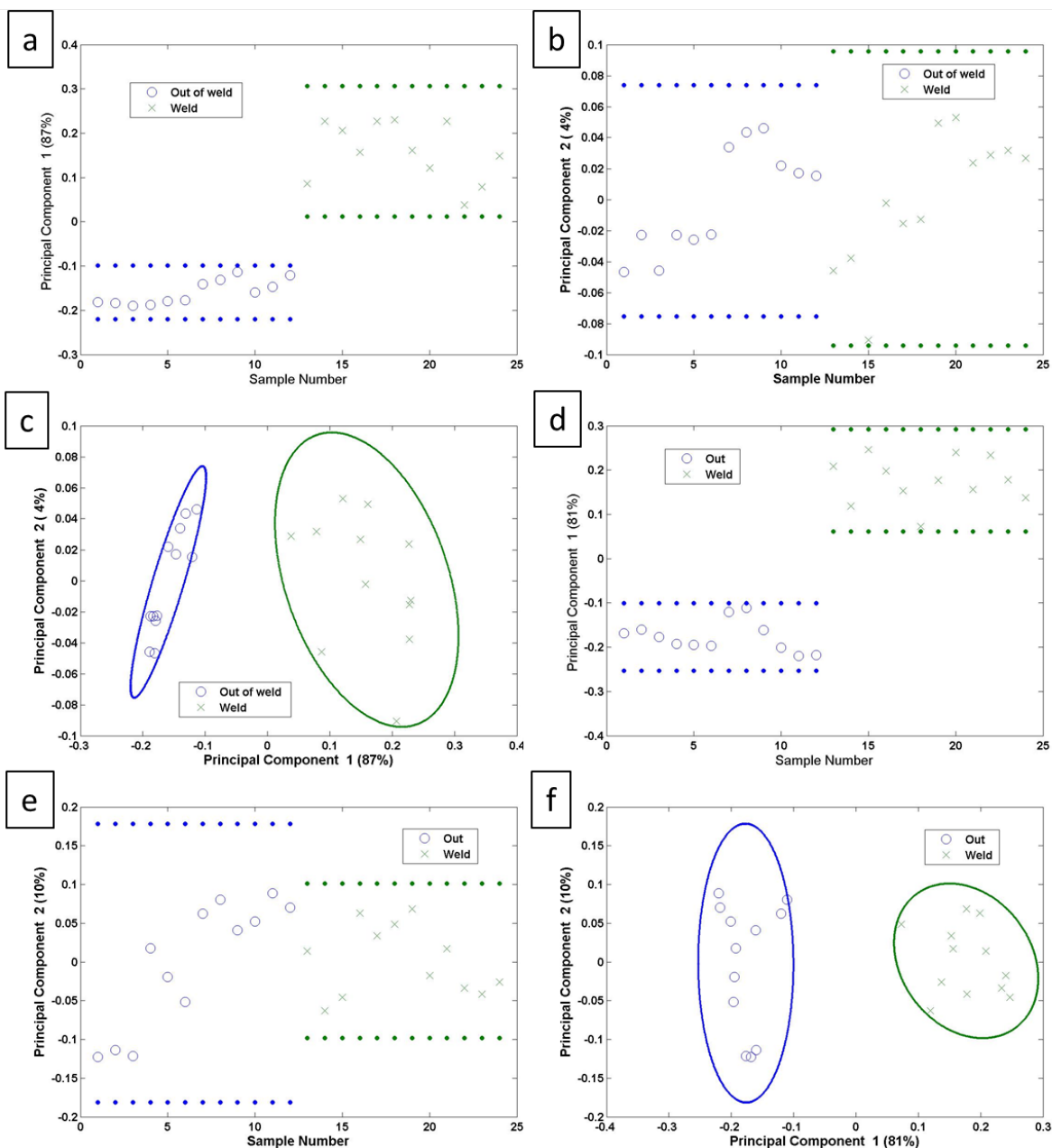


Figure 6.15: Scores of the automatic selected peak list. In the negative mode scores of principal component (a) 1 and (b) 2, (c) PC1 and PC2 plotted together. In the positive mode scores of principal component (d) 1 and (e) 2, (f) PC1 and PC2 plotted together.

of polymer residues after breaking and dissolving the samples. These C-O-Al bonds are likely created by a reaction between the polymer amide groups and the aluminum hydroxide groups. The brief high temperature spike during the welding process allows fast conformation changes of the polymer chains and also enhances the reaction rate between the amide and hydroxyl groups. However, the reaction mechanisms are still speculative and further studies with model samples were carried out to further confirm these hypotheses (see part 6.3 and 6.4).

PCA was used on two different peak lists: the hand-selected peak list and an automatic generated peak list. It shows that the separation is made directly and only with the first

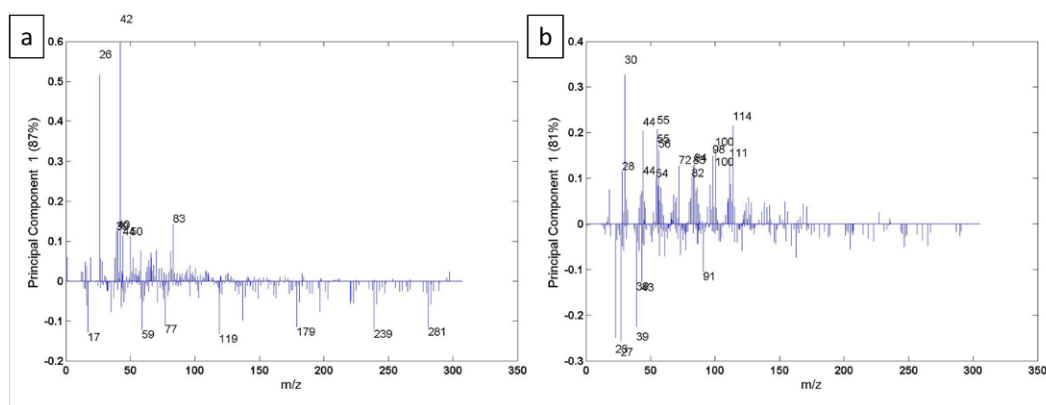


Figure 6.16: Loadings of PC1 (a) in the negative mode and (b) in the positive mode.

principal component. The loadings show that polymer is detected in the weld in both cases and both polarities. This is in good agreement with the XPS data. Nonetheless, the hybrid ions do not appear in the high loadings. So the user is forced to hand-select them to analyze their behavior.

6.2 Ablated welded samples

The goal of these samples is to assess if there are major chemical differences brought about by the surface pretreatment, which could help also to explain the higher shear loads of these samples.

6.2.1 XPS results

Laser ablation as surface pretreatment allows to drastically increase the shear load resistance of the assemblies as demonstrated in Chapter 5 part 5.1 (Surface pretreatment). An optimization process was done, to get the ablation conditions giving the highest shear load resistance, and some samples were analyzed in the same way as the welded samples studied previously. These new samples are called the “ablated welded samples”

Table 6.2 summarizes the surface composition obtained with XPS from the survey spectra of the welded and ablated welded samples out and in the weld. For clarity purposes, the welded samples will be referred to as “W” out and in the weld, while the ablated welded samples will be referred as “AW”. Out of the weld, the composition of the AW samples is comparable to the same surfaces without welding (see Chapter 5 Surface pretreatment) and compared to the W samples some differences can be pointed out: higher oxygen percentage, lower carbon percentage and zero contaminants (magnesium, calcium and zinc). This is very characteristic of surface laser ablation, which cleans the surfaces and oxidizes them. It is also to be noticed, that no fluorine is observed out of the weld, meaning that the trifluoroethanol did not adsorb on the surface during the dissolution process. The solvent induced apparently no surface modification. More interesting is the comparison between the compositions of W and AW samples in the weld. On average there is less oxygen, even if it is still within error bars. There is also less aluminum visible, maybe due to a higher coverage of polymer of the surface. At the same time, there is more carbon, as well as there is more nitrogen, nearly two times more compared to the welded samples. The increase of nitrogen percentage in the AW samples is of more than ten times from the outside to the weld. This is a good hint of a higher polymer coverage. The higher polymer coverage can be explained by a higher anchorage on the surface due to the surface pretreatment.

Table 6.2: Comparison of the XPS average elemental of the out of the weld and the weld for non-ablated and ablated aluminum-polyamide assemblies.

Samples	%O	%Al	%C	%N	%F	%Mg	%Ca	%Zn
Out of weld	43.8 (± 2.0)	28.6 (± 0.7)	24.6 (± 2.5)	0.7 (± 0.3)	1.4 (± 0.2)	0.3 (± 0.1)	0.5 (± 0.1)	0.1 (± 0.1)
Welded ablated out of weld	53.8 (± 2.6)	28.0 (± 2.5)	17.7 (± 4.8)	0.5 (± 0.5)	0.0	0.0	0.0	0.0
Weld	36.6 (± 1.7)	23.9 (± 2.3)	32.8 (± 3.2)	4.4 (± 0.7)	1.7 (± 0.2)	0.1 (± 0.2)	0.5 (± 0.1)	0.0
Welded ablated weld	31.7 (± 3.8)	17.2 (± 3.8)	44.1 (± 5.6)	7.0 (± 1.0)	0.0	0.0	0.0	0.0

In Figure 6.17, presenting the high resolution spectra of the C1s region in the weld of W and AW samples. On the W polymamide-6.6 was easily identified with three peaks: C-C/C-H at 284.8 eV, C-O/C-N at 286.0 eV and C=O at 288.1 eV [282]. For the AW samples four peak were used to interpret the spectra: a C-C/C-H contribution at 284.8 eV, a C-O/C-N contribution at 286.0 eV, a contribution of C=O at 287.9 eV and a O-C=O contribution at 288.9 eV [282]. The characteristic contribution of polyamide-6.6 are identified, and the nitrogen N1s region spectra show a unique peak at 399.6 eV, which is also characteristic of polyamide-6.6 [282, 326, 327]. In conclusion polyamide-6.6 is also binding on the surfaces in the weld after dissolving the polymer. There is an additional contribution of O-C=O, that might come from the adsorption of CO₂ onto the surface. The details of the high resolution spectra out and in the weld for the Al2p, O1s, N1s, and C1s can be found in annex.

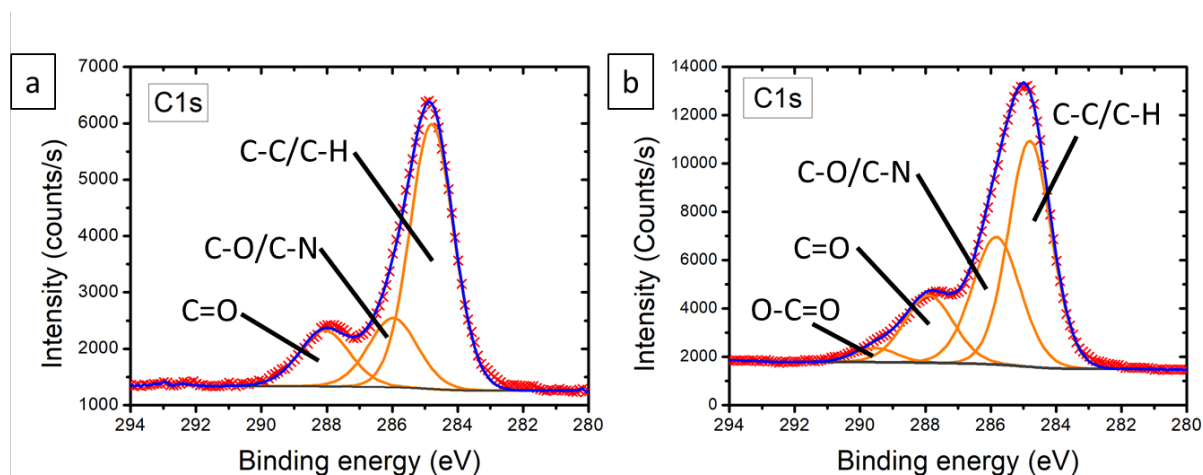


Figure 6.17: XPS high resolution spectra of the C1s region in the weld of (a) a welded sample and (b) a ablated welded sample.

By comparing the carbon C1s high resolution spectra in the weld between the W and the AW samples, it is noticeable that the C-O/C-N contribution is much more intense on the welded ablated samples and especially more intense than the C=O contribution. The ratio between the C-O/C-N and C=O contributions are indeed very different, $1.1 (\pm 0.2)$ for the W samples and $1.7 (\pm 0.3)$ for the AW samples. More bonds with the aluminum surface, which also explains the

higher polymer coverage in the weld, can induce this increase of this ratio. A parasite reaction might have occurred: crosslinking between the polymer chains due to the heat of the welding, which is also consistent with the high polymer coverage in the weld. The failure is cohesive as seen in Chapter 5 part 5.1, and the shear strength does not give any information on the interface.

6.2.2 ToF-SIMS results

Before trying to analyze the data using a PCA, a direct analysis was attempted. The peak lists for both modes were obtained using the same approach as for the welded samples (polymer ions, metal ions, hybrid ions and some contaminations). As the PCA results obtained afterwards are very similar to the welded samples, they will not be discussed here, but the data are visible in annex. In both cases, out and in the weld are discriminated completely with PC1. The positive loadings are associated to high intensities in the weld and negative loadings to high intensities out of the weld. The positive loadings are composed of ions related to the polymer, and the negative loadings to the metal surface and contaminations. This is true for both sets of peak lists (hand-selected and automatic generated peak lists).

The presence of polyamide-6.6 in the weld is also confirmed by ToF-SIMS measurements. Polyamide-6.6 characteristic ions present intensities 3 to 4 times higher intensities in the weld compared to the out of weld, as depicted in Figure 6.18. Unfortunately on those samples, monomeric ions could not be surely identified. The difference between the W and AW samples, is the thermal transfer resistance at the interface (see Chapter 5 part 5.1 surface pretreatments) due to the ablation. Since more heat is transferred to the polymer on the AW samples, the polymer degradation chances are higher, which might explain why no monomer could be identified on the AW samples, compared to the W samples or even the reference polymer spectra (see annex). To support this hypothesis a study on the polymer's degradation should be performed, which is far beyond the aim of this part.

Figure 6.19 presents the normalized intensity for characteristic aluminum ions out and in the weld. The same behavior as for the W samples can be observed; the intensity is nearly twice higher out of the weld than inside the weld. This confirms that a thin polymer layer is covering the metal surface. Here as well, the thickness of the film must be quite low, since metallic ions are still detected in the weld and should be about 1 nm. The layer might present holes, but on the images taken at the border between the weld and the out of weld, no hole can be seen (see Figure 6.20). So if the layer presents holes they must be of sub-micrometer size.

The images and their area integration along the x axis of characteristic ions of the polymer and the metal presented in Figure 6.20, show the same features as those taken on the welded samples (see Figure 6.4). A low intensity and a high intensity zone with a sharp separation between the out and in the weld for the polymer ions. For the aluminum ions, first there is a high intensity zone, then a low intensity zone, also with a sharp separation line. When superimposing the images from the polymer and the metal, the separation line overlays perfectly in both positive and negative mode, giving a complementary pattern. The dashed line in the area integrations represents the separation between the weld and outside the weld. One will also observe that the separation is not at the same place on the x axis between the negative ions ($x \approx 0.75\text{mm}$) and the positive ions ($x = 0.9\text{ mm}$), this is simply due to the fact that both images were not acquired at the same place, which is common when switching from one polarity to another.

The possible chemical reactions were also investigated for these samples. There were less hybrid ions identified on these samples. Hence, no ions of the $\text{C}_x\text{H}_y\text{Al}_z^{-/+}$ and the $\text{C}_x\text{H}_y\text{N}_z\text{Al}_w^{-/+}$ families could be surely identified in the spectra. Having a look at XPS data, no peak related to a carbide bond is identified in the C1s region (see Figure 6.17), as well as no peak related to a nitride can be identified in the N1s region (see annex). These elements support the previous conclusion that there is no C-Al bond and that a C-N-Al bond is rather improbable.

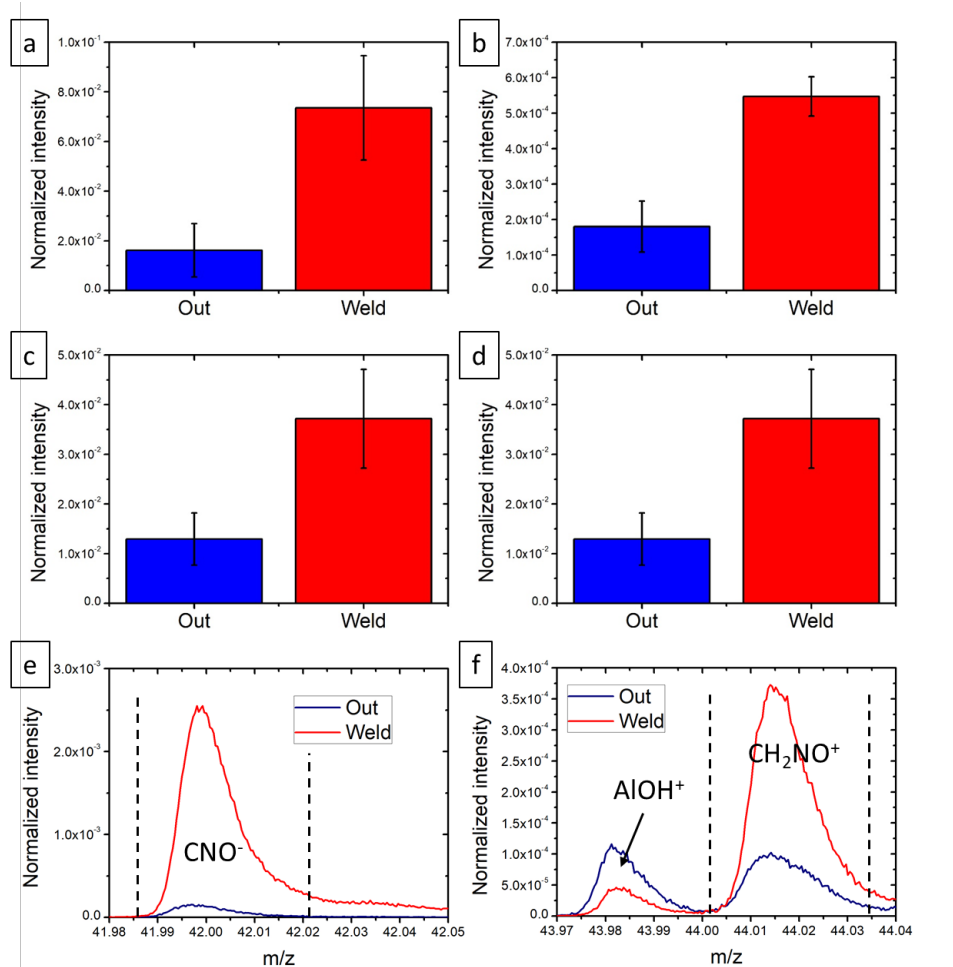


Figure 6.18: ToF-SIMS characteristic polyamide-6.6 ions in the negative and positive mode, presented in intensity normalized to total counts per zone, in blue the out of weld and in red the weld. (a) CNO^- , (b) $\text{C}_3\text{H}_2\text{NO}^-$, (c) CH_4N^+ , and (d) CH_2NO^+ . Mass spectra zone with the range of interest marked by dashed lines of (e) CNO^- , and (f) CH_2NO^+ .

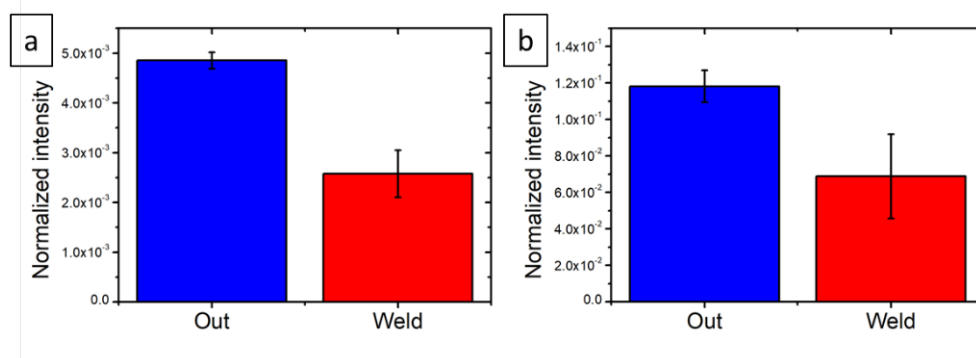


Figure 6.19: ToF-SIMS characteristic aluminum ions in the negative and positive mode, presented in intensity normalized to total counts per zone, in blue the out of weld, and the weld in red. (a) AIO^- , (b) Al^+ .

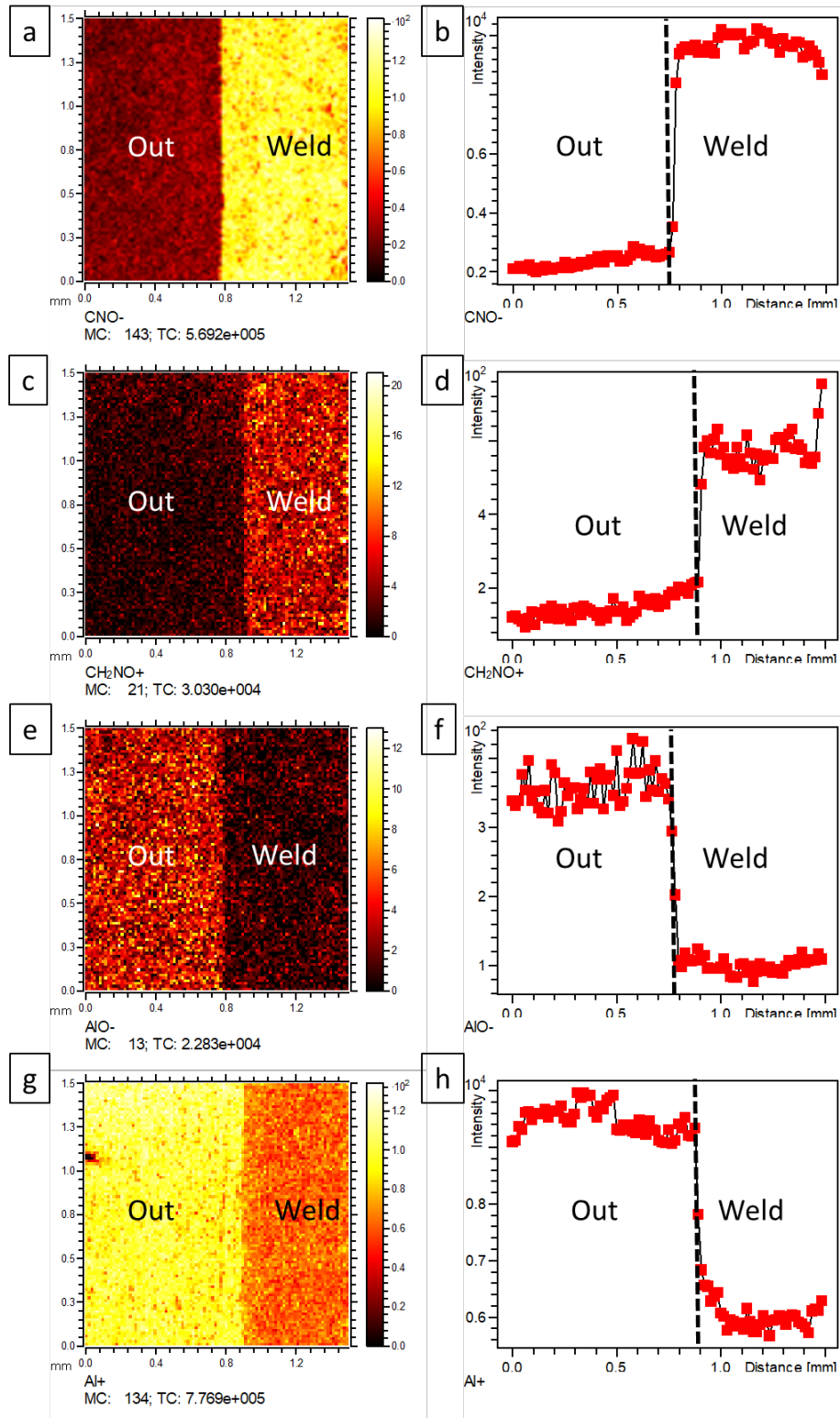


Figure 6.20: ToF-SIMS large area images and their area integration along the x axis (a) and (b) CNO^- , (c) and (d) CH_2NO^+ , (e) and (f) AIO^- , and (g) and (h) Al^+ .

As said above, very limited number of hybrid ions could be surely identified. The list comprises four: CHNOAl^- , CHNO_2Al^- , CHNOAl^+ , and CHNO_2Al^+ . The behavior of CHNOAl^-

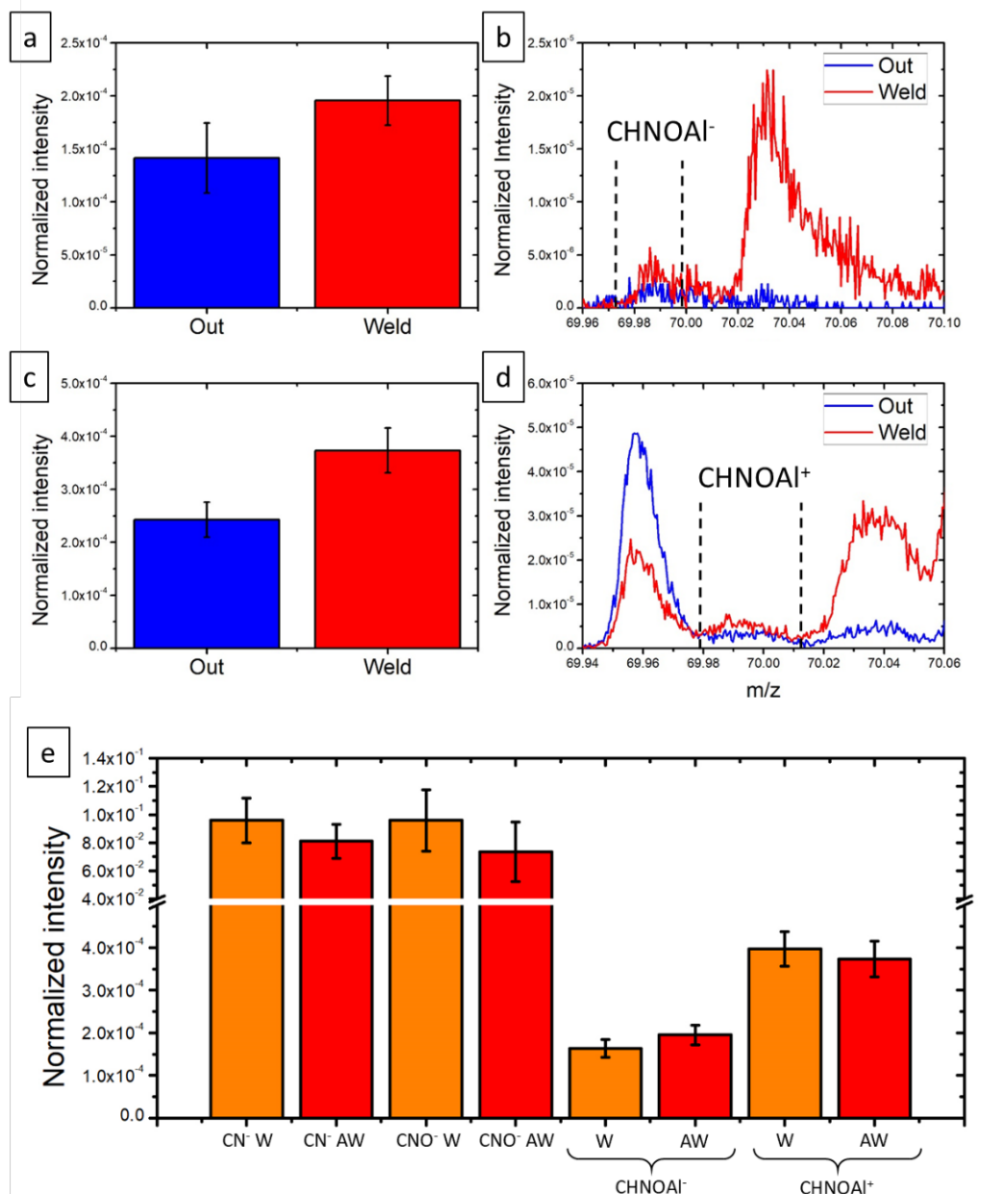


Figure 6.21: ToF-SIMS intensity normalized to total counts of characteristic peaks presented as histograms per zone, in blue the out of weld and in red the weld, and the mass spectra with the range of interest marked by dashed lines of (a) and (b) CHNOAl⁻, (c) and (d) CHNOAl⁺, and (e) comparison of the normalized intensity of CN⁻, CNO⁻, CHNOAl⁻ and CHNOAl⁺ in the welded and ablated welded samples.

are depicted in Figure 6.21 (a) (b), (c) and (d) along with the mass spectra. The intensity is higher in the weld compared to the out of weld, but the intensity difference between both zones is not as high as on the W samples. The relative high intensity out of the weld could be an interference with another ion, possibly C₂H₃OAl^{-/+}. If there is such interference even in the weld, it could also support a C-O-Al bonding. Figure 6.21 (e) depicts the comparison of the normalized intensities in the weld for W and AW samples for several ions: CN⁻, CNO⁻, CHNOAl⁻ and CHNOAl⁺. The normalized intensity of each ion is equivalent for the different samples W

and AW. This is interesting, since the XPS proved that there is more polyamide sticking on the AW samples than on the W samples.

6.2.3 Conclusions on the ablated welded samples

The work on the ablated welded samples allowed to make comparisons with the welded samples and draw interesting results. It demonstrated the strength and the validity of the methodology of the samples preparation to access their interface by first breaking the samples, and dissolve the residue left.

When comparing out and in the weld from the ablated welded samples, it could be observed that polymer is also binding in the weld with XPS and ToF-SIMS. From the XPS data, the amount of polymer is higher on the ablated welded samples than on the simply welded samples. Two possibilities exist to explain this: (1) more bonds at the interface, (2) the crosslinking of the polymer. This would need more investigations to be sure. The images taken at the border of the weld displayed the same features as the ones from the welded samples: more polymer in the weld, a sharp separation between both zones, and a very thin polymer layer.

The chemical reactivity study was more rapid due to the fact that specific hybrid ions in favor for C-Al and C-N-Al bonds were not identified in the mass spectra due to less carbon contamination, and this is supported by the absence of peaks of such nature in XPS. Nonetheless, some ions in support of a C-O-Al bond could be surely identified. They do display higher intensities in the weld than out of it, but the difference of intensity between both zones (even if statistically significantly different) is lower than for the welded samples. Assumption was made that there is some interference with another ion possibly $C_2H_3OAl^{+/+}$. The normalized intensity of CN^- , CNO^- and $CHNOAl^{+/+}$ in the weld of the welded and ablated welded samples were compared and turned out to be equivalent. Naively, one would have expected that the intensity of $CHNOAl^{+/+}$ ions would have been higher, because there are more bonds at the interface between the materials, explaining the higher shear load. But as seen in the Chapter 5 (surface pretreatment), the failure is cohesive and therefore no information on the real adhesive strength is known.

6.3 Spin-coated samples

The spin coated samples were prepared in order to confirm the observations made on the previous samples, but also to investigate even further the reaction mechanism. Moreover the major objective was to study the impact of the welding on at the interface of polymer already in intimate contact with the metal.

6.3.1 Polyamide adsorption/adhering on the aluminum surface

The surface elemental composition measured with XPS is presented in Table 6.3. The nitrogen percentage increases from the reference samples (3.7%) to the weld zone (4.7%), while the out of weld (4.4%) has an intermediate percentage. It is noticeable that the nitrogen percentage in the reference is more than four times higher than on a simple aluminum surface (of the same alloy). In the same time the oxygen percentage decreases from 42.3% to 37.6% from the reference to the weld. These two changes can be caused by the presence of polyamide-6.6 on the surface in the weld, which contains less oxygen than an aluminum oxide surface (12.5% in PA-6.6 and 60% in pure Al_2O_3). The increase of the average carbon percentage from the reference to the weld is not statistically significant, as the standard deviations for each zone overlap each other, but it seems to be slightly increasing in the weld. The average percentage of aluminum decreases from the reference to the weld and is even lower in the out of weld, but

as for the carbon percentage, the standard deviations of each zone overlap each other. These results suggest that polyamide is adsorbed in the reference, the out of weld and in the weld, but not in the same amount. So, the spin-coating process allows the polyamide-6.6 to adsorb on the surface, and the welding increases the amount binding in the weld to amounts comparable to the welded samples. Interestingly, no fluorine is detected, which suggests that the solvent used for dissolution – 2,2,2-trifluoroethanol – does not adsorb on the surface as it did on the welded samples.

Table 6.3: XPS average elemental composition and its standard deviation of an aluminum surface, in the reference, out of the weld and in the weld.

Samples	%O	%Al	%C	%N
Al surface	42.2 (± 1.5)	27.3 (± 1.8)	29.7 (± 2.7)	0.8 (± 0.4)
Reference	42.3 (± 1.3)	27.1 (± 2.5)	27.0 (± 3.2)	3.7 (± 0.5)
Out of weld	39.8 (± 0.9)	24.4 (± 1.2)	31.5 (± 1.8)	4.4 (± 0.3)
Weld	37.6 (± 0.9)	25.7 (± 1.3)	32.0 (± 1.9)	4.7 (± 0.3)

Figure 6.22 (a), (b) and (c) show the high resolution spectra of the C 1s regions in the reference, out of the weld and in the weld. First, a C-C/C-H contribution was fixed at 284.8 eV for each spectra, which served as calibration peak. Then a C-O/C-N contribution was found around 285.8 eV. At last a contribution of C=O around 287.9 eV was added. The calculation of the ratio of the C-O/C-N contribution and the C=O one gives similar result for all the samples: 1.2 (± 0.2) for the reference, 1.3 (± 0.3) out of the weld, and 1.1 (± 0.1) in the weld. All the spectra of carbon C 1s can be interpreted with the characteristic peaks of polyamide-6.6 [283,284,295,296]. This is supported by the spectra from the N 1s region shown in Figure 6.22 (d), (e) and (f), where an amide peak can be identified around 399.8 eV [282,286,298]. It is the only contribution clearly identified. The O 1s region of the reference, the out of weld and in the weld are depicted in Figure 6.22 (g), (h) and (i). Three contribution were identified: one for the aluminum oxide at 531.4 eV, one for the aluminum hydroxide at 532.3 eV, and one for organic molecules in this case polyamide and water at 533.2 eV [150,282,297]. The Al 2p region presented in Figure 6.22 (j), (k) and (l), is fitted using three contribution, one for Al 2p_{3/2} at 72.4 eV, one for Al 2p_{1/2} at 72.8 eV, which are characteristic for metallic aluminum, and the last contribution at 74.5 eV corresponding to oxidized aluminum [282].

The intensity of the most representative ions specific for nylon-6.6 measured in ToF-SIMS are presented in Figure 6.23 (reference polyamide spectra can be found in annex). Their intensity is higher in the weld than outside the weld and the reference and can more than double (see Figure 6.23 (c)). Nonetheless, the intensities of these ions in the reference are already high, meaning that polymer is already present in the reference. This is in good agreement with the observations made in XPS. There is polyamide-6.6 absorbed on the all the different zones due to the spin-coating process, but in the weld there is more polyamide adhering on the surface after the dissolution process. This is due to the heating of the welding.

Figure 6.24 present large area images and their x-axis integration of the intensity of polymer ions at the border region between the weld and outside the weld. It is directly noticeable that the intensity goes from a low intensity plateau to a high intensity one, going from the out of weld to the weld (from left to right). This confirms what was observed in the static mode and in XPS, there is more polyamide in the weld than outside of it and in the reference.

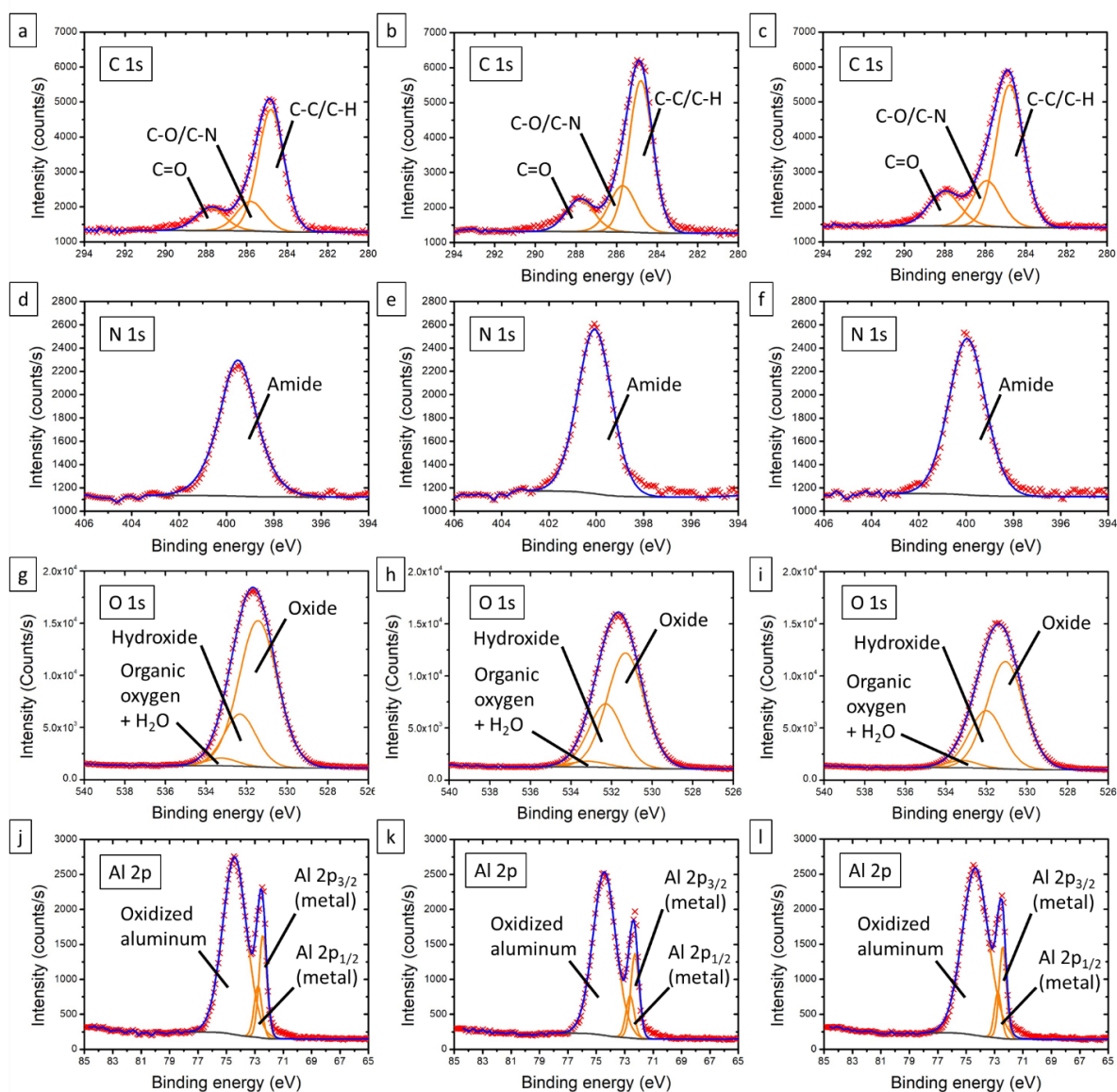


Figure 6.22: XPS high resolution of the C 1s region in (a) the reference, (b) out of the weld and (c) in the weld, of the N 1s region (d) in the reference, (e) the out of weld, (f) in the weld, of the O 1s region (g) the reference, (h) the out of weld, (i) in the weld, and the Al 2p region (j) the reference, (k) out of the weld and (l) in the weld.

6.3.2 Chemical reactivity

As already presented in section 6.1.2, the polymer exhibits different possible reactive sites: carbon sites, a nitrogen site and an oxygen site. The carbon sites will not be discussed here, as the results from the welded samples clearly showed that there is no reaction involving them.

6.3.2.1 Reactivity with the nitrogen sites

Looking at the XPS high resolution spectra from the N 1s region (see Figure 6.22 (d), (e) and (f)), only one contribution at 399.8eV related to the amide function of the polymer is visible. No contribution from an aluminum nitride bond is visible around 396 eV [317–319]. So as on the

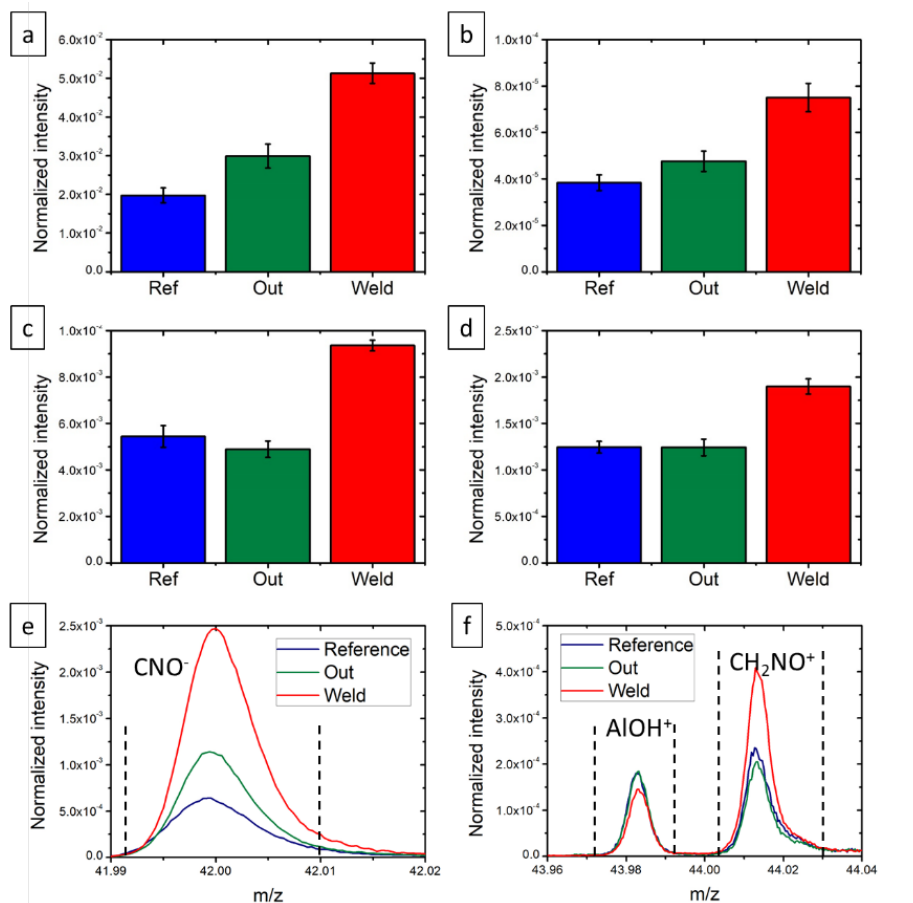


Figure 6.23: ToF-SIMS intensity normalized to total counts of characteristic peaks presented as histograms per zone, in blue the reference, in green the out of weld and in red the weld of (a) CNO^- , (b) $\text{C}_2\text{H}_3\text{NO}^-$, (c) CH_2NO^+ and (d) $\text{C}_2\text{H}_4\text{NO}^+$. Mass spectra zone with the range of interest marked by dashed lines of (e) CNO^- , and (f) $\text{C}_2\text{H}_4\text{NO}^+$.

welded samples, if such bonds do occur their presence is limited and below the detection limit of the XPS system. Ions from the family $\text{C}_x\text{H}_y\text{N}_z\text{Al}_w^{-/+}$ were surely identified, and are presented in Figure 6.25. $\text{CHNAI}^{+/+}$ have a higher relative intensity in the weld – nearly twice more – which would be in favor of a C-N-Al bond. But the following ion CH_2NAI^+ has equivalent relative intensities for all the three zones, while CH_2NAI^- has lower relative intensity in the weld compared to the out of weld and the reference. The same arguments for recombination as for the welded samples can be used here (see 6.1.2.2). These ions have lower relative intensities than the $\text{C}_x\text{H}_y\text{N}_z\text{O}_w\text{Al}_n^{-/+}$ ions as can be seen in Figure 26 in the weld. Moreover the ion CNO^- which could be a source of recombination for the $\text{C}_x\text{H}_y\text{N}_z\text{O}_w\text{Al}_n^{-/+}$ ions, has a lower intensity than CN^- responsible for the recombination of $\text{C}_x\text{H}_y\text{N}_z\text{Al}_w^{-/+}$. As already detailed above (see 6.1.2.2), literature is not supporting a C-N-Al bond at the interface, because nitrides are peculiarly instable in the presence of moisture, which is the case here [320–323].

6.3.2.2 Reactivity with the oxygen sites

In the XPS high resolution spectra from the O 1s region, three different contribution were used to fit the spectra (see Figure 6.22). One at 531.4 eV related to the aluminum oxide, one at 532.3 eV related to the aluminum hydroxide form and one related to organic molecule and water

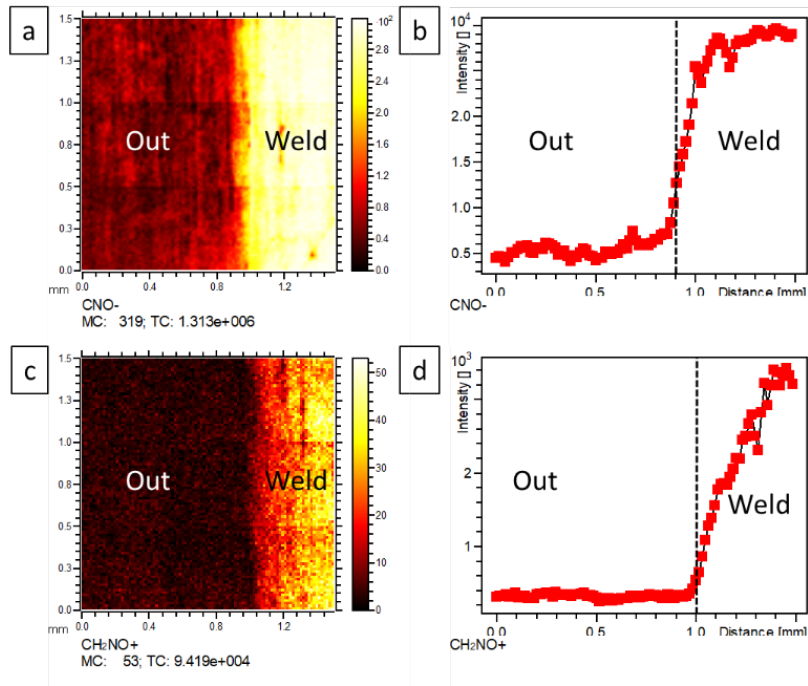


Figure 6.24: ToF-SIMS large area images at the border region between the weld and the out of weld and their x axis area integration (a) and (b) for CNO^- and (c) and (d) for CH_2NO^+ .

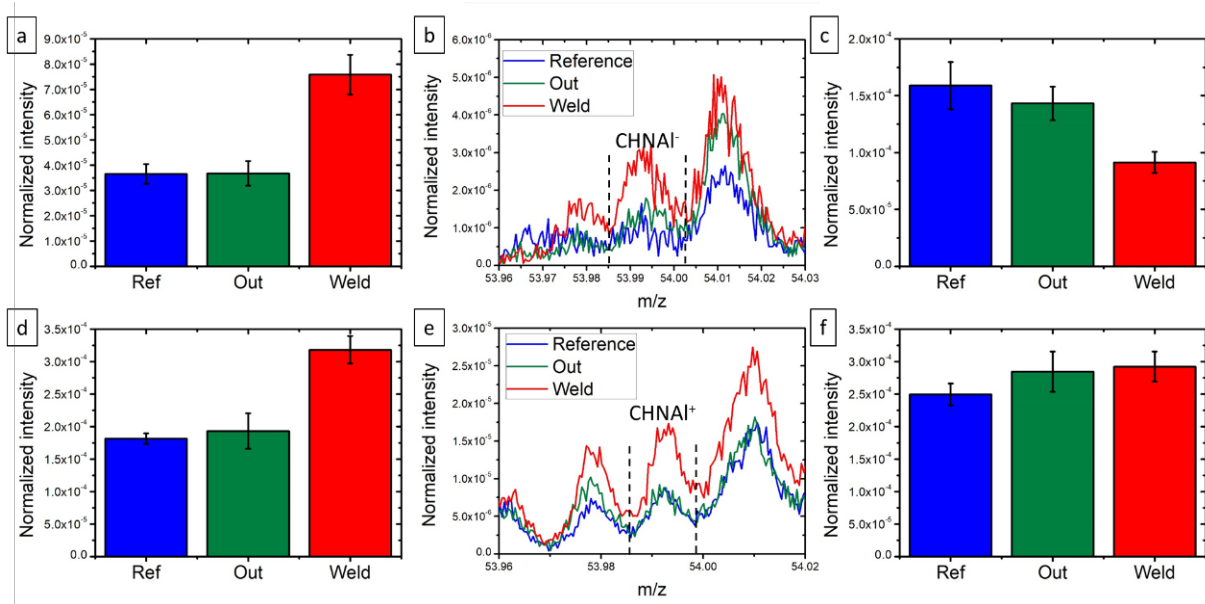


Figure 6.25: ToF-SIMS intensity normalized to total counts of characteristic peaks presented as histograms per zone, in blue the reference, in green the out of weld and in red the weld of (a) CHNAI^- , (c) CH_2NAI^- , (d) CHNAI^+ and (f) CH_2NAI^+ , and the mass spectra zone with the range of interest marked by dashed lines of (b) CHNAI^- , and (e) CHNAI^+ .

at 533.2 eV. The last contribution was related mostly to the amide function and water, but as detailed in section 6.1.2.3, it is reasonable to put a C-O-Al contribution here as well. In the C 1s region such contribution will be mixed in the C-O/C-N peak around 286 eV. This seems

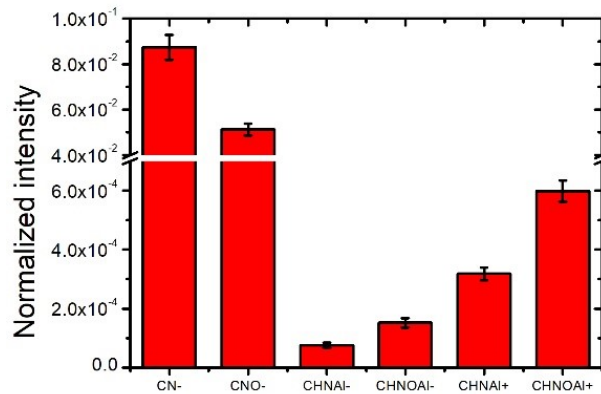


Figure 6.26: Comparison of the normalized intensity of CN⁻, CNO⁻, CHNAI⁻, CHNOAI⁻, CHNAI⁺ and CHNOAI⁺ in the weld.

a reasonable interpretation, but there are no authors to the best of our knowledge describing C-O-Al bonds in XPS.

The SIMS data analysis allowed to identify two families of ions related to a C-O-Al bond: the C_xH_yO_zAl_w^{-/+} and the C_xH_yN_zO_wAl_n^{-/+}.

The ions from the C_xH_yO_zAl_w^{-/+} family have an erratic behavior, indeed some of them have equivalent or lower intensities in the weld than outside (CH₂OAl⁻, C₂H₂OAl⁻, C₂H₃OAl⁻, C₂H₅OAl⁻, and CH₄OAl⁺, C₂H₄OAl⁺, C₃H₄OAl⁺) whereas others have higher intensities in the weld (COAl⁻, CHOAl⁻, C₂OAl⁻, C₂HOAl⁻, CO₂Al⁻ and CHOAl⁺, CH₃OAl⁺, C₂HOAl⁺, C₂H₂OAl⁺, CHO₂Al⁺). The first ions, lower in intensity in the weld, can be explained by adventitious carbon and CO₂ adsorption on the aluminum surface [283, 296, 325]; while the second ions, higher in intensity, can be interpreted as originating from a C-O-Al bond.

Ions from the family C_xH_yN_zO_wAl_n^{-/+} were confidently identified, as CNOAl⁺, CHNOAl⁺, CHNO₂Al⁺, CH₃NO₂Al⁺ and CNOAl⁻, CHNOAl⁻, CH₂NOAl⁻, CHNO₂Al⁻, CH₂NO₂Al⁻, CH₃NO₂Al⁻. They all present higher relative intensity in the weld compared to the out of weld and the reference, as can be seen for some of the ions in Figure 6.27. These ions could originate from a C-O-Al bond, a C-N-Al bond or simply recombination. As discussed above and for the welded samples, a C-N-Al bond is not the favored bond (see section 6.3.2.1). Recombination from CNO⁻, H^{-/+}, and Al^{-/+} to form these ions is probable and some of the ions detected might originate from it. Nonetheless, as can be seen in Figure 6.26, the intensity of CNO⁻ is much lower than the intensity of CN⁻, but at the same time the ions CHNOAl^{-/+} have higher intensities than the CHNAI^{-/+} ions. However, if only recombination occurs, one can suppose that the ions CHNOAl^{-/+} would have lower intensities than CHNAI^{-/+} ions. This is even more true, since the heavier the ion, the lower the probability is to form it by recombination. So, the only explanation possible is that there is a C-O-Al bond formed during the welding. As detailed in section 6.1.2.3, literature shows several examples of such bonds between polyimides and aluminum [180, 324, 328–330]. The polymer already bonds to the surface during the spin-coating process, but the welding process allows the polymer to melt and to rearrange itself again [208, 250], enabling the polymer to react with the aluminum surface and to create even more bonds between both materials. This allows to clearly identify the bond as a C-O-Al bond as depicted in Figure 6.28.

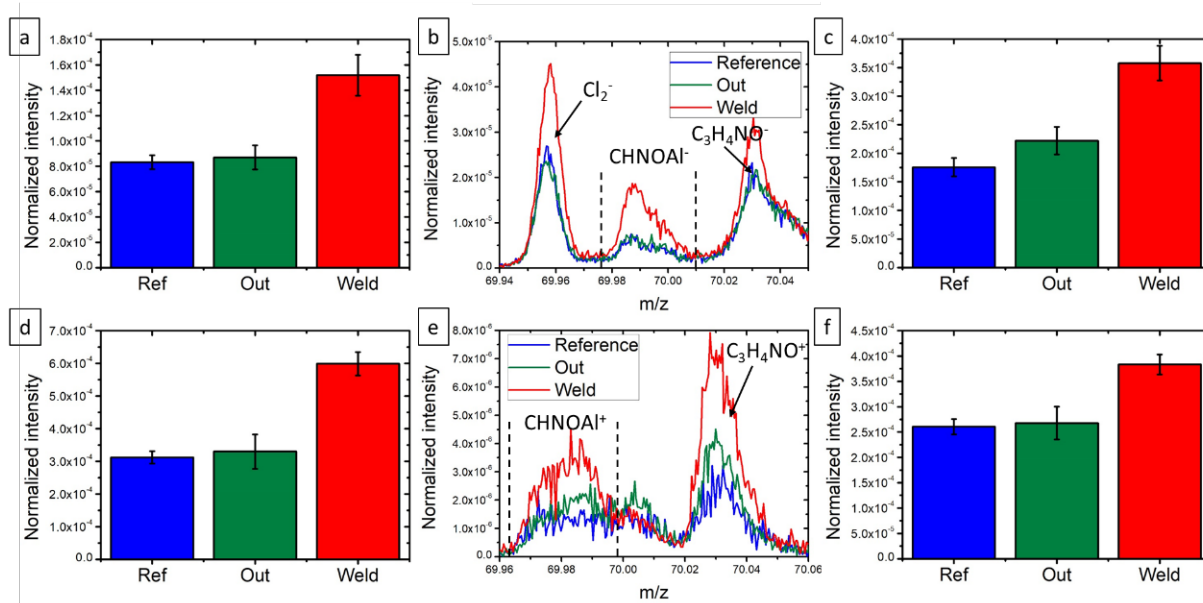


Figure 6.27: ToF-SIMS intensity normalized to total counts of characteristic peaks presented as histograms per zone, in blue the reference, in green the out of weld and in red the weld of (a) CHNOAl^- , (b) CHNO_2Al^- , (c) CHNOAl^+ and (d) CHNO_2Al^+ and the mass spectra zone with the range of interest marked by dashed lines of (b) CHNOAl^- , and (e) CHNOAl^+ .

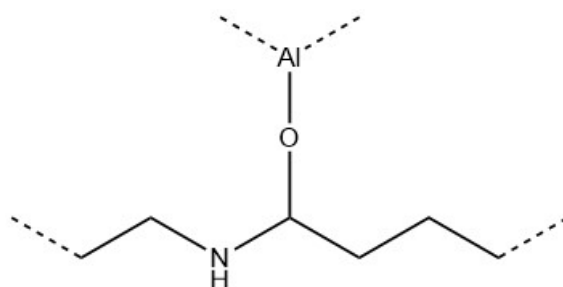


Figure 6.28: Scheme of the chemical bond between the aluminum surface and the polyamide-6.6.

6.3.2.3 Reactivity of the metal

For the welded samples, it was assumed that the metal reacts with the free hydroxyl groups present at the surface. This assumption was made because examples in the literature point in that direction [152, 198, 307]. Figure 6.29 depicts the normalized relative intensity of characteristic ions of aluminum oxide and aluminum hydroxide. The relative intensity of the ions related to the oxide are equivalent for all three zones, while the relative intensity of the ions related to the hydroxide is lower in the weld than in the reference. The out of weld has an intermediate behavior for the hydroxide ions. This is supporting the fact that the polymer reacts with the free hydroxyl groups present at the surface during the welding process.

Figure 6.30 (a) shows the percentage of aluminum obtained from the XPS survey for the three zones. The percentage is equivalent in all zones, especially the reference and the weld. The oxide thickness was calculated using Strohmeier's method [258] from the high resolution spectra in the Al 2p region (see Figure 6.30 (b)). the oxide appears to be thicker in the weld than in the reference, the out of weld being in an intermediate position, even if mostly looking like the reference. The welding seems to oxidize the metal surface deeper. This might partly be due to

the fact that the reaction of the polymer with the metal releases water, as depicted in Figure 6.31. Moreover, water is also present in the polymer naturally, which also might be source of oxygen atoms to oxidize the aluminum surface [87]. The oxygen atoms deep at the interface between the bulk aluminum and the native oxide layer, receive enough energy from the heating of the welding to move further in the bulk, creating lack of oxygen at this interface. These lacks are filled by the oxygen from the layer just above, so that the lacks move up to the interface with the polymer. These lacks are filled by the water from the polymer, and the water released from the reaction with the polymer as depicted in Figure 6.31. This mechanism stops when the samples get colder.

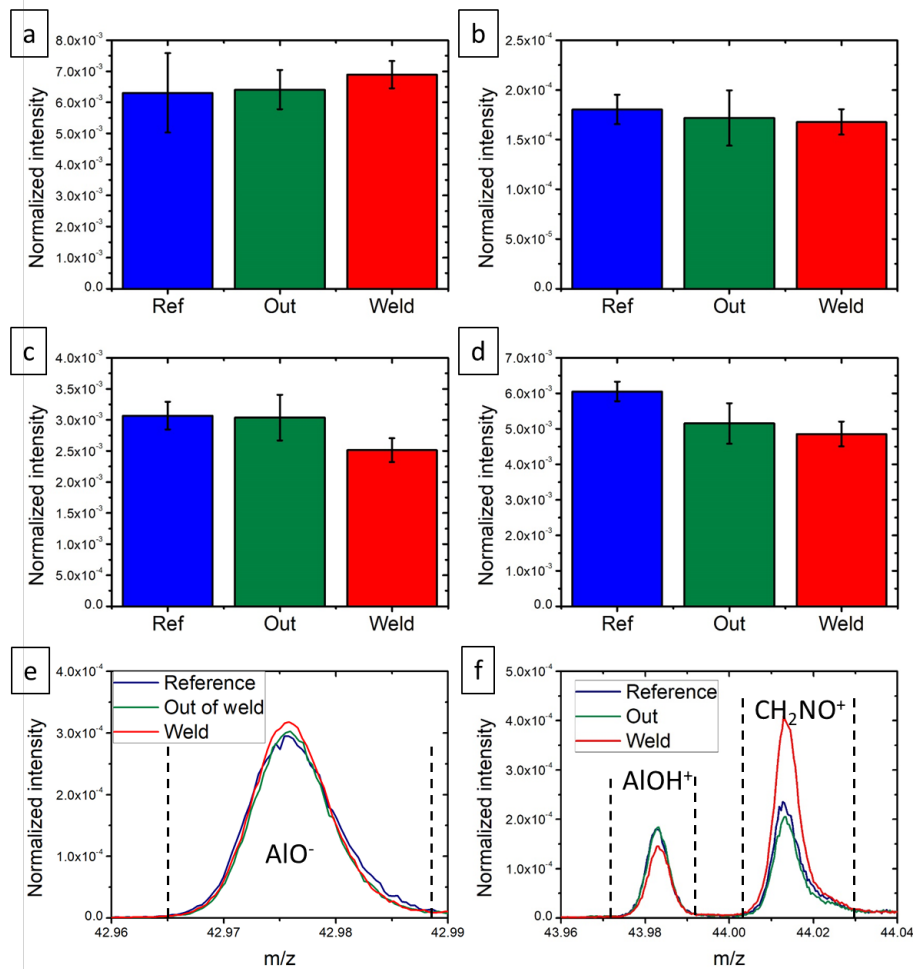


Figure 6.29: ToF-SIMS intensity normalized to total counts of characteristic ions of an oxidized aluminum surface (a) AlO^- , (b) AlO^+ , (c) AlOH^+ , and (d) AlH_2O_2^+ . Mass spectra zone with the range of interest marked by dashed lines of (e) AlO^- , and (f) AlOH^+ .

6.3.3 Discussion about PCA

6.3.3.1 PCA on the hand-selected peak lists

The two polarities display different behavior in the scores as depicted in Figure 6.32. In the negative mode, PC1 separates the weld from the reference and the out of weld. PC2 does not display any sample separation. Plotting PC1 versus PC2 the weld is clearly separated, but the reference and the out of weld are also clearly separated, which was not apparent by looking at

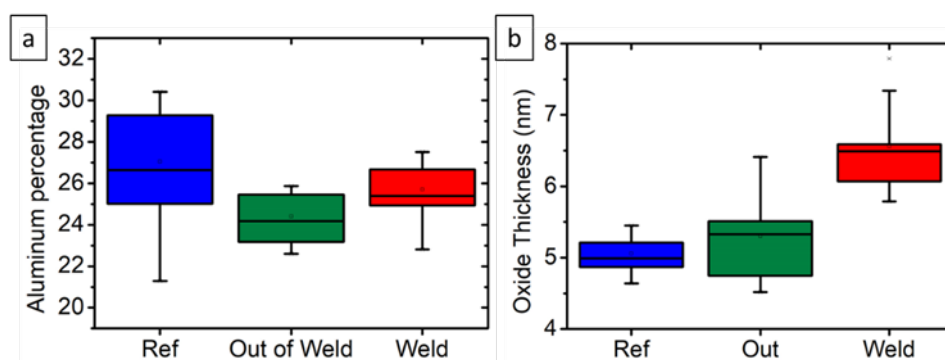


Figure 6.30: (a) percentage of aluminum obtained from the XPS survey spectra per zone, (b) oxide thickness per zone calculated from the XPS Al 2p region using Strohmeier's method [258].

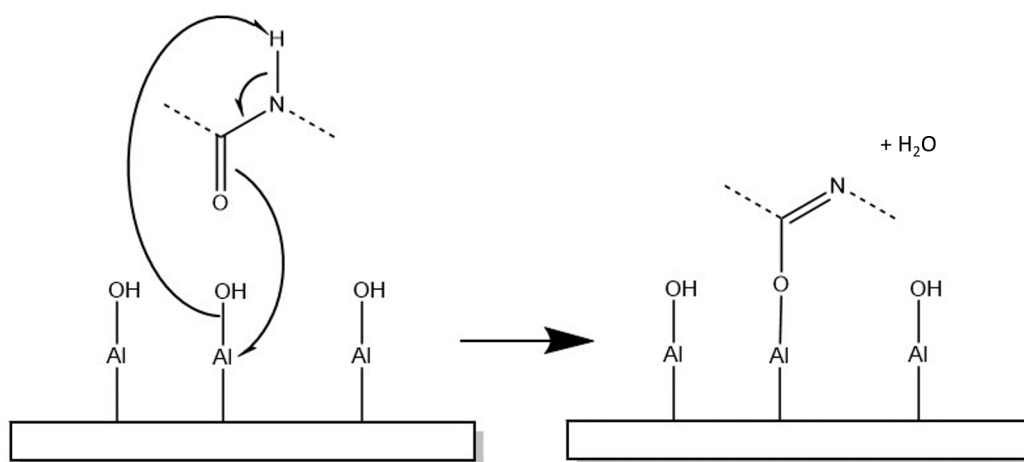


Figure 6.31: Scheme of the reaction mechanism between the polyamide-6.6 and the aluminum surface.

the scores separately. The major cause of difference is the welding process, but also the heat received out of weld is sufficient to differentiate them from the reference samples. In the positive mode, PC1 does not discriminate the different samples. Apparently there is a high variability on the reference samples, which seems to be the major cause of difference between the samples. PC2 clearly discriminates the weld from the reference and the out of weld. Plotting PC1 versus PC2 emphasizes this even more, but also shows that the reference and the out of weld are similar, as the two scores are overlapping.

The loadings of both polarities are depicted in Figure 6.33. In the negative mode, the loadings of PC1 display clear intensity patterns. The ions presenting positive loadings have higher intensities in the weld than in the reference, the out of weld being intermediate. The ions presenting the highest loadings are all related to the polymer. Mass 25 is C_2H^- , mass 26 is CN^- , mass 40 is $C_2H_2N^-$, mass 41 is C_2HO^- , mass 42 is CNO^- , mass 50 is C_3N^- . The ions presenting negative loadings have lower intensities in the weld and out of it than on the reference. The ions presenting the highest negative loadings are associated to contaminations, as mass 19 is F^- , and mass 35 is Cl^- . The loadings of PC2 in the negative mode do not display a clear pattern in the intensity of the ions. The ions presenting the highest positive loadings are related to the polymer and contaminations. Mass 12 is C^- , mass 16 is O^- , mass 17 is OH^- , mass 19 is F^- , mass 26 is CN^- , mass 43 is $C_2H_3O^-$. The ions presenting the highest negative loadings are associated to contaminations, the polymer and the aluminum, as mass 35 is Cl^- , mass 45 is CHO_2^- , mass

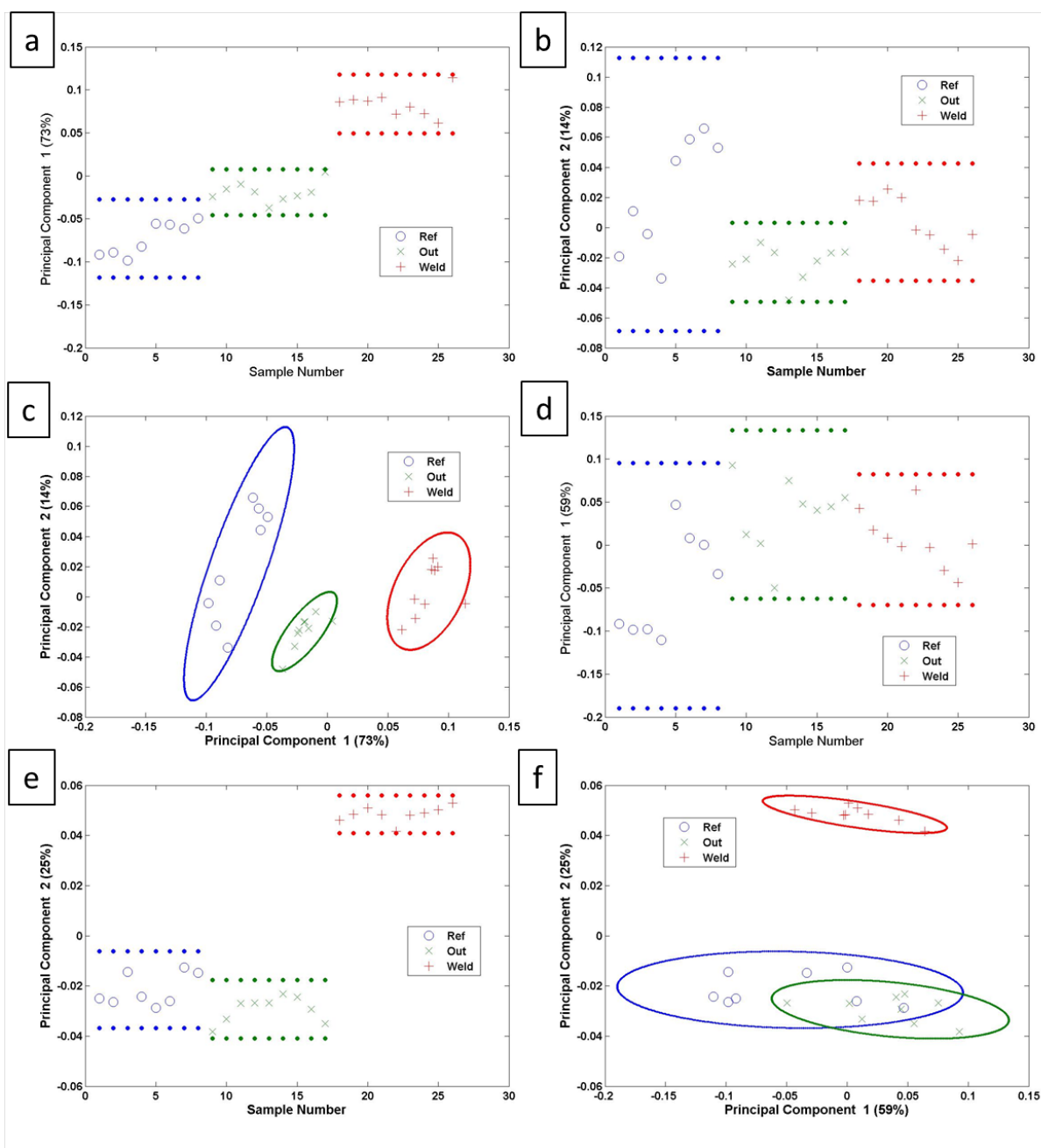


Figure 6.32: Scores of the hand-selected peak list. In the negative mode (a) PC1, (b) PC2, (c) PC1 versus PC2. Scores in the positive mode (d) PC1, (e) PC2, and (f) PC1 versus PC2.

59 is AlO_2^- .

In the positive mode, the loadings of PC1 present a clear pattern. The positive loadings are ions, having a low intensity in the reference, a higher intensity out of weld and an even higher in the weld. The ions presenting the highest loadings are associated to the polymer. Mass 56 is $\text{C}_2\text{H}_2\text{N}^+$, mass 86 is $\text{C}_4\text{H}_8\text{N}^+$ and mass 87 is $\text{C}_4\text{H}_9\text{N}^+$. The negative loadings are associated to ions presenting equivalent intensities in the reference and the weld, but lower intensities out of the weld. The ions with the highest negative loadings are associated to the aluminum, or the polymer. Mass 27 is Al^+ , mass 27 is C_2H_3^+ , mass 29 is CHO^+ , mass 41 is C_3H_5^+ . For PC2, the intensities of the ions presenting positive loadings present a systematic pattern. Their intensity

is systematically higher in the weld than out of the weld, the reference being generally lower than the out of weld, but can also be higher in intensities. These ions are linked to the polymer, for example mass 28 is CH_2N^+ , mass 30 is CH_4N^+ , mass 44 is CH_2NO^+ , mass 55 is $\text{C}_3\text{H}_3\text{O}^+$, mass 86 is $\text{C}_4\text{H}_8\text{NO}^+$. The ions presenting negative loadings have lower intensities in the weld than out of it and than the reference. The ions presenting the highest negative loadings are linked to organics, as mass 70 is $\text{C}_4\text{H}_8\text{N}^+$, mass 72 is C_6^+ , and mass 84 is $\text{C}_5\text{H}_8\text{O}^+$.

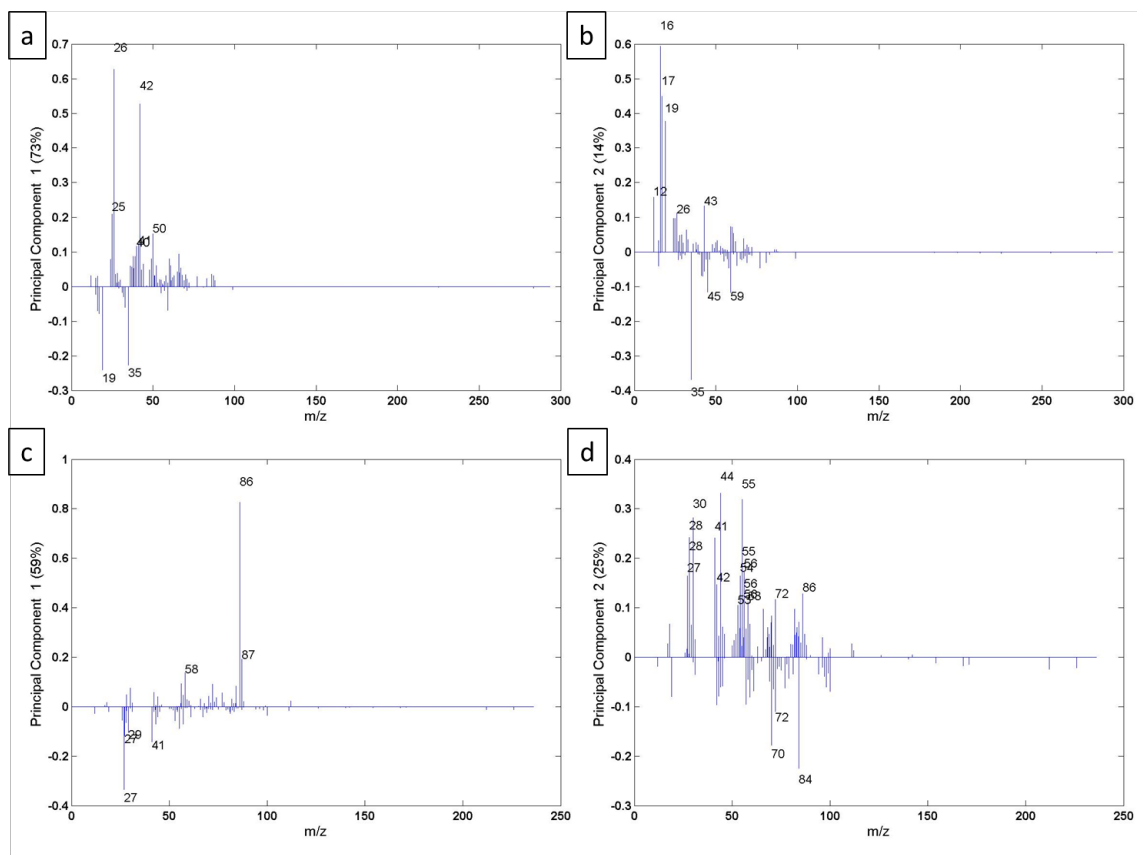


Figure 6.33: Loadings of the hand-selected peak list. In the negative mode (a) PC1, (b) PC2. In the positive mode (c) PC1, (d) PC2.

6.3.3.2 PCA on the automatic generated peak lists

As for the other samples an automatic generated peak list was obtained by applying the following parameters: minimum intensity of 100 counts and a mass range from 0 to 300 m/z. The peak lists are composed of 365 and 420 peaks in the negative and the positive mode respectively.

The scores obtained for the automatic generated peak list behave the same than the ones obtained for the hand-selected peak list, as can be seen in Figure 6.34. In the negative mode, the out of weld and the weld are separated, but the reference is not differentiated. PC2 shows a similar behavior for the sample separation. Plotting PC1 versus PC2, the three samples are clearly discriminated. The scores of the reference show a high variability for both principal components. In the positive mode, as for the hand-selected peak list, the samples are not separated, and the major difference is the high variability on the reference samples. On PC2, the weld is discriminated from the two others. Plotting PC1 versus PC2 emphasizes the separation of the weld from the reference and the out of weld. The reference and the out of weld are overlapping, meaning that they are not very different from one another.

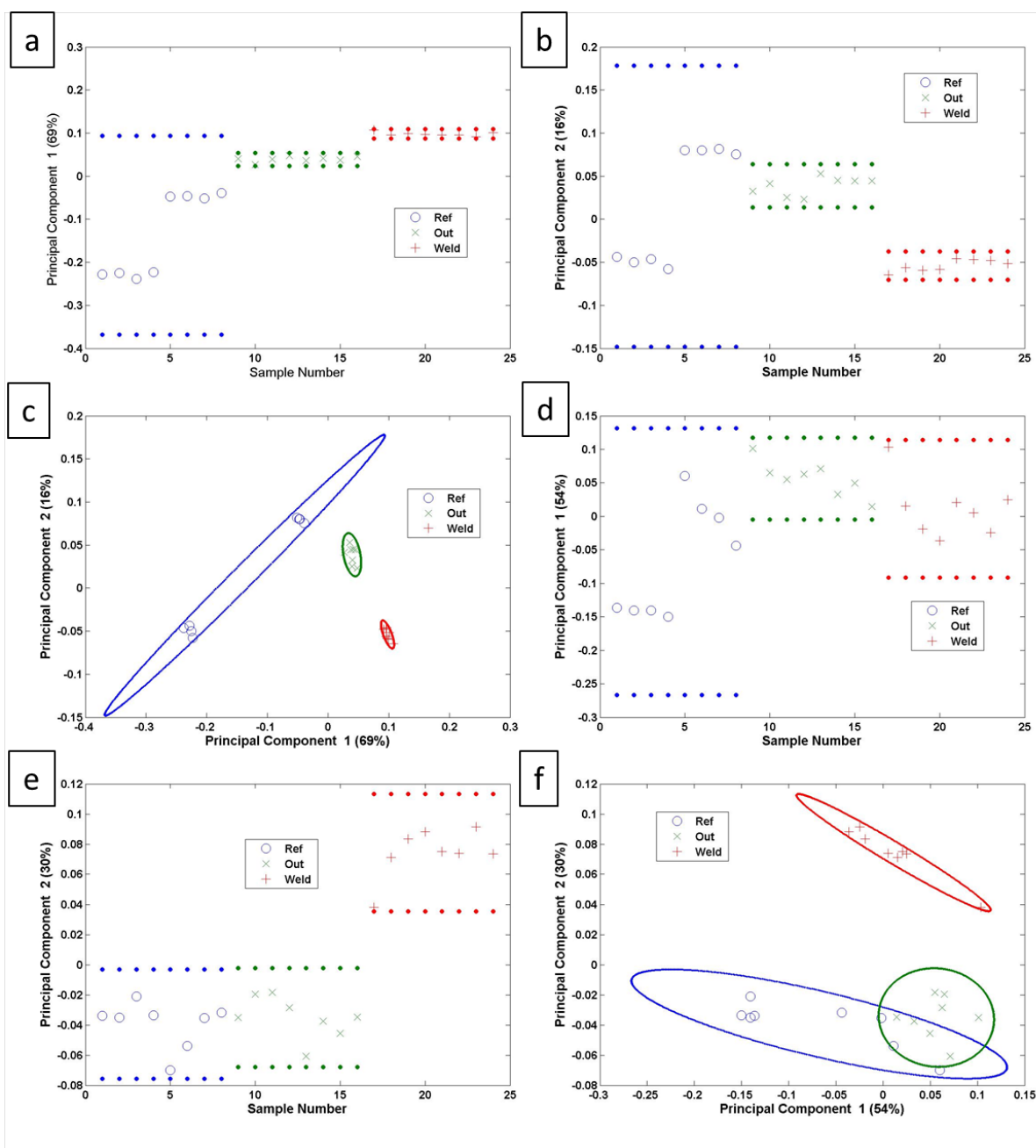


Figure 6.34: Scores of the automatic generated peak list. In the negative mode (a) PC1, (b) PC2, and (c) PC1 versus PC2. In the positive mode (d) PC1, (e) PC2, and (f) PC1 versus PC2.

Having a close look at the loadings in the negative mode in Figure 6.35 (a) and (b), the intensities of the ions display systematic patterns in PC1. The positive loadings are for ions having higher intensities in the weld than out of the weld and than the reference. The interpretation of the ions presenting the highest loadings show the presence of ions of the polymer and contaminations. Mass 25 is C_2H^- , mass 26 is CN^- , mass 42 is CNO^- , mass 63 is $COCl^-$, mass 79 is CO_2Cl^- . In PC1, the negative loadings are for ions presenting lower intensities in the weld than out of the weld and than the reference. The ions presenting the highest negative loadings are related to contaminations, as mass 19 is F^- , mass 35 is Cl^- , mass 37 is $^{37}Cl^-$, mass 79 is Br^- , and mass 81 is $^{81}Br^-$. For PC2, the ions presenting positive loadings have higher intensities on

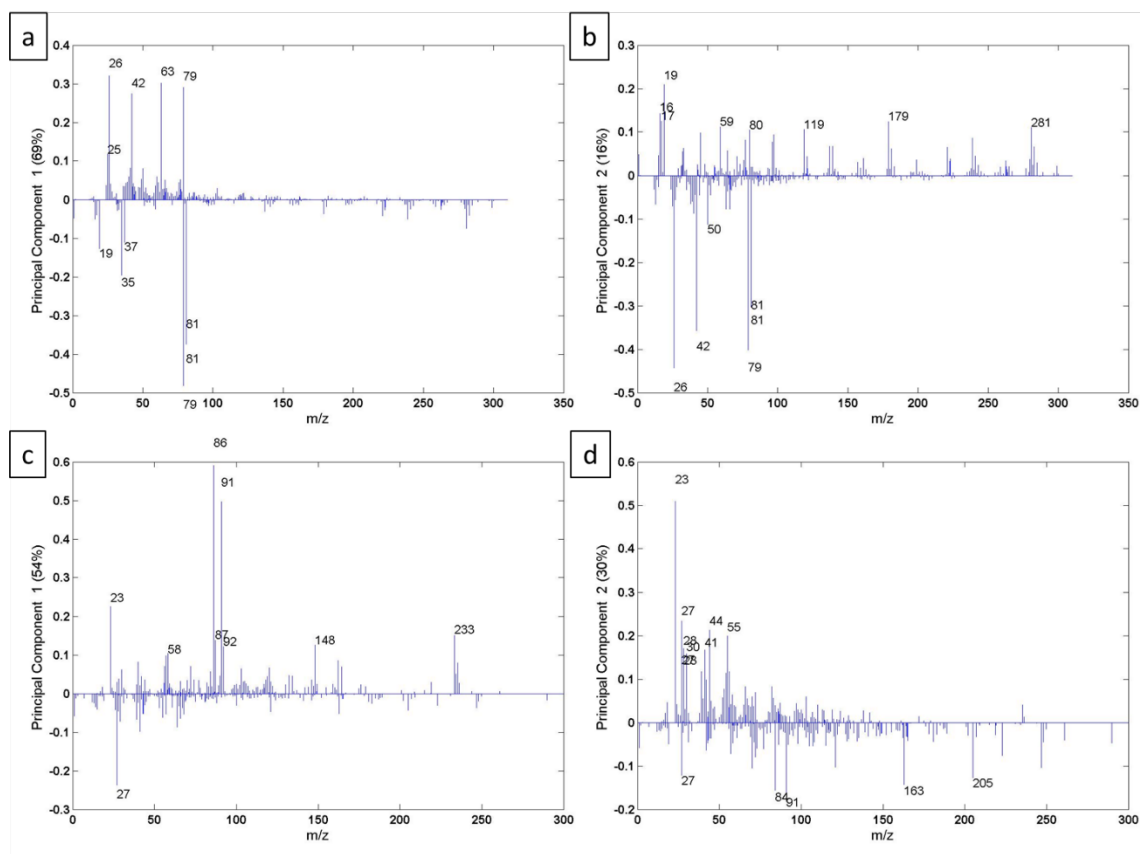


Figure 6.35: Loadings in the negative mode (a) PC1, (b) PC2. Loadings in the positive mode (c) PC1 and (d) PC2.

the reference than the weld, while out of the weld the intensity does not follow a pattern. The ions presenting the highest positive loadings are related to the aluminum and contaminations. Mass 19 is F^- , mass 80 is SO_3^- , mass 179 is $Al_3H_2O_8^-$, or mass 281 is $Al_5H_2O_9^-$. For PC2, the negative loadings do not have a systematic intensity pattern. The ions presenting the highest negative loadings are interpreted to be related to both the polymer and contaminations. Mass 26 is CN^- , mass 42 is CNO^- , mass 50 is $COCl^-$, mass 79 is Br^- , mass 81 is $^{81}Br^-$.

The loadings of the positive mode are visible in Figure 6.35 (c) and (d). For PC1, the positive loadings present higher intensities out of the weld than the reference, the weld being generally lower than the out of weld and higher than the reference but this is not systematical. The ions presenting the highest loadings are linked to the polymer and contaminations. Mass 23 is Na^+ , mass 86 is $C_5H_{12}N^+$, mass 91 is $C_7H_7^+$, mass 148 $C_6H_{16}N_2O_2^+$, or mass 233 is $C_{15}H_{23}NO^+$. The negative loadings present lower intensities out of the weld than the reference, the weld again does not present a systematical pattern. The highest ion presenting negative loadings is related to the aluminum with the ion Al^+ , at mass 27. For PC2, the positive loadings have higher intensities in the weld than out of it, while the intensities on the reference do not follow a pattern. The ions presenting the highest positive loadings are linked to the polymer and contaminations. Mass 23 is Na^+ , mass 28 is CH_2N^+ , mass 30 is CH_4N^+ , mass 44 is CH_2NO^+ , or mass 55 is $C_3H_3O^+$. The negative loadings present lower intensities in the weld than out of it, the reference also does not follow any pattern. The ions are related organics and the aluminum surface. Mass 84 is $C_6H_{12}^+$, mass 91 is $C_7H_7^+$, mass 163 is $Al_3H_2O_5^+$, mass 205 is $Al_2HO_6^+$.

6.3.4 Conclusions on the spin-coated samples

The methodology of spin-coating a thin layer of polymer, which is then dissolved to perform XPS and ToF-SIMS, worked out well. It was proven that polymer is still detected in all zones: reference, out of weld and in the weld. This is due to polymer adsorption during the spin-coating process, but in the weld the polyamide signal is even more intense both in XPS and ToF-SIMS, suggesting that the welding and the subsequent heating has an effect on the chemical reaction at the interface. As for the nature of the bond, a C-Al bond was directly excluded. The possibility of a C-N-Al bond was investigated. XPS data did not support such possibility, while in ToF-SIMS the ions associated to such bond proved to be originating from recombination. The oxygen reactive site were also investigated, and combining the XPS and ToF-SIMS data, it is proven that a C-O-Al bond is formed during the spin-coating and even more during the welding process. At last, the reactivity of the metal could also be investigated. In ToF-SIMS, the specific ions of the oxide have identical intensities in all zones, while the hydroxides ions present lower intensities in the weld. This is supporting the idea of a reaction occurring between the free hydroxyl groups of the metal and the polymer (see Figure 6.31). In XPS, it was observed that the surface is oxidized during the welding, which can be due to the water present in the polymer or the water released during the chemical reaction. Hence the heating due to the welding has a strong effect on the samples, as more polymer is sticking after dissolution, which can be explained by the fact that there are more bonds created because of the welding. The use of a PCA is also discussed at the end and reveals that a direct approach leads to the same conclusions and observations than a PCA. This is why for simplicity a direct approach was preferred. Nonetheless, both PCA also shed light on the role played by the contaminations to differentiate the samples, which was not well studied in the direct approach.

6.4 Model samples

The main idea behind these samples is to investigate the reaction mechanism. As the polymer already adsorbs on the metal surface because of the spin-coating, it is reasonable to think that a smaller molecule presenting only the reactive part of the polymer will interact more easily with the aluminum surface. N-methylformamide was chosen, because N-methylethanamide is not liquid at ambient temperature (mp at 26-28 °C). After the dip coating, some of the samples were heated at 150 °C (the heated samples), which is not the welding temperature, but was chosen below the boiling point of the molecule, which is 182 °C.

6.4.1 Deposition of the molecule on the aluminum surface

Table 6.4 summarizes the average elemental composition obtained by analyzing the XPS survey spectra for the UV cleaned samples, the air-dried samples and the heated samples. The nitrogen percentage is three times higher on the heated samples than the UV cleaned samples, while the air dried samples have a bit more nitrogen than the UV-cleaned samples detected. First observation is that the molecule is deposited on the surface of the air dried and heated samples. Second observation is that the heating has an effect on the molecule's deposition, since there is more nitrogen on the heated samples, than on the air dried samples. The carbon percentage is quite high on the UV cleaned samples. This due to experimental reasons. Indeed, the UV-dried samples were transported in air from the cleaning place to the XPS machine, only for a few minutes, but it was sufficient for recontamination. The carbon percentage is relatively low for the air-dried and the heated samples. Maybe the methylformamide deposited occupies the reactive sites blocking the recontamination of the surface after the dipping. At the same time, the oxygen percentage is higher in the air-dried and heated samples, which would also

support the idea that the methylformamide limits the recontamination by blocking the reactive sites. The aluminum percentage is equivalent on the UV cleaned and the heated samples, but is slightly higher on the air-dried samples.

Table 6.4: XPS average elemental composition and its standard deviation of UV cleaned aluminum, the air-dried and the heated samples.

Samples	%O	%Al	%C	%N
UV-cleaned	44.7 (± 0.9)	28.3 (± 1.2)	26.3 (± 1.7)	0.6 (± 0.2)
Air-dried	53.1 (± 1.5)	32.0 (± 1.7)	14.0 (± 3.1)	1.0 (± 0.2)
Heated	53.9 (± 3.4)	29.0 (± 2.4)	15.3 (± 5.0)	1.8 (± 0.2)

The XPS high resolution spectra of the C1s region depicted in Figure 6.36 (a), (b) and (c), were fitted using four contribution. The first one is attributed to C-C/C-H bonds at 284.8 eV and was used for calibration. The second contribution at 286.1 eV is attributed to C-O and C-N bonds. The third one at 288.2 eV is attributed to a C=O function. The fourth one at 289.5 eV is attributed to carbonate [282]. This shows that the surfaces are contaminated with adventitious carbon (especially the carbonate contribution), but also for the air-dried and the heated samples that methylformamide was deposited on the surface.

The O1s region, which spectra are presented in Figure 6.36 (d), (e) and (f), were fitted using three contribution. The first one at 531.4 eV is interpreted as aluminum oxide, the second one at 532.4 eV is related to aluminum hydroxide, and the last one at 533.5 eV is due to organic molecules and water. This interpretation is relatively classical for an aluminum surface exposed to air [150, 282, 297]. The last contribution is slightly more intense for the air-dried and even more intense on the heated samples, which indicates a chemical difference in the organic oxygen on the top surface. This supports the idea that methylformamide molecules are deposited on the surface.

The XPS high resolution spectra of the N 1s region, shown in Figure 6.36 (g), (h) and (i), are of low intensity, since there is only about 1-2% nitrogen detected in the survey spectra. Even if the noise-to-signal ratio is very low, the interpretation show one contribution at 399.9 eV, which is a characteristic peak for amides [282]. This confirms that some methylformamide is present on the surface after the dip-coating and the two drying process.

For the XPS high resolution spectra of the Al 2p region, presented in Figure 6.36 (j), (k), and (l), three contribution were used for fitting. The two first at 72.8 eV and 73.2 eV are attributed to Al 2p_{3/2} and Al 2p_{1/2} and are both due to aluminum in metallic form. The last contribution at 74.2 eV is attributed to oxidized aluminum. This is a typical spectrum of an aluminum surface [191, 195, 198, 299–305].

In Figure 6.37, the normalized relative intensity of characteristic ions for amide functions are presented CH_4N^+ and CNO^- , but methylformamide molecular ions could also be identified as $\text{C}_2\text{H}_6\text{NO}^+$ $[\text{M}+\text{H}]^+$ and $\text{C}_2\text{H}_4\text{NO}^-$ $[\text{M}-\text{H}]^-$. They all present higher relative intensities for the air-dried and the heated samples. This confirms clearly the deposition of methylformamide after the dip coating. However, by comparing the relative intensities of these ions of the air-dried and heated samples, it seems that more N-methylformamide is deposited on the air-dried samples. This is in contradiction with the XPS data, where more nitrogen is detected on the heated samples. Moreover, the relative intensity of the CNO^- fragment is much higher on the heated samples, while the intensity of $\text{C}_2\text{H}_4\text{NO}^-$ is equivalent for both samples. This is also true for $\text{C}_2\text{H}_4\text{NO}^+$ (see annex). It is interesting to notice that the hydrogen rich ions have lower intensities on the heated samples. This indicates that the heating brings enough energy at the interface to initiate a reaction between the molecule and the aluminum surface. This reaction could be decomposition or bonding. Since there is more nitrogen on the heated samples and

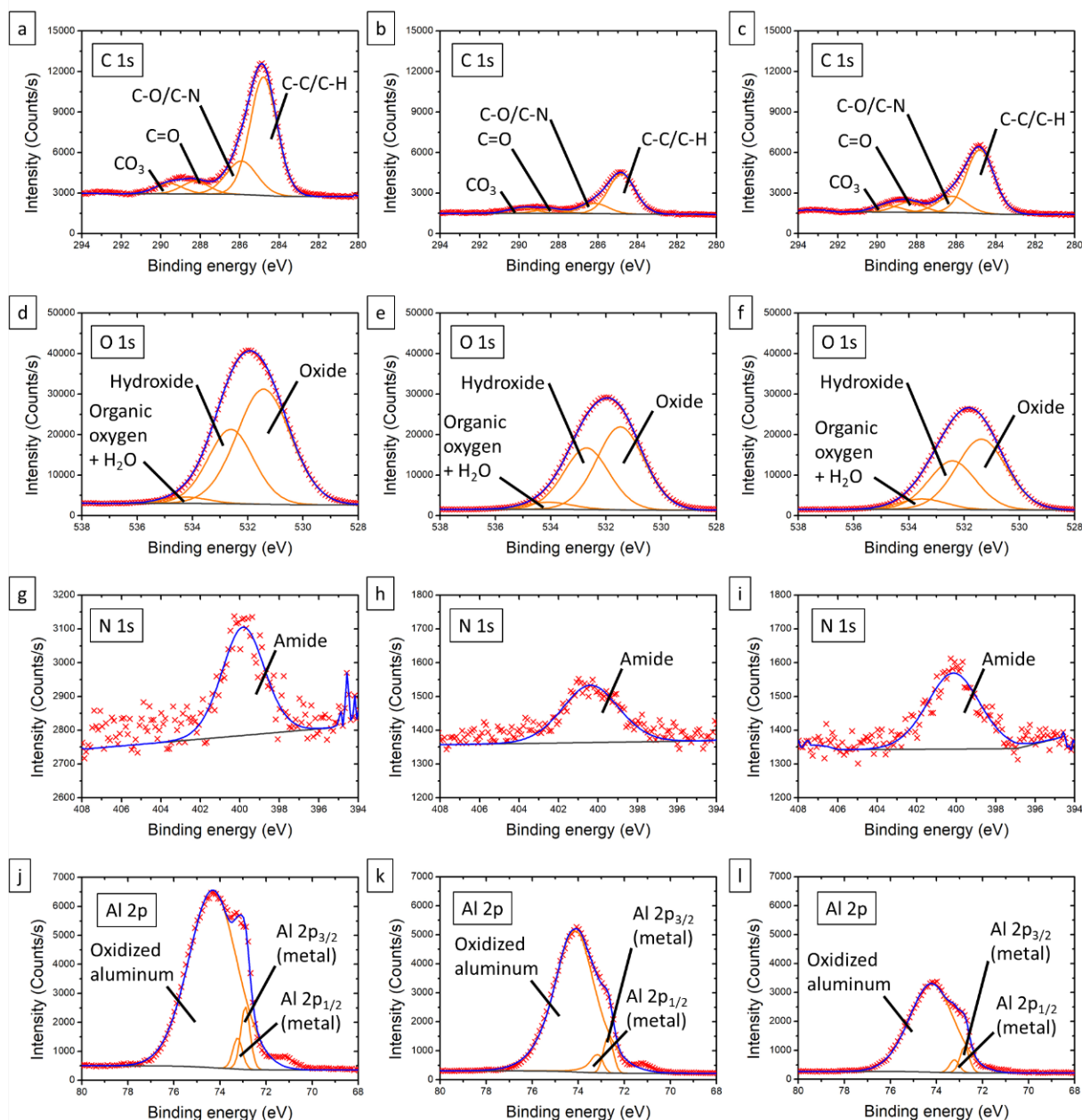


Figure 6.36: XPS high resolution of the C 1s region for (a) the UV cleaned samples, (b) the air-dried samples and (c) the heated samples, of the O 1s region for (d) the UV cleaned samples, (e) the air-dried samples, (f) the heated samples, of the N 1s region for (g) the UV cleaned samples, (h) the air-dried samples, (i) the heated samples, and of the Al 2p region for (j) the UV cleaned samples, (k) the air-dried samples and (l) the heated samples.

that there are equivalent intensities for $C_2H_4NO^{-/+}$, the reaction seems to be bonding.

6.4.2 Chemical reactivity

As already presented in section 6.1.2, the polymer offers different possible reactive sites: carbon sites, a nitrogen site and an oxygen site. As for the spin-coated samples, the reactivity of the carbon sites will not be discussed for the model samples, since part 1 shows clearly no

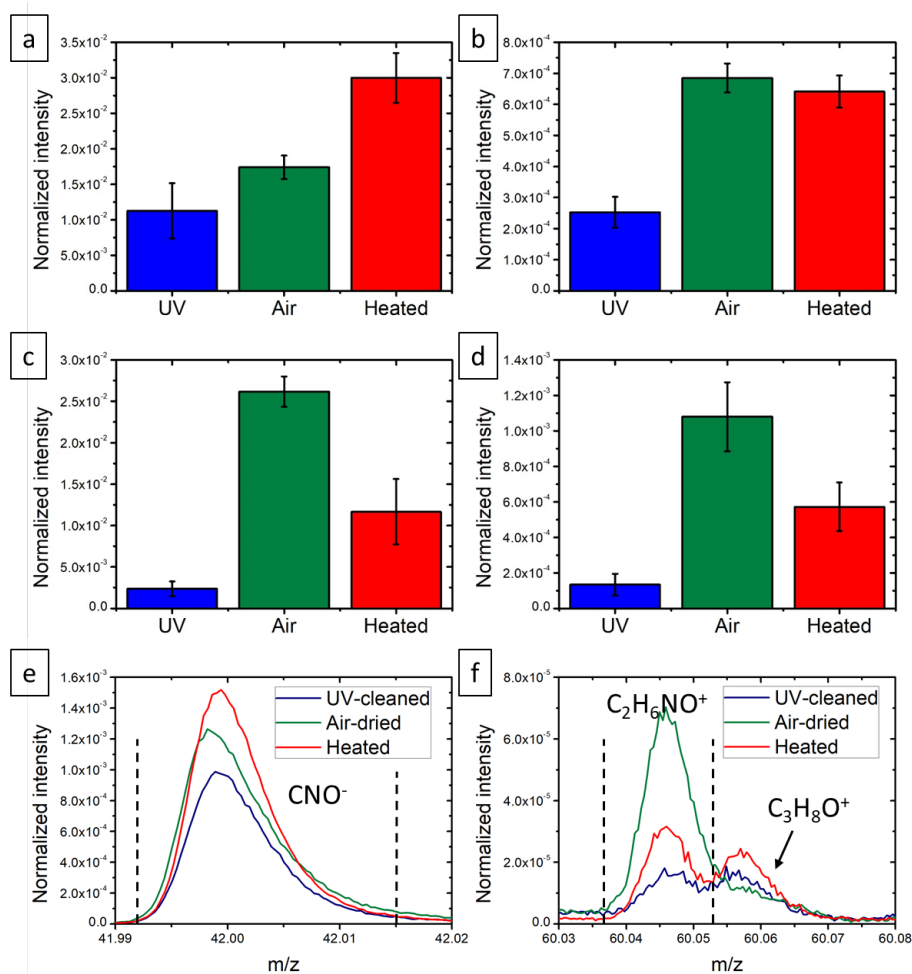


Figure 6.37: ToF-SIMS intensity normalized to total counts of characteristic peaks of N-methylformamide presented as histograms per samples, in blue the UV cleaned samples, in green the air-dried samples and in red the heated samples of (a) CNO^- , (b) $\text{C}_2\text{H}_4\text{NO}^-$, (c) CH_4N^+ and (d) $\text{C}_2\text{H}_6\text{NO}^+$, the mass spectra with the range of interest marked by dashed lines of (e) CNO^- and (f) $\text{C}_2\text{H}_6\text{NO}^+$.

reaction with the carbon sites.

6.4.2.1 Reactivity with the nitrogen sites

From the XPS high resolution spectra of the N 1s region, it appears that there is no Al-N peak around 396 eV [317–319]. However the signal of the nitrogen is very low, because there is only 1-2% on the surfaces, so the interpretation of the spectra is rather uncertain. Nonetheless, it is coherent with the previous experiments on the welded samples and the spin-coated samples.

In ToF-SIMS, only two ions of the $\text{C}_x\text{H}_y\text{N}_z\text{Al}_w^{-/+}$ were identified: CHNAI^+ and CHNAI^- (see Figure 6.38). CHNAI^+ present higher intensities on the air-dried and the heated samples, which is in coherent to the fact that there is less nitrogen present on the UV cleaned samples. The intensity of CHNAI^+ on the air-dried and the heated samples is equivalent, despite the fact that there is more nitrogen and the heating effect on the heated samples. CHNAI^- on the contrary is twice more intense on the heated samples compared to the UV cleaned and air-dried samples. But this ion present a very low relative intensity $\approx 5.10^{-5}$, which tends to indicate a

recombination. For comparison the CHNOAl^- ion has an intensity of $\approx 5 \cdot 10^{-4}$, so ten times more intense. Dissociation of CHNOAl ions in CHNAl ions could also be considered, but even in this case, CHNAl ions do not indicate a nitrogen bonding between the two compounds.

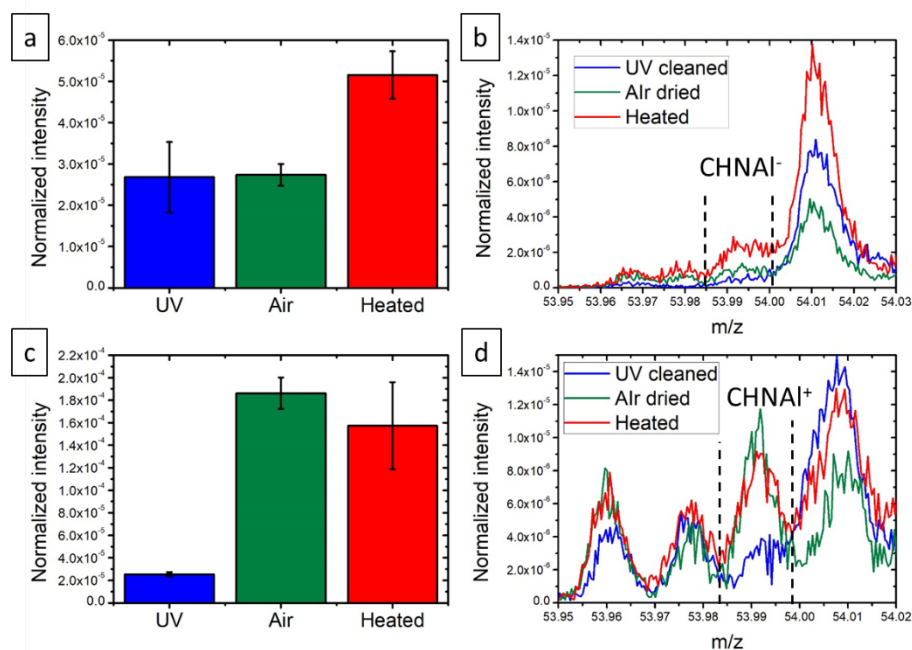


Figure 6.38: ToF-SIMS intensity normalized to total counts of characteristic peaks presented as histograms per zone, in blue the UV cleaned samples, in green the air dried ones and in red the heated samples, and the mass spectra with the range of interest marked by dashed lines of (a) and (b) CHNAI^- , (c) and (d) CHNAI^+ .

6.4.2.2 Reactivity with the oxygen sites

In XPS, in the O 1s region, the peak at 531.4 eV was assigned to organic components and water. As described in sections 6.1.2.3, 6.2.1 and 6.3.2.2, this peak can also be attributed to C-O-Al. This is supported by the spectra of the C 1s region, with the peak at 286.1 eV, which could also correspond to such type of bonds.

The SIMS data analysis allowed to identify two families of ions related to a C-O-Al bond on these samples as well: the $\text{C}_x\text{H}_y\text{O}_z\text{Al}_w^{-/+}$ and the $\text{C}_x\text{H}_y\text{N}_z\text{O}_w\text{Al}_n^{-/+}$.

As on the other samples, the $\text{C}_x\text{H}_y\text{O}_z\text{Al}_w^{-/+}$ ions have an erratic behavior. Some of them have equivalent intensities on all samples, or lower intensities on the heated samples compared to the UV-cleaned or air-dried samples (CH_2OAl^+ , CH_3OAl^+ , CH_4OAl^+ , and C_2OAl^- , C_2HOAl^- , CO_2Al^-). While a few of these ions have higher intensities on the heated samples compared to the UV cleaned and air-dried samples (CHOAl^+ and COAl^- , CHOAl^-). In the negative mode, the ions presenting lower intensities on the heated samples have a composition that looks like components coming from the contamination of carbon dioxide on a metallic surface.

In the negative mode, only three ions of the $\text{C}_x\text{H}_y\text{N}_z\text{O}_w\text{Al}_n^{-/+}$ family could be surely identified: CNOAl^- , CHNOAl^- and CHNO_2Al^- . These ions are more diverse than on the other samples in the positive mode: CHNOAl^+ , CH_3NOAl^+ , CHNO_2Al^+ , $\text{C}_2\text{H}_5\text{NOAl}^+$, $\text{C}_2\text{H}_6\text{NOAl}^+$, $\text{CH}_3\text{NO}_2\text{Al}^+$, and $\text{C}_2\text{H}_5\text{NO}_2\text{Al}^+$. Some of the ions' intensities are represented in Figure 6.39. Out of CHNO_2Al^+ and $\text{C}_2\text{H}_6\text{NOAl}^+$, they all present higher intensities on the heated samples compared to the UV cleaned samples. The behavior of the intensities of these ions on the air

dried samples is catching the attention. For most of the ions' intensity is lower than on the heated samples, which points in the direction of a C-O-Al bond. But for $C_2H_5NO_2Al^+$, the intensity is much higher on the air-dried samples than on the heated samples. This ion is apparently composed of the entire methylformamide molecule and an AlO fragment of the metal surface. In section 6.4.1, the hypothesis of a bonding reaction of the molecule with the surface was proposed. This bonding, or at least the reaction, induces changes in the molecule, explaining why the ions presenting the whole molecule are less intense on the heated samples. The nature of the hybrid ions observed and investigated, the most suitable explanation is a C-O-Al bond.

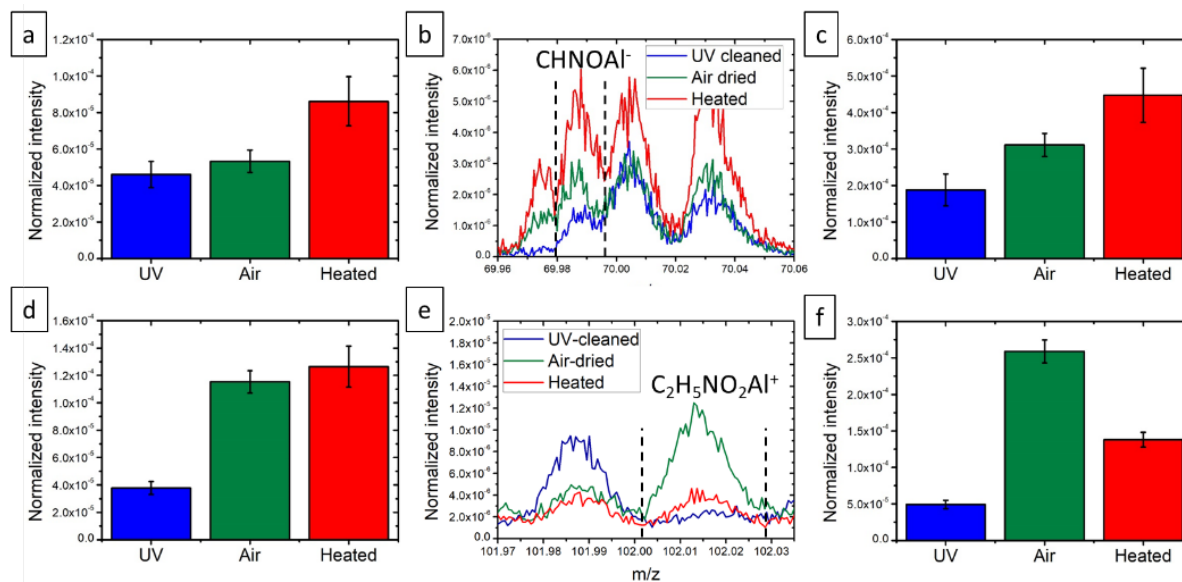


Figure 6.39: ToF-SIMS intensity normalized to total counts of characteristic peaks presented as histograms per zone, in blue the UV cleaned samples, in green the air dried ones and in red the heated samples of (a) $CHNOAl^-$, (c) $CHNO_2Al^-$, (d) $CHNOAl^+$ and (f) $C_2H_5NO_2Al^+$ and the mass spectra zone with the range of interest marked by dashed lines of (b) $CHNOAl^-$, and (e) $C_2H_5NO_2Al^+$.

6.4.2.3 Reaction mechanism

The percentage of aluminum on the UV cleaned and the heated samples is similar, while it is higher on the air-dried samples. The XPS high resolution spectra of the Al 2p region was fitted using three contribution: two interpreted as from metallic aluminum, and one for the oxidized form of aluminum. From this, an estimate of the oxide thickness could be calculated, using Strohmeier's method [258]. For the three samples, there was no statistical difference visible, and an average value of nearly 8 nm for the oxide thickness was obtained for all samples. So the same effect of oxidation as on the spin-coated effect is not observable (see 6.3.2.3). Indeed, the heating is lower than during the welding process, only 150 °C compared to nearly 300 °C, and the methylformamide forms a much thinner deposit than the spin-coated polymer.

In ToF-SIMS some ions can give a clue about the binding mechanism. The relative intensities of some metallic ions are represented in Figure 6.40. It can be observed that the hydroxide ions ($AlHO_2^+$ and $AlH_2O_2^+$) presented have lower intensities on the heated samples compared to the air-dried samples. This indicates a disappearance of hydroxide during the heating process, maybe by reacting with the methylformamide. At the same time, the intensities of the ions of the oxide (AlO^- and AlO_2^-) presented are similar on the air-dried and the heated samples.

Other ions from the metal have intensities varying differently, making it difficult to understand clearly the mechanism. Above in sections 6.4.1 and 6.4.2.2, observation was made, that the molecule on the heated samples, tends to lose hydrogen. This was confirmed with the lower intensity of CH_4N^+ and $\text{C}_2\text{H}_6\text{NO}^+$, and the lower intensity of $\text{C}_2\text{H}_5\text{NO}_2\text{Al}^+$. In Figure 6.41, a possible reaction mechanism is depicted. The possible fragmentations of the formed compound during SIMS measurement, are in good agreement with the measurement. Indeed it explains the lower intensity of $\text{C}_2\text{H}_6\text{NO}^+$ because of the loss of an hydrogen atom during the reaction. The lower intensity of CH_4N^+ can be explained, also because of the loss of a hydrogen atom bound to the nitrogen, but also because this nitrogen atom has a double bond with a carbon, which diminishes the probability of a fragmentation at this point. The explanation of the lower intensity on the heated samples for $\text{C}_2\text{H}_5\text{NO}_2\text{Al}^+$ is also the loss of the hydrogen of the nitrogen. At the same time the intensities of CNO^- and $\text{C}_2\text{H}_4\text{NO}^-$ can be maintained, while the intensity of CHNOAl^{\pm} are also explained.

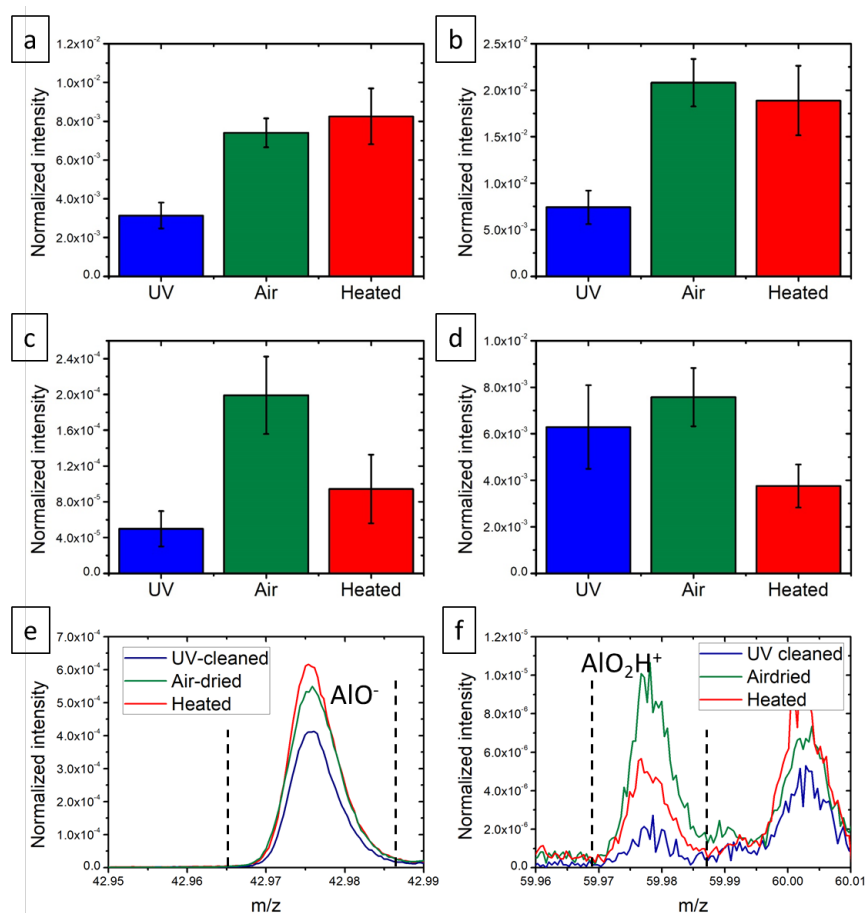


Figure 6.40: ToF-SIMS intensity normalized to total counts of characteristic ions of an oxidized aluminum surface (a) AlO^- , (b) AlO_2^- , (c) AlHO_2^+ , and (d) AlH_2O_2^+ , and the mass spectra zone with the range of interest marked by dashed lines of (e) AlO^- , and (f) AlO_2H^+ .

6.4.3 Discussion about PCA

Even if the SIMS data shown above was analyzed without the help of PCA, it is interesting to discuss it. Indeed, the weakness of the direct approach is the user arbitrary peak selection. This might induce bias in the data analysis and cause misinterpretation or just overlooking important

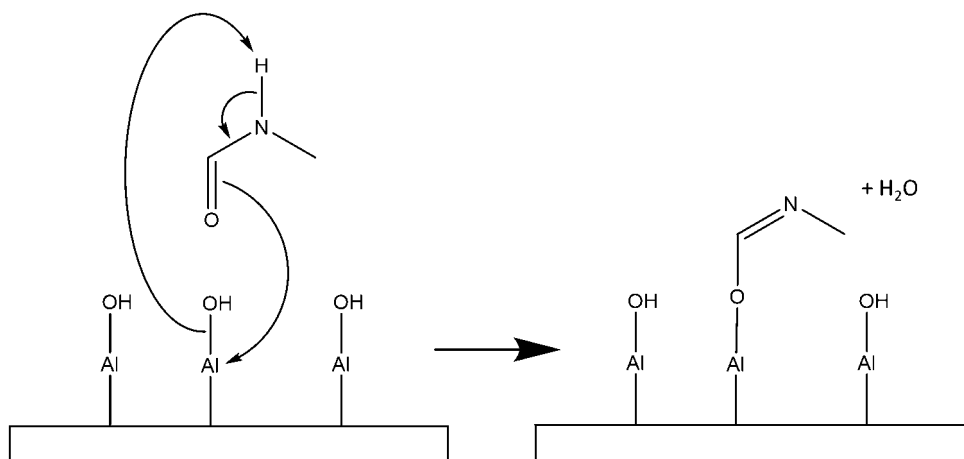


Figure 6.41: Proposition of reaction mechanism between the molecule and the metal surface.

results. In our case, the peak lists were created as carefully as possible by selecting peaks related to the N-methylformamide, the aluminum, some contaminations, and hybrid ions. For the hybrid ions, first the different family of ions were identified, then for each family, the different atomic combinations were tested. If in the mass range of the tested combination there is a peak, it was tested also for potential interferences with other ions. If there is a peak with no interference, the peak was interpreted as the tested hybrid ion. The hand selected peak lists can be found in annex. An automatic peak list was generated by applying the following parameters: an intensity higher than 100 counts, and a mass range between 0 and 300m/z. The peak lists in both the negative and the positive mode are both composed of 394 peaks.

6.4.3.1 PCA on the hand-selected peak lists

The scores of the PCA for both polarities are represented in Figure 6.42. The behavior in both polarities is here very different. Indeed, in the negative mode, PC1 discriminates the UV-cleaned samples from the air-dried and the heated samples, while PC2 discriminates the Air-dried samples from the UV-cleaned and the heated samples. Plotting PC1 versus PC2 allows then to clearly separate the three samples. In the positive mode, the scores of PC1 and PC2 do not discriminate alone the samples. PC1 plotted versus PC2 allows to separate the UV-cleaned samples from the Air-dried and the Heated samples. The air-dried and the heated samples do overlap, underlying the fact that the PCA in the positive mode on the hand-selected peak list does not discriminate them.

In the negative mode, the loadings (see Figure 6.43) of PC1 and PC2 display clearly a pattern. For PC1, the positive loadings are associated to ions presenting higher intensities on the air-dried and the heated samples than on the UV-cleaned samples, while the negative loadings the intensity of the ions are higher on the UV-cleaned samples than on the air-dried and the heated samples. For the interpretation of the ions presenting high loadings, no clear pattern exist, as metal and N-methylformamide ions are detected indistinctively in both positive and negative loadings. For instance, mass 26 is CN^- , mass 41 is C_2HO^- , mass 42 is CNO^- , mass 43 is AlO^- , mass 58 is $\text{C}_2\text{H}_4\text{NO}^-$, or mass 59 is AlO_2^- . PC2 also presents a recurrent pattern for the intensities of the different ions. The positive loadings refer to ions presenting intensities higher on the heated samples than on the air-dried and UV-cleaned samples. Here also the ions are related to both the N-methylformamide and the aluminum, but some two hybrid ions are present in the high loadings. For example, mass 24 C_2^- , mass 40 is C_2O^- , mass 51 is C_2Al^- , mass 67 is

C_2OAl^- , or mass 99 is $\text{Al}_3\text{H}_2\text{O}^-$. The negative loadings are also related to N-methylformamide and the metal, as mass 45 is CHO_2^- and AlO_2^- .

In the positive mode the loadings of PC1 present a pattern of intensity even if the scores do not separate them. The positive loadings refer to ions having low intensities on the UV-cleaned samples, high intensities on the air-dried samples and intermediate intensities on the heated samples. Here also the nature of the ions is from both N-methylformamide and aluminum. For example, mass 15 is CH_3^+ , mass 27 is Al^+ , mass 28 CH_2N^+ , mass 30 is CH_4N^+ , or mass 61 is AlH_2O_2^+ . The negative loadings present high intensities on the UV-cleaned samples compared to the two other samples. The ion presenting the highest loadings can be related to both N-methylformamide or organic contamination as mass 29 is C_2H_5^+ . The loadings of PC2 present the same pattern of intensity for both the positive and negative loadings. This is coherent with the fact that the scores do not separate the samples. So the main differences are not between the type of samples. The ions present low intensities on the heated samples, high intensities on the air-dried samples and intermediate intensities on the heated samples.

From this PCA done on both polarities for the hand-selected peak list, the results are not the most convincing. The peak list of the negative mode is efficient and allows to clearly differentiate the samples, but not in the positive mode. The peak list is certainly not complete enough to be able to understand the differences between the samples.

6.4.3.2 PCA on the automatic generated peak lists

Looking at the scores obtained for the PCA done on the automatic generated peak lists depicted in Figure 6.44, it appears that both polarities clearly discriminate the three samples. In the negative mode PC1 separates the UV-cleaned samples from the air-dried and the heated samples, and PC2 separates the three of them. In the positive mode the scores of PC1 directly separate the three samples. PC2 separates the heated samples from the UV-cleaned and the air-dried samples. Plotting PC1 versus PC2 in both polarities emphasizes the differentiation made by the two first principal components.

The loadings of PC1 in the negative mode have a clear pattern of intensity (see Figure 6.45). The positive loadings are associated to ions having higher intensities on the air-dried samples than on the UV-cleaned samples, the heated samples being even higher or equivalent to the air-dried samples. On the nature of the ions, in majority contaminations are present in the high loadings, but also some aluminum and N-methylformamide ions. Mass 16 is O^- , mass 17 is OH^- , mass 19 is F^- , mass 26 is CN^- , mass 59 is AlO_2^- , or mass 119 is $\text{Si}_3\text{H}_3\text{O}^-$. The negative loadings present decreasing intensities from the UV-cleaned samples to the heated samples. The only ion presenting high loadings at mass 197 is $\text{Al}_3\text{H}_4\text{O}_7^-$. For PC2, the pattern of intensity is visible between the air-dried samples and the heated samples. The positive loadings are ions presenting higher intensities on the heated samples than on the air-dried samples, while the negative loadings are ions having lower intensities on the heated samples than on the air-dried samples. The intensity on the UV-cleaned samples for both positive and negative loadings do not present a recurrent pattern. For PC2 the nature of the ions presenting the highest positive loadings are related to both N-methylformamide and contaminations. Mass 25 is C_2H^- , mass 26 is CN^- , mass 35 is Cl^- , mass 42 is CNO^- , mass 66 is C_3NO^- . The highest negative loadings are related to the aluminum and contaminations. Mass 45 is CHO_2^- , mass 77 is SiO_3H^- , mass 79 is CO_2Cl^- , mass 179 is $\text{Al}_3\text{H}_2\text{O}_6^-$, mass 239 is $\text{Al}_3\text{H}_3\text{O}_6^-$, mass 281 is $\text{Al}_5\text{H}_2\text{O}_9^-$.

In the positive mode the loadings present also an intensity pattern for PC1 and PC2 (see Figure 6.45). For PC1, the positive loadings are linked to ions presenting higher intensities on the air-dried and heated samples than on the UV-cleaned samples. They are linked to ions from the N-methylformamide and the aluminum surface. For instance, mass 27 is Al^+ , mass 30 is CH_4N^+ , mass 32 is CH_6N^+ , mass 42 is $\text{C}_2\text{H}_4\text{N}^+$, or mass 73 is $\text{C}_3\text{H}_9\text{N}_2^+$. The highest negative loadings

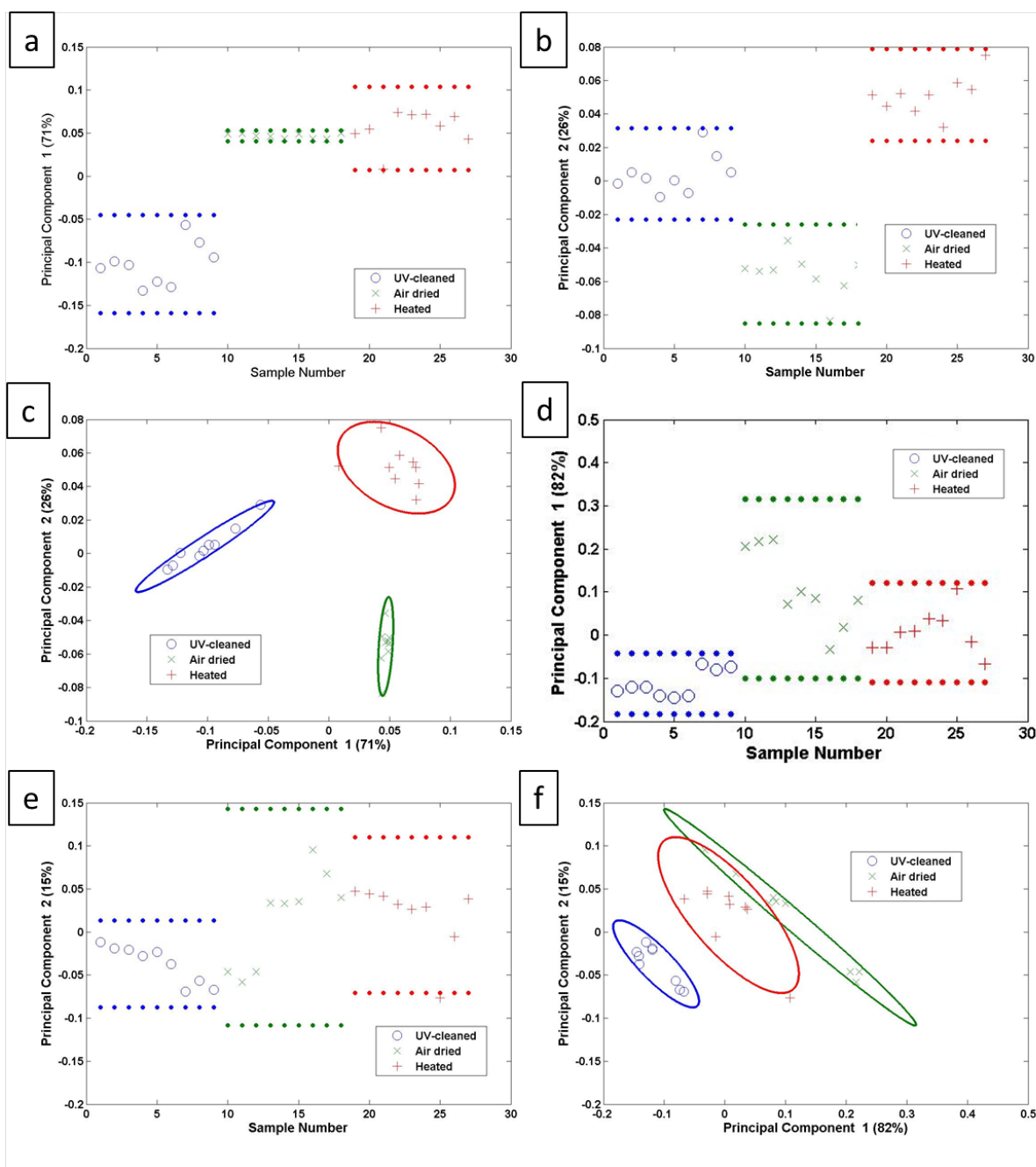


Figure 6.42: Scores of the hand-selected peak list. In the negative mode (a) PC1, (b) PC2, (c) PC1 versus PC2. Scores in the positive mode (d) PC1, (e) PC2, and (f) PC1 versus PC2.

are ions related to organic contaminations, like mass 41 is $C_3H_5^+$, mass 43 is $C_3H_7^+$, mass 55 is $C_4H_7^+$, mass 86 is $C_5H_{12}N^+$ or mass 91 is $C_7H_7^+$. The intensity pattern for the loadings of PC2 is between the air-dried and the heated samples. No clear pattern could be identified for the UV-cleaned samples. The positive loadings present higher intensities on the heated samples than on the air-dried samples. They are linked to contaminations and N-methylformamide, as mass 23 is Na^+ , mass 39 is K^+ , mass 44 is $C_2H_6N^+$, mass 112 is $C_7H_{12}O^+$, mass 140 is $C_8H_{12}O_2^+$. The negative loadings present higher intensities on the air-dried samples than on the heated samples. They can be related to organic contaminations, as mass 29 is $C_2H_5^+$, mass

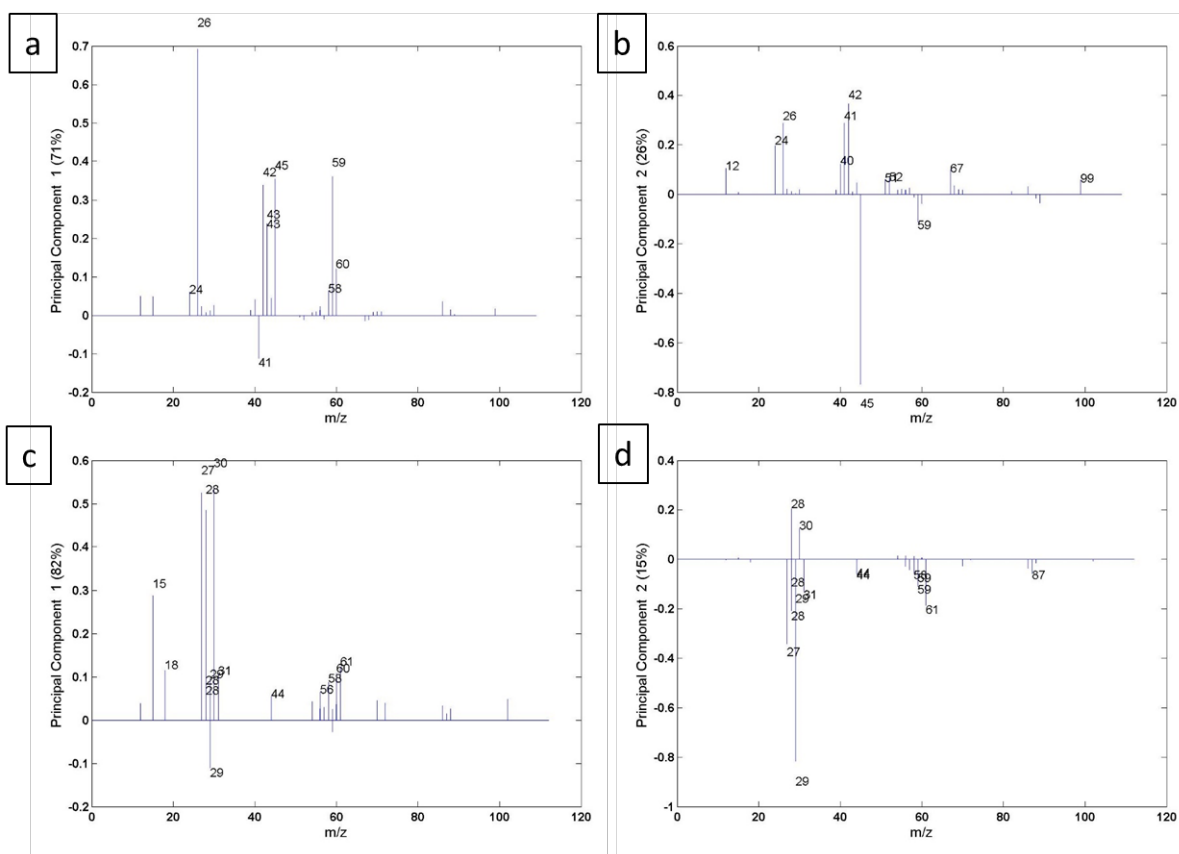


Figure 6.43: Loadings of the hand-selected peak list. In the negative mode (a) PC1, (b) PC2. In the positive mode (c) PC1, (d) PC2.

41 is $C_3H_5^+$, mass 43 is $C_3H_7^+$, and mass 73 is $C_3H_9N_2^+$.

The automatic generated peak list show that the samples are clearly different. In the positive mode the samples are also discriminated unlike the hand-selected peak list. In addition, it shows the role and the determinant impact of contaminations on the results. This emphasizes even more the importance of making the good assumptions in building a peak list.

6.4.4 Conclusions on the model samples

The dip-coating process deposits the methylformamide on a very low scale for the heated samples as well as for the heated samples. The heating fixes more molecule than just air-drying, but at the same time the heating degrades methylformamide, because of its bonding reaction with the aluminum surface. This degradation implies a reaction with the aluminum surface. Two of the reactive sites of the polymer were checked: the nitrogen site and the oxygen site. The carbon reactive site were directly excluded, as sufficient proofs were given to exclude any reaction of this kind in section 4.1.2.1. The analysis of a possible reaction with the nitrogen site demonstrated that the ions of the $C_xH_yN_zAl_w^{-/+}$ originate from recombination effect. The reactivity of the oxygen sites, showed clearly that a C-O-Al bond is formed during the heating process. The last part details why PCA and compares the use of the hand-selected peak list with the automatic generated peak list. In the negative mode the results are very similar for the two peak list, whereas in the positive mode the hand-selected peak list is not able to discriminate the different samples using PCA.

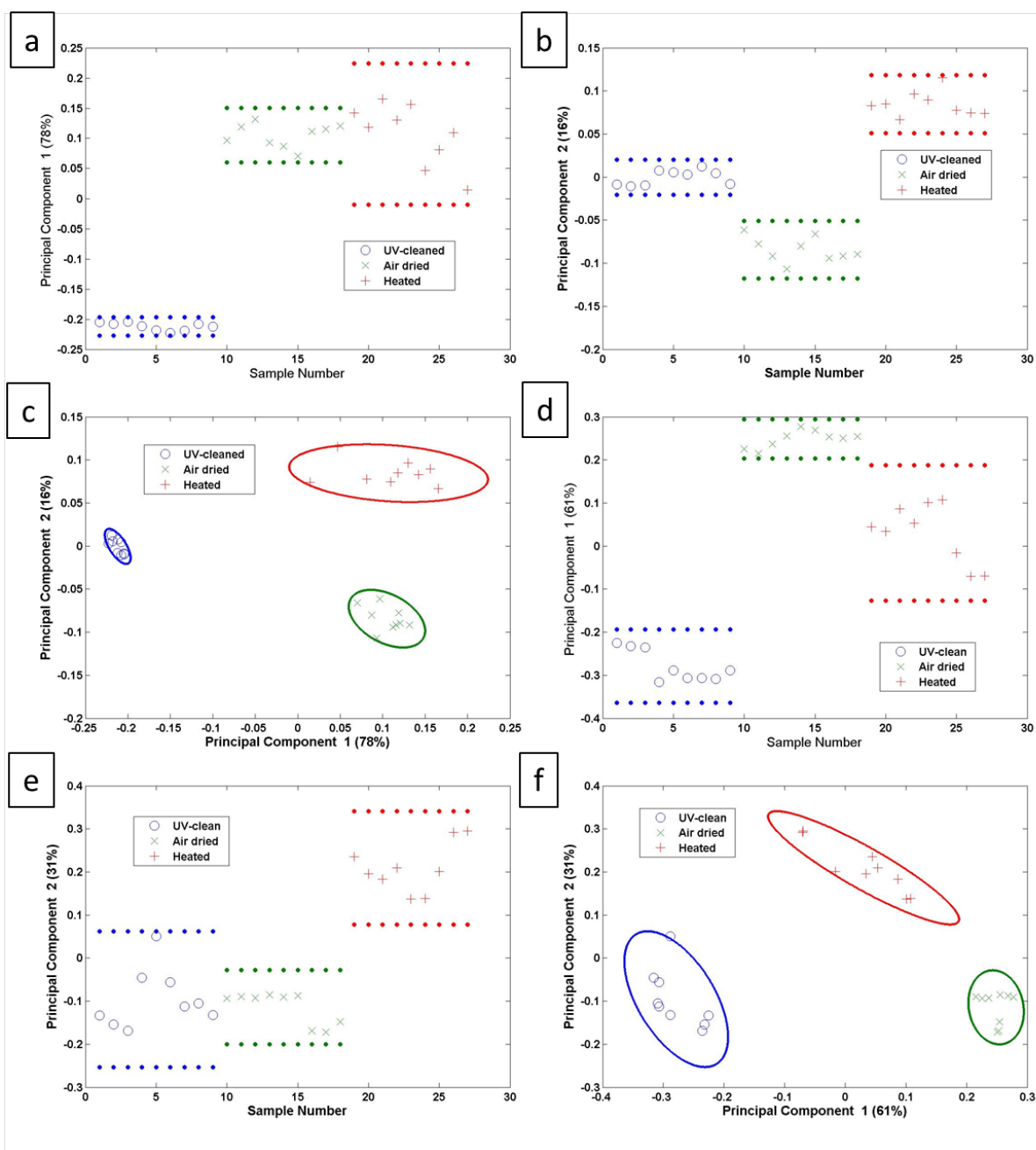


Figure 6.44: Scores of the automatic generated peak list. In the negative mode (a) PC1, (b) PC2, and (c) PC1 versus PC2. In the positive mode (d) PC1, (e) PC2, and (f) PC1 versus PC2.

6.5 Conclusions

In this chapter, the results of four different samples were presented and discussed. To access the interface, three different, yet complementary, approaches were used. The first approach used, by breaking and dissolving the residue, is an innovation. Indeed, breaking the samples was already used several times, as well as dissolving, but never together. This allowed to analyze the interface of thick assemblies: the welded and the ablated welded samples. The second approach is more classical, spin-coating a thin film which is dissolved afterwards. Finally the third approach, consists in depositing a molecule presenting only the reactive part of the polymer studied.

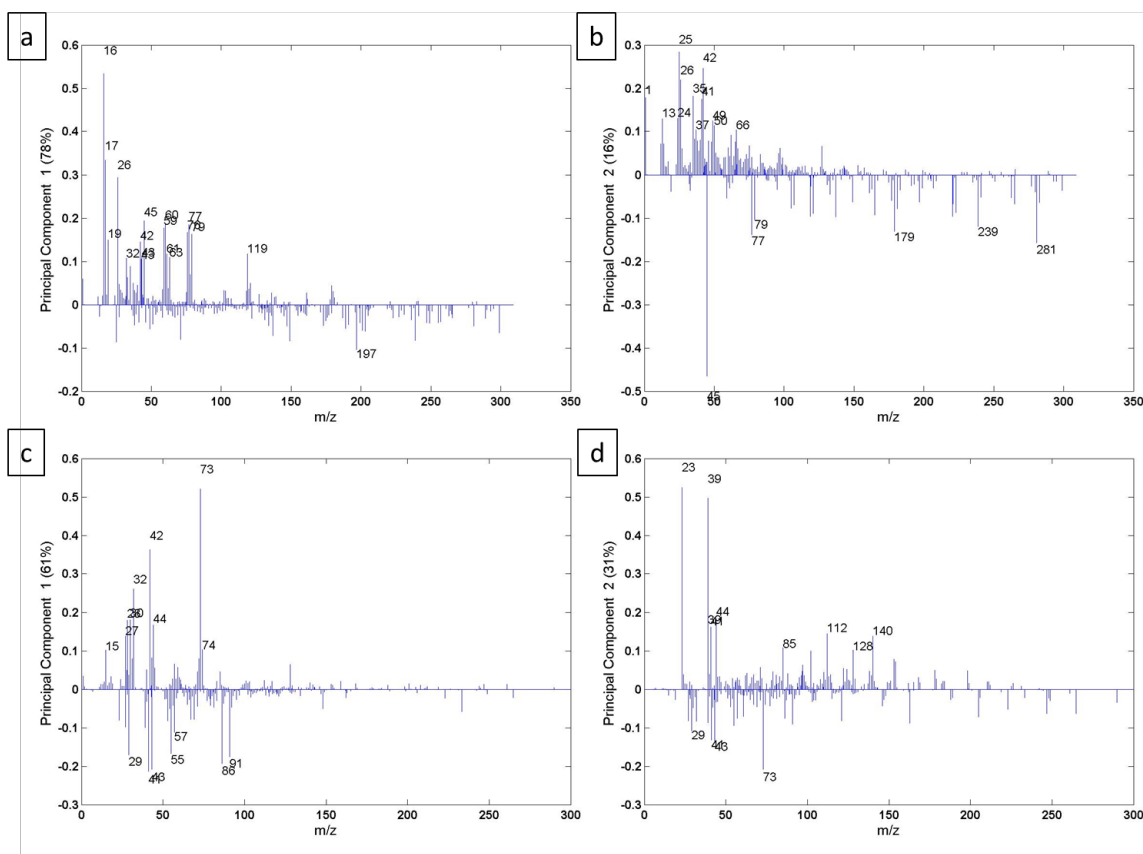


Figure 6.45: Comparison of the loadings obtained for the automatically generated peak list and the hand selected peak list in the negative mode, (a) and (b) PC1, (c) and (d) PC2.

More polymer or methylformamide were detected in the zones or on the samples, which were welded or heated. This even after the dissolution step for the welded, ablated welded, and spin-coated samples. The separation between the weld and the out of weld was a sharp separation line, as observed on the welded, ablated welded and the spin-coated samples as can be seen on the images taken in ToF-SIMS in Figure 6.4, Figure 6.20 and Figure 6.24.

The reactivity of the polymer was studied on all four samples. Three different types of reactive sites were identified: carbons, nitrogen and oxygen sites (see Figure 6.5). All four samples displayed results leading to the same conclusions. First there is no reaction with the carbon sites. Secondly the reaction does not occur on the nitrogen site. Finally the reaction happens at the oxygen site, leading to the formation of a C-O-Al bond, as depicted in Figure 6.12.

The reactivity of the metal was more difficult to assess. Indeed it was possible to study it on the spin-coated and the model samples, as no major differences on the metal behavior could be seen on the welded and the ablated welded samples. Nonetheless, the lower occurrence of hydroxide ions on the welded zone or the heated samples, indicate that the reaction between the polymer and the metal occurs with the free hydroxyl groups on the metallic surface (see Figure 6.28).

The use of PCA for all the samples was also investigated and it appears that a direct approach for all the samples lead to the same conclusions. The samples are well discriminated and the most important difference is the presence or absence of polymer/molecule. The hybrid ions do not present high loadings because they present low intensities compared to the polymer ions for

instance. They are then necessarily hand-selected. Nevertheless the role of the contaminations was put forward through the use of PCA on both the hand-selected and the automatic generated peak lists.

Chapter 7

Titanium-polyamide bonding?

This chapter summarizes the results of the experiments performed to show the existence and the nature of a chemical bond between titanium and polyamide-6.6. As this material combination was tested after the aluminum-polyamide combination and the developed strategy was successful, the same strategy was applied. It was adapted in order to take into account the different behavior of titanium compared to aluminum. First welded samples were prepared as for aluminum, by welding ethanol wiped titanium sheets to polyamide-6.6 plates. To access the interface, the samples were broken and directly analyzed, contrarily to the aluminum welded samples, because the failure mode is mixed on the titanium welded samples with some adhesive and some cohesive parts. So the interface is directly accessible. In a second time, titanium spin-coated samples were prepared, by spin-coating polyamide-6.6 onto mirror polished titanium surfaces. Some of them were welded, some not, to serve as reference. To access the interface, the polyamide-6.6 layer was dissolved using 2,2,2-trifluoroethanol. At last, model samples were prepared. As reference, titanium surfaces were UV-cleaned. After UV-cleaning other titanium surfaces were dipped in N-methylformamide, which presents only the reactive part of polyamide-6.6. After, some of them were let to dry in ambient conditions, while the rest was put on a hot plate and heated up to 150 ° C to simulate welding. N-methylformamide has a boiling point at 186 ° C. All the samples were analyzed by XPS and ToF-SIMS. The complete description of the preparation and explanation of the strategy of the samples can be found in Chapter 4 Materials and Method.

7.1 Welded samples

Contrarily to the aluminum welded samples, where the failure mode was cohesive in the polymer, the titanium samples present a mixed failure mode between an adhesive failure and a cohesive failure mode in the polymer (see Figure 7.1). At first the welded samples of titanium were also dissolved, following the same procedure as for the aluminum welded samples. Doing the XPS and ToF-SIMS analysis on those samples with a dissolution step showed no differences between the weld and out of the weld, even on the zones where there was a cohesive failure mode. Indeed, no polymer traces were detected in the weld and both zones present the features of simple titanium surfaces (see Table 7.1). This demonstrate that the chemical interaction of the polymer is stronger with the solvent, 2,2,2-trifluoroethanol, than with the titanium surface. As the dissolution step washes all the interface information away and as the failure mode is mixed, no dissolution step was performed on the samples presented hereafter. The measurements were done on the adhesive failure part. The analysis of the ToF-SIMS data was done directly at the first place, but PCA was done later and this will be discussed at the end of this part before the conclusion.

Table 7.1: XPS elemental composition of titanium welded samples with a dissolution step out and in the weld.

Samples	%O	%Ti	%C	%N	%Al	%V
Out of weld	45.6 (± 4.6)	32.6 (± 3.8)	16.8 (± 3.6)	2.2 (± 0.5)	2.4 (± 0.8)	0.5 (± 0.1)
Weld	46.3 (± 4.8)	33.1 (± 7.0)	15.3 (± 2.4)	2.3 (± 0.4)	2.5 (± 0.7)	0.5 (± 0.2)

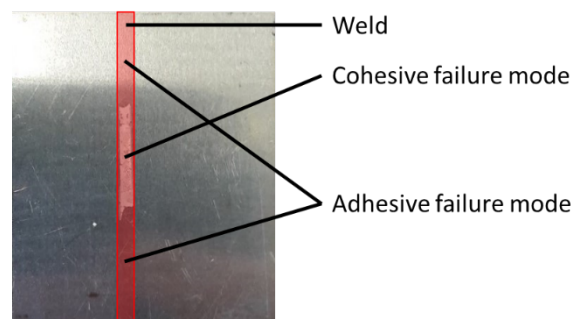


Figure 7.1: Image of the failure mode on the titanium welded samples.

7.1.1 Traces of polyamide-6.6 in the adhesive failure mode zone in the weld

7.1.1.1 XPS data

Table 7.2 summarizes the elemental composition obtained with XPS for a reference of polyamide-6.6, a titanium reference (an ethanol wiped titanium surface of the same alloy), out and in the weld of the welded titanium samples. The nitrogen percentage in the weld is three times higher than out of the weld and the titanium reference. This is a good indication of the presence of polyamide in the weld after breaking the samples. The carbon percentage is equivalent with huge standard variations out and in the weld, but much higher than on the titanium reference. While in the weld the carbon percentage can be explained by the presence of polyamide on top the surface, the carbon out of the weld can be associated to adventitious carbon. This also explains the low percentage of oxygen out and in the weld. The percentage of titanium is equivalent on the reference, out and in the weld. The presence of aluminum and vanadium is expected as they are present in the alloy Ti-64 used. The presence of calcium, silicon, sulfur, zinc and iron is likely due to surface contaminations of the reference samples. This is also the case for fluorine, but the higher percentages out and in the weld is not understood.

The C 1s region high resolution spectra out and in the weld were interpreted using five contributions, as presented in Figure 7.2 (a) and (b). The C-C/C-H contribution was used for calibration of the XPS data and set at 284.8 eV. A titanium carbide contribution was added around 281.4 eV [331, 332] for both zones. Around 286.2 eV [282, 286, 296] a contribution of C-O/C-N bonds was also added. A contribution of C=O was added around 288.2 eV [282, 286, 296]. And finally a contribution of C-F bonds was added around 292.2 eV [282, 286, 296]. The C-F bonds come from the fluorine contamination of the surface out and in the weld. It is noticeable that the intensity of the C-O/C-N and C=O contributions is significantly higher in the weld than out of it. This can be explained by the presence of polyamide-6.6 in the weld and not outside of it. The titanium carbide contribution is equivalent out and in the weld.

The Ti 2p region high resolution spectra out and in the weld are depicted in Figure 7.2 (c) and (d). Surface plasmons were identified around 471.0 eV [286, 289, 290]. The Ti 2p spectra present a spin-orbit splitting, explaining why for each contribution there are two peaks associated to the Ti 2p_{3/2} and the Ti 2p_{1/2}. For simplicity both energies will be given for each contributions,

Table 7.2: XPS elemental composition from the survey spectra for polyamide-6.6, reference titanium, out of the weld and in the weld.

Samples	%O	%Ti	%C	%N	%Al	%V	%Ca	%F	%Si	%S	%Zn	%Fe
PA-6.6	12.3 (\pm 0.3)	0.0	75.9 (\pm 0.1)	11.8 (\pm 0.2)	0.0	0.0	0.0	0.0	0.0	0.0	0.0	0.0
Ti ref	50.3 (\pm 1.3)	17.0 (\pm 0.9)	22.2 (\pm 2.2)	1.3 (\pm 0.5)	0.5 (\pm 0.0)	2.7 (\pm 0.3)	2.1 (\pm 0.2)	0.5 (\pm 0.1)	1.4 (\pm 0.2)	1.0 (\pm 0.2)	0.5 (\pm 0.1)	0.6 (\pm 0.1)
Out of weld	33.4 (\pm 5.6)	14.9 (\pm 3.0)	45.0 (\pm 7.4)	1.3 (\pm 0.4)	0.9 (\pm 0.6)	0.4 (\pm 0.2)	2.9 (\pm 0.3)	1.3 (\pm 0.3)	0.0	0.0	0.0	0.0
Weld	32.7 (\pm 6.5)	15.5 (\pm 1.8)	42.3 (\pm 7.8)	4.7 (\pm 0.6)	0.9 (\pm 0.5)	0.3 (\pm 0.2)	2.5 (\pm 0.2)	1.1 (\pm 0.1)	0.0	0.0	0.0	0.0

without specifying each time that the first and lower energy given is from the Ti 2p_{3/2} and the second and higher energy is from the Ti 2p_{1/2}. Two contributions are associated to Ti(0) and titanium carbide bonds around 453.4 eV and 459.6 eV [286, 289, 290]. These contributions are consistent with the C 1s region high resolution spectra, where a C-Ti peak was identified too. Two other contributions are associated to Ti(II) and titanium nitride bonds around 454.6 eV and 460.3 eV [286, 289, 290]. Two contributions of Ti(III) were identified around 456.8 eV and 462.5 eV [286, 289, 290]. Finally two other contributions related to Ti(IV) were identified around 458.3 eV and 464.1 eV [286, 289, 290]. The peak presented here are characteristic of a titanium surface and are consistent with those found on the reference titanium surface (see Annex). Regarding the intensities of all the contributions, no major differences was noticed between out of the weld and in the weld. The titanium carbide looks more intense in the weld than out of the weld, but looking at the percentages, out of the weld represents on average $20.0 \pm 13.1\%$, while in the weld it accounts for $20.1 \pm 7.7\%$.

The O 1s region high resolution spectra out and in the weld are represented in Figure 7.2 (e) and (f). In both zones, three contributions were identified. The first one around 529.9 eV is associated to titanium oxide [282]. The second and the third, respectively around 531.2 eV and 532.4 eV are associated to Al-O, V-O bonds and oxygen from organic molecules [282]. No significant difference could be identified by looking at the intensities of the different contributions used to fit this region.

The N 1s region high resolution spectra out and in the weld are depicted in Figure 7.2 (g) and (h). Two contribution were identified in each zone. The first one associated to titanium nitride was identified around 396.5 eV [286, 289, 290], while the second one was found around 399.8 eV. In the weld, with this energy and intensity, it is clearly a contribution of polyamide-6.6 [282, 286]. Out of the weld, the peak is not very intense and the FWHM is also very broad. Therefore, no really precise interpretation can be given, it is associated to organic compounds due to surface contaminants.

7.1.1.2 ToF-SIMS data

The normalized intensity of some of the polymer characteristic ions is represented in histograms in Figure 7.3. The intensities of these ions is systematically higher in the weld than out of the weld. This confirms the observations made in XPS, that in the weld polyamide is

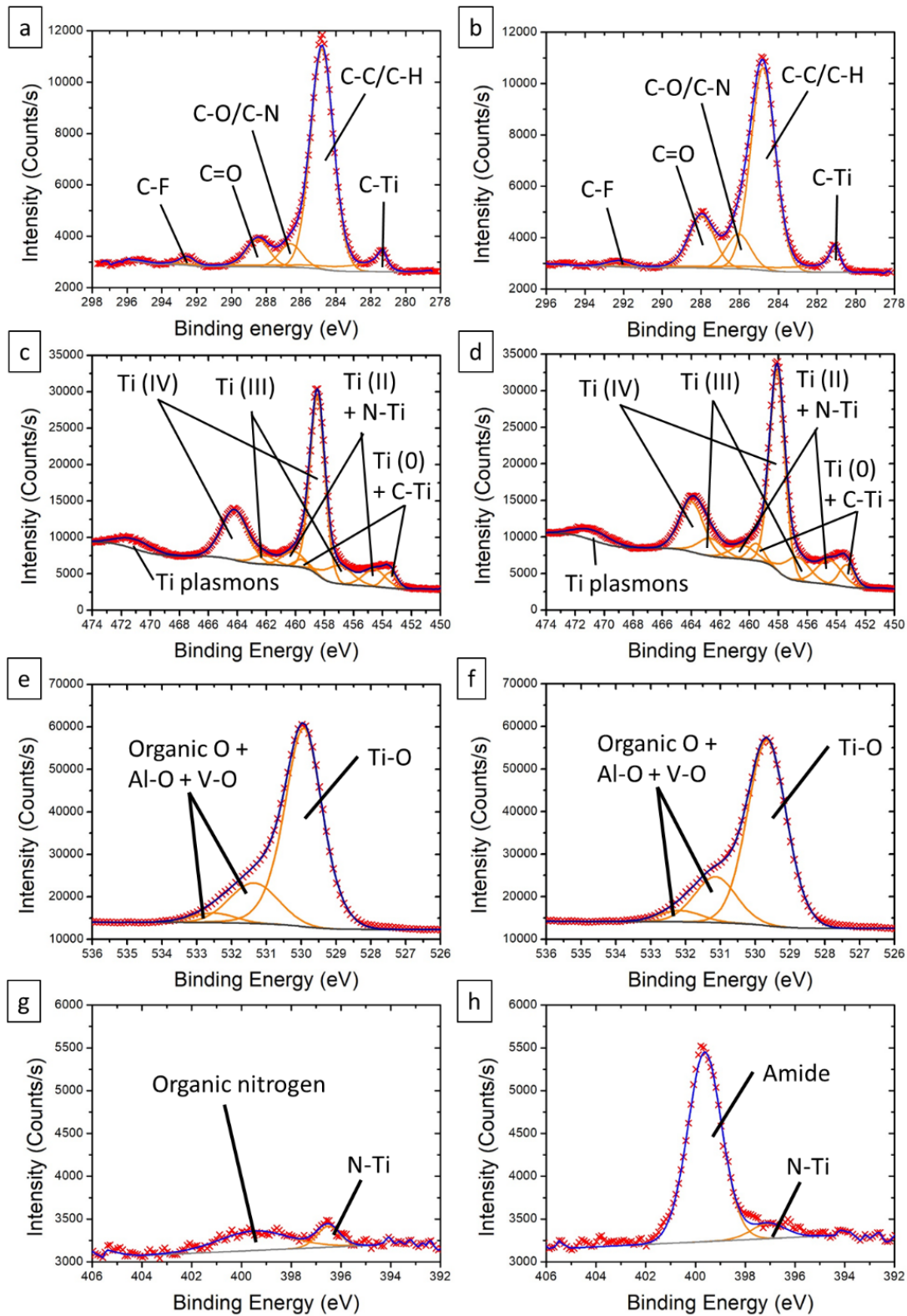


Figure 7.2: XPS high resolution spectra in the C 1s region (a) out and (b) in the weld, of the Ti 2p region (c) out and (d) in the weld, of the O 1s region (e) out and (f) in the weld, and of the N 1s region (g) out and (h) in the weld.

sticking to the surface after breaking the samples in the adhesive failure mode zone. Polyamide fragments are clearly identified, but no monomeric ion could be identified in the spectra, as it was the case on the aluminum welded samples. The characteristic ions of the titanium have on average lower intensities in the weld than out of it, but the variations stay within the error bars, as depicted in Figure 7.4. Since metal is still detected in the weld, it means that the polymer covering the surface is a very thin film. Large area images, taken at the border region between the weld and out of the weld, are presented in Figure 7.5. On the images obtained for the polymer fragments, a low intensity zone on the left hand side can be seen (images (a) and (c)) while a high intensity zone on the right hand side is visible. The transition between both zones is sharp, with no intermediate transition zone. The left hand side was identified as the out of weld and the right side as the weld. The images confirm the observation that polyamide is present in the weld after breaking the samples, and moreover that the separation between both zones is sharp. The images of the titanium oxide ions in Figure 7.5 (e), (f), (g) and (h), show a reversed pattern compared to the polyamide ions. Indeed the high intensity zone here is out of the weld, while the low intensity zone is in the weld. While on the simple spectra the intensity between out and in the weld for the metallic ions evolves within the error bars, on the images and their area integration, the difference between both zones is clearly visible and the transition as sharp as on the images of the polymer's ions. Nonetheless in the weld, metal is still clearly visible and identified, meaning that the polymer film is extremely thin. On the images no hole was identified for the polymer's ions in the weld, so that the film is covering the whole surface, unless the holes are smaller than the images' resolution.

7.1.2 Nature of the chemical bond

The polyamide sticking after breaking the sample must have a strong interaction, at least strong enough to withstand the breaking and remain on the metal surface. This can be explained by a chemical bond between both materials. Indeed, during the welding process, the polymer melts briefly [250, 287], as the temperature at the interface reaches 300 °C. This allows the polymer to flow and react with the titanium native oxide layer at the interface. On the polymer chain, several reactive sites can be identified (marked with red dots in Figure 7.6). Three reactive sites are located on carbons: the one bearing the amide function and his neighbor, and the one linked to the nitrogen atom. One reactive site is the nitrogen of the amide function and the last one is the oxygen atom of the amide function. All these reactive sites will be investigated separately hereafter.

7.1.2.1 Reaction with the carbon sites

In Figure 7.2 (a) and (b) the high resolution spectra of the C 1s region out and in the weld present a peak identified as titanium carbide around 281.4 eV. The intensity of this peak out and in the weld is equivalent, showing no major differences. On the reference titanium, such peak was not observed at all, but maybe it is because it is below the detection limit, as the whole carbon percentage is way lower on the reference titanium (22.2%) than out (45%) and in the weld (42.3%). Nonetheless, this is intriguing, as such peak are not observed on simple titanium anywhere else in litterature [289, 290, 331–333]. Since this peak is observed in similar intensities out and in the weld, one can conclude that this is not due to the welding process and is predominantly caused by surface contaminations.

Looking at specific ions of the $C_xH_yTi_z^{-/+}$ family in ToF-SIMS, several ions were surely identified. In the negative mode only one was identified surely: C_2Ti^- . In the positive mode six were clearly identified: CTi^+ , $CHTi^+$, CH_2Ti^+ , C_2HTi^+ , $C_2H_2Ti^+$, $C_2H_3Ti^+$. Some of the intensities of these ions are represented in Figure 7.7. It is observable that on average, their

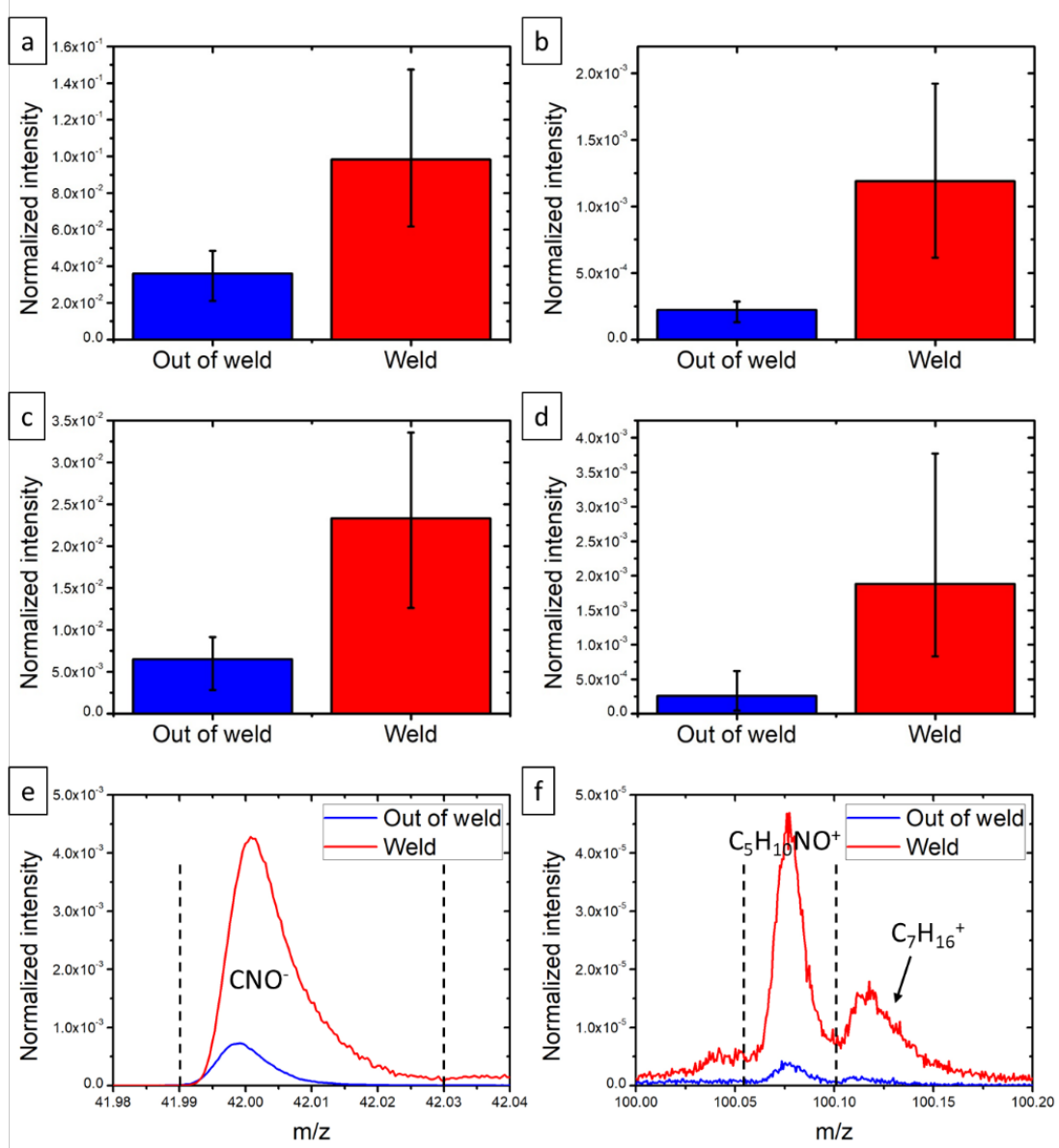


Figure 7.3: ToF-SIMS histograms of the normalized intensity out of the weld in blue and in the weld in red, of (a) CNO^- , (b) $\text{C}_3\text{H}_4\text{NO}^-$, (c) CH_4N^+ , and (d) $\text{C}_5\text{H}_{10}\text{NO}^+$. Mass spectra normalized on total intensity of the region of (e) CNO^- , and (f) $\text{C}_5\text{H}_{10}\text{NO}^+$.

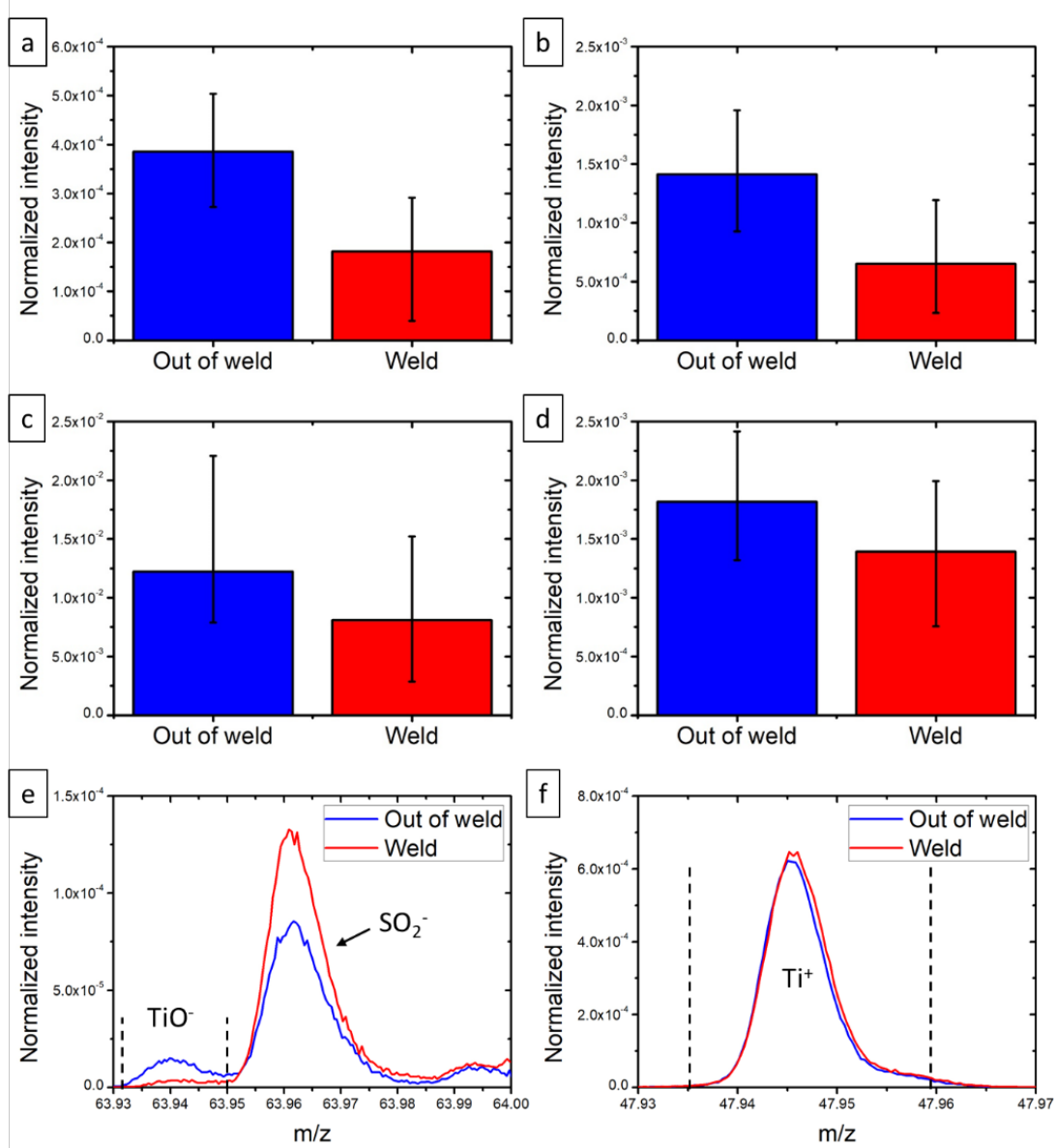


Figure 7.4: ToF-SIMS histograms of the normalized intensity out of the weld in blue and in the weld in red, of (a) TiO^- , (b) TiO_2^- , (c) Ti^+ , and (d) TiO_2H^+ . Mass spectra normalized on total intensity of the region of (e) TiO^- , and (f) Ti^+ .

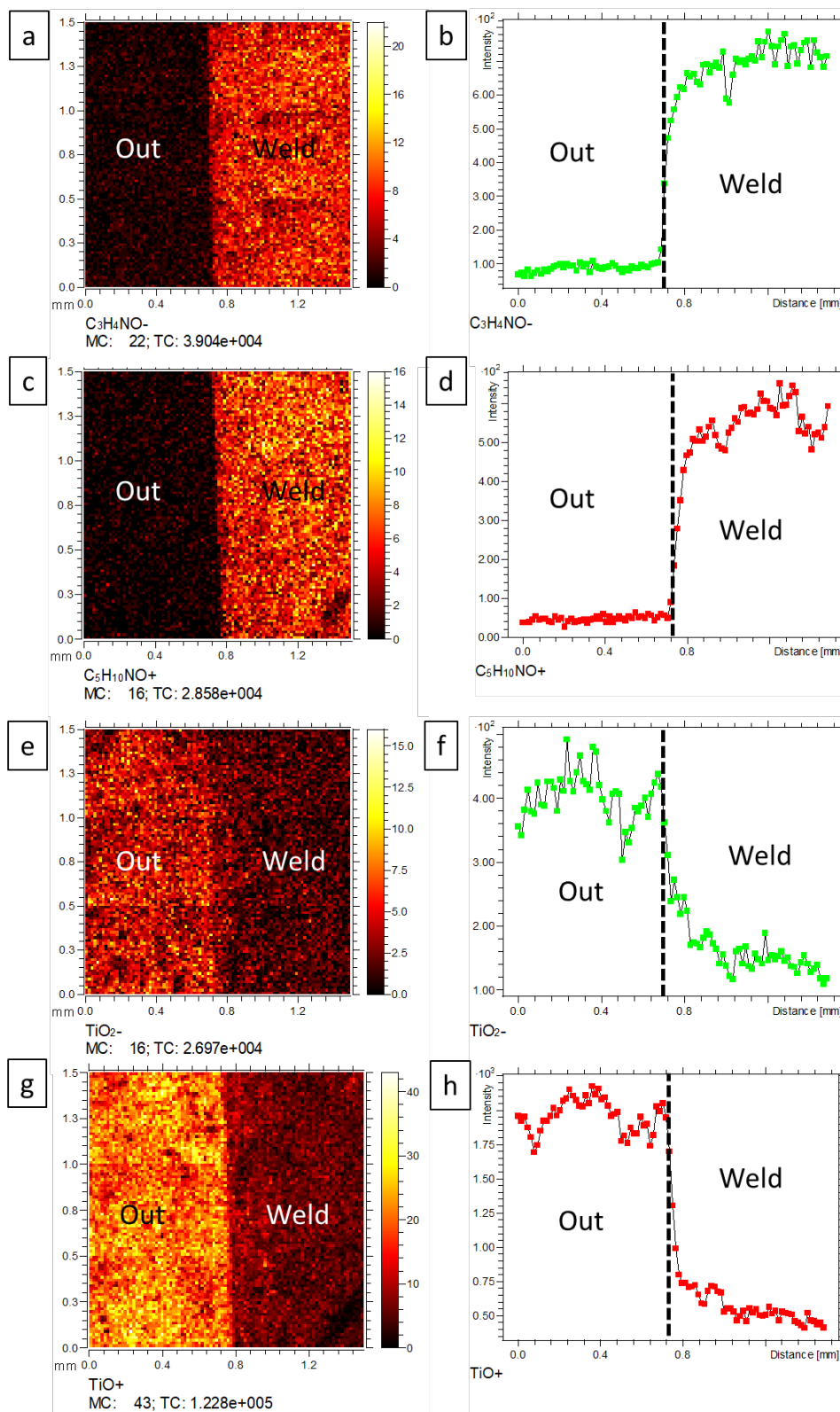


Figure 7.5: ToF-SIMS large area images and their area integration along the x axis (a) and (b) CNO^- , (c) and (d) $C_5H_{10}NO^+$, (e) and (f) TiO_2^- , and (g) and (h) TiO^+ .

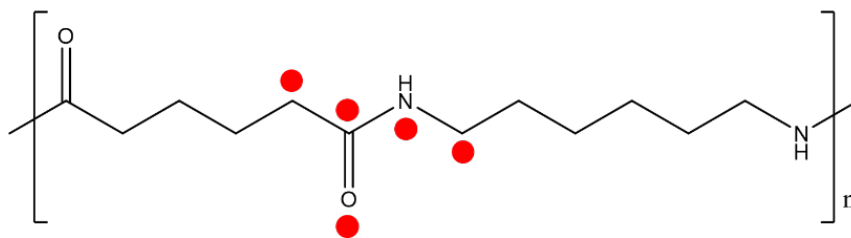


Figure 7.6: Chemical formula of nylon-6.6 showing the reactive sites by red dots of the chain.

intensities is systematically lower in the weld than out of it, while staying within the error bars. This is consistent with the observations made with XPS, where the intensity of the C-Ti bond is similar out and in the weld. This leads to the same conclusion, that there is no C-Ti bond between the polymer and the metal at the interface, and that the ions observed are due to surface contaminations.

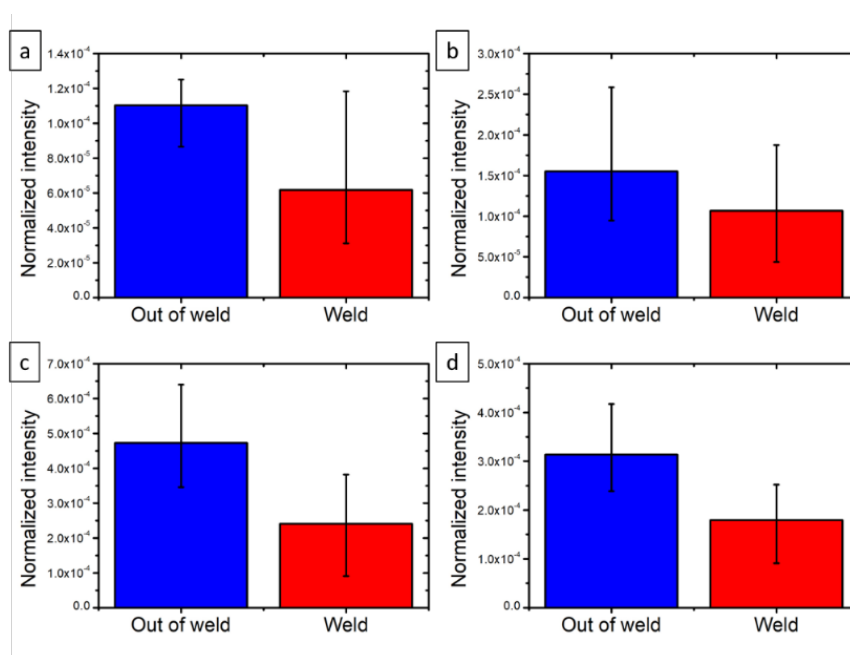


Figure 7.7: ToF-SIMS histograms of the normalized intensity out of the weld in blue and in the weld in red, of (a) C_2Ti^- , (b) CTi^+ , (c) $C_2H_2Ti^+$, and (d) $C_2H_3Ti^+$.

7.1.2.2 Reaction with the nitrogen sites

Looking at the high resolution spectra of the N 1s region out and in the weld depicted in Figure 7.2 (g) and (h), two contributions were identified. The first one was associated to organics out of the weld and to the polyamide in the weld, as stated above. A second contribution around 396.5 eV was identified and interpreted as titanium nitride bond [286,289,290]. The intensity of this peak out and in the weld is equivalent showing no major differences. This shows that the bond is due to contaminations present prior to welding and is not caused by it.

In ToF-SIMS some ions of the $C_xH_yN_zTi_w^{-/+}$ families were identified in the spectra. Strangely no ions of this family could be surely identified in the positive mode, while in the negative mode only two were identified: $CNTi^-$ and $CHNTi^-$. The intensity out and in the weld

of these ions presented in Figure 7.8 does not show much differences between both zones, even if in average the intensity of these ions is slightly lower in the weld than out of the weld. Nonetheless, the low diversity of the ions of the $C_xH_yN_zTi_w^-$ as well as their low normalized intensity (about 10^{-4}) compared to the intensity seen for the Ti-N bond in XPS leads to the conclusion that the compound presenting such bond is not of organic nature, but rather titanium nitride particles. Looking at the titanium reference a similar effect is not seen.

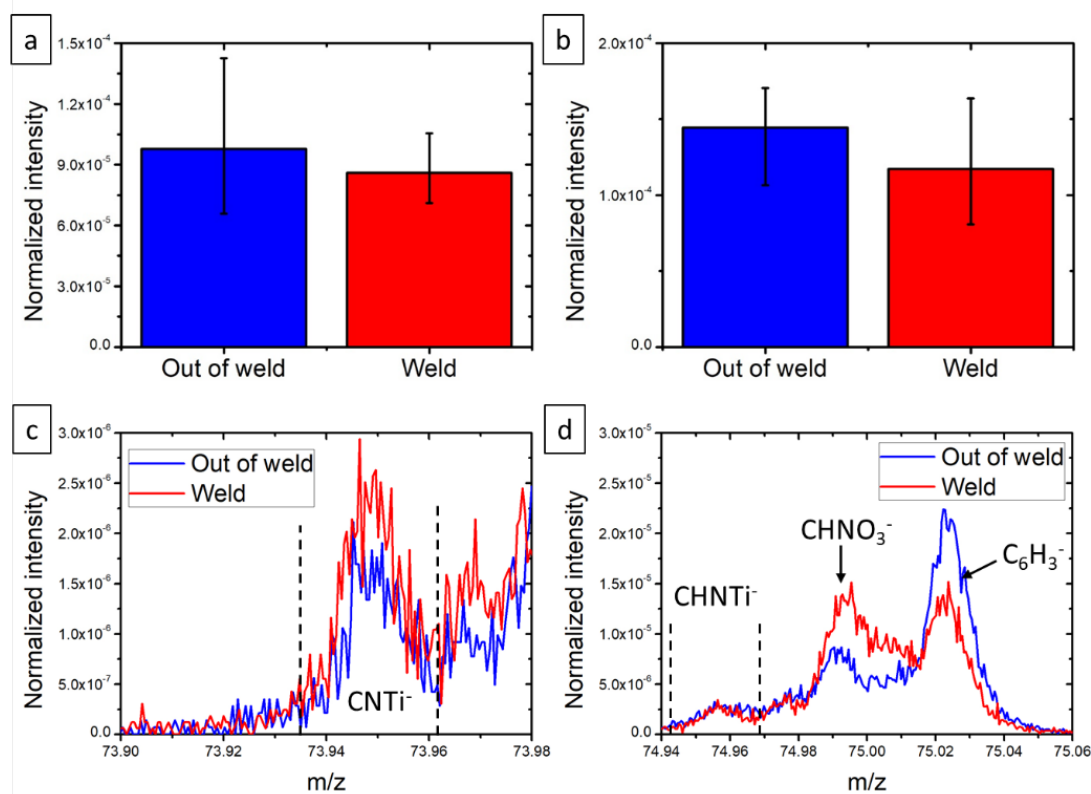


Figure 7.8: ToF-SIMS histograms of the normalized intensity out of the weld in blue and in the weld in red, of (a) $CNTi^-$, (b) $CHNTi^-$. Mass spectra normalized on total intensity of the region of (c) $CNTi^-$, and (d) $CHNTi^-$.

7.1.2.3 Reaction with the oxygen sites

As stated above the O 1s region out and in the weld (Figure 7.2 (e) and (f)) were fitted using three contributions. The first one around 529.9 eV is associated to titanium oxide [282], the second and the third, respectively around 531.2 eV and 532.4 eV are associated to Al-O, V-O bonds and oxygen from organic molecules. The intensity of the different contributions does not present significant variations. Looking at the C 1s spectra, it is noticeable that the contributions associated to the amide have higher intensities in the weld. Indeed the C-O/C-N contribution around 286.2 eV, represents only $5.5 \pm 1.3\%$ of the carbon out of the weld, while in the weld it represents $10.2 \pm 2.1\%$. The C=O bond around 288.2 eV accounts for $6.4 \pm 1.0\%$ out of the weld and $14.0 \pm 1.6\%$ in the weld. Those increases are explained by the presence of polyamide in the weld, but maybe also hide the possibility of a C-O-Ti bond. As for the aluminum to the best of our knowledge, a C-O-Ti has not been described in XPS previously. Nonetheless, it is reasonable to think that such bond should appear in the C 1s region spectrum around this energy. So with just the XPS data no conclusion can be drawn about a possible C-O-Ti bond.

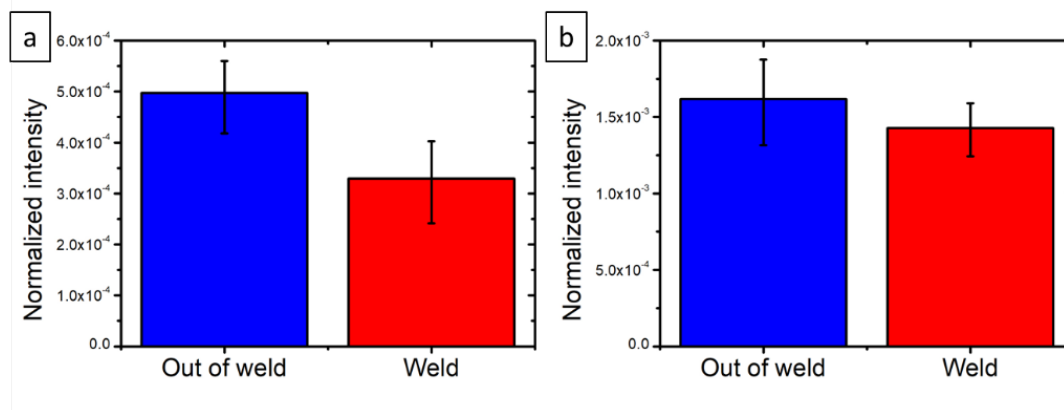


Figure 7.9: ToF-SIMS histograms of the normalized intensity out of the weld in blue and in the weld in red, of (a) C_2OTi^- , (b) $C_2HO_2Ti^-$.

In ToF-SIMS, two different families of ions, which can be related to a C-O-Ti bond, were investigated: $C_xH_yO_zTi_w^{-/+}$ and $C_xH_yN_zO_wTi_n^{-/+}$.

For the $C_xH_yO_zTi_w^{-/+}$ family three ions were identified in the negative mode: C_2OTi^- , $C_2H_2OTi^-$ and $C_2HO_2Ti^-$; while in the positive mode only two ions could be surely identified: CHO_2Ti^+ and $CH_3O_2Ti^+$. They all present the same intensity pattern like shown in Figure 7.9, in average a lower intensity in the weld than outside, but always still within the error bars. This family of ions can also be related to surface contaminations, explaining why the ions present a high intensity out of the weld, which is quite contaminated as already described above. So the ions of this family are not representative of a C-O-Ti bond.

The ions of the $C_xH_yN_zO_wTi_n^{-/+}$ family were easily identified in both modes. In the negative mode five could be surely attributed: $CNOTi^-$, $CHNOTi^-$, CH_3NOTi^- , CNO_2Ti^- and $CH_3NO_2Ti^-$. In the positive mode only two could be surely identified: $CHNOTi^+$ and CH_3NOTi^+ . It is a noticeable trend on those samples that hybrid ions are more intense in the negative mode than in the positive mode, but this trend has no explanation to the best of our knowledge. In Figure 7.10 the intensity of some ions of this family are presented as well as mass spectra zoomed on these specific ions with their range of integration. The intensity of the ions is on average systematically higher in the weld than out of the weld. But while the positive ions' intensity varies within the error bars, in the negative mode the variation always exceeds their respective error bars, so that the intensity of these ions is significantly higher in the weld than out of it. This is a strong hint for a possible C-O-Ti bond (see Figure 7.11 (a)), but these ions could also be an indication for C-N-Ti bonds or for a complexation reaction involving both the nitrogen and the oxygen atom of the amide function in the bond (see Figure 7.11 (b)). The possibility of a C-N-Ti was already discussed above in section 7.1.2.2 and this bond is not the nature of the bond between the two materials. The complexation reaction possibility aroused, since the $C_xH_yO_zTi_w^{-/+}$ are found in similar and even decreasing intensities in the weld than outside. Such a complex has a lot of steric constraints to stay stable, even though several articles state the use of a complex presenting a similar structure [334–337]. This complex has one carbon atom double bonded to two nitrogen atoms, themselves bonded to the same titanium atom. The authors state that the complex is quite fragile and that too much heat (not more than $150^\circ C$) will degrade it. Moreover, the synthesis of such compounds is always done in solution with titanium already in complex form. It seems quite unreasonable for a complex to form at an interface between a solid metal and a momentarily liquid metal. The C-O-Ti bond explanation is preferred. Indeed several examples of other materials, as well as polyamide showed to be

linked by a oxygen atom [338–340].

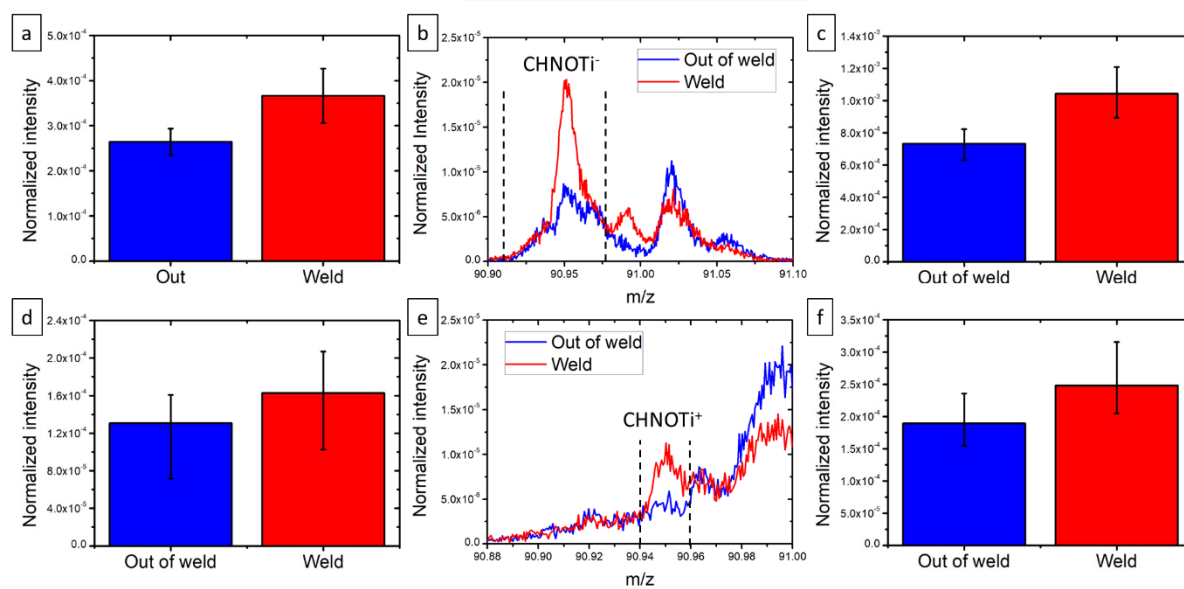


Figure 7.10: ToF-SIMS histograms of the normalized intensity out of the weld in blue and in the weld in red, of (a) CHNOTi^- , (c) CHNO_2Ti^- , (d) CHNOTi^+ , and (f) CH_3NOTi^+ , and the mass spectra zoomed on (b) CHNOTi^- and (e) CHNOTi^+ .

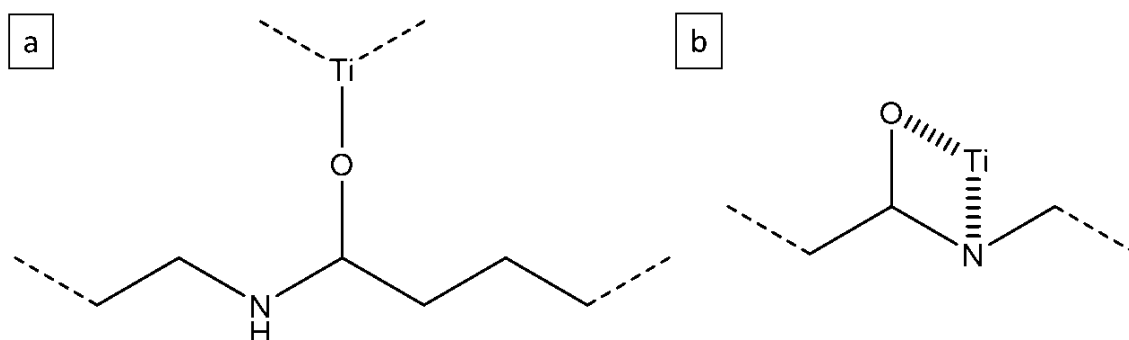


Figure 7.11: Representation of (a) a C-O-Ti bond and (b) the complexation bonding involving both the oxygen and the nitrogen of the amide function.

7.1.3 Discussion about PCA

7.1.3.1 PCA on the hand-selected peak list

The hand-selected peak list was established using some hypotheses based on the XPS measurements: (1) select peaks related to the polymer, (2) select peaks related to the titanium surface, (3) select some contaminations, and (4) search for peaks related to hybrid ions. This peak list was then used for PCA. The scores of the two first principal components in both polarities are presented in Figure 7.12. The two zones (out of the weld and the weld) are well separated with PC1 in both polarities. PC2 does not show any further differences between both zones for both polarities, which indicates that PC1 contains all the differences between the two zones in both polarities. Plotting PC1 versus PC2 emphasizes that even more. To understand the

differences between the zones, only PC1 is needed, and therefore only the loadings of PC1 will be studied in both polarities, as depicted in Figure 7.13. In both polarities the positive loadings are related to masses presenting higher intensities in the weld than out of it, while the negative loadings are related masses presenting lower intensities in the weld than out of it. Looking at the interpretation of the masses presenting the highest loadings in both modes, similar patterns appear. For the positive loadings, the ions are related to the polymer. In the negative mode, mass 26 is CN^- , mass 40 is $\text{C}_2\text{H}_2\text{N}^-$, mass 42 CNO^- or mass 70 is $\text{C}_3\text{H}_4\text{NO}^-$. In the positive mode, mass 30 is CH_4N^+ , mass 44 is CH_2NO^+ , mass 55 is $\text{C}_3\text{H}_3\text{O}^+$ and mass 72 is $\text{C}_3\text{H}_6\text{NO}^+$. For the negative loadings, the masses with high loadings are related to contaminations and the metal. In the negative mode, mass 19 is F^- , mass 25 is C_2H^- , mass 35 is Cl^- , and mass 99 is VO_3^- . In the positive mode, the mass 23 is Na^+ , mass 39 is K^+ , mass 40 Ca^+ , mass 48 is Ti^+ and mass TiO^+ . This is in good agreement with the direct analysis made above. A direct analysis was then preferred for simplicity.

7.1.3.2 PCA on the automatic generated peak list

At last an automatic generated peak list was obtained using the automatic peak selection tool from the SurfaceLab software. The scores obtained are shown in Figure 7.14 for both polarities. Their behavior is similar to the scores obtained for the hand-selected peak list. Indeed, PC1 in both polarities discriminates clearly the two zones, while PC2 does not. So all the differences of both zones are contained in PC1 in both polarities. Because of that only the loadings of PC1 need to be studied. They are represented in Figure 7.15. In both polarities the highest positive loadings have higher intensities in the weld than out of it, and these ions are related to polyamide-6.6. For instance in the negative mode, mass 26 in CN^- , mass 40 is $\text{C}_2\text{H}_2\text{N}^-$, mass 42 is CNO^- and mass 83 is $\text{C}_5\text{H}_7\text{O}^-$. In the positive mode for instance mass 30 is CH_4N^+ , mass 44 is CH_2NO^+ , mass 55 is $\text{C}_3\text{H}_3\text{O}^+$, or mass 114 is $\text{C}_6\text{H}_{12}\text{NO}^+$. The highest negative loadings in both polarities have lower intensities in the weld than out of it, and are also related to contaminations and the metal. For instance, in the negative mode, the mass 16 is O^- , mass 17 is OH^- , mass 19 is F^- , or mass 77 is SiOH_3^- , or mass 99 is $\text{CHOC}_2\text{Cl}_2^-$. While in the positive mode, mass 23 is Na^+ , mass 39 is K^+ , mass 40 is Ca^+ , mass 48 is Ti^+ , mass 64 is TiO^+ , or mass 91 is C_7H_7^+ . These observations are similar to the hand-selected peak list, which gives strength to the hypotheses used to build the peak list. They are also similar to the direct analysis (without PCA). A direct analysis was preferred, because the XPS data already gave some information to analyze the ToF-SIMS measurements (polymer present in the weld and not outside) on one hand. On the other hand the hybrid ions are quite low intensity peaks, which explains why they are not in the highest loadings, and would require an analysis of the data as the one done to build the hand-selected peak. To study the chemical bonding and reactivity, this would have been done anyway. Nonetheless, the role and impact of the contaminations might have been minimized in the hand-selection.

7.1.4 Conclusions on the welded samples

Since the fracture happens with a mixed failure mode, adhesive and cohesive in the polymer, no dissolution step was needed to analyze the interface. Indeed, when the dissolution was tried, no traces of the welding could be seen in XPS and ToF-SIMS. The samples were then analyzed by comparing the out of weld with the weld, and specifically the zone where the adhesive failure happened. Both XPS and ToF-SIMS showed that there is polymer in the weld covering the metal surface. Furthermore, the images showed that the separation between the weld and the out of weld is sharp and no transition zone was observed.

The chemistry of the polymer bond was investigated, by studying several chemical reactions

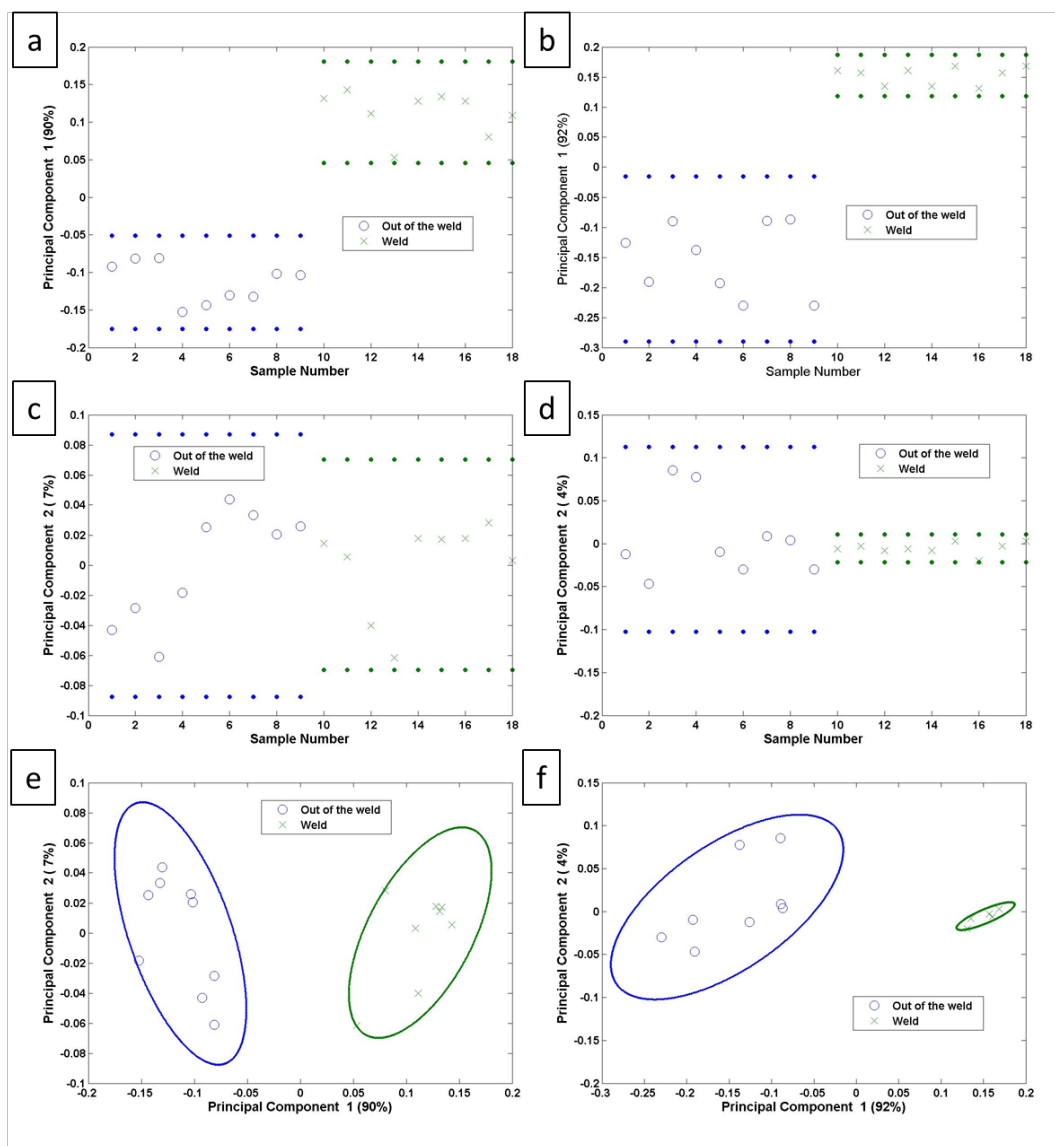


Figure 7.12: Scores of the hand-selected peak list, PC1 in (a) the negative mode, (b) the positive mode, PC2 in (c) the negative mode, (d) the positive mode, and PC1 versus PC2 in (e) the negative mode and (f) the positive mode.

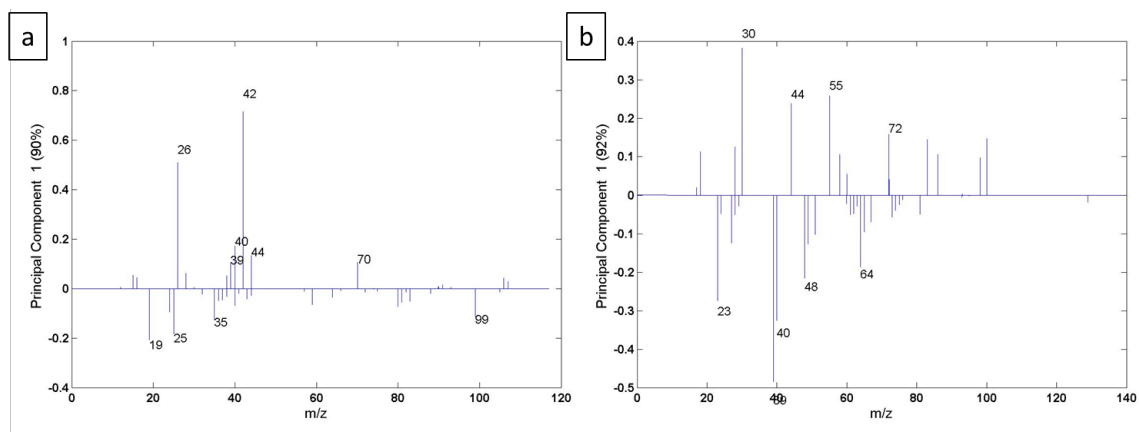


Figure 7.13: Loadings of the PC1 in (a) the negative mode, and (b) the positive mode.

options depending on the reactive sites. A titanium carbide bond is observed out and in the weld, but proved not to be the bond between the polymer and the titanium surface, as the intensity of this bond in XPS and the related ions in ToF-SIMS are identical. The same observation was made for a reaction with nitrogen. Moreover, it was found out that the titanium nitride bond is not of an organic origin. At last the reaction with the oxygen was investigated and the XPS data does not allow to conclude that there is such a bond, but does not exclude it either. ToF-SIMS data is clearly showing that the intensity of the ions presenting the amide function linked to titanium are more intense in the weld than outside of it, which leads us to the conclusion that there is a C-O-Ti bond, which is in good agreement with the literature found on the question.

Using PCA on both the hand-selected peak list and the automatic generated peak list allowed to show that they display similar results and are in good agreement with the direct analysis. Indeed, the ions playing the greatest role to discriminate the zones are ions related to the polymer on one side, and ions related to contaminations and the metal on the other side. The hybrid ions do not display high loadings. This rapid PCA analysis supports the conclusions made by direct analysis. The PCA on the automatic generated peak list supports the hypotheses made to build the hand-selected peak list. It also shows that a PCA analysis was not mandatory to analyze correctly the data.

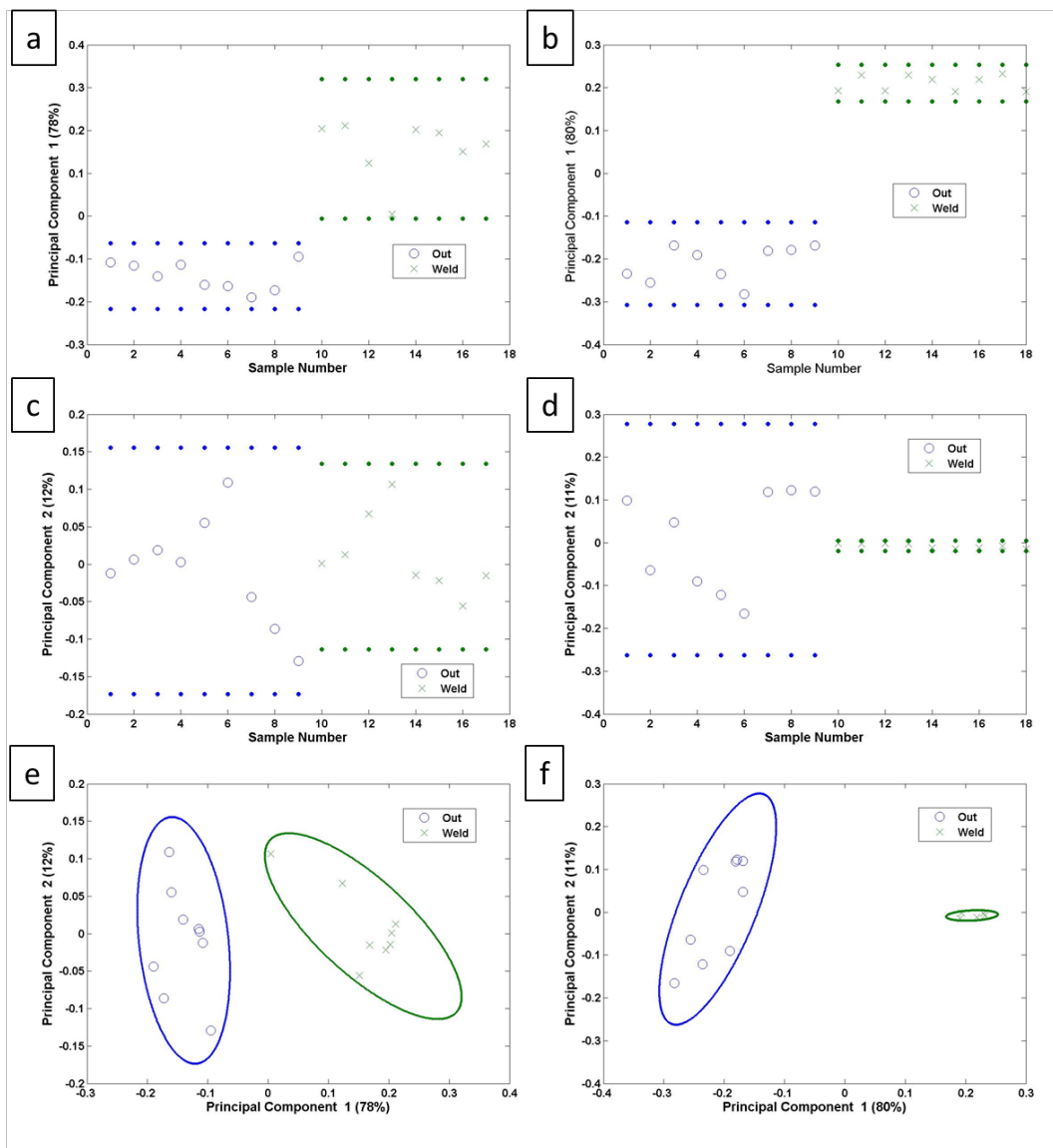


Figure 7.14: Scores of the hand-selected peak list, PC1 in (a) the negative mode, (b) the positive mode, PC2 in (c) the negative mode, (d) the positive mode, and PC1 versus PC2 in (e) the negative mode and (f) the positive mode.

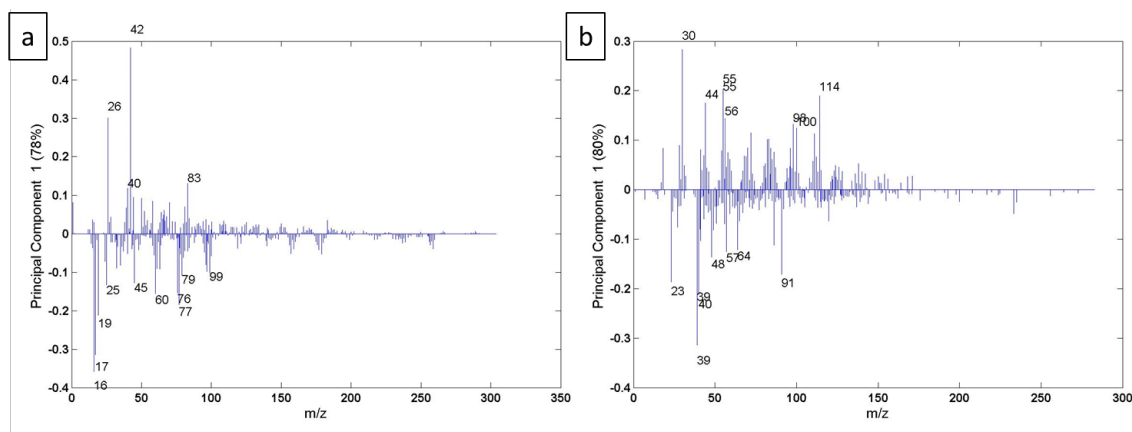


Figure 7.15: Loadings of the PC1 in (a) the negative mode, and (b) the positive mode.

7.2 Spin-coated samples

For the welded samples, a dissolution step was detrimental for the interface analysis, as all the polymer was washed away. Since there were adhesive failure places, the analysis were performed on these spots directly after the breaking. On the spin-coated samples this is not possible and a dissolution step is mandatory to analyze the interface. Therefore the dissolution step has been shortened to the minimum (about 30s, the time to wash the traces of polymer) for the titanium spin-coated samples, compared to the aluminum spin-coated samples.

7.2.1 XPS results

From the elemental composition calculated from the survey spectra, presented in Table 7.3, it is visible that the oxygen and the titanium percentages are significantly lower in the weld than on the reference, while out of the weld the percentages are intermediate. At the same time the carbon percentage increases on average with a high standard deviation. The nitrogen percentage increases slightly on the out of weld and even more in the weld compared to the reference. In the reference the nitrogen percentage is already high (4.8 ± 0.7 %) indicating that polyamide-6.6 is still present on the surface after the dissolution step. Nonetheless, the increase of this percentage clearly shows that the welding –the heating– has an effect on the polyamide-6.6 leading to a higher binding to the titanium. The aluminum percentage is equivalent for all the samples. The vanadium percentage varies a little bit but since the percentages are so low, it is insignificant. The zinc percentage is also equivalent on all the samples in very low quantity. It is clearly a contamination, from an unknown source.

Table 7.3: XPS elemental composition from the survey spectra for the reference, out of the weld and in the weld.

Samples	%O	%Ti	%C	%N	%Al	%V	%Zn
Ref	42.2 (± 2.9)	19.2 (± 3.0)	30.9 (± 3.5)	4.8 (± 0.7)	2.1 (± 0.5)	0.2 (± 0.0)	0.6 (± 0.1)
Out of weld	38.7 (± 3.6)	15.3 (± 1.6)	37.3 (± 4.4)	5.4 (± 1.0)	2.2 (± 0.3)	0.5 (± 0.0)	0.5 (± 0.0)
Weld	36.0 (± 1.0)	13.4 (± 1.1)	40.9 (± 2.4)	7.0 (± 0.4)	2.0 (± 0.3)	0.2 (± 0.0)	0.5 (± 0.1)

The high resolution spectra of the C 1s region of the different samples are depicted in Figure 7.16 (a), (b) and (c). Four contributions were used to fit the data. One contribution at 284.8 eV is associated to C-C/C-H bonds [282,286,296] and was used for calibration. A second contribution around 285.9 eV is associated to C-O/C-N bonds [282,286,296]. The third contribution is around 287.8 eV and was interpreted as a C=O bond [282,286,296]. The fourth contribution is associated to O-C=O bond around 289.0 eV [282,286,296]. The different contribution are consistent with the presence of polyamide-6.6, even if some contaminations are also present characterized by the O-C=O peak around 289.0 eV. By comparing the intensities of the different contributions no significant differences were observed. Since there is no titanium carbide contribution, the polymer does not react with the metal surface through its carbon reactive sites.

To fit the high resolution spectra of the Ti 2p region of the different spectra in Figure 7.16 (d), (e) and (f), nine peak were used. One peak is related to titanium surface plasmons around 471.1 eV [286,289,290]. The left eight peak are related to only four different contributions because of the spin-orbit splitting of Ti 2p_{3/2} and Ti 2p_{1/2}. The energies will be given in this order first for the Ti 2p_{3/2} and then for the Ti 2p_{1/2}. The first contribution is metallic titanium Ti (0) around 453.3 eV and 459.7 eV [286,289,290]. The second contribution is for oxidized titanium Ti (II) around 454.6 eV and 460.9 eV [286,289,290]. The third contribution is around 457.0 eV and 462.7 eV and corresponds to oxidized titanium Ti (III) [286,289,290]. The fourth contribution is related to oxidized titanium Ti (IV) around 458.5 eV and 464.3 eV [286,289,290]. The comparison of the intensities of the different contributions between the samples showed no significant differences.

The high resolution spectra of the O 1s region was fitted using three contributions. The first one around 530.0 eV is related to titanium oxide bonds [282,286,296]. The second and the third one around 531.2 eV and 532.2 eV respectively, are related to Al-O, V-O and organic bonds [282,286,296]. The intensities were not significantly different from one sample to another. The fitting does not prove that a C-O-Ti bond exists, but it does not exclude it either, and the C 1s spectra would also be consistent with it without proving its existence either.

The high resolution spectra of the N 1s region were not fitted in the same manner in the reference and the out of weld than in the weld. Indeed in the reference and out of weld only one contribution was needed to fit correctly the peak around 399.7 eV, which corresponds to an amide bond characteristic for polyamide-6.6. This is in good agreement with the previous observations, that polymer is present on all the samples even after the dissolution step. In the weld the same amide bond contribution is observed around 399.6 eV, which is a bit lower than on the other samples, but still in good agreement with the literature. A second peak had to be added to fit correctly the spectra around 398.2 eV. By comparing this energy to the existing tables, the only possibility is an imine bond. As said previously, the heating due to the welding does have an impact on the interaction between the polymer and the metal surface. This is clearly visible on the elemental composition, and is now confirmed with the apparition of this peak only in the weld. By mimicry with the aluminum (see Chapter 6), where it was shown that the reaction forms an imine, one can suppose that the same reaction happens here with the titanium (see Figure 7.17). At the same time, no titanium nitride peak was identified in the N 1s region, leaving the only chemical reaction possible on the oxygen site.

7.2.2 Principal component analysis on the ToF-SIMS data

The data obtained from the measurement and its analysis in ToF-SIMS proved to be difficult to analyze and a pattern fitting an explanation was hard to find, that's why a principal component analysis was performed. Peak lists containing characteristic ions from the polymer, the metal, some contaminations and the hybrid ions present in the spectra were done in both modes. A second set of peak list was obtained by using the automatic peak selection tool in

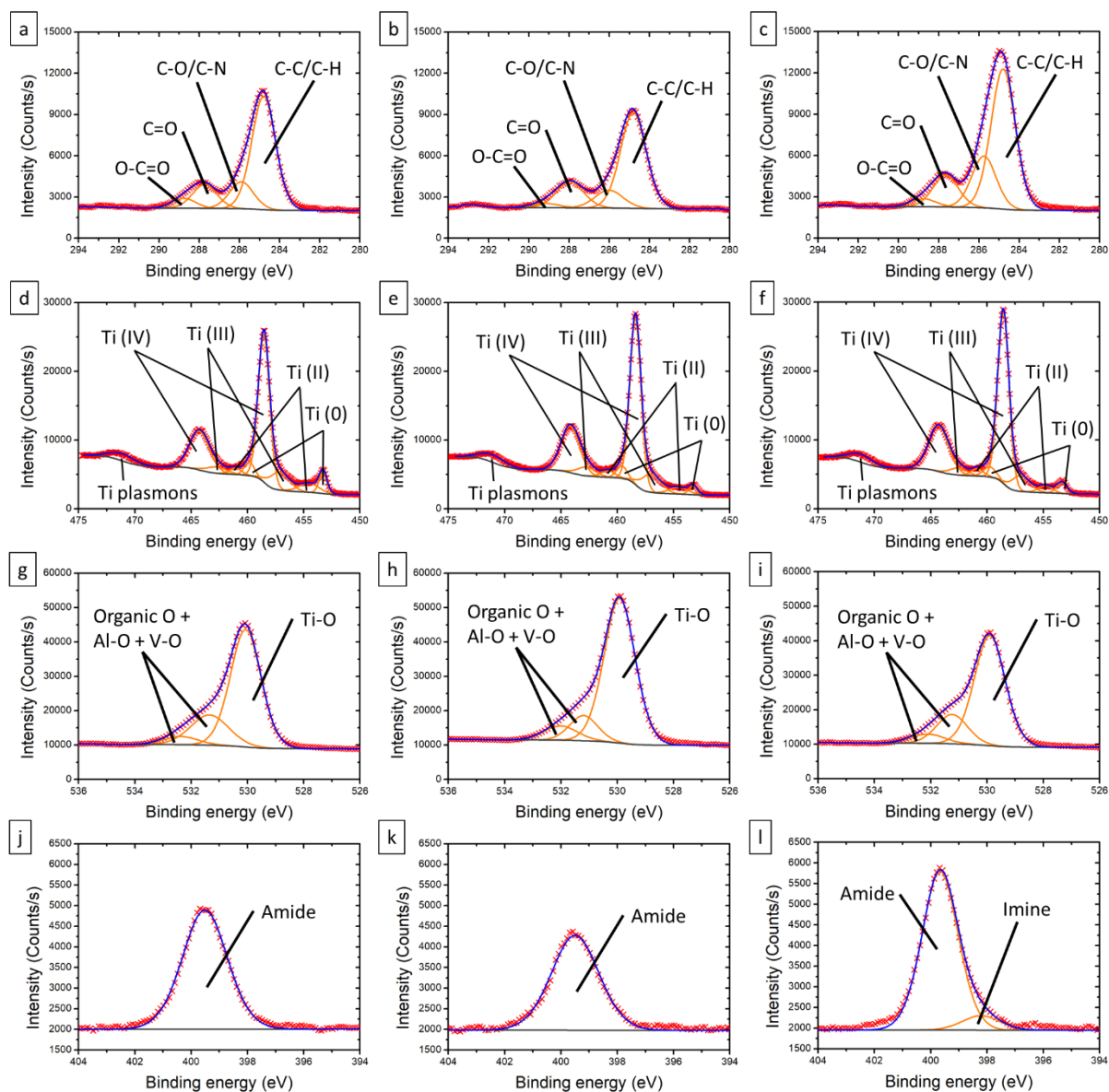


Figure 7.16: XPS high resolution spectra for the reference, out of the weld and in the weld in (a), (b) and (c) the C 1s region, in (d), (e) and (f) the Ti 2p region, in (g), (h) and (i) the O 1s region, and in (j), (k) and (l) the N 1s region.

SurfaceLab 7.0, using the same conditions as for the aluminum samples (300 m/s mass range and an intensity higher than 100 counts). The PCA on the hand selected peak list will be presented first, by looking at the negative mode and then the positive mode. In a second time the PCAs on the automatically generated peak lists in both modes will be discussed.

To use the principal component analysis (PCA), the data of both negative and positive mode was first normalized on the total intensity, and the PCA was run using a square-root mean centering.

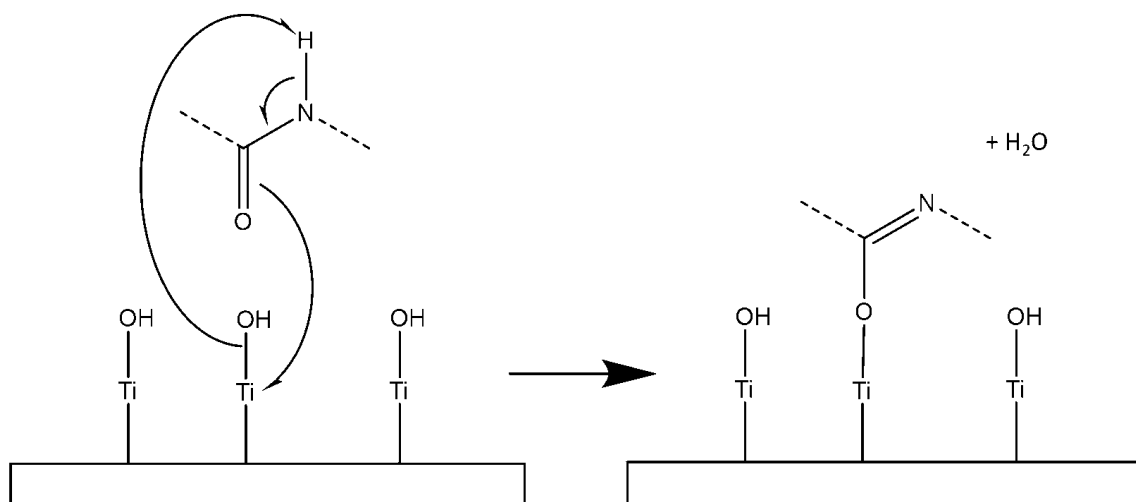


Figure 7.17: Scheme of a possible reaction mechanism between the polyamide-6.6 and the titanium surface.

7.2.2.1 In the negative mode

The scores obtained for the two first principal component on the data from the negative mode are depicted in Figure 7.18, as well as the plot of both principal components together. Looking at the scores of both PC separately (Figure 7.18 (a) and (b)), the samples are not separated at all. This shows that the differences between the samples are quite low, and also justify the use of the PCA in this case. Nonetheless, by plotting the two principal components together (Figure 7.18 (c)), it is visible that the reference and the weld are clearly separated as the blue and the red lines do not cross-over. The lines correspond to the confidence limit of the scores. The out of weld presents at the same time similarities with the reference but also with the weld, because of the crossing-over of the green line. This explains the difficulty to differentiate the different samples on a direct approach. Looking more into details of the scores of the out of weld, three points corresponding to three samples are also in the region of the weld. These three points all come from the same sample, as for each sample three measurement points were taken. The data becomes much easier to understand and to explain by removing these three samples, which is why from now on the data presented will be without these three problematic measurement point.

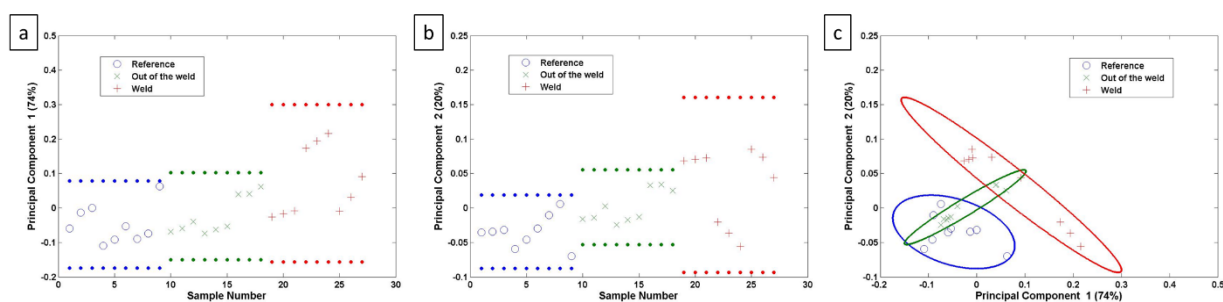


Figure 7.18: (a) scores of principal component 1, (b) scores of principal component 2, (c) principal component 1 versus principal component 2.

The removal of the three problematic points out of the weld allows to calculate new principal

components. These new scores are presented in Figure 7.19. Here also the scores alone of the two first principal components do not differentiate the samples, but plotting them together shows clearly that the weld is completely separated from the reference and the out of weld, which is now completely included in the reference. This emphasizes the impact of the welding and lowers the effect of the heating out of the weld. So now with just the two first principal components, the samples can be differentiated without difficulty. Moreover they explain 95% of the differences between the samples (75% for PC1 and 20% for PC2). The following principal components were not studied.

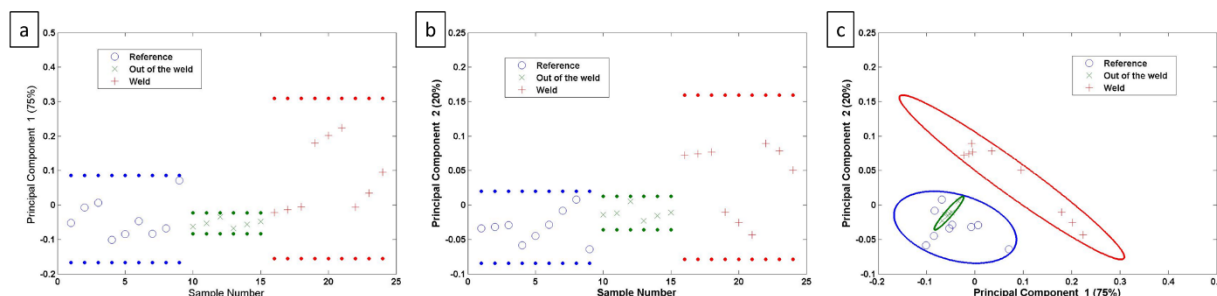


Figure 7.19: (a) scores of principal component 1, (b) scores of principal component 2, (c) principal component 1 versus principal component 2 after removing three points out of the weld.

Looking at the loadings of the two first principal components presented in Figure 7.20, a similar trend is observed in both cases (The exact values of the loadings are presented for each ion of the peak list in a table in annex). The ions related to the metal titanium surface have systematically for both principal component negative loadings. Looking at some of these ions' intensities in Figure 7.21 it is observable that they present lower intensities in the weld at least on average compared to the reference and the out of weld. The polymer related to the polyamide-6.6 are divided into two categories. The first category present systematically positive loadings (CN^- , C_2N^- , C_3H_2^- , C_2HN^- , $\text{C}_2\text{H}_2\text{N}^-$, C_3N^-). The second category is composed of the ions which present for one principal component a negative loading and for the other principal component a positive loading (NH^- , CNO^- , NH_2^- , C_2^- , C_2H^- , C_3^- , C_3H^- , C_3H_3^- , C_2HO^- , C_4H^- , C_6^- , C_2H_3^- , $\text{C}_5\text{H}_4\text{NO}^-$). Looking at some of their intensities of both categories of ions in Figure 7.22, they split also into two categories following the same separation as on the loadings. In the first case, they present systematically significantly higher intensities in the weld than out of the weld and in the reference. In the second case, they present equivalent intensities where the standard deviation overlay for the three samples. In the second category, they have generally an alkane structure or present an oxygen atom. This is in good agreement with the observations made in XPS, where the nitrogen percentage in the weld is significantly higher in the weld than on the reference and the out of weld. Moreover it also complies with the observation of the presence of polymer on all the three samples in XPS. To sum up, the negative loadings of both principal components are associated to ions presenting lower or equivalent intensities in the weld than out of the weld and in the reference, while in the positive loadings the ions present higher intensities in the weld than out of it and the reference. At the same time the ions presenting negative loadings are ions of the metal. This leads to the conclusion that the negative loadings are associated and characterize the reference and the out of weld, while the positive loadings characterize the weld.

For the hybrid ions, different families of hybrid ions were investigated and added into the peak list: the $\text{C}_x\text{H}_y\text{Ti}_z^-$, the $\text{C}_x\text{H}_y\text{N}_z\text{Ti}_w^-$, the $\text{C}_x\text{H}_y\text{O}_z\text{Ti}_w^-$ and $\text{C}_x\text{H}_y\text{N}_z\text{O}_w\text{Ti}_n^-$. For the $\text{C}_x\text{H}_y\text{Ti}_z^-$ family, only one ion was identified in the spectra: C_3Ti^- . This ion presents negative loadings for

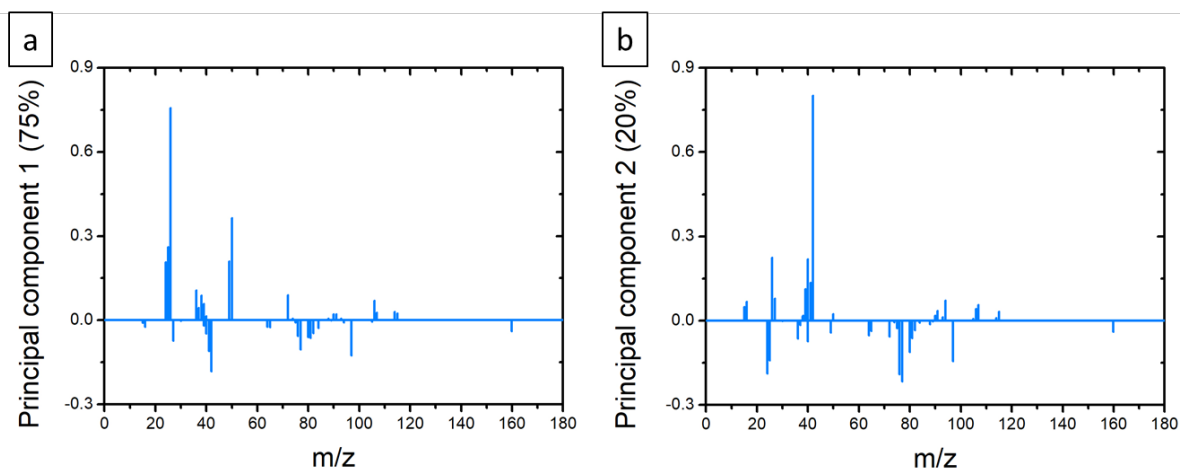


Figure 7.20: (a) loadings of the principal component 1, (b) loadings of the principal component 2.

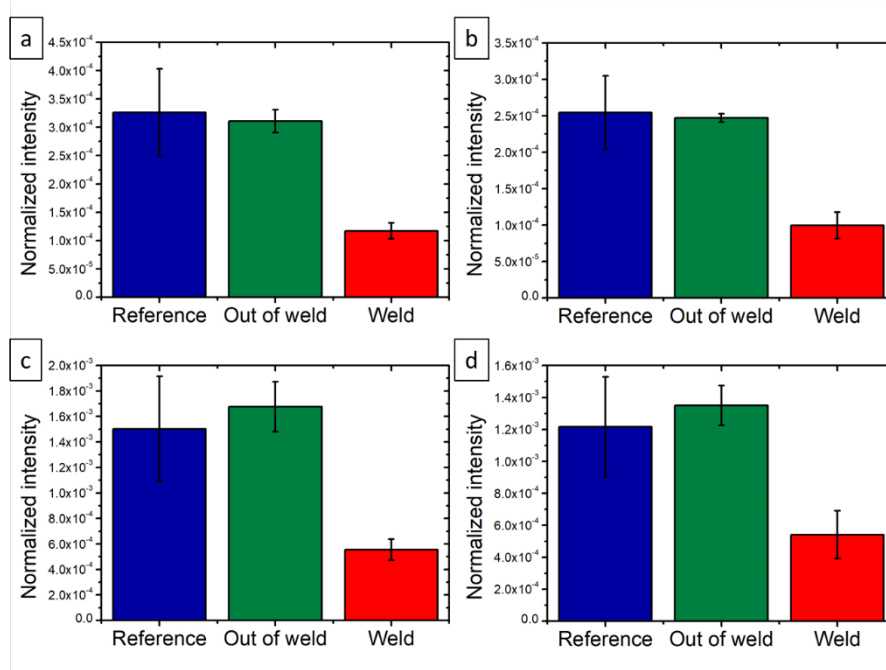


Figure 7.21: ToF-SIMS histograms of the normalized intensity in the reference, out of the weld in blue and in the weld in red, of (a) TiO^- , (b) TiOH^- , (c) TiO_2^- , and (d) TiO_2H^- .

both principal component and has higher intensity in the reference and out of the weld, than in the weld (see Figure 7.23 (a)). This family of ion is associated to a carbide bond between both materials, but the intensity is lower in the weld, and in XPS no carbide bond is observed, leading to the conclusion that the polymer does not bond itself using the carbon reactive sites (see Figure 7.6). The $\text{C}_x\text{H}_y\text{N}_z\text{Ti}_w^-$ are linked with a nitride bond between both materials. Several ions of this family were identified: CNTi^- , CHNTi^- , CH_2NTi^- , and CH_3NTi^- . CNTi^- is the only ion presenting a positive loading in PC1 and a negative loading in PC2. Looking at its intensity in Figure 7.23 (b), it is equivalent for all samples explaining the alternate loadings, as for some of the polymer ions. The other ions of this family present negative loadings in both PC1 and

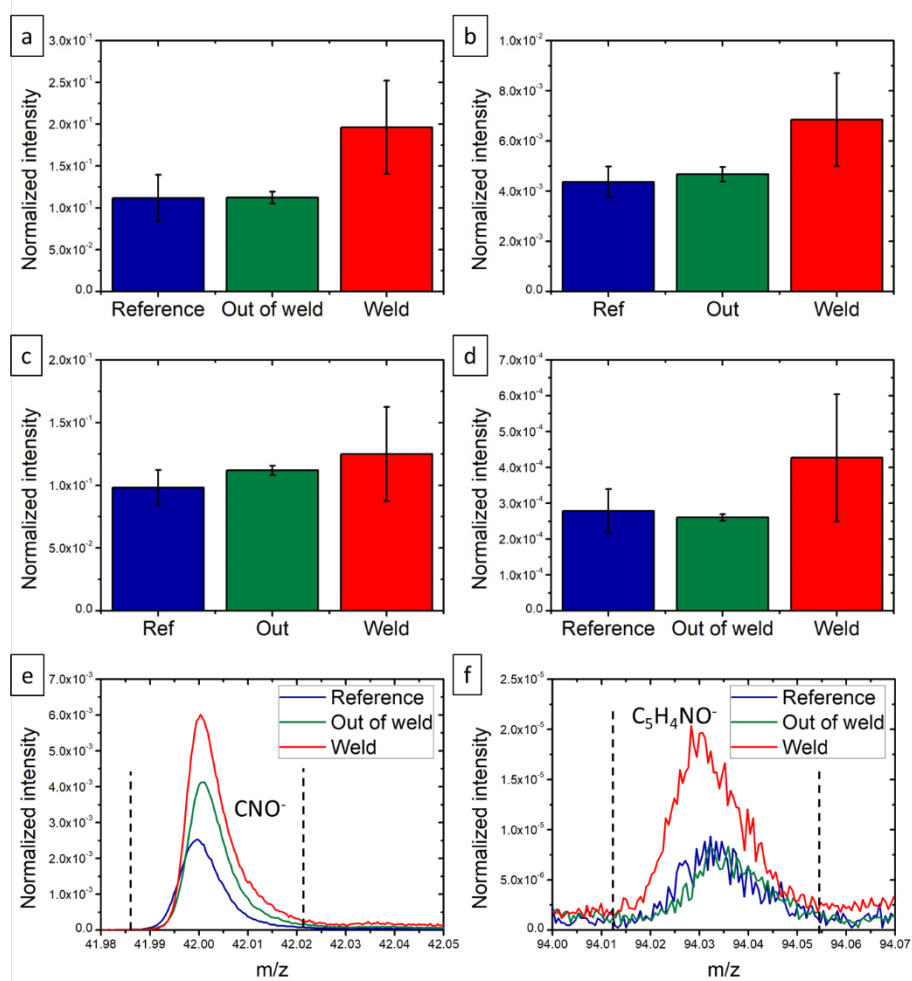


Figure 7.22: ToF-SIMS histograms of the normalized intensity in the reference, out of the weld in blue and in the weld in red, of (a) CN^- , (b) $\text{C}_2\text{H}_2\text{N}^-$, (c) CNO^- , and (d) $\text{C}_5\text{H}_4\text{NO}^-$. Mass spectra normalized on total intensity of the region of (e) CNO^- , and (f) $\text{C}_5\text{H}_4\text{NO}^-$.

PC2. This clearly indicates that a nitride bond can be excluded, which is consistent with the XPS data where no nitride bond has been observed. The $\text{C}_x\text{H}_y\text{O}_z\text{Ti}_w^-$ is related to an oxygen bond between the polymer and the metal, but is also easily associated to surface contaminations. Four ions of this family were surely identified in the spectra: C_2OTi^- , C_2HOTi^- , CHO_2Ti^- , and $\text{C}_2\text{HO}_2\text{Ti}^-$. Looking at their loadings, they are divided in three groups. The first group composed of C_2HOTi^- has negative loadings in PC1 and PC2, but its intensity is equivalent in all the samples. The second group composed of C_2OTi^- and $\text{C}_2\text{HO}_2\text{Ti}^-$ have a negative loading in one principal component and a positive loading in the other one. Here also they present equivalent intensities on all the samples. The third group composed of CHO_2Ti^- present positive loadings for both principal component and has an increased intensity in the weld compared to the out of weld and the reference (see Figure 7.24 (a)). This is a good hint of a C-O-Ti bond. The last family of hybrid ions, $\text{C}_x\text{H}_y\text{N}_z\text{O}_w\text{Ti}_n^-$, presents positive loadings for PC1 and PC2 for all the identified ions: CNOTi^- , CHNOTi^- , CNO_2Ti^- , CHNO_2Ti^- , C_3NOTi^- , C_3HNOTi^- . They also all have higher intensities at least on average in the weld than out of it and the reference (see Figure 7.24 (b) and (c)). This confirms the presence of a C-O-Ti bond. It might already be formed during the spin-coating process, but the heating of the welding clearly has an impact on

the intensity of these ions, explained by the presence of such a bond. Indeed the recombination makes probably a part of the intensity of these ions, but the titanium ions have significantly lower intensities in the weld than elsewhere so that recombination cannot alone explain the higher intensities of these ions in the weld.

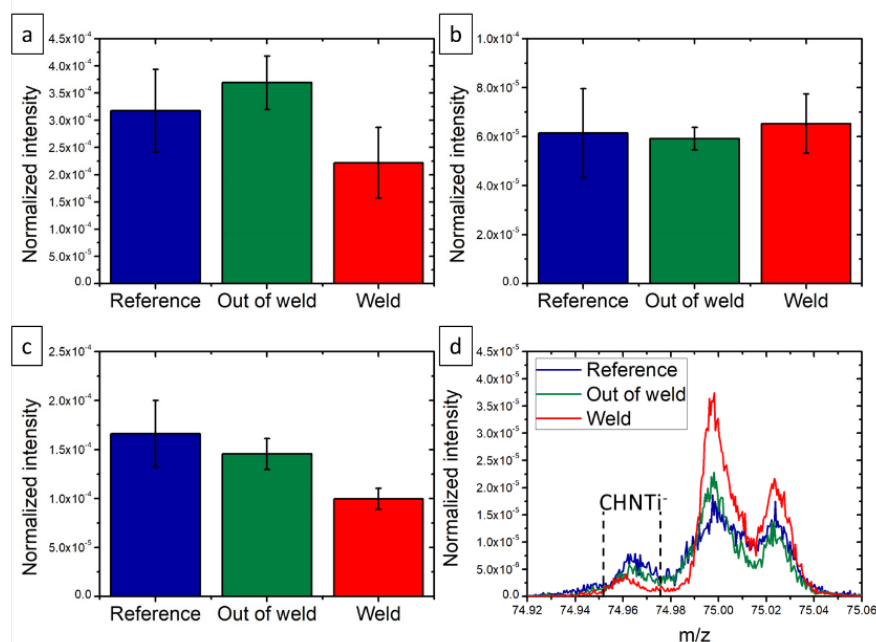


Figure 7.23: ToF-SIMS histograms of the normalized intensity in the reference, out of the weld in blue and in the weld in red, of (a) C_3Ti^- , (b) $CNTi^-$, (c) $CHNTi^-$, and (d) the spectra overlay zoomed on $CHNTi^-$.

For the chemical reaction mechanism, as said above the higher intensities of the polymer ions' presenting a nitrogen atom are consistent with the XPS data and the formation of an imine in the weld, and is consistent with the proposed mechanism (see Figure 7.17). Nonetheless, the intensities of the metallic ions are systematically lower in the weld than elsewhere, which does not allow to draw any conclusion on the reaction of the metal with the surface titanium hydroxide, as proposed earlier.

7.2.2.2 In the positive mode

First a PCA with all the samples was performed, where only the two first principal components are needed to understand the majority of the data set (85%) and differentiate the samples. The scores of PC1 and PC2 and plotted together are presented in Figure 7.25. The principal components separately do not differentiate the samples, which is why a principal component analysis is needed. The scores plotted together in Figure 7.25 (c) shows that the PC1 and PC2 completely differentiate the reference and the weld. The out of weld has an intermediate behavior, as the confidence limit (the green line) crosses over the confidence limit of both the reference and the weld. This shows that the heating due to the welding does also affect the non-welded zone. This is in good agreement with the results observed in the PCA in the negative mode. Looking more into details the scores of the out of weld, three points are clearly separated from the six others, and are close to the points of the weld. It appears that they all are from the same sample, but also from the same sample which was removed in the PCA of the negative mode. So in the same manner as in the negative mode, these points were removed. A new PCA was

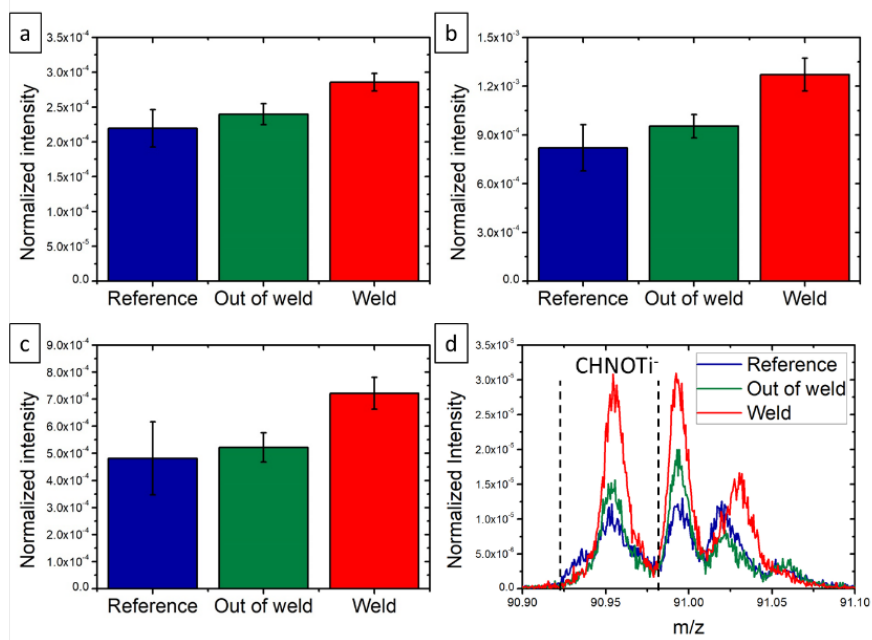


Figure 7.24: ToF-SIMS histograms of the normalized intensity in the reference, out of the weld in blue and in the weld in red, of (a) CHO_2Ti^- , (b) C_3HNOTi^- , (c) CHNOTi^- , and (d) the spectra overlay zoomed on CHNOTi^- .

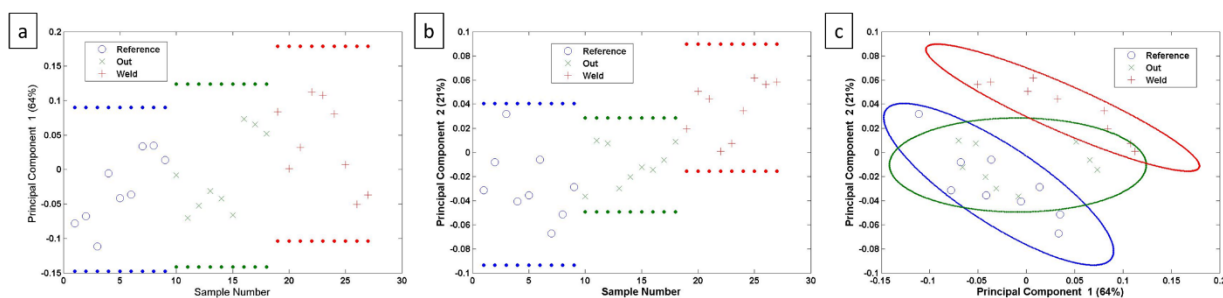


Figure 7.25: (a) scores of principal component 1, (b) scores of principal component 2, (c) principal component 1 versus principal component 2.

performed and the obtained scores are presented in Figure 7.26. Here also only the two first principal components were needed. When plotting the scores of both principal components, the separation between the reference and the weld is maintained, but now the out of weld is clearly separated from the weld and completely included in the reference. This is similar to the result obtained in the negative mode.

To better understand the root causes of this differentiation, the loadings depicted in Figure 7.27 are investigated. The values of the loadings of both principal components of each ion in the peak list can be found in annex. Following the pattern of the loadings of the different ions, four categories can be made.

The first one present negative loadings for PC1 and PC2. In this category only one ion is present Al^+ and presents lower intensities in the weld than out of the weld and in the reference.

The second category is the exact opposite by presenting only positive loadings for both principal components. They present higher intensities in the weld compared to the reference

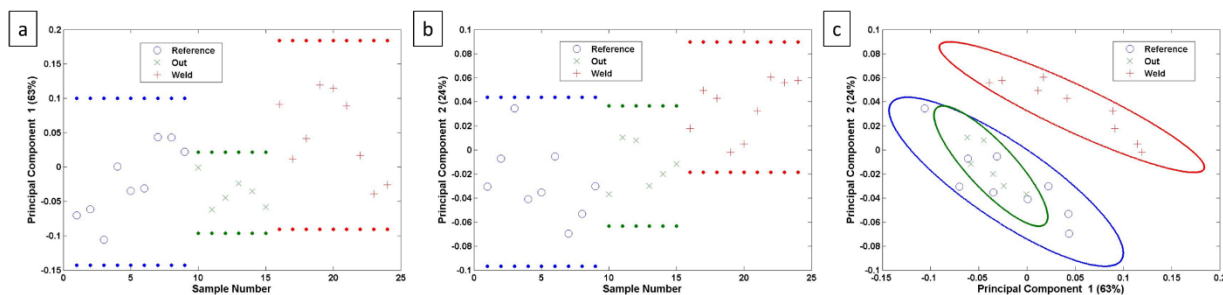


Figure 7.26: (a) scores of principal component 1, (b) scores of principal component 2, (c) principal component 1 versus principal component 2 after removing three points out of the weld.

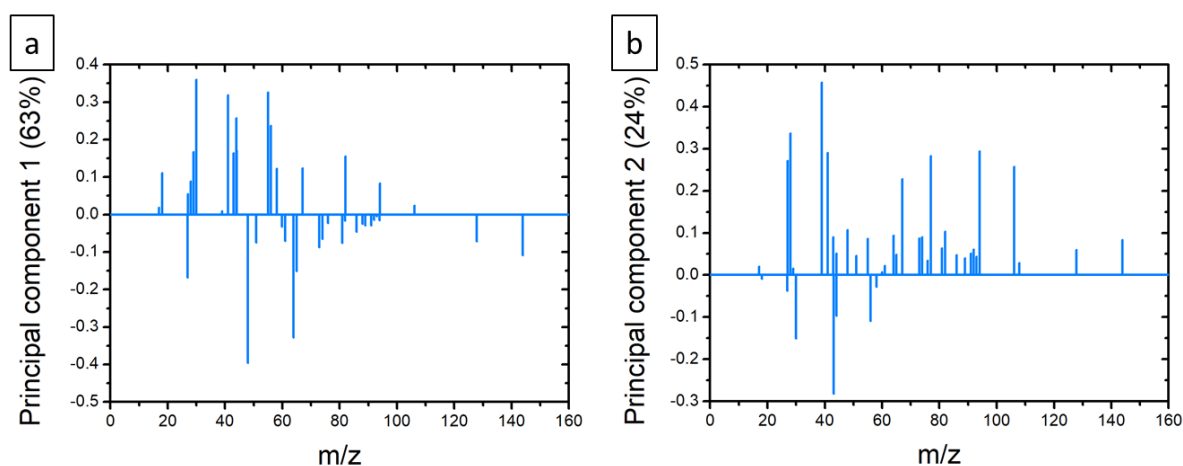


Figure 7.27: (a) loadings of the principal component 1, (b) loadings of the principal component 2.

and the out of weld. These ions are characteristic ions of polyamide-6.6 (NH_3^+ , C_2H_3^+ , CH_2N^+ , C_2H_5^+ , C_3H_3^+ , C_3H_5^+ , $\text{C}_2\text{H}_3\text{O}^+$, CH_2NO^+ , $\text{C}_3\text{H}_3\text{O}^+$, C_5H_7^+ , C_5HO^+ , $\text{C}_5\text{H}_8\text{N}^+$, $\text{C}_6\text{H}_8\text{N}^+$, and $\text{C}_7\text{H}_8\text{N}^+$). Some of their intensities are depicted in Figure 7.28. This confirms that polyamide-6.6 is present in higher amounts in the weld than out of it and the reference, which is in good agreement with the XPS data and negative mode SIMS data. There is also one hybrid ion in this category: $\text{CH}_2\text{NO}_2\text{Ti}^+$. The intensity of this ion (see Figure 7.31 (b)) is on average higher in the weld, but the error bars of the weld and the reference are overlapping. It appears that the positive loadings are linked to the ions presenting higher intensities in the weld, so more generally to the weld itself.

The third category present positive loadings in PC1 and negative loadings in PC2. They generally have a higher intensity in average in the weld than elsewhere, but their standard deviation overlap. These ions are also associated to polyamide-6.6 (NH_4^+ , CH_4N^+ , C_3H_7^+ , $\text{C}_2\text{H}_6\text{N}^+$, $\text{C}_3\text{H}_6\text{N}^+$, and $\text{C}_2\text{H}_4\text{NO}^+$). They also confirm that polyamide-6.6 is more present in the weld, but also show that the quantity of polymer in the reference and the out of weld is not negligible due to the spin-coating preparation method.

The fourth and last category presents negative loadings in PC1 and positive in PC2. Their intensity pattern is more variable and no trend was observed. This category is composed of metallic ions and all the hybrid ions. Let's first have a look at the titanium ions. The intensities of these ions is similar for all of them: a lower average intensity in the weld than out of weld

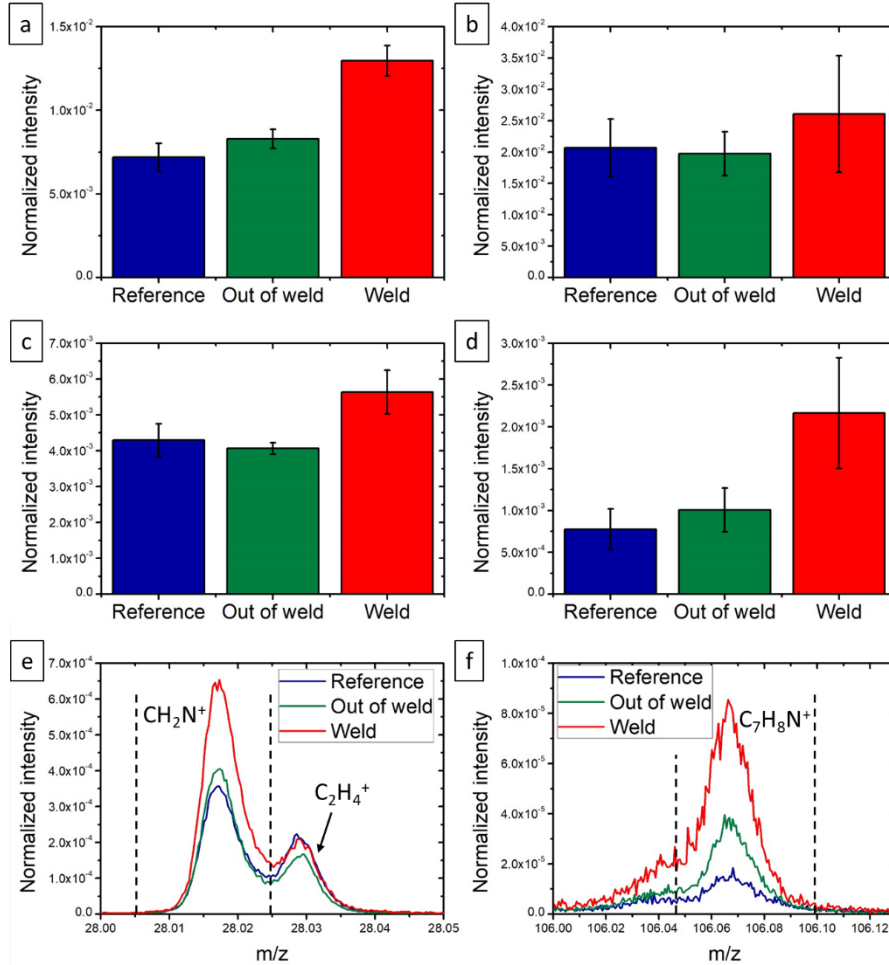


Figure 7.28: ToF-SIMS histograms of the normalized intensity in the reference, out of the weld in blue and in the weld in red, of (a) CH_2N^+ , (b) CH_4N^+ , (c) $\text{C}_2\text{H}_3\text{O}^+$, and (d) $\text{C}_7\text{H}_8\text{N}^+$. Mass spectra normalized on total intensity of the region of (e) CH_2N^+ , and (f) $\text{C}_7\text{H}_8\text{N}^+$.

and the reference. Some of the intensity of these ions are depicted in Figure 7.29. It is visible that the intensity in the reference always presents a high standard deviation overlapping with the standard deviation of the intensity in the weld. Nonetheless, the out of weld generally has a higher intensity than in the weld, the average value being near the one of the reference. So the metal is less intense in the weld, leading to the conclusion that more polymer covers the surface in the weld after the dissolution step. This observation is in good agreement with the XPS data and the SIMS data in the negative mode. For the hybrid ions, four different families were identified: the $\text{C}_x\text{H}_y\text{Ti}_z^+$, the $\text{C}_x\text{H}_y\text{N}_z\text{Ti}_w^+$, the $\text{C}_x\text{H}_y\text{O}_z\text{Ti}_w^+$ and $\text{C}_x\text{H}_y\text{N}_z\text{O}_w\text{Ti}_n^+$. In the $\text{C}_x\text{H}_y\text{Ti}_z^+$ five ions were identified: CTi^+ , CHTi^+ , C_2HTi^+ , $\text{C}_3\text{H}_2\text{Ti}^+$, and $\text{C}_3\text{H}_4\text{Ti}^+$. The intensities of two of them characterizing the behavior of all these ions are presented in Figure 7.30 (a) and (b). Two patterns are visible, one presenting lower intensities in the weld than out of the weld and the reference in average, the second presenting similar intensities in the reference and the weld and the out of weld higher in average. In each case the reference presents a high standard deviation. No clear conclusion can be drawn out from this data, but based on the observation in the negative mode and in XPS, no C-Ti is formed between both materials. From the $\text{C}_x\text{H}_y\text{N}_z\text{Ti}_w^+$ only two ions were identified: CNTi^+ and CH_2NTi^+ . Their intensities as well as a spectra zoom on the CH_2NTi^+ region are depicted in Figure 7.30 (c), (d) and (e).

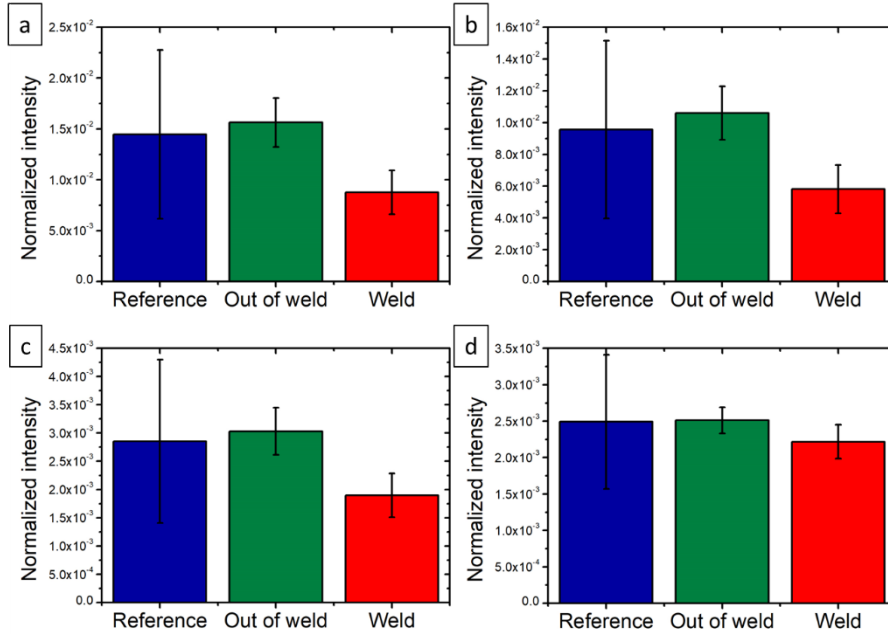


Figure 7.29: ToF-SIMS histograms of the normalized intensity in the reference, out of the weld in blue and in the weld in red, of (a) Ti^+ , (b) TiO^+ , (c) TiOH^+ , and (d) TiO_2H^+ .

Their intensity is equivalent in the reference and in the weld, while out of the weld they are slightly higher in average, which is confirmed on the spectra zoom. The welding does not have an effect on these ions in the positive mode, leading to the conclusion that there is no C-N-Ti bond formed at the interface. This is also supported by the previous observations made in XPS and in the negative mode. From the $\text{C}_x\text{H}_y\text{O}_z\text{Ti}_w^+$, only two ions could be identified: C_2HOTi^+ and $\text{CH}_2\text{O}_2\text{Ti}^+$. They both present equivalent intensities on all the samples as represented in Figure 7.31 (a). Here also no clear conclusion can be done. The last family $\text{C}_x\text{H}_y\text{N}_z\text{O}_w\text{Ti}_n^+$ has four identified members: CHNOTi^+ , CH_2NOTi^+ , CH_3NOTi^+ , and $\text{CH}_2\text{NO}_2\text{Ti}^+$ (already described above). On average the intensity is slightly higher in the weld than out of the weld and the reference, even if sometimes very slightly for CHNOTi^+ . This difference is not significant because of the overlapping error bars. This seems to indicate a C-O-Ti bond, but with just the results from the positive mode in SIMS it would be hard to conclude anything. But by comparing the results in the negative mode and the XPS results it is clear that there is a C-O-Ti bond formed at the interface.

From all this, it appears that for both principal components, negative loadings indicates lower intensities in the weld than in the reference and out of the weld, while positive loadings indicate the opposite. The positive loadings can be associated to the weld, while the negative one are associated to the reference and out of the weld.

7.2.2.3 PCA on the automatically generated peak lists

The automatic generated peak lists resulted in two lists composed of 310 peaks in the negative mode and 300 peaks in the positive mode. The scores obtained for the automatic generated peak list in both negative and positive modes, displayed in Figure 7.32, show a similar behavior than on the hand made peak lists presented above. Indeed, PC1 and PC2 are not able to discriminate the samples separately, but plotted together, the reference and the weld are clearly separated. The out of the weld samples have an intermediate behavior, crossing over the zones of the two

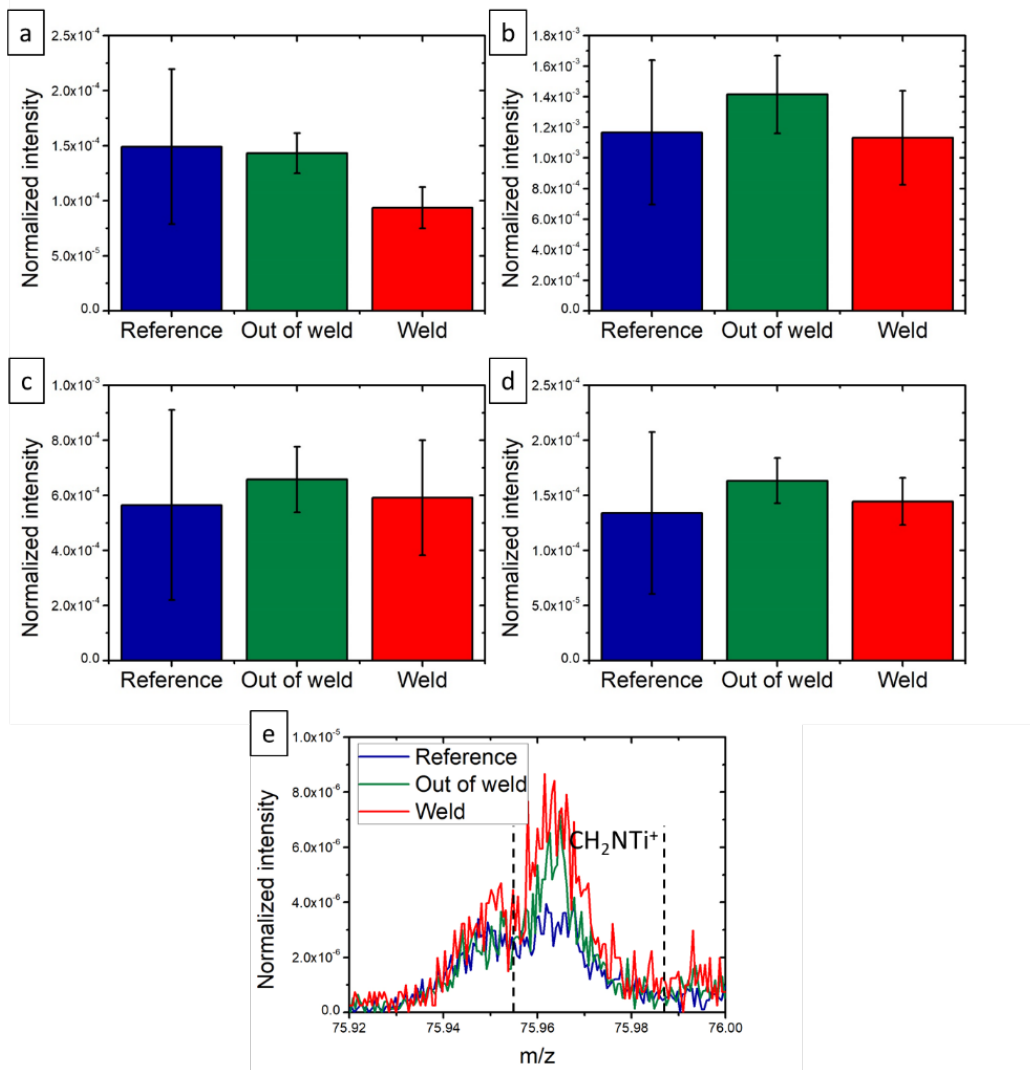


Figure 7.30: ToF-SIMS histograms of the normalized intensity in the reference, out of the weld in blue and in the weld in red, of (a) CTi^+ , (b) $C_3H_4Ti^+$, (c) $CNTi^+$, (d) CH_2NTi^+ , and (e) the spectra overlay zoomed on CH_2NTi^+ .

others. Looking more into details, it appears that there are three out of the weld samples, which behave very differently than the others. They are actually the same samples, which were deleted in the PCAs of the hand made peak lists. So these samples were deleted and two new PCAs were done.

After removing the three out of the weld samples, the PCA is able to discriminate in both modes the weld from the reference and the out of weld (see Figure 7.33). It is noticeable that the reference and the out of weld are undistinguishable, underlying the fact that heat is not diffused further than the weld zone. Again the behavior is similar than for the hand made peak lists.

The loadings are presented in Figure 7.34. Having a close look on the loadings of the PC1 in both negative and positive mode, it is observable that the ions presenting positive loadings also present higher intensities in the weld than out of the weld and the reference. Interpreting these ions, they are all related to the polymer. For instance in the negative mode, mass 26 is CN^- , mass 49 is C_4H^- , mass 50 is C_3N^- , or mass 79 is C_5N^- which can be related to the polymer.

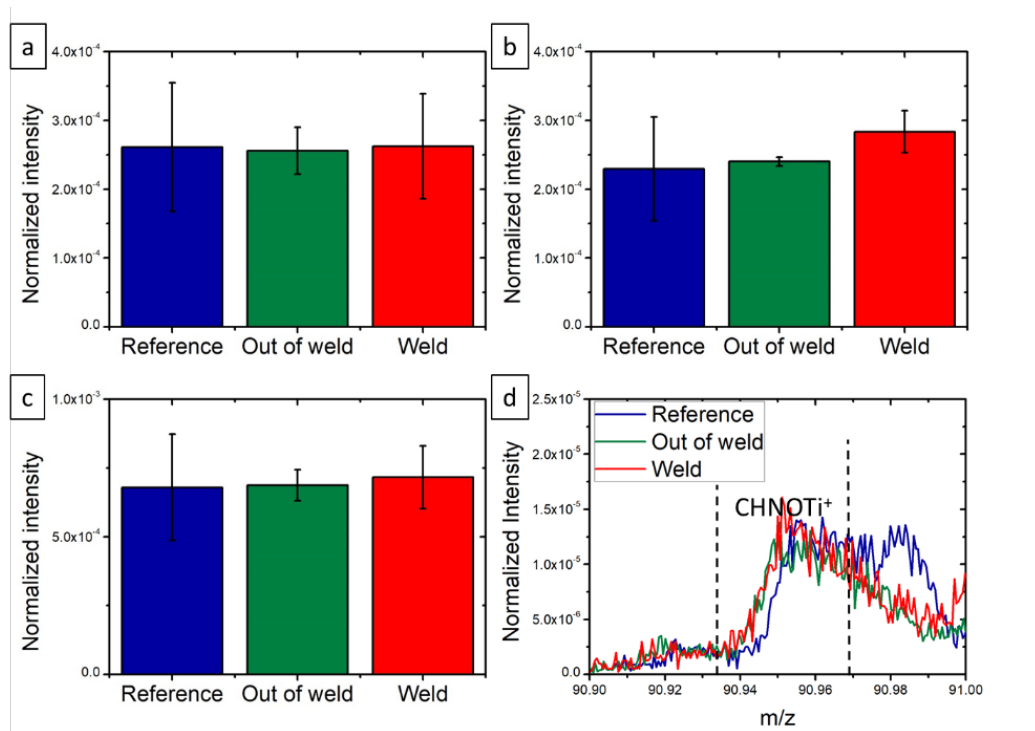


Figure 7.31: ToF-SIMS histograms of the normalized intensity in the reference, out of the weld in blue and in the weld in red, of (a) C_2HOTi^+ , (b) $CH_2NO_2Ti^+$, (c) $CHNOTi^+$, and (d) the spectra overlay zoomed on $CHNOTi^+$.

While in the positive mode, mass 30 is CH_4N^+ , mass 41 is $C_3H_5^+$, mass 44 is CH_2NO^+ , mass 55 is $C_3H_3O^+$, or mass 80 is $C_5H_6N^+$, which are also related to the polymer. The negative loadings present lower intensities in the weld than elsewhere and are related to the metal surface but also to contaminations. In the negative mode the metal is present at mass 96 TiO_3^- , mass 97 TiO_3H^- , or mass 59 AlO_2^- , while typical contaminations are seen at mass 35 Cl^- , mass 45 CHO_2^- , mass 63 $COCl^-$, or mass 63 CO_2Cl^- . In the positive mode the metal is represented with mass 48 Ti^+ , and mass 64 TiO^+ , while the other ions are contaminations such as Na^+ mass 23, K^+ mass 39, and Ca^+ mass 40. The peak at mass 86 could not be surely attributed, the only reasonable ion only regarding the mass is $C_5H_{12}N^+$, but as it presents lower intensities in the weld, it cannot be an ion related to the polymer. The loadings of the PC2 are very different for both polarity. In the negative mode, no clear pattern appears looking at the intensity of the different ions. In the positive mode a pattern exist. The positive loadings are ions presenting lower intensities in the out of weld compared to the reference, while the intensity in the weld can be higher or lower. They are related to organics, for instance mass 55 is $C_3H_3O^+$, mass 43 is supposedly $C_3H_7^+$ or mass 100 is $C_5H_{10}NO^+$. The negative loadings present higher intensities in the out of weld than on the reference. The ions can be related to contaminations like mass 39 K^+ , the metal mass 48 Ti^+ , or the polymer mass 39 $C_3H_3^+$, mass 65 $C_5H_5^+$ or mass 115 $C_4H_7N_2O_2^+$.

A similar conclusion can be drawn out than for the aluminum spin-coated samples. The hand selected peak lists display the same results than the automatically generated, and the hybrid ions also are not part of the ions presenting the highest loadings. Hence the user bias from the hand selected peak lists will be introduced also in the automatically generated peak lists. The hybrid ions would have to be selected by the user anyway. It also shows that the construction of the hand-selected peak list is robust, by selecting peaks related to the polymer, the metal and

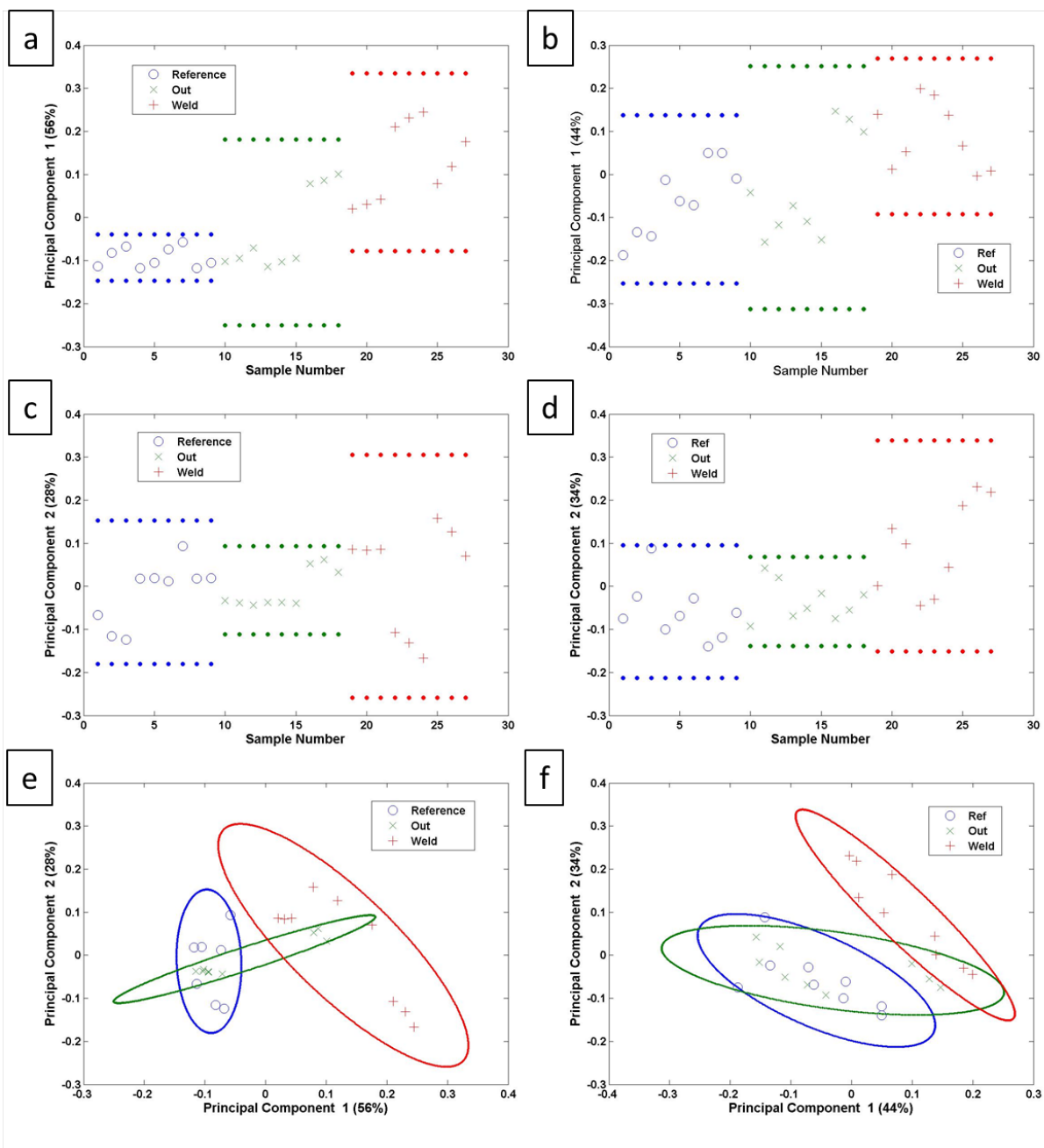


Figure 7.32: Scores for the automatic generated peak list in the negative mode (a) PC1, (c) PC2, (e) PC1 versus PC2 and in the positive mode (b) PC1, (d) PC2, and (f) PC1 versus PC2.

some contaminations, and adding the hybrid ions. The peaks related to contaminations were neglected in the hand-made selection, diminishing their impact to differentiate the samples.

7.2.3 Conclusions on the spin-coated samples

On the welded samples, the dissolution proved to remove the interface information. Therefore, the dissolution step on the titanium spin-coated samples was shortened to the minimum, in order to avoid the dissolution of everything related to the polymer. This proved to be efficient. Indeed, the XPS data as well as the two PCA performed on the SIMS data, showed that more

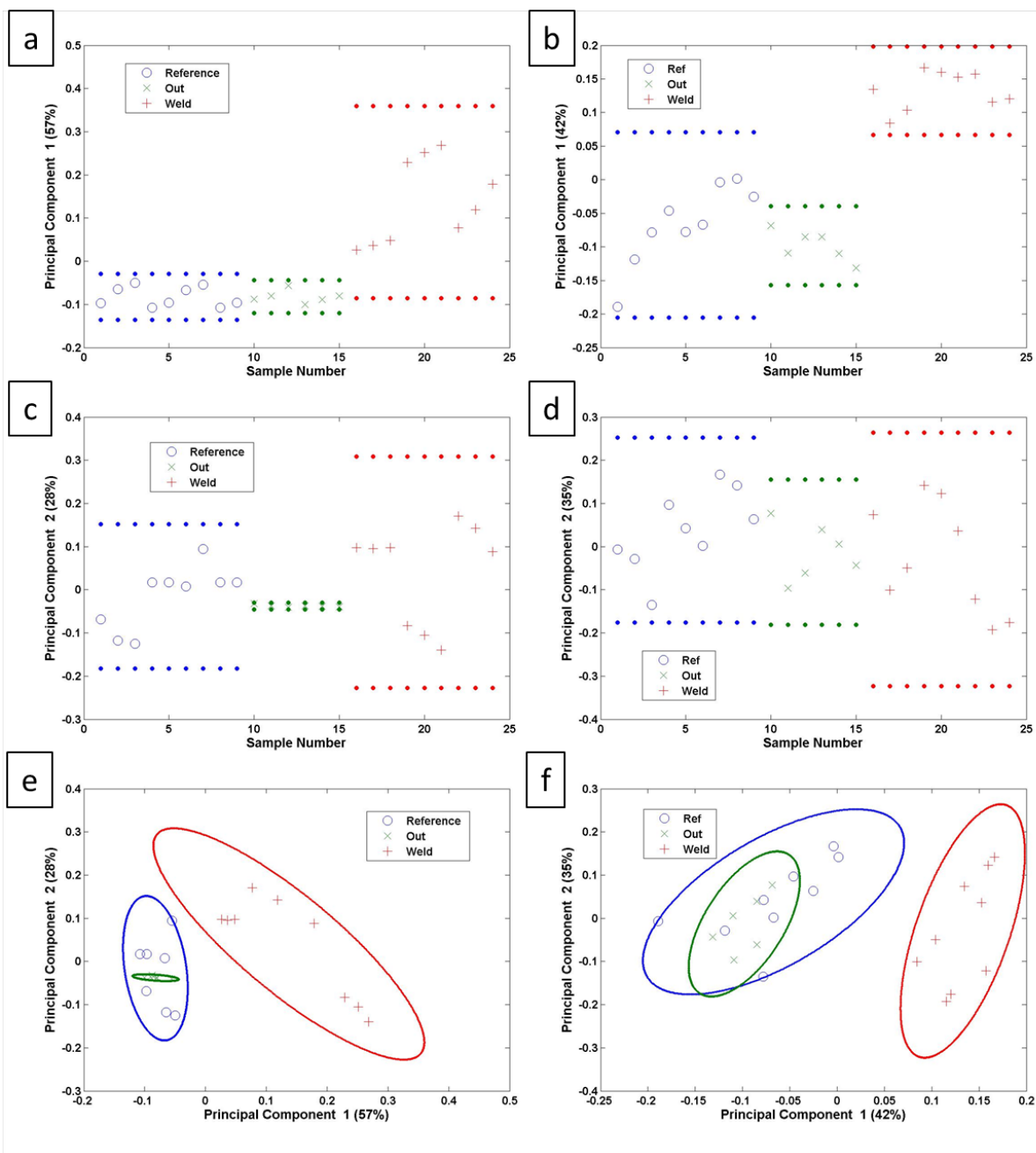


Figure 7.33: Scores for the automatic generated peak list with six out of the weld samples in the negative mode (a) PC1, (c) PC2, (e) PC1 versus PC2 and in the positive mode (b) PC1, (d) PC2, and (f) PC1 versus PC2.

polymer is present in the weld compared to the out of the weld and the reference. Moreover, the information from the titanium and the metal in general is less intense in the weld than elsewhere, emphasizing the fact that a thicker polymer layer covers the surface. This also shows that the welding has an effect on the interface, the heat given allows the polymer to form more bonds with the metal at the interface.

As for the chemical reactivity, the XPS data showed different things. Apparently no reaction between the titanium and the carbon was observed, as no C-Ti bond was observed. In the same manner, no N-Ti bond was observed, which allows to conclude that no nitride bond is formed

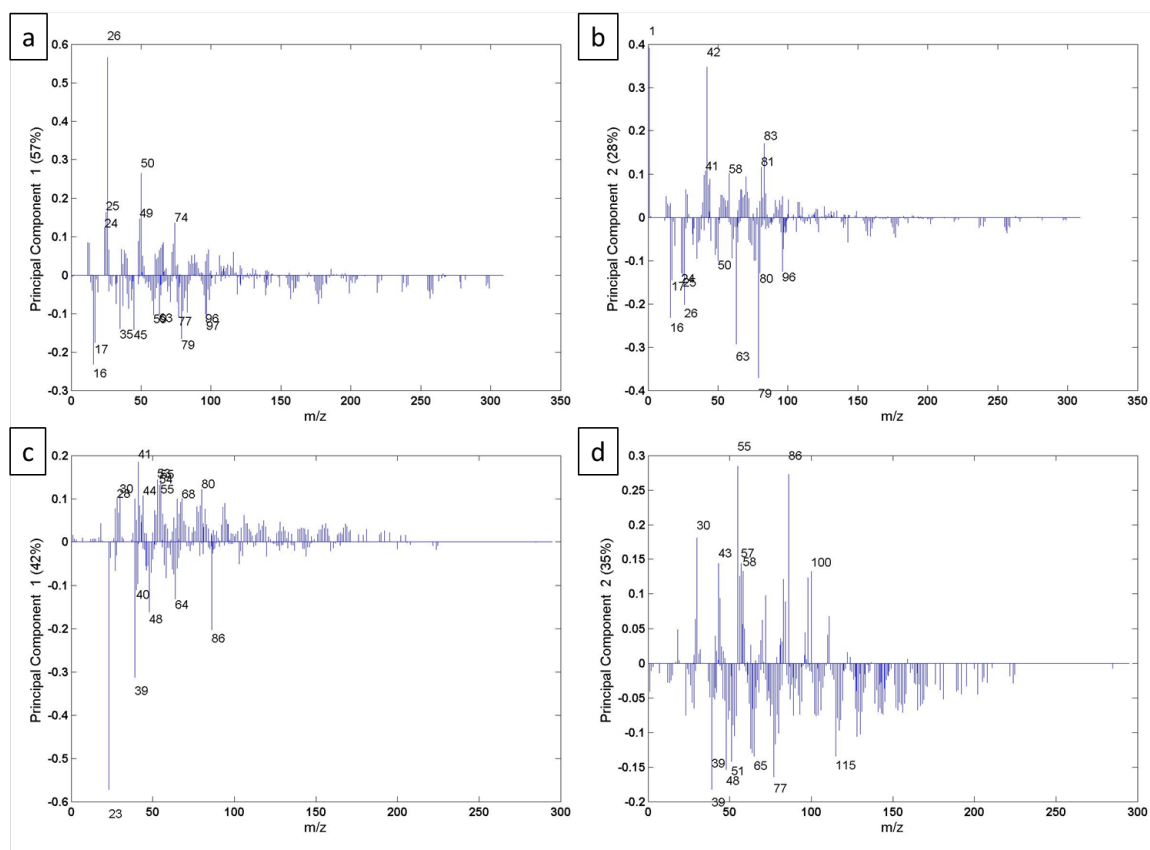


Figure 7.34: Loadings of the PCA in the negative mode (a) PC1, (b) PC2, and in the positive mode (c) PC1 and (d) PC2.

due to the welding. The only possibility left is a C-O-Ti bond. The XPS data is not confirming nor infirming such possibility. Indeed, the peaks of such bond would appear near to already existing contributions, and no clear difference was observed between the samples directly linked to such a bond. Nonetheless, a peak interpreted as an imine bond in the N 1s region appears in the weld and is absent out of the weld and the reference. This is a hint at a possible reaction mechanism shown in Figure 7.17.

To analyze the SIMS data, PCA were performed for each polarity. In the negative mode the PCA showed clear result. As in XPS, it was shown that no reaction occurs to form a carbide bond nor a nitride bond. Here the ions related to a C-O-Ti bond, proved to have a higher intensity in the weld than out of the weld and in the reference, which allows to conclude that a C-O-Ti bond is formed. In the positive mode the results are less clear, but points also to the direction of a C-O-Ti bond. PCAs on automatic generated peak lists was also done for comparison purposes, and it appears that the data behave similarly in both modes than the PCA on the hand-selected peak lists.

7.3 Model samples

The main idea behind these samples is to investigate the reaction mechanism (see Chapter 4 part 4.1.2.3). As the polymer already adsorbs on the metal surface because of the spin-coating, it is reasonable to think that a smaller molecule presenting only the reactive part of the polymer will interact more easily with the titanium surface. N-methylformamide was chosen,

Table 7.4: XPS elemental composition from the survey spectra for the UV-cleaned, the air-dried and the heated samples.

Samples	%O	%Ti	%C	%N	%Al	%V	%F	%S
UV-cleaned	58.3 (± 1.3)	24.8 (± 1.7)	10.5 (± 1.3)	1.0 (± 0.1)	3.9 (± 0.8)	0.5 (± 0.1)	0.6 (± 0.1)	0.4 (± 0.1)
Air-dried	56.2 (± 3.1)	21.4 (± 2.6)	16.0 (± 3.8)	1.9 (± 0.2)	4.2 (± 0.7)	0.4 (± 0.1)	0.0	0.0
Heated	54.7 (± 2.0)	18.4 (± 1.0)	20.8 (± 2.4)	1.5 (± 0.3)	4.3 (± 0.3)	0.3 (± 0.1)	0.0	0.0

because N-methylethanamide is not liquid at ambient temperature (mp at 26-28 °C). After the dip coating, some of the samples were heated at 150 °C (the heated samples), which is not the welding temperature, but the boiling point of the molecule is of 182 °C.

7.3.1 Deposition of the molecule

The elemental composition of the different surfaces obtained by analyzing the survey spectra of the XPS measurement is detailed in Table 7.4. The oxygen and titanium percentages decrease from the UV-cleaned samples to the heated samples, while the carbon percentage increases from the UV-cleaned samples to the heated samples. The UV-cleaning step removes the adventitious carbon, but since there is a certain time to get the samples from the UV-cleaner to the analysis chambers, the samples are slightly recontaminated. The nitrogen percentage is lower on the UV-cleaned samples (1.0%), intermediate on the heated samples (1.5%) and at the highest on the air-dried samples (1.9%). Since the nitrogen percentage is higher on the air-dried and the heated samples than on the UV-cleaned samples, N-methylformamide has been deposited on the samples. Nonetheless, the nitrogen percentage is on average lower on the heated samples, indicating that there is a chemical reaction or desorption happening due to the heating, explaining why less nitrogen is observed on the heated samples. The aluminum percentage is equivalent on all samples and the vanadium percentage is a bit lower on the heated samples. Traces of fluorine and sulfur are detected on the UV-cleaned samples, but their origin is unknown.

In Figure 7.35 (a), (b) and (c), the high resolution spectra of the C 1s region of the different samples are depicted. For the UV-cleaned samples, four contributions were used for the interpretation. The first one at 284.8 eV, used as calibration, was attributed to C-C/C-H bonds [282, 286, 296]. The second contribution attributed to C-O/C-N bonds is around 286.0 eV [282, 286, 296]. The third one is around 287.8 eV and was linked to C=O bonds [282, 286, 296]. The last one is around 289.6 eV and is interpreted as carbonate [282, 286, 296]. This spectra is typical of adventitious carbon contamination [283, 295, 296, 325]. For the air-dried and the heated samples the same interpretation was used. Here also four contributions were applied: a C-C/C-H bond at 284.8 eV, a C-O/C-N bond around 286.2 eV, a C=O bond around 287.8 eV and a O-C=O contribution around 288.8 eV [282, 286, 296]. On the air-dried and the heated samples, the contributions of C-O/C-N and C=O bonds are more intense than on the UV-cleaned samples, which is a good indication that the molecule has been deposited on the surfaces.

The high resolution spectra of the Ti 2p region of all the samples can be seen in Figure 7.35 (d), (e) and (f) and were interpreted in the same manner. A plasmonic contribution was found around 471.7 eV [286, 289, 290]. Because of the spin-orbit splitting the eight other peaks used to fit the spectra are linked to four bonding states. Both energies will be given, but first the energies linked to the Ti 2p_{3/2} will be written and then the energies of the Ti 2p_{1/2}. The first binding state is the metallic titanium found around 453.7 eV and 460.2 eV [286, 289, 290]. The second binding

state is Ti(II) with energies around 455.3 eV and 461.6 eV [286, 289, 290]. The third binding state is linked to Ti(III) around 457.4 eV and 463.4 eV [286, 289, 290]. And the fourth binding state is related to Ti(IV) with energies around 458.7 eV and 464.6 eV [286, 289, 290]. Looking at the intensities of the different contribution showed that there are no significant differences between the samples.

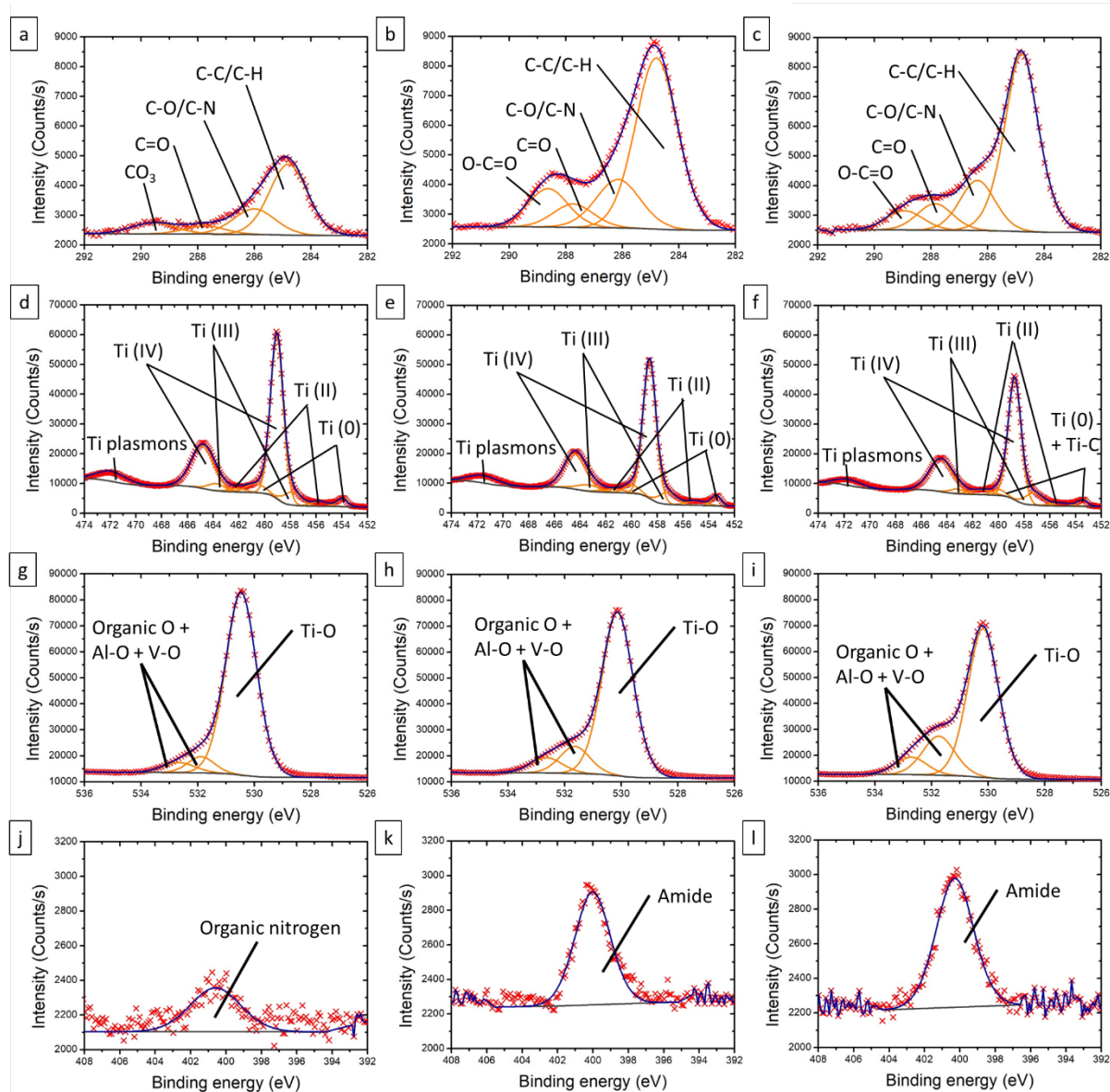


Figure 7.35: XPS high resolution spectra for the UV-cleaned, the air dried and the heated samples in (a), (b) and (c) the C 1s region, in (d), (e) and (f) the Ti 2p region, in (g), (h) and (i) the O 1s region, and in (j), (k) and (l) the N 1s region.

The high resolution spectra of the O 1s region are presented in Figure 7.35 (g), (h) and (i). Three contributions were used to fit the spectra. The first contribution is associated to titanium oxide around 530.2 eV [286, 289, 290]. Then two contributions were added around 531.7 eV and 532.7 eV respectively. Both are related to organic materials present on the surface but also Al-O and V-O bonds [286, 289, 290]. The intensity of the first contribution (Ti-O) is in average lower on the heated samples ($66.9 \pm 2.7\%$) than on the air-dried samples ($74.5 \pm 9.2\%$), but

significantly lower than on the UV-cleaned samples ($83.6 \pm 6.1 \%$). At the same time the second contribution (at 531.7 eV) is in average more intense on the heated samples ($22.9 \pm 3.4 \%$) than on the air-dried samples ($16.0 \pm 4.6 \%$), and significantly higher than on the UV-cleaned samples ($9.2 \pm 3.7 \%$). The third contribution shows less variation than the two others, but is in average higher on the heated samples ($10.2 \pm 1.9 \%$), intermediate on the air-dried samples ($9.5 \pm 47 \%$) and the lowest on the UV-cleaned samples ($7.1 \pm 2.7 \%$). The higher intensities of the second and the third contributions while the first one is less intense, on the air-dried and the heated samples, are good indication that the N-methylformamide is deposited on the surface.

On the high resolution spectra of the N 1s region, depicted in Figure 7.35 (j), (k) and (l), it is visible that only one contribution was used to fit the spectra. This contribution is around 400.8 eV, while around 400.0 eV on the air-dried and the heated samples. The binding energy on the air-dried and the heated samples correspond to the binding energy of an amide function [282, 286, 298], while on the UV-cleaned samples it corresponds to organic compounds [282, 286, 298]. Moreover, the intensity is much higher on the air-dried and the heated samples, in agreement with the elemental percentages calculated from the survey spectra. This all also confirms the deposition of N-methylformamide on the air-dried and the heated samples.

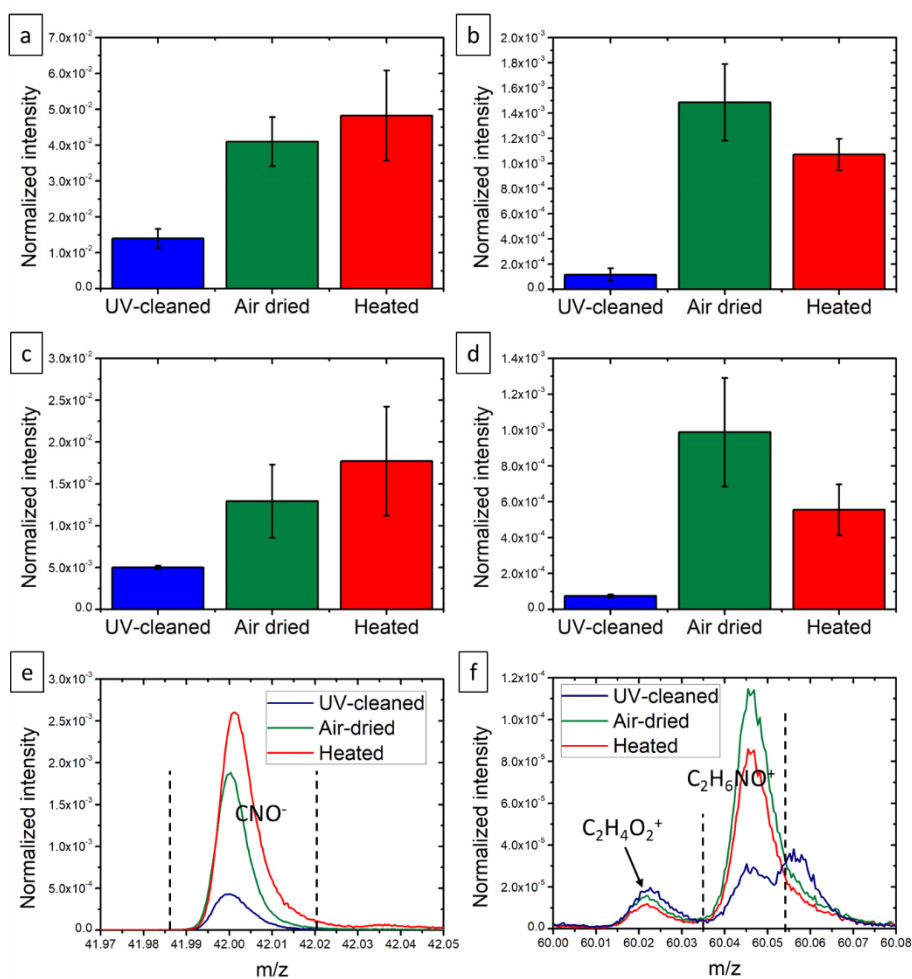


Figure 7.36: ToF-SIMS histograms of the normalized intensity on the UV-cleaned samples in blue of the air dried samples in green and the heated samples in red, of (a) CNO^- , (b) $\text{C}_2\text{H}_4\text{NO}^-$, (c) CH_4N^+ , and (d) $\text{C}_2\text{H}_6\text{NO}^+$. Mass spectra normalized on total intensity of the region of (e) CNO^- , and (f) $\text{C}_2\text{H}_6\text{NO}^+$.

With ToF-SIMS several ions could be identified as related to N-methylformamide. They present higher intensities on the air-dried and the heated samples, than on the UV-cleaned samples, as presented in Figure 7.36. This shows clearly the deposition of the molecule on the air-dried and the heated samples which is in good agreement with the XPS data. Nonetheless, it is visible that the ions of the whole molecule $C_2H_4NO^-$ and $C_2H_6NO^+$ are less intense on the heated samples than on the air-dried samples, while for smaller ions, fragments of the molecule, the intensity is equivalent on both samples. This indicates that the heating as an effect, leading to a chemical reaction between the molecule and the titanium surface.

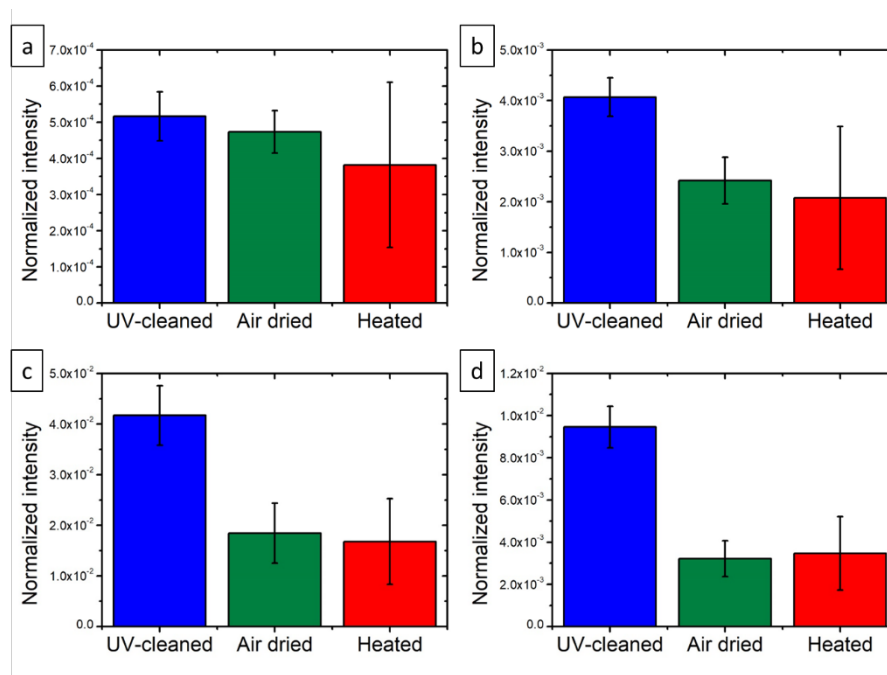


Figure 7.37: ToF-SIMS histograms of the normalized intensity on the UV-cleaned samples in blue of the air dried samples in green and the heated samples in red, of (a) TiO^- , (b) TiO_2^- (c) Ti^+ , and (d) $Ti_2O_3^+$.

In Figure 7.37 the intensity of several ions characteristic of a titanium surface are presented. In the negative mode the intensity of these ions is lower on the air-dried and the heated samples than on the heated samples. In the positive mode, the intensity is systematically equivalent for the air-dried and the heated samples, while less intense than the UV-cleaned samples. Such drop of intensity cannot be fully explained by the coverage of the layer of N-methylformamide, since it is deposited as an ultra-thin film. The only explanation possible is a matrix effect, where the molecule deposited changes the ionization probability of the titanium. The same effect is possible in the negative mode, but it is less clear than in the positive mode.

7.3.2 Chemical reactivity

As for the other samples the chemical reactivity was investigated on the molecule represented in Figure 7.38. Since N-methylformamide mimics the reactive part of polyamide-6.6, the same reactive sites can be observed: carbon reactive sites, nitrogen reactive site and an oxygen reactive site. On these samples, the metal's reactivity was also investigated.

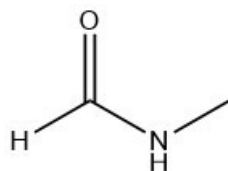


Figure 7.38: Chemical formula of N-methylformamide.

7.3.2.1 Carbon reactive sites

On the high resolution spectra of the C 1s region presented in Figure 7.35 (a), (b) and (c), no titanium carbide peak was identified. However, the signal of the bond C-Ti might be below the detection limit. Indeed, the deposited molecule forms an extremely thin layer so that the detection limit for bonds at the interface might not be reached.

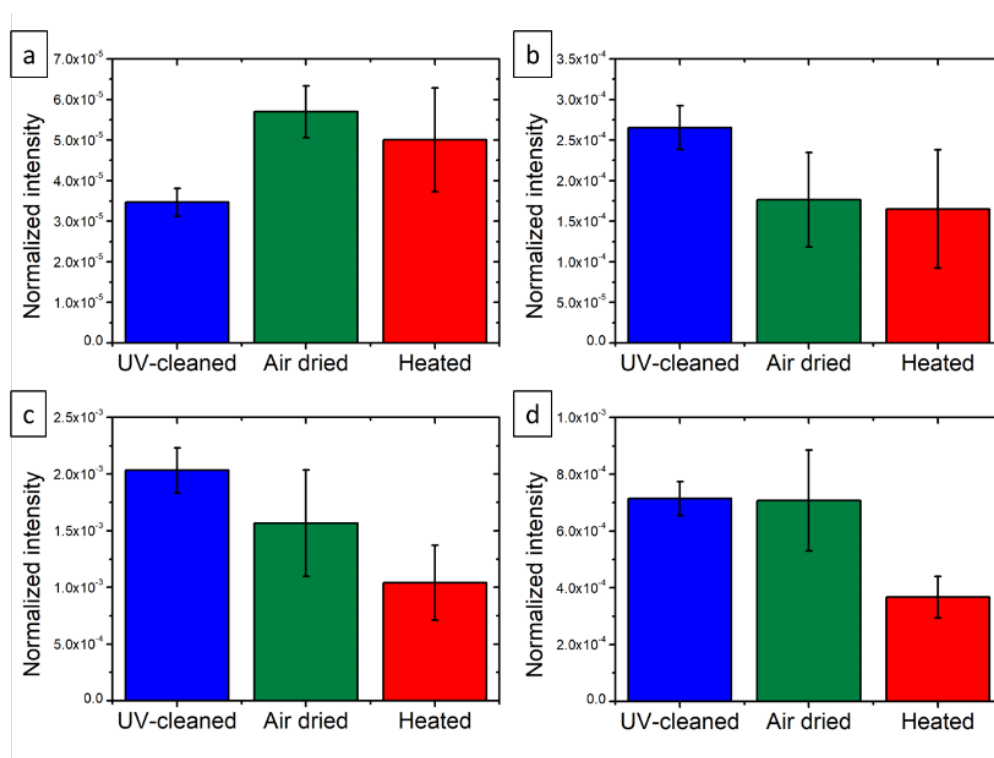


Figure 7.39: ToF-SIMS histograms of the normalized intensity on the UV-cleaned samples in blue of the air dried samples in green and the heated samples in red, of (a) C_2Ti^- , (b) CTi^+ , (c) C_2HTi^+ , and (d) $C_3H_2Ti^+$.

In ToF-SIMS several ions of the $C_xH_yTi_z^{-/+}$ family could be surely identified, some of their intensities are represented in Figure 7.39. In the negative mode, only one ion was found: C_2Ti^- . In the positive mode, nine ions were found: CTi^+ , $CHTi^+$, CH_2Ti^+ , CH_3Ti^+ , C_2HTi^+ , $C_2H_2Ti^+$, C_3Ti^+ , $C_3H_2Ti^+$, and $C_3H_3Ti^+$. While in the negative mode the ion C_2Ti^- present higher intensities on the air-dried and the heated samples than on the UV-cleaned samples, in the positive mode the intensities of all the ions of the family present at least lower intensities on the heated samples than on the UV-cleaned samples. The air-dried samples present an intermediate behavior sometimes on the same level than the heated samples, sometimes in between the UV-cleaned and the heated samples, and sometimes on the same level than the UV-cleaned samples. This

points to the direction of no reaction with the carbon sites. Moreover, the presence of ions containing more than one carbon also points to the direction of a reaction with surface contaminants or simply a recombination after sputtering in the selvedge. Adding the fact that only one ion of this family could be identified in the negative mode, the conclusion is clearly that no reaction happens between the molecule and the titanium surface on the carbon reactive sites.

7.3.2.2 Nitrogen reactive sites

On the XPS high resolution spectra of the N 1s region, in Figure 7.35 (j) (k) and (l), only a peak related to organics for the UV-cleaned samples and a peak related to an amide function were found. This lowers the probability of a C-N-Ti bond, but the signal of the bond might be below the detection limit of the XPS machine.

In ToF-SIMS some ions of the $C_xH_yN_zTi_w^{-/+}$ family were surely identified. In the negative mode, three were found: $CNTi^-$, CH_2NTi^- , and CH_3NTi^- . In the positive mode, only two ions were found: $CHNTi^+$ and CH_2NTi^+ . The normalized intensities of four of these ions are represented in Figure 7.40 along with zooms of the mass spectra. In the negative mode only $CNTi^-$ presents significantly higher intensities on the air-dried samples and the heated samples, while for the two other ions, the intensities are lower on those samples compared to the UV-cleaned ones. In the positive mode for both ions the pattern is the same. The intensity is higher on the air-dried samples than on the UV-cleaned samples, while on the heated samples it is higher in average than the UV-cleaned samples, but with a high standard deviation. Since the intensity of this ions on the heated samples variates that much and is on some samples lower than on the UV-cleaned samples, it is reasonable to think that there is no C-N-Ti bond and that these ions are due to recombination. This is confirmed by the high intensity of these ions on the air-dried samples, where the highest nitrogen percentage was found.

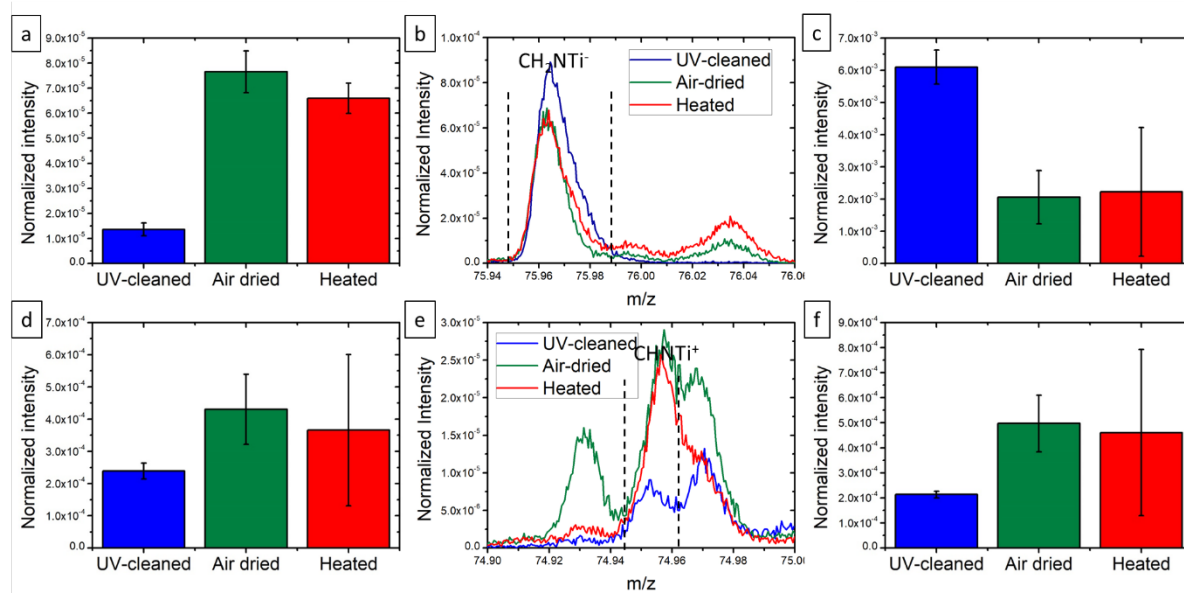


Figure 7.40: ToF-SIMS histograms of the normalized intensity on the UV-cleaned samples in blue of the air dried samples in green and the heated samples in red, of (a) $CNTi^-$, (c) CH_2NTi^- , (d) $CHNTi^+$, and (f) CH_2NTi^+ and the spectra zoomed on (b) CH_2NTi^- and (e) $CHNTi^+$.

7.3.2.3 Oxygen reactive sites

The high resolution spectra of the O 1s (see Figure 7.35 (i), (j) and (k)) do not present a specific peak for a C-O-Ti bond. Nonetheless, the second and the third contribution respectively at 531.7 eV and 532.7 eV present higher intensities, which is first associated to the fact that N-methylformamide has been deposited on the samples. It can also be characteristic of a C-O-Ti bond, but just with the XPS data it is hard to conclude on this matter.

In ToF-SIMS, two different family of ions, which can be related to a C-O-Ti bond, were investigated: $C_xH_yO_zTi_w^{-/+}$ and $C_xH_yN_zO_wTi_n^{-/+}$.

For the $C_xH_yO_zTi_w^{-/+}$ in the negative mode only two ions were found: CH_3OTi^- , CHO_2Ti^- . In the positive mode eight ions were identified: $CHOTi^+$, CH_2OTi^+ , CH_3OTi^+ , C_2HOTi^+ , CHO_2Ti^+ , $CH_2O_2Ti^+$, $CH_3O_2Ti^+$, and $CH_4O_2Ti^+$. In the negative mode, the ion CH_3OTi^- presents a significantly lower intensity on the air-dried and even lower on the heated samples than on the UV-cleaned samples. At the same time CHO_2Ti^- has a way higher intensity on the air-dried samples and even higher on the heated samples. In the positive mode, the ions can be separated into three categories. The first one is where the intensities are equivalent for all the samples and no significant difference can be observed. This category includes the following ions: $CHOTi^+$, CH_2OTi^+ , C_2HOTi^+ , CHO_2Ti^+ , and $CH_2O_2Ti^+$. The second category comprises the only ion presenting lower intensities on the air-dried and the heated samples: CH_3OTi^+ . The last category comprises the ions presenting higher intensities on the air-dried and even higher on the heated samples: $CH_3O_2Ti^+$ and $CH_4O_2Ti^+$. Looking at all this data, a pattern seems to appear, the lower the mass, so the less distinctive the ion, the more the intensities of them are equivalent between all the samples. Since they are lower masses and so less distinctive of the molecule binding to the surface, they can be associated to contamination as well as recombination. Consequently the heavier the ions, the more specific to the binding between the molecule and the titanium surface they get, explaining the higher intensities of such ions on the air-dried and the heated samples. Since these ions also have higher intensities on the heated samples than the air-dried samples, one can easily conclude that the heating process does have an impact on the system and that it creates C-O-Ti bonds between the molecule and the metal surface.

For the $C_xH_yN_zO_wTi_n^{-/+}$ more ions were identified in both negative and positive mode. In the negative mode seven ions were found: $CNOTi^-$, $CHNOTi^-$, $CHNO_2Ti^-$, CH_2NOTi^- , $C_2NO_2Ti^-$, $C_2HNO_2Ti^-$, and $C_2H_5NOTi^-$. In the positive mode five ions were identified: $CHNOTi^+$, CH_2NOTi^+ , CH_3NOTi^+ , $C_2H_4NOTi^+$, and $C_2H_5NOTi^+$. In the negative mode the intensities vary in the same manner for almost all the ions: the intensities are higher on the heated samples than on the air-dried samples (at least on average) and than the UV-cleaned samples. For $CHNOTi^-$ the intensity is indeed higher on the air-dried and the heated samples, but is equivalent on these both samples as shown in Figure 7.41 (a). Only for $C_2HNO_2Ti^-$ the intensities are equivalent on all the samples. In the positive mode the pattern of the intensities is every time the same with low intensities on the UV-cleaned samples, high intensities on the air-dried samples and the heated samples are always in between, on average, with sometimes the standard deviation overlapping with the one of the air-dried samples. The intensities in the negative mode clearly indicate a C-O-Ti bonding, while the intensities in the positive mode suggest a degradation of the molecule after heating since $C_2H_4NOTi^+$, and $C_2H_5NOTi^+$ present lower intensities on the heated samples than on the air-dried samples.

7.3.2.4 Reaction mechanism

The top surface of the titanium in contact with the N-methylformamide, is present in two forms: the oxide form and the hydroxide form. By analogy, one could think that the reaction

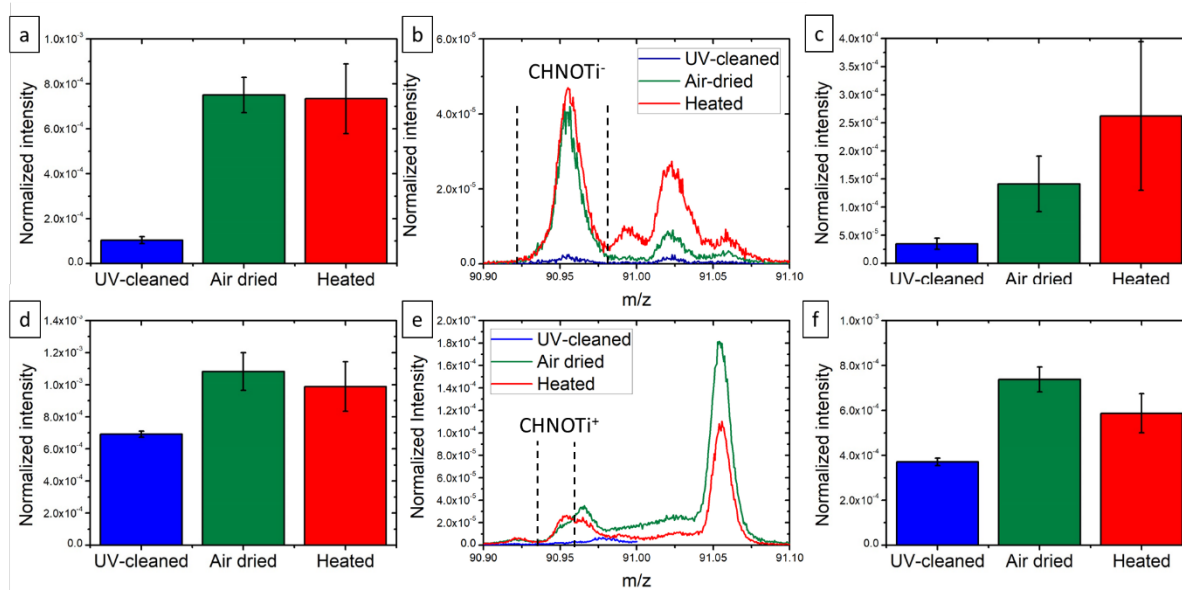


Figure 7.41: ToF-SIMS histograms of the normalized intensity on the UV-cleaned samples in blue of the air dried samples in green and the heated samples in red, of (a) CHNOTi^- , (c) $\text{C}_2\text{H}_5\text{NOTi}^-$, (d) CHNOTi^+ , and (f) $\text{C}_2\text{H}_4\text{NOTi}^+$ and the spectra zoomed on (b) CHNOTi^- and (e) CHNOTi^+ .

mechanism on the titanium is the same as on the aluminum (see Figure 7.42). It is reasonable to think that the amide reacts with the free hydroxyl groups to form C-O-Ti bonds. The intensities of ions related to the oxide depicted in Figure 7.37, show that in the negative mode the intensities have on average lower intensities going from the UV-cleaned samples to the heated samples through the air-dried samples. In the positive mode a matrix effect was observed explaining the lower intensities for both air-dried and heated samples compared to the UV-cleaned samples. Specific ions related to the titanium hydroxide were also identified in the spectra (see Figure 7.43). In the negative mode the hydroxide ions present a high standard deviation on the heated samples making no significant differences with the UV-cleaned and air-dried samples. The air-dried samples present, at least on average, higher intensities than the UV-cleaned ones. By comparing the hydroxide ions with the oxide ions, one could simply think that the reaction happens at the oxide and not at the hydroxyl free groups. In the positive mode, the oxide and hydroxide ions present the same pattern of intensities, equivalent intensities on the air-dried and the heated samples, while significantly lower than on the UV-cleaned samples. Since they present no difference of behavior no conclusion can be drawn about the reaction mechanism.

Having a second look on the ions related to the N-methylformamide (see Figure 7.36), it was already noticed that the molecular ions presented lower intensities on the heated samples than on the air-dried samples. It was interpreted as the molecule reacting with the titanium surface. Nonetheless, the hybrid ion $\text{C}_2\text{H}_5\text{NOTi}^-$, being the strict combination between the N-methylformamide and a titanium atom is higher in intensity on the heated samples than on the air-dried ones. At the same time, no $\text{C}_2\text{H}_4\text{NOTi}^-$ could be identified. This would indicate an other reaction mechanism than the one which is similar to the reaction of N-methylformamide and aluminum as depicted in Figure 7.42. However this possibility is not confirmed with the data from the positive mode. Indeed the hybrid ions $\text{C}_2\text{H}_4\text{NOTi}^+$ and $\text{C}_2\text{H}_5\text{NOTi}^+$ present both lower intensities on the heated samples than on the air-dried ones. This observation can be compliant with the proposed mechanism. It means that the reaction does not bind the molecule

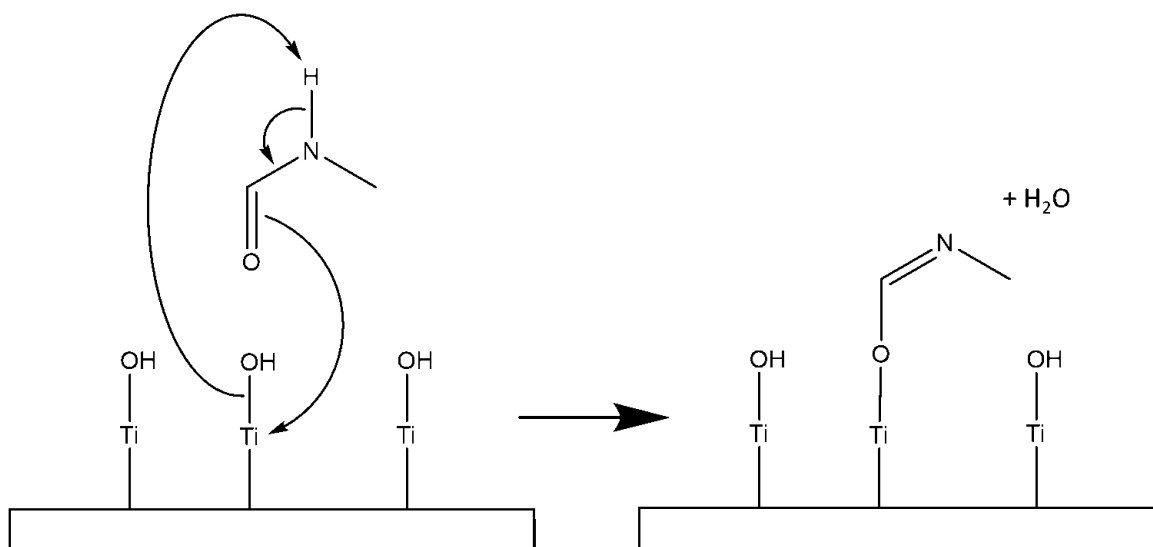


Figure 7.42: Proposition of reaction mechanism between the molecule and the metal surface.

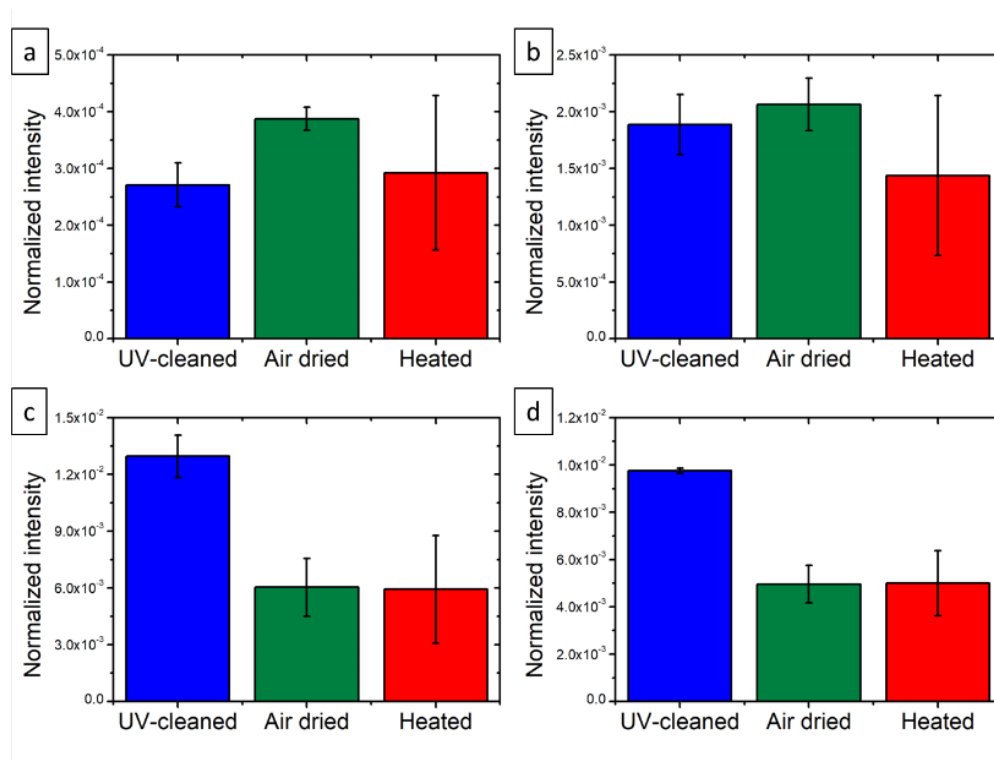


Figure 7.43: ToF-SIMS histograms of the normalized intensity on the UV-cleaned samples in blue of the air dried samples in green and the heated samples in red, of (a) $TiOH^-$, (b) TiO_2H^- , (c) $TiOH^+$ and (d) TiO_2H^+ .

to the surface, but that the molecule also degrades during the heating process. This is reasonable since titanium is nowadays regularly used as catalyst for different chemical reactions and not just for photocatalysis [341, 342].

7.3.3 Discussion about PCA

7.3.3.1 PCA on the hand-selected peak lists

The scores obtained for the PCA in both polarities are depicted in Figure 7.44. In both modes, PC1 discriminates the UV-cleaned samples from the air-dried and heated samples. The first difference is associated to the deposition of N-methylformamide. Looking at the loadings of PC1 in both polarities in Figure 7.45 (a) and (c), it appears that the positive loadings, present higher intensities on the air-dried and the heated samples than on the UV-cleaned samples. The opposite pattern, higher intensities on the UV-cleaned samples than on the air-dried and the heated samples, is observed for the negative loadings. For the interpretation, the positive loadings are related to the N-methylformamide in both polarities. For instance, in the negative mode the mass 25 is C_2HN^- , mass 26 is CN^- , mass 42 is CNO^- , and mass 43 $C_2H_3O^-$. In the positive mode, mass 28 is CH_2N^+ , mass 30 CH_4N^+ , and mass 32 is CH_6N^+ . The negative loadings of PC1 are related to contaminations and the metal. For example, in the negative mode, mass 59 is AlO_2^- , mass 96 TiO_3^- , mass 79 was first interpreted as CH_3OTi^- , but it should rather be interpreted as CO_2Cl^- , and mass 76 was first interpreted as CH_2NTi^- , but could also be interpreted as SiO_3^- . In the positive mode for example, mass 27 is Al^+ , mass 48 is Ti^+ , mass 64 is TiO^+ , or mass 144 is $Ti_2O_3^+$. PC2 and the following principal components do not discriminate the air-dried and the heated samples. This is confirmed by looking at the loadings of PC2 in Figure 7.45 (b) and (d). The intensities do not show any pattern to differentiate the air-dried and the heated samples. The hand-selected peak list is not complete enough to make the differentiation. This might be because the contaminations were left out of the construction of the peak lists in both modes.

7.3.3.2 PCA on the automatic generated peak lists

The PCA on the automatic generated peak list was more successful as can be seen in the scores of PC1 and PC2 in both polarities depicted in Figure 7.46. In both modes PC1 separates the UV-cleaned samples from the air-dried and the heated samples. So, as seen on the hand-selected peak list the greatest difference is the deposition of N-methylformamide. The loadings of PC1 shown in Figure 7.47 (a) and (c) display the same behavior for both polarities. The positive loadings have higher intensities on the air-dried and the heated samples than on the UV-cleaned samples, and are related to the N-methylformamide and contaminations. For instance, in the negative mode mass 1 is H^- , mass 26 is CN^- , mass 41 C_2HN^- , mass 42 is CNO^- . In the positive mode mass 23 is Na^+ , mass 39 is K^+ , mass 42 is $C_2H_3N^+$, or mass 73 is $C_2H_3NO^+$. The negative loadings present lower intensities on the air-dried and the heated samples than on the UV-cleaned samples. They are related to ions from the metal and contaminations. In the negative mode mass 16 is O^- , mass 62 is NO_3^- , mass 79 is CO_2Cl^- , or mass 96 is TiO_3^- . In the positive mode mass 27 is Al^+ , mass 48 is Ti^+ , mass 64 is TiO^+ , mass 91 is $C_7H_7^+$. PC2 discriminates the air-dried samples from the heated samples (see Figure 7.46). The heating treatment is the second cause of difference between the samples. The loadings in both polarities do not behave the same way. In the negative mode the positive loadings are related to ions presenting higher intensities on the heated samples than on the air-dried samples. While in the positive mode, the ions related to positive loadings have lower intensities on the heated samples than on the air-dried samples. For the negative loadings, in the negative mode the intensities are lower on the heated samples than on the air-dried samples and in the positive mode the intensities are higher on the heated samples than on the air-dried samples. The ions presenting high positive and negative loadings in PC2 for both modes can be related to contaminations, the metal and N-methylformamide indistinctively. For the positive loadings in the negative mode, mass 71 is $C_4H_7O^-$, mass 80 is $TiNH_2^-$, mass 96 is TiO_3^- , mass 97 is TiO_3H^- . Still in the negative

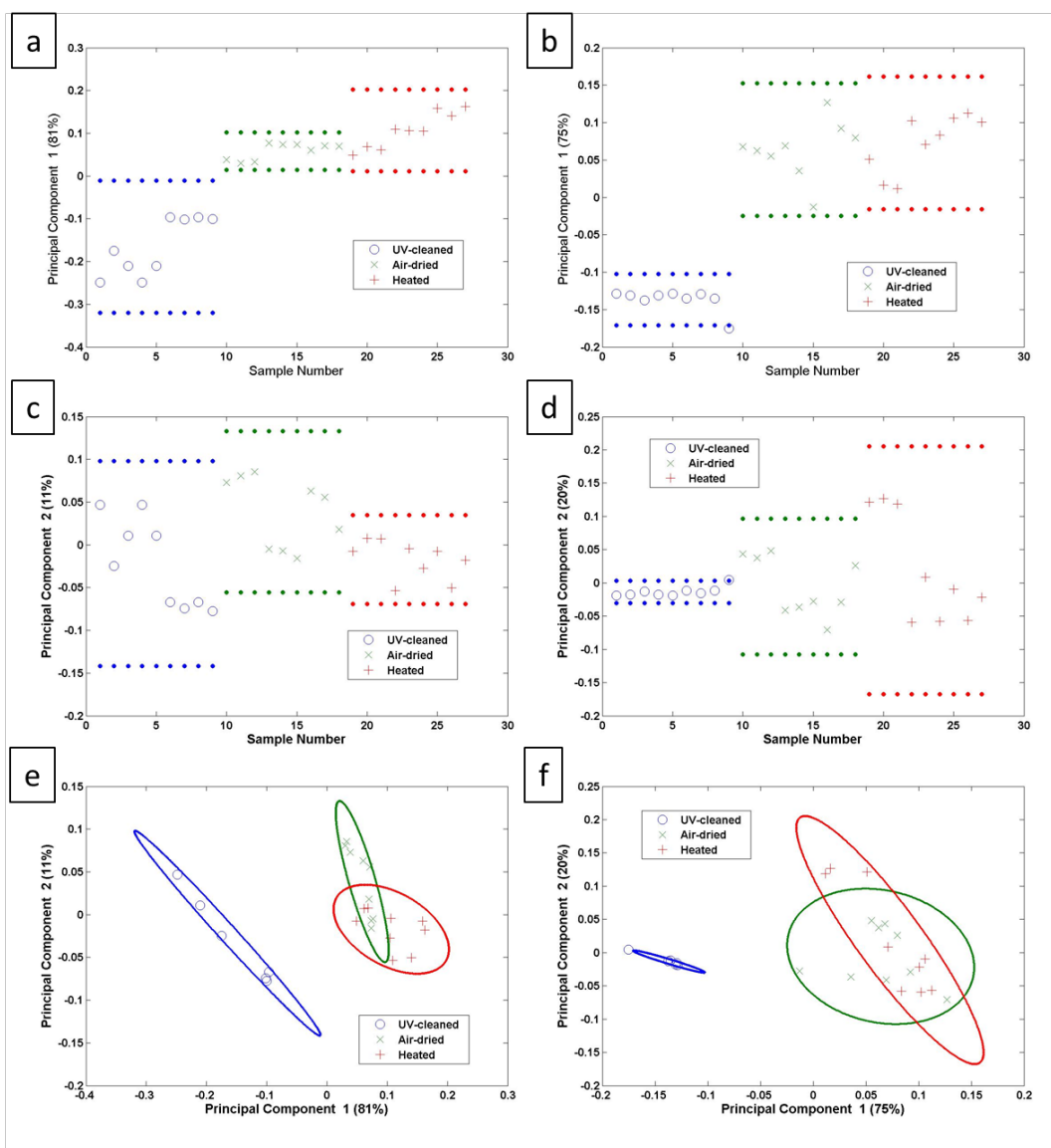


Figure 7.44: Scores of the PCA on the hand-selected peak list, PC1 (a) for the negative mode, (b) for the positive mode, PC2 (c) for the negative mode, (d) for the positive, PC1 versus PC2 (e) for the negative mode, (f) for the positive mode.

mode the negative loadings mass 17 is OH^- , mass 26 is CN^- , mass 63 COCl^- , mass 79 is CO_2Cl^- . In the positive mode for the positive loadings, mass 32 is CH_6N^+ , mass 40 is Ca^+ , mass 57 is CaOH^+ , mass 73 is $\text{C}_3\text{H}_7\text{N}_2^+$. For the negative loadings in the positive mode mass 23 is Na^+ , mass 29 is C_2H_5^+ , mass 55 is $\text{C}_3\text{H}_3\text{O}^+$. This explains why in for hand-selected peak list the PCA was unable to separate the air-dried samples from the heated samples. Indeed, the role and the presence of contaminations was neglected in the construction of the peak list. The PCA allows to draw similar conclusion than the direct analysis, but the also emphasizes the fact that the peak list should be build carefully.

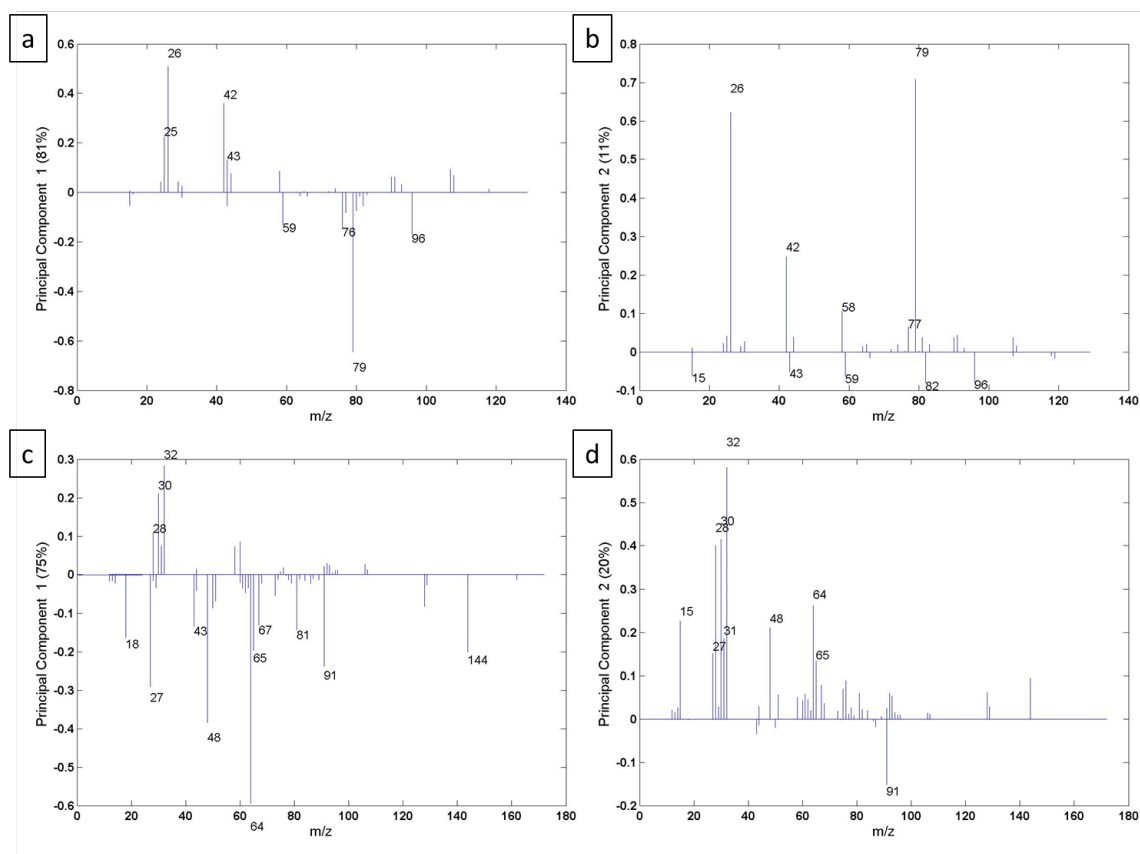


Figure 7.45: Loadings for the negative mode (a) of PC1, (b) of PC2, in the positive mode (c) of PC1 and (d) of PC2.

7.3.4 Conclusions on the model samples

In this part it was demonstrated that the molecule N-methylformamide is deposited on the titanium surfaces after dip-coating, but also that the molecule undergoes a chemical reaction degrading it. The potential chemical reaction was studied, by looking to the different reactive sites, carbon, nitrogen and oxygen as for the previous presented samples. The study of the carbon sites revealed that the molecule does not react with its carbon atoms on the titanium surface. The same conclusion could be made with the nitrogen sites. It was shown that the chemical reaction happens on the oxygen reactive sites. The goal of the preparation of those samples was also to see if a reaction mechanism could be observed as it was on the aluminum samples. The study revealed that the reaction mechanism on titanium is more complicated and that the molecule not only binds to the surface but also undergoes a degradation upon heating.

The PCA on the automatic generated peak lists leads to the same conclusions: deposition of the molecule, but also its degradation by heating. The direct analysis was preferred for simplicity. Comparing the PCA on the automatic generated peak list and the hand-selected peak list, it appears that the role of the contamination, and the degradation of the molecule was underestimated.

7.4 Conclusions

In this chapter, the interface between polyamide-6.6 and titanium was investigated in a similar approach than for polyamide-6.6 and aluminum. Indeed, similar samples were prepared:

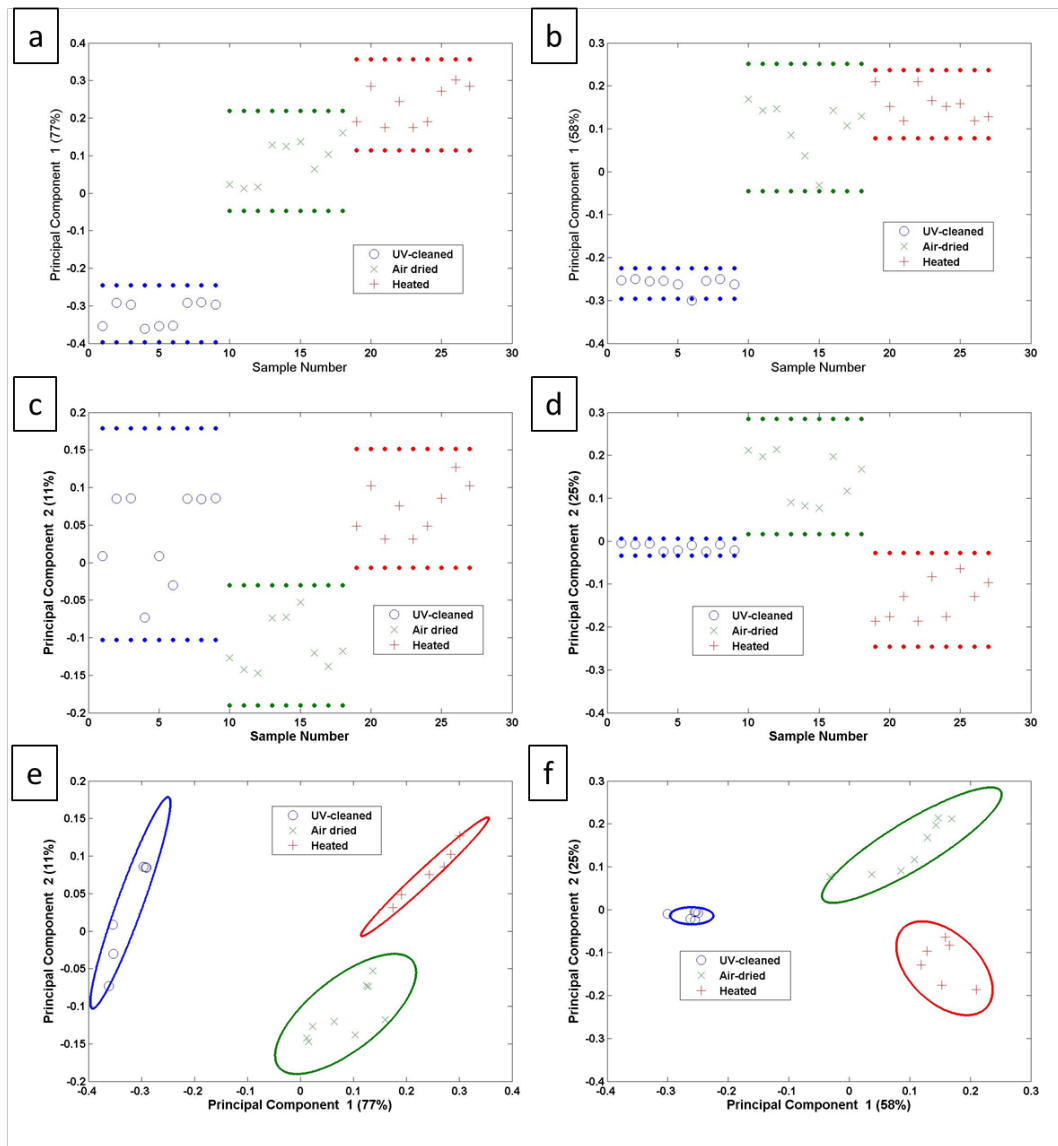


Figure 7.46: Scores of the PCA on the automatic generated peak list, PC1 (a) for the negative mode, (b) for the positive mode, PC2 (c) for the negative mode, (d) for the positive, PC1 versus PC2 (e) for the negative mode, (f) for the positive mode

welded samples, spin-coated samples and model samples. Adaptations had to be made on the welded samples, the breaking step leads to a mixed failure mode of adhesive and cohesive failure in the polymer. The dissolution step on these samples lead to a perfectly clean titanium surface without any trace of welding and polymer. Since there is an adhesive failure mode zone, the welded samples were analyzed directly after breaking them in this zone. This allows to conclude that the interaction between the polymer and the titanium is not as strong as the interaction between the polymer and the aluminum. Because of that the procedure of the spin-coated samples was also adapted and the dissolution step was shortened to the minimum. For the model samples no adaptation was needed.

For the welded samples, the adaptation of the process allowed to observe the presence of polyamide-6.6 in the weld. And as for the aluminum the separation line between the weld and the out of weld is a straight sharp line. As for the chemistry, titanium carbide is observed in

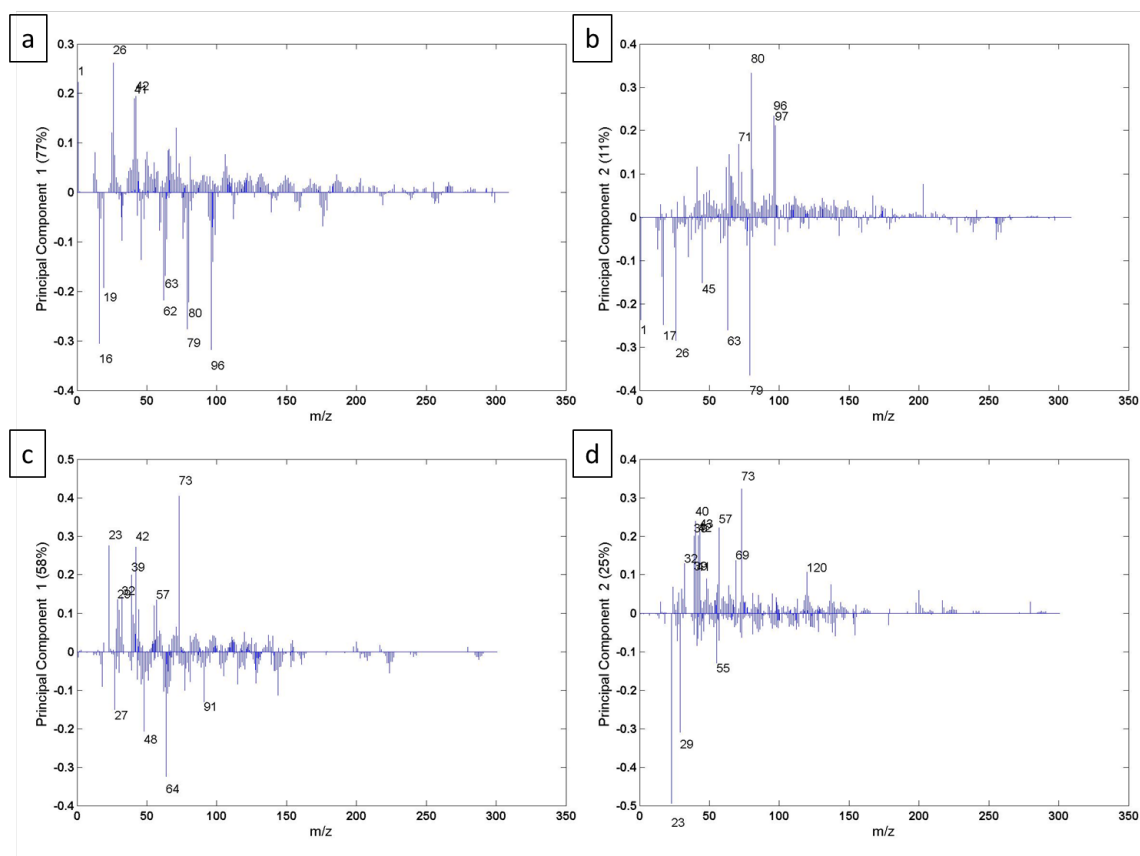


Figure 7.47: Loadings for the negative mode (a) of PC1, (b) of PC2, in the positive mode (c) of PC1 and (d) of PC2.

XPS and in ToF-SIMS in similar amounts out and in the weld. At the same time, no titanium nitride is observed in both XPS and ToF-SIMS. As for a reaction with the oxygen reactive site, the XPS data does not help to conclude anything. The ToF-SIMS data allows to conclude that a C-O-Ti bond is formed which is in good agreement with the literature found on the matter.

On the spin-coated samples in XPS, polyamide-6.6 was detected on all three samples, but in higher amounts in the weld. The high resolution spectra of the different regions showed no formation of titanium carbide, no titanium nitride, while the reaction with an oxygen site is not proven but not excluded. In the weld in the N 1s region an imine bond was observed, but not elsewhere. This is a hint to the reaction mechanism depicted in Figure 7.17. To analyze the ToF-SIMS data, two principal components analysis were performed, one in the negative mode and one in the positive mode. For both modes, three points out of the weld were excluded from the data set. In the negative mode, the results showed clearly that polyamide-6.6 is more present in the weld than elsewhere. It was also shown that no reaction forming titanium carbide and titanium nitride is observed. The PCA clearly shows that a C-O-Ti bond is formed at the interface, and in even higher amounts due to the welding. In the positive mode, the results were less clear, but still allowed to observe more polymer in the weld than elsewhere. As for the chemical reaction, the results point to the direction of a C-O-Ti bond but not as clearly as in the negative mode.

At last on the model samples, the molecule N-methylformamide is present in higher amounts on the air-dried samples than on the heated samples. For the reactivity, as for the previous samples, no reaction with the carbon nor the nitrogen was observed. Here also the same ob-

servation was made that the reaction happens with the oxygen to form a C-O-Ti bond. These samples were also prepared in order to investigate the reactivity of the metal and the reaction mechanism. Unfortunately, the results obtained did not allow to draw any conclusion on this matter.

The realization of PCA on the hand-selected peak list and the automatic generated peak list allowed to show that the conclusions are the same for all samples than the direct analysis (welded and model samples). The comparison between the PCA on both peak lists allowed to show that for the welded and spin-coated samples, the peak lists and the hypotheses used to build them were sound enough. For the model samples the role and the presence of contaminations was underestimated, and the PCA on the hand-selected peak list did not allow to discriminate the air-dried from the heated samples.

Chapter 8

Diffusion

This chapter presents the exploratory work done on diffusion during the welding process. To the best of our knowledge, a diffusion phenomenon has never been reported on hybrid laser welded systems. The samples were prepared by spin-coating a thin layer of polyamide-6.6 on mirror polished aluminum. Welding was performed on the sample by shining the laser on the aluminum plate backside. Depth profiling was performed with ToF-SIMS out of the weld and in the weld. The complete and detailed description of the samples' preparation strategy and preparation parameters can be found in Chapter 4 Materials and Methods.

8.1 Results and discussion

The depth profiling was performed in ToF-SIMS using a Cs^+ gun at 500 eV combined interlaced with the classical Bi_3^+ gun for analysis. The advantage to profile with a Cs^+ gun is its capacity to profile organics as well as metals [165], which is peculiarly adequate for hybrid materials analysis. In Figure 8.1, slices of the X-Z and the Y-Z planes of the total ion intensity are presented for both zones: out of weld and in the weld. The intensity varies from a high intensity zone to a low intensity zone quite abruptly. This transition zone corresponds to the transition from the polymer to the metal, so the interface. Generally depth profiles are not normalized, but here two different profiles will be compared. The normalization is then mandatory for comparison purposes. Different methods of normalization exist. To allow a better comparison between out and in the weld profiles, a total count normalization is the best suited. In addition, as the total intensity vary a lot in the profile, a point-to-point normalization was chosen. So, the profiles were normalized point-to-point on the total intensity.

The roughness of the mirror polished aluminum surface was measured (see Chapter 4 part 4.4.1) and gave a R_a value of 10 nm. The spin-coated polyamide layer thickness was also measured by doing a scratch and using profilometry (see Chapter 4 part 4.4.2) and was evaluated at 110 ± 20 nm. Knowing this, it is possible to attempt a depth calibration of the profiles, but the main difficulty is now to place correctly the interface on the measured data. Several methods to place the interface exist. The oldest and most commonly used, is to monitor specific ions, having a drop or an increase of intensity; the interface is than simply put at 50% of their intensity variation, which is classical for non-normalized brute profiles. Another possibility is to use two characteristic ions, one for each layer and possibly with high intensities and to put the interface at their crossing point. This methodology works only if the profile is normalized in such a way that both ions maximal values are identical. In our case, the crossing of the lines of CNO^- and AlO_2^- could be used to place the interface. The last possibility is to use the automatic interface searching of the SurfaceLab 7.0 software. A specific ion must be selected, the tool will then look for the highest variations of intensity and classify them by range. The variation of the

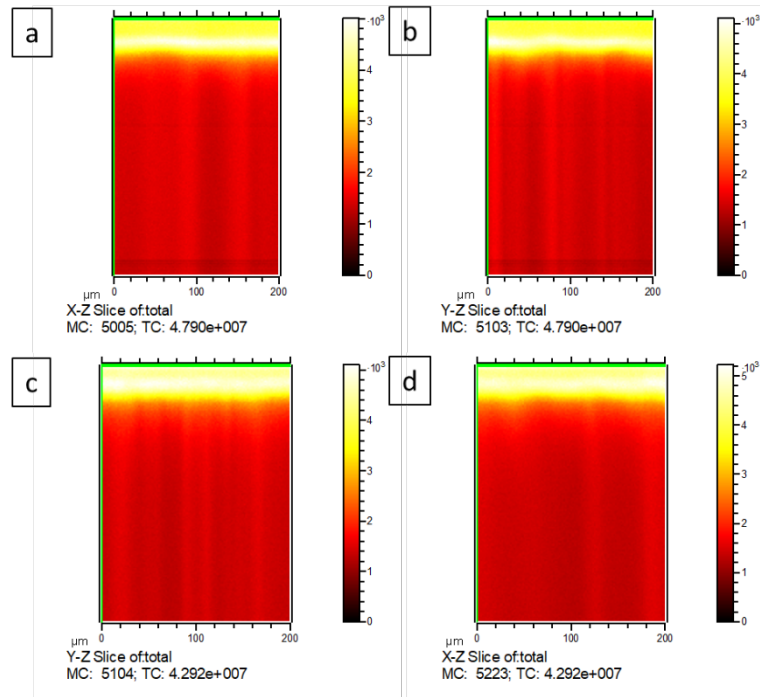


Figure 8.1: ToF-SIMS profile slices of the total intensity of the spectra in X-Z and Y-Z planes for (a) and (b) the out of weld, and (c) and (d) in the weld.

ion is modeled by an error function, allowing to derivate it into a Gaussian function. From the Gaussian function two points of 84%/16% intensity are calculated. If the ion's intensity increases (like the metal in the studied case), the second point of 84%/16% intensity will be chosen. If the ion's intensity decreases (like the polymer in the studied case), the first point of 16%/84% will be chosen as interface. In practice, the interface is then placed on the nearest measured point. The method showing the best results, meaning the best overlay of the profiles out and in the weld, was the automatic tool from the SurfaceLab 7.0 software. In this operation, choosing the ion to calibrate the interface is a crucial step. As can be observed in Figure 8.2, where the slices X-Z and Y-Z of CNO^- and AlO_2^- are depicted, the interface is not located at the same depth depending if polymer ions or metal ions are selected. Indeed, the intensity of the polymer ions decreases deeper than the intensity of the metal ions increases. Therefore it seems more reliable to place the interface using the metallic ions, even if the purpose is to study the diffusion of the metal in the polymer layer. Since the aluminum oxide presents a native oxide layer, the ion selected is an ion related to an oxide. The idea is to take a simple ion, and in this case there two possibilities were identified: AlO^- and AlO_2^- (other ions exist, but these ones are the most simple and common for aluminum). The choice was made in favor of AlO_2^- , because this ion is more intense than AlO^- . So using the interface tool and knowing the polymer layer thickness, the depth calibration could be done, and the interface placed at 110 nm. This depth calibration is valid till the interface is reached. The software puts automatically a constant sputter rate on the whole profile, but this is not the reality. The sputter rate is different from one material to another, and at interfaces, it can be assumed that the sputter rate evolves continuously from one material to another. However to make a complete depth scaling, the sputter rate of the native oxide should be measured separately, which is far beyond the purpose of this part. Nonetheless, the thickness of the oxide can be estimated, by making two assumptions. The first is that the sputter rate of the oxide is similar to the sputter rate of the pure metal. The second is that the

density is similar between the oxide and the metal. These assumptions allow to use Yamamura's formula to calculate the sputter rate of pure compounds [343]. Using this equation the estimated thickness of the metal profiled was of 14 nm for the out of weld and 13 nm in the weld. The thickness difference of the two zones is due to the fact that the sputter time of the different profiles is different. However, these values are rough estimations, and for presentation purposes they were not used to scale the profiles in Figure 8.3. For presentation purposes the sputter rate of the profiles was kept constant over the whole profiles, but after the interface the depth scaling was hidden, since it does not represent the reality.

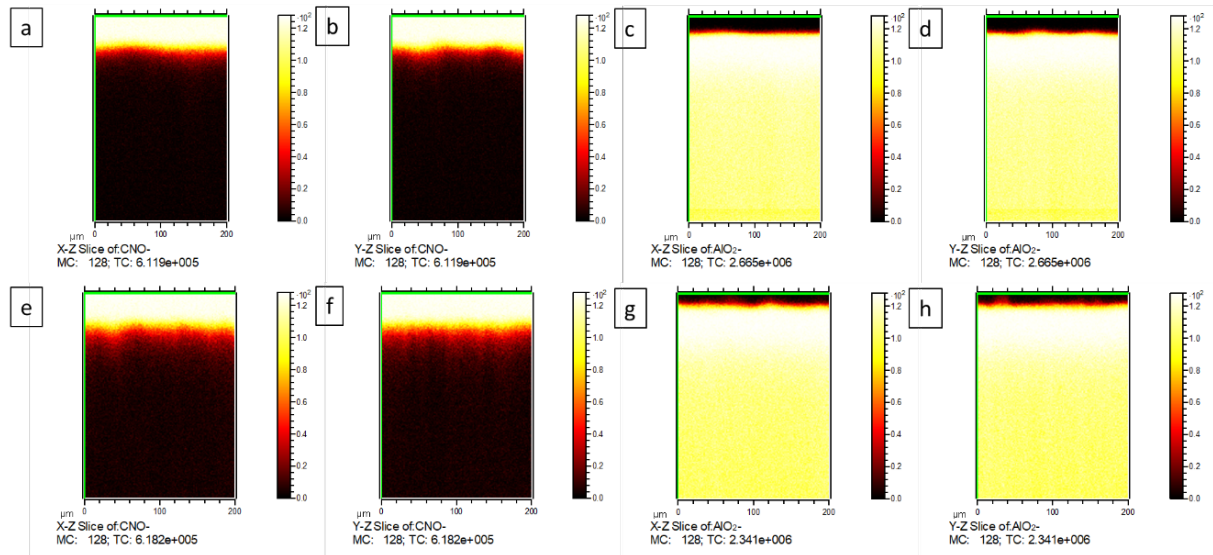


Figure 8.2: ToF-SIMS profile slices in X-Z and Y-Z plans of CNO^- (a) and (b) the out of weld, and (e) and (e) in the weld, and of AlO_2^- (c) and (d) out of the weld, and (g) and (h) in the weld.

Figure 8.3 (a) shows the profiles of both zones for two characteristic ions of the polymer: CNO^- and $\text{C}_2\text{H}_4\text{NO}^-$. The normalized intensities of the two ions are equivalent out and in the weld. Their intensities begin to diminish at the same depth, but do not diminish as fast. The intensity of these ions diminish faster in the out of weld than in the weld. The interpretation of polymer diffusion in the metal is rather improbable, because a long polymer chain has low probability to move freely in the crystalline structure of the aluminum. The reason might be because the polymer is more chemically bonded to the metal in the weld, which explains why more time is needed to sputter the polymer completely. In Figure 8.3 (b) the intensity of two characteristic ions of the metal are depicted: Al^- and AlO_2^- . These ions were chosen because they are quite intense, and are not in the same range of intensity for their plateau after the interface. These ions start to be detectable out of the weld at the same depth, around 30 nm. On the other hand, these ions are already detected from the beginning (the surface) in the weld. This clearly shows that a diffusion phenomenon occurs due to the welding. To evaluate the diffusion length a methodology must be chosen. Taking the distance where the intensity of the metal ions begins to increase is not relevant to evaluate the diffusion length, as it depends on the detection limit of this ion and the signal-to-noise ratio. Another choice would be to use the distance of mid height intensity of the ion. The distances of mid height intensity of the metal ions are summarized in Table 8.1. The mid-height intensity is reached sooner in the weld than out of it. The roughness parameter R_a has been used as standard deviation value for this distance estimation. Out the weld the value found is for both ions 95 nm, while in the weld the process gives 85 and 88 nm respectively. So the diffusion length obtained from the

interface to the distance mid-height intensity are respectively 15 ± 10 nm and 25 ± 10 nm for Al^- out and in the weld, and 15 ± 10 nm and 22 ± 10 nm for AlO_2^- out and in the weld. The diffusion out of the weld can be explained by the spin-coating process, where some metal can be dissolved, also some diffusion might be due to the welding process. Indeed, as seen in the previous chapters centered on the chemical bonding, out of weld, the heating has an impact, lower than in the weld, but still present. The last methodology to estimate the diffusion length is to fit the intensity curves with an exponential function:

$$I(x) = y_0 + Ae^{-\frac{x}{d}} \quad (8.1)$$

with $I(x)$ being the intensity of the ion, x the distance, y_0 and A fitting parameters, and d the diffusion parameter. The fitting was done using the Origin software, and the fitting parameters for both ions out and in the weld can be found in Table 8.2. The diffusion length D was obtained by subtracting the diffusion parameter d out and in the weld for the same ion, as follow:

$$D = d_{Weld} - d_{Out} \quad (8.2)$$

The diffusion length value obtained for Al^- is of 39 nm and 23 nm for AlO_2^- . The value obtained for AlO_2^- is very similar than for the first method (22 nm). The difference between the two diffusion length can be explained because the increase of Al^- out of the weld is slower than for AlO_2^- even if they begin to increase at quasi the same distance. This is due to the oxide layer on the metal before reaching the pure bulk aluminum. As the interface is placed using AlO_2^- , the fitting is more adequate for this ion and this value should be taken.

Table 8.1: depth in nm at mid-height intensity for the ions of the aluminum studied.

Ions	AlO_2^-	Diffusion length	Al^-	Diffusion length
Out of Weld	95 ± 10 nm	$15 \pm$ nm	95 ± 10 nm	$15 \pm$ nm
Weld	85 ± 10 nm	$25 \pm$ nm	88 ± 10 nm	$22 \pm$ nm

Table 8.2: fitting parameters out and in the weld for the curves of intensity of Al^- and AlO_2^- .

	y_0	A	$1/d$	d	R^2	Diffusion legnth
Al^- Out	0.00967	-0.02329	0.01659	60 ± 0.0008 nm	90%	/
Al^- Weld	0.00928	-0.01180	0.01010	99 ± 0.0004 nm	93%	39 ± 10 nm
AlO_2^- Out	0.17711	-0.40124	0.01514	66 ± 0.0006 nm	93%	/
AlO_2^- Weld	0.17648	-0.23080	0.01120	89 ± 0.0005 nm	92%	23 ± 10 nm

8.2 Conclusion

As a conclusion, these experiments showed the existence of a diffusion effect due to the welding. An estimate of this diffusion has been made with two different methodologies and is of 22 ± 10 nm or 23 ± 10 nm in the weld. Even if these results are encouraging, the measurement should be repeated to validate the results. Furthermore, the diffusion phenomena should be investigated on other laser welded material combinations. Even if the proof of concept of diffusion effect is now measured and established, its impact on the adhesion, and by extension on the mechanical resistance is not understood at all, and should be investigated even further.

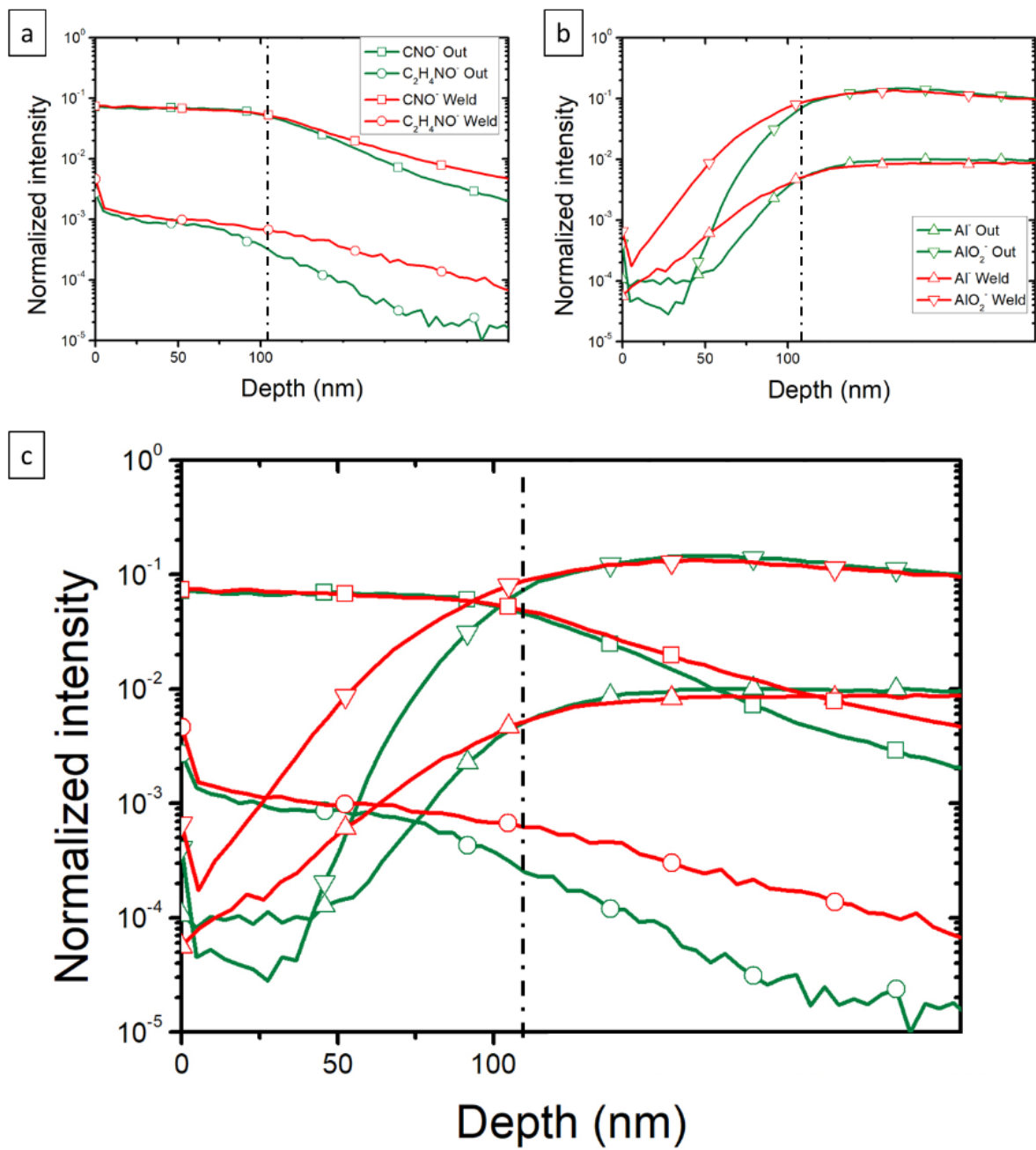


Figure 8.3: ToF-SIMS depth profiles (a) for characteristic polymer ions, (b) for characteristic aluminum ions and (c) an overlay of both types of ions using the same legend.

Chapter 9

Conclusions

Several aspects of the adhesion between a polymer and a metal after laser welding were investigated in this PhD thesis, conducted within the framework of the M.Era-Net project named “LASERSTAMP” (Laser and Surface Treatment Assisted Metal Polymer assembly). First, in chapter 2 a review was given on the assembling methods with a deep focus on laser welding at the end. In chapter 3 a state of the art of adhesion science with a focus on hybrid assemblies was then proposed.

From the two chapters of literature review, two major issues were identified: understanding the root causes of adhesion and accessing the interface. These were the two main objectives of this work. To explain adhesion four phenomena are used: mechanical interlocking, chemical bonding, diffusion and electrostatic attraction. In this work, mechanical interlocking was not considered, because the question is presently quite well developed and because it was excluded from the Laser-STAMP project. Electrostatic attraction is generally described as a secondary effect. Moreover, in our case where an insulating polymer is welded to a metal, the experimental characterization of this phenomenon is extremely difficult. Some attempts were made in this direction, but were not successful and the results are not presented here. The two last phenomena are chemical bonding and diffusion. Diffusion was never characterized in the case of laser welding and seldom observed in hybrid assemblies. Chemical bonding in hybrid assemblies is well studied in general, but in the specific case of laser welding, this work represents the first attempt to characterize this phenomenon. Several options were found in literature to achieve that goal. The first consists in depositing a small molecule mimicking the reactive part of the organic molecule on the surface and characterizing the surface covered with this molecule. A second possibility is to deposit a thin film, generally by spin-coating, then to dissolve this film to characterize the interface. In the case of larger and thicker samples, simply breaking the samples can be a solution, but this is only working if the samples break with an adhesive failure mode. Hence characterizing chemical bonding at the interface is not a trivial question.

The materials and methods are summarized in chapter 4. The sample preparation is detailed from the strategy of preparation and analysis to the analysis parameters used.

Chapter 5 is centered on the effect of surface pretreatment on the weld. Throughout the Laser-STAMP project different surface pretreatment were tested: laser ablation, anodization, plasma treatment and silanization. Here only the results on laser ablation were presented, because they are the most complete but also because they exhibit the best mechanical properties. Laser ablation was applied on both aluminum and titanium. The results were similar on both metals. The shear load increases linearly with the joint area. The joint area can be increased by decreasing the thermal contact resistance (TCR). The TCR depends on several parameters: the oxide thickness, the roughness and the chemical nature of the oxidized layer. The oxide thickness and the roughness are the most determining factors, and for both of them, the lower

they are the higher the joint area hence higher shear load. The chemical nature, meaning the ratio of oxide/hydroxide of the oxidized layer seems also to be playing a role in the thermal diffusion. The samples presenting a purer oxide (so less hydroxide) also presented the highest joint area and so the highest shear load. The "chemical homogeneity" could be a factor to favor the thermal transfer. Even if these results are interesting, the cristallographic state of the different layers was not investigated and this could help to better understand the whole thermal transfer mechanism.

The two following chapters investigated the existence and the nature of a chemical bond at the interface between polyamide-6.6 and aluminum (chapter 6) then titanium (chapter 7).

For aluminum four different types of samples were prepared. First welded samples and ablated/welded samples were prepared. To prepare them, aluminum sheets were laser welded to the polyamide plates. In the case of ablated/welded samples, the aluminum sheets were laser ablated prior to welding. The main issue on these samples is that they are quite thick (5 mm), which makes the access to the interface quite delicate. Therefore a new methodology was proposed and successfully carried out. The idea is first to break the assembly, which leads to a cohesive failure mode in the polymer leaving a thick polymer residue on the metal surface. This residue is then dissolved using an adequate solvent, in our case 2,2,2-trifluoroethanol. The idea of breaking the samples or to dissolve them has already been performed several times by other research groups, but the novelty in this work resides in the combination of both processes to access the interface. The third type is the spin-coated samples, where a thin polyamide-6.6 film is spin-coated on mirror polished aluminum sheets. The thin film was then welded. The interface was once again reached through a dissolution step. The fourth and last type of samples is the model samples, where a small molecule mimicking the reactive part of the polymer, N-methylformamide, is dip-coated onto aluminum sheets. Some of these samples were heated to simulate the welding process. The analysis of all the samples showed that more polyamide-6.6 or N-methylformamide was detected on the welded or heated zones. On the welded, ablated/welded and the spin-coated samples, the images done in ToF-SIMS show that the separation between the weld and the out of weld is a sharp line. Polyamide-6.6 exhibits three potential reaction sites: carbon, nitrogen and oxygen sites. All the measurements lead to the same conclusion: the bonding occurs primarily through the formation of C-O-Al bonds at the interface between the metal and the polymer. Studying the reactivity of the metal was only possible on the spin-coated and model samples. The results indicate that the polymer reacts with the surface free hydroxyl groups of the aluminum surface.

In the case of titanium, only three types of samples were studied, inspired from the work done previously on aluminum: welded samples, spin-coated and model samples. First welded samples were prepared, similarly to the aluminum welded samples with a titanium sheet laser welded to a polyamide-6.6 plate. The samples break following a mixed failure mode: adhesive and cohesive in the polymer. The dissolution step was tried anyway, but proved to be detrimental to the interface analysis, as all the polymer traces got washed away during the process. Henceforth the samples were analyzed in the adhesive failure zone directly after breaking them. The results show that polymer is present in the weld after the fracture. A potential chemical reaction was investigated. A titanium carbide bond exists prior to welding and does not seem to be affected by the welding process. The data do not show a reaction with the nitrogen reactive site. On the contrary the data show the formation of a C-O-Ti bond after welding, which is in good agreement with the literature found on the matter. The second type of samples was the spin-coated samples. Like aluminum, a thin polyamide-6.6 film was spin-coated on mirror polished titanium sheets. Both the XPS and the ToF-SIMS data show similar results: (1) more polymer is detected in the weld and (2) no formation of titanium carbide nor titanium nitride was observed. The data also pointed to a reaction forming C-O-Ti bonds at the polymer/metal interface. Furthermore,

the XPS data suggested the presence of an imine bond after welding, which fits the formation of a C-O-Ti bond model proposed. The last type of samples are the model samples, where, as for aluminum a small molecule, N-methylformamide, was dip coated onto titanium sheets. The formation of a C-O-Ti bond is also observed on the model samples, but the data seem to indicate that the molecule not only binds to the surface but is also degraded during the heating process. This did not allow to get further information on the bonding mechanism as expected.

PCA were performed for all the samples of chapters 5 and 6 in both polarities, using a hand-selected peak list and an automatic generated peak list. By comparing the results of the two peak lists, they are generally similar and show the same results. This implies that the hypotheses used to build the hand-selected peak list were quite accurate. These hypotheses were done upon the results of the analysis of the XPS data, showing the presence of the aluminum or titanium and polyamide-6.6 or N-methylformamide. The only weakness detected is the role of the contaminations of the different samples and therefore their impact in the differentiation of the different samples was a bit neglected. Nonetheless, the results point to the same direction as the direct analysis, which was preferred. A direct analysis might be more user dependent, but as the data were quite clear to begin with, the need for PCA was low. The only samples where it was surely needed were the titanium spin-coated samples, and the PCA revealed that some of the out of weld samples presented problems, as they were similar to the weld, explaining the failure of the direct analysis.

Chapter 8 summarizes the work done on the diffusion phenomenon. This is an exploratory work, as diffusion has never been studied in hybrid laser welded assemblies. The samples were prepared by spin-coating a thin layer of polyamide-6.6 on mirror polished aluminum sheets. They were then welded. Depth profiles were subsequently performed in and out of the weld by ToF-SIMS. The results are promising, as diffusion of aluminum was observed in the polyamide-6.6 layer in the weld. The diffusion length was estimated to be about 25 ± 10 nm. These results are extremely encouraging, but need more investigation. Unfortunately, the impact of this diffusion on the adhesion and the mechanical resistance could not be evidenced yet.

The objectives of this thesis were to access the interface of thick samples and to investigate the chemical bond, its existence, its nature and its formation mechanism in laser welded aluminum/polyamide-6.6 and titanium/polyamide-6.6 systems. All the goals were hit. Indeed a new methodology, breaking and dissolving of thicker samples, was proposed and carried out successfully. The methodology was adapted to the failure mode, mixed or cohesive, by translating it from the aluminum to the titanium samples. Other samples were also prepared to support and complete the results obtained on the welded samples: the spin-coated samples and the model samples. They all together allowed to understand that for both combinations the bond is of C-O-M (M=Al, Ti) nature. The bond is formed by the reaction of the carboxyl group of the polymer with a free hydroxyl group at the top surface of the metal, by releasing water and forming an imine bond. In addition to these results, the surface of laser ablated samples was investigated with XPS, pointing to the direction of an impact of the chemical composition of the oxidized layer on the thermal conduction, tuning the joint area and so the shear load. This impact is secondary compared to the roughness or the thickness of the oxidized layer. At last a diffusion phenomenon was observed and characterized in the weld, but its impact is still to be investigated.

As perspectives, several axes could be explored. Since the main part of this work is centered on interfacial chemical binding, other material combinations should be explored. Several polymers are eligible, one of them would be polyetheretherketone (PEEK). In terms of chemistry and reactive sites, it would be interesting to test polymers presenting other types of reactive sites (no oxygen reactive site), such as polyethylene (PE), polystyrene (PS), or polyacrylonitrile (PAN). Other metals can also be tested, such as steel and stainless steel, but also different alloys of

aluminum and titanium. Another interesting axis would be to investigate more thoroughly the diffusion phenomenon, in order to better understand its impact on the adhesion but more generally on the weld. For instance, when breaking the assemblies, they fail at least partially in the cohesive mode. In this cases the weak point is in the polymer base material. The origin of this weak point is not yet fully understood and needs to be investigated in order to further increase the mechanical resistance of the assemblies and increase the attractiveness of laser welding even further. A third axis of development would be to probe the electrostatic effect at the interface. The main issue is that the polymer used in our assemblies is an electrical insulator. However, in future works it could be easily tackled by using conductive polymers, such as PEEK, or the more commonly known poly(3,4-ethylenedioxythiophene), or polystyrene sulfonate (PEDOT:PSS). The interfaces of such polymers with other materials (metals generally) are studied to get the best interfacial electrical conductivity, and very rarely with an adhesion purpose. The development of an experimental method to characterize this electrical contact between an insulator and a metal is at the moment quite difficult and would represent a major breakthrough. Classical electrical contact measurements are not possible and UPS is only possible on extremely thin films (about ten nanometers) deposited on metals. This could also be studied by simulation and theoretical calculations. Simulation and theoretical calculations could be attempted for a broader approach of adhesion, which might help to disentangle how the different phenomena interfere with one another. For the moment the adhesion phenomena are studied separately but it could represent an interesting development and help to create a more complete model to describe adhesion. The work could then be used not only for laser welded samples, but also for adhesives and other assembling methods. At last, one of the main questions and difficulty encountered during this work, was to differentiate recombination effects and chemical bonding with the hybrid ions in the ToF-SIMS data. Experimental works dedicated to understanding recombination effects in the SIMS community are still missing. This may not come as a surprise as the discrimination between the two processes is extremely difficult, as it was evidenced several times in this work.


Appendix to surface pretreatments

Laser ablation on aluminum

Full article "Influence of aluminum laser ablation on interfacial thermal transfer and joint quality of laser welded aluminum-polyamide assemblies" published in *Coatings* in 2019

Article

Influence of Aluminum Laser Ablation on Interfacial Thermal Transfer and Joint Quality of Laser Welded Aluminum–Polyamide Assemblies

Adham Al-Sayyad ^{1,*} , Julien Bardon ², Pierre Hirchenhahn ³, Regis Vaudémont ², Laurent Houssiau ³ and Peter Plapper ¹

¹ Faculty of Science, Technology and Communication (FSTC), University of Luxembourg, L1359 Luxembourg, Luxembourg; peter.plapper@uni.lu

² Materials Research and Technology (MRT), Luxembourg Institute of Science and Technology, L4362 Esch-sur-Alzette, Luxembourg; julien.bardon@list.lu (J.B.); regis.vaudemont@list.lu (R.V.)

³ Namur Institute of Structured Materials (NISM), LISE laboratory, University of Namur, 5000 Namur, Belgium; pierre.hirchenhahn@unamur.be (P.H.); laurent.houssiau@unamur.be (L.H.)

* Correspondence: adham.alsayyad@uni.lu; Tel.: +352-466-644-6034

Received: 29 September 2019; Accepted: 12 November 2019; Published: 19 November 2019



Abstract: Laser assisted metal–polymer joining (LAMP) is a novel assembly process for the development of hybrid lightweight products with customized properties. It was already demonstrated that laser ablation of aluminum alloy Al1050 (Al) prior to joining with polyamide 6.6 (PA) has significant influence on the joint quality, manifested in the joint area. However, profound understanding of the factors affecting the joint quality was missing. This work investigates the effects of laser ablation on the surface properties of Al, discusses their corresponding impact on the interfacial thermal transfer between the joining partners, and evaluates their effects on the joint quality. Samples ablated with different parameters, resulting in a range from low- to high-quality joints, were selected, and their surface properties were analyzed by using 2D profilometry, X-ray photoelectron spectroscopy (XPS), scanning electron microscope (SEM), and energy-dispersive X-ray spectroscopy (EDX). In order to analyze the effects of laser ablation parameters on the interfacial thermal transfer between metal and polymer, a model two-layered system was analyzed, using laser flash analysis (LFA), and the thermal contact resistance (TCR) was quantified. Results indicate a strong influence of laser-ablation parameters on the surface structural and morphological properties, influencing the thermal transfer during the laser welding process, thus affecting the joint quality and its resistance to shear load.

Keywords: laser welding; metal–polymer; laser ablation; thermal contact resistance

1. Introduction

Joining metals to polymers has gained prominent interest among researchers and industries because of its ability to produce lightweight hybrid structures with tailored properties. Conventional metal–polymer joining methods, such as adhesive bonding, mechanical fastening, friction stir welding, and ultrasonic joining, have their drawbacks, as they either require high processing time, involve hazardous chemicals, cause excessive tool wear, involve geometrical constraints, or require the addition of weight to the component. The thermal joining of metals to polymers is challenging because of the significant difference of the thermal properties and melting temperatures of both materials. However, Laser-Assisted Metal–Polymer joining (LAMP) provides the ability to precisely control the energy input into the materials, giving the opportunity to thoroughly melt the polymer at the interface of the joint, while, at the same time, avoiding its degradation. In addition, LAMP has its advantages over

conventional joining methods in being rapid, autogenous, and a non-contact process that offers design flexibility, along with the ability to produce miniaturized joints and minimize overlapping dimensions.

So far, research in LAMP has shown the reliability of the laser welding process in a variety of material combinations [1–4]. Preliminary surface treatments before welding have shown a significant impact on the joint strength and quality. Researchers [3–12] reported the effects of several surface pretreatments on LAMP, including mechanical, chemical, electrochemical, and laser pretreatments for metals, as well as plasma and UV ozone pretreatment for polymers. Similar to adhesive bonding, two main factors were reported in the literature as affecting the LAMP joint properties: mechanical interlocking and physicochemical bonding. However, although LAMP is a thermal joining process, the effect of surface pretreatments on the thermal transfer between the joining partners during the laser welding process, and on the joint quality, has not been investigated.

Increased surface roughness has shown to have a positive effect on enhancing LAMP joint strength by increasing mechanical interlocking effects [9,10,12]. Furthermore, an increased surface roughness might increase the surface wettability of treated metal, which in turns allows a better wetting of the molten polymer during the laser welding process. However, an increase in surface roughness results in an increase in the thermal contact resistance (TCR) across the interface of the two solid materials in contact [13,14]. When two solid surfaces come into contact, the flow of heat across the interface is mainly governed by solid-to-solid conduction at the points of contact, and conduction through the fluid occupying the noncontact area, resulting in restrictions to the heat flow [15]. Yovanovich [16] summarizes forty years of research in the field of thermal contact resistance, and in particular introduces the development of a geometric–mechanical–thermal model called the Cooper–Mikic–Yovanovich (CMY) model to predict the thermal contact resistance of conforming rough surfaces.

Researchers [17–22] developed several theoretical models to calculate thermal contact resistance. Three mechanical models—elastic, plastic, or elastic–plastic deformation of the surface asperities—were considered, assuming that surface asperities follow Gaussian height distributions about a mean plane passing through each surface, and assuming that surface asperities are randomly distributed over the apparent contact area. Yovanovich [23] summarized the TCR model developed by Cooper et al. [20] and proposed compact expression to calculate the TCR between two nominally flat solid surfaces (1 and 2) in contact assuming plastic deformation of asperities as given by Equation (1). Given that σ_1 , m_1 , k_1 are properties of material 1, and σ_2 , m_2 , k_2 are properties of material 2, $\sigma = (\sigma_1^2 + \sigma_2^2)^{0.5}$ is the effective root mean square roughness (RMS) so that $\sigma_{1,2} = \sqrt{\frac{1}{L} \int_0^L y^2(x) dx}$, where L is the profile traced length; $m = (m_1^2 + m_2^2)^{0.5}$ is the effective mean asperity slope, and $m_{1,2} = \frac{1}{L} \int_0^L \left| \frac{dy(x)}{dx} \right| dx$ is the mean absolute asperity slope. H is the microhardness of the softer material, P is the applied pressure, and k_h is the harmonic mean thermal conductivity at the interface where $k_h = 2k_1k_2/(k_1 + k_2)$. It is clear from Equation (1), which can be utilized in describing the TCR between metal and polymer in their solid state, prior to the laser joining process [24], that TCR has a proportional relation to the ratio of the root mean square roughness σ to the asperities slope, m .

$$TCR = \frac{0.8\sigma}{mk_h} \left(\frac{H}{P} \right)^{0.95} \quad (1)$$

Laser ablation was proven to be an effective and rapid surface pretreatment technique for aluminum (Al 1050) to enhance the bonding strength when welded with polyamide (PA 6.6) [1,5,25]. It was already demonstrated that laser-ablation parameters have a strong impact on the joint quality, demonstrated by the joint area and its resistance to failure, but no effect on the joint strength, i.e., its stress to failure [5]. Results have shown the prominence of cohesive failure mode indicating that interfacial adhesion is not the only factor influencing the joint quality. Preliminary results showed that the joint resistance to failure is influenced by the topography of the ablated aluminum surface, in particular by topography parameters representing the density of peaks on the surface. From the knowledge of TCR models quoted before, it is therefore hypothesized that laser-ablation parameters

affect the thermal transfer between the joining partners, which would reflect on the joint area and quality, impacting its resistance to shear load. This research aims at understanding the effects of surface properties on the interfacial thermal transfer between laser ablated Al 1050 joined to PA 6.6 using laser-beam welding. It correlates the influence of surface topography and the chemistry of aluminum modified layer to the TCR and reports their consecutive effects on the joint quality. To the best of the authors' knowledge, this is the first time that the prominence of the TCR for the welding quality is evidenced in LAMP.

2. Experimental Method

2.1. Materials

In those experiments, 0.5 mm thick EN-AW1050A aluminum (Al) in half-hard state, with geometry of 30 mm × 60 mm, and 4 mm thick polyamide 6.6 (PA) purchased from Dutec (Ahaus, Germany), with the dimensions of 25 mm × 75 mm were used. Prior to the joining process, Al samples were prepared by laser ablation, and PA samples were wiped with ethanol, to remove potential surface contaminants.

2.2. Laser Ablation

Al surfaces were ablated, using a short-pulsed (ns) Nd:YVO₄ laser (TruMark 6130 from TRUMPF, Ditzingen, Germany), with a wavelength of 1064 nm and spot size of 45 μm. Al-Sayyad et al. [5] already demonstrated that, from seven different ablation parameters, namely pulse frequency (f_p), beam guidance speed (V), lines, focal position, Al rolling direction, ablation hatching orientation, and laser beam power percentage, only f_p and V had a significant influence on laser welded Al-PA joints' resistance to shear failure. This research focuses on further evaluating the effects of those significant laser-ablation conditions, as shown in Table 1, on Al surface properties, thermal transfer across the joining partners, and corresponding joint quality. Based on previous investigations [5], six ablation conditions (see Table 1) were chosen for this research, as they resulted in a wide range of joint quality. Since ablation was performed with a q-switched laser, increasing pulse frequency results in decreasing the peak pulse power and fluence of the laser beam. However, overlap ratio between consecutive laser pulses (see Figure 1) depends on both pulse frequency and beam guidance speed, as described by Equation (2).

$$O (\%) = 100 \times \left(1 - \frac{V \left(\frac{mm}{s} \right)}{f_p (\text{Hz}) \times O (mm)} \right) \quad (2)$$

Table 1. Laser-ablation parameters and attributes.

Parameter	Frequency (kHz)	Speed (mm/s)	Peak Pulse Power (kW)	Fluence (J/cm ²)	Overlap Ratio (%)
P1	85	250	11	15.2	93
P2	40	1000	35	28.6	44
P3	70	1000	15	17.9	68
P4	85	1750	11	15.2	54
P5	120	1750	5	9.12	68
P5-95%	Same as Al_5 but with 95% power		4.75	8.66	68

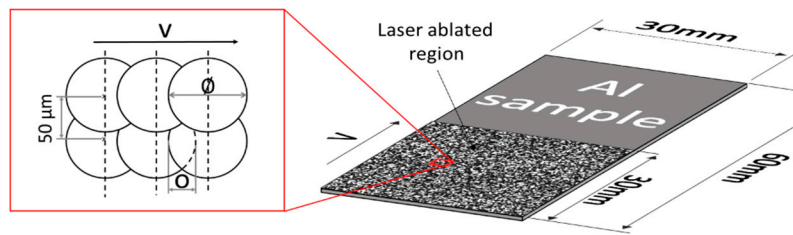


Figure 1. Schematic drawing illustrating six laser pulses irradiating Al surface during laser-ablation process and demonstrating laser pulses overlap ratio (O) between two consecutive pulses.

2.3. Laser-Beam Welding

Laser welding was performed with a fiber laser (TruFiber 400 from TRUMPF), with a wavelength of 1070 nm and a calculated spot size of 58 μm, irradiated on the Al surface after clamping the parts in an overlap configuration, as shown in Figure 2. A peak pulse power of 400 W was modulated with a pulse frequency of 25 kHz and pulse duration of 35 μs. The laser beam followed a spiral trajectory, with a feed velocity (v_f) of 88.8 mm/s. Part of the irradiated laser-beam energy gets absorbed, converted to heat energy, conducted through the Al, and transferred to melt PA, thereby joining Al to PA. However, heat transfer across the interface depends on the TCR. Figure 3 shows a simplified illustration of the hypothesized thermal-energy transfer of the irradiated laser beam across the interface in the case of (a) ideal flat surfaces and (b) across rough ablated Al surfaces in contact with smooth PA modeling “real life” conditions. The presence of surface asperities at the interface causes the thermal transfer by conduction to take place mostly at the points of contact [16], thereby increasing TCR and reducing the thermal energy transfer across the interface. Single lap shear tests were performed by using Z010 from Zwick/Roell (Ulm, Germany). Samples were clamped in a vertical alignment, with a jaw-to-jaw distance of 75 mm. The crosshead pulling speed was set at 2.21 mm/min.

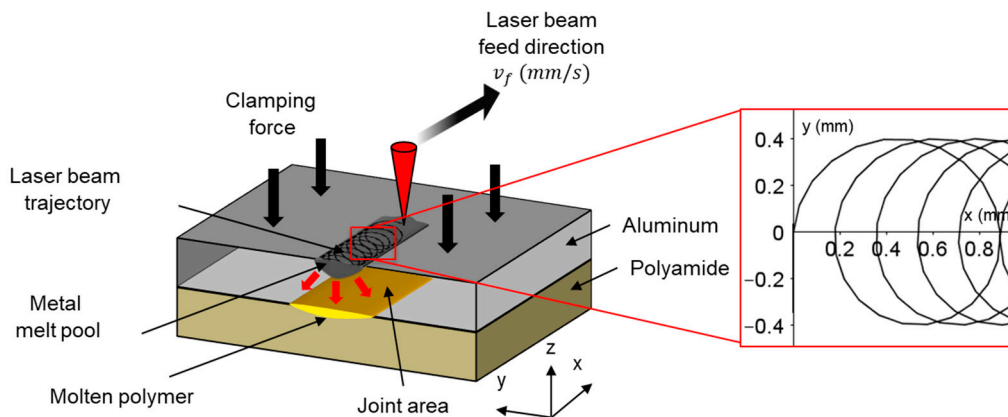


Figure 2. Schematic drawing of laser-beam-welding setup.

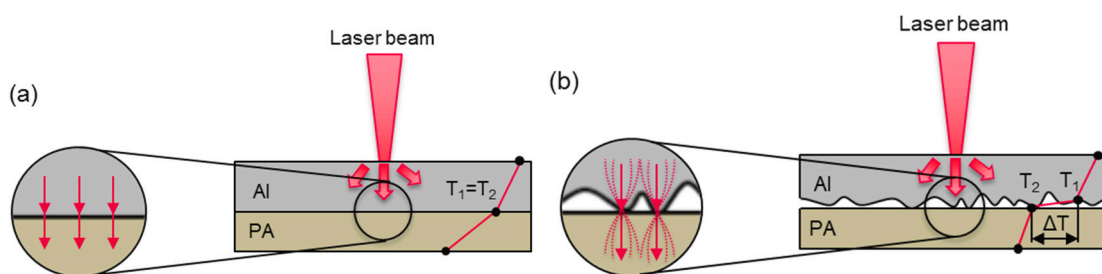


Figure 3. Schematic of hypothesized interfacial thermal-energy transfer during laser-welding process across (a) ideally flat conforming surfaces and (b) ablated aluminum surfaces in contact with smooth polyamide.

2.4. Joint-Area Assessment

In order to quantify the joint area, a dedicated experimental approach was developed. First, macroscopic images of the joint interface after failure were obtained by using a digital FUJIFILM X-Pro2 camera (Tokyo, Japan). Next, the dimensions of a single pixel were measured, using GIMP software (2.10), by correlating to a predefined scale positioned on the sample close to the weld zone. Then, the coordinates outlining the joint area were allocated, and the joint area was measured by counting the number of pixels and correlating them to the measured pixel dimension. Polarized and stitched microscopic images of the joint area were used to confirm the measurements.

2.5. X-Ray Photoelectron Spectroscopy (XPS)

The atomic composition of treated surfaces and its chemical-bonding states were investigated, using a K-alpha from Thermo Scientific (Waltham, MA, USA). An X-ray beam (Al K α , 1486.6 eV) with a spot size of 300 μm was used in the analysis. Six regions of 1 cm^2 area were ablated on an Al sample, each region with different ablation condition (see Table 1). Six points per ablated region were investigated by measuring a survey spectrum (3 scans, 200 eV energy pass) and high-resolution spectra for the regions of Al 2p, O 1s, and C 1s (20 scans, 20 eV pass energy) atoms.

2.6. Scanning Electron Microscope (SEM)

A pressure-controlled FEI Quanta FEG 200 scanning electron microscope (SEM) from FEI Company (Hillsboro, OR, USA) was used in secondary electron mode, in order to get information about the samples' morphology. The acceleration voltage was generated at 15 kV. Six regions of 1 cm^2 area were ablated on an Al sample. The sample conductivity was enhanced by depositing a fine layer of conductive lacquer in contact with the untreated aluminum part of the sample. The area that was coated by this lacquer was not observed.

2.7. Energy-Dispersive X-Ray Spectroscopy (EDX)

EDX spectra were obtained in the SEM with an EDAX GENESIS XM 4i energy-dispersive X-ray spectrometer (EDX, Mahwah, NJ, USA). The analytical distance used for X-ray measurement was 10 mm, which corresponded to a take-off angle of 35°. The measurement was performed at a pressure of 3×10^{-4} Pa (water vapor) and an accelerating voltage of 15 kV. A $0.15 \times 0.13 \text{ mm}^2$ area was scanned and an average spectrum was obtained on the whole area. The elemental composition is calculated from this spectrum, assuming the sample is only composed of aluminum, oxygen, and carbon. This assumption is made after observing the whole EDX spectra and identifying the peaks exhibiting a significant height.

2.8. Surface Topography

Surface profile was obtained for the ablated Al by means of a P17 (KLA Tencor, Milpitas, CA, USA) mechanical profilometer equipment with a scanning load of 0.5 mg. Measurements were performed by using acquisition rate of 50 Hz, a scanning speed of 20 $\mu\text{m/s}$, and a scanning length of 2 mm, resulting in a scanning time of 100 s and 5000 measured points. Six regions of 1 cm^2 area were ablated on an Al sample. Four measurements were performed on each region; two along the axis of applied pulling forces during shear testing, and two perpendicular to it. The roughness profile was calculated with a cut-off length of 0.25 mm. Roughness parameters R_q (average quadratic height or "root-mean-square" roughness) and R_dq (average quadratic slope) were calculated following ISO 4287 [26], and their average value is reported.

Similar measurements performed on PA sample show that its average quadratic height (R_q) is close to 40 nm. Raw or ablated aluminum exhibit R_q values close to 400 nm or in the range of 0.9–6 μm , respectively. It shows that the PA is very smooth compared to ablated aluminum and that the schematic drawing in Figure 3b is a reasonable representation of "real life" conditions.

2.9. Laser Flash Analysis (LFA)

In order to prepare ablated samples for LFA, they were cut to 1 cm² squared geometry, using an Accutom 50 dicing tool from Struers (Ballerup, Denmark). Then, ablated samples were arranged in layered configuration, together with a 1 mm thick polished aluminum sample with the same dimensions as the ablated ones, as shown in Figure 4. Samples were coated on both external faces using Graphit 33 spray from Kontakt Chemie (Iffezheim, Germany) containing 1–5 w/w % of graphite powder in order to have a consistent absorbance to the laser beam and consistent emissivity to the IR detector.

Laser flash analysis (LFA) test was performed by a Netzsch LFA 457 Microflash machine (Selb, Germany) at room temperature. A single flash (0.5 ms) from Nd-Yag laser was irradiated on the untreated surface of the ablated aluminum sample, as illustrated in Figure 4. The LFA chamber was filled with dry argon gas during the experimentation in order to reduce the influence of moisture on the measurement of the thermal properties. An infrared detector (InSb photodiode) was used to monitor the temperature transient at the back face. The output voltage of the laser was fixed at 1922 V for all experiments. A duration of 60 ms was used for the acquisition time of the IR detector.

Layered configuration (see Figure 4) was used in order to calculate the TCR generated by the particular geometry of the rough ablated surface in contact with a flat surface [27]. It is difficult to calculate the exact TCR between PA and Al by using LFA with such layered configuration, due to experimental challenges resulting from the low thermal conductance of PA. Therefore, the rough ablated aluminum is brought into contact with another flat aluminum sample. Thermal diffusivity of the layered system is evaluated from the measurement of temperature increase as a function of time at the back face of the polished aluminum, i.e., the side facing the IR sensor. Then, the density, thickness, thermal diffusivity, and specific heat of both materials were predefined to that of pure aluminum, kept constant for all tested samples, and used to calculate the TCR based on the algorithm developed by Hartmann et al. [28].

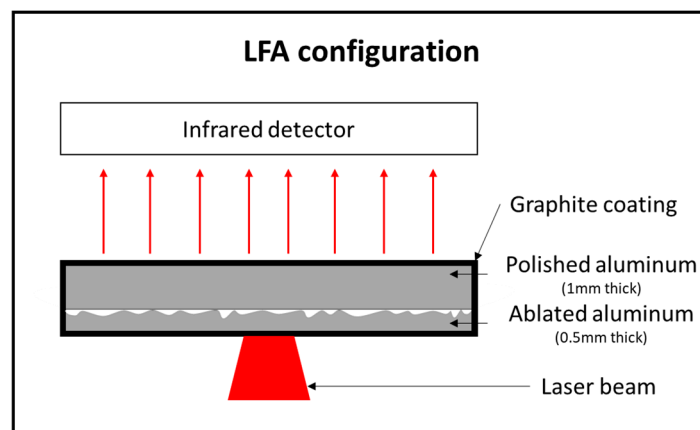


Figure 4. Schematic drawing of laser flash analysis layered configuration.

3. Results

3.1. Joint Strength

The joint area was identified at the joint interface after failure as the area of residues/damages on both materials. The joint area measured in the case of ethanol-wiped aluminum (Al ref) showed 58% of the joint area measured on the corresponding PA indicating a mixture between adhesive and cohesive failure modes. Figure 5 plots the joint area versus shear load at failure for samples that had their aluminum ablated prior to the joining process with the six parameters discussed in this article. Although shear load at failure of the tested samples varies from 524 to 1632 N, linear relation between joint area and shear load indicates constant strength across all samples. A descriptive model

was generated to describe the relation between all data points. High coefficient of determination (R^2) of 0.98 illustrates very low variability in the calculated strength, as indicated by a slope of 34.69 MPa. In addition, results show equal and matching joint area on corresponding Al and PA samples, demonstrating prominence of cohesive failure mode for the ablated aluminum and indicating that the reported variation in joint quality is less likely to be a result of variations in interfacial chemical-bonding behavior. Results confirm that laser-ablation parameters have a significant influence on the joint quality, manifested in the joint area as shown in Figure 6, but no influence on the joint strength. Table 2 shows the effect of laser-ablation parameters on joint resistance to shear load.

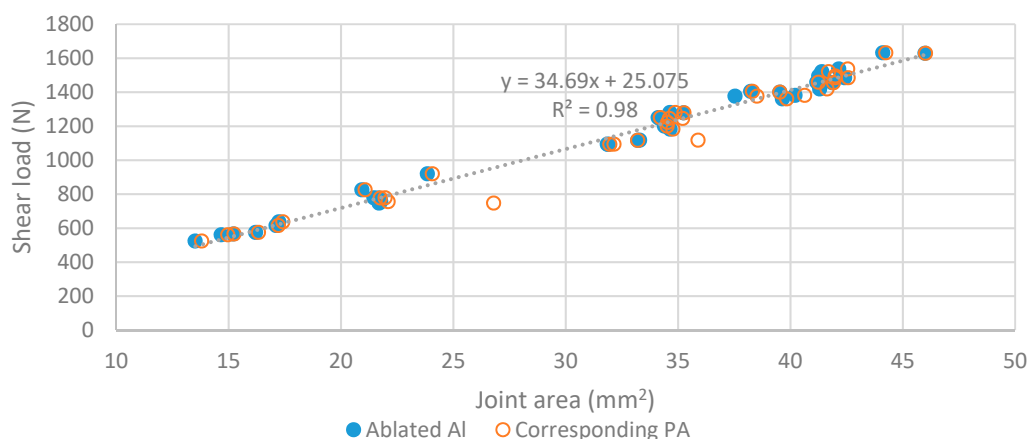


Figure 5. Evolution of joint area, along with increasing joint's resistance to failure.



Figure 6. Stacked microscopic images of PA joint area after failure (dark areas), illustrating effect of laser-ablation parameters on joint quality.

Table 2. Effect of laser-ablation parameters on joint resistance to failure.

Ablation Parameters	P1	P2	P3	P4	P5	P5-95%
Average shear load (N)	580 ± 41	800 ± 65	1222 ± 143	1341 ± 172	1415 ± 113	1465 ± 65

3.2. X-Ray Photoelectron Spectroscopy (XPS)

As far as the general composition of the treated aluminum surfaces (see Figure 7) is concerned, it is first observed that laser ablation removes a large part of the adsorbed carbon on the surface, as well as other impurities, resulting in a “cleaning” effect. Concerning the sample which had its surface wiped only with ethanol (Al ref), a high carbon content is visible (29.5 at.%) and a relatively low oxygen concentration (41.1 at.%). After laser pretreatment, a significant decrease in the carbon content on the surface could be noticed, along with an increase in oxygen content. It corresponds to the effects which are generally expected for laser ablation of aluminum: the high energy density of the laser beam has two possible effects, either acting separately or in combination. First, laser ablation certainly causes the

removal of surface contaminants, thereby lowering the “masking” effect of the aluminum surface by the contamination top layer. Second, it might contribute to the regeneration of a thicker oxide layer on the Al surface due to high surface temperature during the ablation process. While a minor nitrogen content of 0.7, 0.7, and 0.5 at.% was detected on P1, P2, and P3, samples ablated with parameters P4, P5, and P5-95% illustrated the presence of only aluminum, oxygen, and carbon elements.

Surface chemistry of the different laser-ablated samples do not significantly differ in aluminum, oxygen, and carbon composition. Since no metallic aluminum at 72.7 eV can be found in the high-resolution Al 2*p* spectra of the ablated samples, Strohmeier’s method [29] cannot be used to estimate the oxide thickness. The oxide of the reference samples thickness has been estimated at 5.5 nm by using this method. This implies that the oxide layer is much thicker than the depth limit probed in XPS, which is evaluated in its wide range at 20 nm [30]. The details of the high-resolution spectra of the different elements (C 1*s*, O 1*s*, and Al 2*p*) were very similar across the ablated surfaces, meaning that the surface chemistry is almost identical regardless of the laser-ablation parameters and the resulted joint’s strength.

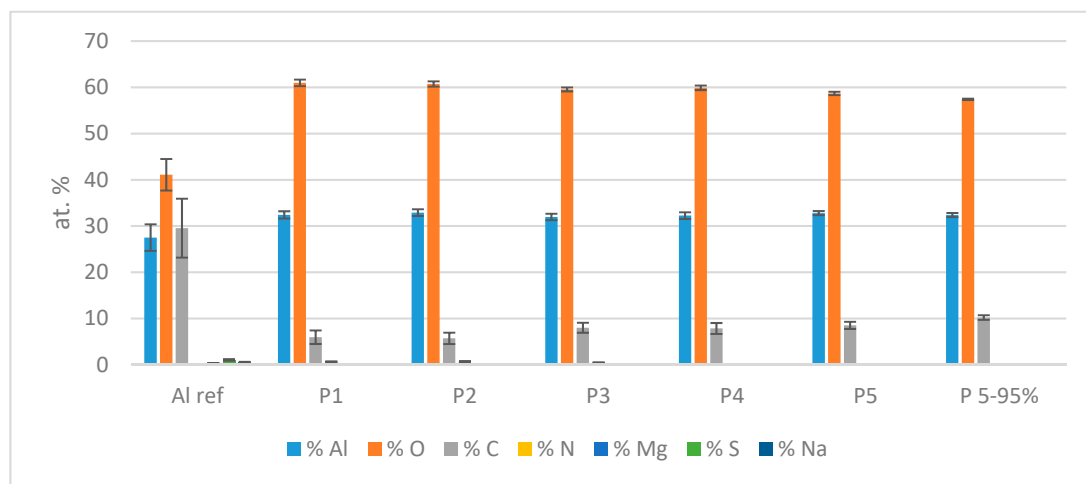


Figure 7. XPS elemental composition of aluminum surfaces.

3.3. Scanning Electron Microscope (SEM)

SEM results shown in Figure 8 illustrates the morphology of the aluminum oxide resulted from the laser-ablation process. The red square shown in 1000× magnification illustrates the area where EDX analysis was performed. Samples ablated with parameter P1, which demonstrated the lowest joint quality, shows relatively high peaks and deep valleys with relatively coarse structures. However, as the joint quality increases, ablated aluminum surfaces are shown to exhibit a smoother surface with finer peak structures, as can be clearly seen on sample P5-95, which resulted in the highest average resistance to failure. Since the failure occurs close to the Al-PA interface (typically 10–15 μm in depth in the PA), the influence of mechanical interlocking cannot be excluded a priori. However, it would be expected that a rougher surface is responsible for a greater mechanical interlocking, thereby reinforcing the joint. The opposite effect is observed here, i.e., the samples exhibiting higher roughness show lower joint quality. It is therefore assumed that mechanical interlocking does not govern the difference of joint resistance to failure.

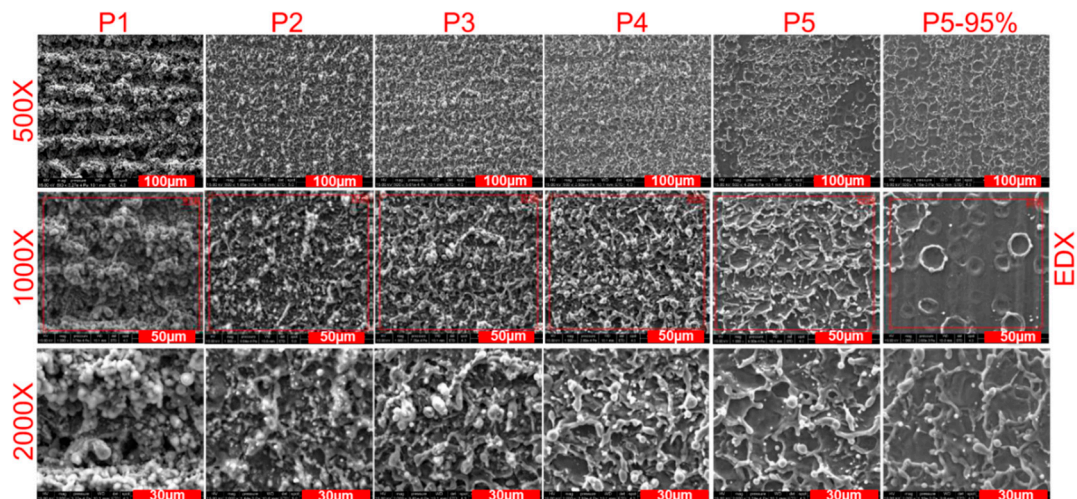


Figure 8. SEM images of ablated surfaces.

3.4. Energy-Dispersive X-Ray Spectroscopy (EDX)

EDX results shown in Figure 9 illustrate atomic percentage of oxygen, carbon, and aluminum. While XPS analyzes a depth which is smaller than 20 nm [30], EDX depth of analysis with the current EDX parameters in use and in case of aluminum oxide would yield a depth close to 2 µm. The carbon element cannot be correctly quantified by the EDX technique and will not be considered in this study.

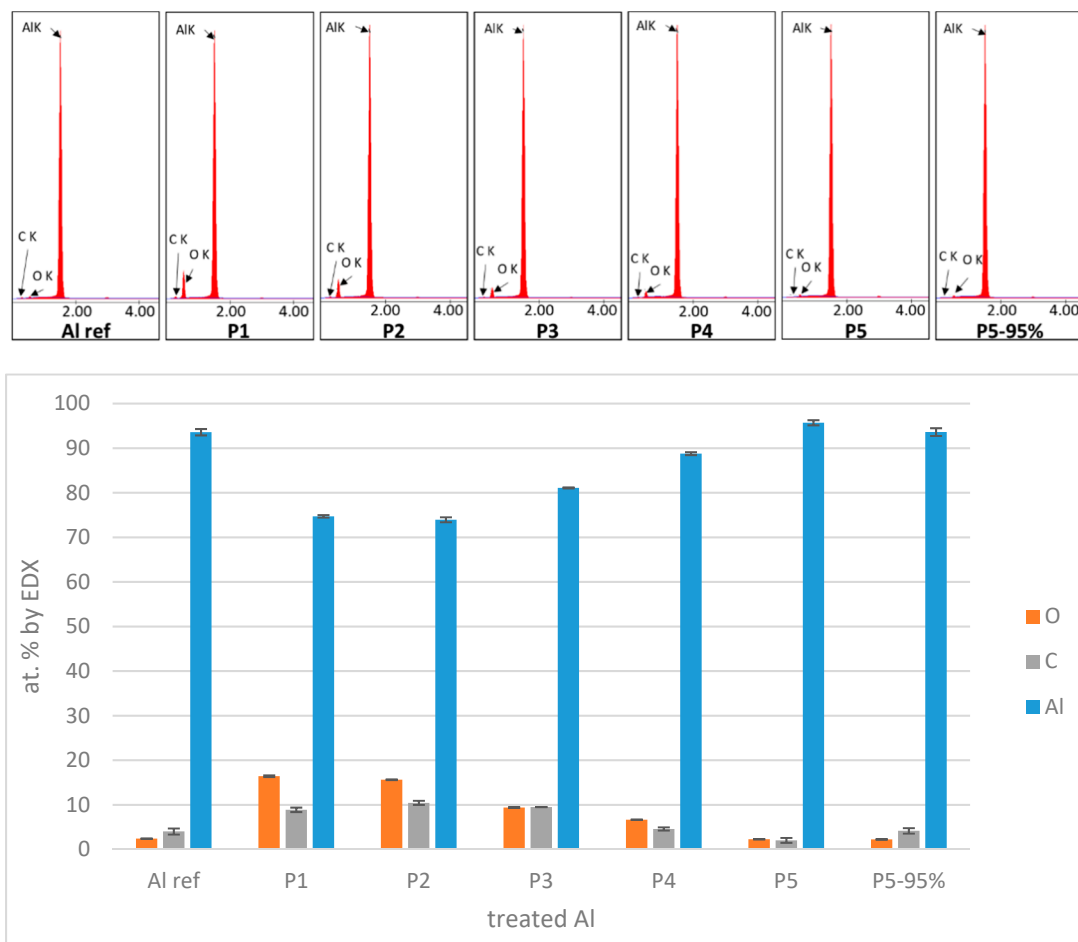


Figure 9. EDX elemental composition of aluminum surfaces.

Interestingly, oxygen concentration detected by EDX increases for the ablation condition. More precisely, this increase is very significant for ablation conditions P1 and P2 (16.4% and 15.6%, respectively), and it is significant to a lesser extent for P3 and P4 (9.4% and 6.7%, respectively), compared to untreated aluminum (2.4%). This leads to the assumption that oxidation of aluminum occurs for ablation conditions P1 to P4 and is particularly large for conditions P1 and P2. This is consistent with XPS results that lead to the conclusion that oxidation occurs at a larger depth than 20 nm for conditions P1 to P4.

A decline in the oxygen peak intensity along the ablated samples from P1 to P5 suggests a decline in aluminum oxide and/or hydroxide layer thickness along the ablation conditions (P1 to P5). EDX is not conclusive for conditions P5 and P5-95%, probably because it is not precise enough at these low concentrations of oxygen (close to 2.4%).

3.5. Surface Topography

The reference aluminum (cleaned with ethanol) exhibited relatively low surface roughness ($R_q = 0.43 \pm 0.26 \mu\text{m}$). Regarding the laser-ablated Al, several topography parameters' values were investigated for correlations with the achieved joint quality. However, no strong correlation was found between R_dq , R_q , and the joint's resistance to failure indicated by the Pearson correlation coefficients of -0.77 and -0.83 , respectively. Figure 10 shows the relation between roughness profile parameters ratio R_q/R_dq involved in the TCR model (Equation (1)) with the corresponding joint's resistance to failure, where σ reflects R_q (μm) and m reflects R_dq measured on ablated aluminum surfaces. The correlation between ratio R_q/R_dq and joint's resistance indicated by the Pearson correlation coefficient is -0.93 .

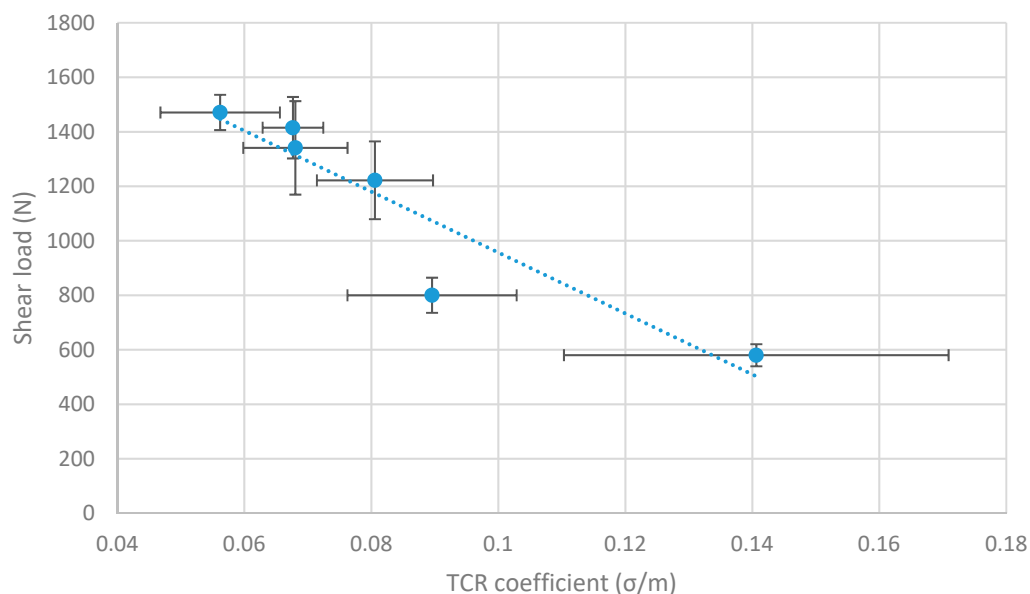


Figure 10. Relation between surface topography and joint's resistance to failure.

3.6. Laser Flash Analysis

In order to fully understand the combined effects of laser-ablation parameters on the thermal transfer through a rough Al surface, LFA layered tests were conducted. Results in Figure 11 show that a decreased TCR across the interface of the layered setup correlates significantly with an increase in the joint's resistance to failure, with a Pearson correlation coefficient of $r = -0.94$. Results confirm that the improvement in joint quality, which is manifested by enhanced joint area and increased resistance to failure, is very likely to be a result of reduced TCR across the interface of the joining partners during the welding process.

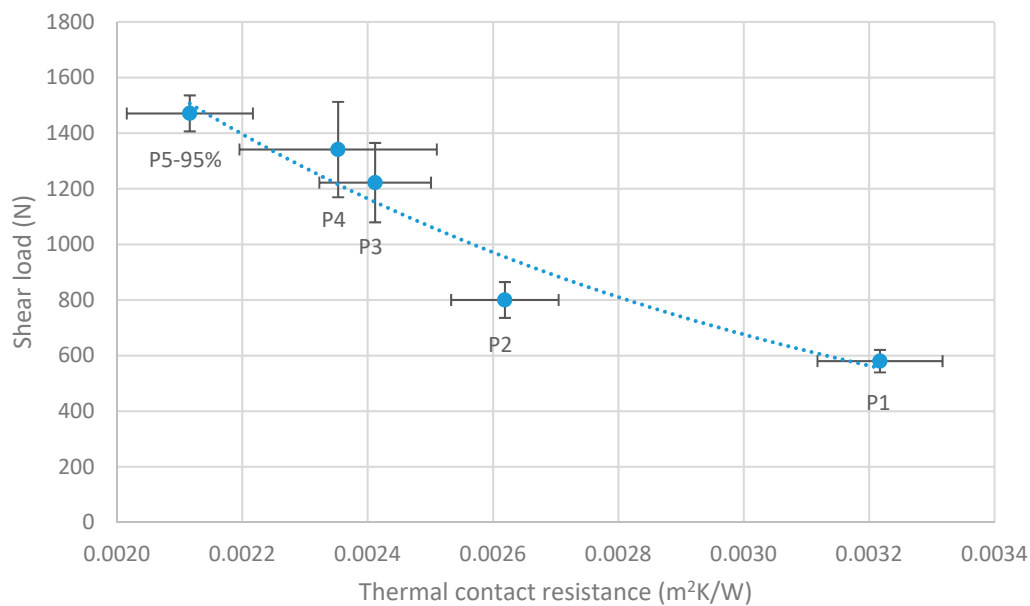


Figure 11. Relation between thermal contact resistance and joint's resistance to failure.

4. Discussion

The lower mechanical resistance of the joint for untreated (reference, only ethanol cleaning) aluminum compared to laser-ablated samples is easily linked to the different surface chemistry. More precisely, laser ablation is responsible to a lower level of carbon contamination and the formation of a relatively thick oxide layer on aluminum. This certainly creates a strong interaction with molten PA during welding, resulting in cohesive failure mode. This is not the case for reference aluminum, which is responsible for the observation of areas of adhesive failure at the interface, thereby reducing the joint resistance.

The difference in joint resistance between laser-ablation conditions clearly comes from a difference in joint area, as stated in 3.1. However, this difference in joint area is difficult to explain. When surface chemistry (as evaluated by XPS) is considered, the only correlation that can be observed is a slight increase of carbon content and a slight decrease of oxygen content from P1 to P5-95, i.e., when shear load increases. An increase in carbon content at the aluminum surface is expected to weaken the interactions at the interface between aluminum and PA and makes the joint weaker. This is contradictory to what is actually observed, in particular if it is also mentioned that failure for ablated samples occurs in PA (cohesive failure), i.e., adhesion at the interface is certainly not responsible for the failure of the assembly.

Interestingly, two good correlations between ablated aluminum properties and shear load are observed. The first one is the decrease of the oxygen concentration, as evaluated by EDX, when shear load increases, and the second is the decrease of Rq/Rdq ratio when shear load increases.

The inverse correlation (Pearson coefficient $r = -0.98$) between EDX oxygen concentration and shear load could probably be explained by a different thermal behavior of the aluminum sample as a function of its content of oxide or hydroxide relatively to metal aluminum. For instance, if it is hypothesized that aluminum oxide is more stable than hydroxide and that it is formed as a layer close to the surface of aluminum, then the aluminum sample can be considered as a two-layer system: metal aluminum in the bulk and aluminum oxide layer at the surface. Since the thermal diffusivity of aluminum oxide ($12 \text{ mm}^2/\text{s}$) is lower than pure aluminum ($94 \text{ mm}^2/\text{s}$) at 300 K [31], this means that a thicker aluminum oxide layer would act as a larger thermal insulator for the transmission of heat to PA during welding. Thus, an increase in oxygen concentration would result in a decrease in volume of molten polymer during welding, leading to a smaller joint area and a decline in the joint's resistance to failure.

Otherwise, the inverse correlation between the Rq/Rdq ratio and shear load (Pearson's correlation $r = -0.93$) has to be interpreted in the light of Equation (1), which links the thermal contact resistance and the σ/m ratio as a surface topography characteristic. In terms of phenomena, it means that, when thermal conduction across a "rough interface" (see Figure 3b) is governed by the area of microcontacts, the thermal contact resistance (TCR) increases as the area of microcontacts decreases. A lower value of Rq/Rdq ratio leads to a lower value of TCR, meaning that a greater heat flow is conducted across the interface. This leads to the melting of a greater volume of PA during welding, which results in a larger joint and a larger shear load. Furthermore, the fact that TCR evaluated by LFA experiments following Hartmann's method is also well correlated to shear load makes these arguments stronger.

Both phenomena (thermal insulation by aluminum oxide and change of TCR by means of different topography) convincingly explain the increase in shear load from P1 to P5-95. Nevertheless, the authors are currently not able to quantify which phenomenon has the larger effect on this increase, or if one of the two phenomena shall be neglected. Further investigations shall be necessary to answer this question.

Moreover, the correlation between topography and shear load explains why, a posteriori, no correlation was found between the Ra topography value (which is strongly correlated to Rq value) and shear load in our former article [5]. In such a case, the critical characteristic of the surface topography is its morphology of peaks, evaluated by Rq/Rdq ratio, and not its amplitude, which is evaluated by Ra or Rq .

5. Conclusions

The link between the aluminum surface characteristics after laser ablation and the shear resistance of dissimilar joints formed by laser welding of ablated aluminum with polyamide was investigated. It is observed that shear load at failure of the joint depends on the joint area demonstrating constant joint strength regardless of the ablation parameters. Good correlations between surface characteristics and shear load lead us to make two possible assumptions for explaining the reduction in joint area.

First, it is observed that laser ablation leads to a significant increase of oxygen content in the first micrometers (in depth) of aluminum surface. This might be responsible for a reduction of thermal conduction in the oxygen-rich volume (formation of aluminum oxide/hydroxide), which in turn reduces the quantity of heat transmitted to melt PA during welding.

Second, it is observed that the different topography characteristics obtained after laser ablation of aluminum exhibit different morphology of peaks, which might in turn influence the thermal contact resistance (TCR) between the rough aluminum and the flat PA during welding.

Experimental evaluation of TCR by LFA confirms that thermal-transfer phenomena are probably responsible of changes in shear-load resistance.

This article shed light on the prominence of interfacial thermal-transfer phenomena in the quality of joints obtained by laser welding of a rough ablated aluminum with a polymer.

Author Contributions: Conceptualization, A.A.-S. and J.B.; methodology, A.A.-S., J.B., and P.H.; formal analysis, A.A.-S., J.B., and P.H.; investigation, A.A.-S., J.B., P.H., and R.V.; writing—original draft preparation, A.A.-S.; writing—review and editing, J.B., P.H., R.V., L.H., and P.P.; supervision, L.H. and P.P.; project administration, P.P.; funding acquisition, P.P., J.B., and L.H.

Funding: This research was funded by FNR (Luxembourg) and DGO6 (Belgium) through M-era.net, under project LaserSTAMP.

Acknowledgments: Jean-Luc Biagi (LIST) is gratefully acknowledged for his skillful characterization of aluminum surfaces by SEM. The authors would like to thank Sébastien Depaifve (LIST) and Daniel Schmidt (LIST) for the interesting insights they provided about thermal interface materials and thermal transfer across interfaces.

Conflicts of Interest: The authors declare no conflicts of interest. The funders had no role in the design of the study; in the collection, analyses, or interpretation of data; in the writing of the manuscript, or in the decision to publish the results.

References

1. Lamberti, C.; Solchenbach, T.; Plapper, P.; Possart, W. Laser assisted joining of hybrid polyamide-aluminum structures. *Phys. Procedia* **2014**, *56*, 845–853. [[CrossRef](#)]
2. Katayama, S.; Kawahito, Y. Laser direct joining of metal and plastic. *Scr. Mater.* **2008**, *59*, 1247–1250. [[CrossRef](#)]
3. Wahba, M.; Kawahito, Y.; Katayama, S. Laser direct joining of AZ91D thixomolded Mg alloy and amorphous polyethylene terephthalate. *J. Mater. Process. Technol.* **2011**, *211*, 1166–1174. [[CrossRef](#)]
4. Arai, S.; Kawahito, Y.; Katayama, S. Effect of surface modification on laser direct joining of cyclic olefin polymer and stainless steel. *Mater. Des.* **2014**, *59*, 448–453. [[CrossRef](#)]
5. Al-Sayyad, A.; Bardon, J.; Hirchenhahn, P.; Santos, K.; Houssiau, L.; Plapper, P. Aluminum pretreatment by a laser ablation process: Influence of processing parameters on the joint strength of laser welded aluminum—Polyamide assemblies. *Procedia CIRP* **2018**, *74*, 495–499. [[CrossRef](#)]
6. Bergmann, J.P.; Stambke, M. Potential of laser-manufactured polymer-metal hybrid joints. *Phys. Procedia* **2012**, *39*, 84–91. [[CrossRef](#)]
7. Zhang, Z.; Shan, J.G.; Tan, X.H.; Zhang, J. Effect of anodizing pretreatment on laser joining CFRP to aluminum alloy A6061. *Int. J. Adhes. Adhes.* **2016**, *70*, 142–151. [[CrossRef](#)]
8. Klotzbach, A.; Langer, M.; Pautzsch, R.; Standfuß, J.; Beyer, E. Thermal direct joining of metal to fiber reinforced thermoplastic components. *J. Laser Appl.* **2017**, *29*, 022421. [[CrossRef](#)]
9. Amend, P.; Pfindel, S.; Schmidt, M. Thermal joining of thermoplastic metal hybrids by means of mono- and polychromatic radiation. *Phys. Procedia* **2013**, *41*, 98–105. [[CrossRef](#)]
10. Holtkamp, J.; Roesner, A.; Gillner, A. Advances in hybrid laser joining. *Int. J. Adv. Manuf. Technol.* **2010**, *47*, 923–930. [[CrossRef](#)]
11. Georgiev, G.L.; Baird, R.J.; McCullen, E.F.; Newaz, G.; Auner, G.; Patwa, R.; Herfurth, H. Chemical bond formation during laser bonding of Teflon® FEP and titanium. *Appl. Surf. Sci.* **2009**, *255*, 7078–7083. [[CrossRef](#)]
12. Roesner, A.; Scheik, S.; Olowinsky, A.; Gillner, A.; Reisingen, U.; Schleser, M. Laser assisted joining of plastic metal hybrids. *Phys. Procedia* **2011**, *12*, 373–380. [[CrossRef](#)]
13. Cui, T.; Li, Q.; Xuan, Y. Characterization and application of engineered regular rough surfaces in thermal contact resistance. *Appl. Therm. Eng.* **2014**, *71*, 400–409. [[CrossRef](#)]
14. Zhang, P.; Cui, T.; Li, Q. Effect of surface roughness on thermal contact resistance of aluminium alloy. *Appl. Therm. Eng.* **2017**, *121*, 992–998. [[CrossRef](#)]
15. Prasher, R. Thermal interface materials: Historical perspective, status, and future directions. *Proc. IEEE* **2006**, *94*, 1571–1586. [[CrossRef](#)]
16. Yovanovich, M.M. Four decades of research on thermal contact, gap, and joint resistance in microelectronics. *IEEE Trans. Compon. Packag. Technol.* **2005**, *28*, 182–206. [[CrossRef](#)]
17. Greenwood, J.A.; Williamson, J.B.P. Contact of nominally flat surfaces. *Proc. R. Soc. London Ser. A Math. Phys. Sci.* **1966**, *295*, 300–319. [[CrossRef](#)]
18. Greenwood, J.A. The area of contact between rough surfaces and flats. *J. Lubr. Technol.* **1967**, *89*, 81–87. [[CrossRef](#)]
19. Greenwood, J.A.; Tripp, J.H. The contact of two nominally flat rough surfaces. *Proc. Inst. Mech. Eng.* **1970**, *185*, 625–633. [[CrossRef](#)]
20. Cooper, M.G.; Mikic, B.B.; Yovanovich, M.M. Thermal contact conductance. *Int. J. Heat Mass Transf.* **1969**, *12*, 279–300. [[CrossRef](#)]
21. Mikić, B.B. Thermal contact conductance; theoretical considerations. *Int. J. Heat Mass Transf.* **1974**, *17*, 205–214. [[CrossRef](#)]
22. Sayles, R.S.; Thomas, T.R. Thermal conductance of a rough elastic contact. *Appl. Energy* **1976**, *2*, 249–267. [[CrossRef](#)]
23. Yovanovich, M.M.; Marotta, E.E. Thermal spreading and contact resistances. In *Heat Transfer Handbook*; Bejan, A., Kraus, A.D., Eds.; Wiley: Hoboken, NJ, USA, 2003; pp. 261–395.
24. Bahrami, M.; Yovanovich, M.M.; Marotta, E.E. Thermal joint resistance of polymer-metal rough interfaces. *J. Electron. Packag.* **2006**, *128*, 23. [[CrossRef](#)]

25. Al-Sayyad, A.; Bardon, J.; Hirchenhahn, P.; Mertz, G.; Haouari, C.; Houssiau, L.; Plapper, P. Influence of laser ablation and plasma surface treatment on the joint strength of laser welded aluminum-polyamide assemblies. In Proceedings of the JNPLI 2017, Strasbourg, France, 13–14 September 2017.
26. ISO 4287—Geometrical Product Specifications (GPS)—Surface Texture: Profile Method—Terms, Definitions and Surface Texture Parameters; International Organization for Standardization: Geneva, Switzerland, 1997.
27. Corbin, S.F.; Turriff, D.M. Thermal diffusivity by the laser flash technique. *Charact. Mater.* **2002**. [[CrossRef](#)]
28. Hartmann, J.; Nilsson, O.; Fricke, J. Thermal diffusivity measurements on two-layered and three-layered systems with the laser-flash method. *High Temp. Press.* **1993**, *25*, 403.
29. Strohmeier, B.R. An ESCA method for determining the oxide thickness on aluminum alloys. *Surf. Interface Anal.* **1990**, *15*, 51–56. [[CrossRef](#)]
30. Ratner, B.D.; Castner, D.G. Electron spectroscopy for chemical analysis. In *Surface Analysis—The Principal Techniques*; John Wiley & Sons, Ltd.: Chichester, UK, 2009; pp. 47–112.
31. King, J.A. *Materials Handbook for Hybrid Microelectronics*; Artech House: Boston, MA, USA, 1988.



© 2019 by the authors. Licensee MDPI, Basel, Switzerland. This article is an open access article distributed under the terms and conditions of the Creative Commons Attribution (CC BY) license (<http://creativecommons.org/licenses/by/4.0/>).

XPS measurements on laser ablated aluminum

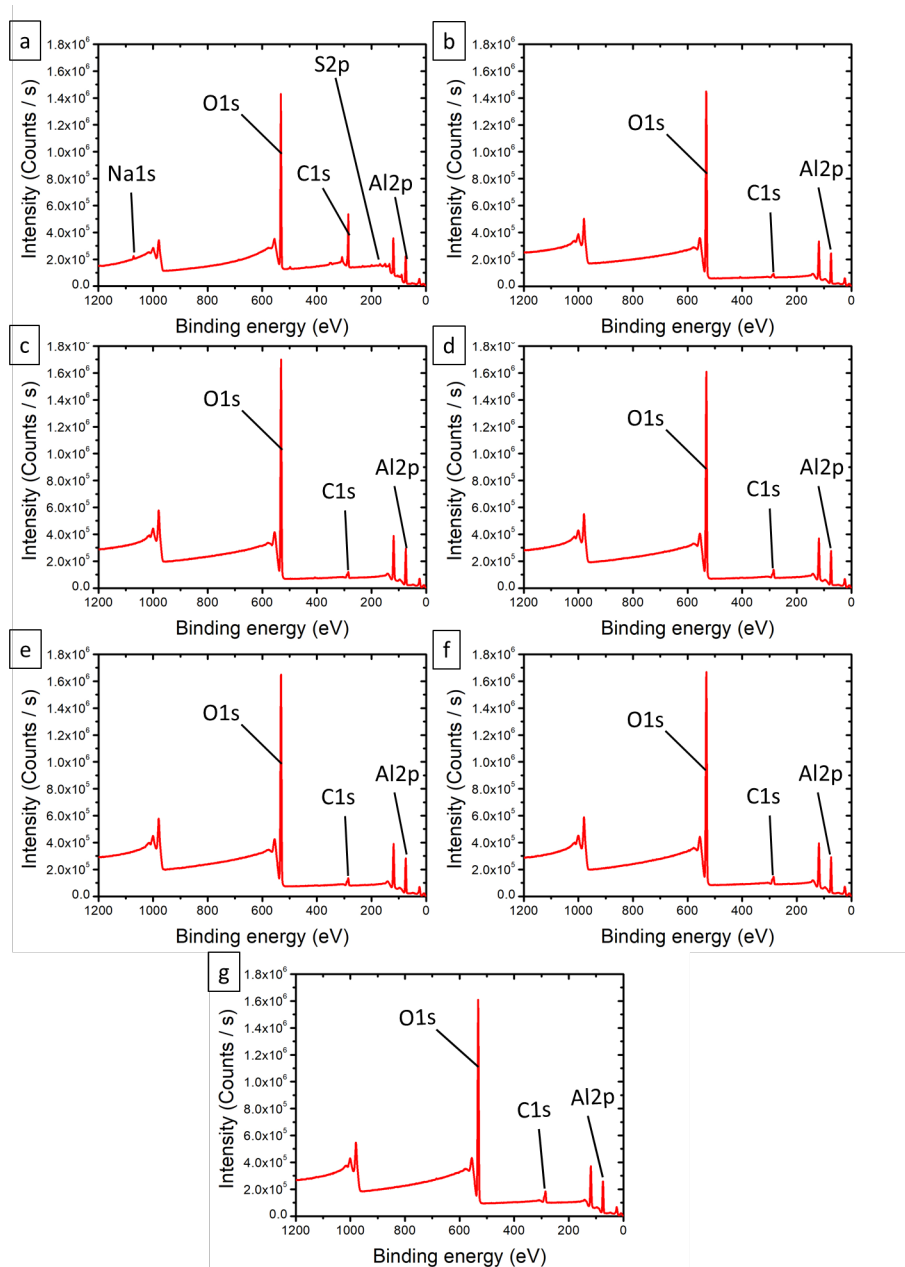


Figure 1: XPS survey spectra of (a) on the reference, (b) on Al_1, (c) on Al_2, (d) on Al_3, (e) on Al_4, (f) on Al_5, (g) on Al_6.

Laser ablation on Titanium

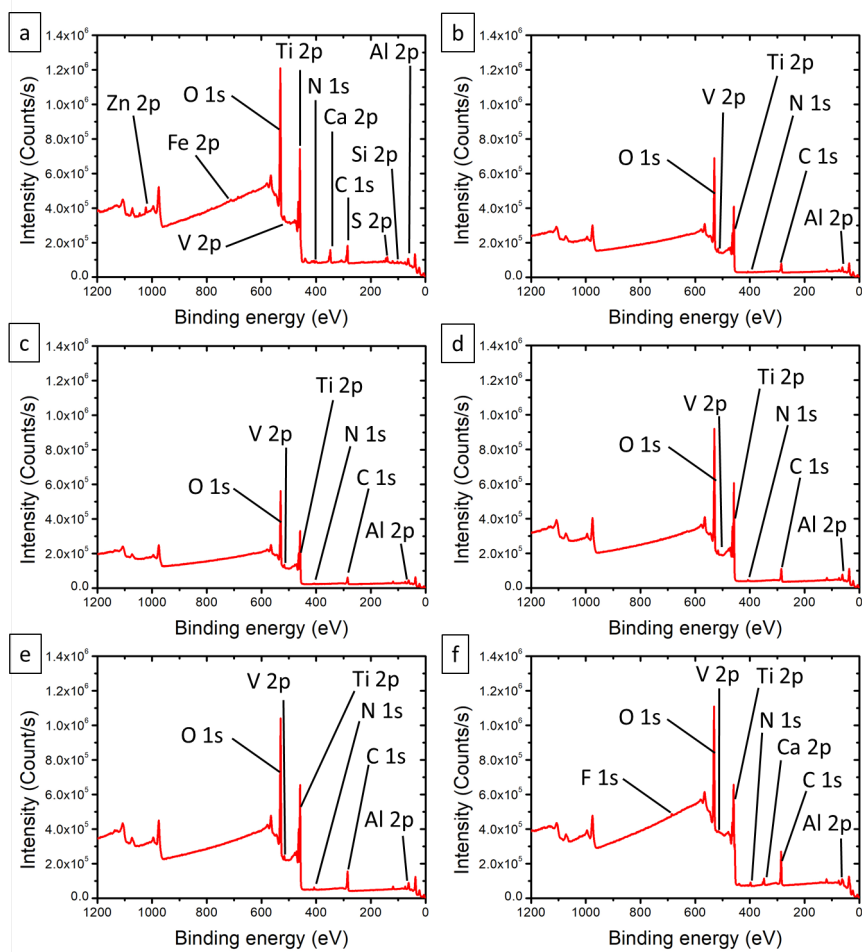


Figure 2: XPS survey spectra of (a) on the reference, (b) on Ti_1, (c) on Ti_2, (d) on Ti_3, (e) on Ti_4, and (f) on Ti_5.

Appendix to aluminum and polyamide bonding?

Welded samples

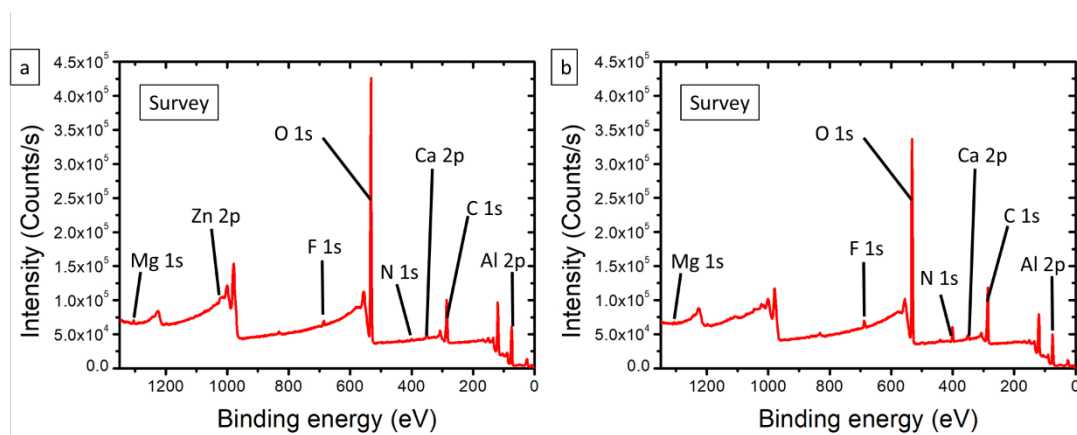


Figure 3: XPS survey of (a) the out of weld and (b) in the weld.

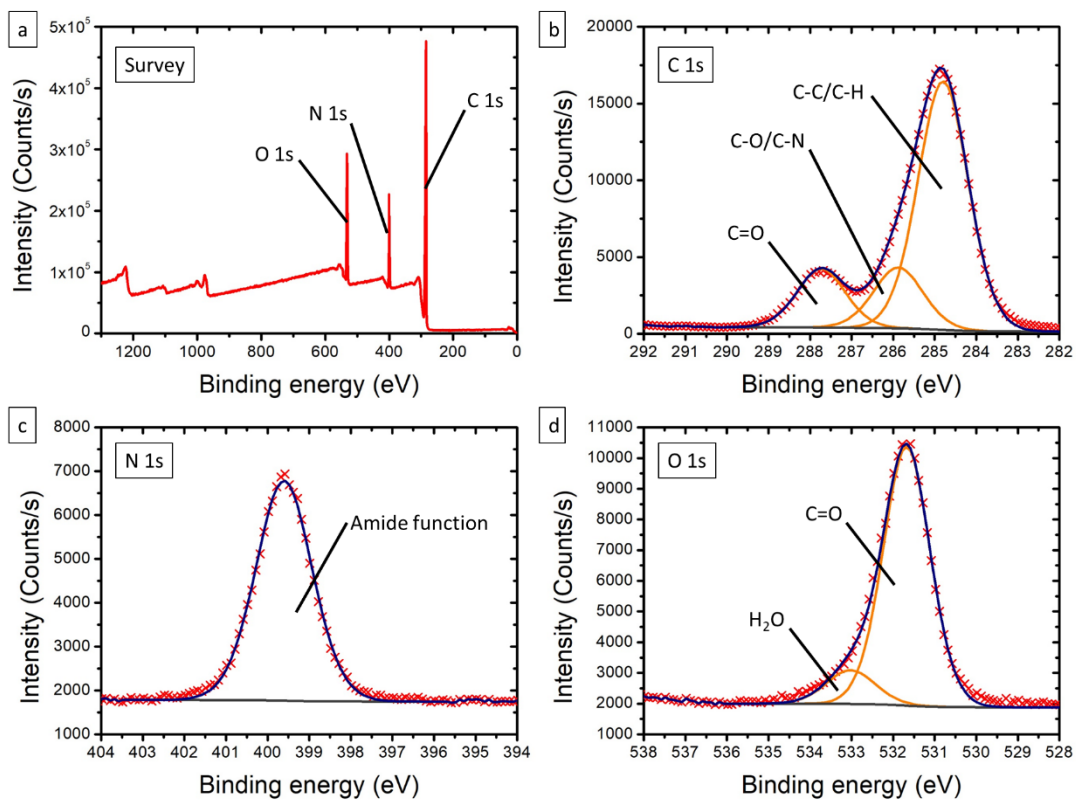


Figure 4: XPS high resolution of bulk polyamide-6.6, in (a) the survey, in (b) the C 1s region, in (c) the N 1s region and in (d) the O 1s region.

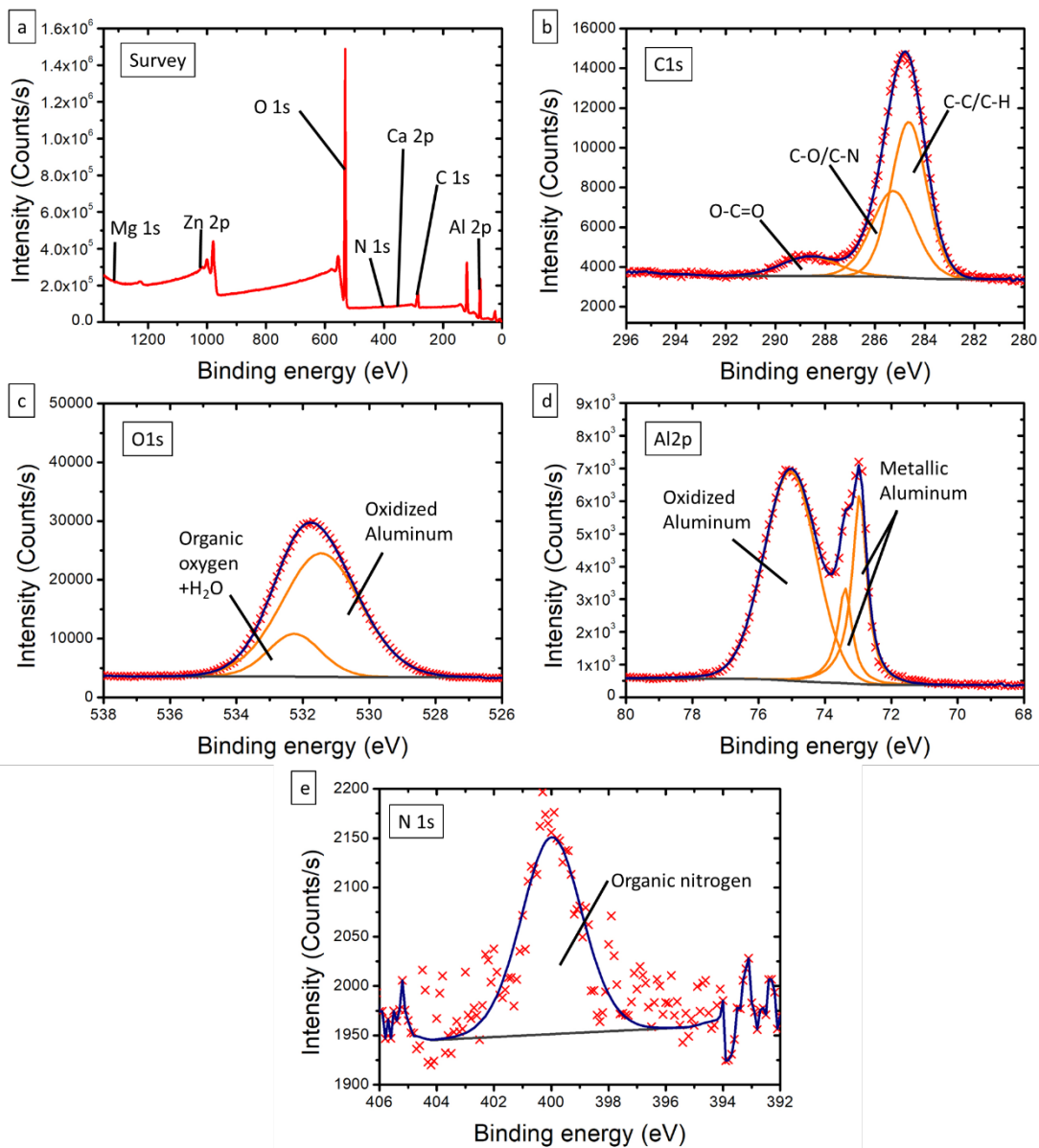


Figure 5: XPS spectra of ethanol wiped aluminum in (a) the survey, in (b) the C 1s region, in (c) the O 1s region, in (d) the Al 2p, and in (e) the N 1s region.

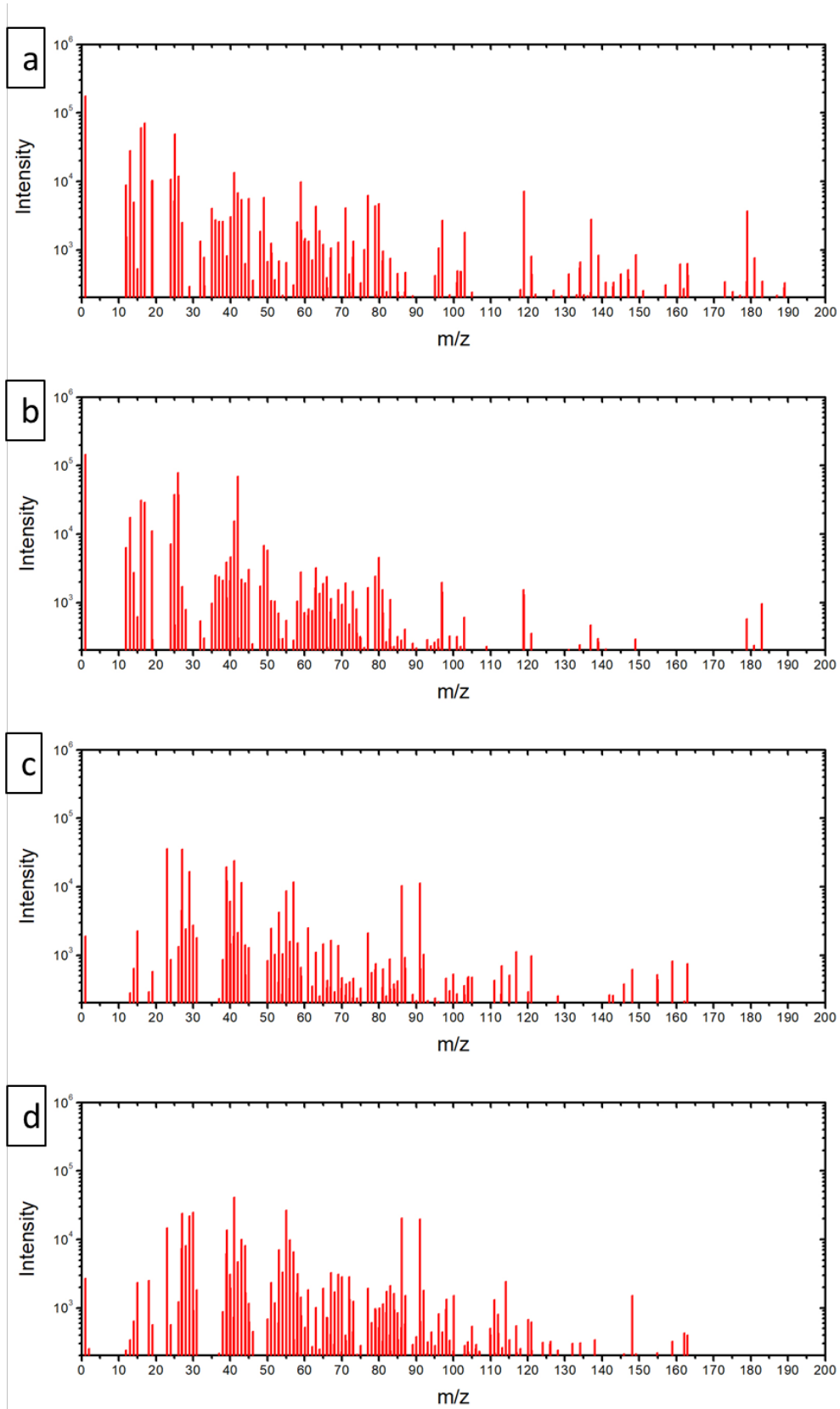


Figure 6: ToF-SIMS spectra of (a) the out of weld, (b) the weld both in negative mode, and (c) the out of weld and (d) the weld both in positive mode.

Table 1: Hand selected peak list in the negative mode.

	Mass (u)	C_3N-	50.0045	C_5H_9N-	83.0685
C-	12.0002	C_2Al-	50.9817	CHNO_2Al-	85.982
CH-	13.0083	C_4H_3-	51.0247	HO_2Al_2-	86.9612
CH_2-	14.0163	C_3O-	51.9948	CH_2NO_2Al-	86.9861
NH-	15.011	C_3H_2N-	52.0204	CH_3NO_2Al-	87.9986
CH_3-	15.0259	C_4H_5-	53.0422	Al_3H_2O-	98.9564
O-	15.9954	CHNAI-	53.9932	C_2H_2OF_3-	99.0107
NH_2-	16.0193	C_3H_4N-	54.0381	C_5H_2OCl-	112.9852
OH-	17.0032	COAl-	54.9774	C_9H_14NO_3-	184.1061
F-	18.9988	CH_2NAI-	54.9995	C_10H_16NO_3-	198.1187
C_2-	24.0007	C_3H_3O-	55.0205	C_12H_22NO_2-	212.1391
C_2H-	25.0089	CHOAl-	55.9837	C_12H_21N_2O_2-	225.1557
CN-	26.0054	C_2H_2NO-	56.0167	C_15H_29NO_2-	255.2339
Al-	26.981	C_3H_6N-	56.0504	C_17H_33NO_2-	283.2662
C_2H_3-	27.0259	AlNO-	56.9786		
Si-	27.9763	CH_2OAl-	56.9957		
AlH-	27.9895	C_2H_3NO-	57.0204		
CH_2N-	28.0211	C_3H_5O-	57.0362		
SiH-	28.9844	C_2H_2O_2-	58.0064		
CHO-	29.004	C_2H_4NO-	58.0342		
NO-	29.9983	AlO_2-	58.9719		
CH_4N-	30.0359	C_2H_3O_2-	59.0156		
P-	30.9726	SiO_2-	59.9658		
CF-	30.9982	AlO_2H-	59.9808		
CH_3O-	31.0194	C_5-	60.0007		
S-	31.9726	SiHO_2-	60.9734		
O_2-	31.99	AlH_2O_2-	60.9885		
O_2H-	32.9977	C_5H-	61.0077		
Cl-	34.9692	NO_3-	61.9895		
C_3-	36.0002	C_4HN-	63.0094		
³⁷ Cl-	36.9675	C_5H_3-	63.0243		
C_3H-	37.0085	C_4HO-	65.0046		
C_2N-	38.0031	C_5H_5-	65.0402		
C_3H_2-	38.0162	C_3NO-	65.9992		
CAI-	38.9804	C_4H_4N-	66.0359		
C_2HN-	39.0098	C_2OAl-	66.9757		
C_3H_3-	39.0243	C_4H_3O-	67.0195		
C_2O-	39.9958	C_2HOAl-	67.9819		
CN_2-	40.0064	C_3H_2NO-	68.015		
C_2H_2N-	40.0205	C_4H_6N-	68.0559		
C_2HO-	41.0047	C_2H_2OAl-	68.9968		
CNO-	42.0017	C_4H_5O-	69.0368		
AlO-	42.9762	CHNOAl-	69.9858		
AlNH_2-	43.0003	C_2H_3OAl-	70.0044		
C_2H_3O-	43.0195	C_3H_4NO-	70.0325		
CO_2-	43.9888	CO_2Al-	70.9686		
CH_2NO-	44.0171	CH_2NOAl-	70.9945		
CHO_2-	44.9987	C_6-	71.9989		
NO_2-	45.9946	C_2H_5OAl-	72.0163		
C_4-	48.0006	AlH_2O_3-	76.9841		
C_4H-	49.008	C_5H_5O-	81.0372		

Table 2: Hand selected peak list in the positive mode.

	Mass (u)	C_4H_4+	52.0286	C_3H_5NO+	71.0322	C_7H_14+	98.1073
C+	11.998	CH_2ONa+	52.9984	C_4H_7O+	71.0492	C_2F_3H_2O+	99.0028
CH+	13.006	C_4H_5+	53.0379	C_4H_9N+	71.0699	C_5H_9NO+	99.0652
CH_2+	14.0143	Al_2+	53.9596	C_5H_11+	71.0914	C_6H_13N+	99.1089
CH_3+	15.0232	CHNAH+	53.9912	CHO_2AH+	71.9771	C_5H_10NO+	100.0754
NH_3+	17.0258	C_2H_3AH+	54.0081	C_6+	72.003	C_7H_16+	100.1313
NH_4+	18.0355	C_3H_4N+	54.0331	C_3H_6NO+	72.0434	C_6H_7O_2+	111.0543
H_3O+	19.0181	C_4H_6+	54.0461	C_4H_10N+	72.0846	C_6H_10NO+	112.0804
Na+	22.9897	HAl_2+	54.9837	C_3H_7NO+	73.0531	C_7H_12NO+	126.0938
Mg+	23.9851	C_3H_3O+	55.0184	C_4H_11N+	73.0977	C_7H_12N_2O+	140.1093
C_2H_2+	26.0137	C_4H_7+	55.0573	C_3H_8NO+	74.0595	C_7H_14N_2O+	142.1203
Al+	26.9815	CHOAH+	55.9808	C_4H_12N+	74.1008	C_9H_16NO+	154.1253
C_2H_3+	27.0231	C_2H_2NO+	56.0104	C_6H_3+	75.0223	C_10H_18NO+	168.1376
Si+	27.9745	C_3H_4O+	56.0233	C_4H_2AH+	76.9946	C_9H_19N_2O+	171.1504
AlH+	27.9878	C_3H_6N+	56.0523	C_6H_5+	77.0383	C_10H_16NO_2+	182.1477
CH_2N+	28.019	C_3H_5O+	57.0327	C_4NO+	77.9752	C_12H_22NO_2+	212.1449
C_2H_4+	28.0305	C_3H_7N+	57.0539	C_5H_4N+	78.0423	C_12H_22N_2O_2+	226.173
CHO+	29.0019	C_4H_9+	57.0717	C_3HN_3+	79.0088		
CH_3N+	29.0248	CH_3OAH+	57.9989	C_6H_7+	79.0525		
C_2H_5+	29.0394	C_2H_4NO+	58.0296	C_5H_6N+	80.0494		
CH_2O+	30.0086	C_3H_8N+	58.0679	H_5O_3Si+	81.0016		
CH_4N+	30.0359	CH_4OAH+	59.0072	C_5H_5O+	81.0334		
CH_3O+	31.0176	C_2H_5NO+	59.0358	C_6H_9+	81.0707		
CH_5N+	31.0408	C_3H_7O+	59.051	COAl_2+	81.9582		
CH_3Na+	38.0135	C_3H_9N+	59.0767	C_2H_4Al_2+	81.997		
K+	38.964	CH_5OAH+	60.0206	C_4H_4NO+	82.0341		
C_2 ¹³ CH_2+	39.0214	C_2H_6NO+	60.0469	C_5H_8N+	82.0659		
Ca+	39.9615	C_3H_10N+	60.0848	CHOAl_2+	82.9737		
C_2 ¹³ CH_3+	40.029	AlH_2O_2+	60.9861	C_3H_4OAH+	83.0072		
C_3H_5+	41.0395	C_2H_5O_2+	61.0295	C_5H_7O+	83.0508		
C_2H_2O+	42.0085	C_3AH+	62.9879	CH_2OAl_2+	83.974		
C_2H_4N+	42.0326	C_5H_3+	63.0209	C_2H_6Al_2+	84.0109		
C_2H_4CH_2+	42.0441	Zn+	63.9286	C_4H_6NO+	84.0401		
AlO+	42.9753	C_5H_5+	65.0366	C_5H_8O+	84.0562		
C_2H_3O+	43.0175	CAI_2+	65.9635	C_5H_10N+	84.0871		
C_2H_5N+	43.0403	C_3H_3AH+	66.0055	C_5H_9O+	85.0654		
C_3H_7+	43.0557	C_2H_4F_2+	66.0295	CHNO_2AH+	85.9826		
AlOH+	43.9826	C_5H_6+	66.0444	C_4H_8NO+	86.0582		
CH_2NO+	44.0137	C_5H_7+	67.0529	C_5H_12N+	86.1001		
C_2H_6N+	44.0514	CH_2Al_2+	67.9798	HO_2Al_2+	86.9578		
AlH_2O+	44.9914	C_2H_2N_3+	68.0225	C_4H_9NO+	87.0676		
CH_3NO+	45.0178	C_4H_6N+	68.051	C_5H_13N+	87.1025		
C_2H_5O+	45.0337	C_2H_2OAH+	68.9911	H_2O_2Al_2+	87.9655		
C_2H_7N+	45.058	C_2H_3N_3+	69.0329	CH_3NO_2AH+	87.9963		
CH_4NO+	46.0293	C_4H_7N+	69.0544	C_4H_10NO+	88.0739		
C_2H_8N+	46.0681	C_5H_9+	69.0737	C_5H_14N+	88.1186		
C_4H_2+	50.013	Al_2O+	69.9553	C_5H_3AH+	90.0088		
C_2AH+	50.9809	CHNOAH+	69.9908	C_6H_8N+	94.0631		
C_4H_3+	51.0222	C_3H_4NO+	70.0311	C_5H_6NO+	96.0425		
C_2HAH+	51.9874	C_4H_8N+	70.0678	C_6H_10N+	96.0851		
CH_3NNa+	52.0144	C_2H_4OAH+	71.0082	C_6H_11N+	97.0967		

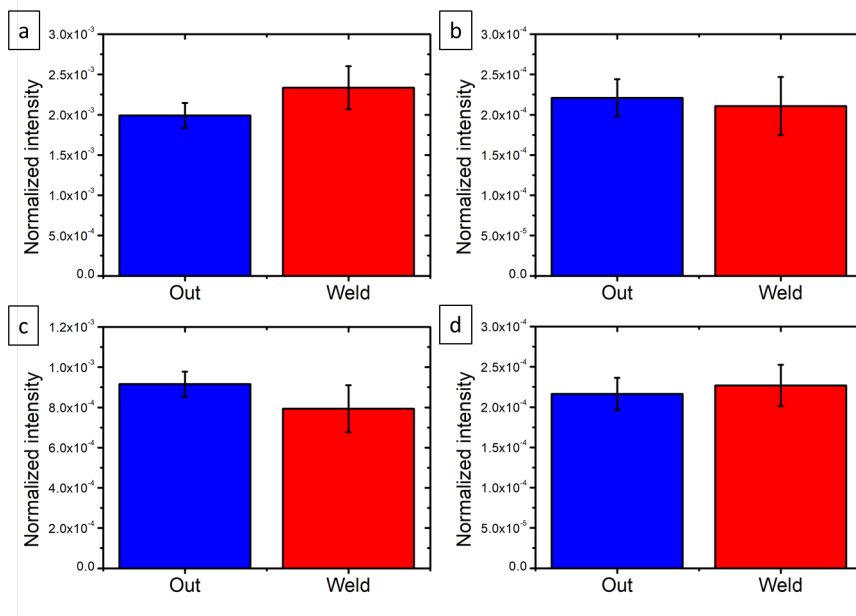


Figure 7: ToF-SIMS characteristic 2,2,2-trifluoroethanol ions in negative and positive mode, presented in total counts relative intensity per zone, in blue the out of weld and in red the weld. (a) CF_3^- , (b) $\text{C}_2\text{H}_2\text{OF}_3^-$, (c) CF_3^+ and (d) $\text{C}_2\text{H}_2\text{OF}_3^+$.

Ablated welded samples

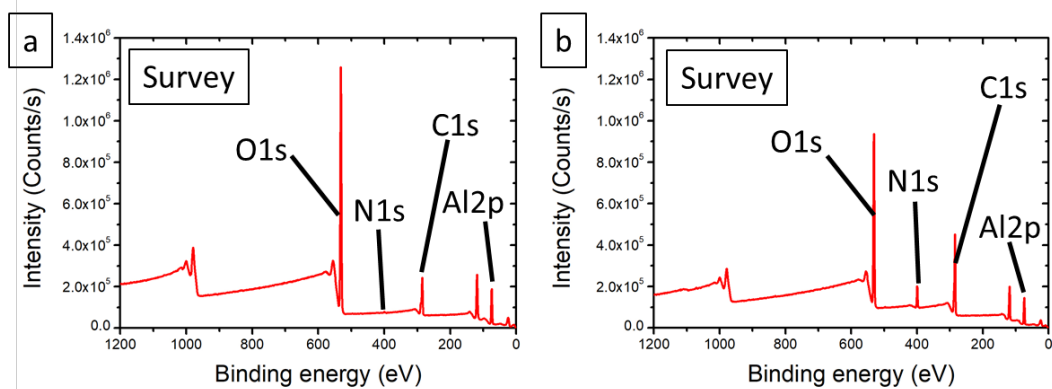


Figure 8: Survey spectra (a) in the weld and (b) out of the weld.

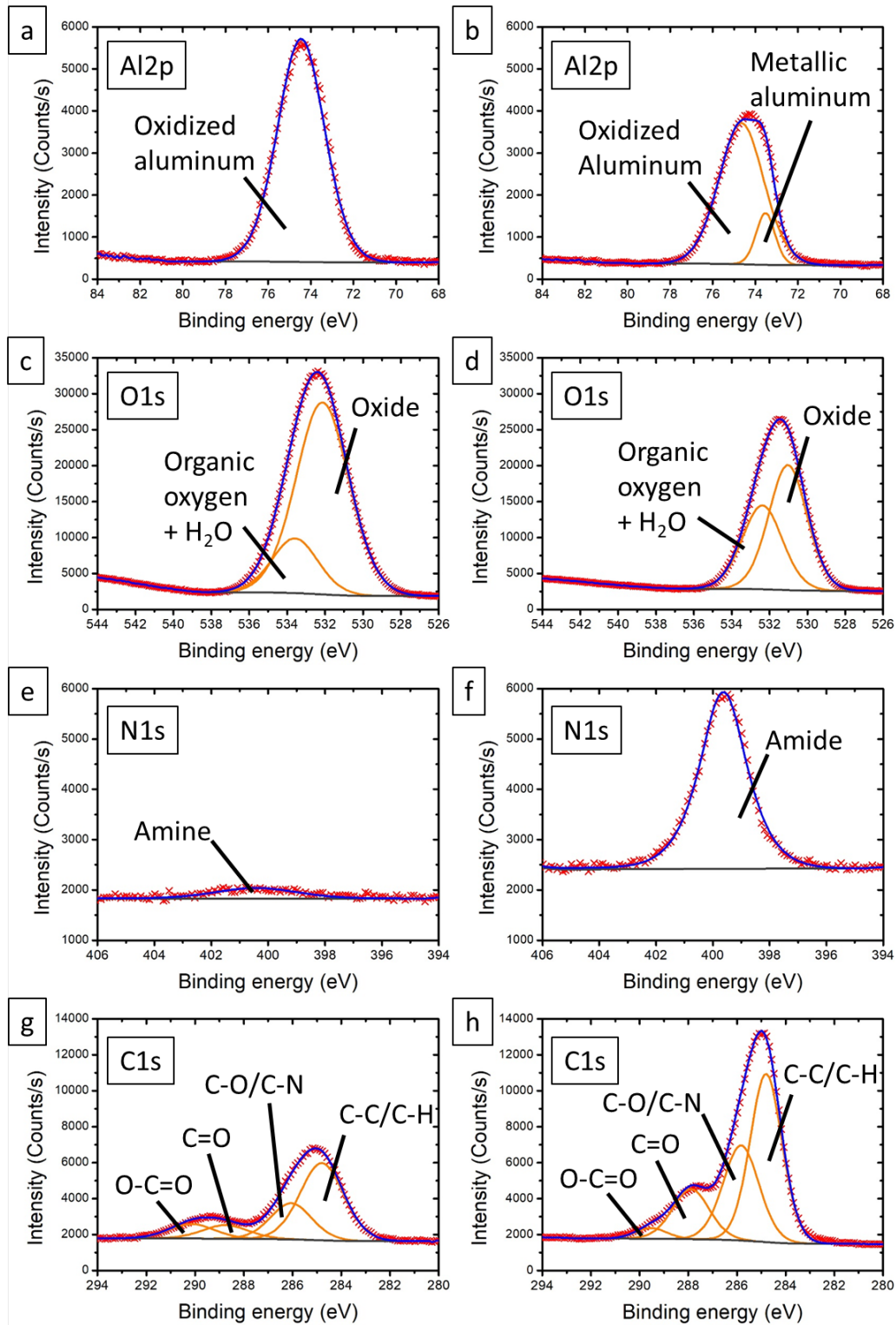


Figure 9: High resolution spectra of the Al 2p region (a) out and (b) in the weld, of the O 1s region (c) out and (d) in the weld, of the N 1s region (e) out and (f) in the weld, and of the C 1s region (g) out and (h) in the weld.

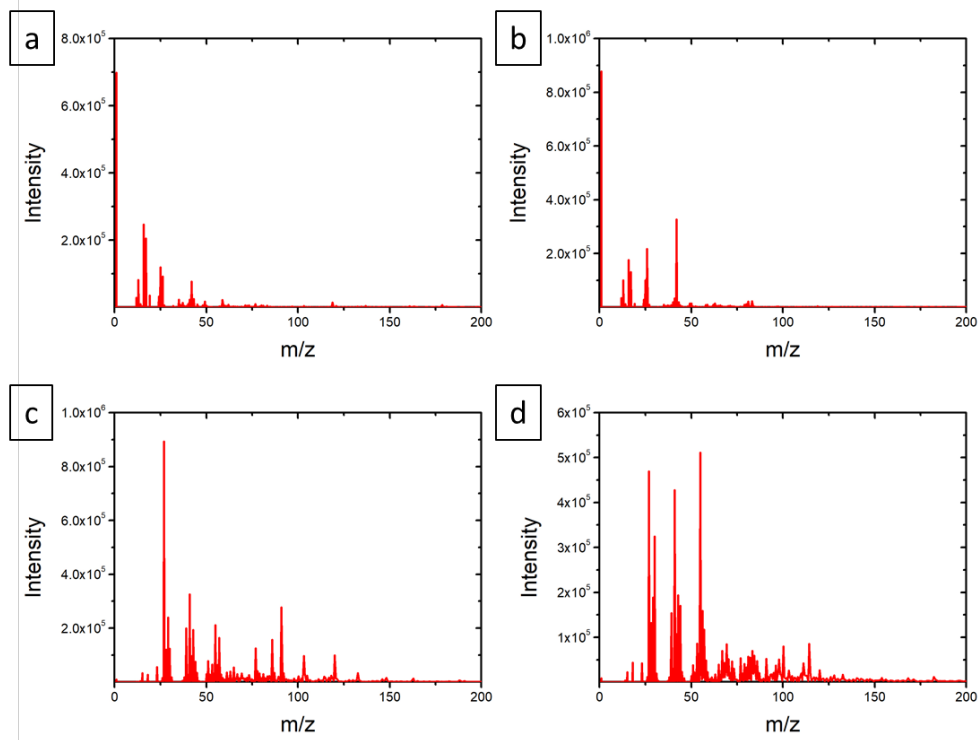


Figure 10: ToF-SIMS spectra of (a) the out of weld, (b) the weld both in the negative mode, and (c) the out of weld and (d) the weld both in the positive mode.

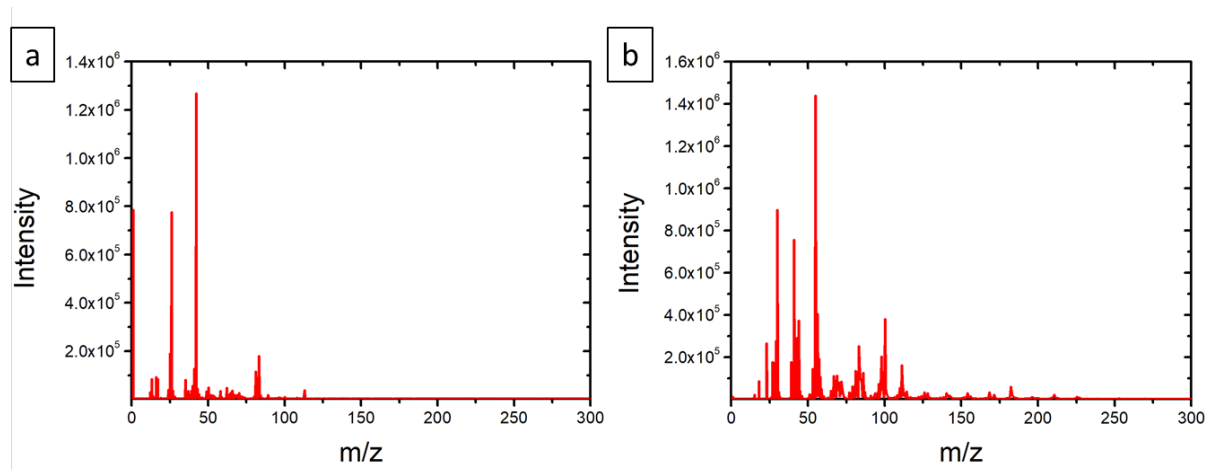


Figure 11: ToF-SIMS reference spectra of polyamide-6.6 (a) in the negative mode, and (b) in the positive mode.

Table 3: Hand selected peak list in the negative mode.

	Mass (u)
Al-	26.9816
AlO-	42.9774
AlO ₂ -	58.9729
Al ₂ O ₃ -	101.9465
AlOH-	43.9884
AlH ₂ O ₂ -	60.9859
AlO ₂ H-	59.98
Al ₃ O ₄ -	144.9252
HO ₃ Al ₂ -	102.9572
NH-	15.0112
CN-	26.0049
CNO-	42.0009
NH ₂ -	16.0195
C ₂ -	23.9999
C ₂ H-	25.0082
NO-	29.997
C ₃ -	36.0003
C ₃ H-	37.0077
C ₂ HN-	39.0111
C ₂ O-	39.996
C ₂ H ₂ N-	40.0216
C ₂ HO-	41.0057
C ₃ NO-	66.0004
C ₄ H ₄ N-	66.0375
C ₂ Al-	50.9821
C ₃ H ₂ NO-	68.0147
CHNO ₂ Al-	85.9822
CHNOAl-	69.9957
C ₂ OAl-	66.9768
CF ₃ -	68.999
F-	18.9987
Cl-	34.9701

Table 4: Hand selected peak list in the positive mode.

	Mass (u)
Al⁺	26.9828
AlH⁺	27.9881
Al₂⁺	53.963
AlO⁺	42.9753
AlOH⁺	43.9843
AlH₂O⁺	44.9932
NH₄⁺	18.0358
CH₄N⁺	30.0356
CH₂NO⁺	44.0123
C₂H₃⁺	27.0232
CH₂N⁺	28.0196
C₂H₄⁺	28.0308
C₂H₅⁺	29.0396
C₃H₃⁺	39.0228
C₂H₃O⁺	43.0184
C₃H₇⁺	43.0566
C₂H₆N⁺	44.0531
C₃H₃O⁺	55.0212
C₄H₇⁺	55.0572
C₃H₆N⁺	56.0591
C₅H₇⁺	67.0554
CHO⁺	29.0017
CF₃⁺	68.9951
Mg⁺	23.9849
Ca⁺	39.9622
C₂HAl⁺	51.9899
CHNAI⁺	53.9922
CHNOAI⁺	69.9959
C₂HOAI⁺	67.9846

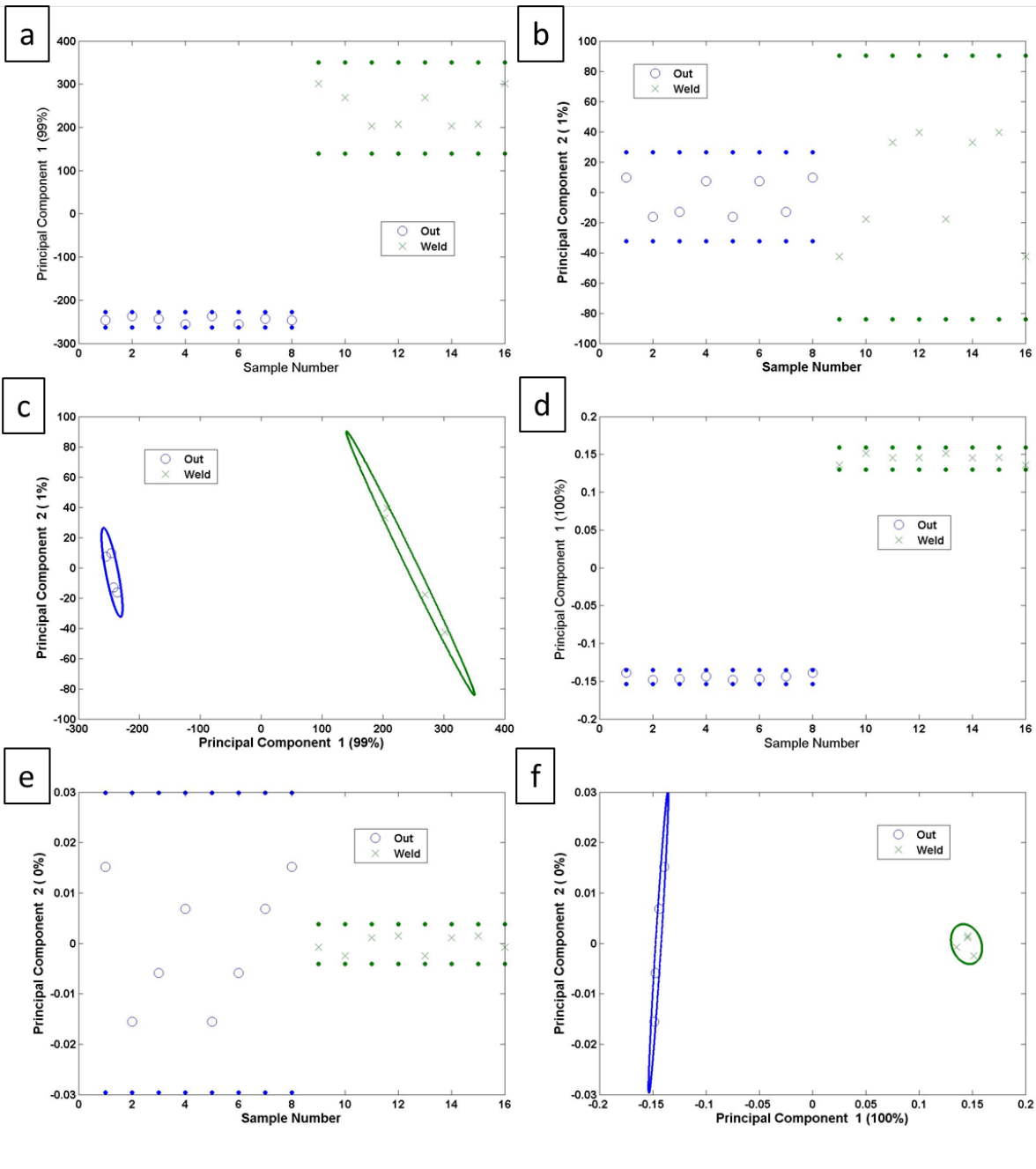


Figure 12: Scores of the hand-selected peak list. In the negative mode (a) PC1, (b) PC2, and (c) PC1 versus PC2. In the positive mode (d) PC1, (e) PC2, and (f) PC1 versus PC2.

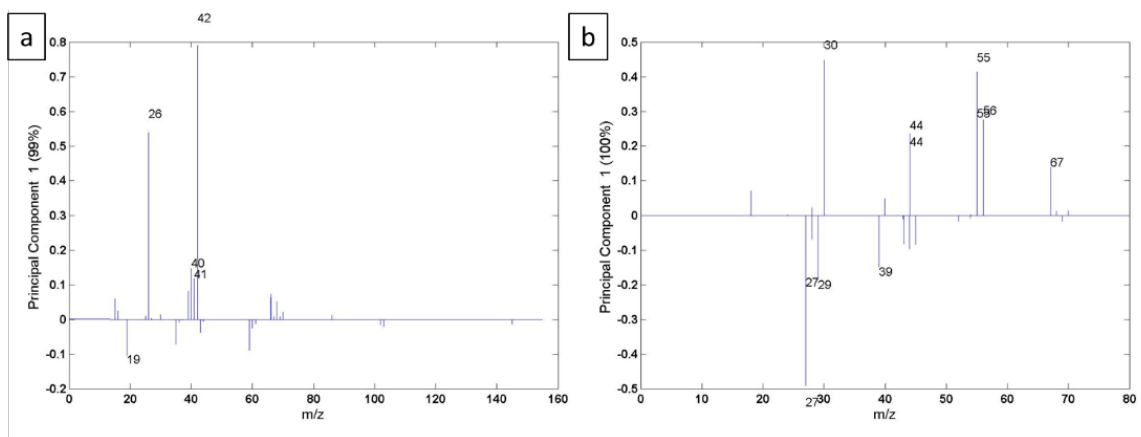


Figure 13: Loadings of PC1 for the hand-selected peak list (a) in the negative mode and (b) in the positive mode.

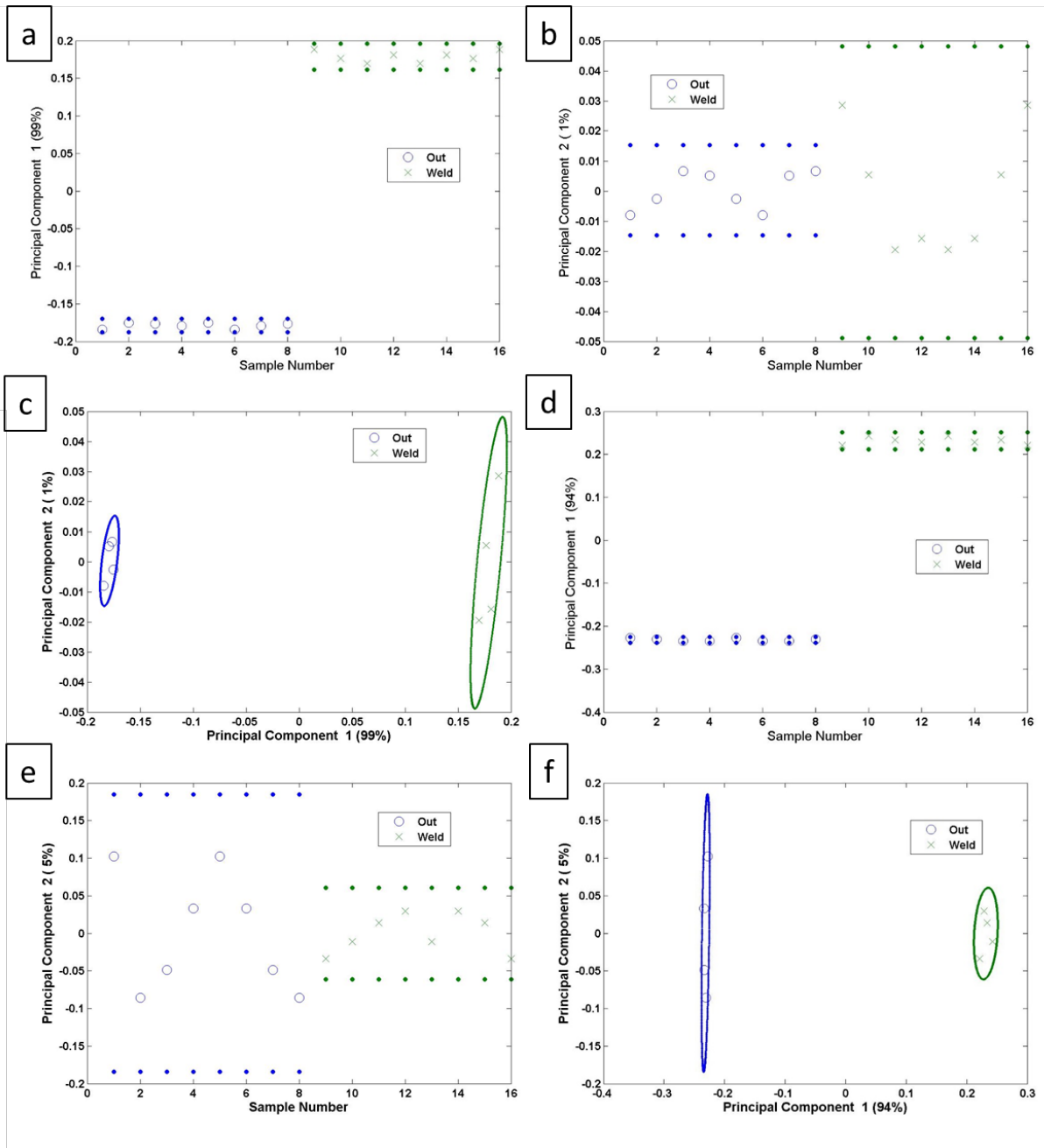


Figure 14: Scores of the automatic generated peak list. In the negative mode (a) PC1, (b) PC2, and (c) PC1 versus PC2. In the positive mode (d) PC1, (e) PC2, and (f) PC1 versus PC2.

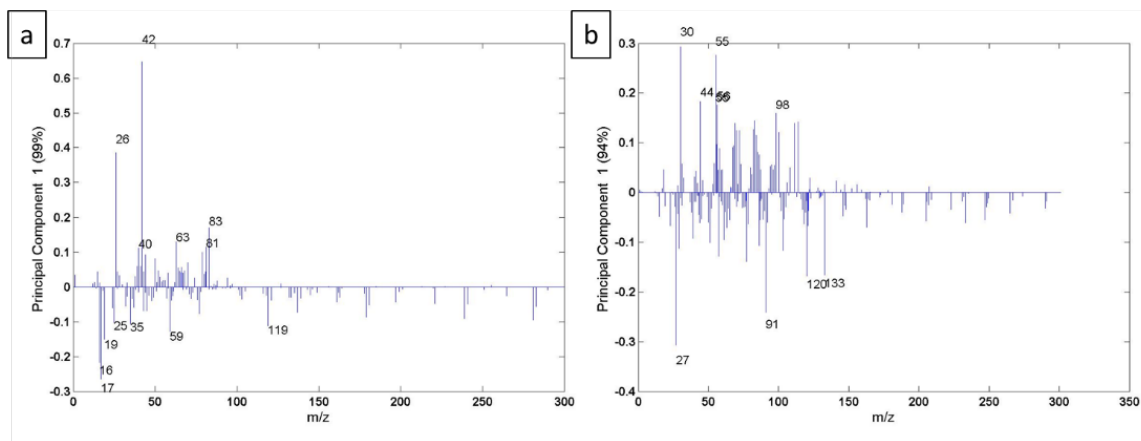


Figure 15: Loadings of PC1 of the automatic generated peak list (a) in the negative mode and (b) in the positive mode.

Spin-coated samples

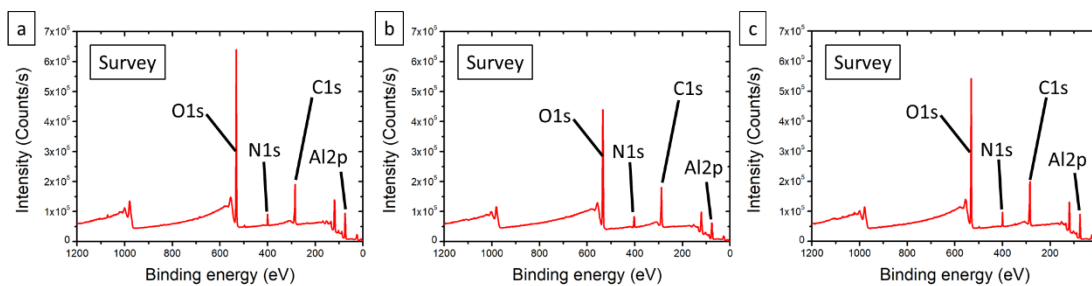


Figure 16: Survey spectra (a) in the reference, (b) out of the weld, and (c) in the weld.

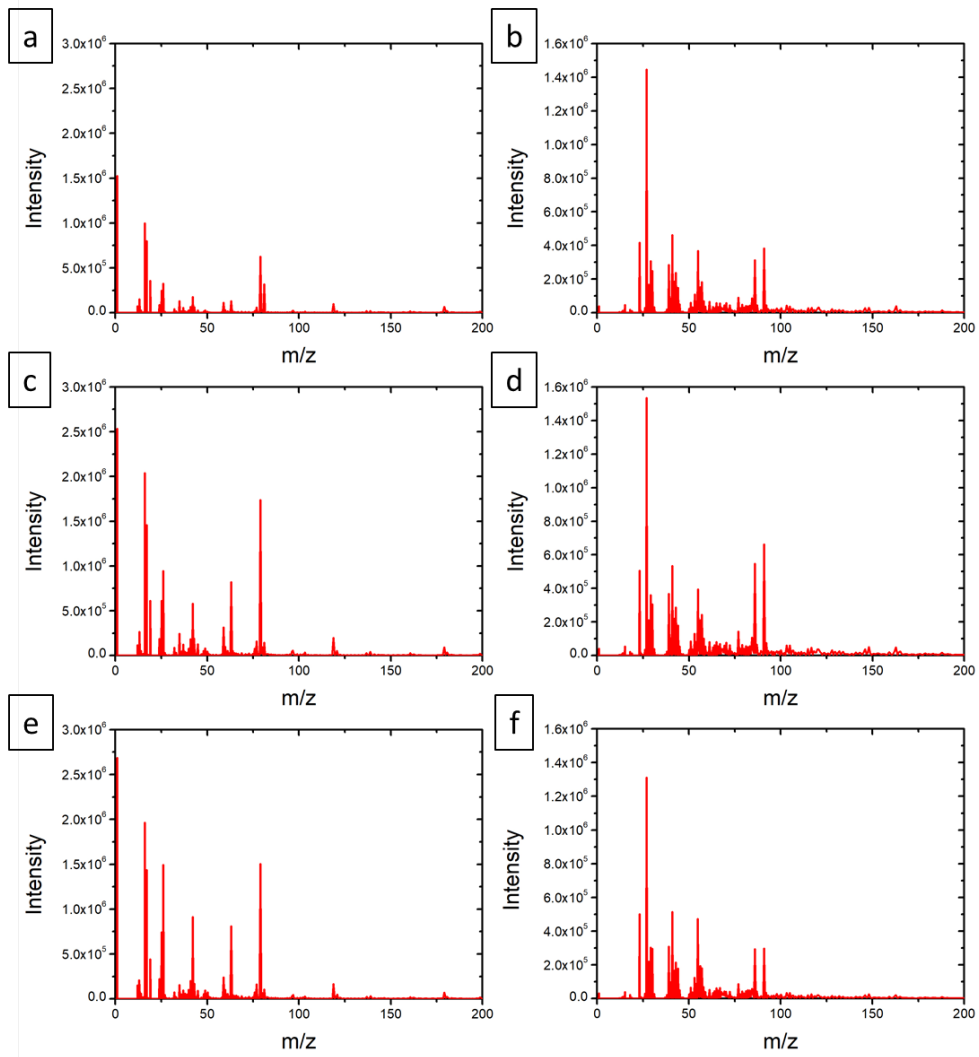


Figure 17: ToF-SIMS spectra in negative and positive mode of (a) and (b) the reference, (c) and (d) the out of weld, and (e) and (f) in the weld.

Table 5: Hand selected peak list in the negative mode.

	Mass (u)	C_4H_5-	53.0419	CH_3NO_2-	88.0157
C-	12.0006	CHNAI-	53.9929	Al_3H_2O-	98.955
NH-	15.0114	C_3H_4N-	54.0378	C_9H_14N-	184.1502
CH_3-	15.0262	COAI-	54.9766	C_10H_16-	198.112
O-	15.9961	CH_2NAI-	55.0004	C_12H_22-	212.1696
NH_2-	16.0194	C_3H_3O-	55.0201	C_12H_21-	225.1435
OH-	17.0036	CHOAI-	55.9772	C_15H_29-	255.2229
F-	18.999	C_2H_2NC-	56.0149	C_17H_33-	283.2537
C_2-	24.001	C_3H_6N-	56.0559		
C_2H-	25.0089	AINO-	56.9787		
CN-	26.0052	CH_2OAI-	56.9949		
AI-	26.9806	C_2H_3NC-	57.0203		
C_2H_3-	27.0258	C_3H_5O-	57.0357		
Si-	27.9762	C_2H_2O-	58.0061		
AIH-	27.9898	CH_4N_3-	58.0326		
CH_2N-	28.021	AlO_2-	58.9721		
SiH-	28.9845	C_2H_3O-	59.0145		
CHO-	29.0045	SiO_2-	59.9673		
NO-	29.9969	AlO_2H-	59.9814		
CH_4N-	30.0342	C_5-	60.0008		
CH_3O-	31.0194	SiHO_2-	60.9748		
O_2-	31.99	AIH_2O_2-	60.989		
O_2H-	32.9979	C_5H-	61.0078		
Cl-	34.9687	NO_3-	61.9739		
C_3-	36.0004	CH_3O_3-	63.0095		
C_3H-	37.0087	C_5H_3-	63.0243		
C_2N-	38.0034	C_4HO-	65.0048		
C_3H_2-	38.0163	C_5H_5-	65.0401		
CAI-	38.9807	H_2O_4-	65.9988		
C_2HN-	39.0107	C_4H_4N-	66.0352		
C_3H_3-	39.025	C_2OAI-	66.9758		
C_2O-	39.9959	C_4H_3O-	67.0192		
CN_2-	40.0071	C_2HOAI-	67.9837		
C_2H_2N-	40.02	C_3H_2NC-	68.0141		
C_2HO-	41.0042	C_4H_6N-	68.0536		
CNO-	42.0005	CNOAI-	68.9766		
AlO-	42.976	C_2H_2OAI-	68.9958		
AlNH_2-	43.0001	C_4H_5O-	69.0356		
C_2H_3O-	43.0194	CHNOAI-	69.9828		
CO_2-	43.9878	C_2H_3OAI-	70.0044		
CH_2NO-	44.0155	C_3H_4NC-	70.0314		
CHO_2-	44.9982	CO_2AI-	70.969		
NO_2-	45.9963	CH_2NOAI-	70.9928		
C_4-	48.0008	C_6-	71.9996		
C_4H-	49.008	C_2H_5OAI-	72.0193		
C_3N-	50.0042	AIH_2O_3-	76.974		
C_2AI-	50.9815	C_5H_5O-	81.0331		
C_4H_3-	51.0246	C_5H_9N-	83.0587		
C_3O-	51.9951	CHNO_2AI-	85.9787		
C_3H_2N-	52.02	HO_2AI_2-	86.9592		
CNAI-	52.9824	CH_2NO_2-	86.9858		

Table 6: Hand selected peak list in the positive mode.

	Mass (u)	CHOAl+	55.9818	C_4H_2Al+	76.9954
C+	11.9979	C_2H_2NO+	56.0132	C_6H_5+	77.0406
NH_3+	17.0251	C_3H_4O+	56.0258	C_4NO+	77.9954
NH_4+	18.0342	C_3H_6N+	56.0525	C_5H_4N+	78.0458
H_3O+	19.0172	C_3H_5O+	57.0352	C_3HN_3+	79.021
C_2H_2+	26.0139	C_3H_7N+	57.0575	C_6H_7+	79.0554
Al+	26.9825	C_4H_9+	57.0724	C_5H_6N+	80.0529
C_2H_3+	27.0233	CH_3OAl+	58.0007	C_5H_5O+	81.0362
AlH+	27.9879	C_2H_4NO+	58.0319	C_6H_9+	81.0738
CH_2N+	28.0187	C_3H_8N+	58.0682	COAl_2+	81.962
C_2H_4+	28.0297	CH_4OAl+	59.01	C_2H_4Al_2+	82.0015
CHO+	29.0015	C_2H_5NO+	59.0383	C_4H_4NO+	82.0303
CH_3N+	29.0247	C_3H_7O+	59.0528	C_5H_8N+	82.069
C_2H_5+	29.0391	C_3H_9N+	59.0727	CHOAl_2+	82.9699
CH_2O+	30.0083	C_2H_6NO+	60.0472	C_3H_4OAl+	83.0098
CH_4N+	30.0349	C_3H_10N+	60.086	C_5H_7O+	83.0541
CH_3O+	31.0174	AlH_2O_2+	60.9875	CH_2OAl_2+	83.9783
CH_5N+	31.0403	C_2H_5O_2+	61.0295	C_4H_6NO+	84.047
C_3H_5+	41.0401	C_3Al+	62.9872	C_5H_8O+	84.0623
C_2H_2O+	42.0091	C_5H_3+	63.0228	C_5H_10N+	84.0906
C_2H_4N+	42.0337	C_5H_5+	65.0395	C_5H_9O+	85.0694
C_2H_4CH_2	42.0446	CAI_2+	65.9656	CHNO_2Al+	85.9833
AlO+	42.9742	C_4H_2O+	66.01	C_4H_8NO+	86.0635
C_2H_3O+	43.0183	C_5H_6+	66.0471	C_5H_12N+	86.1026
C_2H_5N+	43.0419	C_5H_7+	67.0567	HO_2Al_2+	86.9609
C_3H_7+	43.0558	C_2HOAl+	67.9834	C_4H_9NO+	87.0717
AlOH+	43.9831	C_2H_2N_3+	68.0268	C_5H_13N+	87.1036
CH_2NO+	44.0139	C_4H_6N+	68.0526	H_2O_2Al_2+	87.971
C_2H_6N+	44.051	CNOAl+	68.9774	CH_3NO_2Al+	87.9997
AlH_2O+	44.9918	C_2H_2OAl+	68.9938	C_4H_10NO+	88.0785
CH_3NO+	45.0197	C_2H_3N_3+	69.0363	C_5H_14N+	88.1142
C_2H_5O+	45.0343	C_4H_7N+	69.0584	C_5H_3Al+	90.0142
C_2H_7N+	45.058	C_5H_9+	69.0743	C_6H_8N+	94.0681
CH_4NO+	46.0295	Al_2O+	69.9574	C_5H_6NO+	96.049
C_2H_8N+	46.0674	CHNOAl+	69.9902	C_6H_10N+	96.0876
C_4H_2+	50.0148	C_3H_4NO+	70.0326	C_6H_11N+	97.0989
C_2Al+	50.9813	C_4H_8N+	70.0697	C_7H_14+	98.1056
C_4H_3+	51.0232	C_2H_4OAl+	71.0106	C_5H_9NO+	99.0725
C_2HAl+	51.9884	C_3H_5NO+	71.0365	C_6H_13N+	99.1107
C_4H_4+	52.0301	C_4H_7O+	71.0525	C_5H_10NO+	100.0815
CNAH+	52.9823	C_4H_9N+	71.0725	C_7H_16+	100.1262
C_4H_5+	53.0397	C_5H_11+	71.0902	C_6H_7O_2+	111.0548
Al_2+	53.9614	CHO_2Al+	71.9811	C_6H_10NO+	112.0842
CHNAH+	53.9926	C_6+	72.0069	C_7H_12NO+	126.0974
C_3H_2O+	54.0093	C_3H_6NO+	72.0465	C_7H_12N_2O+	140.114
C_3H_4N+	54.0358	C_4H_10N+	72.0868	C_7H_14N_2O+	142.13
C_4H_6+	54.048	C_3H_7NO+	73.054	C_9H_16NO+	154.1317
HAl_2+	54.9727	C_4H_11N+	73.09	C_10H_18NO+	168.1481
CH_2NAH+	54.9867	C_3H_8NO+	74.0623	C_9H_19N_2O+	171.1579
C_3H_3O+	55.0196	C_4H_12N+	74.098	C_12H_22NO_2+	212.1431
C_4H_7+	55.0578	C_6H_3+	75.0245	C_12H_22N_2O_2+	226.2119

Model samples

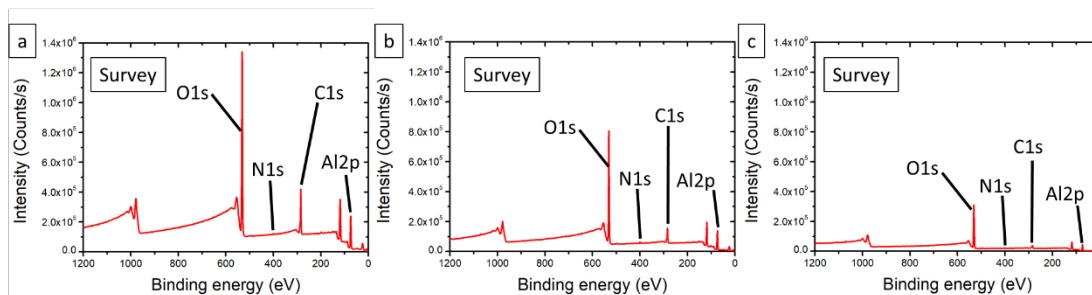


Figure 18: XPS survey spectra of (a) the UV-cleaned samples, (b) the air-dried samples, and (c) the heated samples.

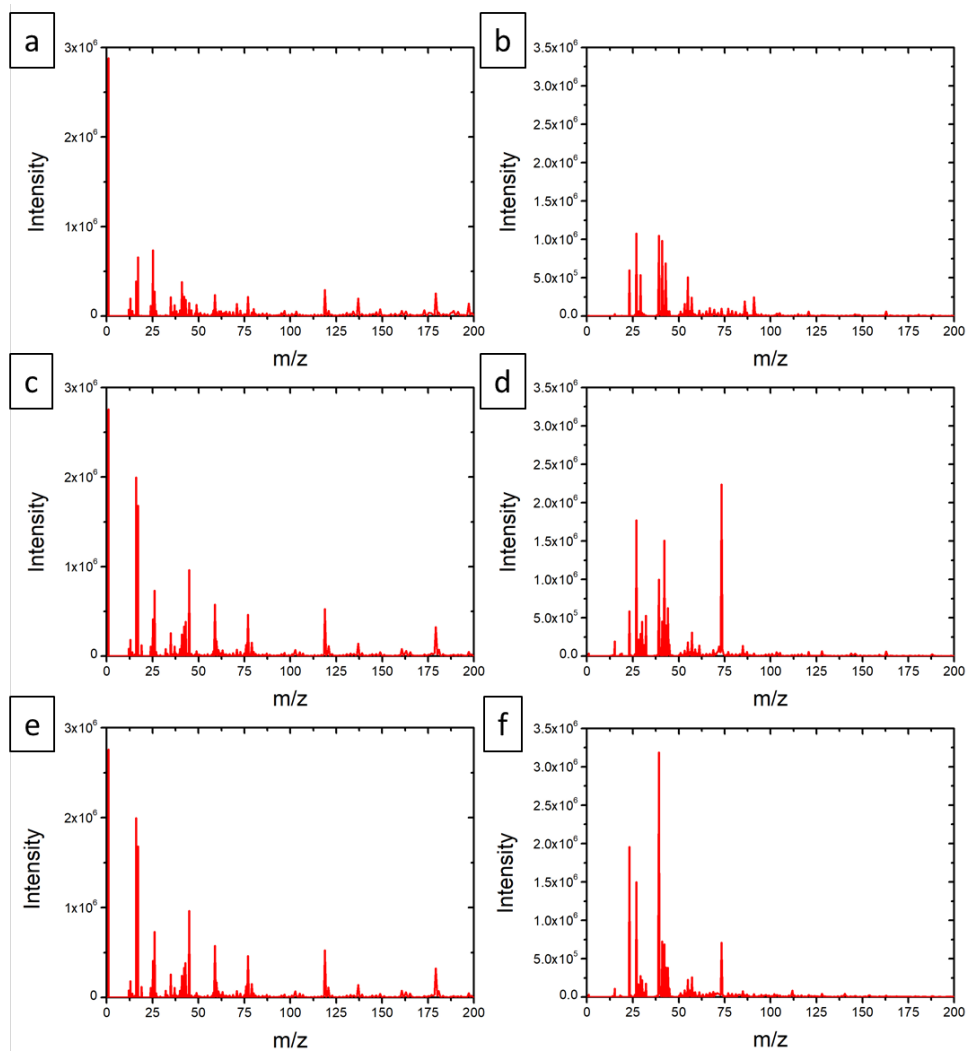


Figure 19: ToF-SIMS spectra in negative and positive mode of (a) and (b) the UV-cleaned samples, (c) and (d) the air-dried samples, and (e) and (f) the heated samples.

Table 7: Hand selected peak list in the negative mode.

	Mass (u)
C-	12.0004
NH-	15.0113
F-	18.9989
Na-	22.9901
C ₂ -	24.0008
CN-	26.005
Al-	26.9814
Si-	27.9768
AlH-	27.9897
CHO-	29.0042
CH ₄ N-	30.036
Cl-	34.9699
CAI-	38.9826
C ₂ O-	39.9958
C ₂ HO-	41.0045
CNO-	42.0008
AlO-	42.9763
AlNH ₂ -	43.0002
CO ₂ -	43.9891
CH ₂ NO-	44.0155
CHO ₂ -	44.9985
C ₂ Al-	50.9818
C ₃ O-	51.9954
CHNAI-	53.9936
COAl-	54.9772
C ₂ HNO-	55.0051
CHOAl-	55.985
C ₂ H ₂ NO-	56.0143
AlNO-	56.9795
C ₂ H ₃ NO-	57.0193
C ₂ H ₄ NO-	58.0307
AlO ₂ -	58.9723
AlO ₂ H-	59.9811
C ₂ OAl-	66.9766
C ₂ HOAl-	67.9844
CNOAl-	68.9785
CHNOAl-	69.9877
CO ₂ Al-	70.9694
COAl ₂ -	81.9577
CHNO ₂ Al-	85.9808
CHO ₃ Al-	87.9744
CH ₂ O ₃ Al-	88.982
Al ₃ H ₂ O-	98.952

Table 8: Hand selected peak list in the positive mode.

	Mass (u)
C+	11.9981
CH_3+	15.023
NH_4+	18.0348
Na+	22.9914
Mg+	23.9843
Al+	26.9812
AlH+	27.9878
CH_2N+	28.0189
C_2H_4+	28.0304
CHO+	29.0023
C_2H_5+	29.039
CH_4N+	30.0349
CH_3O+	31.0179
AlOH+	43.9829
CH_2NO+	44.0115
CHNAH+	53.9924
CHOAH+	55.9815
C_2H_2NO+	56.0114
CH_2OAH+	56.9917
CH_3OAH+	57.9999
C_2H_4NO+	58.0292
AlO_2+	58.9713
CH_4OAH+	59.0088
C_2H_5NO+	59.0356
AlO_2H+	59.9783
C_2H_6NO+	60.0465
AlH_2O_2+	60.9872
Al_2O+	69.9564
CHNOAH+	69.9859
CH_3NOAH+	72.0015
CHNO_2AH+	85.9776
C_2H_5NOAH+	86.015
C_2H_6NOAH+	87.0217
CH_3NO_2AH+	87.9993
C_2H_5NO_2AH+	102.0151

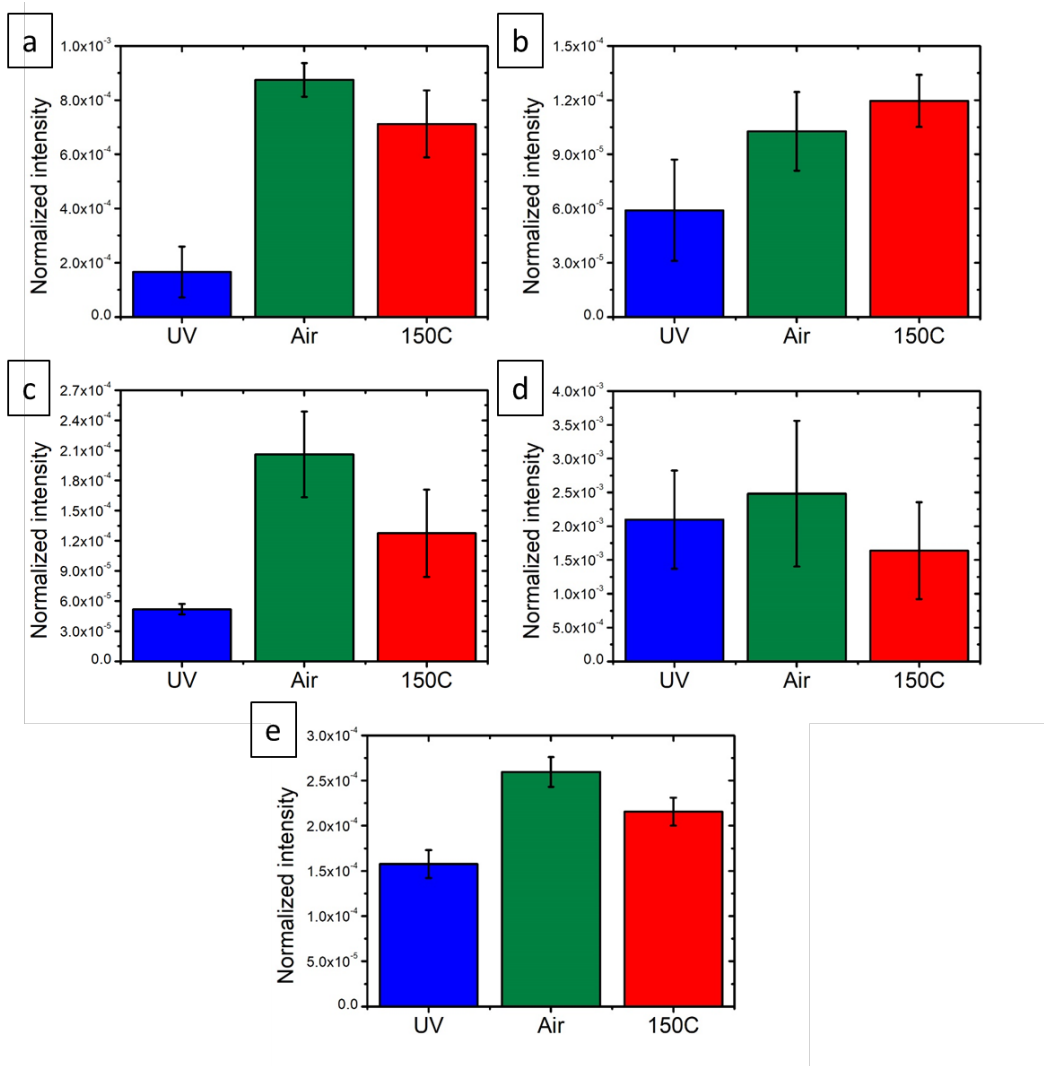


Figure 20: ToF-SIMS total counts normalized intensity of characteristic peaks of methylamide presented as histograms per samples, in blue the UV cleaned samples, in green the air-dried samples and in red the heated samples of (a) $C_2H_4NO^+$, (b) AlO_2^+ , (c) AlO^+ , (d) $AlOH^+$, and (e) $C_2H_5NOAl^+$.

Appendix to titanium and polyamide bonding?

Welded samples

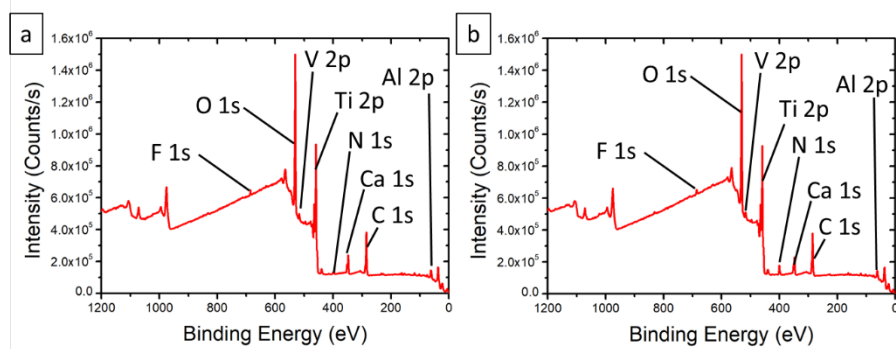


Figure 21: XPS survey spectra for (a) out of the weld, and (b) in the weld.

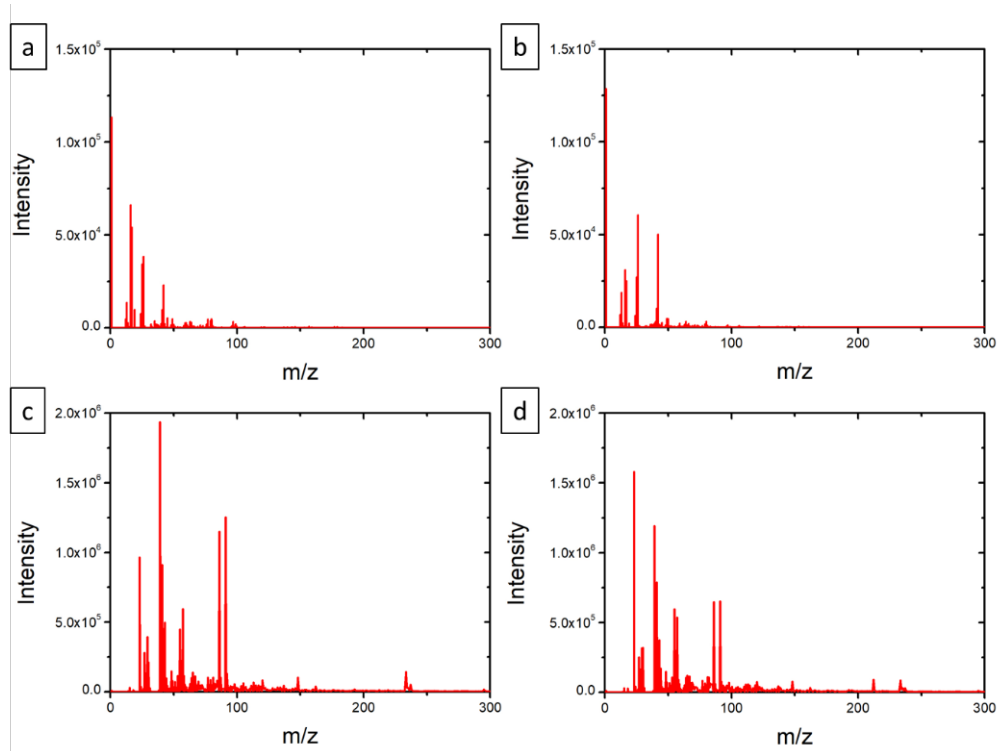


Figure 22: ToF-SIMS spectra in negative mode of (a) out of the weld and (b) in the weld, and in positive mode (c) out of the weld and (d) in the weld.

Table 9: Hand selected peak list in the negative mode.

	Mass (u)
C-	12.001
NH-	15.0112
NH ₂ -	16.0199
F-	18.9985
C ₂ -	24.0005
C ₂ H-	25.0095
CN-	26.0061
CH ₂ N-	28.0227
NO-	29.9961
S-	31.9722
Cl-	34.9697
C ₃ -	36.0001
C ₃ H-	37.0086
C ₂ N-	38.0037
C ₃ H ₂ -	38.0169
C ₂ HN-	39.0111
C ₂ O-	39.9961
C ₂ H ₂ N-	40.0211
C ₂ HO-	41.0052
CNO-	42.0007
AlO-	42.9771
CO ₂ -	43.9906
CH ₂ NO-	44.0168
AlNO-	56.9794
AlO ₂ -	58.9717
TiO-	63.9404
TiH ₂ O-	65.9588
C ₃ H ₄ NO-	70.0332
C ₂ Ti-	71.9489
CNTi-	73.9473
CHNTi-	74.9537
TiO ₂ -	79.9342
VNO-	80.9428
TiH ₂ O ₂ -	81.9551
VO ₂ -	82.9336
C ₂ OTi-	87.9425
C ₂ H ₂ OTi-	89.9592
CNOV-	92.9411
CH ₃ NOTi-	92.9665
VO ₃ -	98.9309
C ₂ HO ₂ Ti-	104.9442
CNO ₂ Ti-	105.9419
CHNO ₂ Ti-	106.9424
CHNOTi-	90.9495
CNOTi-	89.9399

Table 10: Hand selected peak list in the positive mode.

	Mass (u)
NH ₃ ⁺	17.0264
NH ₄ ⁺	18.0356
Na ⁺	22.9909
Mg ⁺	23.9847
Al ⁺	26.9809
C ₂ H ₃ ⁺	27.0232
Si ⁺	27.9757
CH ₂ N ⁺	28.0191
C ₂ H ₅ ⁺	29.0398
CH ₄ N ⁺	30.0356
K ⁺	38.9647
Ca ⁺	39.9615
CH ₂ NO ⁺	44.0143
C ₂ H ₆ N ⁺	44.0518
Ti ⁺	47.9461
TiH ⁺	48.9533
V ⁺	50.9426
C ₃ H ₃₀ ⁺	55.0191
C ₂ H ₄ NO ⁺	58.0306
CTi ⁺	59.9458
C ₂ H ₆ NO ⁺	60.0477
CHTi ⁺	60.9561
CH ₂ Ti ⁺	61.9614
TiNH ⁺	62.9566
TiO ⁺	63.9419
TiOH ⁺	64.9479
VO ⁺	66.9387
C ₃ H ₆ NO ⁺	72.0454
C ₄ H ₁₀ N ⁺	72.0833
C ₂ HTi ⁺	72.9543
C ₂ H ₂ Ti ⁺	73.9623
C ₂ H ₃ Ti ⁺	74.9702
TiO ₂ H ⁺	80.9446
C ₅ H ₇₀ ⁺	83.0502
C ₄ H ₈ NO ⁺	86.061
CHNOTi ⁺	90.9485
CH ₃ NOTi ⁺	92.9668
C ₅ H ₈ NO ⁺	98.0615
C ₅ H ₁₀ NO ⁺	100.0772
Ti ₂ O ₂ H ⁺	128.8965
CH ₂ NTi ⁺	75.9663
CHO ₂ Ti ⁺	92.9422
CH ₃₀ ₂ Ti ⁺	94.9573

Spin-coated samples

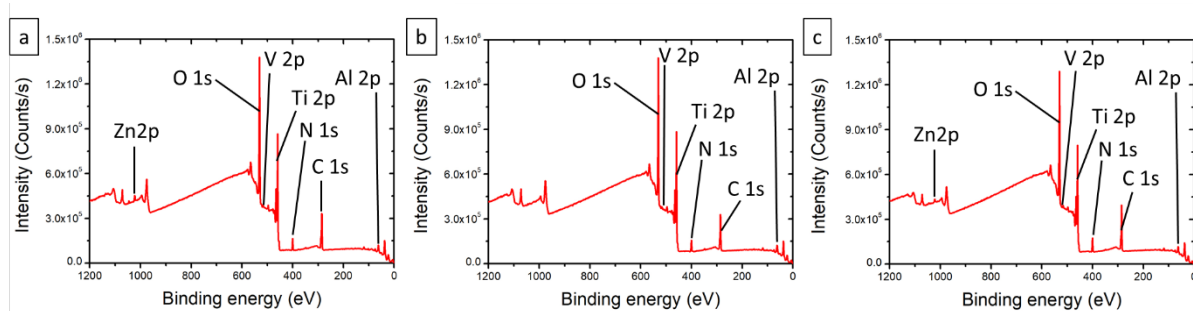


Figure 23: XPS survey spectra for (a) the reference, (b) out of the weld, and (c) in the weld.

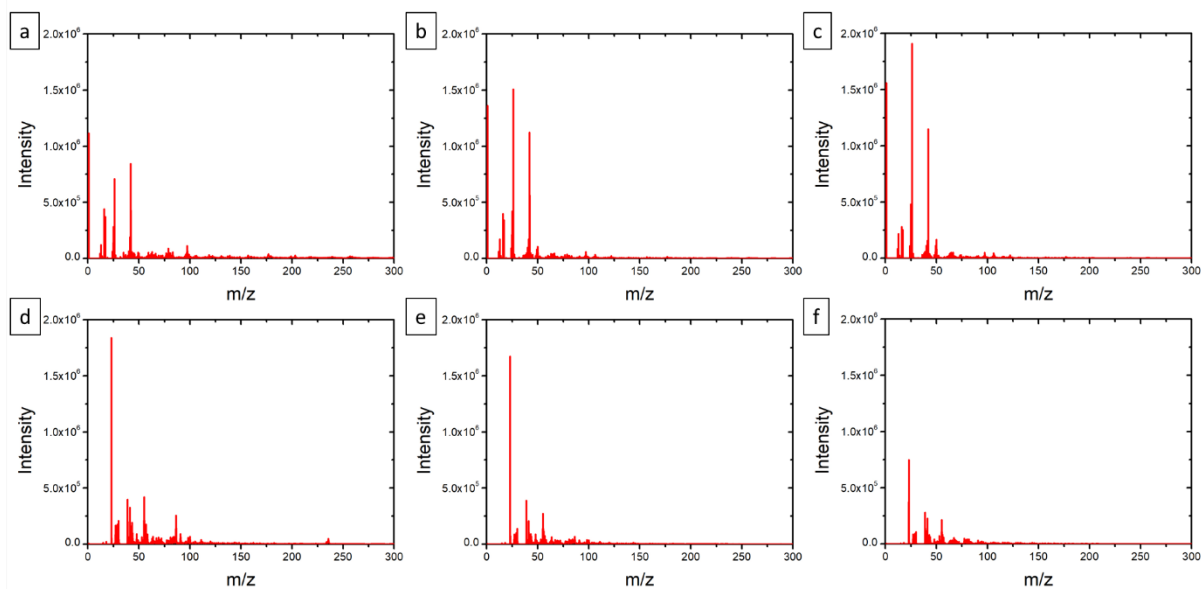


Figure 24: ToF-SIMS spectra in negative mode of (a) the reference, (b) out of the weld and (c) in the weld, and in positive mode (d) in the reference, (e) out of the weld and (f) in the weld.

Table 11: Loadings from the two first principal components in negative mode associated to the masses and the ions.

	Mass (u)	Loadings 1	Loadings 2
NH_4+	18.0347	0.1109	-0.0093
CH_4N+	30.034	0.3594	-0.1511
CH_2NO+	44.0134	0.2575	0.0511
NH_3+	17.0257	0.0185	0.0199
C_2H_3+	27.022	0.0549	0.2713
CH_2N+	28.0178	0.0882	0.3368
C_2H_5+	29.0387	0.1671	0.0154
C_3H_3+	39.0227	0.009	0.4574
C_3H_5+	41.039	0.3184	0.2898
C_3H_7+	43.0549	0.1634	-0.2818
C_2H_3O+	43.0175	0.0724	0.0901
C_2H_6N+	44.0507	0.1699	-0.0967
C_3H_3O+	55.0175	0.326	0.0864
C_3H_6N+	56.0513	0.2365	-0.1091
C_2H_4NO+	58.0305	0.1225	-0.028
C_5H_7+	67.0567	0.1232	0.2284
C_6H_8N+	94.0649	0.0834	0.2938
C_5HO+	77.0032	0.0012	0.2829
C_5H_8N+	82.0654	0.1556	0.1001
Al+	26.9795	-0.168	-0.0377
V+	50.9425	-0.075	0.0457
Ti+	47.9443	-0.3954	0.1069
TiO+	63.9413	-0.3281	0.0937
Ti_2O_2+	127.883	-0.0713	0.0599
Ti_2O_3+	143.8786	-0.1084	0.0838
TiOH+	64.9473	-0.1512	0.0485
TiH_2O_2+	81.9554	-0.0163	0.1037
TiO_2H+	80.9457	-0.0754	0.0636
CHNOTi+	90.9611	-0.029	0.0511
CH_2NOTi+	91.9646	-0.0142	0.0607
CH_3NOTi+	92.9691	-0.0051	0.0441
C_7H_8N+	106.0656	0.0237	0.2572
CH_2NO_2Ti+	107.9588	0.0003	0.029
CH_2O_2Ti+	93.9509	-0.0149	0.004
C_2HOTi+	88.9497	-0.0293	0.0398
C_3H_4Ti+	87.9783	-0.0246	0.0007
CTi+	59.9433	-0.0327	0.0067
CHTi+	60.9536	-0.0702	0.0223
C_2HTi+	72.9528	-0.0879	0.0875
C_3H_2Ti+	85.9593	-0.0456	0.048
CNTi+	73.9525	-0.0651	0.0898
CH_2NTi+	75.964	-0.0222	0.0342

Table 12: Loadings from the two first principal components in positive mode associated to the masses and the ions.

	Mass (u)	Loadings 1	Loadings 2
NH_4+	18.0347	0.1109	-0.0093
CH_4N+	30.034	0.3594	-0.1511
CH_2NO+	44.0134	0.2575	0.0511
NH_3+	17.0257	0.0185	0.0199
C_2H_3+	27.022	0.0549	0.2713
CH_2N+	28.0178	0.0882	0.3368
C_2H_5+	29.0387	0.1671	0.0154
C_3H_3+	39.0227	0.009	0.4574
C_3H_5+	41.039	0.3184	0.2898
C_3H_7+	43.0549	0.1634	-0.2818
C_2H_3O+	43.0175	0.0724	0.0901
C_2H_6N+	44.0507	0.1699	-0.0967
C_3H_3O+	55.0175	0.326	0.0864
C_3H_6N+	56.0513	0.2365	-0.1091
C_2H_4NO+	58.0305	0.1225	-0.028
C_5H_7+	67.0567	0.1232	0.2284
C_6H_8N+	94.0649	0.0834	0.2938
C_5HO+	77.0032	0.0012	0.2829
C_5H_8N+	82.0654	0.1556	0.1001
Al+	26.9795	-0.168	-0.0377
V+	50.9425	-0.075	0.0457
Ti+	47.9443	-0.3954	0.1069
TiO+	63.9413	-0.3281	0.0937
Ti_2O_2+	127.883	-0.0713	0.0599
Ti_2O_3+	143.8786	-0.1084	0.0838
TiOH+	64.9473	-0.1512	0.0485
TiH_2O_2+	81.9554	-0.0163	0.1037
TiO_2H+	80.9457	-0.0754	0.0636
CHNOTi+	90.9611	-0.029	0.0511
CH_2NOTi+	91.9646	-0.0142	0.0607
CH_3NOTi+	92.9691	-0.0051	0.0441
C_7H_8N+	106.0656	0.0237	0.2572
CH_2NO_2Ti+	107.9588	0.0003	0.029
CH_2O_2Ti+	93.9509	-0.0149	0.004
C_2HOTi+	88.9497	-0.0293	0.0398
C_3H_4Ti+	87.9783	-0.0246	0.0007
CTi+	59.9433	-0.0327	0.0067
CHTi+	60.9536	-0.0702	0.0223
C_2HTi+	72.9528	-0.0879	0.0875
C_3H_2Ti+	85.9593	-0.0456	0.048
CNTi+	73.9525	-0.0651	0.0898
CH_2NTi+	75.964	-0.0222	0.0342

Model samples

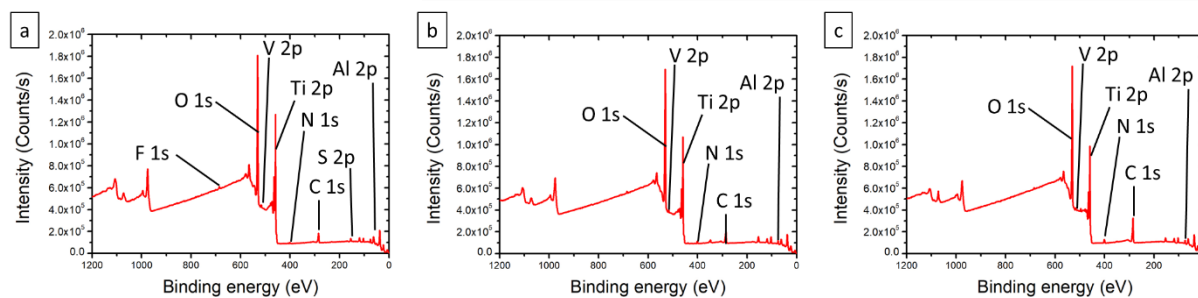


Figure 25: XPS survey spectra for (a) the UV cleaned samples, (b) the air dried samples, and (c) the heated samples.

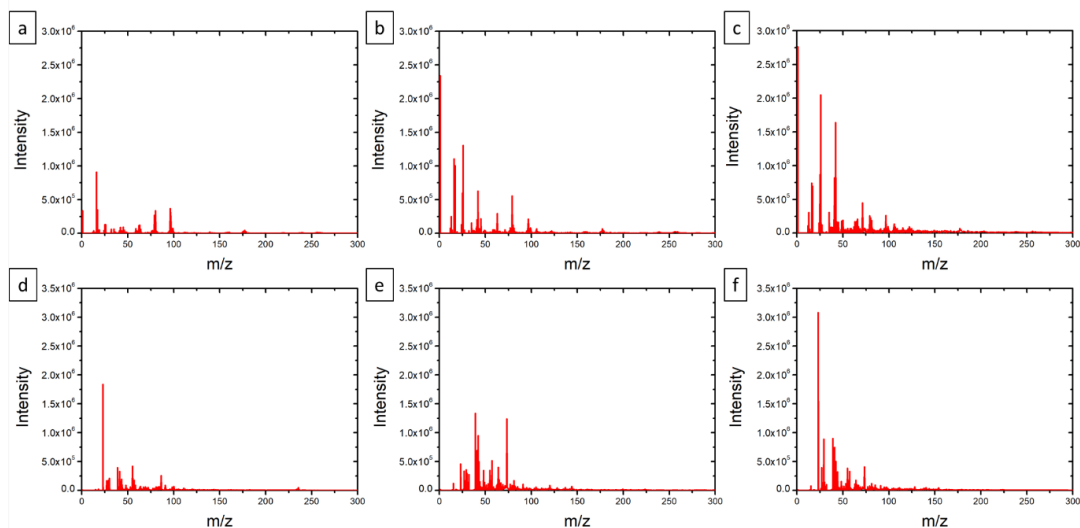


Figure 26: ToF-SIMS spectra in negative mode of (a) the UV-cleaned samples, (b) the air-dried samples and (c) the heated samples, and in positive mode (d) the UV-cleaned samples, (e) the air-dried samples and (f) the heated samples.

Table 13: Hand selected peak list in the negative mode.

	Mass (u)
TiO-	63.9421
TiO_2-	79.9367
TiO_3-	95.9323
TiOH-	64.9505
TiH_2O-	65.9618
TiH_2O_2-	81.9566
TiO_2H-	80.9452
AlO-	42.9771
AlO_2-	58.9726
VO_2-	82.9368
NH-	15.011
CH_3-	15.0266
CN-	26.0077
CNO-	42.0028
NH_2-	16.0205
C_2-	24.0005
C_2H-	25.0098
NO-	29.9979
C_2H_4NO-	58.0329
C_2H_3O-	43.0208
CH_2NO-	44.0165
CHO-	29.0045
CH_4N-	30.0365
CNTi-	73.9519
CH_2NTi-	75.9648
CH_3NTi-	76.9742
CH_3OTi-	78.9614
CHO_2Ti-	92.9442
C_2Ti-	71.9494
CNOTi-	89.9511
CHNOTi-	90.9559
CHNO_2Ti-	106.9484
CH_2NO_2Ti-	107.9538
C_2HNO_2Ti-	118.9503
C_2NO_2Ti-	117.9428
C_2H_5NOTi-	106.9864

Table 14: Hand selected peak list in the positive mode.

	Mass (u)	CH_2O_2T	93.9534
Ti+	47.9455	CH_3O_2T	94.9596
TiO+	63.943	CH_4O_2T	95.9685
Ti_2O_2+	127.8852	CH_2NTi+	75.9669
Ti_2O_3+	143.881	C_2H_5NO	106.9645
TiOH+	64.9486	C_2H_4NO	105.9727
TiH_2O_2+	81.9545		
Ti_2O_2H+	128.8912		
TiO_2H+	80.9457		
H_2O_4Ti_2+	161.8898		
Al+	26.9814		
AlOH+	43.9835		
AlH+	27.9921		
V+	50.9433		
VO+	66.9403		
VOH+	67.9464		
CH_3+	15.0228		
NH_4+	18.035		
CH_4N+	30.0355		
CHO+	29.0035		
CH_3O+	31.0177		
CH_5N+	31.042		
CH_6N+	32.0519		
CH_2NO+	44.0131		
CH_2N+	28.0189		
C_2H_4NO+	58.0309		
C_2H_6NO+	60.0444		
C_2H_3O+	43.0176		
C_4H_2+	50.0132		
C_7H_7+	91.0548		
CTi+	59.9446		
CHTi+	60.9552		
CH_2Ti+	61.9626		
CH_3Ti+	62.9702		
C_2H_2Ti+	73.9623		
C_2HTi+	72.9548		
C_3Ti+	83.9455		
C_3H_2Ti+	85.9602		
C_3H_3Ti+	86.9701		
C+	11.9977		
CH+	13.0059		
CH_2+	14.0138		
CHNTi+	74.9555		
CHNOTi+	90.9601		
CH_2NOTi+	91.9634		
CH_3NOTi+	92.9688		
CHOTi+	76.9497		
CH_2OTi+	77.961		
CH_3OTi+	78.9643		
C_2HOTi+	88.9504		
CHO_2Ti+	92.9429		

Appendix to diffusion

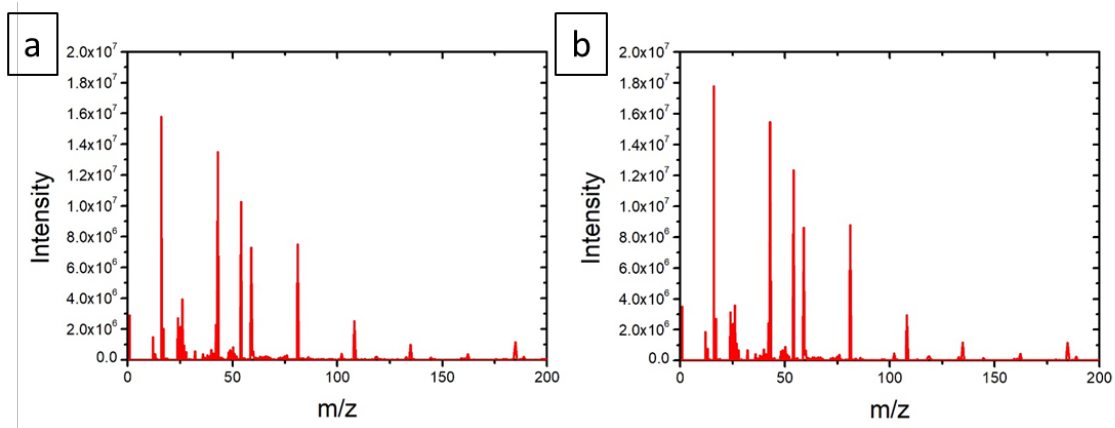


Figure 27: ToF-SIMS mass spectra of the profiles (a) in the reference, (b) out of weld and (c) in the weld.

Bibliography

- [1] S. A. de Beaune. *L'homme et l'outil. L'invention technique durant la préhistoire*. Number 17. CNRS éditions, Paris, 2008.
- [2] J. P. Bergmann and M. Stambke. Potential of Laser-manufactured Polymer-metal hybrid Joints. *Physics Procedia*, 39:84–91, 2012.
- [3] P Amend, S Pfindel, and M Schmidt. Thermal joining of thermoplastic metal hybrids by means of mono- and polychromatic radiation. In *Physics Procedia*, volume 41, pages 98–105, 2013.
- [4] A. Roesner, S. Scheik, A. Olowinsky, A. Gillner, U. Reisgen, and M. Schleser. Laser assisted joining of plastic metal hybrids. In *Physics Procedia*, volume 12, pages 373–380, 2011.
- [5] S. Katayama and Y. Kawahito. Laser direct joining of metal and plastic. *Scripta Materialia*, 59(12):1247–1250, 2008.
- [6] M. Wahba, Y. Kawahito, and S. Katayama. Laser direct joining of AZ91D thixomolded Mg alloy and amorphous polyethylene terephthalate. *Journal of Materials Processing Technology*, 211(6):1166–1174, 2011.
- [7] Oxford Dictionaries. Definition of adhesion in English by Oxford Dictionaries, 2018.
- [8] C. Bischof, A. Bauer, W. Possart, and R. D. Schulze. Zur Adhäsion in Metall-Polymer-Grenzschichten und ihrer praktischen Nutzung. *Acta Polymerica*, 40(3):214–221, 1989.
- [9] A. Baldan. Adhesion phenomena in bonded joints. *International Journal of Adhesion and Adhesives*, 38:95–116, 2012.
- [10] J.W. McBain and D.G. Hopkins. On Adhesives and Adhesive Action. *The Journal of Physical Chemistry*, 29(2):188–204, jan 1925.
- [11] L. H. Sharpe and H. Schonhorn. Surface Energetics, Adhesion, and Adhesive Joints. pages 189–201. jan 1964.
- [12] S. S. Voyutskiï and Yu L. Margolina. The Nature of Self-Adhesion (Tack) of Polymers. I. *Rubber Chemistry and Technology*, 30(2):531–543, mar 1957.
- [13] B V Derjaguin and V P Smilga. Electronic theory of adhesion. *Journal of Applied Physics*, 38(12):4609–4616, 1967.
- [14] B. Bonpain and M. Stommel. Influence of surface roughness on the shear strength of direct injection molded plastic-aluminum hybrid-parts. 2018.

- [15] J. Bardon, D. Del Frari, A. Al-Sayyad, P. Hirchenhahn, L. Houssiau, and P. Plapper. Laser Welding of Polyamide-6.6 and Aluminium: Effect of Preliminary Aluminium Anodisation Treatment. In *Extended Abstracts of Adhesion'19*, Bristol, 2019.
- [16] A. Al-Sayyad, J. Bardon, P. Hirchenhahn, G. Mertz, C. Haouari, L. Houssiau, and P. Plapper. Influence of laser ablation and plasma surface treatment on the joint strength of laser welded aluminum-polyamide assemblies. *Jnpli 2017*, 2017.
- [17] A. Al-Sayyad, J. Bardon, P. Hirchenhahn, K. Santos, L. Houssiau, and P. Plapper. Aluminum pretreatment by a laser ablation process: influence of processing parameters on the joint strength of laser welded aluminum – polyamide assemblies. *Procedia CIRP*, 74:495–499, 2018.
- [18] S.T. Amancio-Filho and J.F. Dos Santos. Joining of Polymers and Polymer-Metal Hybrid Structures: Recent Developments and Trends. *Polymer engineering and Science*, 49:1461–1476, 2009.
- [19] J. Rotheiser. *Joining of Plastics: Handbook for Designers and Engineers*. Carl Hanser Verlag, Munich, 1999.
- [20] L. Chanson. *Traité d'ébénisterie*. Vial edition, 2003.
- [21] W. Graubner, G. Daleiden, E. Fline, W. Gronder, and K. Schenkel. *Assemblages du bois*. Vial edition, 2020.
- [22] P. P. A. Mazza, F. Martini, B. Sala, M. Magi, M. P. Colombini, G. Giachi, F. Landucci, C. Lemorini, F. Modugno, and E. Ribechini. A new Palaeolithic discovery: tar-hafted stone tools in a European Mid-Pleistocene bone-bearing bed. *Journal of Archaeological Science*, 33(9):1310–1318, sep 2006.
- [23] A Baldan. Adhesively-bonded joints and repairs in metallic alloys, polymers and composite materials: Adhesives, adhesion theories and surface pretreatment. *Journal of Materials Science*, 39(1):1–49, 2004.
- [24] C. Ageorges, L. Ye, and M. Hou. Advances in fusion bonding techniques for joining thermoplastic matrix composites: a review. *Composites Part A: Applied Science and Manufacturing*, 32(6):839–857, jun 2001.
- [25] R. J. Crawford and Y. Tam. Friction welding of plastics. *Journal of Materials Science*, 16(12):3275–3282, dec 1981.
- [26] A. Yousefpour, M. Hojjati, and J.-P. Immarigeon. Fusion Bonding/Welding of Thermoplastic Composites. *Journal of Thermoplastic Composite Materials*, 17(4):303–341, 2004.
- [27] D. Grewell, A. Benatar, and J.B. Park. *Plastics and Composites Welding Handbook*. Carl Hanser Verlag, Munich, 2003.
- [28] V. K. Stokes. Vibration welding of thermoplastics. Part I: Phenomenology of the welding process. *Polymer Engineering & Science*, 28(11):718–727, 1988.
- [29] H. Potente, J. Natrop, T. K. Pedersen, and M. Uebbing. Comparative Investigations into the Welding of Glass-Fiber-Reinforced PES. *Journal of Thermoplastic Composite Materials*, 6(2):147–159, apr 1993.

- [30] H. Potente and M. Uebbing. Friction welding of polyamides. *Polymer Engineering and Science*, 37(4):726–737, apr 1997.
- [31] P. Bates, D. Couzens, and J. Kendall. Vibration Welding of Continuously Reinforced Thermoplastic Composites. *Journal of Thermoplastic Composite Materials*, 14(4):344–354, jul 2001.
- [32] C. J. Nonhof and G a Luiten. Estimates for process conditions during the ultrasonic welding of thermoplastics. *Polymer Engineering and Science*, 36(9):1177–1183, aug 1996.
- [33] F. Balle, G. Wagner, and D. Eifler. Ultrasonic spot welding of aluminum sheet/carbon fiber reinforced polymer – joints. *Materialwissenschaft und Werkstofftechnik*, 38(11):934–938, 2007.
- [34] S. R. Strand, C. D. Sorensen, and T. W. Nelson. Effects of friction stir welding on polymer microstructure. In *Annual Technical Conference - ANTEC, Conference Proceedings*, volume 1, pages 1078–1082, 2003.
- [35] Z. Kiss and T. Czigány. Applicability of friction stir welding in polymeric materials. *Periodica Polytechnica*, 51(1):15–18, 2007.
- [36] F. Simoes and D. M. Rodrigues. Material flow and thermo-mechanical conditions during Friction Stir Welding of polymers: Literature review, experimental results and empirical analysis. *Materials and Design*, 59:344–351, 2014.
- [37] N Mendes, P Neto, M A Simão, A Loureiro, and J N Pires. A novel friction stir welding robotic platform: welding polymeric materials. *International Journal of Advanced Manufacturing Technology*, 85(1-4):37–46, 2016.
- [38] S. Eslami, P. J Tavares, and P. M.G.P. Moreira. Friction stir welding tooling for polymers: review and prospects. *International Journal of Advanced Manufacturing Technology*, 89(5-8):1677–1690, 2017.
- [39] Y. Huang, Xi. Meng, Y. Xie, L. Wan, Z. Lv, J. Cao, and J. Feng. Friction stir welding/processing of polymers and polymer matrix composites. *Composites Part A: Applied Science and Manufacturing*, 105:235–257, 2018.
- [40] E. D. Nicholas. Developments in the Friction Stir Welding of Metals. In *Proc. of ICAA-6*, pages 139–151, 1998.
- [41] V. A. Kagan. Benefits of Induction Welding of Reinforced Thermoplastics in High Performance Applications. *Journal of Reinforced Plastics and Composites*, 24(13):1345–1352, sep 2005.
- [42] V. K. Stokes. Experiments on the induction welding of thermoplastics. *Polymer Engineering and Science*, 43(9):1523–1541, sep 2003.
- [43] R Velthuis and P Mitschang. Induction welding technology - Joining fibre reinforced thermoplastic polymers (composites) for aerospace applications. 1(October):1727–1734, 2003.
- [44] M. Hou, L. Ye, and Y.-W. Mai. An Experimental Study of Resistance Welding of Carbon Fibre Fabric Reinforced Polyetherimide (CF Fabric/PEI) Composite Material. *Applied Composite Materials*, 6(1):35–49, 1999.

- [45] S. Poyraz, L. Zhang, A. Schroder, and X. Zhang. Ultrafast Microwave Welding/Reinforcing Approach at the Interface of Thermoplastic Materials. *ACS Applied Materials and Interfaces*, 7(40):22469–22477, 2015.
- [46] C. Ageorges and L. Ye. State of the Art in Fusion Bonding of Polymer Composites. pages 7–64. Springer, London, 2002.
- [47] A. P. da Costa, E. C. Botelho, M.L. Costa, N. E. Narita, and J. R. Tarpani. A review of welding technologies for thermoplastic composites in aerospace applications. *Journal of Aerospace Technology and Management*, 4(3):255–265, 2012.
- [48] K. Mistry. Tutorial Plastics welding technology for industry. *Assembly Automation*, 17(3):196–200, sep 1997.
- [49] J. Hunt. Joining Thermoplastic Pipe. *Chemical engineering*, 97(2):110, 1990.
- [50] J. R. Atkinson and I. M. Ward. The joining of biaxially oriented polyethylene pipes. *Polymer Engineering & Science*, 29(23):1638–1641, dec 1989.
- [51] R A Grimm. FUSION WELDING TECHNIQUES FOR PLASTICS. 1990.
- [52] C. Ageorges. Experimental investigation of the resistance welding of thermoplastic-matrix composites. Part II: optimum processing window and mechanical performance. *Composites Science and Technology*, 60(8):1191–1202, 2000.
- [53] P. Michel. An analysis of the extrusion welding process. *Polymer Engineering & Science*, 29(19):1376–1381, oct 1989.
- [54] X. Lu, C. Zhang, G. Zhao, Y. Guan, L. Chen, and A. Gao. State-of-the-art of extrusion welding and proposal of a method to evaluate quantitatively welding quality during three-dimensional extrusion process. *Materials and Design*, 89:737–748, 2016.
- [55] A. Yousefpour, M. Hojjati, and J.-P. Immarigeon. Fusion Bonding/Welding of Thermoplastic Composites. *Journal of Thermoplastic Composite Materials*, 17(4):303–341, jul 2004.
- [56] C. Ageorges and L. Ye. Simulation of impulse resistance welding for thermoplastic matrix composites. *Applied Composite Materials*, 8(2):133–147, 2001.
- [57] A. P. da Costa, E. C. Botelho, M. L. Costa, N. E. Narita, and J. R. Tarpani. A review of welding technologies for thermoplastic composites in aerospace applications. *Journal of Aerospace Technology and Management*, 4(3):255–265, 2012.
- [58] A. J. Demaria, R. Gagosz, and G. Barnard. Ultrasonic-refraction shutter for optical maser oscillators. *Journal of Applied Physics*, 34(3):453–455, 1963.
- [59] E. M. Petrie. Alternative fabric-joining technologies. In *Garment Manufacturing Technology*, pages 337–371. Elsevier, may 2015.
- [60] C. Brecher. Multi-technology platforms (MTPs). In *Integrative Production Technology: Theory and Applications*, pages 369–513. Springer International Publishing, jan 2017.
- [61] C. Innocenti, G. Pieri, M. Yanagishita, R. Pini, S. Siano, and A. Zanini. Application of laser welding to the restoration of the ostensory of the martyr St. Ignatius from Palermo. *Journal of Cultural Heritage*, 4(SUPPL. 1):362–366, jan 2003.

- [62] J. F. Asmus. Non-divestment laser applications in art conservation. *Journal of Cultural Heritage*, 4(SUPPL. 1):289–293, jan 2003.
- [63] S. T. Auwal, S. Ramesh, F. Yusof, and S. M. Manladan. A review on laser beam welding of titanium alloys. *International Journal of Advanced Manufacturing Technology*, 97(1-4):1071–1098, 2018.
- [64] B. Fotovvati, S. F. Wayne, G. Lewis, and E. Asadi. A Review on Melt-Pool Characteristics in Laser Welding of Metals. *Advances in Materials Science and Engineering*, 2018, 2018.
- [65] M. Mehrpouya, A. Gisario, and M. Elahinia. Laser welding of NiTi shape memory alloy: A review. *Journal of Manufacturing Processes*, 31:162–186, jan 2018.
- [66] K. F. Tamrin, Y. Nukman, and N. A. Sheikh. Laser spot welding of thermoplastic and ceramic: An experimental investigation. *Materials and Manufacturing Processes*, 30(9):1138–1145, 2015.
- [67] K. Sato, Y. Kurosaki, T. Saito, and I. Satoh. Laser welding of plastics transparent to near-infrared radiation. In Koji Sugioka, Malcolm C. Gower, Richard F. Haglund, Jr., Alberto Pique, Frank Traeger, Jan J. Dubowski, and Willem Hoving, editors, *Photon Processing in Microelectronics and Photonics*, volume 4637, page 528. SPIE, jun 2002.
- [68] I. Jones. Laser welding for plastic components. *Assembly Automation*, 22(2):129–135, 2002.
- [69] I. Jones. Laser welding of plastics. In *Handbook of Laser Welding Technologies*, pages 280–300. Wiley-VCH, 2013.
- [70] C. Lamberti, T. Solchenbach, P. Plapper, and W. Possart. Laser assisted joining of hybrid polyamide-aluminum structures. In *Physics Procedia*, volume 56, pages 845–853, 2014.
- [71] Z Sun and J C Ion. Laser welding of dissimilar metal combinations. *Journal of Materials Science*, 30(17):4205–4214, 1995.
- [72] A. Cenigaonaindia, F. Liébana, A. Lamikiz, and Z. Echegoyen. Novel Strategies for Laser Joining of Polyamide and AISI 304. *Physics Procedia*, 39:92–99, 2012.
- [73] C. Engelmann, A. Roesner, A. Olowinsky, and V. Mamuschkin. Lasermikrostrukturen zum lasergestützten Fügen von Kunststoff und Metall. In *Große Schweißtechnische Tagung*, pages 179–183, Essen, 2013.
- [74] A Fortunato, G Cuccolini, A Ascari, L Orazi, G Campana, and G Tani. Hybrid metal-plastic joining by means of laser. *International Journal of Material Forming*, 3(SUPPL. 1):1131–1134, 2010.
- [75] Y. Kawahito, A. Tange, S. Kubota, and S. Katayama. Development of direct laser welding for metal and plastics. In *International Congress on Applications of Laser and Electro-Optics*, 2006.
- [76] Y. Niwa, Y. Kawahito, S. Kubota, and S. Katayama. Development and improvement in laser direct joining of metal and plastic. In *26th International Congress on Applications of Lasers and Electro-Optics, ICALEO 2007 - Congress Proceedings*, volume 2007, page 902. Laser Institute of America, sep 2007.

- [77] K. Hao, W. Liao, T. Zhang, and M. Gao. Interface formation and bonding mechanisms of laser transmission welded composite structure of PET on austenitic steel via beam oscillation. *Composite Structures*, 235, mar 2020.
- [78] H. Gower, R. Pieters, and I. Richardson. Pulsed laser welding of metal-polymer sandwich materials using pulse shaping. *ICALEO 2004 - 23rd International Congress on Applications of Laser and Electro-Optics, Congress Proceedings*, 548, 2004.
- [79] F. Yusof, M. Yukio, M. Yoshiharu, and M. H. Abdul Shukor. Effect of anodizing on pulsed Nd:YAG laser joining of polyethylene terephthalate (PET) and aluminium alloy (A5052). *Materials and Design*, 37:410–415, 2012.
- [80] X. Wang, P. Li, Z. Xu, X. Song, and H. Liu. Laser transmission joint between PET and titanium for biomedical application. *Journal of Materials Processing Technology*, 210(13):1767–1771, 2010.
- [81] X. Wang, H. Chen, H. Liu, P. Li, Z. Yan, C. Huang, Z. Zhao, and Y. Gu. Simulation and optimization of continuous laser transmission welding between PET and titanium through FEM, RSM, GA and experiments. *Optics and Lasers in Engineering*, 51(11):1245–1254, nov 2013.
- [82] C.W. Chan and G. C. Smith. Fibre laser joining of highly dissimilar materials: Commercially pure Ti and PET hybrid joint for medical device applications. *Materials and Design*, 103:278–292, 2016.
- [83] G. L Georgiev, R. J Baird, E. F McCullen, G. Newaz, G. Auner, R. Patwa, and H. Herfurth. Chemical bond formation during laser bonding of Teflon ® FEP and titanium. *Applied Surface Science*, 255(15):7078–7083, 2009.
- [84] A. Mian, G. Newaz, L. Venda, N. Rahman, D. G. Georgiev, G. Auner, R. Witte, and H. Herfurth. Laser bonded microjoints between titanium and polyimide for applications in medical implants. *Journal of Materials Science: Materials in Medicine*, 16(3):229–237, mar 2005.
- [85] K. Schricker, M. Stambke, and J. P. Bergmann. Adjustment and Impact of the Thermoplastic Microstructure of the Melting Layer in Laser-based Joining of Polymers to Metals. 2015.
- [86] K. Schricker, S. Diller, and J. P. Bergmann. Bubble formation in thermal joining of plastics with metals. *Procedia CIRP*, 74:518–523, 2018.
- [87] C. P S Kuda-Malwathumullage and G.W Small. Determination of moisture content of polyamide 66 directly from combination region near-infrared spectra. *Journal of Applied Polymer Science*, 131(16):40645, 2014.
- [88] J. D. Venables. Adhesion and durability of metal-polymer bonds. *Journal of Materials Science*, 19(8):2431–2453, aug 1984.
- [89] V. A. Kagan. Moisture Effects on Mechanical Performance of Laser-welded Polyamide. *Journal of Reinforced Plastics and Composites*, 24(11):1213–1223, jul 2005.
- [90] C. Ageorges and J.F. Dos Santos. Moisture Effects on Mechanical Performance of Laser-welded Polyamide. *Physics Procedia*, 39(3):1213–1223, jun 2011.

- [91] S. S. Voyutskii. Adhesion and Autohesion of Polymers. *Interscience Publication*, 145:16–17, 1963.
- [92] F. Awaja, M. Gilbert, G. Kelly, B. Fox, and P. J. Pigram. Adhesion of polymers. *Progress in Polymer Science (Oxford)*, 34(9):948–968, sep 2009.
- [93] AFNOR. Spécification géométrique des produits (GPS) État de surface : Méthode du profil Termes, définitions et paramètres d'état de surface. *NF EN ISO 4287*, 1998.
- [94] S. Sunil Kumar and K. Ramamurthi. Influence of flatness and waviness of rough surfaces on surface contact conductance. *Journal of Heat Transfer*, 125(3):394–402, 2003.
- [95] K. Autumn, M. Sitti, Y. A. Liang, A. M. Peattie, W. R. Hansen, S. Sponberg, T. W. Kenny, R. Fearing, J. N. Israelachvili, and R. J. Full. Evidence for van der Waals adhesion in gecko setae. *Proceedings of the National Academy of Sciences of the United States of America*, 99(19):12252–12256, sep 2002.
- [96] G. Huber, S. N. Gorb, N. Hosoda, R. Spolenak, and E. Arzt. Influence of surface roughness on gecko adhesion. *Acta Biomaterialia*, 3(4):607–610, jul 2007.
- [97] R. Hensel, K. Moh, and E. Arzt. Engineering micropatterned dry adhesives – from contact theory to handling applications. *Advanced Functional Materials*, 1800865, 2018.
- [98] M. Seong, H.H. Park, I. Hwang, and H. E. Jeong. Strong and reversible adhesion of interlocked 3D-microarchitectures. *Coatings*, 9(1):48, jan 2019.
- [99] W. S. Kim, I.H. Yun, J. J. Lee, and H. T. Jung. Evaluation of mechanical interlock effect on adhesion strength of polymer-metal interfaces using micro-patterned surface topography. *International Journal of Adhesion and Adhesives*, 30(6):408–417, sep 2010.
- [100] C. Hopmann, S. Kreimeier, J. Keseberg, and C. Wenzlau. Joining of Metal-Plastics-Hybrid Structures Using Laser Radiation by Considering the Surface Structure of the Metal. *Journal of Polymers*, 2016:1–10, 2016.
- [101] K. Schricker, M. Stambke, J. P. Bergmann, K. Bräutigam, and P. Henckell. Macroscopic surface structures for polymer-metal hybrid joints manufactured by laser based thermal joining. In *Physics Procedia*, volume 56, pages 782–790. Elsevier, jan 2014.
- [102] J. Haubrich, M. Löbbecke, P. Watermeyer, F. Wilde, G. Requena, and J. da Silva. Buried interfaces – A systematic study to characterize an adhesive interface at multiple scales. *Applied Surface Science*, 433:546–555, mar 2018.
- [103] J. P.B. van Dam, S. T. Abrahams, A. Yilmaz, Y. Gonzalez-Garcia, H. Terry, and J. M.C. Mol. Effect of surface roughness and chemistry on the adhesion and durability of a steel-epoxy adhesive interface. *International Journal of Adhesion and Adhesives*, 96:102450, jan 2020.
- [104] S. G. Prolongo, G. Rosario, and A. Ureña. Study of the effect of substrate roughness on adhesive joints by SEM image analysis. *Journal of Adhesion Science and Technology*, 20(5):457–470, 2006.
- [105] M. Zou, S. Beckford, R. Wei, C. Ellis, G. Hatton, and M. A. Miller. Effects of surface roughness and energy on ice adhesion strength. *Applied Surface Science*, 257(8):3786–3792, feb 2011.

- [106] Y. Li and Z.-H. Lu. Failure of Fermi Level in Referencing Chemical Shift of Molecules on Solid Surfaces. *Advanced Materials Interfaces*, 1800150:1800150, 2018.
- [107] L. Pan, J. Hu, Y. Lv, W. Ma, W. Ding, Y. Wang, A. Zhang, F. Wang, X. Pang, and J. Tao. Modification of Ti-6Al-4V plates with Schiff base complex and adhesive performance of Ti-6Al-4V/PEEK. *Materials and Design*, 144:271–280, apr 2018.
- [108] T. Kleffel and D. Drummer. Investigating the suitability of roughness parameters to assess the bond strength of polymer-metal hybrid structures with mechanical adhesion. *Composites Part B: Engineering*, 117:20–25, 2017.
- [109] Zhou Zhang, Ji-Guo Shan, Xiang-Hu Tan, and Jing Zhang. Effect of anodizing pretreatment on laser joining CFRP to aluminum alloy A6061. *International Journal of Adhesion and Adhesives*, 70:142–151, 2016.
- [110] Zhiqiang Gao, Shujing Peng, Jie Sun, Lan Yao, and Yiping Qiu. Influence of processing parameters on atmospheric pressure plasma etching of polyamide 6 films. *Applied Surface Science*, 255(17):7683–7688, 2009.
- [111] Y. Wang, K. Jia, C. Xiang, J. Yang, X. Yao, and Z. Suo. Instant, Tough, Noncovalent Adhesion. *ACS Applied Materials & Interfaces*, 2019.
- [112] C. Sun, J. Min, J. Lin, H. Wan, S. Yang, and S. Wang. The effect of laser ablation treatment on the chemistry, morphology and bonding strength of CFRP joints. *International Journal of Adhesion and Adhesives*, 84:325–334, aug 2018.
- [113] M. Nosonovsky and B. Bhushan. Roughness-induced superhydrophobicity: A way to design non-adhesive surfaces. *Journal of Physics Condensed Matter*, 20(22), 2008.
- [114] W. Gao and R. Huang. Effect of surface roughness on adhesion of graphene membranes. *Journal of Physics D: Applied Physics*, 44(45), 2011.
- [115] B. N.J. Persson and M. Scaraggi. Theory of adhesion: Role of surface roughness. *Journal of Chemical Physics*, 141(12):124701, sep 2014.
- [116] W. Gutowski. Thermodynamics of Adhesion. In *Fundamentals of Adhesion*, pages 87–135. Springer US, Boston, MA, 1991.
- [117] I. Newton. *Opticks: Or, a Treatise of the Reflexions, Refractions, Inflexions and Colours of Light. Also Two Treatises of the Species and Magnitude of Curvilinear Figures*. Smith and Walford, London, 1st edition, 1704.
- [118] IUPAC. *Gloassary of Terms Used in Physical Organic Chemistry*. 1994.
- [119] T. Steiner. The whole palette of hydrogen bonds REVIEWS The Hydrogen Bond in the Solid State. *Angew. Chem. Int. Ed.*, 41:48–76, 2002.
- [120] J. D. Smith, C. D. Cappa, K. R. Wilson, B. M. Messer, R. C. Cohen, and R. J. Saykally. Energetics of hydrogen bond network rearrangements in liquid water. *Science*, 306(5697):851–853, oct 2004.
- [121] M. L. Cowan, B. D. Bruner, N. Huse, J. R. Dwyer, B. Chugh, E. T.J. Nibbering, T. Elsaesser, and R. J.D. Miller. Ultrafast memory loss and energy redistribution in the hydrogen bond network of liquid H₂O. *Nature*, 434(7030):199–202, mar 2005.

- [122] G. N. Pairas and P. G. Tsoungas. H-Bond: éhe Chemistry-Biology H-Bridge. *Chemistry-Select*, 1(15):4520–4532, sep 2016.
- [123] N. Diaz, F.X. Simon, M. Schmutz, M. Rawiso, G. Decher, J. Jestin, and P. J. Mésini. Self-assembled diamide nanotubes in organic solvents. *Angewandte Chemie - International Edition*, 44(21):3260–3264, may 2005.
- [124] E. Christ, C. Blanc, A. Al Ouahabi, D. Maurin, R. Le Parc, J. L. Bantignies, J. M. Guenet, D. Collin, and P.J. Mésini. Origin of Invariant Gel Melting Temperatures in the c-T Phase Diagram of an Organogel. *Langmuir*, 32(19):4975–4982, may 2016.
- [125] L. Penn and F. Larsen. Physicochemical properties of kevlar 49 fiber. *Journal of Applied Polymer Science*, 23(1):59–73, 1979.
- [126] Organisation of Protein: 4 Structures.
- [127] G. Cavallo, P. Metrangolo, R. Milani, T. Pilati, A. Priimagi, G. Resnati, and G. Terraneo. The halogen bond. *Chemical Reviews*, 116(4):2478–2601, feb 2016.
- [128] P. J. Costa. The halogen bond: Nature and applications. *Physical Sciences Reviews*, 2(11):1–16, 2019.
- [129] W. Wang, B. Ji, and Y. Zhang. Chalcogen bond: A sister noncovalent bond to halogen bond. *Journal of Physical Chemistry A*, 113(28):8132–8135, jul 2009.
- [130] S. Scheiner. Detailed comparison of the pnicoen bond with chalcogen, halogen, and hydrogen bonds. *International Journal of Quantum Chemistry*, 113(11):1609–1620, jun 2013.
- [131] G. N. Lewis. The atom and the molecule. *Journal of the American Chemical Society*, 38(4):762–785, apr 1916.
- [132] W. Heitler and F. London. Wechselwirkung neutraler Atome und homöopolare Bindung nach der Quantenmechanik. *Zeitschrift für Physik*, 44(6-7):455–472, jun 1927.
- [133] P. G. Howe, D. P. Benton, and I. E. Puddington. London – Van Der Waals Attractive Forces Between Glass Surfaces. *Canadian Journal of Chemistry*, 33(9):1375–1383, sep 1955.
- [134] S. P. Koenig, N. G. Boddeti, M. L. Dunn, and J. S. Bunch. Ultrastrong adhesion of graphene membranes. *Nature Nanotechnology*, 6(9):543–546, 2011.
- [135] Z. Lu and M. L. Dunn. Van der Waals adhesion of graphene membranes. *Journal of Applied Physics*, 107(4), 2010.
- [136] F. Didier and J. Jupille. Contribution of the van der Waals forces to the work of adhesion at metal / oxide interfaces. *Journal of Adhesion Science and Technology*, 10(4):373–382, 1996.
- [137] D. M Lipkin, J. N Israelachvili, and D. R Clarke. Estimating the metal-ceramic van der waals adhesion energy. *Philosophical Magazine A: Physics of Condensed Matter, Structure, Defects and Mechanical Properties*, 76(4):715–728, 1997.
- [138] F.W. Delrio, M. P. De Boer, J.A. Knapp, E. D. Reedy, P. J. Clews, and M. L. Dunn. The role of van der Waals forces in adhesion of micromachined surfaces. *Nature Materials*, 4(8):629–634, jul 2005.

- [139] P. Loskill, H. Hähl, T. Faidt, S. Grandthyll, F. Müller, and K. Jacobs. Is adhesion superficial? Silicon wafers as a model system to study van der Waals interactions. *Advances in Colloid and Interface Science*, 179-182:107–113, nov 2012.
- [140] R. C. Thomas, J. E. Houston, R. M. Crooks, T. Kim, and T. A. Michalske. Probing Adhesion Forces at the Molecular Scale. *Journal of the American Chemical Society*, 117(13):3830–3834, 1995.
- [141] C. R. Frihart. Specific adhesion model for bonding hot-melt polyamides to vinyl. *International Journal of Adhesion and Adhesives*, 24(5):415–422, oct 2004.
- [142] J. Kajtna, B. Alič, M. Krajnc, and U. Šebenič. Influence of hydrogen bond on rheological properties of solventless UV crosslinkable pressure sensitive acrylic adhesive prepolymers. *International Journal of Adhesion and Adhesives*, 49:103–108, mar 2014.
- [143] H.K. Park, B. Se. Kong, and E. S. Oh. Effect of high adhesive polyvinyl alcohol binder on the anodes of lithium ion batteries. *Electrochemistry Communications*, 13(10):1051–1053, oct 2011.
- [144] D. K. Owens. The mechanism of corona and ultraviolet light-induced self-adhesion of poly(ethylene terephthalate) film. *Journal of Applied Polymer Science*, 19(12):3315–3326, 1975.
- [145] A. Faghihnejad, K. E. Feldman, J. Yu, M. V. Tirrell, J. N. Israelachvili, C. J. Hawker, E. J. Kramer, and H. Zeng. Adhesion and surface interactions of a self-healing polymer with multiple hydrogen-bonding groups. *Advanced Functional Materials*, 24(16):2322–2333, 2014.
- [146] E. Papirer, J. M. Perrin, G. Nanse, and P. Fioux. Adsorption of poly(methylmethacrylate) on an α alumina: evidence of formation of surface carboxylate bonds. *European Polymer Journal*, 30(8):985–991, 1994.
- [147] S. R. Leadley and J. F. Watts. The use of XPS to examine the interaction of poly(acrylic acid) with oxidised metal substrates. *Journal of Electron Spectroscopy and Related Phenomena*, 85(1-2):107–121, jul 1997.
- [148] J. Marsh, L. Minel, M. G. Barthés-Labrousse, and D. Gorse. Interaction of epoxy model molecules with aluminium, anodised titanium and copper surfaces: An XPS study. *Applied Surface Science*, 133(4):270–286, aug 1998.
- [149] J. F. Watts, S. R. Leadley, J. E. Castle, and C. J. Blomfield. Adsorption of PMMA on oxidized Al and Si substrates: An investigation by high-resolution X-ray photoelectron spectroscopy. *Langmuir*, 16(5):2292–2300, mar 2000.
- [150] M R Alexander, G Beamson, C J Blomfield, G Leggett, and T M Duc. Interaction of carboxylic acids with the oxyhydroxide surface of aluminium: Poly(acrylic acid), acetic acid and propionic acid on pseudoboehmite. *Journal of Electron Spectroscopy and Related Phenomena*, 121(1-3):19–32, 2001.
- [151] C. L Loch, D. Ahn, C. Chen, J. Wang, and Z. Chen. Sum frequency generation studies at poly(ethylene terephthalate)/silane interfaces: Hydrogen bond formation and molecular conformation determination. *Langmuir*, 20(13):5467–5473, 2004.

- [152] S. Pletinx, L. L. I. Fockaert, J. M. C. Mol, T. Hauffman, and H. Terryn. Probing the formation and degradation of chemical interactions from model molecule/metal oxide to buried polymer/metal oxide interfaces. *npj Materials Degradation*, 3(1):1–12, dec 2019.
- [153] P. S. Ho, P. O. Hahn, J. W. Bartha, G. W. Rubloff, F. K. LeGoues, and B. D. Silverman. Chemical bonding and reaction at metal/polymer interfaces. *Journal of Vacuum Science & Technology A: Vacuum, Surfaces, and Films*, 3(3):739–745, 1985.
- [154] J. F. Watts. The Interfacial Chemistry of Adhesion: Novel Routes to the Holy Grail? In *Adhesion: Current Research and Applications*, pages 1–16. Wiley-VCH Verlag GmbH & Co. KGaA, Weinheim, FRG, apr 2006.
- [155] J. Melngailis. Focused ion beam technology and applications. *Journal of Vacuum Science & Technology B: Microelectronics and Nanometer Structures*, 5(2):469, mar 1987.
- [156] T. Ishitani and T. Yaguchi. Cross-sectional sample preparation by focused ion beam: A review of ion-sample interaction. *Microscopy Research and Technique*, 35(4):320–333, nov 1996.
- [157] J. H Daniel, D.F Moore, J. F Walker -, J. Bai, S. Reyntjens, and R. Puers. A review of focused ion beam applications in microsystem technology. *Journal of Micromechanics and microengineering*, 11:287–300, 2001.
- [158] R. Jiang, M. Li, Y. Yao, J. Guan, and H. Lu. Application of BIB polishing technology in cross-section preparation of porous, layered and powder materials: A review. *Frontiers of Materials Science*, 13(2):107–125, jun 2019.
- [159] S. J. Hinder, J. F. Watts, and C. Lowe. Interface analysis and compositional depth profiling by XPS of polymer coatings prepared using ultra-low-angle microtomy. *Surface and Interface Analysis*, 36(8):1032–1036, aug 2004.
- [160] S. J. Hinder, C. Lowe, J. T. Maxted, and J. F. Watts. Migration and segregation phenomena of a silicone additive in a multilayer organic coating. *Progress in Organic Coatings*, 54(2):104–112, oct 2005.
- [161] S. Adhami, M. L. Abel, C. Lowe, and J. F. Watts. The role of the adhesion promoter in a model water-borne primer. *Surface and Interface Analysis*, 46(10-11):1005–1008, oct 2014.
- [162] J. C. Vickerman and I.S Gilmore. *Surface analysis: the principal techniques*. John Wiley & Sons, 2009.
- [163] J. C. Vickerman and D. Briggs. *ToF-SIMS: Surface Analysis by Mass Spectrometry*. IM Publications, 2nd edition, 2013.
- [164] L. Houssiau, C. Noël, N. Mine, K. W. Jung, W. J. Min, and D. W. Moon. Investigation of Cs surface layer formation in Cs-SIMS with TOF-MEIS and SIMS. *Surface and Interface Analysis*, 46(S1):22–24, 2014.
- [165] C. Noël and L. Houssiau. Hybrid Organic/Inorganic Materials Depth Profiling Using Low Energy Cesium Ions. *Journal of the American Society for Mass Spectrometry*, 27(5):908–916, 2016.

- [166] C. Noël, S. Pescetelli, A. Agresti, A. Franquet, V. Spampinato, A. Felten, A. di Carlo, L. Houssiau, and Y. Busby. Hybrid perovskites depth profiling with variable-size argon clusters and monatomic ions beams. *Materials*, 12(5):726, mar 2019.
- [167] C. Noël, Y. Busby, N. Mine, and L. Houssiau. ToF-SIMS Depth Profiling of Organic Delta Layers with Low-Energy Cesium Ions: Depth Resolution Assessment. *Journal of the American Society for Mass Spectrometry*, 30(8):1537–1544, 2019.
- [168] K Konstadinidis, B Thakkar, A Chakraborty, L W Potts, R Tannenbaum, M Tirrell, and J F Evans. Segment Level Chemistry and Chain Conformation in the Reactive Adsorption of Poly(methyl methacrylate) on Aluminum Oxide Surfaces. *Langmuir*, 8(5):1307–1317, 1992.
- [169] R. Tannenbaum, S. King, J. Lecy, M. Tirrell, and L. Potts. Infrared study of the kinetics and mechanism of adsorption of acrylic polymers on alumina surfaces. *Langmuir*, 20(11):4507–4514, may 2004.
- [170] M. Brogly, M. Nardin, and J. Schultz. Evidence of acid-base interfacial adducts in various polymer/metal systems by IRAS: Improvement of adhesion. *Journal of Adhesion*, 58(3-4):263–279, 1996.
- [171] J.M. Chalmers and P.R. Griffith. *Handbook of vibrational spectroscopy*. John Wiley & Sons, Chichester, UK, 2002.
- [172] Y. Suzuki, M. Osawa, A. Hatta, and W. Suëtaka. Mechanism of absorption enhancement in infrared ATR spectra observed in the Kretschmann configuration. *Applied Surface Science*, 33-34(C):875–881, sep 1988.
- [173] M. Öhman, D. Persson, and C. Leygraf. In situ ATR-FTIR studies of the aluminium/polymer interface upon exposure to water and electrolyte. *Progress in Organic Coatings*, 57(1):78–88, sep 2006.
- [174] M. Öhman and D. Persson. An integrated in situ ATR-FTIR and EIS set-up to study buried metal-polymer interfaces exposed to an electrolyte solution. *Electrochimica Acta*, 52(16):5159–5171, apr 2007.
- [175] P. Taheri, J. H.W. De Wit, H. Terryn, and J. M.C. Mol. In situ study of buried metal-polymer interfaces exposed to an aqueous solution by an integrated ATR-FTIR and electrochemical impedance spectroscopy system. *Journal of Physical Chemistry C*, 117(40):20826–20832, oct 2013.
- [176] T. Van Schaftinghen, S. Joiret, C. Deslouis, and H. Terryn. In-situ Raman Spectroscopy and Spectroscopic Ellipsometry study of the iron/Polypyrrole interface. In *Passivation of Metals and Semiconductors, and Properties of Thin Oxide Layers*, pages 691–696. Elsevier Science, jan 2006.
- [177] G. Xue, Y. Lu, and J. Zhang. Stable SERS Substrates Used for In Situ Studies of the Polymer-Metal Interface at Elevated Temperature. *Macromolecules*, 27(3):809–813, may 1994.
- [178] L. Li, T. Hutter, A. S. Finnemore, F. M. Huang, J. J. Baumberg, S. R. Elliott, U. Steiner, and S. Mahajan. Metal oxide nanoparticle mediated enhanced Raman scattering and its use in direct monitoring of interfacial chemical reactions. *Nano Letters*, 12(8):4242–4246, aug 2012.

- [179] S. Pletincx, L. Trotochaud, L.-L. Fockaert, J.M C Mol, A. R Head, O. Karshoğlu, H. Bluhm, H. Terryn, and T. Hauffman. In Situ Characterization of the Initial Effect of Water on Molecular Interactions at the Interface of Organic/Inorganic Hybrid Systems. *Scientific Reports*, 7(November 2016):45123, 2017.
- [180] S. Pletincx, K. Marcoen, L. Trotochaud, L. L. Fockaert, J. M.C. Mol, A. R. Head, O. Karshoğlu, H. Bluhm, H. Terryn, and T. Hauffman. Unravelling the chemical influence of water on the PMMA/Aluminum oxide hybrid interface in situ. *Scientific Reports*, 7(1):1–11, 2017.
- [181] A. González-Orive, I. Giner, T. de los Arcos, A. Keller, and G. Grundmeier. Analysis of polymer/oxide interfaces under ambient conditions – An experimental perspective. *Applied Surface Science*, 442:581–594, 2018.
- [182] P. W. Bohn. Localized optical phenomena and the characterization of materials interfaces. *Annual Review of Materials Science*, 27(1):469–498, aug 1997.
- [183] J. Van Den Brand, O. Blajiev, P. C.J. Beentjes, H. Terryn, and J. H.W. De Wit. Interaction of anhydride and carboxylic acid compounds with aluminum oxide surfaces studied using infrared reflection absorption spectroscopy. *Langmuir*, 20(15):6308–6317, jul 2004.
- [184] P. C.J. Beentjes, J. Van Den Brand, and J. H.W. De Wit. Interaction of ester and acid groups containing organic compounds with iron oxide surfaces. *Journal of Adhesion Science and Technology*, 20(1):1–18, 2006.
- [185] P. Taheri, T. Hauffman, J. M.C. Mol, J. R. Flores, F. Hannour, J. H.W. De Wit, and H. Terryn. Electrochemical analysis of the adsorption and desorption behaviors of carboxylic acid and anhydride monomers onto zinc surfaces. *Electrochimica Acta*, 56(25):9317–9323, oct 2011.
- [186] M. A. Ramin, G. Le Bourdon, N. Daugey, B. Bennetau, L. Vellutini, and T. Buffeteau. PM-IRRAS investigation of self-assembled monolayers grafted onto SiO₂/Au substrates. *Langmuir*, 27(10):6076–6084, jun 2011.
- [187] J. Wielant, T. Hauffman, O. Blajiev, R. Hausbrand, and H. Terryn. Influence of the iron oxide acid-base properties on the chemisorption of model epoxy compounds studied by XPS. *Journal of Physical Chemistry C*, 111(35):13177–13184, sep 2007.
- [188] O. L. Blajiev, A. Ithurbide, A. Hubin, C. Van Haesendonck, and H. Terryn. XPS study of the assembling morphology of 3-hydroxy-3-phosphono-butiric acid tert-butyl ester on variously pretreated Al surfaces. *Progress in Organic Coatings*, 63(3):272–281, oct 2008.
- [189] P. Taheri, J. Wielant, T. Hauffman, J. R. Flores, F. Hannour, J. H.W. De Wit, J. M.C. Mol, and H. Terryn. A comparison of the interfacial bonding properties of carboxylic acid functional groups on zinc and iron substrates. In *Electrochimica Acta*, volume 56, pages 1904–1911. Pergamon, jan 2011.
- [190] S. T. Abrahami, T. Hauffman, J. M.M. De Kok, J. M.C. Mol, and H. Terryn. XPS Analysis of the Surface Chemistry and Interfacial Bonding of Barrier-Type Cr(VI)-Free Anodic Oxides. *Journal of Physical Chemistry C*, 119(34):19967–19975, aug 2015.
- [191] L. I. Fockaert, P. Taheri, S. T. Abrahami, B. Boelen, H. Terryn, and J. M.C. Mol. Zirconium-based conversion film formation on zinc, aluminium and magnesium oxides and their interactions with functionalized molecules. *Applied Surface Science*, 423:817–828, nov 2017.

- [192] J. F. Watts and J. E. Castle. The application of X-ray photoelectron spectroscopy to the study of polymer-to-metal adhesion - Part 1 Polybutadiene coated mild steel. *Journal of Materials Science*, 18(10):2987–3003, oct 1983.
- [193] J. F. Watts and J. E. Castle. The application of X-ray photoelectron spectroscopy to the study of polymer-to-metal adhesion - Part 2 The cathodic disbondment of epoxy coated mild steel. *Journal of Materials Science*, 19(7):2259–2272, jul 1984.
- [194] V. Di Ruocco, M. Morra, E. Occhiello, and F. Garbassi. On the failure of water-immersed steel-acrylic adhesive joints. *Journal of Materials Science Letters*, 10(11):649–652, jan 1991.
- [195] A. Rattana, J.D. Hermes, M. L. Abel, and J. F. Watts. The interaction of a commercial dry film adhesive with aluminium and organosilane treated aluminium surfaces: A study by XPS and ToF-SIMS. *International Journal of Adhesion and Adhesives*, 22(3):205–218, 2002.
- [196] M. Ghaffari, M. R. Saeb, B. Ramezanzadeh, and P. Taheri. Demonstration of epoxy/carbon steel interfacial delamination behavior: Electrochemical impedance and X-ray spectroscopic analyses. *Corrosion Science*, 102:326–337, jan 2016.
- [197] Y. Yoshida, B. VanMeerbeek, Y. Nakayama, J. Snauwaert, L. Hellemans, P. Lambrechts, G. Vannerle, and K. Wakasa. Evidence of chemical bonding at biomaterial-hard tissue interfaces. *Journal of Dental Research*, 79(2):709–714, 2000.
- [198] S. Pletincx, J. M.C. Mol, H. Terryn, A. Hubin, and T. Hauffman. An in situ spectro-electrochemical monitoring of aqueous effects on polymer/metal oxide interfaces. *Journal of Electroanalytical Chemistry*, 848:113311, sep 2019.
- [199] M. Kiguchi, K. Saiki, and A. Koma. Effects of anharmonicity of ionic bonds on the lattice distortion at the interface of alkali halide heterostructures. *Surface Science*, 470(1-2):81–88, 2000.
- [200] C. M. Bowers, K. C. Liao, H. J. Yoon, D. Rappoport, M. Baghbanzadeh, F.C. Simeone, and G. M. Whitesides. Introducing ionic and/or hydrogen bonds into the SAM//Ga₂O₃ top-interface of AgTS/S(CH₂)_nT//Ga₂O₃/EGaIn junctions. *Nano Letters*, 14(6):3521–3526, jun 2014.
- [201] M. Wróbel, J. Ossowski, M. Krawiec, K. Kozieł, P. Dąbczyński, and P. Cyganik. Oscillation in the stability of consecutive chemical bonds at the molecule-metal interface-the case of ionic bonding. *Physical Chemistry Chemical Physics*, 21(25):13411–13414, 2019.
- [202] D. J. Siegel, L. G. Hector, and J.B. Adams. Adhesion, atomic structure, and bonding at the (formula presented) interface: A first principles study. *Physical Review B - Condensed Matter and Materials Physics*, 65(8):1–19, 2002.
- [203] P. W. Peacock and J. Robertson. Bonding, Energies, and Band Offsets of [Formula presented] and [Formula presented] Gate Oxide Interfaces. *Physical Review Letters*, 92(5):4, 2004.
- [204] J. M. Hu and C. B. Eom. Magnetic-field control of ionic bonds on ferroelectric surfaces. *Applied Physics Letters*, 114(9), 2019.
- [205] A. Fick. Ueber Difusion;. *Annalen der Physik*, 1855.

- [206] S. S. Voyutskii and Y. L. Margolina. O prirode samoslipaniya (autogezii) vysokomolekul-yarnykh veshchestv. *Uspekhi khimii*, 18(4):449–461, 1949.
- [207] S. S. Voyutskii and V. L. Vakula. The role of diffusion phenomena in polymer-to-polymer adhesion. *Journal of Applied Polymer Science*, 7(2):475–491, 1963.
- [208] P. G. de Gennes. Reptation of a Polymer Chain in the Presence of Fixed Obstacles. *The Journal of Chemical Physics*, 55(2):572–579, 1971.
- [209] G. Fourche. An overview of the basic aspects of polymer adhesion. Part I: Fundamentals. *Polymer Engineering & Science*, 35(12):957–967, 1995.
- [210] F. Brochard-Wyart. Kinetics of Polymer—Polymer Interdiffusion. In *Fundamentals of Adhesion*, pages 181–206. Springer US, Boston, MA, 1991.
- [211] C M Roland and G. G.A. Bohm. Macromolecular Diffusion and the Autoadhesion of Polybutadiene. *Macromolecules*, 18(6):1310–1314, 1985.
- [212] H. R. Brown, A. C.M. Yang, T. P. Russell, W. Volksen, and E. J. Kramer. Diffusion and self-adhesion of the polyimide PMDA-ODA. *Polymer*, 29(10):1807–1811, 1988.
- [213] A. G. Mikos and N.A. Peppas. Polymer chain entanglements and brittle fracture: 2. Autohesion of linear polymers. *Polymer*, 30(1):84–91, jan 1989.
- [214] J. J. Sahlin and N. A. Peppas. Enhanced hydrogel adhesion by polymer interdiffusion: Use of linear poly(ethylene glycol) as an adhesion promoter. *Journal of Biomaterials Science, Polymer Edition*, 8(6):421–436, jan 1997.
- [215] A. Ghanem and Y. Lang. Introduction to Polymer Adhesion. *Polymer Blends Handbook*, (August):1–122, 2003.
- [216] C. Zhang, Y. Bai, B. Cheng, and W. Liu. Adhesion properties of atactic polypropylene/acrylate blend copolymer and its adhesion mechanism for untreated polypropylene materials. *International Journal of Adhesion and Adhesives*, 80:7–15, jan 2018.
- [217] A Mocellin, G Régnier, J Peixinho, N Schmitt, and S Roux. Adhesion mechanisms at the interface between two polytetrafluoroethylene (PTFE) films. 2019.
- [218] J J Pireaux. Is there an interaction at the aromatic site(s) in a metal/polymer interface? An XPS and HREELS review. *Synthetic Metals*, 67(1-3):39–46, 1994.
- [219] F. Faupel, R. Willecke, and A. Thran. Diffusion of metals in polymers. *Materials Science and Engineering: R: Reports*, 22(1):1–55, 1998.
- [220] E. Sacher. *Polymer Metallization*. Springer Science, New York, 2nd edition, 2002.
- [221] P. Bébin and R. E. Prud’Homme. Comparative XPS study of copper, nickel, and aluminum coatings on polymer surfaces. *Chemistry of Materials*, 15(4):965–973, feb 2003.
- [222] I. Campos-Silva, S. Bernabé-Molina, D. Bravo-Bárceñas, J. Martínez-Trinidad, G. Rodríguez-Castro, and A. Meneses-Amador. Improving the Adhesion Resistance of the Boride Coatings to AISI 316L Steel Substrate by Diffusion Annealing. *Journal of Materials Engineering and Performance*, 25(9):3852–3862, sep 2016.

- [223] E. M.F. Vieira, J F Ribeiro, R Sousa, M M Silva, L Dupont, and L. M. Gonçalves. Titanium Oxide Adhesion Layer for High Temperature Annealed Si/Si₃N₄/TiO_x/Pt/LiCoO₂ Battery Structures. *Journal of Electronic Materials*, 45(2):910–916, 2016.
- [224] D. d. Ma, Y. p. Xue, J. Gao, Y. Ma, S. w. Yu, Y. s. Wang, C. Xue, H. j. Hei, and B. Tang. Effect of Ta diffusion layer on the adhesion properties of diamond coating on WC-Co substrate. *Applied Surface Science*, 527:146727, oct 2020.
- [225] S. S. Voyutskii. Some Comments on the Series of Papers "Interfacial Contact and Bonding in Autohesion". *The Journal of Adhesion*, 3(1):69–76, 1971.
- [226] R. P. Champion. The Influence of Structure on Autohesion (Self-Tack) and Other forms of Diffusion into Polymers. *The Journal of Adhesion*, 7(1):1–23, 1975.
- [227] K. He, L. Li, and J. Wang. Diffusive–stochastic–viscoelastic model for specific adhesion of viscoelastic solids via molecular bonds. *Acta Mechanica Sinica/Lixue Xuebao*, 35(2):343–354, 2019.
- [228] Z. Du and X. Zhu. Molecular Dynamics Simulation to Investigate the Adhesion and Diffusion of Asphalt Binder on Aggregate Surfaces. *Transportation Research Record*, 2673(4):500–512, 2019.
- [229] J. Martinez, S. B. Sinnott, and S.R. Phillpot. Adhesion and diffusion at TiN/TiO₂ interfaces: A first principles study. *Computational Materials Science*, 130:249–256, apr 2017.
- [230] Y. Han, M. C. Tringides, J. W. Evans, and P. A. Thiel. Adsorption, intercalation, diffusion, and adhesion of Cu at the 2 H - Mo S 2 (0001) surface from first-principles calculations. *Physical Review Research*, 2(1):013182, feb 2020.
- [231] W. Mönch. *Semiconductor Surfaces and Interfaces*. Springer Berlin Heidelberg, 2001.
- [232] C. Kittel. *Introduction to Solid State Physics*. John Wiley & Sons, 8th editio edition, 2004.
- [233] K. Seeger. *Semiconductor Physics. An Introduction*. Springer Berlin Heidelberg, 2004.
- [234] Z. Zhang and J. T Yates. Band bending in semiconductors: Chemical and physical consequences at surfaces and interfaces. *Chemical Reviews*, 112(10):5520–5551, 2012.
- [235] W Salaneck. The electronic structure of polymer–metal interfaces studied by ultraviolet photoelectron spectroscopy. *Materials Science and Engineering: R: Reports*, 34(3):121–146, 2001.
- [236] M P De Jong, R Friedlein, W Osikowicz, R Salaneck, and M Fahlman. Molecular Crystals and Liquid Crystals Ultraviolet Photoelectron Spectroscopy of Polymers. *Mol. Cryst. Liq. Cryst.*, 1406(August 2012):193–203, 2006.
- [237] H. Ishii and K. Seki. Energy level alignment at organic/metal interfaces studied by UV photoemission: breakdown of traditional assumption of a common vacuum level at the interface. *IEEE Transactions on Electron Devices*, 44(8):1295–1301, 1997.
- [238] H. Ishii, K. Sugiyama, E. Ito, and K. Seki. Energy level alignment and interfacial electronic structures at organic/metal and organic/organic interfaces. *Advanced Materials*, 11(8):605–625, 1999.

- [239] T. Kugler, W.R. Salaneck, H Rost, and A.B. Holmes. Polymer band alignment at the interface with indium tin oxide: consequences for light emitting devices. *Chemical Physics Letters*, 310(5-6):391–396, 1999.
- [240] N. Hayashi, H. Ishii, Y. Ouchi, and K. Seki. Examination of band bending at buckminsterfullerene (C 60)/metal interfaces by the Kelvin probe method. *Journal of Applied Physics*, 92(7):3784–3793, 2002.
- [241] H. Ishii, N. Hayashi, E. Ito, Y. Washizu, K. Sugi, Y. Kimura, M. Niwano, Y. Ouchi, and K. Seki. Kelvin probe study of band bending at organic semiconductor/metal interfaces: Examination of fermi level alignment. *Physica Status Solidi (A) Applied Research*, 201(6):1075–1094, 2004.
- [242] M. Timpel, H. Li, M. V. Nardi, B. Wegner, J. Frisch, P. J. Hotchkiss, S.R. Marder, S. Barlow, J. L. Brédas, and N. Koch. Electrode Work Function Engineering with Phosphonic Acid Monolayers and Molecular Acceptors: Charge Redistribution Mechanisms. *Advanced Functional Materials*, 28(8):1–12, 2018.
- [243] W. Possart. Experimental and theoretical description of the electrostatic component of adhesion at polymer/metal contacts. *International Journal of Adhesion and Adhesives*, 8(2):77–83, 1988.
- [244] S. A. Brazovskii and N. N. Kirova. Towards the Theory of Metal-Polymer Contact. *Synthetic metals*, 57:4385–4392, 1993.
- [245] E. Ettetdgui, H. Razafitrimo, Y. Gao, and B. R. Hsieh. Band bending modified tunneling at metal/conjugated polymer interfaces. *Applied Physics Letters*, 67(1995):2705, 1995.
- [246] A. A. Griffith. The phenomena of rupture and flow in solids. *Philosophical Transactions of the Royal Society of London. Serie A, Containing Papers of a Mathematical or Physical Character*, (221):163–198, 1921.
- [247] J. Cognard. *Science et Technologie du Collage*. PPUR, 1st editio edition, 2003.
- [248] S. M. Weidner, U. Just, W. Wittke, F. Gruber, and J. F. Friedrich. Analysis of modified polyamide 6.6 using coupled liquid chromatography and MALDI-TOF-mass spectrometry. *International Journal of Mass Spectrometry*, 238(3 SPEC. ISS.):235–244, nov 2004.
- [249] W. M. Haynes, D. R. Lide, and T. J. Bruno. CRC handbook of chemistry and physics: a ready-reference book of chemical and physical data. *Choice Reviews Online*, 47(07):47–3553–47–3553, 2010.
- [250] C. Lamberti, T. Solchenbach, P. Plapper, and W. Possart. Laser assisted joining of hybrid polyamide-aluminum structures. *Physics Procedia*, 56(C):845–853, 2014.
- [251] S. F. Corbin and D. M. Turriff. Thermal Diffusivity by The Laser Flash Technique. In *Characterization of Materials*. 2012.
- [252] J. Hartmann, O. Nilsson, and J. Fricke. Thermal Diffusivity Measurements on Two-Layered and Three-Layered Systems with the Laser-Flash Method. *High Temperatures-High Pressures*, 25(January 1993):403, 1993.
- [253] G. Greczynski and L. Hultman. X-ray photoelectron spectroscopy: Towards reliable binding energy referencing, 2020.

- [254] S. Tanuma, C. J. Powell, and D. R. Penn. Calculations of electron inelastic mean free paths. IX. Data for 41 elemental solids over the 50 eV to 30 keV range. *Surface and Interface Analysis*, 43(3):689–713, 2011.
- [255] B. Vincent Crist. XPS in industry—Problems with binding energies in journals and binding energy databases, 2019.
- [256] R. G. Copperthwaite and J. Lloyd. Photoinduced decomposition of sodium perchlorate and sodium chlorate when studied by X-ray photoelectron spectroscopy. *Journal of the Chemical Society, Dalton Transactions*, (11):1117–1121, 1977.
- [257] J. C. Klein, Chung Ping L., D.M. Hercules, and J. F. Black. Decomposition of Copper Compounds in X-Ray Photoelectron Spectrometers. *Applied Spectroscopy*, 38(5):729–734, sep 1984.
- [258] B R Strohmeier. an Esca Method for Determining the Oxide Thickness on Aluminum-Alloys. *Surface and Interface Analysis*, 15(1):51–56, 1990.
- [259] W. M. Mullins and B. L. Averbach. The electronic structure of anodized and etched aluminum alloy surfaces. *Surface Science*, 206(1-2):52–60, 1988.
- [260] T.A. Carlson. No Title. *Surf. Interface Anal.*, (4):125, 1982.
- [261] B. P. Payne, M. C. Biesinger, and N. S. McIntyre. X-ray photoelectron spectroscopy studies of reactions on chromium metal and chromium oxide surfaces. *Journal of Electron Spectroscopy and Related Phenomena*, 184(1-2):29–37, 2011.
- [262] F. Honda, G.M. Lancaster, Y. Fukuda, and J. W. Rabalais. SIMS study of the mechanism of cluster formation during ion bombardment of alkali halides. *The Journal of Chemical Physics*, 69(11):4931–4937, dec 1978.
- [263] P.T. Murray and J. W. Rabalais. Ejection Dynamics and Electronic Processes Governing Secondary Particle Emission in SIMS. *Journal of the American Chemical Society*, 103(5):1007–1013, 1981.
- [264] S. J. Pachuta and R. G. Cooks. Mechanisms in Molecular SIMS. *Chemical Reviews*, 87(3):647–669, 1987.
- [265] A. Benninghoven. Molecular Secondary Ion Emission. pages 116–121. Springer, Berlin, Heidelberg, 1979.
- [266] R. J. Colton. Molecular Secondary Ion Mass Spectrometry (Sims). *Journal of vacuum science & technology*, 18(3):737–747, 1980.
- [267] P.A. Lyon. Desorption mass spectrometry, 1985.
- [268] JA Van den Berg. Neutral and ion beam SIMS of non-conducting materials. *Vacuum*, 36(11-12):981–989, 1986.
- [269] W. J. Van Ooij and R. H.G. Brinkhuis. Interpretation of the fragmentation patterns in static SIMS analysis of polymers. Part I. Simple aliphatic hydrocarbons. *Surface and Interface Analysis*, 11(8):430–440, 1988.
- [270] R.A. Cocco, C. Papageorgopoulos, and B.J. Tatarchuk. Static SIMS measurements during explosive desorption: desorption-induced recombination and cationization. *Surface Science*, 218:167–177, 1989.

- [271] G. J. Leggett and J. C. Vickerman. The structure of the PET m/z 152 ion and implications for ion formation mechanisms in static SIMS. *Surface and Interface Analysis*, 18(8):637–639, 1992.
- [272] R. D. Harris, M. J. Van Stipdonk, and E. A. Schweikert. Kiloelectron volt cluster impacts: Prospects for cluster-SIMS. *International Journal of Mass Spectrometry and Ion Processes*, 174(1-3):167–177, mar 1998.
- [273] N. Kh. Dzhemilev and A. Wucher. Formation of sputtered clusters: a multistep model. In *Proceedings of the 12th International Conference on Secondary Ion Mass Spectrometry*, pages 157–160, Brussels, 1999.
- [274] K. Pearson. LIII. On lines and planes of closest fit to systems of points in space. *The London, Edinburgh, and Dublin Philosophical Magazine and Journal of Science*, 2(11):559–572, 1901.
- [275] H. Hotelling. Relations between two Sets of Variables. 28(3):321–377, 1936.
- [276] General Introduction to Principal Component Analysis.
- [277] A. Al-Sayyad, J. Bardon, P. Hirchenhahn, R. Vaudémont, L. Houssiau, and P. Plapper. Influence of aluminum laser ablation on interfacial thermal transfer and joint quality of laser welded aluminum-polyamide assemblies. *Coatings*, 9(11), 2019.
- [278] Adham Al-Sayyad, Julien Bardon, Pierre Hirchenhahn, Kevin Santos, Laurent Houssiau, and Peter Plapper. Aluminum pretreatment by a laser ablation process: Influence of processing parameters on the joint strength of laser welded aluminum - Polyamide assemblies. *Procedia CIRP*, 74:495–499, 2018.
- [279] JA King. *Material Handbook for Hybrid Microelectronics*. Artech House, Boston, 1988.
- [280] B.D. Ratner and D. G. Castner. Electron Spectroscopy for Chemical Analysis. In *Surface Analysis– The Principal Techniques*, pages 47–112. John Wiley & Sons, Ltd, Chichester, UK, 2009.
- [281] P. Hirchenhahn, A. Al-Sayyad, J. Bardon, A. Felten, P. Plapper, and L. Houssiau. Highlighting chemical bonding between nylon-6.6 and the native oxide from an aluminum sheet assembled by laser welding. *ACS Applied Polymer Materials*, 2(7):2517–2527, 2020.
- [282] G Beamson and D. Briggs. *High resolution XPS of organic polymers, the scienta ESCA300 database*. John Wiley & Sons, Ltd, oct 1992.
- [283] T. L. Barr and S. Seal. Nature of the use of adventitious carbon as a binding energy standard. *Journal of Vacuum Science & Technology A: Vacuum, Surfaces, and Films*, 13(3):1239–1246, 1995.
- [284] H. Piao and N.S. McIntyre. Adventitious carbon growth on aluminium and gold-aluminium alloy surfaces. *Surface and Interface Analysis*, 33(7):591–594, 2002.
- [285] Francesca Cavezza, Sven Pletincx, Reynier I. Revilla, Jehan Weaytens, Matthieu Boehm, Herman Terryn, and Tom Hauffman. Probing the Metal Oxide/Polymer Molecular Hybrid Interfaces with Nanoscale Resolution Using AFM-IR. *Journal of Physical Chemistry C*, 123(43):26178–26184, oct 2019.

- [286] C. D. Wagner, W. M. Riggs, L. E. Davis, J. F. Moulder, and G. E. Muilenberg. *Handbook of x-ray photoelectron spectroscopy : a reference book of standard spectra for identification and interpretation of XPS data - Catalog - UW-Madison Libraries*. Physical Electronics, 1995.
- [287] A. Al-Sayyad, P. Lama, J. Bardou, P. Hirchenhahn, L. Houssiau, and P. Plapper. Laser joining of titanium alloy to polyamide: influence of process parameters on the joint strength and quality. *The International Journal of Advanced Manufacturing Technology*, 2020.
- [288] M. C. Biesinger, L. W.M. Lau, A. R. Gerson, and R. St C. Smart. Resolving surface chemical states in XPS analysis of first row transition metals, oxides and hydroxides: Sc, Ti, V, Cu and Zn. *Applied Surface Science*, 257(3):887–898, nov 2010.
- [289] M.C. Biesinger, B. P. Payne, A. P. Grosvenor, L.W.M. Lau, A. R. Gerson, and R. St C. Smart. Resolving surface chemical states in XPS analysis of first row transition metals, oxides and hydroxides: Cr, Mn, Fe, Co and Ni. *Applied Surface Science*, 257(7):2717–2730, nov 2011.
- [290] F. Variola, J.H. Yi, L. Richert, J. D. Wuest, F. Rosei, and A. Nanci. Tailoring the surface properties of Ti6Al4V by controlled chemical oxidation. *Biomaterials*, 29(10):1285–1298, 2008.
- [291] J. Vaynberg and L. M. Ng. Surface chemistry of fluoroethanols II. A FTIR study of the reaction of 2,2,2-trifluoroethanol on Al₂O₃ surface. *Surface Science*, 577(2-3):188–199, mar 2005.
- [292] R. H. Friend, R. W. Gymer, A. B. Holmes, J. H. Burroughes, R. N. Marks, C. Taliani, D. D.C. Bradley, D. A. Dos Santos, J. L. Brédas, M. Lögdlund, and W. R. Salaneck. Electroluminescence in conjugated polymers. *Nature*, 397(6715):121–128, 1999.
- [293] S. J. Ding, Q. Q. Zhang, D. W. Zhang, J.T. Wang, Y.D. Zhou, and W.W. Lee. XPS characterization of the interface between low dielectric constant amorphous fluoropolymer film and evaporation-deposited aluminum. *Applied Surface Science*, 178(1-4):140–148, 2001.
- [294] W. X. Gong, J. H. Qu, R. P. Liu, and H. C. Lan. Effect of aluminum fluoride complexation on fluoride removal by coagulation. *Colloids and Surfaces A: Physicochemical and Engineering Aspects*, 395:88–93, feb 2012.
- [295] P. Swift. Adventitious carbon—the panacea for energy referencing? *Surface and Interface Analysis*, 4(2):47–51, 1982.
- [296] D. J. Miller, M. C. Biesinger, and N. S. McIntyre. Interactions of CO₂ and CO at fractional atmosphere pressures with iron and iron oxide surfaces: One possible mechanism for surface contamination? *Surface and Interface Analysis*, 33(4):299–305, 2002.
- [297] M. R. Alexander, G. E. Thompson, and G. Beamson. Characterization of the oxide/hydroxide surface of aluminum using X-ray photoelectron spectroscopy: A procedure for curve fitting the O 1s core level. *Surface and Interface Analysis*, 29(7):468–477, 2000.
- [298] A. Mohtasebi, T. Chowdhury, L. H.H. Hsu, M. C. Biesinger, and P. Kruse. Interfacial Charge Transfer between Phenyl-Capped Aniline Tetramer Films and Iron Oxide Surfaces. *Journal of Physical Chemistry C*, 120(51):29248–29263, dec 2016.

- [299] M. L. Abel, A. Rattana, and J. F. Watts. Interaction of γ -glycidoxypropyltrimethoxysilane with oxidized aluminum substrates: The effect of drying temperature. *Journal of Adhesion*, 73(2-3):313–340, 2000.
- [300] J.F. Watts, A. Rattana, and M. L. Abel. Interfacial chemistry of adhesives on hydrated aluminium and hydrated aluminium treated with an organosilane. *Surface and Interface Analysis*, 36(11):1449–1468, 2004.
- [301] J. Van den Brand, P C Snijders, W G Sloof, H Terryn, and J. H.W. De Wit. Acid-base characterization of aluminum oxide surfaces with XPS. *Journal of Physical Chemistry B*, 108(19):6017–6024, 2004.
- [302] J. Van den Brand, W. G. Sloof, H. Terryn, and J. H.W. De Wit. Correlation between hydroxyl fraction and O/Al atomic ratio as determined from XPS spectra of aluminium oxide layers. *Surface and Interface Analysis*, 36(1):81–88, 2004.
- [303] M. L. Abel, R. Joannic, M. Fayos, E. Lafontaine, S. J. Shaw, and J. F. Watts. Effect of solvent nature on the interaction of γ -glycidoxy propyl trimethoxy silane on oxidised aluminium surface: A study by solution chemistry and surface analysis. *International Journal of Adhesion and Adhesives*, 26(1-2):16–27, feb 2006.
- [304] K. Shimizu, M.L. Abel, and J. F. Watts. Evaluation of the interaction and adsorption of γ -glycidoxy propyl trimethoxy silane with grit-blasted aluminium: A ToF-SIMS and XPS study. *Journal of Adhesion*, 84(8):725–741, sep 2008.
- [305] S. T Abrahamsi, T. Hauffman, J.M.M. De Kok, J. M.C. Mol, and H. Terryn. Effect of Anodic Aluminum Oxide Chemistry on Adhesive Bonding of Epoxy. *Journal of Physical Chemistry C*, 120(35):19670–19677, 2016.
- [306] K. Shimizu, C. Phanopoulos, R. Loenders, M. L. Abel, and J. F. Watts. The characterization of the interfacial interaction between polymeric methylene diphenyl diisocyanate and aluminum: A ToF-SIMS and XPS study. *Surface and Interface Analysis*, 42(8):1432–1444, 2010.
- [307] S. T. Abrahamsi, J. M. M. de Kok, V. C. Gudla, R. Ambat, H. Terryn, and J. M. C. Mol. Interface strength and degradation of adhesively bonded porous aluminum oxides. *npj Materials Degradation*, 1(1):1–8, dec 2017.
- [308] M Bou, J M Martin, Th Le Mogne, and L. Vovelle. Chemistry of the interface between aluminium and polyethyleneterephthalate by XPS. *Applied Surface Science*, 47(2):149–161, 1991.
- [309] F C Liu, P Dong, W Lu, and K Sun. On formation of Al–O–C bonds at aluminum/polyamide joint interface. *Applied Surface Science*, 466(September 2018):202–209, 2019.
- [310] T. P.D. Rajan, R M Pillai, and B C Pai. Reinforcement coatings and interfaces in aluminium metal matrix composites. *Journal of Materials Science*, 33(14):3491–3503, 1998.
- [311] E Pippel, J Woltersdorf, M Doktor, J Blucher, and H P Degischer. Interlayer structure of carbon fibre reinforced aluminum wires. *Journal of Materials Science*, 35(9):2279–2289, 2000.

- [312] J T Blucher, J Dobranszky, and U Narusawa. Aluminium double composite structures reinforced with composite wires. *Materials Science and Engineering A*, 387-389(1-2 SPEC. ISS.):867–872, 2004.
- [313] T Etter, P Schulz, M Weber, J Metz, M Wimmeler, J F Löffler, and P J Uggowitzer. Aluminium carbide formation in interpenetrating graphite/aluminium composites. *Materials Science and Engineering A*, 448(1-2):1–6, 2007.
- [314] M. Yang and V.D. Scott. Carbide formation in a carbon fibre reinforced aluminium composite. *Carbon*, 29(7):877–879, 1991.
- [315] A. M.K. Esawi, K. Morsi, A. Sayed, M. Taher, and S. Lanka. Effect of carbon nanotube (CNT) content on the mechanical properties of CNT-reinforced aluminium composites. *Composites Science and Technology*, 70(16):2237–2241, 2010.
- [316] S. H. Li and C. G. Chao. Effects of carbon fiber/Al interface on mechanical properties of carbon-fiber-reinforced aluminum-matrix composites. *Metallurgical and Materials Transactions A: Physical Metallurgy and Materials Science*, 35 A(7):2153–2160, 2004.
- [317] F. Malengreau, V. Hautier, M. Vermeersch, R. Sporcken, and R. Caudano. Chemical interactions at the interface between aluminium nitride and iron oxide determined by XPS. *Surface Science*, 330(1):75–85, 1995.
- [318] I. Bertóti. Characterization of nitride coatings by XPS. *Surface and Coatings Technology*, 151-152:194–203, 2002.
- [319] L. Rosenberger, R. Baird, E. McCullen, G. Auner, and G. Shreve. XPS analysis of aluminum nitride films deposited by plasma source molecular beam epitaxy. *Surface and Interface Analysis*, 40(9):1254–1261, 2008.
- [320] J. Bauer, L. Biste, and D. Bolze. Optical properties of aluminium nitride prepared by chemical and plasmachemical vapour deposition. *physica status solidi (a)*, 39(1):173–181, jan 1977.
- [321] H. Okano, N. Tanaka, Y. Takahashi, T. Tanaka, K. Shibata, and S. Nakano. Preparation of aluminum nitride thin films by reactive sputtering and their applications to GHz-band surface acoustic wave devices. *Applied Physics Letters*, 64(2):166–168, 1994.
- [322] T. Tsuchida, T. Hasegawa, T. Kitagawa, and M. Inagaki. Aluminium nitride synthesis in air from aluminium and graphite mixtures mechanically activated. *Journal of the European Ceramic Society*, 17(15-16):1793–1795, 1997.
- [323] J. Carlos Rojo, Glen A. Slack, Kenneth Morgan, Balaji Raghothamachar, Michael Dudley, and Leo J. Schowalter. Report on the growth of bulk aluminum nitride and subsequent substrate preparation. *Journal of Crystal Growth*, 231(3):317–321, 2001.
- [324] J. W. Bartha, P. O. Hahn, F. LeGoues, and P. S. Ho. Photoemission spectroscopy study of aluminum–polyimide interface. *Journal of Vacuum Science & Technology A: Vacuum, Surfaces, and Films*, 3(3):1390–1393, 2002.
- [325] C.H. Yu, C. H. Huang, and C.S. Tan. A review of CO₂ capture by absorption and adsorption. *Aerosol and Air Quality Research*, 12(5):745–769, 2012.

- [326] G. Borcia, C. A. Anderson, and N. M.D. Brown. The surface oxidation of selected polymers using an atmospheric pressure air dielectric barrier discharge. Part II. *Applied Surface Science*, 225(1-4):186–197, 2004.
- [327] Anna Kuzminova, Artem Shelemin, Ondřej Kylián, Andrei Choukourov, Helena Valentová, Ivan Krakovský, Jan Nedbal, Danka Slavínská, and Hynek Biederman. Study of the effect of atmospheric pressure air dielectric barrier discharge on nylon 6,6 foils. *Polymer Degradation and Stability*, 110:378–388, 2014.
- [328] Z. Lin, H. M. Meyer, J. H. Weaver, S.G. Anderson, and Lj. Atanasoska. Aluminum/polyimide interface formation: An x-ray photoelectron spectroscopy study of selective chemical bonding. *Journal of Vacuum Science & Technology A: Vacuum, Surfaces, and Films*, 5(6):3325–3333, 2002.
- [329] H. Zhu, Z. Chen, Y. Sheng, and T. T. Luong Thi. Flaky polyacrylic acid/aluminium composite particles prepared using in-situ polymerization. *Dyes and Pigments*, 86(2):155–160, jul 2010.
- [330] K Vermöhlen, H Lewandowski, H. D. Narres, and E Koglin. Adsorption of polyacrylic acid on aluminium oxide: DRIFT spectroscopy and ab initio calculations. *Colloids and Surfaces A: Physicochemical and Engineering Aspects*, 170(2-3):181–189, sep 2000.
- [331] J. E. Krzanowski and R. E. Leuchtner. Chemical, mechanical, and tribological properties of pulsed-laser-deposited titanium carbide and vanadium carbide. *Journal of the American Ceramic Society*, 80(5):1277–1280, 1997.
- [332] J. Luthin and Ch Linsmeier. Characterization of electron beam evaporated carbon films and compound formation on titanium and silicon. In *Physica Scripta T*, volume 91, pages 134–137. IOP Publishing, 2001.
- [333] P. S. Bagus, C.J. Nelin, C. R. Brundle, and S.A. Chambers. A New Mechanism for XPS Line Broadening: The 2p-XPS of Ti(IV). *Journal of Physical Chemistry C*, (Iv), 2018.
- [334] A. Goodwin and B. M Novak. Synthesis of New Rigid Rod Helical Polymers through the Living Polymerization of Carbodiimides Using Titanium(IV) Complexes. *Macromolecules*, 27(19):5520–5522, 1994.
- [335] S. Pritchett, P. Gantzel, and P. J. Walsh. Synthesis and crystal structures of chiral titanium bis(sulfonamido) bis(amide) complexes: Differences in ligand hapticity caused by crystal packing forces. *Organometallics*, 16(24):5130–5132, nov 1997.
- [336] P.J. Stewart, A. J. Blake, and P. Mountford. New titanium complexes containing an amidinate-imide supporting ligand set: Cyclopentadienyl, alkyl, borohydride, aryloxide, and amide derivatives. *Organometallics*, 17(15):3271–3281, jul 1998.
- [337] S. Pritchett, P. Gantzel, and P. J. Walsh. Synthesis and Structural Study of Titanium Bis(sulfonamido) Bis(amide) Complexes. *Organometallics*, 18(5):823–831, 1999.
- [338] A. Michiardi, G. Hélarý, P. C.T. Nguyen, L. J. Gamble, F. Anagnostou, D. G. Castner, and V. Migonney. Bioactive polymer grafting onto titanium alloy surfaces. *Acta Biomaterialia*, 6(2):667–675, feb 2010.

- [339] M. Reggente, P. Masson, C. Dollinger, H. Palkowski, S. Zafeiratos, L. Jacomine, D. Passeri, M. Rossi, N. E. Vrana, G. Pourroy, and A. Carradò. Novel Alkali Activation of Titanium Substrates to Grow Thick and Covalently Bound PMMA Layers. *ACS Applied Materials and Interfaces*, 10(6):5967–5977, 2018.
- [340] K. Kondoh and J. Umeda. C–O bond enhancing direct bonding strength between plastic and pure titanium. *Materials Letters*, 211:331–334, jan 2018.
- [341] M. J Mckay and H. M Nguyen. Recent Advances in Transition Metal-Catalyzed Glycosylation. *ACS Catalysis*, (2):1563–1595, 2012.
- [342] Z. Zhang, Z. Wang, R. Zhang, and K. Ding. An Efficient Titanium Catalyst for Enantioselective Cyanation of Aldehydes: Cooperative Catalysis. *Angewandte Chemie*, 122(38):6898–6902, 2010.
- [343] N. Matsunami, Y. Yamamura, Y. Itikawa, N. Itoh, Y. Kazumata, S. Miyagawa, K. Morita, R. Shimizu, and H. Tawara. Energy dependence of the ion-induced sputtering yields of monatomic solids, 1983.

(french version) L'industrie des transports a besoin de structures de plus en plus légères pour permettre de diminuer les émissions de gaz polluants, et donc leur impact environnemental. Par ailleurs, l'industrie biomédicale cherche à développer des implants de plus en plus fonctionnalisés mais qui soient biocompatibles. Ces deux problèmes, en apparence très éloignés, mènent en réalité à la même solution : des assemblages hybrides polymères-métaux. Une des difficultés est d'assembler ces matériaux qui sont très différents par nature. Parmi toutes les techniques qui existent -la fixation mécanique, le collage, et la soudure- une technique attire de plus en plus l'attention : la soudure laser. Cette technique est prometteuse car elle est rapide, permet une grande liberté de conception et ne nécessite pas de matériaux intermédiaires. Néanmoins, les causes du phénomène d'adhésion ne sont pas encore bien comprises. La théorie de l'adhésion prévoit quatre phénomènes pour l'expliquer : l'ancrage mécanique, des liaisons chimiques, la diffusion et des interactions électrostatiques. Ce travail de thèse s'est penché sur deux combinaisons de matériaux présentant un fort intérêt industriel pour étudier les liaisons chimiques à l'interface : la combinaison aluminium/polyamide-6.6 et la combinaison titane/polyamide-6.6. Pour les deux combinaisons, trois types d'échantillons différents ont été préparés : des échantillons soudés, des échantillons spin-coatés et des échantillons modèles. Les échantillons soudés ont été préparés en soudant une plaque de métal au polymère. Pour analyser leurs interfaces, une nouvelle méthodologie a été élaborée en combinant fracture des échantillons et dissolution du résidu de polymère restant. Les échantillons spin-coatés ont été réalisés en déposant une fine couche de polymère sur du métal poli miroir. Les échantillons modèles ont été obtenus en déposant une molécule composée uniquement de la partie réactive du polymamide-6.6, le N-méthylformamide. Les résultats XPS et ToF-SIMS de ces trois types d'échantillons ont permis de montrer l'existence, la nature et le mécanisme de formation de la liaison chimique entre les deux matériaux : une liaison C-O-M (M= Al ou Ti). Enfin l'existence d'un phénomène de diffusion est aussi mis en évidence dans la combinaison aluminium/polyamide-6.6.

(english version) On one hand, to lower the impact of the transport industry on the greenhouse gas emissions, hence their environmental impact, it is urgent to create lightweight structures. On the other hand, the biomedical industry is striving for more biocompatible and more functionalized implants. The two problems lead to the same solution: hybrid polymer-metal assemblies. The question now is to assemble such extremely different materials. Amongst all the technique available -mechanical fastening, adhesive bonding, and welding- one technique is catching more and more attention: laser welding. This technology presents many advantages, such as fast processing, easy automation, high design freedom and no need for intermediate materials. Nonetheless, the root causes of adhesion are still not well understood. The adhesion theory proposes four phenomena to explain it: mechanical interlocking, chemical bonding, diffusion and electrostatic interaction. In this thesis the chemical bonding at the interface was thoroughly investigated for two materials combinations of interest for the industry: aluminum/polyamide-6.6 and titanium/polyamide-6.6. For the two combinations three types of samples were prepared: welded samples, spin-coated samples and model samples. The welded samples consist in near industrial samples with thick metal and polymer sheets welded together. To analyze those samples, a new methodology was developed combining breaking the samples and dissolving the polymer residue to access the interface for XPS and ToF-SIMS analysis. The spin-coated samples consist simply in a spin-coated layer of polymer on mirror polished metal. The model samples consist in the deposition of a molecule presenting only the reactive part of the polymer structure, N-methylformamide. The combination of the XPS and ToF-SIMS results of the three samples allowed to determine the existence, the nature of the bond, a C-O-M bond (M=Al or Ti), and the reaction mechanism. The proof of concept of diffusion in the case of laser welding on the combination aluminum/polyamide-6.6 is also done at the end.